

# The University of Sheffield



## Investigation of Flux Reversal Permanent Magnet Machines

**Huayang Li**

**A thesis submitted for the degree of Doctor of Philosophy**

Department of Electronic and Electrical Engineering

The University of Sheffield

Sheffield, UK

**June 2019**

## ABSTRACT

Flux reversal permanent magnet (FRPM) machines, as one kind of stator-PM machines, are ideally suited to low-speed and high-torque applications due to their robust rotor structure, simple stator structure, and easy heat management. This thesis presents a thorough investigation into the FRPM machines, with particular reference to the working principle and performance improvement.

Based on the air-gap field modulation theory, the PM magnetomotive force (MMF)-permeance model is adopted to analyse the working principle of the FRPM machines. The feature of multi-working harmonics in FRPM machines is revealed, i.e. all PM MMF harmonics together with the fundamental permeance contribute to the torque production. Based on the analytical model, the critical design parameters are parametrically investigated. It shows that the machine performance is sensitive to the PM thickness, since the PMs increase the equivalent air-gap length, thus restricting the field modulation effect and associated torque performance.

Various aspects of improving the torque density of FRPM machines are then investigated in detail, including the PM polarities of adjacent teeth, the number of PMs on each stator tooth, alternate consequent-pole PM (CPM) topology, and toroidal-windings (TWs). It shows that opposite PM polarities of adjacent teeth are preferred compared to identical PM polarities, due to the more effective interactions between the PM and armature fields. Thanks to the additional back-EMF produced by the auxiliary PM MMF harmonic, a 76% higher torque density can be achieved in a prototype FRPM machine by properly increasing the number of PM pairs on each stator tooth. The FRPM machines with various CPM topologies are analysed and compared, from which the topology with the highest torque density is identified. Because of the improved armature field, the CPM-FRPM machine can exhibit more than 15% higher torque density than the conventional FRPM machine, even with halved PM volume. The FRPM machines with TWs are also proposed and compared with the machines using conventional concentrated-windings. For specific stator slot/rotor pole combinations, the torque density of the proposed machines with TWs can be improved by 80%, which resulted from the improved pitch factor.

Finally, the performance of various FRPM machines are summarised and compared with the popular Vernier machine, which works based on the air-gap field modulation as well. Results show that although a large DC permeance component is utilised to produce torque in the Vernier machine, the FRPM machines can have competitive or even higher torque density, while their PM volumes are significantly reduced.

All theoretical analyses are validated experimentally on various prototypes.

## **ACKNOWLEDGEMENTS**

I would like to extend my sincere gratitude to my supervisor, Professor Zi-Qiang Zhu, without whom there would be no completion of this thesis. Throughout this research work, his invaluable guidance and constructive comments have helped me to cultivate good research habits which benefit me a lot. His continuous support and trust also encourage me to pursue higher achievement in my career.

Great thanks also go to the members of the Electrical Machines and Drives Group at the University of Sheffield, for their help and useful discussions. In particular, Mr. Karl Rotchell and Mr. Lawrence Obodo for their assistance in prototyping.

Thank the Rolls-Royce plc for their financial support.

Finally, I would like to thank all my friends and family members for their endless love and support.

# CONTENTS

<b>Abstract.....</b>	<b>2</b>
<b>Acknowledgements .....</b>	<b>3</b>
<b>Nomenclatures.....</b>	<b>8</b>
<b>CHAPTER 1 General Introduction .....</b>	<b>13</b>
1.1 Various Permanent Magnet Machine Topologies for Low-Speed and High-Torque Applications .....	13
1.1.1 Rotor Permanent Magnet Machines.....	14
1.1.2 Stator Permanent Magnet Machines .....	17
1.1.3 Other Permanent Magnet Machine Topologies .....	23
1.2 Development of Flux Reversal Permanent Magnet Machines.....	24
1.2.1 Torque Improvement and Topology Evolution.....	27
1.2.2 Torque Ripple Mitigation.....	32
1.2.3 Analysis Methodology .....	34
1.2.4 Other Related Issues.....	35
1.3 Magnetic Gearing Effect/Air-Gap Field Modulation and Magnetically Geared Machines ..	35
1.3.1 Magnetic Gears .....	36
1.3.2 Various Magnetically Geared Machines Working Based on Magnetic Gearing Effect ...	37
1.3.3 Analysis of Magnetic Gearing Effect/Air-Gap Field Modulation in Flux Reversal Permanent Magnet Machines.....	43
1.4 Scope of Research and Contributions of Thesis .....	46
1.4.1 Scope of Research.....	46
1.4.2 Main Contributions of Thesis .....	52
<b>CHAPTER 2 Influence of PM Polarities of Adjacent Teeth on Electromagnetic Performance of Flux Reversal Permanent Magnet Machine .....</b>	<b>53</b>
2.1 Introduction.....	53
2.2 Working Principle of FRPM Machines with Different PM Arrangements Considering PM Polarities of Adjacent Teeth.....	55
2.2.1 Flux Linkage Variation .....	56
2.2.2 Air-gap Field Produced by PM MMF.....	59
2.2.3 Equivalent Pole-Pair Number and Armature Field .....	70
2.2.4 Torque Contribution of Working Field Harmonics .....	72
2.3 Influence of Rotor Pole Number .....	76
2.3.1 Two Magnet Pieces on Each Stator Tooth.....	76
2.3.2 Four Magnet Pieces on Each Stator Tooth.....	79

2.4	Performance Comparison of Four 14-Rotor-Pole FRPM Machines with Different PM Arrangements .....	81
2.4.1	No-Load Performance .....	83
2.4.2	On-Load Torque Performance .....	86
2.4.3	Losses and Efficiency .....	90
2.4.4	Power Factor .....	93
2.4.5	Demagnetisation Withstand Capability.....	95
2.5	Experimental Validation .....	97
2.6	Conclusion .....	102
<b>CHAPTER 3 Optimal Number of PM Pieces on Single Stator Tooth of Flux Reversal Permanent Magnet Machine.....</b>		<b>104</b>
3.1	Introduction.....	104
3.2	Working Principle of FRPM Machines with Different Number of PM Pieces on Single Stator Tooth .....	105
3.2.1	Machine Configuration .....	105
3.2.2	Analytical Derivation of Machine Performance with Opposite PM Polarities of Adjacent Teeth	107
3.3	Analysis of FRPM Machines with Different Numbers of PM Pieces.....	112
3.3.1	Optimal Rotor Pole Number .....	112
3.3.2	Identification of Working Harmonics of PM MMF.....	114
3.3.3	Influence of Number of PM Pieces on Cogging Torque.....	117
3.4	Influence of Design Parameters .....	118
3.4.1	Stator Slot Opening Ratio .....	118
3.4.2	Split Ratio .....	120
3.4.3	PM Thickness.....	121
3.4.4	Rotor Slot Ratio .....	123
3.4.5	Stator Slot Number.....	124
3.5	Performance Validation by Finite Element Analysis.....	126
3.5.1	Optimal Number of PM Pieces .....	126
3.5.2	No-Load Performance.....	128
3.5.3	On-Load Performance.....	134
3.6	Experimental Validation .....	137
3.7	Conclusion .....	141
<b>CHAPTER 4 Analysis of Flux Reversal Permanent Magnet Machines with Consequent-Pole PM Topologies.....</b>		<b>142</b>
4.1	Introduction.....	142
4.2	Torque Improvement Mechanism of CPM-FRPM Machines.....	144
4.3	Average Torque Comparison of SPM- and CPM-FRPM Machines Having Different Stator Slot/Rotor Pole Combinations .....	148

4.3.1	Influence of Rotor Pole Number .....	148
4.3.2	Comparison of 12/14 and 12/16 FRPM Machines.....	149
4.3.3	Influence of Stator Slot Number .....	152
4.4	Analysis of FRPM Machines with Different CPM Topologies .....	154
4.4.1	Air-Gap Flux Density.....	156
4.4.2	Torque Contribution of Working Harmonics.....	162
4.4.3	Influence of PM Dimensions .....	164
4.4.4	Torque Improvement over SPM Topologies.....	168
4.5	Performance Comparison of 14-Rotor-Pole SPM and CPM-FRPM Machines.....	171
4.5.1	On-Load Torque and Flux Density Distribution.....	171
4.5.2	No-Load Performance.....	174
4.5.3	Over-Load Torque Capability and Inductance.....	177
4.5.4	Losses and Efficiency .....	179
4.5.5	Power Factor .....	181
4.5.6	Demagnetisation Withstand Capability.....	182
4.5.7	3-D End-Effect Analysis.....	182
4.6	Experimental Validation .....	186
4.7	Conclusion .....	192
<b>CHAPTER 5 Comparative Analysis of Flux Reversal Permanent Magnet Machines with Toroidal and Concentrated Windings .....</b>		<b>194</b>
5.1	Introduction.....	194
5.2	Working Principle and Pitch Factor Improvement of FRPM Machine .....	198
5.2.1	Working Principle and Influence of Rotor Pole Number of CW-FRPM Machine .....	198
5.2.2	Pitch Factor Improvement by Using Toroidal Winding .....	201
5.3	Optimisation and Critical Design Parameters .....	202
5.3.1	Optimisation of FRPM Machines .....	202
5.3.2	Influence of Critical Design Parameters .....	206
5.4	Performance Comparison of FRPM Machines .....	207
5.4.1	Air-Gap Field and Winding Pole-Pair Number .....	208
5.4.2	No-Load Performance.....	211
5.4.3	On-Load Torque Performance .....	212
5.4.4	Inductance.....	214
5.4.5	Losses and Efficiency .....	215
5.4.6	Torque-Current Characteristic .....	217
5.4.7	Power Factor .....	218
5.5	Preferred Slot/Pole combinations for TW-FRPM Machine.....	219
5.6	Experimental Validation .....	220

5.7	Conclusion .....	225
<b>CHAPTER 6 Comparative Study of Air-gap Field Modulation in Flux Reversal and Vernier Permanent Magnet Machines.....226</b>		
6.1	Introduction.....	226
6.2	Machine Configuration and Working Principle .....	228
6.2.1	FRPM Machine .....	229
6.2.2	Vernier Machine .....	230
6.2.3	Different Working Harmonics of Two Kinds of Machines .....	231
6.3	Influence of Critical Design Parameters .....	235
6.3.1	PM Thickness.....	235
6.3.2	Slot Width Ratio .....	237
6.4	Finite Element and Experimental Validation.....	238
6.4.1	Finite Element Validation .....	238
6.4.2	Experimental Validation .....	247
6.5	Performance Summary of Various FRPM Machines and Vernier Machine.....	251
6.6	Conclusion .....	256
<b>CHAPTER 7 General Conclusions and Future Work .....258</b>		
7.1	General Conclusions .....	258
7.1.1	Working Mechanism and analysis methods of FRPM machines.....	258
7.1.2	Developed FRPM Machine Topologies.....	260
7.1.3	Performance Improvement and Comparison .....	261
7.2	Future Works .....	263
<b>References.....264</b>		
<b>Appendix A CAD Drawings of Prototypes .....276</b>		
<b>Appendix B Cogging Torque and Static Torque Measuring Method.....286</b>		
<b>Appendix C Analytical Performance Derivation of Flux Reversal Permanent Magnet Machines with Identical PM Polarities of Adjacent Teeth .....288</b>		
<b>Appendix D Publications.....295</b>		

# NOMENCLATURES

## Variables

$B$	Air-gap flux density (T)
$B_r$	Remanence of PMs (T)
$B_{rn}, B_{tm}$	Radial and tangential components of the $n$ th air-gap flux density (T)
$D$	Stator outer diameter (mm)
$E$	Back-EMF (V)
$f$	Electric frequency (Hz)
$F_i$	PM MMF (A/m)
$f_s$	Slot filling factor
$g$	Air-gap length (mm)
$G_r$	Gear ratio
$h_m$	PM thickness (mm)
$h_{st}$	Height of stator tooth (mm)
$I$	Armature current (A)
$I_a, I_b, I_c,$	Currents of phases a, b, c (A)
$I_d, I_q$	$D$ - and $q$ -axis currents (A)
$I_{rated}$	Rated current (A)
$k_d$	Distribution factor
$k_p$	Pitch factor
$k_{sr}$	Split ratio
$l$	Axial length (mm)
$L_d, L_q$	$D$ - and $q$ -axis inductances
$l_{end}$	End-winding length (mm)



$m$	Phase number
$n$	Rotor speed (rpm)
$n_c$	Number of turns per coil
$N_m$	Number of iron pieces of modulation ring
$N_{ph}$	Number of series turns per phase
$n_{pp}$	Number of PM pairs on each stator tooth
$N_r$	Number of rotor poles
$N_s$	Number of stator slots
$p_a$	Pole-pair number of armature MMF
$p_{cu}$	Copper loss (W)
$p_{cu\_total}$	Total copper loss (W)
$p_{em}$	Electromagnetic power (W)
$p_{eq}$	Equivalent pole pair number
$p_f$	Power factor
$p_h$	Pole-pair number of high-speed element
$p_l$	Pole-pair number of low-speed element
$p_m$	Pole-pair number of PM MMF
$q$	Number of slots per pole per phase
$Q$	Number of coil-EMF phasors per phase
$R$	Air-gap radius (mm)
$R_{ro}$	Outer radius of rotor (mm)
$R_{si}$	Inner radius of stator (mm)
$S$	Slot area (mm <sup>2</sup> )
$T_{avg}$	Average torque (Nm)
$T_c$	Cogging torque (Nm)
$T_n$	Instantaneous torque (Nm)

$t_{sy}$	Thickness of stator yoke (mm)
$U_d, U_q$	$D$ - and $q$ -axis voltages (V)
$V_{ac}$	Active machine volume (mm <sup>3</sup> )
$V_{PM}$	PM volume (mm <sup>3</sup> )
$W_c$	Magnetic field energy (W)
$w_i^f$	Weight factor of the $i$ th PM MMF harmonic in FRPM machine
$w_q^v$	Weight factor of the $q$ th permeance harmonic in Vernier machine
$w_{ro}$	Width of rotor slot opening (mm)
$w_{rt}$	Width of rotor tooth (mm)
$w_{so}$	Width of stator slot opening (mm)
$w_{st}$	Width of stator tooth (mm)
$\alpha$	Electric angle between two adjacent coil-EMF phasors (elec. deg.)
$\alpha_m$	Pole pitch of PMs (rad)
$\theta_{rn}$	Phase of radial component of the $n$ th air-gap field (rad)
$\theta_{tn}$	Phase of tangential component of the $n$ th air-gap field (rad)
$\lambda$	Flux linkage (Wb)
$\Lambda_q$	The $q$ th air-gap permeance harmonic (H <sup>-1</sup> )
$\mu_0$	Vacuum permeability (H/m)
$\mu_r$	Relative permeability of PMs
$\tau_r$	Rotor pole pitch (rad)
$\tau_s$	Stator slot pitch (rad)
$\psi_m$	Flux linkage per pole (Wb)
$\omega$	Electrical angular frequency (rad/s)
$\Omega_h$	Mechanical angular speed of high-speed element (rad/s)
$\Omega_l$	Mechanical angular speed of low-speed element (rad/s)
$\Omega_m$	Mechanical angular speed of modulation ring (rad/s)

$\Omega_r$  Mechanical angular speed of rotor (rad/s)

### **Abbreviations**

2D	Two-dimensional
3D	Three-dimensional
Back-EMF	Back electromotive force
BLAC	Brushless alternating current
BLDC	Brushless direct current
CAD	Computer aided design
CPM	Consequent-pole permanent magnet
CPM-FRPM	FRPM machine with CPM
CVT	Continuously variable transmission
CW	Concentrated-winding
CW-FRPM	FRPM machine with CW
DC	Direct current
DSPM	Doubly salient permanent magnet
DW	Distributed-winding
DW-FRPM	FRPM machine with DW
EV	Electric vehicle
FE	Finite element
FEA	Finite element analysis
FMP	Flux modulation pole
FRPM	Flux reversal permanent magnet
GCD	Greatest common divisor
HEV	Hybrid electric vehicle
IPM	Interior-permanent magnet
LCM	Lowest common multiple

MG	Magnetic gear
MGd	Magnetically geared
MMF	Magnetomotive force
PM	Permanent magnet
PMSM	Permanent magnet synchronous machine
PS	Partitioned-stator
PS-FRPM	Partitioned-stator flux reversal permanent magnet
PWM	Pulse width modulation
SFPM	Switched flux permanent magnet
SPM	Surface-mounted permanent magnet
SPM-FRPM	FRPM machine with SPM
SR	Switched reluctance
THD	Total harmonic distortion
TW	Toroidal winding
TW-FRPM	FRPM machine with TW

# CHAPTER 1

## GENERAL INTRODUCTION

With the increasing exploitation of non-renewable energy and the continuous deterioration of the environment, it is of great significance and urgency to develop and apply novel technologies relevant to energy saving and pollution mitigation in various aspects of human society. In the field of electrical machines, both academia and industry have made great efforts to achieve this goal, mainly from the following two aspects. Firstly, the applications of electrical machines have been greatly broadened. For example, the electric drives have now been successfully commercialised to replace the conventional gasoline/diesel engines in many vehicles, which are beneficial to reducing the pollution and the dependence on non-renewable energy [ZHU07]. Secondly, the performance of electrical machine systems has been continuously improved, which enables high energy utilisation, thus reducing the energy consumption.

It would be expected that the ever-higher requirements placed on system performance will continuously motivate the innovations of electrical machines, from design and analysis methodology to topology evolution. A promising machine topology, i.e. the flux reversal permanent magnet (FRPM) machine, will be comprehensively investigated in this thesis, which should be an effective supplement to the knowledge of high-performance electrical machines. In this chapter, the relevant backgrounds and developments of FRPM machines will be introduced and reviewed. The research scope and contributions of this thesis will also be presented.

Some sections of this chapter are published as “Recent developments and comparative study of magnetically geared machines,” *CES Trans. Elect. Mach. Syst.*, vol. 2, no.1, pp. 13-22, Mar. 2018, doi: 10.23919/TEMS.2018.8326448.

### **1.1 Various Permanent Magnet Machine Topologies for Low-Speed and High-Torque Applications**

Along with the emergence and development of high-energy-product permanent magnet (PM) materials in last decades, PM machines have now been widely used for various applications at different power and speed levels, thanks to the superior torque density, efficiency, and topology

diversity [REF10] [LEV08] [ZHU12].

For those applications with low-speed and high-torque requirements, e.g. electric/hybrid electric vehicles (EV/HEVs) [CHA07a] [CHA07b], wind power generation [POL06], ship propulsion [REF13], rail traction [HEL09] etc., the mainstream system solutions consist of conventional medium/high-speed electrical machines and mechanical gearboxes [ATA01]. However, the systems are inevitably accompanied with drawbacks brought by the mechanical gearboxes, such as strict lubrication and maintenance demand, high vibration and noise, short lifecycle and so on. Therefore, research on electric drive systems with simplified or even eliminated gearboxes has aroused great attention from both academia and industry. The systems without any gearboxes are so-called direct-drive systems.

Up to now, many PM machine topologies have been extensively investigated for direct-drive systems. According to different PM locations, there are mainly two PM machine categories, which are rotor permanent magnet machines (designated as rotor-PM machines) and stator permanent magnet machines (designated as stator-PM machines), respectively. The basic concepts and topologies of these two kinds of machines will be given in the following.

### 1.1.1 Rotor Permanent Magnet Machines

Rotor-PM machines, commonly referred to as permanent magnet synchronous machines (PMSMs), are the most conventional and widely-commercialised PM machine topologies. The working principle of rotor-PM machines is quite explicit and has been thoroughly analysed [HAN03] [GRE10] [HEN10]. For a rotor-PM machine, by properly arranging and energising the armature windings in the stator, a certain rotating armature field is produced in the air-gap with its fundamental pole pair-number being  $p_a$  and excitation frequency being  $f$ . If the PMs arrayed on the rotor are with the same pole-pair number (i.e.  $p_m=p_a$ ) and the rotor rotational speed  $n$  equals  $60f/p_m$ , a synchronous rotating PM field can be produced in the air-gap and a steady electromagnetic torque/power transmission between the stator and the rotor can thus be achieved.

As distinguished by the number of slots per pole per phase ( $q=N_s/2mp_m$ , where  $N_s$  is the number of stator slots and  $m$  is the phase number), there are mainly two categories of PMSMs, i.e. integer-slot and fractional-slot machines. For integer-slot PMSMs,  $q$  is an integer and the overlapping windings are always used to achieve a high winding factor. For example, a 24-stator-slot/4-rotor-pole (abbreviated as 24/4) three-phase PMSM with integer-slot distributed-

windings (i.e.  $q=2$ ) is shown in Fig. 1.1 (a) and a 12/4 PMSM with integer-slot concentrated-windings (i.e.  $q=1$ ) is shown in Fig. 1.1 (b). The main advantages of an integer-slot machine include the high utilisation of reluctance torque and the sinusoidal armature field distribution in the air-gap, which are desirable for high torque density and high efficiency. Such features have prompted integer-slot machines to be used in many applications, such as wind power generation [CHE00a] [POL06]. As for fractional-slot PMSMs,  $q$  is a fraction and the non-overlapping concentrated-windings can be accommodated to achieve short end-windings and high winding factor simultaneously [BIA06]. Either all teeth wound windings or alternate teeth wound windings (sometimes also designated as double layer or single layer windings) can be used, as shown in Fig. 1.2. Clearly, the short end-windings and resulted low copper loss make the fractional-slot machines promising candidates for applications where the axial-length is limited. Moreover, the fractional-slot machines always feature with high packing factor, low cogging torque and high fault-tolerance capability, although the field harmonics are more abundant [ISH06] [REF10]. Thanks to these merits mentioned above, the fractional-slot PMSMs have been a hot research topic over the past few decades and attempted for many applications, such as in-wheel driven EV [WAN08] [IFE12].

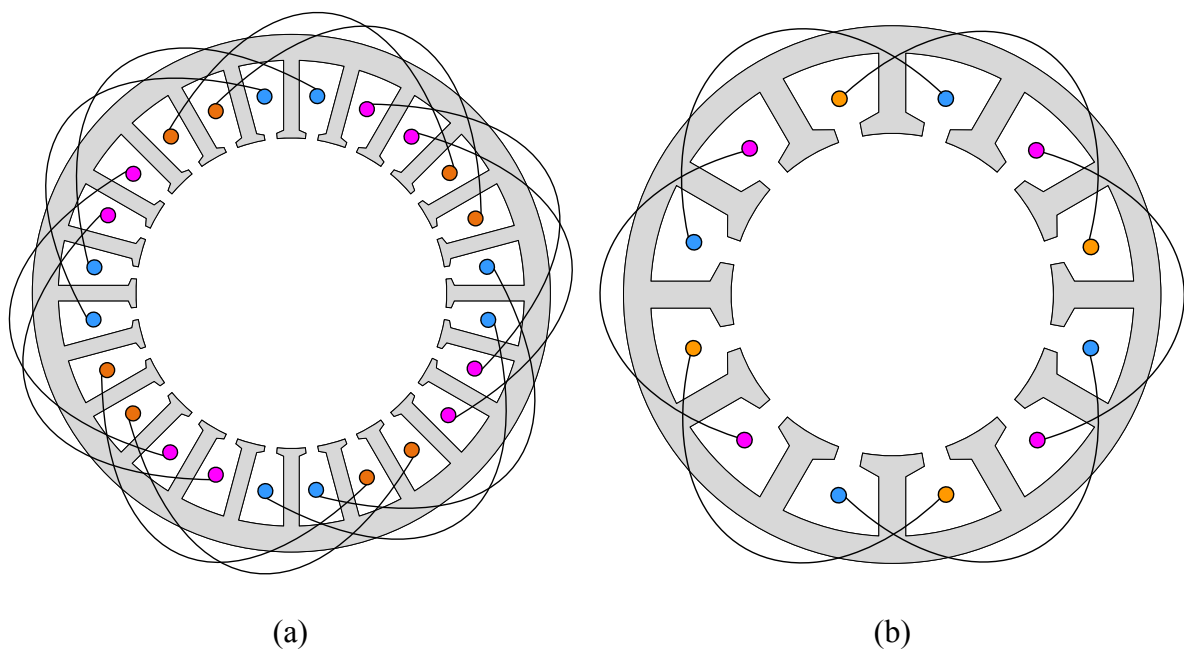


Fig. 1.1 Integer-slot PMSMs with overlapping windings. (a) 24/4 PMSM with distributed windings ( $q=2$ ). (b) 12/4 PMSM with concentrated windings ( $q=1$ ).

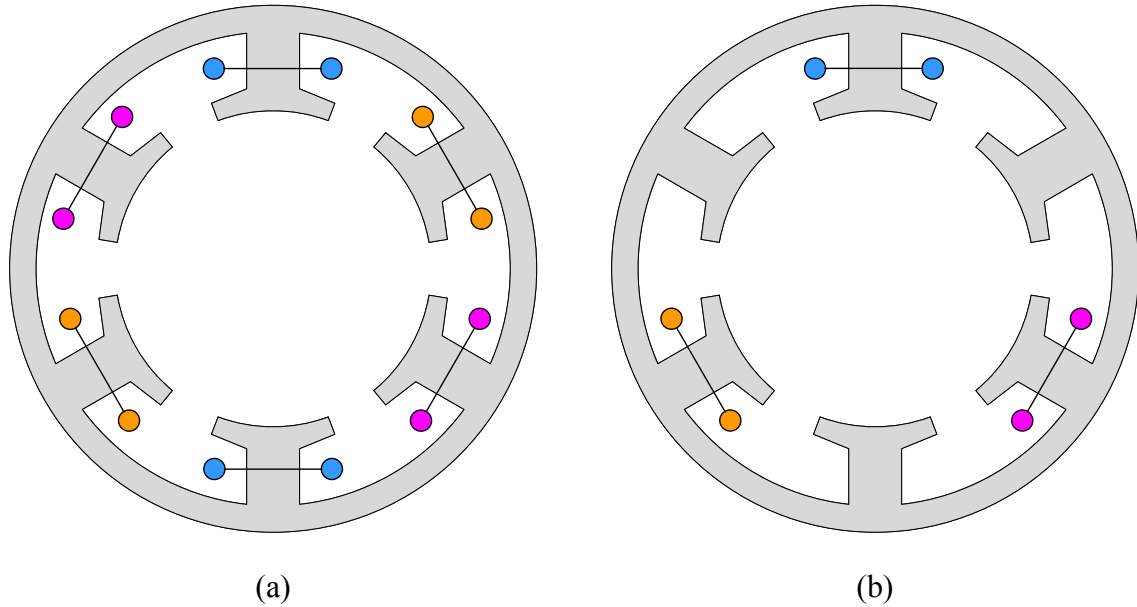


Fig. 1.2 Fractional-slot PMSMs with non-overlapping windings. (a) 6/4 PMSM with all teeth wound windings ( $q=0.5$ ). (b) 6/4 PMSM with alternate teeth wound windings ( $q=0.5$ ).

For either integer-slot or fractional-slot rotor-PM machines, there exist various PM rotor topologies, which can be roughly classified into four types [ZHU07], as shown in Fig. 1.3. Among these rotor topologies, the surface-mounted-PM (SPM) rotor, Fig. 1.3 (a), is the most widely used topology due to its simplicity. However, there is no reluctance torque for a SPM machine and the PMs may suffer local demagnetisation since they directly face the armature field in the air-gap. To utilise the reluctance torque, the inset-PM rotor topology has been proposed and is shown in Fig. 1.3 (b). The iron between the PM pieces would facilitate the positioning of the PMs and produce additional reluctance torque since the  $q$ -axis inductance is larger than the  $d$ -axis inductance. To further boost the reluctance torque, other PM configurations with PMs accommodated within the rotor core have gained a lot of interests [ZHU07]. An example of the interior-PM (IPM) rotor topology is shown in Fig. 1.3 (c). Such a topology may offer high reluctance torque due to the big difference between  $d$ - and  $q$ -axis inductances, and the risk of local demagnetisation of PMs is effectively mitigated since the PMs are kept away from the air-gap and shielded by the irons. It should be noted that the number of PM layers and the shape of PM arrays can be adjusted to maximise the reluctance torque or utilise the flux-focusing effect [ZHU16]. A special case to utilise the flux-focusing effect is depicted in Fig. 1.3 (d), i.e. spoke-PM topology. As can be seen, the PMs are circumferentially magnetised, and the utilised PM volume can be increased to intensify the PM field. It should be noted that there is always a trade-off between the mechanical strength and the electromagnetic performance of an IPM machine, which is reflected in the design of the



thin iron bridges between the PM pieces and the rotor surfaces. Thin iron bridges are desirable to reduce the flux leakage and improve the output torque; however, the rotor deformation and manufacturability turn to be a challenging issue.

In general, each of these PM rotor topologies has unique advantages and disadvantages, and the determination of the PM rotor topology for a specific application should be well considered according to the specific requirements of electromagnetic performance, mechanical performance, thermal performance and manufacturability etc.

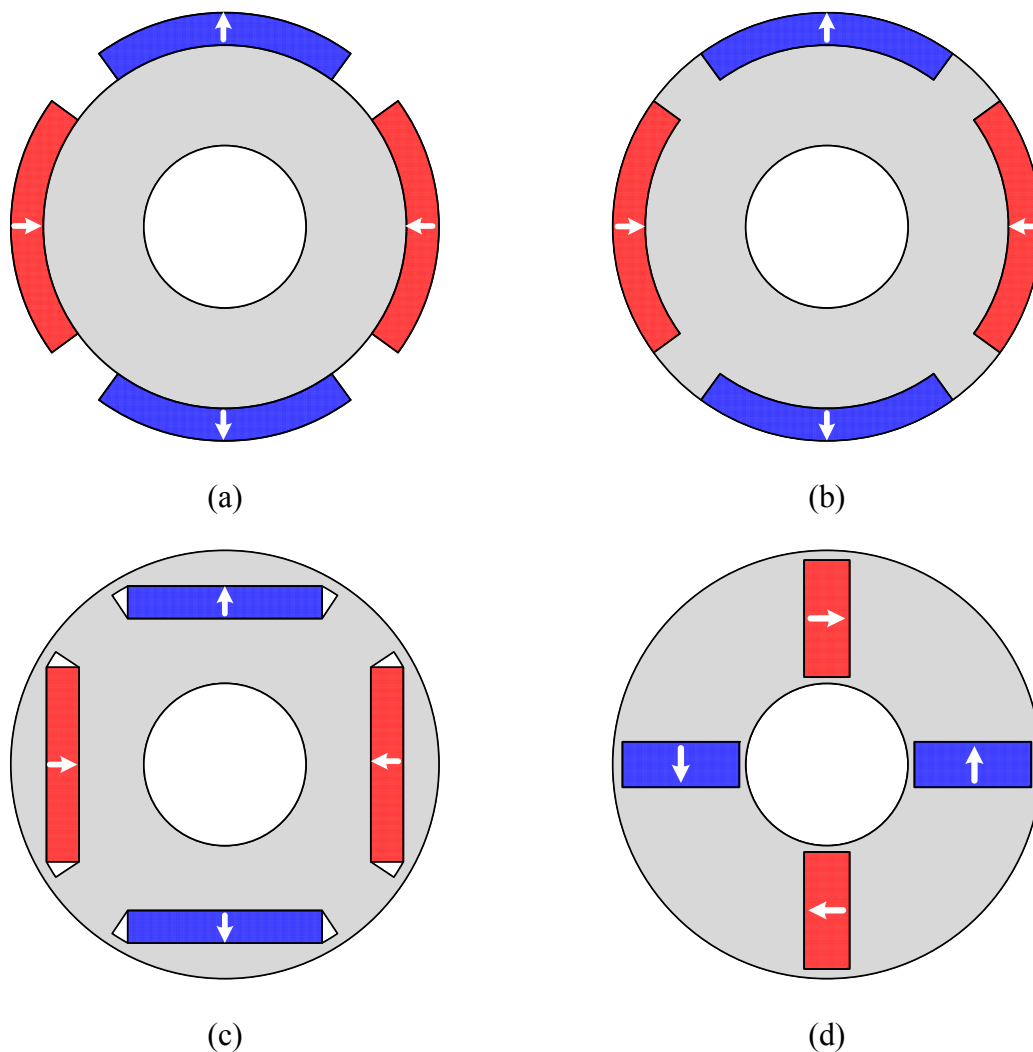


Fig. 1.3 Various PM rotor topologies. (a) Surface-mounted-PM type. (b) Inset-PM type. (c) Interior-PM type. (d) Spoke-PM type.

### 1.1.2 Stator Permanent Magnet Machines

Unlike rotor-PM machines, both PMs and armature windings are accommodated on the stator side in a stator-PM machine while the rotor is of a simple salient pole structure [ZHU07]. Some

distinctive features make the stator-PM machines attractive for low-speed and high-torque applications [CHE11a], which can be summarised as follows:

- Without any coils or PMs, the rotor structure is very simple and robust, and it is very convenient to employ high rotor pole number, both of which are suited to the low-speed and high-torque applications;
- Non-overlapping concentrated tooth coils are usually adopted, resulting in short end-windings and low copper loss;
- The PMs are placed on the stationary component, making it possible to equip more effective cooling systems, and thus, the heat dissipation and temperature rise of PMs can be more easily managed especially under heavy load conditions.

Considering the different placement methods of PMs on stator, the stator-PM machines can be mainly grouped into four categories, which are:

- Doubly salient PM machines (PMs are inserted into stator yoke);
- Switched flux PM machines (PMs are inserted into stator teeth);
- Stator slot PM machines (PMs are placed in stator slot-openings);
- Flux reversal PM machines (PMs are attached on stator bore).

The basic topologies and features of these four kinds of stator-PM machines will be introduced in the following.

#### ***1.1.2.1 Doubly Salient Permanent Magnet Machine***

The doubly salient permanent magnet (DSPM) machines can be developed from the conventional switched reluctance (SR) machines, with an aim to improve the torque density [LIA95]. Taking a three-phase 12/8 DSPM machine as an example, its cross-section is shown in Fig. 1.4 (a), which can be derived from a conventional 12/8 SR machine by inserting four PM pieces into the stator yoke [CHE00b]. By introducing PMs into a SR machine, the pre-magnetisation is achieved in phase coils, which is helpful to increase the flux level and the torque performance. Moreover, the control of a DSPM machine is more flexible than a SR machine since the conventional bipolar converter for PMSMs can be used to supply bipolar current waveforms [LIA95].

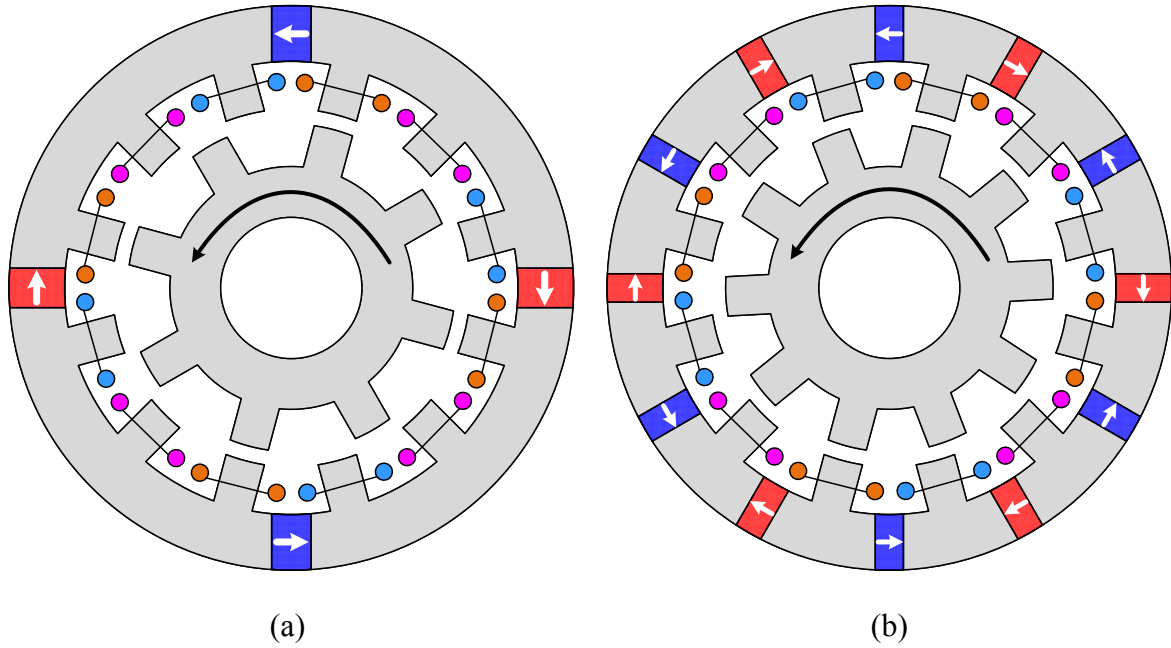


Fig. 1.4 Three-phase DSPM machines with different  $N_s/N_r$  combinations. (a) 12/8 DSPM machine with asymmetric magnetic flux paths for different phases [CHE00b]. (b) 12/10 DSPM machine with symmetrical magnetic flux paths for different phases [WU14].

However, as pointed out in [WU15a], the conventional DSPM machines suffer asymmetric magnetic flux paths for different phases, which will cause asymmetric phase back-EMF waveforms and large torque ripple. To achieve symmetrical magnetic flux paths for different phases, more feasible stator slot/rotor pole ( $N_s/N_r$ ) combinations for a DSPM machine other than those directly derived from a SR machine are investigated in [WU14]. For example, a novel 12/10 DSPM machine with symmetrical flux paths for different phases is reported in [WU14] and its cross-section is shown in Fig. 1.4 (b). As analysed in [WU14], symmetrical and sinusoidal phase back-EMF waveforms can be obtained in this 12/10 DSPM machine, resulting in low torque ripple. However, the number of PM pieces and the corresponding PM volume of the 12/10 DSPM machine are significantly increased while its torque density is even slightly lower than that of the conventional 12/8 DSPM machine [WU15a].

Although the DSPM machines can exhibit higher torque density than the SR machines, the drawback of DSPM machines is obvious since the coil flux linkage is unipolar, which largely restricts the torque density [CHE11a]. Moreover, the stator structure of the DSPM machines is not rigid since PMs are inserted into the stator yoke, which will make the manufacture and assembly more difficult.

### ***1.1.2.2 Switched Flux Permanent Magnet Machine***

Switched flux permanent magnet (SFPM) machines are another typical stator-PM machine topology, in which the PMs are inserted into stator teeth [HOL97]. In comparison with the DSPM machines, the SFPM machines feature with bipolar flux linkage and sinusoidal back-EMF waveform, and thus have much better torque performance [HUA05]. In the past two decades, the investigation of SFPM machines has drawn a lot of attention and many novel SFPM machine topologies have been proposed and have been systematically reviewed in [ZHU11a]. A good example is that different shapes of stator core segment have been employed, as shown in Fig. 1.5. The most popular three-phase 12/10 U-core SFPM machine is shown in Fig. 1.5 (a). As can be seen, a PM piece is inserted into each stator tooth and the adjacent circumferentially magnetised PM pieces enable a flux-focusing effect [CHE10a] [CHE10b], which is similar to the spoke-PM type shown in Fig. 1.3 (d). By halving the stator slot number, a new SFPM machine topology, i.e. the C-core SFPM machine, is proposed in [CHE11b], and a 6/10 C-core SFPM machine is shown in Fig. 1.5 (b). With the aid of finite element analysis (FEA), it is proven that the C-core SFPM machines (i.e. the rotor pole number is around twice of the stator slot number) can significantly improve the torque density over the conventional U-core SFPM machines (i.e. the rotor pole number is similar to the stator slot number) and the PM volume is also largely reduced [CHE11b]. Based on the C-core SFPM machine, by adding additional stator teeth without PMs, the E-core SFPM machine is proposed in [CHE11c] and a 12/10 E-core SFPM machine is shown in Fig. 1.5 (c). FE results show that the E-core SFPM machines can have higher torque density than the U-core SFPM machines, while the PM usage is halved. Although the torque density of an E-core SFPM machine is always lower than that of a C-core SFPM machine, its redundant teeth can be used to accommodate additional field windings, from which some novel hybrid-excited SFPM machines can be obtained, as highlighted in [CHE11d]. Moreover, in [ZHU08], a novel SFPM machine with multi-tooth structure is proposed. The further increased rotor pole number makes such a topology particularly suitable for low-speed direct-drive applications.

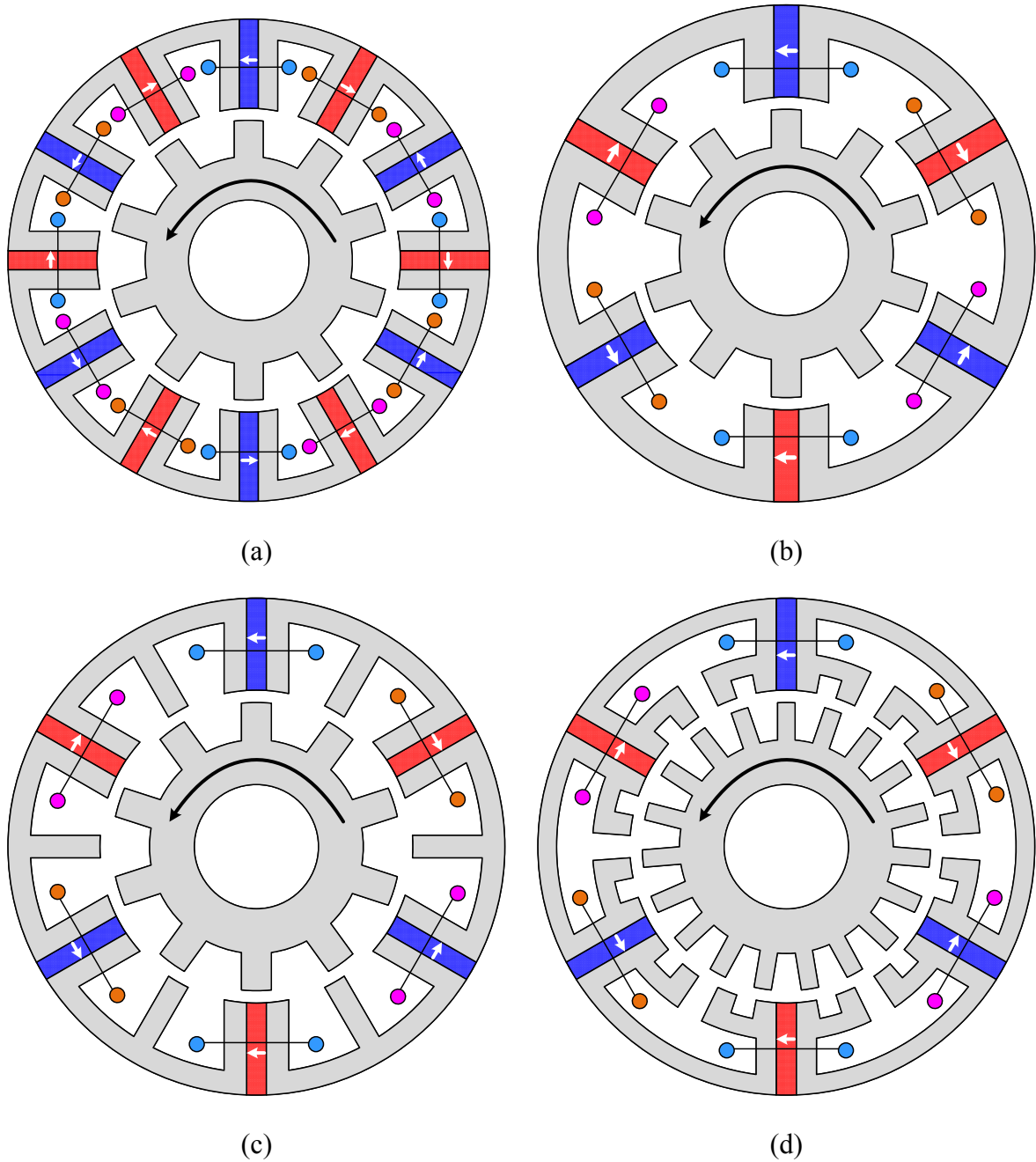


Fig. 1.5 Three-phase SFPM machines with different shapes of stator core segment. (a) 12/10 U-core SFPM machine [HOL97]. (b) 6/10 C-core SFPM machine [CHE11b]. (c) 12/10 E-core SFPM machine [CHE11c]. (d) 6/19 multi-tooth SFPM machine [ZHU08].

Although the SFPM machines especially the C-core SFPM machines can exhibit superior torque density, the saturation in stator core is quite severe, making the over-load capability of the SFPM machines very limited [ZHU08]. Besides, similar to the DSPM machines, the modular stator structure tends to introduce more manufacturing tolerance in SFPM machines [ZHU09a], making the mass production very challenging.

### 1.1.2.3 Stator Slot Permanent Magnet Machine

The stator slot permanent magnet (SSPM) machines are initially proposed as PM-assisted SR machines by introducing PMs in stator slot-openings of the SR machines [NAK07] [AND14]. Fig. 1.6 (a) shows a three-phase 12/8 SSPM machine derived from the conventional 12/8 SR machine. The intention of employing circumferentially magnetised PMs in stator slot-openings of a SR machine is to mitigate the stator saturation, and thus enhancing the torque density. By using the same drive circuit as the conventional 12/8 SR machine (i.e. with unipolar current waveforms injected), a 25% higher output torque of the 12/8 SSPM machine is reported in [NAK07]. Further, by injecting sinusoidal bipolar currents, more feasible  $N_s/N_r$  combinations of the SSPM machines are identified, such as 12/10, 12/11, 12/13, 12/14 etc. [AFI16]. By way of example, the cross-section and winding layouts of a 12/10 SSPM machine are shown in Fig. 1.6 (b). Under open-circuit condition, the main PM fluxes of a SSPM machine are short-circuited within the stator, which differs from the vast majority of PM machines. Therefore, the no-load back-EMF of the SSPM machines is always negligible, providing superior fault tolerant capability especially for high-speed operations. However, the PMs may suffer high risk of demagnetisation and the machine performance is very sensitive to manufacture tolerances [AFI16] [ZHE18].

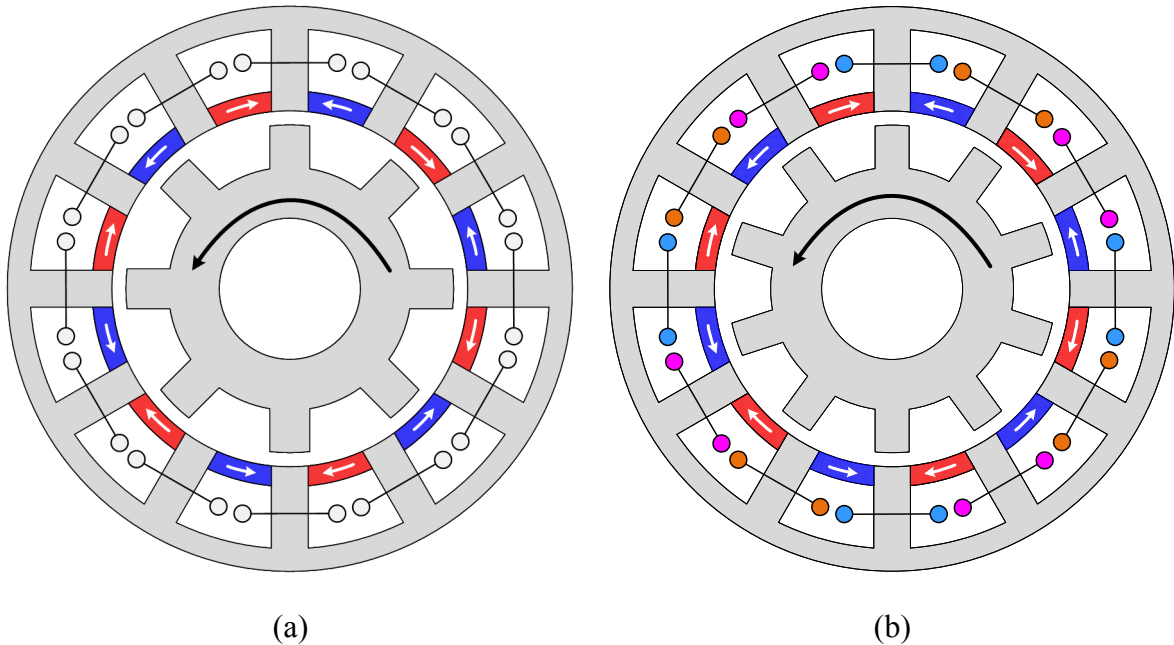


Fig. 1.6 Three-phase SSPM machines with different  $N_s/N_r$  combinations. (a) 12/8 SSPM machine with unipolar excitation [NAK07]. (b) 12/10 SSPM machine with bipolar excitation [AFI16].

#### 1.1.2.4 Flux Reversal Permanent Magnet Machine

By mounting PMs on the inner surface of each stator tooth, another kind of stator-PM machines, i.e. the flux reversal permanent magnet (FRPM) machines are developed. The single-phase, two-phase, and three-phase FRPM machines are firstly proposed in [DEO97], [IWA94], and [WAN99], respectively. Fig. 1.7 shows two conventional three-phase FRPM machines with different  $N_s/N_r$  combinations, i.e. 12/10 FRPM machine with two PM pieces on each stator tooth [HUA10] and 6/14 FRPM machine with four PM pieces on each stator tooth [MOR10a]. As rotor rotates, a bipolar flux linkage variation can be achieved in each coil, making the torque density of the FRPM machines higher than that of the DSPM machines [CHE11a]. In comparison with the DSPM and SFPM machines, the stator structure of the FRPM machines is quite robust and the PM assembling is also simpler than the SSPM machines. Therefore, the FRPM machines will be the focus of this thesis and the detailed developments of FRPM machines will be reviewed later.

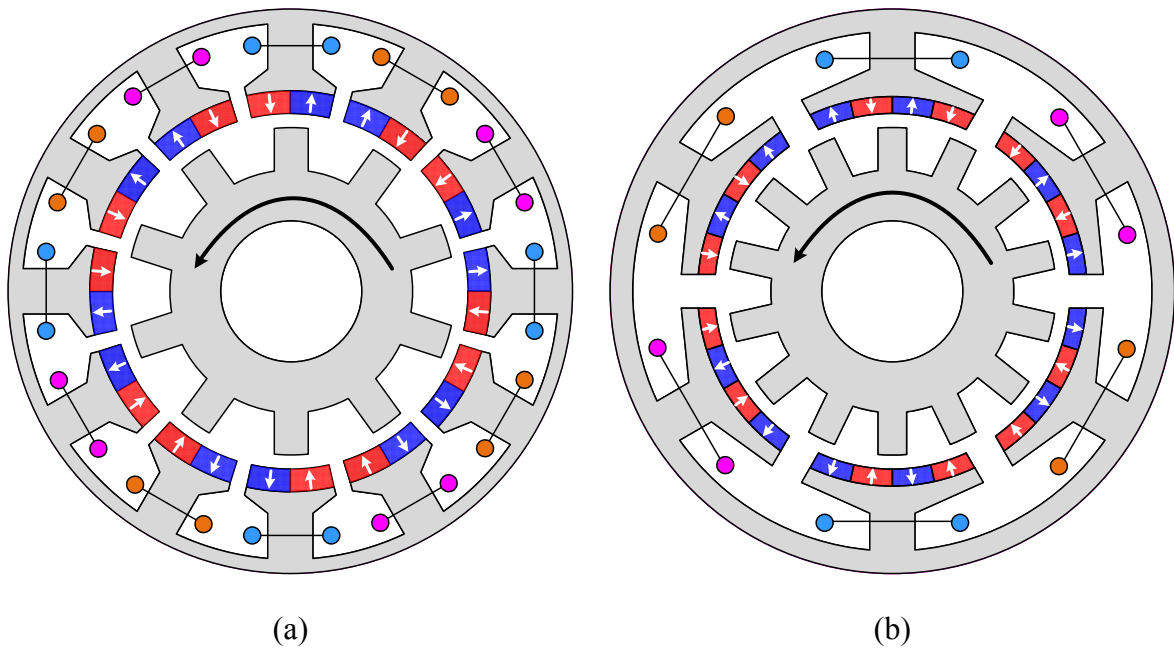


Fig. 1.7 Three-phase FRPM machines with different  $N_s/N_r$  combinations. (a) 12/10 FRPM machine with two PM pieces on each stator tooth [HUA10]. (b) 6/14 FRPM machine with four PM pieces on each stator tooth [MOR10a].

### 1.1.3 Other Permanent Magnet Machine Topologies

It should be noted that only radial-field PM machines are introduced and presented in the previous sections. In practice, various concepts of rotor-PM and stator-PM configurations can be also employed in axial-field [KAH14], linear [LU18], and transverse-flux machines

[HUS17], depending on the requirements of the specific direct-drive applications. A good example is that the YASA axial-field machines with dual rotors and single stator have been commercialised and attempted for many direct-drive applications, such as EV/HEVs [YAS16]. Besides, for transverse-flux machines, the rotor pole number can be increased without sacrificing stator slot area, which results in a high electric loading and a high torque density [WEH88] [HUS17]. The high torque density makes the transverse-flux machines ideally suited to many direct-drive applications, such as wave energy conversion [POL05]. However, the complex mechanical structure and relatively low power factor are main obstacles for applying transverse-flux machines [ZHU07].

## 1.2 Development of Flux Reversal Permanent Magnet Machines

As a member of stator-PM machines, the FRPM machine is believed to be a very promising candidate for low-speed and high-torque direct-drive applications due to the reasons of: 1) the FRPM machines can exhibit superior torque density when compared to those machines without PMs, such as the SR machines; 2) the FRPM machines have simple and robust rotor structure when compared to those machines with PMs mounted on the rotor, i.e. the rotor-PM machines; 3) the FRPM machines have rigid stator structure when compared to the other stator-PM machines, i.e. the DSPM machines and the SFPM machines. However, it is noteworthy that the FRPM machines also have some disadvantages. For example, since the PMs are attached on the inner surface of stator teeth and the air-gap fields are rich of harmonics, the eddy current loss and pulsating radial force of PMs may be high. The relatively large equivalent air-gap length also restricts the rotor-tooth modulation, which may cause lower torque density especially compared with the SFPM machines [CHE11a]. For clarity, the main features, advantages and disadvantages of the FRPM machines are summarised in Table 1.1.

This thesis will provide a thorough investigation into the FRPM machines. To begin with, the relevant backgrounds and developments of FRPM machines will be described in this section.

Although the idea of arranging PMs on stator can date back to the 1950s [RAU55], it is not until the 1990s that the detailed topologies of the FRPM machines are proposed. To the author's knowledge, the concept of mounting PMs on the inner surface of stator teeth is firstly described in [IWA94], as a two-phase linear reluctance machine shown in Fig. 1.8 (a), and the term of "flux reversal" is then used by Prof. Boldea *et al.* [BOL96]. As shown in Fig. 1.8 (b), a single-phase rotatory FRPM machine is proposed in [DEO97], from which the FRPM machines are



regarded as one special type of stator-PM machines. The FRPM machines are then extended to three phases (see Fig. 1.10) and investigated for many applications, such as EVs [WAN01], servo system [BOL02], wind power generation [MOR10a], urban rail traction [ZHA14], angular grinder [DMI16], pump/fan [PRA17], and etc. Various aspects of current research and relevant literatures are briefly summarised in Fig. 1.9.

Table 1.1 Main features, advantages and *disadvantages* of FRPM machines

Features	Advantages and <i>disadvantages</i>
1. Salient pole rotor structure	<ul style="list-style-type: none"> <li>a. No slip ring and brush required</li> <li>b. Robust rotor and fast dynamic response</li> <li>c. Easy to adjust rotor pole number for different applications</li> </ul>
2. PMs attached on the inner surface of stator teeth	<ul style="list-style-type: none"> <li>a. Still a very simple and robust stator</li> <li>b. <i>High PM eddy current loss</i></li> <li>c. <i>Large equivalent air-gap length and relatively weak air-gap field modulation effect</i></li> <li>d. <i>High pulsating radial force on PMs</i></li> </ul>
3. Non-overlapping concentrated-windings	<ul style="list-style-type: none"> <li>a. High winding packing factor</li> <li>b. Short end-windings and compact volume</li> <li>c. Good fault-tolerance capability</li> </ul>

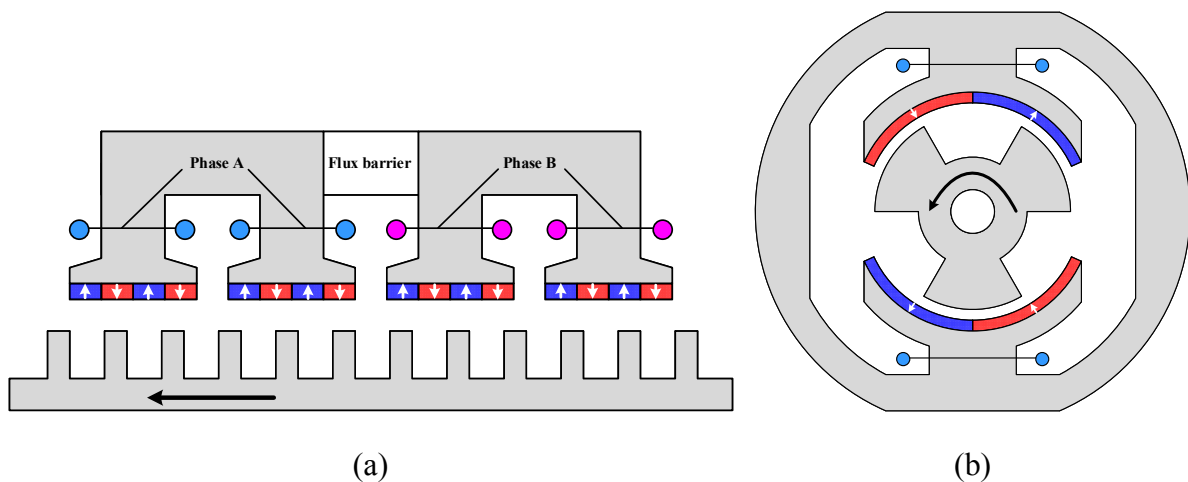


Fig. 1.8 Initial concepts of FRPM machines. (a) Two-phase linear FRPM machine [IWA94].  
(b) Single-phase rotary FRPM machine [DEO97].

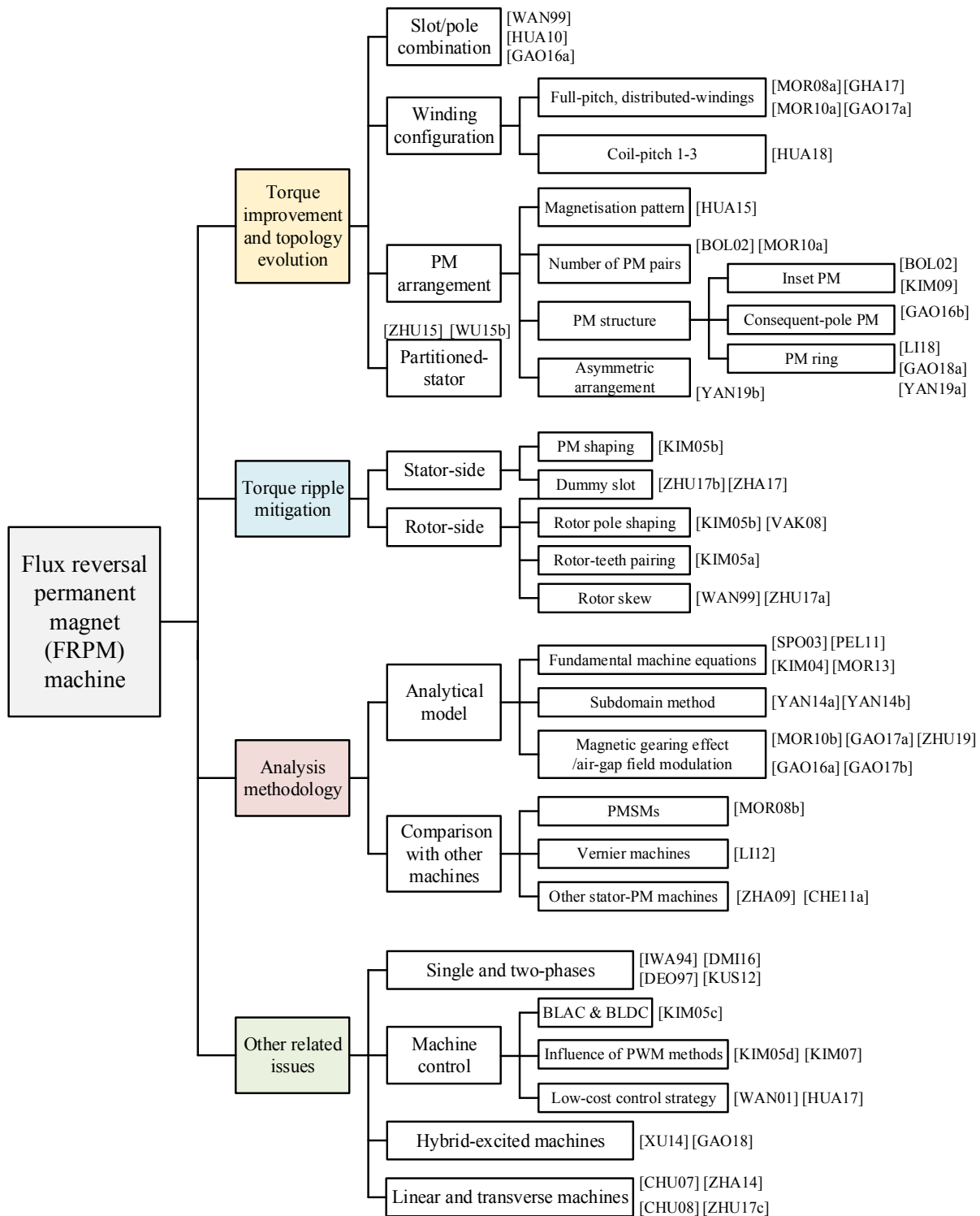


Fig. 1.9 Recent developments of FRPM machines and relevant references.

As can be seen from Fig. 1.9, among the existing literatures, quite a few focuses on torque improvement and topology evolution of the FRPM machines since a high torque density is always the most critical requirement for direct-drive applications. Correspondingly, many novel FRPM machine topologies have been proposed. Some literatures also dedicate to

reducing the torque ripple of the FRPM machines since the cogging torque/torque ripple may be severe for machines with doubly salient structure. Besides, the analysis methodology of FRPM machines has attracted many researcher's attention due to the more complex working principle in stator-PM machines. Some related issues, such as the high-performance control strategy and the extension of FRPM machines to hybrid-excited machines, have also been investigated. These research hotspots of the FRPM machines will be addressed in more detail.

## 1.2.1 Torque Improvement and Topology Evolution

### 1.2.1.1 Stator Slot/Rotor Pole Combination

The three-phase FRPM machines are firstly investigated in [WAN99]. According to some simple analytical analyses, the general relationship between the number of stator slot ( $N_s$ ) and the number of rotor pole ( $N_r$ ) is summarised as  $N_s/N_r = m/(m+1)$  [WAN99], and a group of three-phase (i.e.  $m=3$ ) FRPM machines are then proposed. By way of example, a conventional three-phase 6/8 FRPM machine is shown in Fig. 1.10 (a). Other feasible  $N_s/N_r$  combinations have also been identified and analysed. For example, in [HUA10], a 12/10 FRPM machine is proposed (see Fig. 1.7 (a)), in which the even-order back-EMF harmonics can be cancelled out; in [GAO16a], the optimal  $N_s/N_r$  combination is identified based on the analytical expressions of machine performance. It shows that the 6/7 FRPM machine is preferred to achieve the highest average torque (for  $N_s=6$ ), while the range of  $N_r$  from 10 to 16 is preferred for  $N_s=12$ . In general, the similar numbers of  $N_s$  and  $N_r$  are suggested to maximise the torque density.

### 1.2.1.2 Winding Configuration

Although the non-overlapping concentrated-windings are usually adopted in FRPM machines for the sake of short end-windings and compact machine design, the other winding configurations can be also used to boost the machine torque in some specific cases. In [MOR08a], the overlapping windings are firstly employed in a 6/8 FRPM machine and are then extended to other  $N_s/N_r$  combinations, e.g. 6/14 in [MOR10a] and 18/17 in [GHA17]. Results show that for these specific  $N_s/N_r$  combinations, the overlapping windings can effectively improve the machine torque due to the improved winding factor. A more general guideline for using overlapping windings in FRPM machines is provided in [GAO17a], from which the  $N_s/N_r$  combinations ideally suited to full-pitch overlapping windings are identified. Besides, in [HUA18], the influences of  $N_s/N_r$  combinations and coil pitch (from 1 to 3) on machine performance are investigated, with a particular emphasis on harmonic elimination of back-EMFs. However, it should be noted that the end-windings are all neglected in these literatures,

which is actually an important issue in selecting winding configurations. In practice, the long end-windings and low packing factor of the full-pitch overlapping windings will definitely counteract the advantages stated in these literatures.

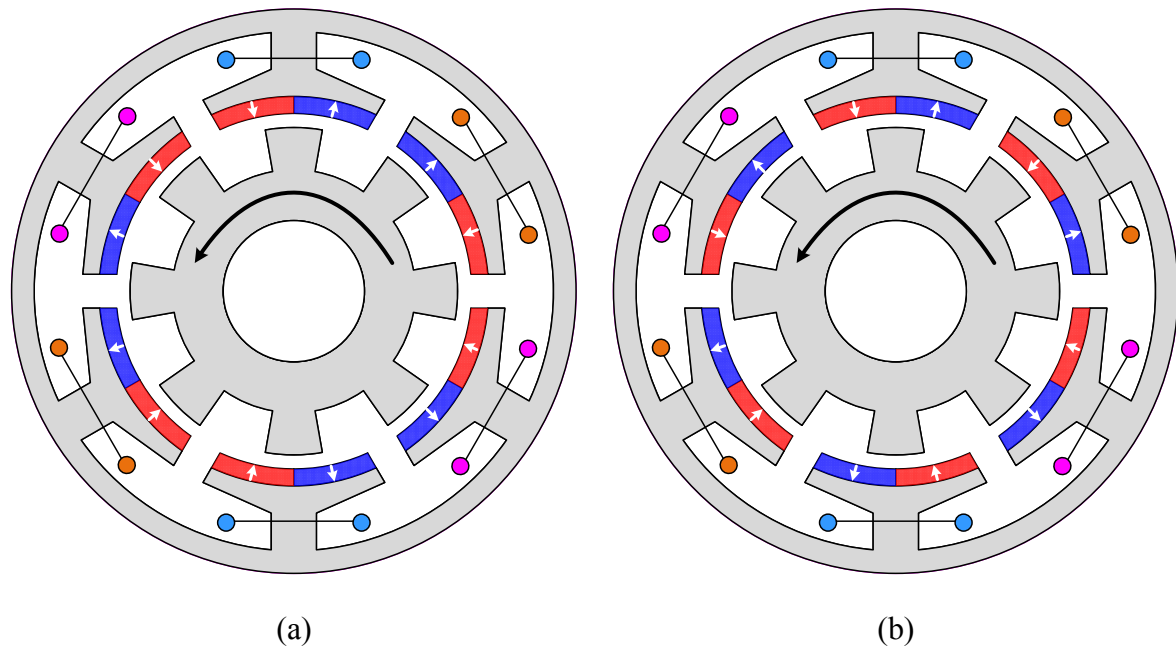


Fig. 1.10 Conventional three-phase 6/8 FRPM machines with different PM magnetisation patterns. (a) PM polarities of adjacent teeth are identical [WAN99]. (b) PM polarities of adjacent teeth are opposite [HUA15].

### 1.2.1.3 PM Arrangement

Since the PMs are simply mounted on the inner stator surface of the FRPM machines, it is quite flexible to adjust the PM arrangements, including the magnetisation pattern, the number of PM pair, and the PM structure etc. From existing literatures, it has been proven that the different PM arrangements have a significant influence on machine performance and some novel FRPM topologies have been proposed, which will be detailed in the following.

A. *Magnetisation pattern*: the polarities of the adjacent PM pieces belonging to two stator teeth can be either identical or opposite, as depicted in Fig. 1.10. Most literatures focus on the FRPM machines with PM polarities of adjacent teeth being identical (see Fig. 1.10 (a)), and only few literatures focus on the other magnetisation pattern (see Fig. 1.10 (b)). In [HUA15], a simple comparison between the two PM magnetisation patterns is provided in terms of the back-EMF waveform. It is stated that the 6/8 FRPM machine shown in Fig. 1.10 (a) is more likely to exhibit a trapezoidal back-EMF waveform while the 6/8 FRPM machine shown in Fig. 1.10 (b) tends to have a sinusoidal back-EMF waveform, thus suitable for brushless DC (BLDC)

and brushless AC (BLAC) drives, respectively. However, the lack of theoretical support and systematic study makes the conclusion in [HUA15] not valid for other  $N_s/N_r$  combinations. In addition, the influence of PM polarities of adjacent teeth on machine torque has not been clearly addressed yet.

B. *Number of PM pairs*: for conventional FRPM machines, a pair of PMs is mounted on each stator tooth, as the 6/8 FRPM machine shown in Fig. 1.10 (a) [WAN99]. Under the same  $N_s$ , the number of PM pairs mounted on each stator tooth can be increased and the corresponding rotor pole number will also be increased. As for the 6/14 FRPM machine shown in Fig. 1.7 (b) [MOR10a], by mounting two pairs of PMs instead of one PM pair on each stator tooth, the rotor pole number is largely increased from 8 to 14. Another example of mounting two pairs of PMs is that in [BOL02], a 12/28 FRPM machine is investigated for a specific low-speed servo drive application where a large rotor pole number is desired. However, it is worth noting that the influence of number of PM pairs on machine performance has not been addressed yet.

C. *PM structure*: in addition to the conventional SPM topology, other PM topologies can be also used in FRPM machines with reference to the different PM structures shown in Fig. 1.3. To utilise the flux-focusing effect, the FRPM machines with inset-PM topology are investigated in [BOL02] [KIM09]. In [KIM09], a 6/8 FRPM machine with inset-PM topology is proposed (see Fig. 1.11 (a)) and compared with its counterpart 6/8 FRPM machine with SPM topology. It is revealed that to achieve the same output torque, the PM volume of the inset-PM topology is only 60% of that of the SPM topology, from which the flux-focusing effect in the inset-PM topology is verified. However, due to the space limitation of stator tooth tips, the inset-PM topology is more sensitive in terms of the mechanical strength. Besides, a 12/16 FRPM machine with consequent-pole PM (CPM) topology is proposed in [GAO16b], as shown in Fig. 1.11 (b). By simply replacing the S-pole PMs in the SPM topology with iron poles, the PM volume of the resulted CPM topology is halved while its torque density can be even higher, thanks to the reduced flux leakage and enhanced flux modulation effect [GAO16b]. However, the influence of  $N_s/N_r$  combinations on the performance of FRPM machine with CPM topology has not been addressed. Moreover, in [LI18], the idea of using a PM ring is proposed (i.e. the space under the stator slot opening is also used to mount PMs), which brings more freedoms to modify the PM excitation. A 12/16 FRPM machine with 36 PM pieces evenly attached on the entire inner stator surface is shown in Fig. 1.12 (a) [LI18]. Not like the conventional 12-stator-slot FRPM machines with PM pole-pair number of 6, the PM pole-pair number in such a machine is changed to 18. FE results show that a 30% higher average torque can be achieved. Further, in [GAO18a] the unevenly attached PM ring is used (i.e. the widths of PM pieces are

different), as shown in Fig. 1.12 (b). The PMs can be arranged to improve the magnitudes of the required PM MMF harmonics, and the multi PM MMF harmonics can be utilised simultaneously. The higher torque density of such a novel FRPM machine is verified by FEA [GAO18a]. However, the process of winding coils and assembling PMs will be more complex in these FRPM machines.

D. *Asymmetric arrangement*: more recently, Yang *et al.* [YAN19a] [YAN19b] propose another two novel FRPM machines, as shown in Fig. 1.13. The first one is a FRPM machine with shifted CPM topology, as shown in Fig. 1.13 (a). The main feature is that the position of the iron pole on each stator tooth can be adjusted to maximise the average torque [YAN19a]. With the optimal position of the iron poles, the novel 6/11 FRPM machine can exhibit much higher torque than the counterpart 6/11 FRPM machine with normal CPM topology (see Fig. 1.11 (b)). A FRPM machine with unequal stator teeth is then proposed and analysed in [YAN19b], as shown in Fig. 1.13 (b). The idea behind this topology is that the flux leakage between the PM poles can be largely reduced especially for the stator teeth with only one PM piece. FE results show that a 12/17 FRPM machine with unequal stator teeth can exhibit 24% higher torque than the conventional 12/17 FRPM machine. However, it should be noted that the feasibility of these novel topologies with other  $N_s/N_r$  combinations has not been clearly addressed yet.

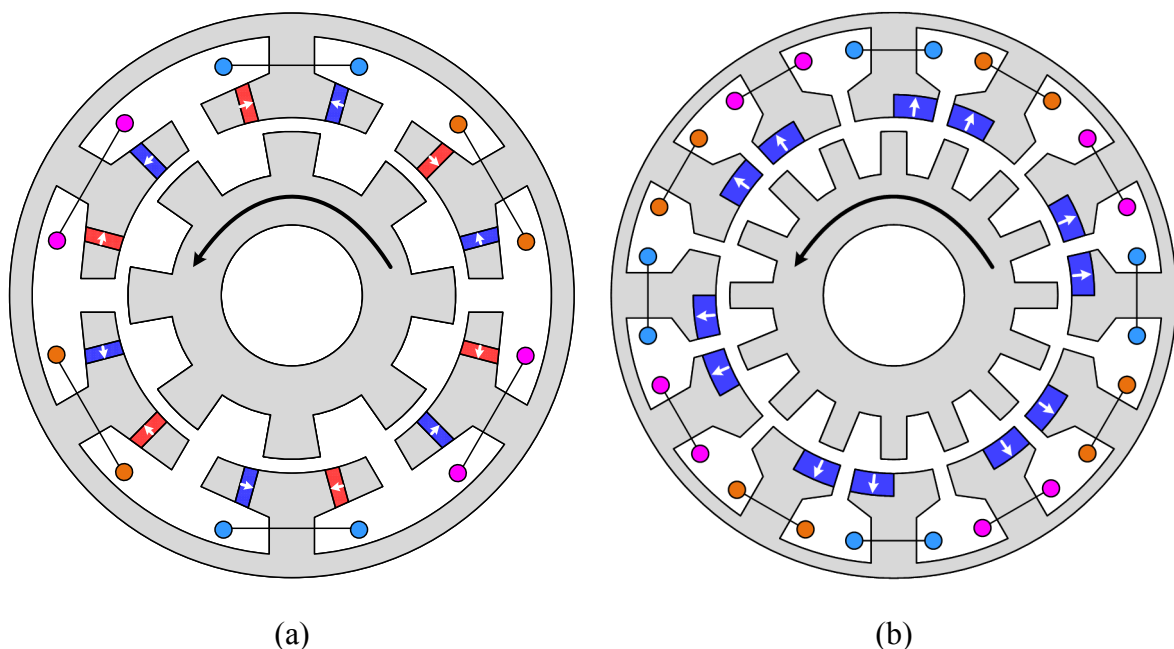


Fig. 1.11 Three-phase FRPM machines with different PM topologies. (a) 6/8 FRPM machine with inset-PM topology [KIM09]. (b) 12/16 FRPM machine with consequent-pole PM topology [GAO16b].

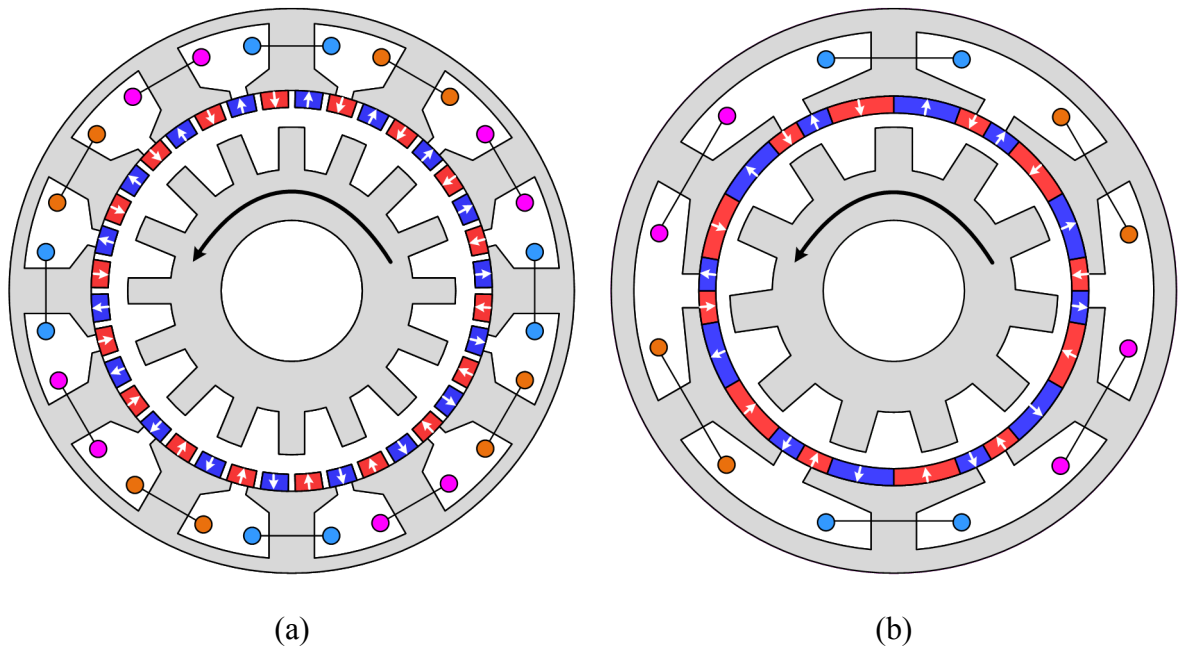


Fig. 1.12 Three-phase FRPM machines with PMs attached on entire inner stator surface. (a) 12/16 FRPM machine with 36 PM pieces evenly attached [LI18]. (b) 6/11 FRPM machine with 24 PM pieces unevenly attached [GAO18a].

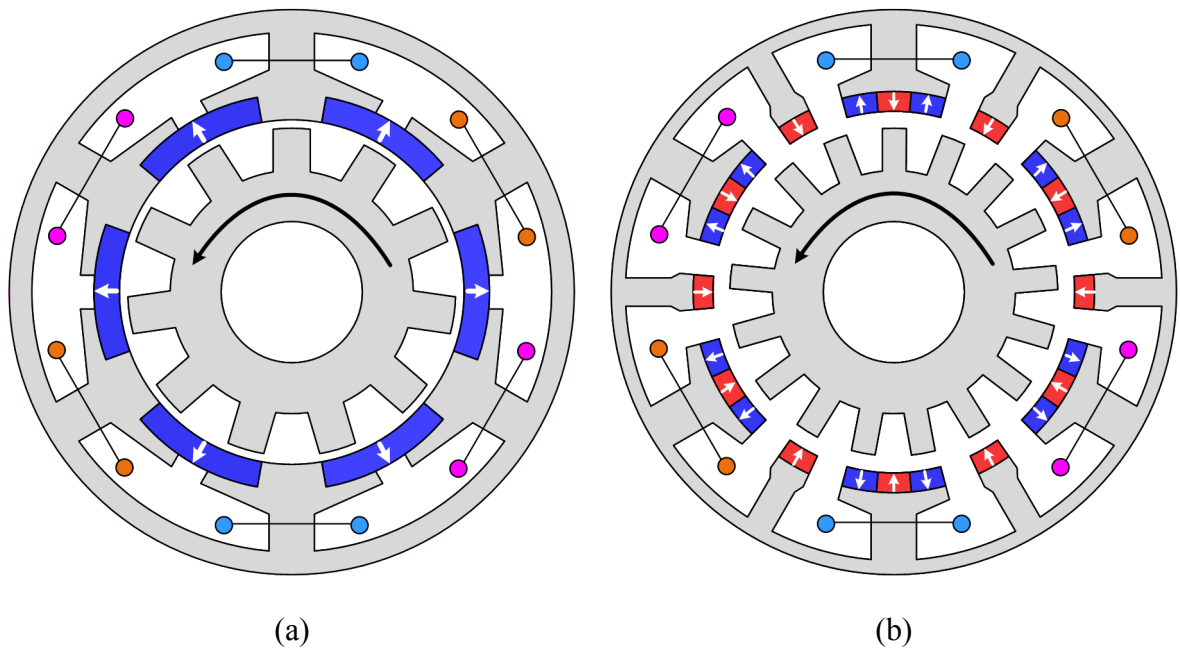


Fig. 1.13 Three-phase FRPM machines with other PM arrangements. (a) 6/11 FRPM machine with shifted consequent-pole PM topology [YAN19a]. (b) 12/17 FRPM machine with unequal stator teeth [YAN19b].

#### 1.2.1.4 Partitioned-Stator Machine

Recently, the partitioned-stator (PS) FRPM machines are proposed by Prof. Zhu *et al.* [ZHU15] [WU15b], as shown in Fig. 1.14. As can be seen, in comparison with the conventional FRPM machines of which the armature windings and the PMs are accommodated in the same stator, the two excitation sources are now separated with one more inner PM stator arranged. Therefore, the inner space of the machines can be utilised which is beneficial to improve the torque and the different PM topologies can also be used, such as the SPM inner stator in Fig. 1.14 (a) [ZHU15] and the CPM inner stator in Fig. 1.14 (b) [WU15b]. However, the dual air-gaps make the mechanical structure of the PS-FRPM machines more complex. More importantly, it is found that the PS-FRPM machines also integrate the features of the magnetically geared machines [ZHU15], which will provide a new perspective to analyse the FRPM machines. More details of using magnetic gearing effect/air-gap field modulation theory to analyse the FRPM machines will be illustrated later.

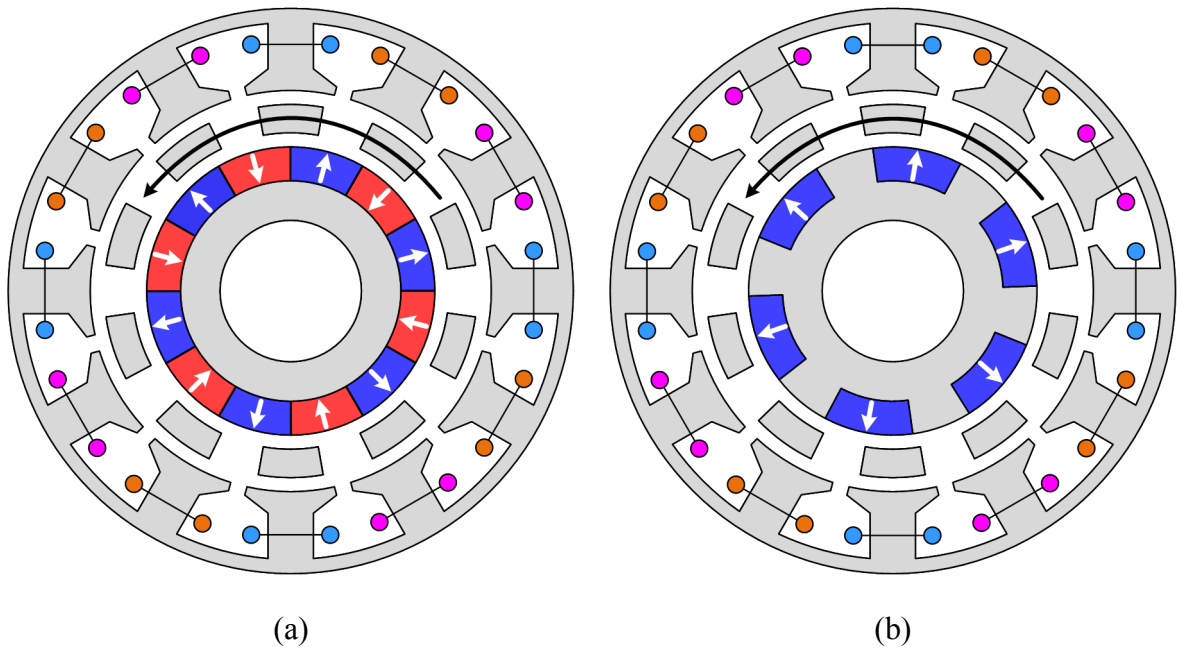


Fig. 1.14 Three-phase 12/10 PS-FRPM machines. (a) SPM inner stator [ZHU15]. (b) CPM inner stator [WU15b].

#### 1.2.2 Torque Ripple Mitigation

In addition to the torque improvement of the FRPM machines, the torque ripple mitigation has also attracted many researcher's attention since the cogging torque and the torque ripple may be severe in such machines with a salient pole rotor structure. As firstly pointed out in [WAN99], the conventional three-phase 6/8 FRPM machine has a very high torque ripple due



to large cogging torque. Thus, the rotor skewing is proposed, as shown in Fig. 1.15 (a) [WAN99]. The optimal rotor skew angle is suggested as  $2\pi/LCM(N_s, N_r)$  ( $LCM$  is the lowest common multiple), which would ideally cancel out the cogging torque. Moreover, the rotor step skewing is investigated in [ZHU17a], which can largely reduce the cogging torque while its rotor manufacture is much simpler. Besides, as shown in Fig. 1.15, many other torque ripple mitigation methods have been proposed, such as rotor teeth pairing [KIM05a], dummy slot on rotor [KIM05b], PM shaping [KIM05b], rotor pole shaping [KIM05b] [VAK08], and dummy slot on stator [ZHU17b] [ZHA17]. The effectiveness of all these techniques has been verified on the conventional three-phase 6/8 FRPM machine with an inherently high cogging torque. However, all these techniques are inevitably accompanied with torque reduction. It is worthwhile to mention that the  $N_s/N_r$  combinations and PM arrangements have a significant influence on cogging torque [GAO17b]. By properly selecting  $N_s/N_r$  combinations of a FRPM machine, the cogging torque and the torque ripple would be inherently low.

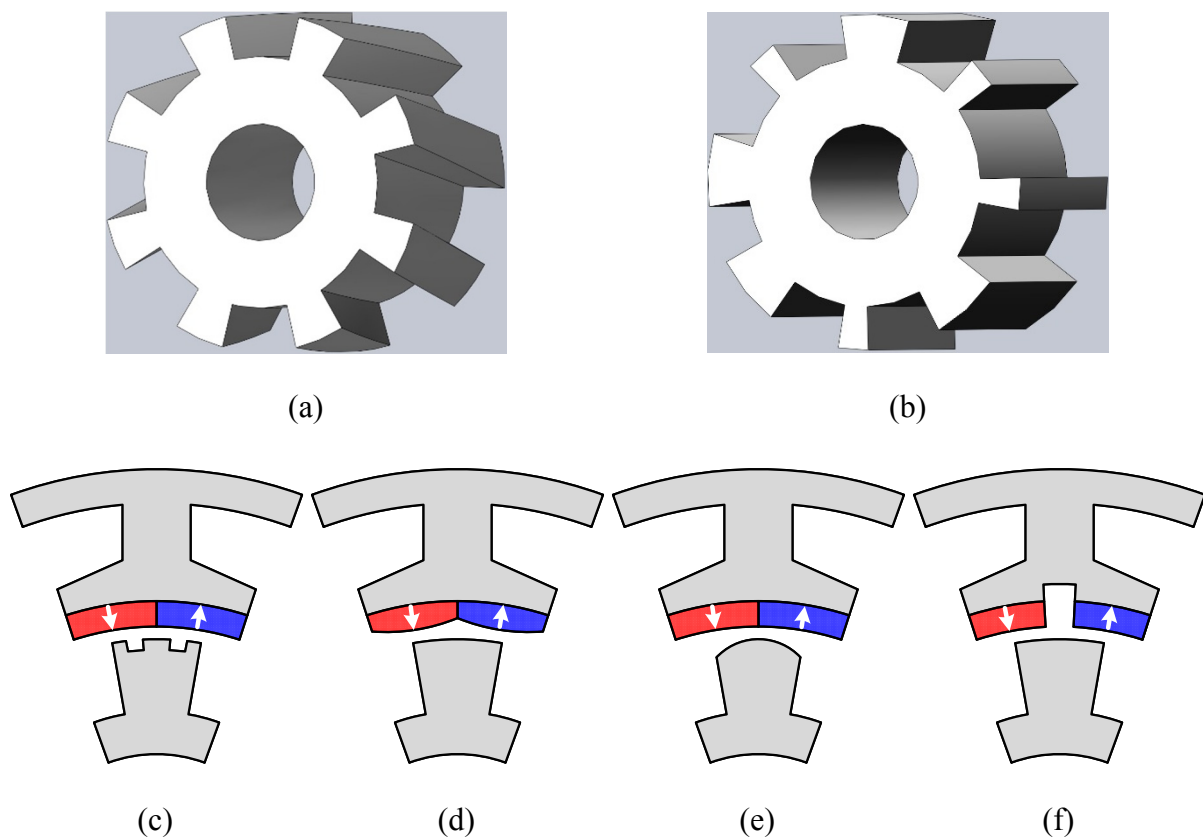


Fig. 1.15 Various techniques for torque ripple mitigation. (a) Rotor skewing. (b) Rotor teeth pairing. (c) Dummy slot on rotor. (d) PM shaping. (e) Rotor pole shaping. (f) Dummy slot on stator.

### 1.2.3 Analysis Methodology

The principle analysis of a FRPM machine is always a challenging task due to its complex working mechanism compared with the conventional PMSMs. In many literatures, the fundamental machine equations, such as the shear stress [SPO03] [PEL11] [MOR13] and the  $d$ - and  $q$ -axis equivalent circuits [MOR13], are used to analyse and design the FRPM machines. However, all these equations are simple one-dimensional (1D) analytical analysis and empirical magnetic loading and/or electrical loading is always required to evaluate the machine performance, which may cause considerable errors. To accurately calculate the air-gap magnetic field and the machine performance, the subdomain analytical method is used in [YAN14a] [YAN14b]. By dividing a FRPM machine into several subdomains and solving the governing equations under specific boundary conditions, the machine performance can be analytically derived although the saturation cannot be considered. However, it should be noted that for analytical methods based on machine equations and sub-domain, a clear understanding of the distinct working mechanism in FRPM machines cannot be fulfilled. With the recently developed theories of magnetic gearing effect and/or air-gap field modulation [CHE17], the working principle of the FRPM machines can now be analysed from a new perspective [MOR10b]. More specifically, the PM magnetomotive force (MMF)-permeance model can be used to deduce the machine performance, from which the rotor-tooth modulation can be accounted for and the working harmonics of PM MMF, permeance distribution, and air-gap fields can be identified. In this thesis, the air-gap field modulation theory will be used to analyse the machine performance and a detailed introduction of this theory will be given in next section.

Although the FRPM machines exhibit some unique advantages (see Table 1.1), it is necessary and also very interesting to compare the FRPM machines with other machine topologies, particularly for torque density. In [MOR08b], a 6/14 FRPM machine with concentrated-windings is compared with a 24/28 fractional-slot PMSM under specific constraints of machine size, electric loading and magnetic loading. A 50% higher power density in the 6/14 FRPM machine is declared. In [LI12], a 6/22 FRPM machine with concentrated-windings is compared with a 6/22 Vernier machine with concentrated-windings in generator mode. FE results show that the generated voltage of the FRPM machine is 7.3% lower. Moreover, the FRPM machine is compared with the other two kinds of stator-PM machines in [ZHA09] [CHE11a]. In [ZHA09], a general power equation is proposed to compare the three stator-PM machine types. However, it is found that the comparison results are greatly influenced by some design conditions, such as the radial length of the stator. An overview of stator-PM machines is

presented in [CHE11a], and it is stated that the FRPM machines tend to have lower torque density compared to the SFPM machines because of the larger equivalent air-gap length. In short, although the mentioned literatures have tried to compare the FRPM machine with other machine topologies, there is no general conclusions can be drawn since the most comparisons are based on FEA and only several limited examples are provided.

#### **1.2.4 Other Related Issues**

Apart from the performance improvement mentioned above, the related control issues of the FRPM machines have also been investigated. In [KIM05c], the two drive methods i.e. BLAC and BLDC drives, are compared based on a 6/8 FRPM machine. It reveals that the BLAC drive is preferred to achieve a smooth output torque. Then, the influence of different pulse width modulation (PWM) methods on the machine performance is investigated in [KIM05d] [KIM07], and several low-cost control strategies and circuits are also proposed [WAN01] [HUA17a].

Although the vast majority of literatures focus on the three-phase radial-field FRPM machine, the investigation has also been extended to FRPM machines with different phase numbers (e.g. one-phase in [KUS12]), excitation types (e.g. hybrid-excited type in [XU14] [GAO18b]), and field directions (e.g. linear machine in [CHU07] [CHU08] [ZHA14], transverse-flux machine in [ZHU17c]). The advantages of simple stator and rotor structures still remain in these FRPM machine topologies.

### **1.3 Magnetic Gearing Effect/Air-Gap Field Modulation and Magnetically Geared Machines**

Thanks to the development of magnetic gear (MG) in the past 20 years, the theories of magnetic gearing effect and/or air-gap field modulation have been developed, which facilitate the evolution of many novel machine topologies and also provide a new perspective to analyse the existing machine topologies, e.g. the FRPM machines. Therefore, in this section, the development of MG and corresponding magnetically geared (MGd) machines will be presented. The utilisation of magnetic gearing effect and/or air-gap field modulation theory in analysing FRPM machines will also be introduced.

### 1.3.1 Magnetic Gears

With reference to various mechanical gears, different MG topologies can be easily developed by simply replacing the teeth of mechanical gear with PM poles. However, most of them have poor torque density due to the insufficient utilisation of PMs. Hence, MGs have not attracted much attention until a novel coaxial MG is proposed [ATA01], which gets rid of the concept of mechanical gear and largely improves the torque density ( $>100\text{kNm/m}^3$ ).

As shown in Fig. 1.16, the MG consists of three components: a high-speed element, a low-speed element, and a magnetic modulation ring [ATA01]. Both high-speed and low-speed elements are made of PMs but with different pole-pair numbers, and the magnetic modulation ring consists of a certain number of ferromagnetic iron pieces. Normally, the magnetic modulation ring locates between the other two elements, aiming to effectively modulate the PM fields, and the positions of the other two PM elements can be swapped (see Fig. 1.16).

The basic configuration of a MG is expressed as

$$N_m = p_h + p_l \quad (1.1)$$

$$N_m \Omega_m = p_h \Omega_h + p_l \Omega_l \quad (1.2)$$

where  $N_m$  is the number of iron pieces of the modulation ring,  $\Omega_m$  is its mechanical angular velocity;  $p_h$  is the pole-pair number of the high-speed element and  $\Omega_h$  is its mechanical angular velocity;  $p_l$  is the pole-pair number of the low-speed element and  $\Omega_l$  is its mechanical angular velocity.

From (1.2), it is clear that all three components of the MG can be rotating and thus the gear ratio (speed ratio)  $G_r$  of any two movable components can be freely adjusted by controlling the speed of the other component, which is so-called continuously variable transmission (CVT). Alternatively, any one of the three components can be fixed at standstill and thus the MG has a constant  $G_r$  between the other two components, which is always used for speed/torque conversion, similar to a conventional mechanical gear.

Many studies have been conducted to further improve the performance of the MG: (a) for high/low-speed element, apart from the SPM rotor structure, other structures can be used to improve the torque density or reduce the PM volume, such as CPM [SHE17a], IPM [RAS05], pure reluctance [SHE17b], and Halbach PM rotor [JIA09a] etc.; (b) the pure reluctance rotor

structure of the magnetic modulation ring can be replaced by CPM or IPM structure, thus providing additional excitation and boosting the torque [PEN14]; (c) the radial-field type can be changed to the axial-field or transverse-flux type, and the shape of iron pieces can be modified to enhance the field modulation and mitigate the flux leakage [CHE14]. Up to now, the maximum torque density of a MG with various torque-boosting techniques adopted has already reached over  $250\text{kNm/m}^3$ , making its competitive for practical applications [YIN15].

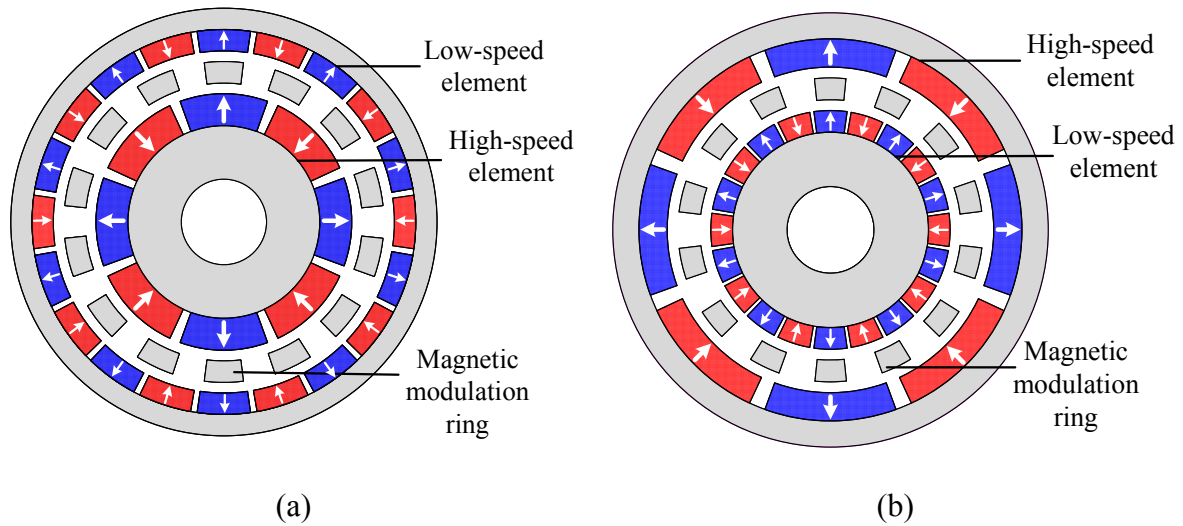


Fig. 1.16 Typical MGs. (a) MG with low-speed element outside. (b) MG with high-speed element outside.

### 1.3.2 Various Magnetically Geared Machines Working Based on Magnetic Gearing Effect

Although a MG shown in Fig. 1.16 can have high torque density, it is simply a passive transmission part without any electrical output port or input port. For the sake of practical application, its integration with electrical machines needs to be well considered. Instead of a simple replacement of a mechanical gear, numerous artful integration methods aiming at compact system volume have been proposed, which greatly enriches the development of this new class of electrical machine, i.e. MGd machines.

As shown in Fig. 1.17, most MGd machines can be directly derived from a MG. In addition, many existing PM machine topologies, such as FRPM machines [MOR10b], SFPM machines [WU15c], and Vernier PM machines [QU11] etc., have now been re-recognized and/or proven to work based on magnetic gearing effect. The MG-derived machines will firstly be reviewed and the air-gap field modulation in FRPM machines will be presented later.

According to different evolutions from a MG, MG-derived machines can be mainly categorized into four types, which are mechanically coupled machines (Type 1), Pseudo machines (Type 2), mechanically and magnetically coupled machines (Type 3), and partitioned-stator machines (Type 4), respectively. For Type 1, the subordinate MG and electrical machine can be easily identified since they are just mechanically coupled without changing their original structures. In contrast, other three types have more compact integration between the MG and electrical machine, as shown in Fig. 1.18. More detailed introduction and review of each type will be given below.

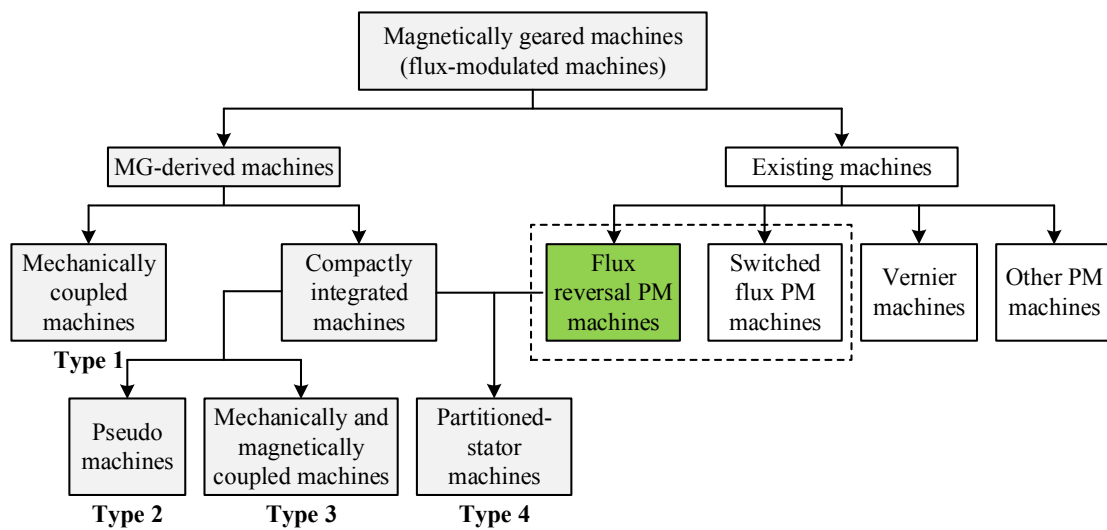


Fig. 1.17 Breakdown of different types of MGd machines.

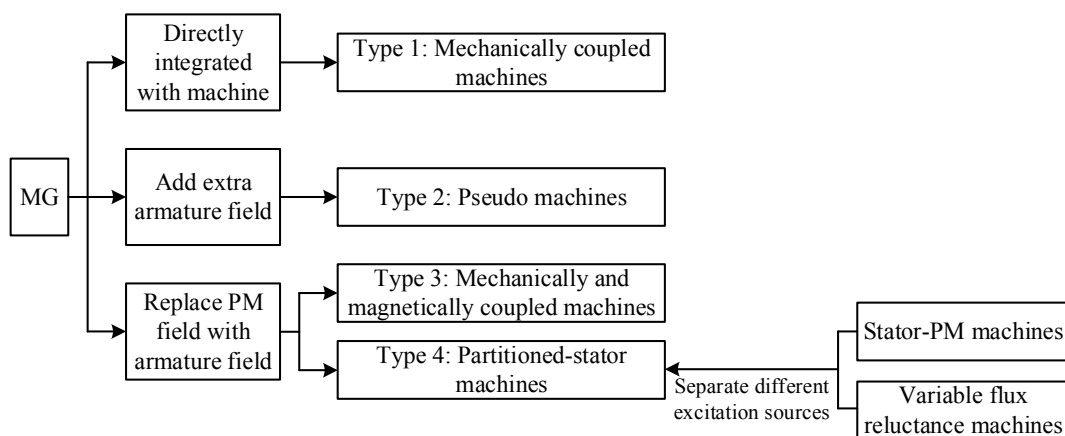


Fig. 1.18 Breakdown of different types of MG-derived machines.

### 1.3.2.1 Type 1: Mechanically Coupled Machines

The basic concept of mechanically coupled machines, Fig. 1.19, is that a MG and a conventional electrical machine are physically connected by sharing the same rotor [CHA07c].

When the machines operate in motor mode, one of the PM rotors (normally the high-speed element) of the MG is shared by the machine and driven by the armature field, then the speed/torque conversion can be achieved by setting the other PM rotor and/or magnetic modulation ring as output rotor. Ideally, the subordinate MG and machine are magnetically decoupled since the magnetic field of the machine does not cause flux distortion in the MG and vice versa.

According to the different relative positions of the MG to the machine, mechanically coupled machines can be further classified into MG-outside machine, Fig. 1.19 (a) [CHA07c], MG-inside machine, Fig. 1.19 (b) [WAN11], and MG-sandwiched machine (one MG with both PM rotors shared by other machines) [JIA09b]. It should be noted that the number of the connected MG and/or machine can be larger than 1, i.e. the cascade level of the mechanically coupled machines can be improved.

Mechanically coupled machines always have high torque density due to their good space utilisation ratio, and they have been investigated and applied for some applications, such as EV and wind power generation [JIA09c] [FRA15]. In addition, as many as three rotors with one of the speeds controllable also make these machines capable of achieving CVT [ATA12].

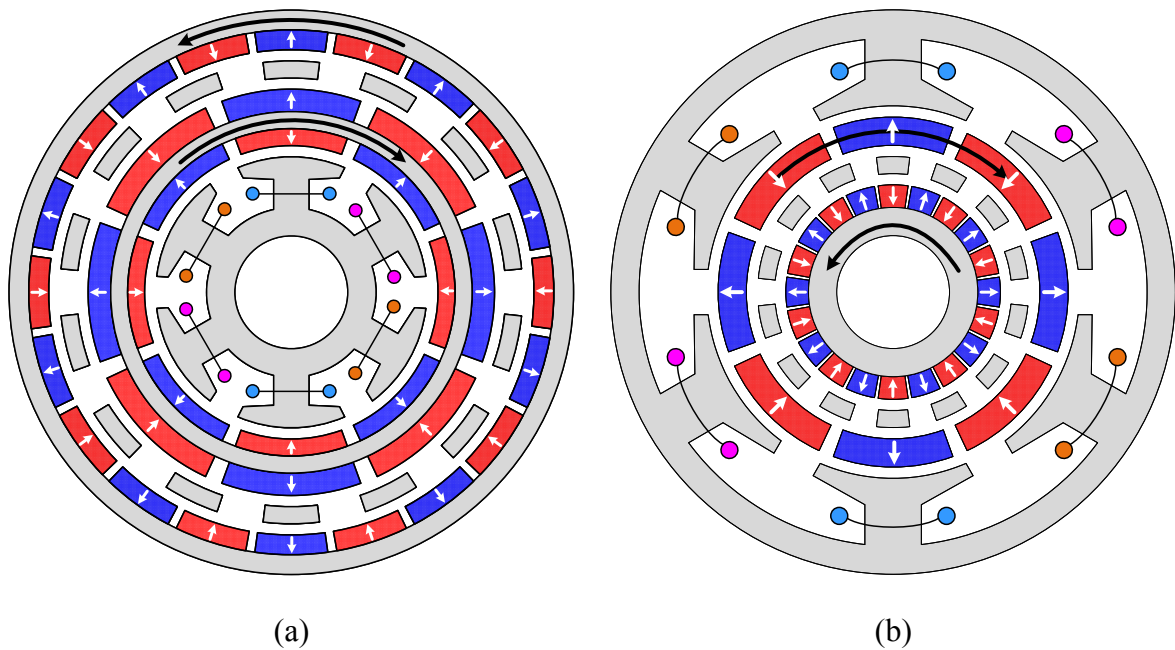
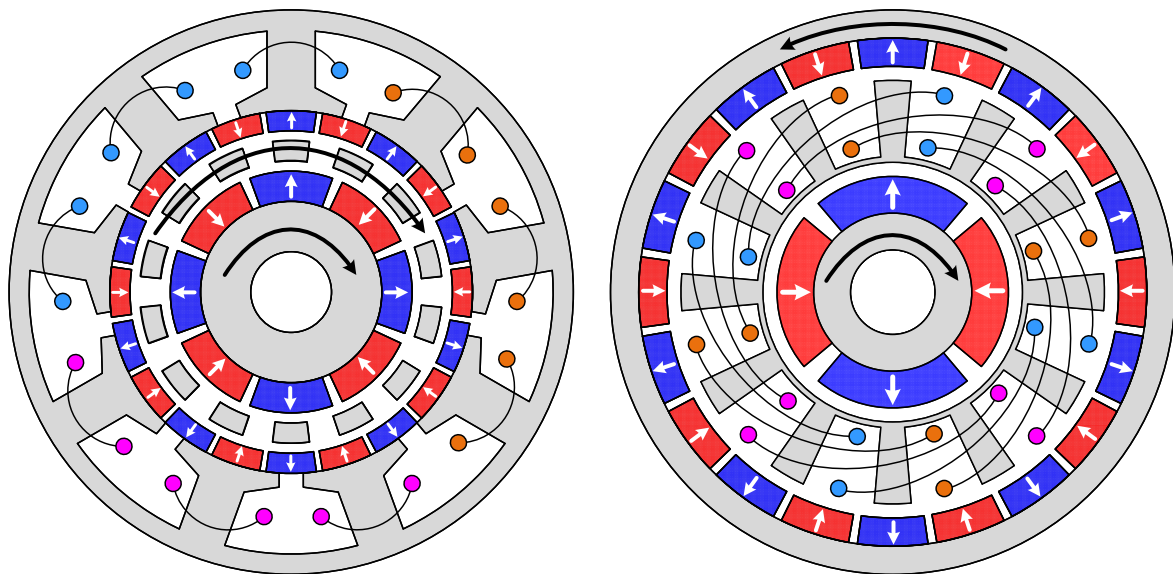


Fig. 1.19 Type1: mechanically coupled machines. (a) MG-outside [CHA07c]. (b) MG-inside [WAN11].

### 1.3.2.2 Type 2: Pseudo Machines

To drive the high-speed rotor of the MG, another approach is to add an extra set of armature windings on the low-speed element, Fig. 1.20 (a), the evolved machine is termed as Pseudo machine [ATA08]. The added armature winding can be either fractional-slot windings or integer-slot concentrated/distributed windings, it produces additional rotating field with the same pole-pair number of the high-speed rotor, thus controlling its rotational speed and direction. Since the PMs of the low-speed element are mounted on the inner surface of the fixed stator, the magnetic modulation ring and the high-speed rotor rotate in the same direction under a fixed speed ratio of  $G_r$ . Basically, the Pseudo machine can be regarded as the combination of a MG with fixed low-speed element and a SPM machine with large air-gap. In [ATA08], it shows that the Pseudo machine can have a high torque density of  $60\text{kNm/m}^3$  even with a small current density of  $2\text{A/mm}^2$ , then it has also been investigated for assorted applications, such as wind power generation and flight control surface actuation etc. [TLA16] [HUS16]. In terms of the placement of armature winding, it can be also placed on the magnetic modulation ring [JIA12] [ZHU18a]. In these cases, the modulation ring is fixed with additional overlapping (see Fig. 1.20 (b)) or non-overlapping windings (see Fig. 1.20 (c)) adopted, the low-speed PM rotor and high-speed PM rotor rotate in reverse under a fixed speed ratio of  $G_r$ .



(a)

(b)



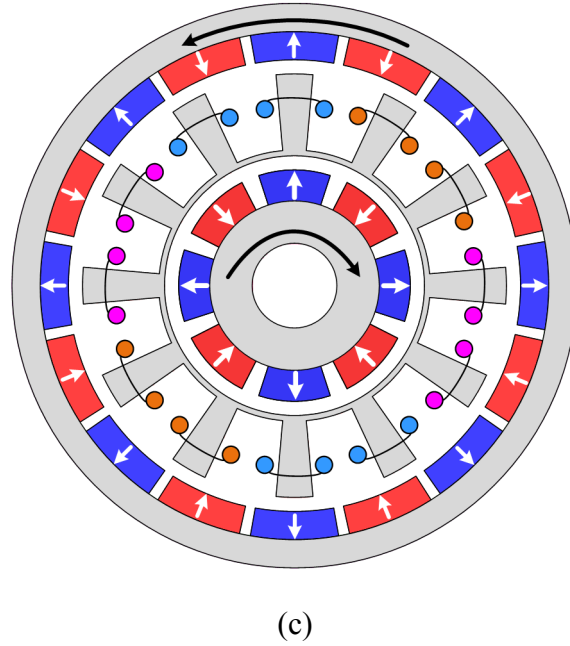


Fig. 1.20 Type 2: Pseudo machines. (a) Outer-stator [ATA08]. (b) Sandwiched-stator with overlapping windings [JIA12]. (c) Sandwiched-stator with non-overlapping windings [ZHU18a].

### 1.3.2.3 Type 3: Mechanically and Magnetically Coupled Machines

The rotating magnetic field produced by the PM rotor of the MG can be replaced by employing a stator equipped with multi-phase sinusoidal excited windings, from which the mechanically and magnetically coupled machines are derived [WAN08b]. As shown in Fig. 1.21 (a), the inner PM rotor of the MG is replaced by the armature winding. In terms of the low-speed PM rotor and the magnetic modulation ring, either one or all of them can be rotating. When the modulation ring is stationary, the machine is similar to a conventional outer-rotor machine but with dual air-gaps. For certain slot/pole number combinations, it is possible to remove the air-gap between the stationary modulation ring and wound stator by merging them into one stator with multi-tooth structure, Fig. 1.21 (b), which is identical to a typical Vernier machine. Hence, the inherent relationship between the Vernier machine and MGd machine is revealed [QU11].

By swapping the positions of the PM rotor and wound stator, the inner-rotor MGd machines have also been proposed [CRI15], which are easier to assemble for most applications. Besides, by setting both inner PM element and magnetic modulation ring as rotor, the machine can achieve functions of power split and CVT, which are suitable for HEVs [ZHE13].

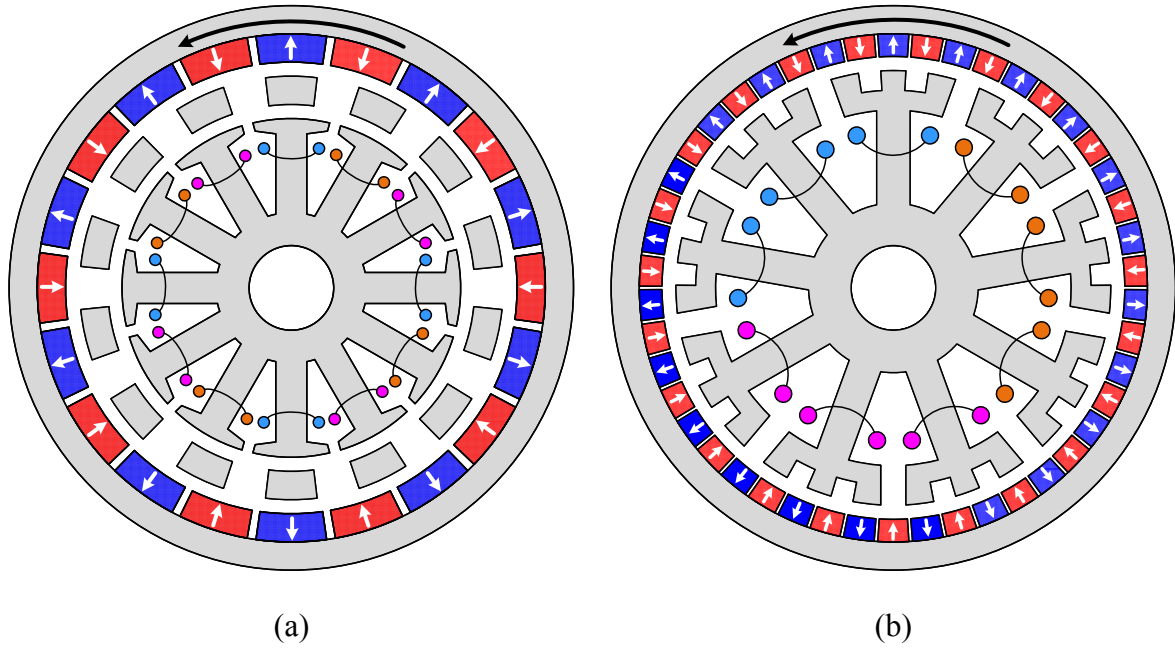


Fig. 1.21 Type 3: mechanically and magnetically coupled machines. (a) Dual air-gap [WAN08b]. (b) Single air-gap (Vernier machine) [QU11].

#### 1.3.2.4 Type 4: Partitioned Stator Machines

As depicted in Fig. 1.14, another type of MGd machines, i.e. partitioned stator machine, is newly developed based on the synergies of MGs and stator-PM machines [ZHU14]. The PS machine can be directly evolved from the stator-PM machine by separating the windings and PMs to two stators, and it always has improved torque density, thanks to the removal of space conflict between the winding and PM. Based on this concept, all kinds of stator-PM machines can be easily converted to PS machines. The difference among various PS machines lies in the pole-pair number, PM structure and relative angular position to the wound stator of the PM stator. An overview of various PS machines has been presented in [ZHU18b].

By comparing Type 4 (PS machines), Fig. 1.14 (a), with Type 3 (mechanically and magnetically coupled machines), Fig. 1.21 (a), it is found that they share many similarities in machine structure, i.e. a PM element, a wound stator, and a magnetic modulation ring. The working principle of Type 4 and their stator-PM counterparts are then analysed from the new perspective of air-gap field modulation, from which the inherent magnetic gearing effect is revealed [WU16a]. It should be noted that for Type 4, only modulation ring can rotate while the modulation ring and/or the PM element can rotate for Type 3.

### 1.3.3 Analysis of Magnetic Gearing Effect/Air-Gap Field Modulation in Flux Reversal Permanent Magnet Machines

As shown in Fig. 1.17, the MG-derived machines can directly integrate a MG into a machine, thus having very high torque density. However, due to the complex mechanical structure of these machines (i.e. dual air-gaps), the system simplification is still very necessary and challengeable to improve the system reliability and guarantee the torque benefit [FRA15]. Moreover, the development of MGs and MGd machines enable a new perspective to analyse the existing machines with single air-gap. For example, the relationship between the MG-derived machine and the Vernier machine can be directly interpreted in Fig. 1.21.

For conventional electromagnetic devices with two sets of excitation sources, a steady average force/torque can be generated only when the pole-pair number and rotational speed of the fields produced by the two sources are identical [TAN10]. However, for a MG, the average torque can be produced by two PM excitation sources with different pole-pair numbers and rotational speeds. More specifically, the torque production is resulted from the indirect interaction instead of the direct interaction of the two sources since the field provided by any PM source is firstly modulated by iron pieces so as to match the pole-pair number and speed of the other PM source. This phenomenon can thus be termed as magnetic gearing effect [TOB00] and/or air-gap field modulation [CHE17].

In terms of FRPM machines, the PM MMF harmonic  $F_{PM}$  and armature MMF harmonic  $F_{armature}$  can be expressed as

$$F_{PM} = F_m \cos(p_m \theta) \quad (1.3)$$

$$F_{armature} = F_a \cos(p_a \theta - \omega_a t - \theta_a) \quad (1.4)$$

where  $F_m$ ,  $F_a$  are the magnitudes of MMF harmonics,  $\omega_a$  is the electric frequency of armature winding and  $\theta_a$  is the initial phase of the armature MMF.

Considering the air-gap permeance distribution produced by salient pole rotor, it is

$$\Lambda_{rotor} = \Lambda_0 + \Lambda_1 \cos N_r (\theta - \Omega_r t - \theta_r) \quad (1.5)$$

where  $\Lambda_0$ ,  $\Lambda_1$  are the magnitudes of permeance distribution,  $\Omega_r$  is the mechanical angular speed of rotor, and  $\theta_r$  is the initial position of rotor.

Since both PM MMF and armature MMF are subjected to rotor-tooth modulation, the air-gap PM field  $B_{PM}$  and armature field  $B_{armature}$  can be written as

$$B_{PM} = F_{PM} \Lambda_{rotor} = \Lambda_0 F_m \cos(p_m \theta) + \Lambda_1 F_m \cos[(N_r \pm p_m) \theta - N_r (\Omega_r t + \theta_r)] \quad (1.6)$$

$$B_{armature} = F_{armature} \Lambda_{rotor} = \Lambda_0 F_a \cos(p_a \theta - \omega t - \theta_a) + \Lambda_1 F_a \cos[(N_r \pm p_a) \theta - (N_r \Omega_r \pm \omega_a) t - (\theta_r \pm \theta_a)] \quad (1.7)$$

The orders and frequencies of air-gap field harmonics are then summarised in Table 1.2.

Before rotor-tooth modulation, the air-gap PM field harmonics are all static (i.e.  $\omega=0$ ) since PMs are mounted on stator. In contrast, the frequencies of air-gap armature field harmonics are all equal to  $\omega_a$ . Therefore, there would be no steady torque component since PM and armature field harmonics are with different rotational speeds (i.e. frequencies).

After rotor-tooth modulation, more PM and armature field harmonics are produced. A steady torque component can be produced when a PM field harmonic has the same order and frequency as any armature field harmonic, which can be expressed as

$$p_m \pm p_a = N_r \quad (1.8)$$

$$N_r \Omega_r \pm \omega_a = 0 \quad (1.9)$$

Table 1.2 Orders and frequencies of air-gap field harmonics

		Order	Frequency $\omega$
Before modulation	PM field	$p_m$	0
	Armature field	$p_a$	$\omega_a$
After modulation	PM field	$p_m$	0
		$N_r \pm p_m$	$N_r \Omega_r$
	Armature field	$p_a$	$\omega_a$
		$N_r \pm p_a$	$N_r \Omega_r \pm \omega_a$

Up to now, several literatures have tried to analyse the inherent magnetic gearing effect and/or air-gap field modulation effect in FRPM machines.

From the perspective of torque production (i.e. magnetic gearing effect), the FRPM machine is interpreted as the combination of a fictitious gear and a conventional PMSM [MOR10b], as shown in Fig. 1.22. Such a fictitious gear reflects the ratio of the flux pattern variation speed over the rotor rotational speed. Taking the 6/14 FRPM machine as an example (see Fig. 1.7 (b)), its flux pattern inside the stator and rotor cores is equivalent to a 2-pole PMSM and the flux pattern variation speed is  $N_r$  times of the rotor shaft speed  $n$  [MOR10b]. Thus, the electrical frequency  $f$  of the FRPM machine is  $nN_r/60$  instead of  $n/60$ . However, the schematic diagram shown in Fig. 1.22 cannot be used to quantify the machine performance since the torque of the 6/14 FRPM machine can never be improved by  $N_r$  times of a conventional 2-pole PMSM. This can be explained by the fact that the magnitude of the 2-pole flux pattern in the FRPM machine is much lower than the normal level in a conventional 2-pole PMSM. In fact, there are multi working harmonic pairs of the air-gap PM and armature fields, which differs from the PMSMs (only one harmonic pair produces torque). The detailed analysis of multi working harmonic pairs in FRPM machines will be given in the following chapters.

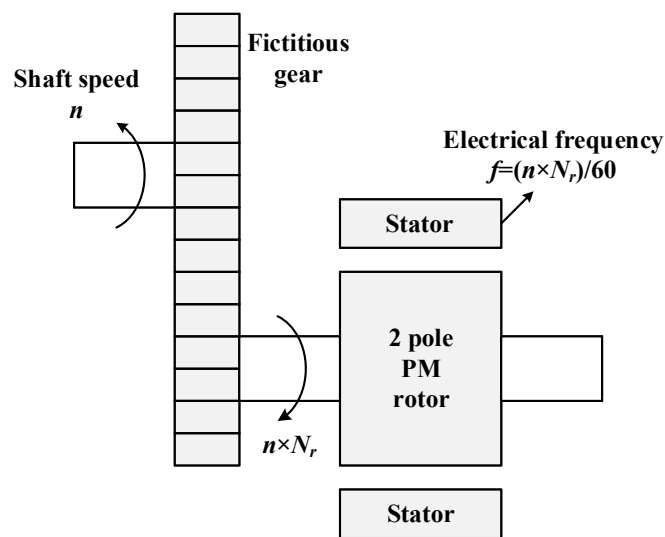


Fig. 1.22 Schematic of the fictitious gear in 6/14 FRPM machine [MOR10b].

From the perspective of air-gap field (i.e. field modulation effect), a number of literatures have recently been published, aiming to more clearly demonstrate the working principle of FRPM machines [GAO16a] [GAO17a] [GAO17b] [ZHU19]. In these papers, the PM MMF-permeance analytical model is established for FRPM machines, from which the no-load air-gap PM field can be accurately calculated (see (1.6)). By further introducing the winding functions, the back-EMF of the machines can be obtained. It reveals that several harmonics of the no-load air-gap field contribute to the back-EMF, which differs from the conventional

PMSM (i.e. only the fundamental no-load air-gap field produces back-EMF). The influence of  $N_s/N_r$  combinations and dimensional parameters on the machine performance can then be investigated. However, in these papers, only the working harmonics of the no-load air-gap field are focused while the contributions of working harmonics of the originated PM MMF and permeance distributions have not been quantified, which are actually very useful in analysing and designing the high-performance FRPM machines. For example, if the contributions of different PM MMF harmonics are quantified, the PM arrangements of the machines can be optimally adjusted to intensify the magnitudes of the most critical PM MMF harmonics. Therefore, a more comprehensive analysis of air-gap field modulation in FRPM machines will be addressed in this thesis.

## **1.4 Scope of Research and Contributions of Thesis**

### **1.4.1 Scope of Research**

This thesis systematically investigates and analyses the flux reversal permanent magnet machines, with a particular focus on torque improvement. Various aspects of PM arrangement and different winding configurations are investigated in detail, and several FRPM machine topologies with superior torque density are proposed as well. The air-gap field modulation theory is adopted and developed throughout the thesis, from which the working mechanism of the FRPM machines is clearly explained, and the principle comparison between the FRPM machine and the Vernier machine is presented. The conclusions and findings of this thesis are validated by both FEA and experiment.

The research scope of this thesis and arrangement of chapters are shown in Fig. 1.23. Various FRPM machine topologies investigated in this thesis are shown in Fig. 1.24. The aims and contents of each chapter are summarised as follows:

#### **Chapter 1**

*Aims: to identify the significances and necessities of this thesis.*

This chapter reviews the relevant backgrounds and developments of the FRPM machine. It shows that the torque improvement is critical to promote the development of the FRPM machine, and various aspects of boosting the machine performance still need to be

systematically investigated, such as the PM arrangement methods and winding configurations. Besides, a clear illustration of the working mechanism in the FRPM machine is also necessary.

## **Chapter 2**

*Aims: to investigate the influence of PM polarities of adjacent teeth on machine performance.*

In this chapter, the most commonly adopted four PM arrangements in FRPM machines will be comprehensively analysed and compared, with the aid of FEA. For each PM arrangement, the working harmonics of air-gap fields and their contributions to the torque production will be identified. The influence of stator slot/rotor pole combinations will then be investigated. Based on the optimal  $N_s/N_r$  combinations, the electromagnetic performance of the four machines will be compared with a particular focus on the influence of PM polarities of adjacent teeth. Results show that opposite PM polarities of adjacent teeth are preferred in terms of torque density. Four prototype FRPM machines corresponding to four different PM arrangements will be manufactured and tested to validate the analyses.

## **Chapter 3**

*Aims: to identify the optimal number of PM pieces on each stator tooth.*

In this chapter, a unified PM MMF-permeance analytical model of FRPM machines having different numbers of PM pieces on single stator tooth will be established, from which the optimal number of PM pieces on single stator tooth and the corresponding rotor pole number can be identified. By using the developed analytical model, the influence of critical design parameters, including stator slot opening ratio, split ratio, PM thickness, and rotor slot ratio etc. will also be investigated. Results show that by employing the optimal number of PM pieces instead of the conventional two on each stator tooth of the FRPM machine, additional fundamental back-EMF improvement can be generated which is beneficial to improve the torque. Three prototype FRPM machines having different numbers of PM pieces on each stator tooth will be manufactured and tested to validate the analyses.

## **Chapter 4**

*Aims: to provide a comprehensive evaluation of the FRPM machines with various consequent-pole PM topologies.*

In this chapter, the FRPM machines with various CPM topologies will be comprehensively investigated. The torque improvement mechanism of CPM-FRPM machines over SPM-FRPM machines and the influence of stator slot/rotor pole combinations of CPM-FRPM machines will firstly be analysed. Then four CPM topologies will be introduced and compared, from which the CPM topology with the highest torque density can be identified. The influence of critical design parameters especially the PM dimensions on the machine performance will also be parametrically investigated. By comparing the electromagnetic performance of CPM topologies with their SPM counterparts, the advantages and disadvantages of CPM topologies in FRPM machines, will be clearly revealed. Four FRPM prototypes will be manufactured and tested to verify the analyses.

## **Chapter 5**

*Aims: to develop a high torque density FRPM machine with toroidal windings.*

In this chapter, the FRPM machine with toroidal windings will be proposed and analysed with reference to conventional concentrated windings. Firstly, the influence of rotor pole numbers on the performance of FRPM machines with conventional concentrated windings will be investigated. By adopting toroidal windings instead of concentrated windings in FRPM machines under specific stator slot/rotor pole combinations, the pitch factor and resulted torque performance can be effectively improved. The critical design parameters and electromagnetic performance of the 12/13 FRPM machines with both winding types will also be analysed and compared. It is shown that the 12/13 FRPM machine with toroidal windings has higher torque, efficiency, power factor, and lower torque ripple. Finally, two FRPM prototypes with toroidal windings and concentrated windings will be manufactured and tested to validate the analyses.

## **Chapter 6**

*Aims: to compare the performance of FRPM machines and Vernier machines.*

In this chapter, the torque production mechanisms of FRPM machines and Vernier machines will be compared based on the unified airgap field modulation theory. Working harmonics of PM MMF and airgap permeance in two conventional 6/10 machines will be analytically identified and compared. Influence of critical dimensional parameters on the machine performance, such as PM thickness and slot width ratio of the flux modulation pole, will also be investigated. It is revealed that the torque density of a Vernier machine is more likely to be higher than that of a conventional FRPM machine, due to the utilised large DC component of



the airgap permeance. Both FEA and experimental validation will be conducted to verify the conclusions. In addition to the conventional FRPM machine, the performance of several promising FRPM machines proposed and analysed in the previous chapters will also be compared with that of the Vernier machine. Results show that these FRPM machines can have similar or even higher torque density than the Vernier machine while their PM volume can be largely reduced.

## Chapter 7

The general conclusions of this thesis and potential future work are summarised in this chapter.

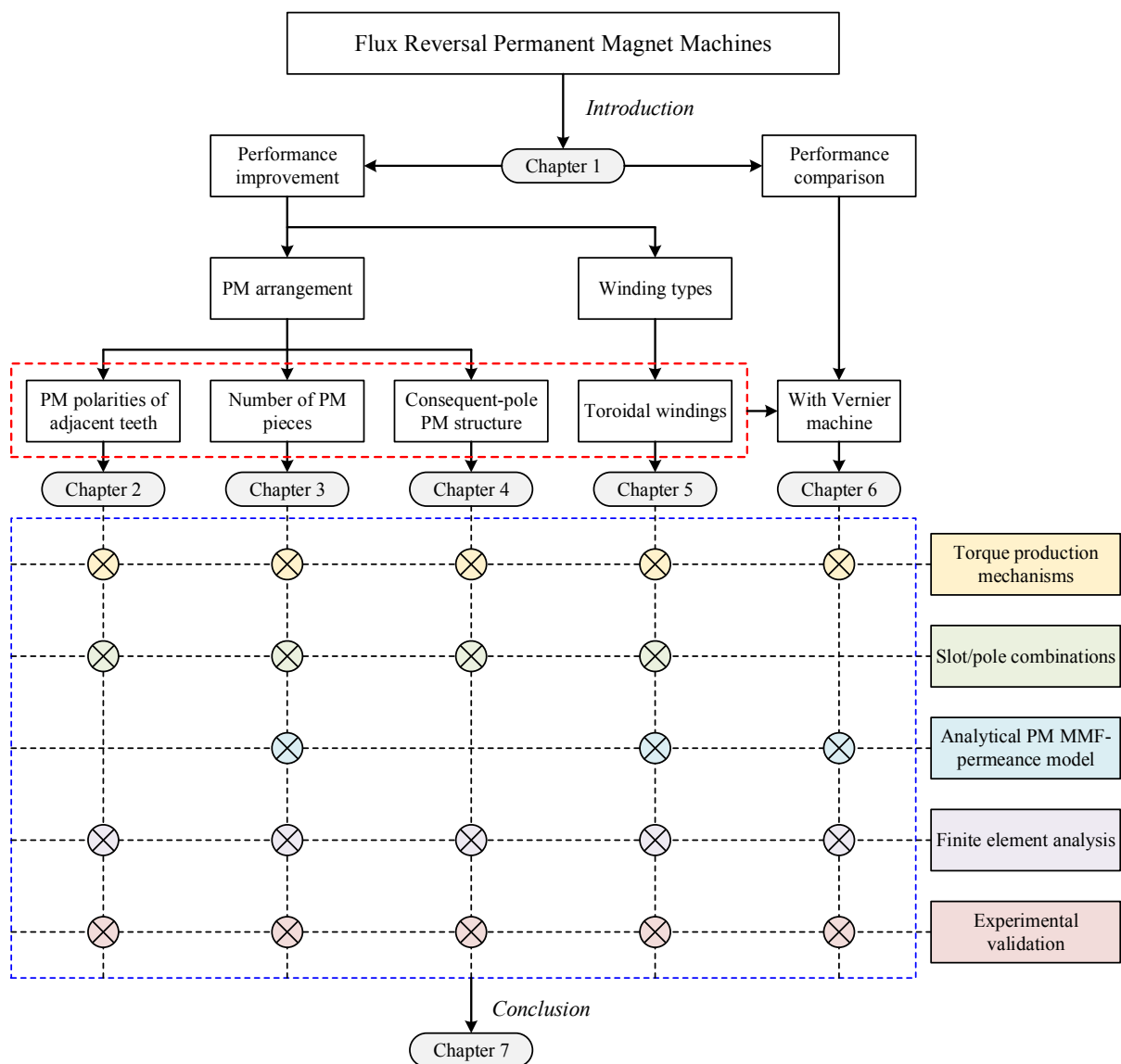
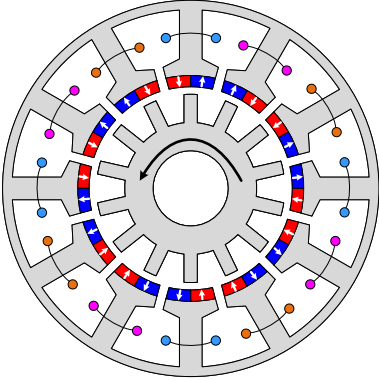
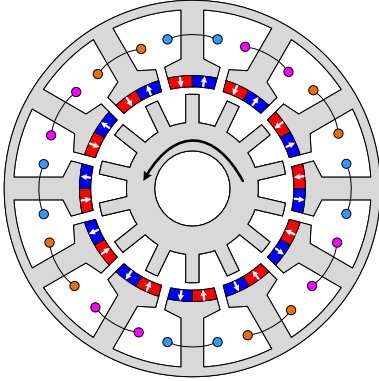
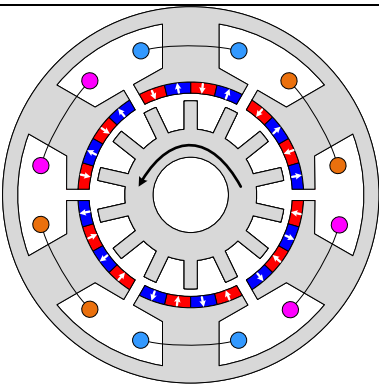
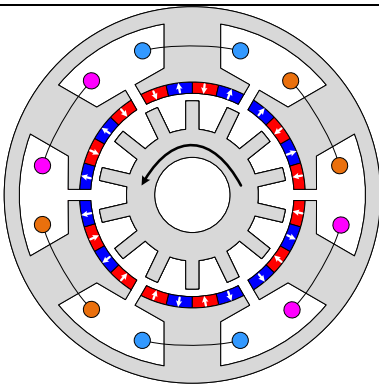
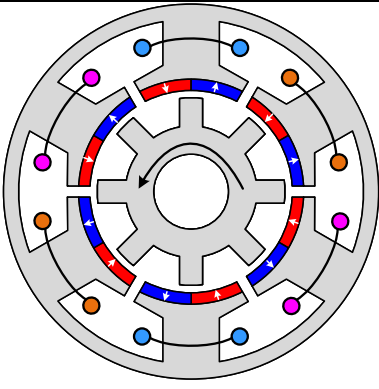
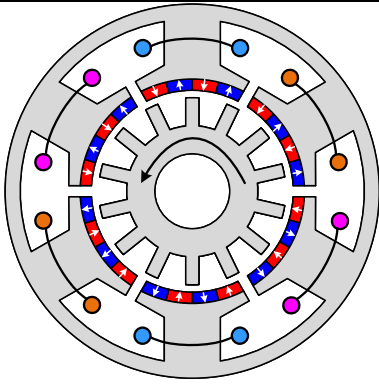
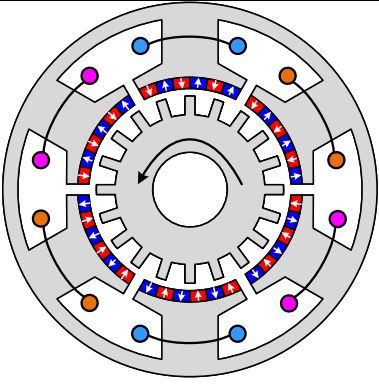


Fig. 1.23 Research scope and arrangement of chapters.

<p>Chapter 2</p>		
<p>Four PM arrangements</p>		
<p>Chapter 3</p>		
<p>Different numbers of PM pieces</p>		

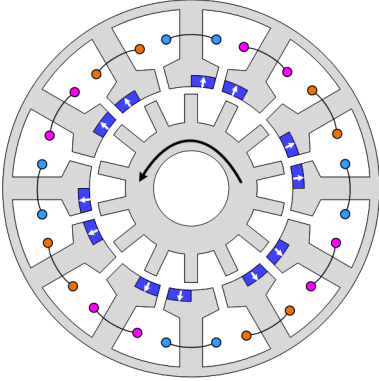
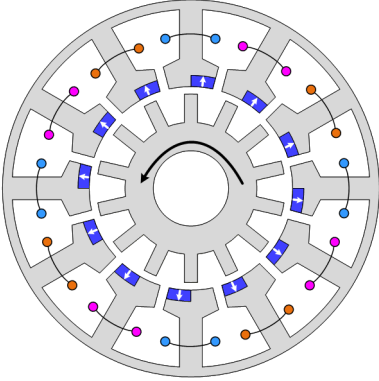
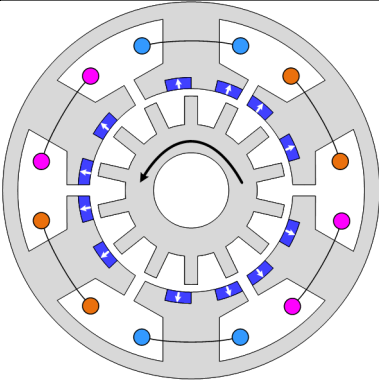
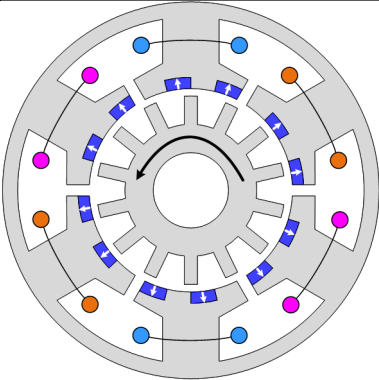
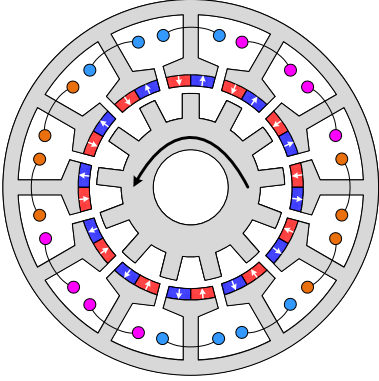
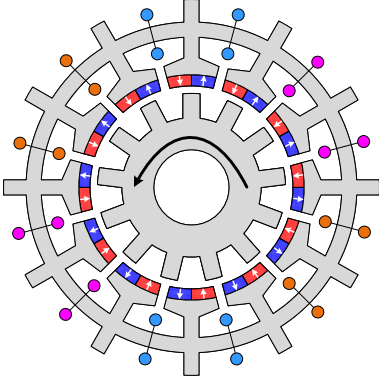
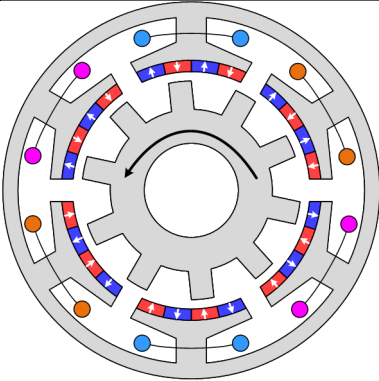
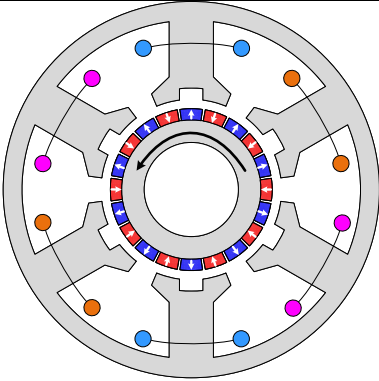
<p>Chapter 4</p> <p>Four CPM topologies</p>		
		
<p>Chapter 5</p> <p>CWs and TWs</p>		
<p>Chapter 6</p> <p>Comparison with Vernier machine</p>		

Fig. 1.24 Various FRPM machine topologies investigated in this thesis.

## 1.4.2 Main Contributions of Thesis

The contributions of this thesis are summarised as follows:

- Based on the theory of air-gap field modulation, the working harmonics of PM MMF and permeance are identified and the contribution of each working harmonic to machine torque is quantified, which provide a deeper understanding of the torque production mechanism in FRPM machines;
- The influences of PM polarities of adjacent teeth and number of PM pairs on each stator tooth are comprehensively investigated, which provide a useful guidance to the design of high-performance FRPM machines;
- Applying various CPM topologies and toroidal windings to FRPM machines, which effectively improves the torque density, efficiency, power factor, and enriches the topologies of the FRPM machines;
- Comparing FRPM machines with Vernier machines based on the unified air-gap field modulation theory, from which the inherently higher torque density of the Vernier machine over the conventional FRPM machine is revealed. However, by using the torque improvement techniques presented in this thesis, several novel FRPM machines are proven to have competitive or even higher torque density than the Vernier machine.

# CHAPTER 2

## INFLUENCE OF PM POLARITIES OF ADJACENT TEETH ON ELECTROMAGNETIC PERFORMANCE OF FLUX REVERSAL PERMANENT MAGNET MACHINE

For FRPM machines, there exist several kinds of PM arrangement which can be characterised by the number of PM pieces on each stator tooth and the PM polarities of adjacent teeth. Taking a three-phase and 14-rotor-pole FRPM machine as an example, in total four PM arrangements, which are most commonly adopted, will be comprehensively compared in this chapter. With the aid of FE analysis, the influence of PM arrangement, particularly the PM polarities of adjacent teeth, on electromagnetic performance of FRPM machine will be demonstrated, and the most promising PM arrangement in terms of the maximum average torque will also be identified. Four prototype FRPM machines corresponding to four different PM arrangements will be manufactured and tested to validate the analyses.

This chapter is published in *IEEE Trans. Ind. Appl.*, vol. 55, no.1, 2019, doi: 10.1109/TIA.2018.2867818.

### 2.1 Introduction

In comparison with the conventional rotor-PM machines, the stator-PM machines feature a salient pole rotor without any coil or PM and a possible high rotor pole number, which make them suitable for low-speed and high-torque applications where high torque density and high mechanical strength are required [CHE11a]. In addition, the stator-PM machines are likely to have superior heat dissipation capability since both heat sources (coils and PMs) are in the stator, which are static, and thus easy to equip efficient cooling design [ZHU10]. According to different PM placements, the stator-PM machines are normally categorised into four groups, which are DSPM machines, SFPM machines, SSPM machines and FRPM machines, respectively. In comparison with the other three kinds of stator-PM machines, a FRPM machine has unique advantage of rigid stator structure, thus exhibiting promising prospect for various applications [BOL02] [KIM04].

The most conventional three-phase FRPM machine was firstly proposed in [WAN99] and is shown in Fig. 2.1. As can be seen, two PM pieces with alternate polarities (labelled as ‘PM1’ and ‘PM2’) are mounted on the inner surface of each stator tooth, and the adjacent two PM pieces belonging to two adjacent stator teeth (labelled as ‘PM2’ and ‘PM3’) have the same magnetisation polarities. For the sake of clarity, such PM arrangement is designated as NS-SN, and a simple schematic is given in Fig. 2.2 (a).

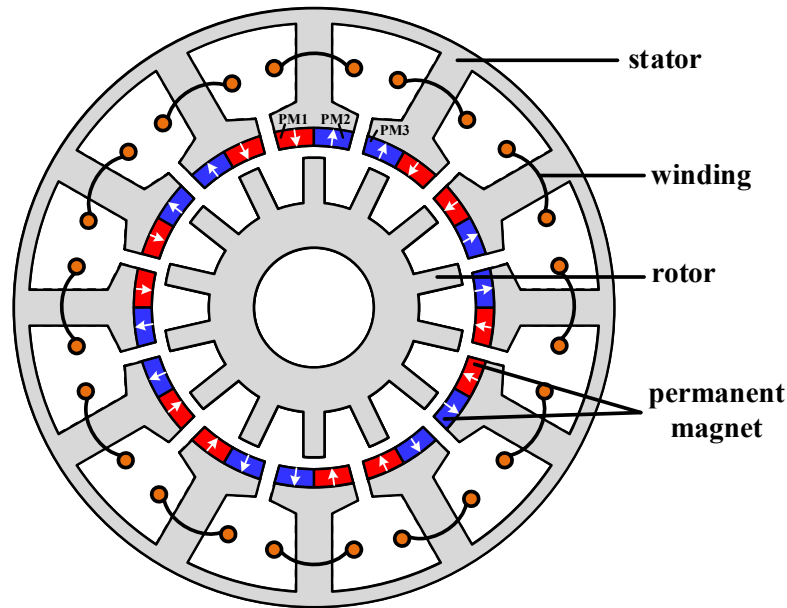


Fig. 2.1 Cross section of the most conventional three-phase FRPM Machine.

Except for the original NS-SN, other PM arrangements have also been successively proposed. By changing the PM polarities of adjacent teeth from identical to opposite, the PM arrangement (denoted as NS-NS) was firstly proposed in a linear FRPM machine in [CHU08] and then investigated for three-phase rotating FRPM machines [PEL11] [HUA18]. As depicted in Fig. 2.2 (b), in comparison with NS-SN, still two PM pieces are mounted on each stator tooth in NS-NS, but the relative PM polarities of all the stator teeth are the same. In addition, based on NS-SN, by mounting two pairs of PM pieces instead of one on a single stator tooth, the PM arrangement of NSNS-SNSN is shown in Fig. 2.2 (c). The two adjacent PM pieces on different stator teeth still have identical polarities in NSNS-SNSN, and such arrangement was firstly proposed in a three-phase rotating FRPM machine for low-speed servo applications [BOL02]. Similarly, by changing the PM polarities of adjacent teeth of NSNS-SNSN from identical to opposite, another PM arrangement is shown in Fig. 2.2 (d) and is designated as NSNS-NSNS. For each PM arrangement, concentrated-windings are always adopted, offering advantage of

short end-winding. However, the winding connections of different PM arrangements differ with each other, which will be explained later.

Although NS-SN, NS-NS, NSNS-SNSN, and NSNS-NSNS have been proposed separately, the existing literatures are all focused on the performance of a single FRPM machine with one specific PM arrangement instead of comparing the influence of different PM arrangements. Besides, the analysis of NSNS-NSNS is incomplete since it is only mentioned in a two-phase linear FRPM machine in [IWA94] and no other literature can be found. It is expected that the PM arrangement of the FRPM machine is worthy of further investigation since it directly affects the air-gap field distribution and corresponding performance. Therefore, in this chapter, the four PM arrangements are all extended to three-phase rotating FRPM machines and a comprehensive analysis of performance difference among the different PM arrangements will be given, and particularly, the influence of PM Polarities of adjacent teeth will be emphasised.

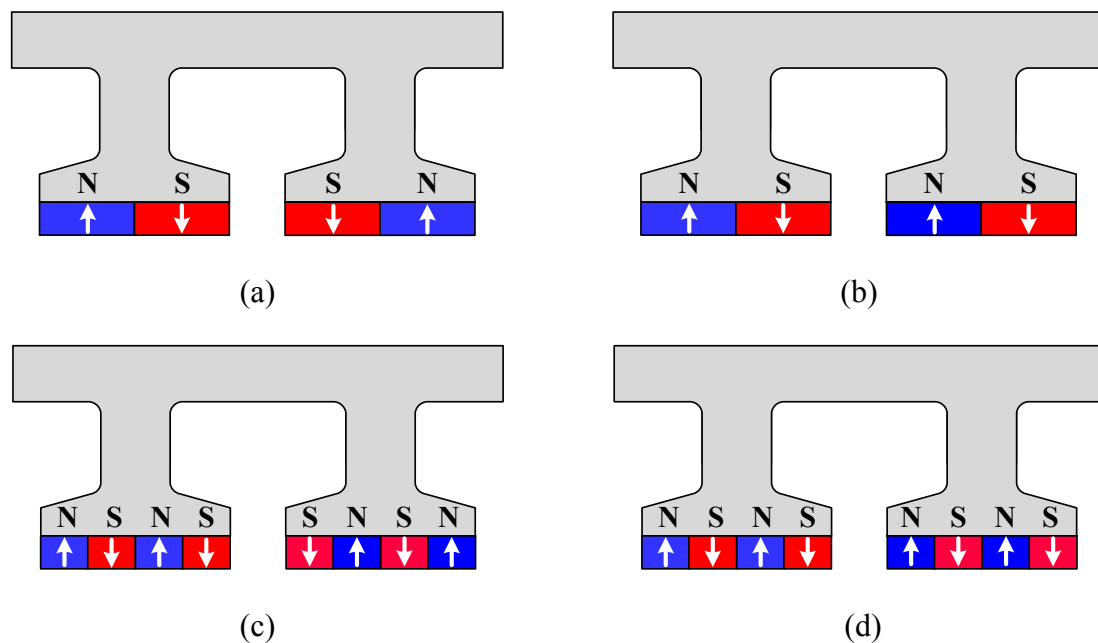


Fig. 2.2 Schematics of four kinds of PM arrangements in FRPM machines. (a) NS-SN. (b) NS-NS. (c) NSNS-SNSN. (d) NSNS-NSNS.

## 2.2 Working Principle of FRPM Machines with Different PM Arrangements Considering PM Polarities of Adjacent Teeth

The working principle of a PM machine can be mainly investigated from two perspectives. The first is from the perspective of a generator, i.e. how the back-EMF is induced as rotor rotates; the second is from the perspective of a motor, i.e. how the air-gap harmonic pairs having the

same pole-pair number, rotational speed and direction are produced when the current is injected. In this chapter, the working principle of FRPM machines will be demonstrated from both perspectives. More specifically, the flux linkage variations of FRPM machines against rotor position will be presented firstly, from which an intuitive understanding of working mechanisms of different PM arrangements can be obtained. Then, the air-gap field harmonics produced by either PM MMF or armature MMF will be analysed in detail, from which the working harmonics contributing to the torque production can be identified and the influence of PM arrangement on the machine performance can be well explained.

### 2.2.1 Flux Linkage Variation

For the FRPM machine with conventional NS-SN arrangement, its inherent characteristic of bipolar flux linkage has been pointed out and investigated in some literatures [CHE11a] [HUA18], as shown in Fig. 2.3. This typical flux linkage variation waveform can be also extended to other PM arrangements.

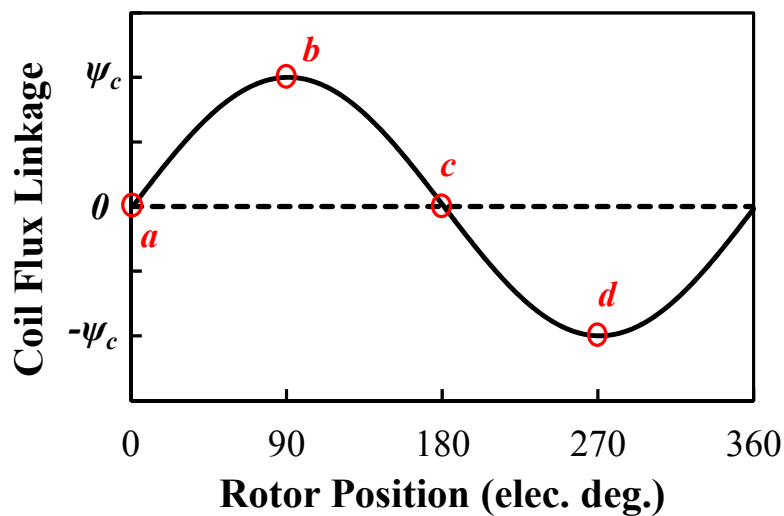


Fig. 2.3 Typical variation of flux linkage in a single coil of FRPM machines.

Taking the conventional 14-rotor-pole FRPM machines as an example, the no-load flux distributions through a single coil A1 of four PM arrangements under different rotor positions are presented in Fig. 2.4, Fig. 2.5, Fig. 2.6, and Fig. 2.7, respectively. As depicted in Fig. 2.4, at rotor position *a*, a rotor tooth is aligned with the stator tooth (i.e. the axis of the coil A1), and no flux passes through the coil A1 since the fluxes directly circle through the stator tooth tip and the rotor tooth.



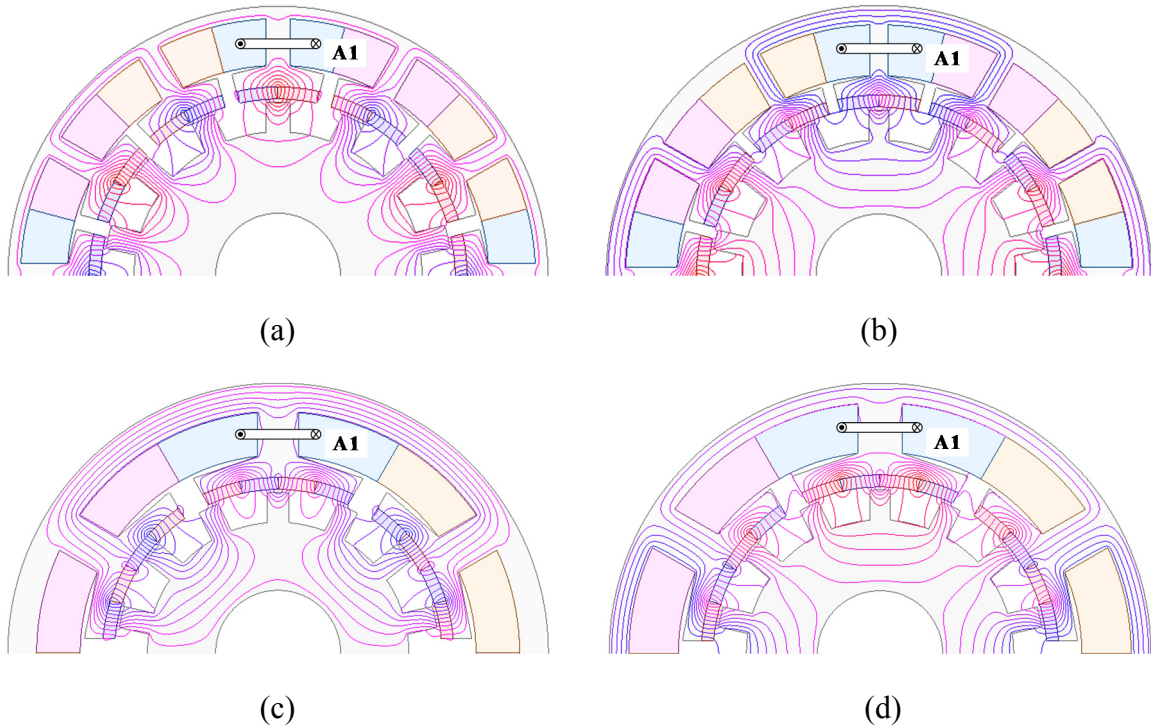


Fig. 2.4 No-load field distributions of 14-rotor-pole FRPM machines at rotor position  $a$  (flux linkage of coil A1 is zero). (a) NS-SN. (b) NS-NS. (c) NSNS-SNSN. (d) NSNS-NSNS.

At rotor position  $b$  (see Fig. 2.5), for both NS-SN and NS-NS, a rotor tooth is aligned with the N magnet on the stator tooth, having maximum positive fluxes linking the coil A1 (assuming that the magnetisation direction of N magnet is outward and is defined as positive). For both NSNS-SNSN and NSNS-NSNS, there are two rotor teeth aligning with the two N magnet pieces on the stator tooth, and the flux linkage of the coil A1 achieves the maximum value as well. As shown in Fig. 2.6, at rotor position  $c$ , when the rotor slot is aligned with the stator tooth, the flux linkage of the coil A1 returns to zero. At rotor position  $d$  (see Fig. 2.7), for NS-SN and NS-NS, a rotor tooth is aligned with the S magnet; for NSNS-SNSN and NSNS-NSNS, two rotor teeth are aligned with the two S magnet pieces. Thus, the coil flux linkage achieves the negative maximum value.

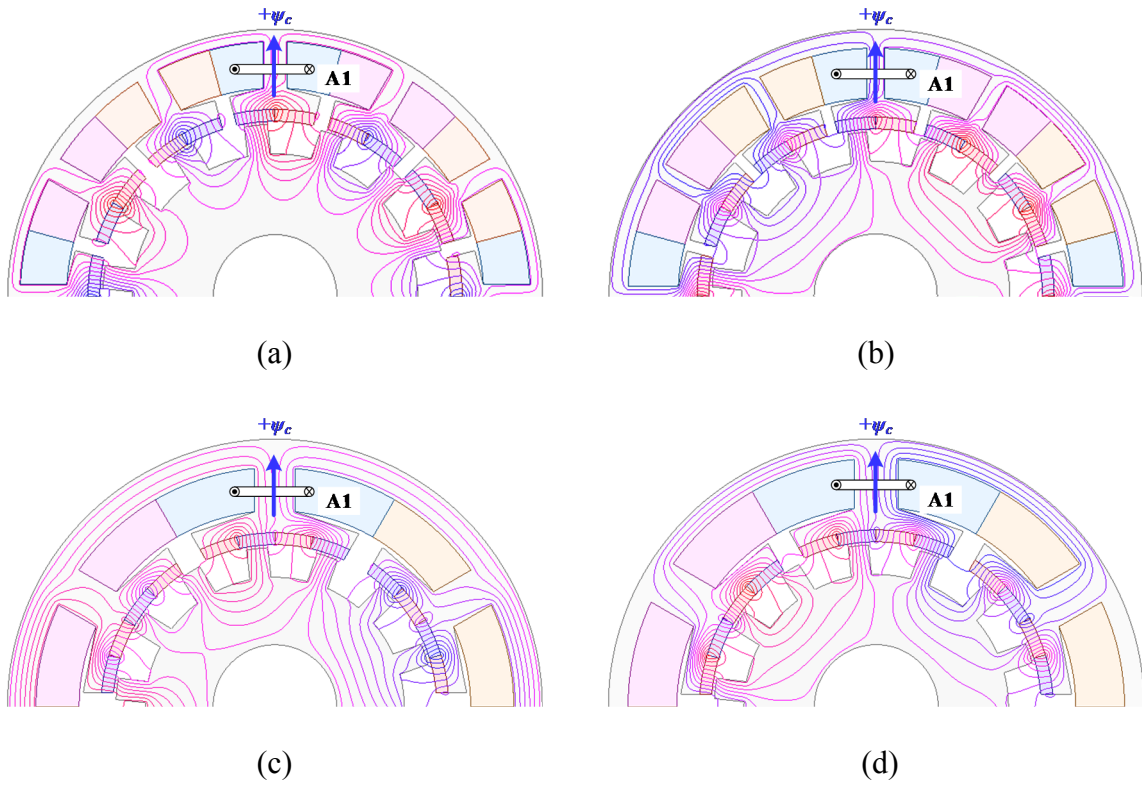


Fig. 2.5 No-load field distributions of 14-rotor-pole FRPM machines at rotor position  $b$  (flux linkage of coil A1 is the positive max.). (a) NS-SN. (b) NS-NS. (c) NSNS-SNSN. (d) NSNS-NSNS.

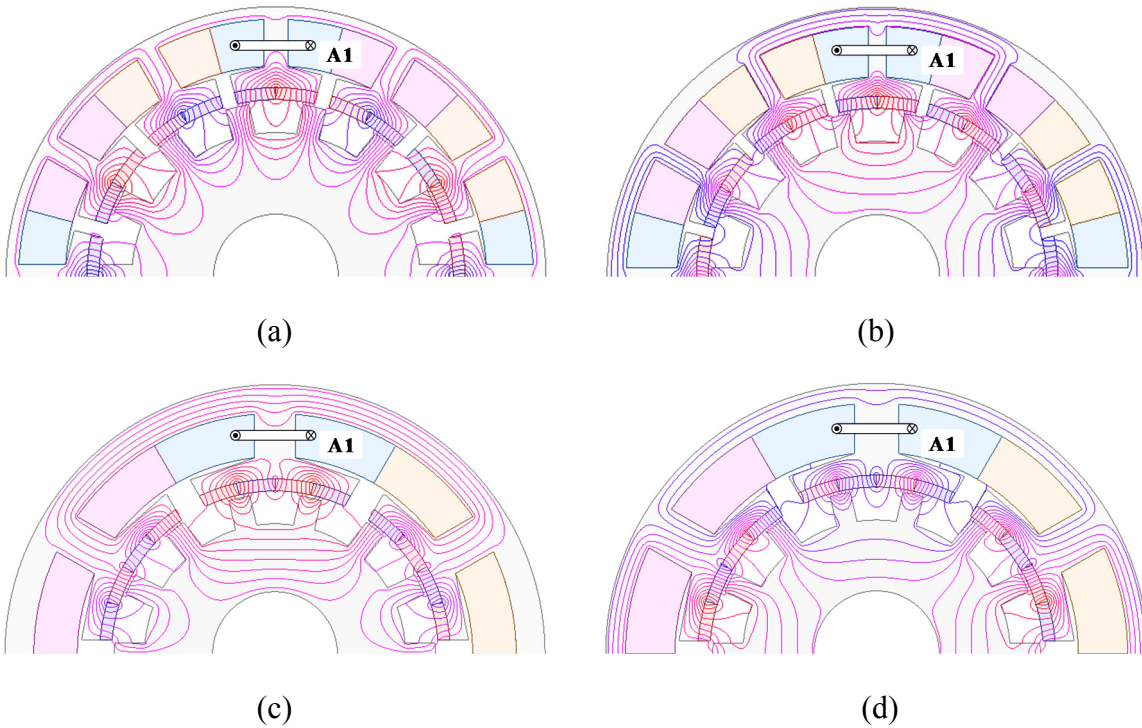


Fig. 2.6 No-load field distributions of 14-rotor-pole FRPM machines at rotor position  $c$  (flux linkage of coil A1 is zero). (a) NS-SN. (b) NS-NS. (c) NSNS-SNSN. (d) NSNS-NSNS.

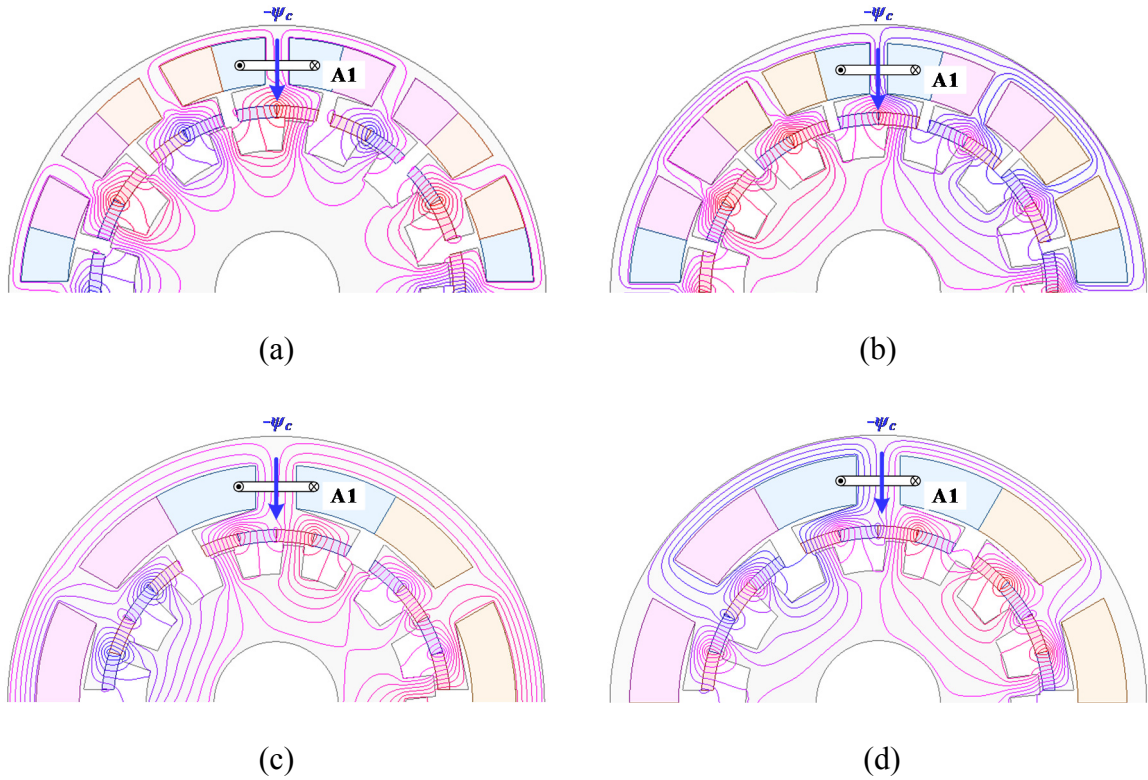


Fig. 2.7 No-load field distributions of 14-rotor-pole FRPM machines at rotor position  $d$  (flux linkage of coil A1 is the negative max). (a) NS-SN. (b) NS-NS. (c) NSNS-SNSN. (d) NSNS-NSNS.

Therefore, for each PM arrangement, the coil flux linkage of FRPM machine varies against rotor position. By properly connecting the different coils in one phase, the phase flux linkage and the corresponding phase back-EMF waveform can be obtained. Consequently, by injecting three-phase currents into the windings, a steady torque can be produced.

### 2.2.2 Air-gap Field Produced by PM MMF

Although the flux linkage variation can be used to understand the working principle of FRPM machines with different PM arrangements, it is still difficult to quantify the influence of PM arrangement on the machine performance. Thus, the air-gap field harmonics will be calculated and analysed in detail, with the aid of FEA.

It is well known that in a conventional rotor-PM machine, the torque is produced by the interaction between the fundamental fields originated from PM MMF and armature MMF. However, the working principle becomes more complex in a FRPM machine since both PM MMF and armature MMF are subjected to the rotor-tooth modulation [GAO16a], resulting in

abundant field harmonics in the air-gap. The pole-pair numbers and rotational speeds of these harmonics can be expressed as [ATA01]

$$p_{m,k} = |mp + kN_r| \quad (2.1)$$

$$\Omega_{m,k} = \frac{mp}{mp + kN_r} \Omega_a + \frac{kN_r}{mp + kN_r} \Omega_r \quad (2.2)$$

where  $p$  is the fundamental pole-pair number of the PM MMF or armature MMF,  $m$  is the corresponding order of Fourier series,  $N_r$  is the rotor pole number,  $k$  is the order of Fourier series of permeance ratio produced by salient rotor teeth,  $\Omega_a$  is the rotational speed of the fundamental armature MMF or PM MMF, and  $\Omega_r$  is the mechanical rotational speed of the rotor.

From (2.1), it is obvious that PM arrangement directly affects the PM field since the fundamental pole-pair number of PM MMF ( $p_m$ ) varies with PM arrangement. Four 14-rotor-pole FRPM machines with different PM arrangements are firstly optimized aiming at the maximum torque by using genetic-algorithm-based global optimization in Maxwell FE software, and their key design parameters are listed in Table 2.1. The stator slot number  $N_s$  of the NS-SN and the NS-NS is 12, while for the NSNS-SNSN and the NSNS-NSNS,  $N_s=6$ . The concentrated winding is adopted for all the machines, resulting in short end windings. The effective copper loss of all the machines is fixed at 20W. It should be noted that although the obtained optimum value of PM thickness  $h_m$  is slightly less than 2mm,  $h_m$  is manually adjusted to 2mm due to the consideration of manufacturability and demagnetisation withstand capability. The influence of  $h_m$  on machine performance will be demonstrated later.

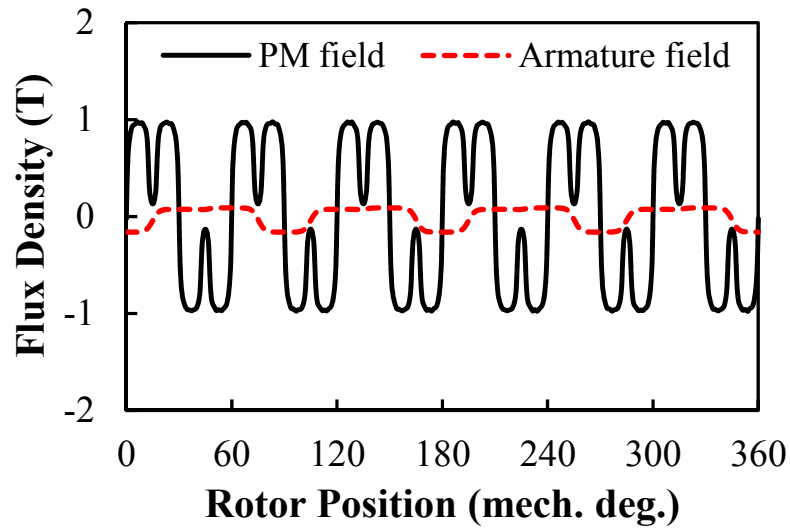
Based on the optimum FE models, the air-gap field distributions of different PM arrangements are calculated and analysed. In terms of the air-gap field produced by PM MMF (i.e. no-load air-gap field), both the PM fields with/without rotor-tooth modulation are considered. In the calculation of air-gap fields without rotor-tooth modulation, a slot-less rotor is adopted in FE software (i.e. no rotor slot exists, and the air-gap length is kept as 0.5mm).

For the 12/14 stator-slot/rotor-pole NS-SN, Fig. 2.8 shows the air-gap PM field without rotor-tooth modulation (at a fixed time of  $t=0s$ ), while the PM field with rotor-tooth modulation is shown in Fig. 2.9. Based on (2.1), the harmonic orders of the PM MMF and permeance ( $m_1, k_1$ ) are labelled as well. As can be seen from Fig. 2.8,  $p_m=N_s/2=6$  and the PM field harmonics

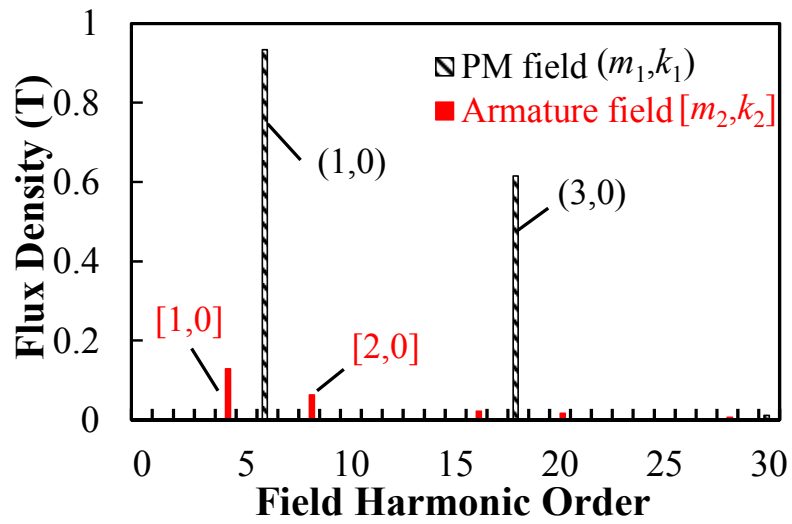
which are odd times of  $p_m$  exist, e.g., the 6th and the 18th. It should be noted that both the 6th ( $m_1=1$ ) and the 18th ( $m_1=3$ ) harmonics are of considerable magnitude due to the specific distribution of the PM MMF [GAO16a]. In terms of the rotor-tooth modulation effect, as shown in Fig. 2.9, it is clear that the PM MMF is mainly subjected to the modulation of the fundamental permeance distribution, i.e.,  $k_1=\pm 1$ , thus producing additional field harmonics, e.g., the 4<sup>th</sup> ( $m_1=3, k_1=-1$ ), the 8<sup>th</sup> ( $m_1=1, k_1=-1$ ), and the 20<sup>th</sup> ( $m_1=1, k_1=1$ ).

Table 2.1 Parameters of the optimum FRPM FE models with four PM arrangements

	NS-SN	NS-NS	NSNS-SNSN	NSNS-NSNS
Stator outer diameter $D$ (mm)			90	
Axial length $l$ (mm)			25	
Air-gap length $g$ (mm)			0.5	
Remanence of PM $B_r$ (T)			1.2	
Relative permeability of PM $\mu_r$			1.05	
Thickness of stator yoke $t_{sy}$ (mm)	2.1	3.2	4.8	3.3
Width of stator tooth $w_{st}$ (mm)	4	3	6.8	7.4
Width of stator slot opening $w_{so}$ (mm)	2.5	1.9	4.6	4.1
Split ratio $k_{sr}$	0.7	0.67	0.65	0.66
PM thickness $h_m$ (mm)	2	2	2	2
Width of rotor tooth $w_{rt}$ (mm)	3.9	3.2	3.6	3.4

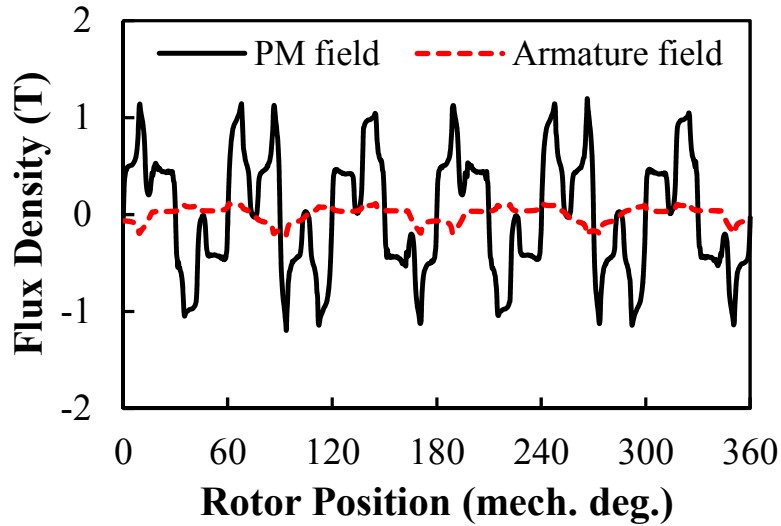


(a)

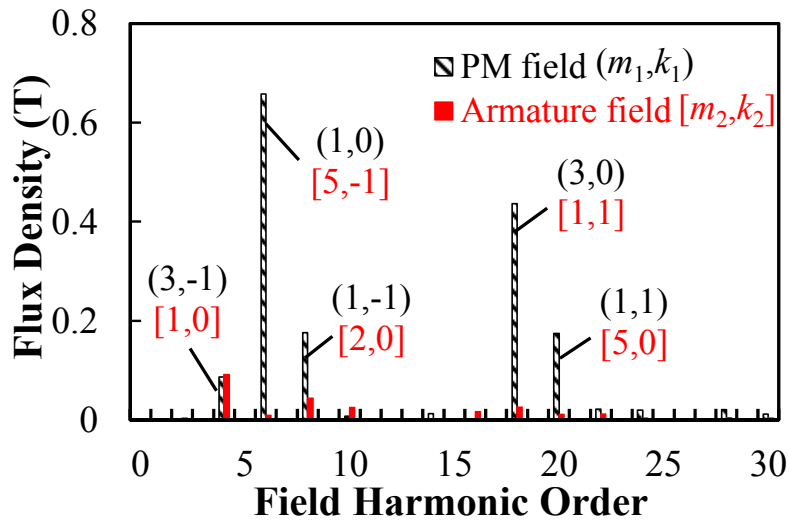


(b)

Fig. 2.8 Air-gap flux density produced by PM MMF and armature MMF in the 12/14 NS-SN without rotor-tooth modulation ( $t=0$ ). (a) Waveforms. (b) Harmonic spectra.



(a)

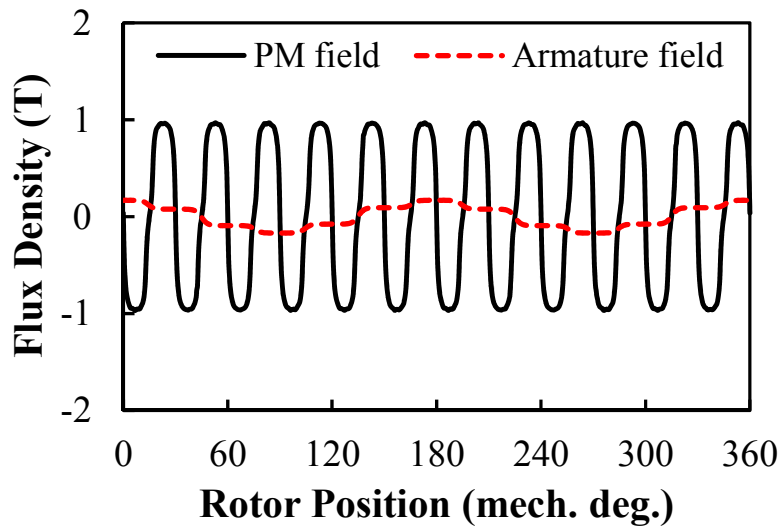


(b)

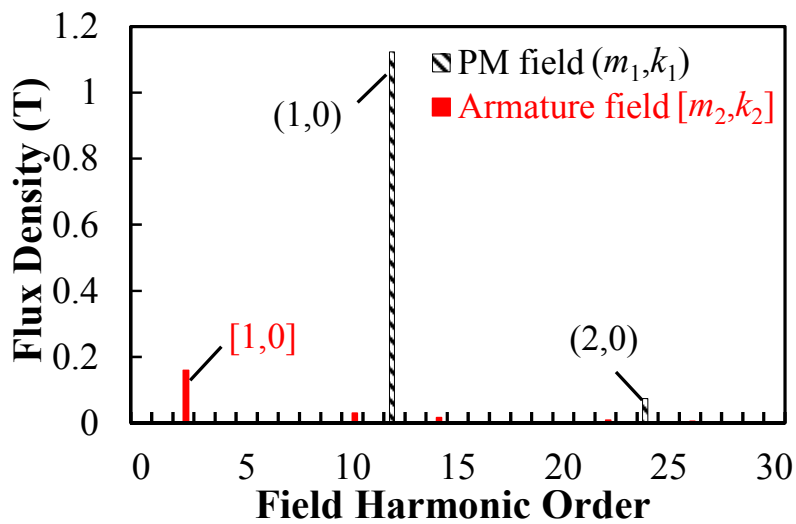
Fig. 2.9 Air-gap flux density produced by PM MMF and armature MMF in the 12/14 NS-SN with rotor-tooth modulation ( $t=0$ ). (a) Waveforms. (b) Harmonic spectra.

For the 12/14 NS-SN, Fig. 2.10 shows the air-gap PM field without rotor-tooth modulation, while the PM field with rotor-tooth modulation is shown in Fig. 2.11. In comparison with the NS-SN, there is a large variation of the air-gap PM field in the NS-SN. For NS-SN,  $p_m=N_s=12$  and the  $p_m$ th harmonic is of the largest magnitude while other harmonics with order being  $m_1 p_m$ th ( $m_1 > 1$ ) are very small, which are clearly shown in Fig. 2.10. In addition, considerable 2<sup>nd</sup> ( $m_1=1, k_1=-1$ ) and 26<sup>th</sup> ( $m_1=1, k_1=1$ ) harmonics appear due to the rotor-tooth modulation, as shown in Fig. 2.11. In general, the PM field of the NS-SN has less harmonics than that of

the NS-SN, i.e. when the PM polarities of adjacent teeth are opposite, the fundamental field harmonic is the dominant.



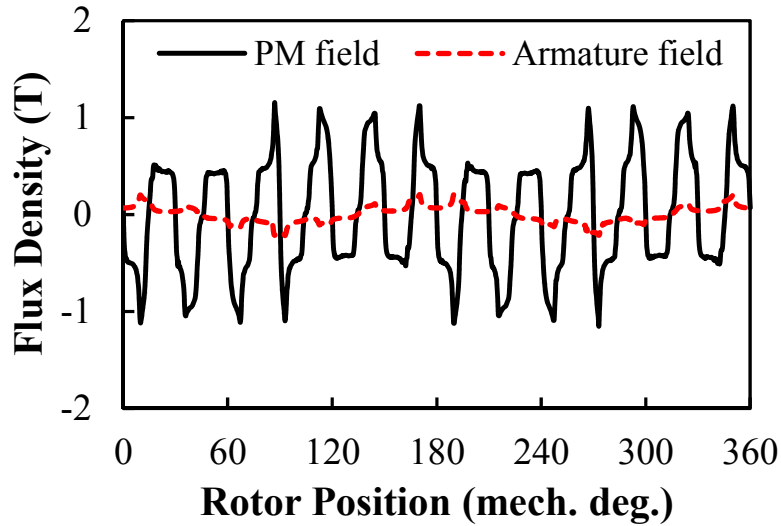
(a)



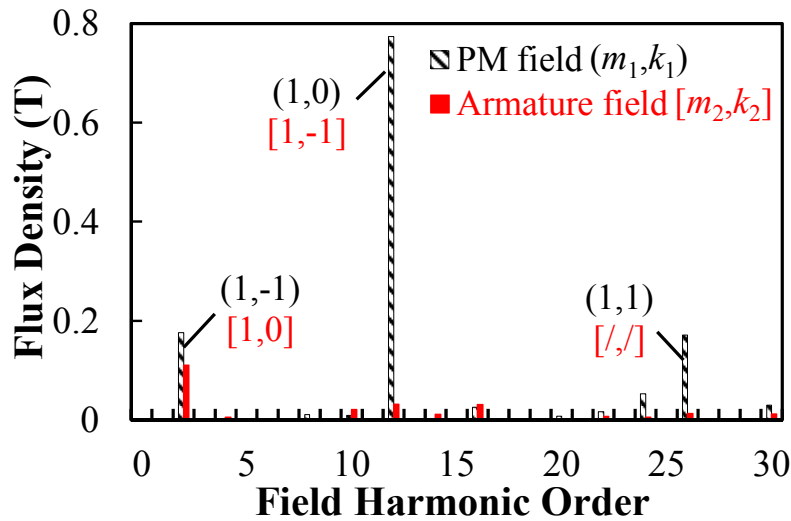
(b)

Fig. 2.10 Air-gap flux density produced by PM MMF and armature MMF in the 12/14 NS-NS without rotor-tooth modulation ( $t=0$ ). (a) Waveforms. (b) Harmonic spectra.





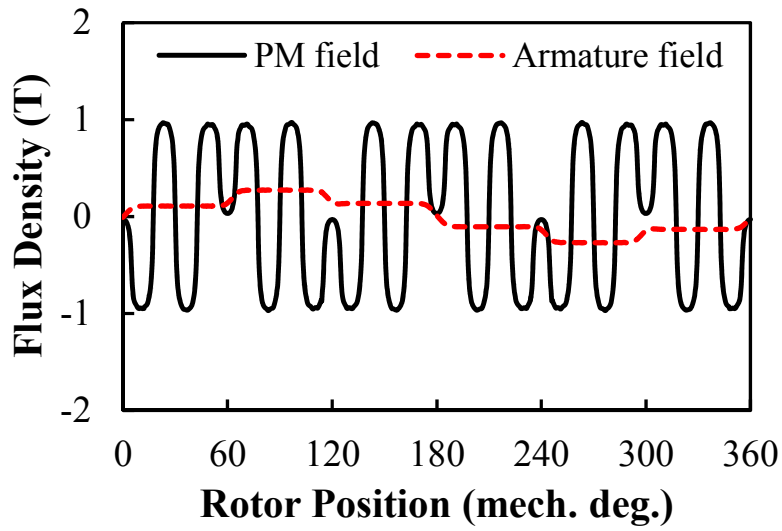
(a)



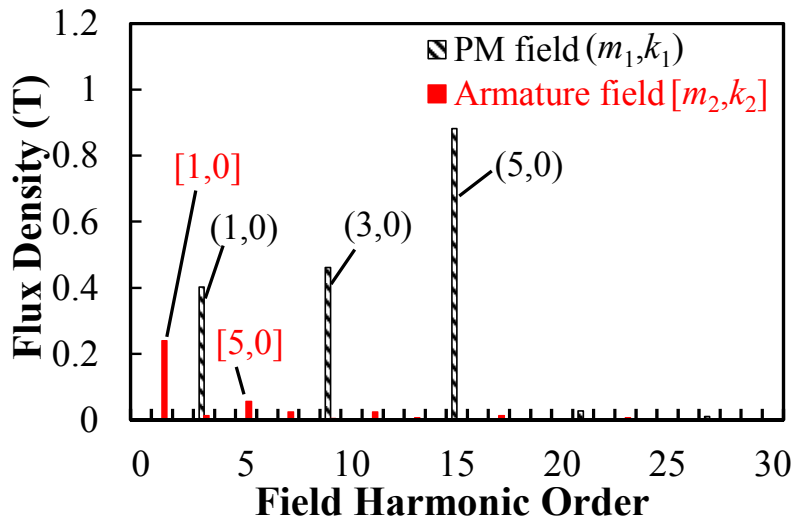
(b)

Fig. 2.11 Air-gap flux density produced by PM MMF and armature MMF in the 12/14 NS-NS with rotor-tooth modulation ( $t=0$ ). (a) Waveforms. (b) Harmonic spectra.

In terms of the other two PM arrangements with four PM pieces on each stator tooth, more abundant PM field harmonics exist. For the 6/14 NSNS-SNSN, Fig. 2.12 shows the air-gap PM field without rotor-tooth modulation, while the PM field with rotor-tooth modulation is shown in Fig. 2.13. As can be seen from Fig. 2.12, for NSNS-SNSN,  $p_m=N_s/2=3$  and harmonics which are odd times of  $p_m$  always have large magnitude, particularly the 3rd, 9<sup>th</sup>, and the 15th, i.e.,  $m_1=1, 3$ , and 5. Similarly, as shown in Fig. 2.13, additional harmonics appear due to the rotor-tooth modulation, e.g., the 1st ( $m_1=5, k_1=-1$ ), the 5th ( $m_1=3, k_1=-1$ ), and the 11th ( $m_1=1, k_1=-1$ ).

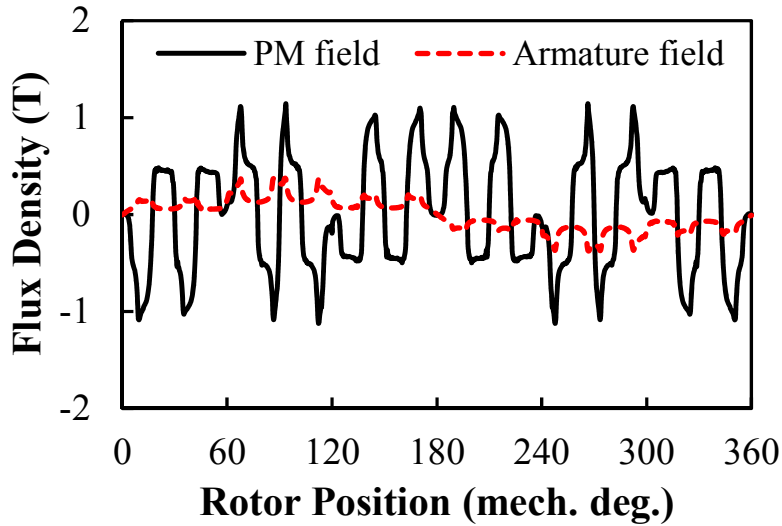


(a)

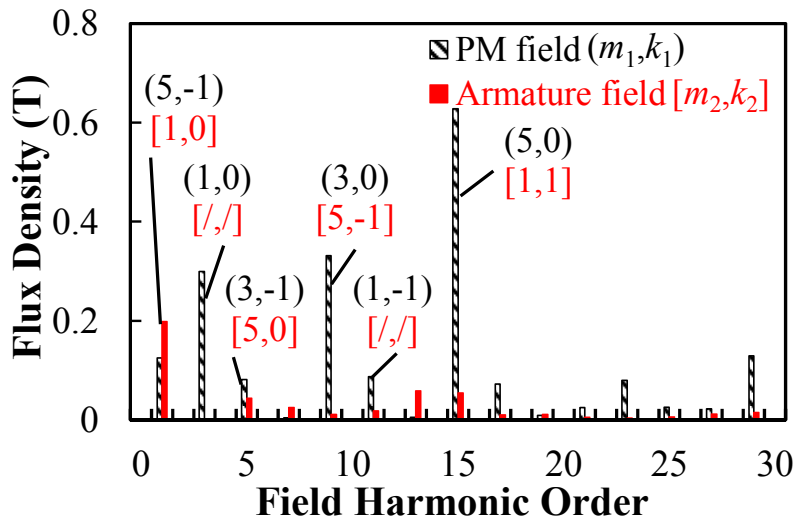


(b)

Fig. 2.12 Air-gap flux density produced by PM MMF and armature MMF in the 6/14 NSNS-SNSN without rotor-tooth modulation ( $t=0$ ). (a) Waveforms. (b) Harmonic spectra.



(a)

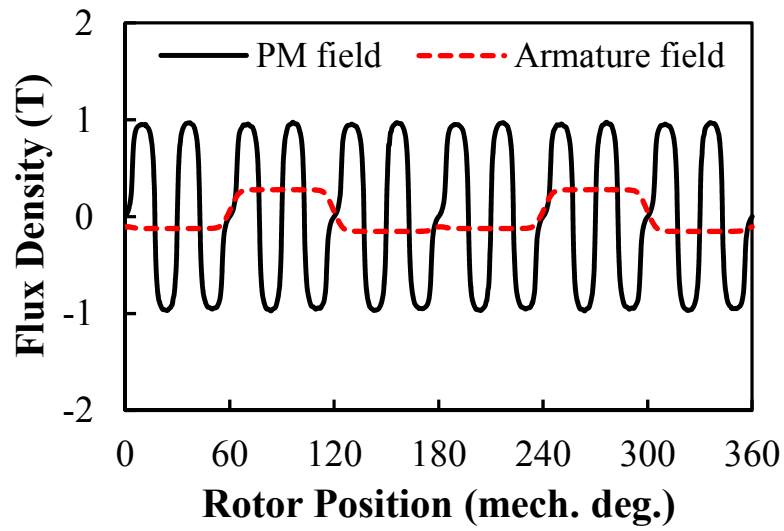


(b)

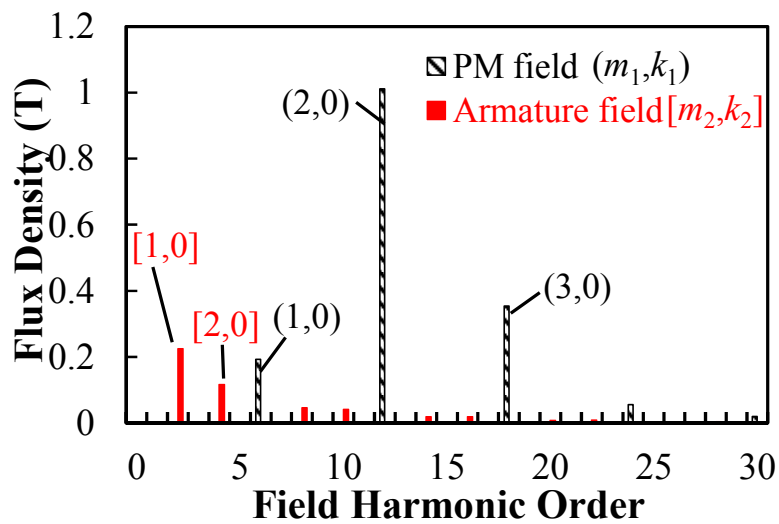
Fig. 2.13 Air-gap flux density produced by PM MMF and armature MMF in the 6/14 NSNS-SNSN with rotor-tooth modulation ( $t=0$ ). (a) Waveforms. (b) Harmonic spectra.

For the 6/14 NSNS-NSNS, Fig. 2.14 shows the air-gap PM field without rotor-tooth modulation, while the PM field with rotor-tooth modulation is shown in Fig. 2.15. As shown in Fig. 2.14, for NSNS-NSNS,  $p_m=N_s=6$  and both odd- and even-times harmonics of  $p_m$  exist, e.g., the 6th ( $m_1=1$ ), the 12th ( $m_1=2$ ) and the 18th ( $m_1=3$ ). It should be noted that the 12th harmonic has much larger magnitude than that of others. Again, after rotor-tooth modulation, abundant modulated harmonics emerge, e.g., the 2nd ( $m_1=2, k_1=-1$ ), the 4th ( $m_1=3, k_1=-1$ ), and the 8th ( $m_1=1, k_1=-1$ ). In comparison with the NSNS-SNSN, the PM field harmonic contents of the NSNS-NSNS are more concentrated, i.e. when the PM polarities of adjacent teeth are

opposite, the PM field has less harmonics, and the magnitude of the main harmonic (the  $2p_m$ th in NSNS-NSNS, and the  $5p_m$ th in NSNS-SNSN) is also larger.

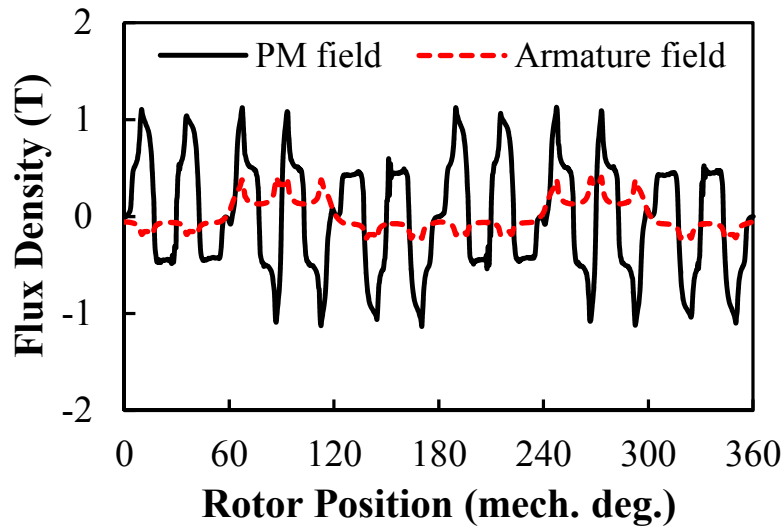


(a)

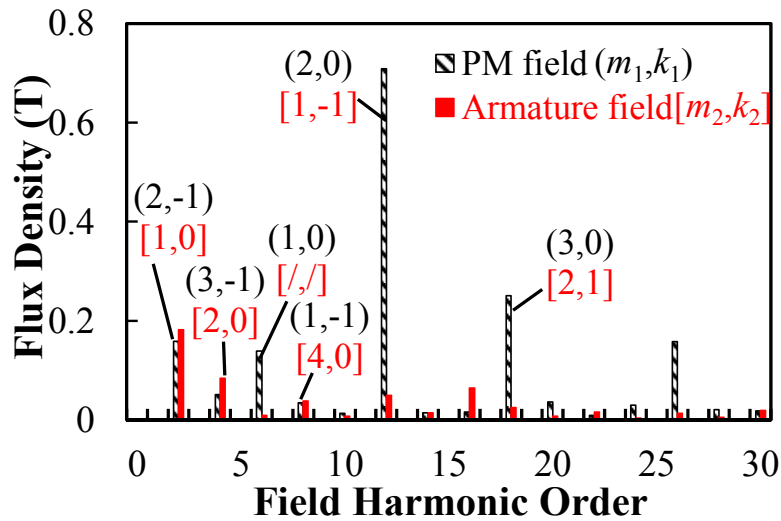


(b)

Fig. 2.14 Air-gap flux density produced by PM MMF and armature MMF in the 6/14 NSNS-NSNS without rotor-tooth modulation ( $t=0$ ). (a) Waveforms. (b) Harmonic spectra.



(a)



(b)

Fig. 2.15 Air-gap flux density produced by PM MMF and armature MMF in the 6/14 NSNS-NSNS with rotor-tooth modulation ( $t=0$ ). (a) Waveforms. (b) Harmonic spectra.

To sum up, the PM fields of four PM arrangements are totally different due to the changed PM MMF distribution. For each arrangement,  $p_m$  and the corresponding major PM field harmonics are summarized in Table 2.2. As can be seen,  $p_m$  is  $N_s$  for NS-NS and NSNS-NSNS since the PM arrangements are exactly the same for two adjacent stator teeth while it is  $N_s/2$  for NS-SN and NSNS-SNSN due to the different PM arrangements on two adjacent stator teeth. In terms of the major harmonics of the PM MMF and air-gap flux density, they are related to not only the relative polarities of the PMs but also the number of PM pieces. From Fig. 2.9, the major harmonics of NS-SN are the  $N_s/2$ th and the  $3N_s/2$ th, while it is the  $N_s$ th for NS-NS (see Fig.

2.11). As for NSNS-SNSN, three major harmonics exist, which are the  $N_s/2$ th,  $3N_s/2$ th, and the  $5N_s/2$ th (see Fig. 2.13). In addition, the  $2N_s$ th is the major harmonic in NSNS-NSNS (see Fig. 2.15). Therefore, when the PM polarities of adjacent teeth are opposite, the PM field harmonic contents are more concentrated; when the PM polarities of adjacent teeth are identical, the PM field harmonic contents are more scattered.

Table 2.2 Pole-pair numbers of different PM arrangements

PM arrangement	NS-SN	NS-NS	NSNS-SNSN	NSNS-NSNS
Fundamental pole-pair number of PM MMF $p_m$	$N_s/2$	$N_s$	$N_s/2$	$N_s$
Major PM MMF harmonics	$N_s/2, 3N_s/2$	$N_s$	$N_s/2, 3N_s/2, 5N_s/2$	$2N_s$
Equivalent pole-pair number $p_{eq}$	$\min( N_s/2 - N_r ,  3N_s/2 - N_r )$	$ N_s - N_r $	$\min( N_s/2 - N_r ,  3N_s/2 - N_r ,  5N_s/2 - N_r )$	$ 2N_s - N_r $

### 2.2.3 Equivalent Pole-Pair Number and Armature Field

In [MOR10b], a FRPM machine of NS-SN arrangement is analysed based on a ‘fictitious’ magnetic gear, from which the performance expressions are analytically derived. Further, the equivalent pole pair number  $p_{eq}$  of NS-SN is proposed in [MOR10b] [GAO16a], which reflects the flux distribution inside the stator and rotor core and can be used to determine the winding connections according to the star of slots of the conventional rotor-PM machine, of which the fundamental pole-pair number of the armature winding is  $p_{eq}$ .

Since the PM arrangement directly determines the PM field,  $p_{eq}$  of four PM arrangements are totally different and significantly influence the winding connections and resulted armature field of the corresponding FRPM machine. Considering the fact that: 1) the flux paths of air-gap PM field harmonics without rotor-tooth modulation mainly circle through the stator tooth-tips and the air-gap; 2) the air-gap PM field harmonics after rotor-tooth modulation and with relatively high pole-pair number are more likely to short-circuit through the stator tooth-tips and the rotor teeth, the fields circle through the stator yoke and rotor yoke are those subjected to the rotor-tooth modulation and with low pole pair number simultaneously. Based on the major PM field

harmonics,  $p_{eq}$  of different PM arrangements can be obtained and summarized in Table 2.2. Fig. 2.16 shows the no-load flux distributions and equivalent flux paths of the four FRPM machines (at rotor position  $a$ ). As can be seen, although all the machines have 14 rotor poles, the flux distributions in stator and rotor cores are totally different. For the NS-SN,  $p_{eq}=4$ ; for the NS-NS,  $p_{eq}=2$ ; for the NSNS-SNSN,  $p_{eq}=1$ ; for the NSNS-NSNS,  $p_{eq}=2$ . The smaller the  $p_{eq}$ , the longer the magnetic length.

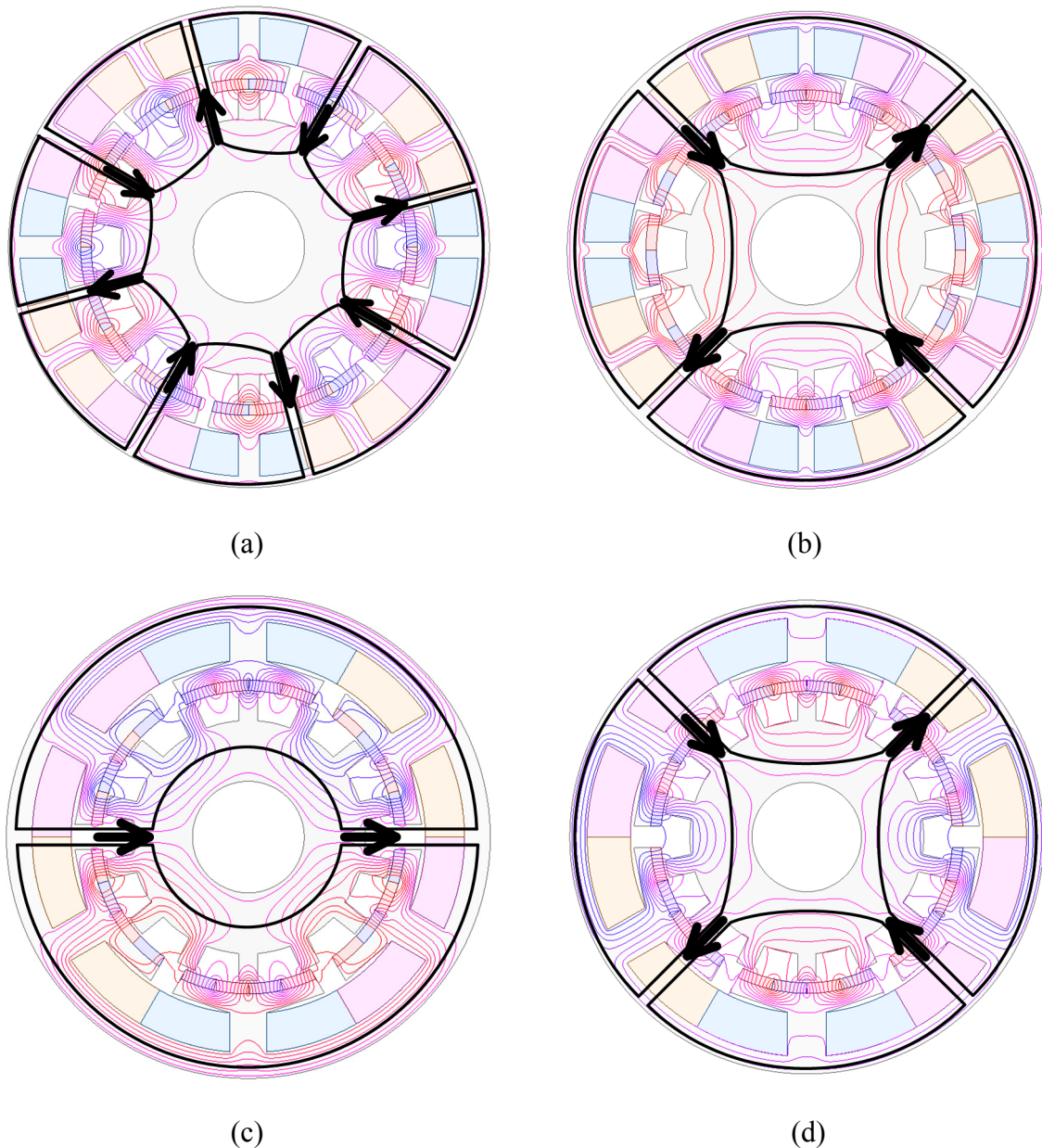


Fig. 2.16 No-load field distributions and equivalent flux paths of the machines. (a) 12/14 NS-SN. (b) 12/14 NS-NS. (c) 6/14 NSNS-SNSN. (d) 6/14 NSNS-NSNS.

According to different  $p_{eq}$ , the winding connections of the four machines can be determined and the resulted armature fields under rated current are calculated. It should be noted that the

concentrated windings are adopted in all the machines. The armature fields of different PM arrangements without rotor-tooth modulation are firstly shown in Fig. 2.8, Fig. 2.10, Fig. 2.12, and Fig. 2.14, respectively. Based on (2.1), the harmonic orders of the armature MMF and permeance  $[m_2, k_2]$  are also labelled. As can be seen from the harmonic spectra,  $p_{eq}$  of different PM arrangements is verified once again. Moreover, the armature fields of different PM arrangement with rotor-tooth modulation are shown in Fig. 2.9, Fig. 2.11, Fig. 2.13, and Fig. 2.15, respectively. As can be seen, more abundant harmonics of the armature field emerge due to the rotor-tooth modulation. By way of example, for the 12/14 NS-SN,  $p_{eq}=4$ , and the winding connection is equivalent to a conventional 12/8 stator-slot/rotor-pole rotor-PM machine. Therefore, both 1, 2, and 5-times harmonics of  $p_{eq}$  exist, i.e., the 4th, the 8th, and the 20th. After rotor-tooth modulation, additional field harmonics emerge, such as the 6th  $[m_2=5, k_2=-1]$  and the 18th  $[m_2=1, k_2=1]$ . Moreover, it is clearly shown that without rotor-tooth modulation, there is no PM and armature field harmonic pair with the same pole number and the same rotating speed in the air-gap; after rotor-tooth modulation, some armature field harmonics emerge in pairs with the PM field, which may contribute to the torque production. Therefore, the FRPM machines with various PM arrangements are all working based on air-gap field modulation.

#### 2.2.4 Torque Contribution of Working Field Harmonics

For the machines working based on air-gap field modulation, although abundant field harmonics exist, only some of them contribute to the torque production. To identify the working harmonics in such machines, there are mainly two approaches. The first one is that only PM field is considered and the contribution to back-EMF of each PM field harmonic can be analytically quantified. Based on this approach, the working harmonics of no-load air-gap field of NS-SN have been well analysed in some papers [GAO17b]. The second approach is that both PM field and armature field are considered, and the working field harmonics contributing to torque production can be directly obtained in FEA by using Maxwell stress tensor [WU15c], as

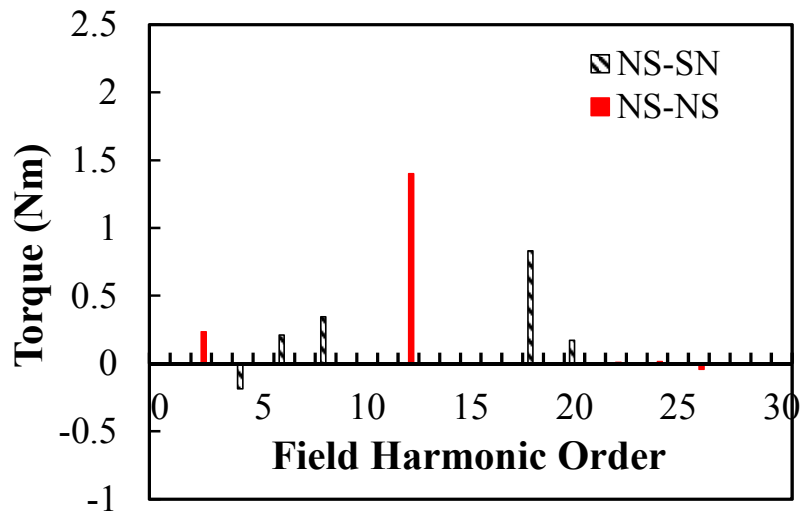
$$T_n(t) = \frac{\pi R^2 L}{\mu_0} B_{rn} B_{in} \cos[\theta_{rn}(t) - \theta_{in}(t)] \quad (2.3)$$

where  $T_n(t)$  is the instantaneous torque produced by the  $n$ th harmonic,  $R$  is the air-gap radius,  $\mu_0$  is the vacuum permeability,  $L$  is the effective axial length,  $B_{rn}$  and  $B_{in}$  are the magnitudes of

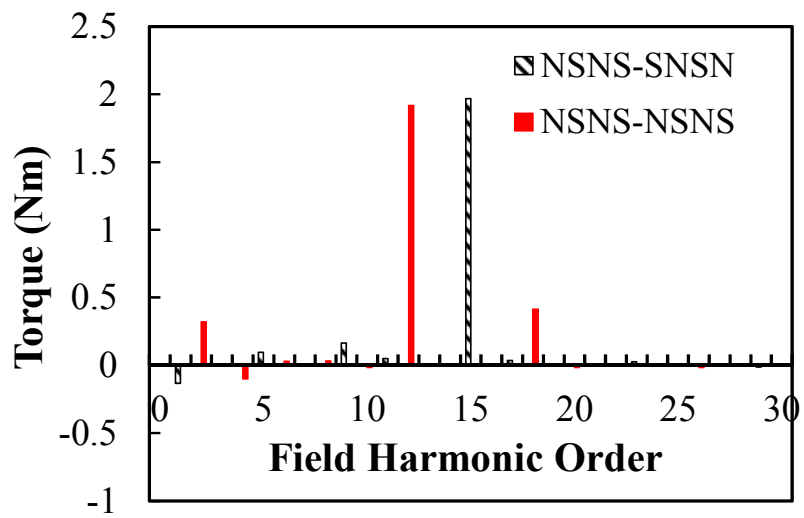


the radial and tangential components of the  $n$ th harmonic,  $\theta_{rn}(t)$  and  $\theta_{tn}(t)$  are the phases of the radial and tangential components of the  $n$ th harmonic.

In this chapter, the second approach is used to analyse and compare the working harmonics of different PM arrangements. Fig. 2.17 shows the torque contribution of each field harmonic in the four machines. It can be found that the torques of all the FRPM machines are contributed by several dominant working field harmonics regardless of PM arrangement, which is different from the conventional rotor-PM machine. However, the contribution of each harmonic and the machine average torque are largely related to the PM arrangement. It is well known that a steady torque component can be produced by the interaction of one PM field harmonic and one armature field harmonic when they have the same pole-pair number and rotational speed. The resulted torque is proportional to the product of the pole-pair number, magnitudes of both the PM and armature field harmonics, and the relative phase angle between them [TAN10]. Based on Fig. 2.9, Fig. 2.11, Fig. 2.13, Fig. 2.15, Fig. 2.17, (2.1), and (2.2), the order, speed, torque proportion of dominant working harmonics (with torque contribution >3%), and the magnitudes of corresponding PM field and armature field harmonics are listed in Table 2.3. As can be seen, for the NS-NS, the torque contribution is concentrated since mainly two working harmonics have considerable torque contribution. In contrast, for the other three PM arrangements, the torque contributions are more scattered with more than four dominating harmonics having proportion higher than 3%. It should be noted that although some harmonic pairs are static, i.e., the rotational speed is zero, a steady torque component can still be produced, which is similar with the SFPM machine analysed in [WU15c].



(a)



(b)

Fig. 2.17 Torque contribution of air-gap field harmonics. (a) NS-SN and NS-NS. (b) NSNS-SNSN and NSNS-NSNS.

Table 2.3 Torque Proportion of Working Harmonics

PM arrangement	$p_{m,k}$ & torque proportion	PM field & $(m_1, k_1)$	Armature field & $[m_2, k_2]$	Speed
NS-SN ( $T_{avg}=1.35\text{Nm}$ )	4 <sup>th</sup> (-13.8%)	0.09T (3,-1)	0.09T [1,0]	-14/4 $\Omega_r$
	6 <sup>th</sup> (15.6%)	0.66T (1,0)	0.01T [5,-1]	0
	8 <sup>th</sup> (25.6%)	0.18T (1,-1)	0.04T [2,0]	14/8 $\Omega_r$
	18 <sup>th</sup> (61.7%)	0.44T (3,0)	0.03T [1,1]	0
	20 <sup>th</sup> (12.6%)	0.17T (1,1)	0.01T [5,0]	14/20 $\Omega_r$
NS-NS ( $T_{avg}=1.60\text{Nm}$ )	2 <sup>nd</sup> (14.5%)	0.18T (1,-1)	0.11T [1,0]	14/2 $\Omega_r$
	12 <sup>th</sup> (87.5%)	0.77T (1,0)	0.03T [1,-1]	0
NSNS-SNSN ( $T_{avg}=2.21\text{Nm}$ )	1 <sup>st</sup> (-6.0%)	0.13T (5,-1)	0.20T [1,0]	-14/1 $\Omega_r$
	5 <sup>th</sup> (4.4%)	0.08T (3,-1)	0.04T [5,0]	14/5 $\Omega_r$
	9 <sup>th</sup> (7.4%)	0.33T (3,0)	0.01T [5,-1]	0
	15 <sup>th</sup> (88.9%)	0.63T (5,0)	0.05T [1,1]	0
NSNS-NSNS ( $T_{avg}=2.59\text{Nm}$ )	2 <sup>nd</sup> (12.4%)	0.16T (2,-1)	0.18T [1,0]	14/2 $\Omega_r$
	4 <sup>th</sup> (-3.8%)	0.05T (3,-1)	0.08T [2,0]	14/4 $\Omega_r$
	12 <sup>th</sup> (73.9%)	0.71T (2,0)	0.05T [1,-1]	0
	18 <sup>th</sup> (16.0%)	0.25T (3,0)	0.02T [2,1]	0

In terms of the total average torque of different PM arrangements, some findings can be concluded as:

1. The 12/14 NS-NS has higher torque than the 12/14 NS-SN. This can be explained by the fact that for the NS-NS, the magnitude of the 12th armature field is large which can interact with the dominant 12th PM field. In contrast, there are mainly two PM field harmonics with large magnitude in the NS-SN, i.e., the 6th and 18th. However, the 6th armature field is of very low magnitude, making the large 6th PM field not fully utilized.
2. The 6/14 NSNS-SNSN and NSNS-NSNS have higher torque than the other two PM arrangements with 12 stator slots. This phenomenon can be attributed to the large magnitude

of armature field in the former two machines when concentrated-windings are adopted. By way of example, for both the 12/14 NS-NS and 6/14 NSNS-NSNS,  $p_{eq}=2$ . However, the magnitude of the 2nd armature field is only 0.11T in the former, which is much smaller than that in the latter (0.18T).

3. The 6/14 NSNS-NSNS has higher torque than the 6/14 NSNS-SNSN, thus exhibiting the highest average torque among four machines. The torque difference between two 6-slot-stator machines can be explained by the different torque contribution effects of the  $p_{eq}$ th field harmonic. For the NSNS-NSNS, the 2nd field harmonic pair produces a positive torque component, thus boosting the torque while the 1st field harmonic pair of the NSNS-SNSN produces a negative torque component and impair the overall torque. This can be further explained by the rotational direction of the  $p_{eq}$ th field harmonic. Based on (1.2), the 1st field harmonic of the NSNS-SNSN rotates to the reverse direction, producing a negative torque component, while the 2nd harmonic of the NSNS-NSNS is of positive rotation, thus producing a positive torque component.

## 2.3 Influence of Rotor Pole Number

The torque performance of a FRPM machine is significantly affected by the rotor pole number  $N_r$ . In [GAO17b], the influence of  $N_r$  on performance of NS-SN is investigated based on analytical equations. It is proven that the optimal  $N_r$  is 14 for 12-slot NS-SN machines in terms of the average torque. In this chapter, the influence of  $N_r$  on performance of FRPM machines regarding PM arrangement will be investigated based on FEA.

### 2.3.1 Two Magnet Pieces on Each Stator Tooth

Fig. 2.18 shows the average torque variation against  $N_r$  of NS-SN and NS-NS. It should be noted that all the machines utilize concentrated-winding and are optimized aiming at the maximum torque density under the fixed stator outer diameter, axial length and copper loss shown in Table 2.1. As can be seen, both NS-SN and NS-NS have relatively high torque when  $N_r$  ranges from 8 to 20, and the torques are the highest when  $N_r=14$ . This can be explained by that: 1) the back-EMF is proportional to  $N_r$ ; 2) the flux of PMs can be sufficiently utilized when  $N_r$  is close to the number of PM pairs which is 12 in this case.

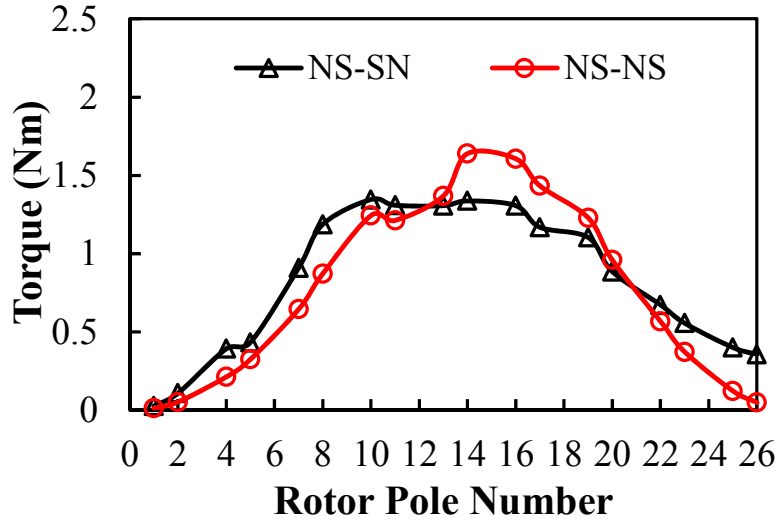


Fig. 2.18 Torque variation against  $N_r$  in NS-SN and NS-NS. ( $N_s=12$ )

In addition, each PM arrangement shows its superiority in a specific range of  $N_r$ . When  $N_r$  ranges from 8 to 12, the torque of the NS-SN is higher while that of the NS-NS is higher within the range from 13 to 20. The winding factors of two machines are utilized to simply explain the different torque variation trends against  $N_r$ . Typically, two approaches can be adopted to calculate the winding factor. The first approach is that the FRPM machine can be regarded as the conventional rotor-PM machine with pole-pair number of  $p_{eq}$ , which is listed in Table 2.2. Then the winding factor can be obtained, e.g. the winding factor of the 12/14 NS-SN is the same as the conventional 12-stator-slot rotor-PM machine with pole pair number of PMs being 4, which is 0.866. Another approach is that the winding factor of the FRPM machine can be directly calculated by using the star of slots with additional consideration of relative polarities of adjacent stator teeth, which is similar to the winding factor calculation in SFPM machine [CHE10]. In this thesis, the winding factor of the FRPM machines will be calculated based on the second approach.

Fig. 2.19 shows the back-EMF phasors of the 12/14 NS-SN. Considering the opposite PM arrangement of two adjacent stator teeth and the influence on the phase shift of the back-EMF phasor, the phasors of the even-number slots are marked with a (^), as shown in Fig. 2.19 (a). Correspondingly, the coil-EMF phasors of the double-layer concentrated-winding are shown in Fig. 2.19 (b). For the 12/14 NS-NS, since the PM arrangements of all stator teeth are identical, its star of slots is just the same as the conventional rotor-PM machine, as shown in Fig. 2.20 (a). Also, the coil-EMF phasors of the double-layer concentrated-winding are shown in Fig. 2.20 (b).

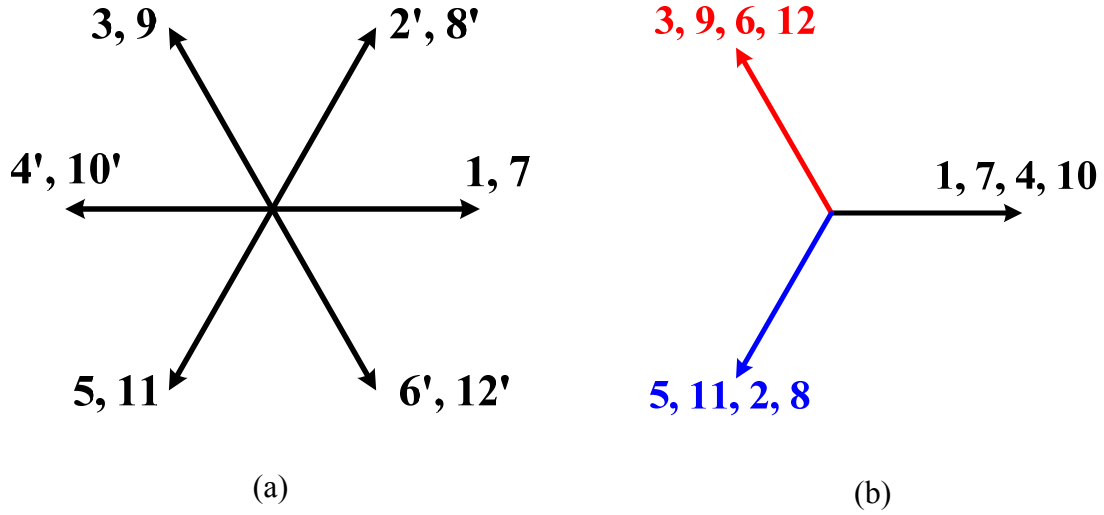


Fig. 2.19 Back-EMF phasors of 12/14 NS-SN. (a) Star of slots. (b) Coil-EMF phasors.

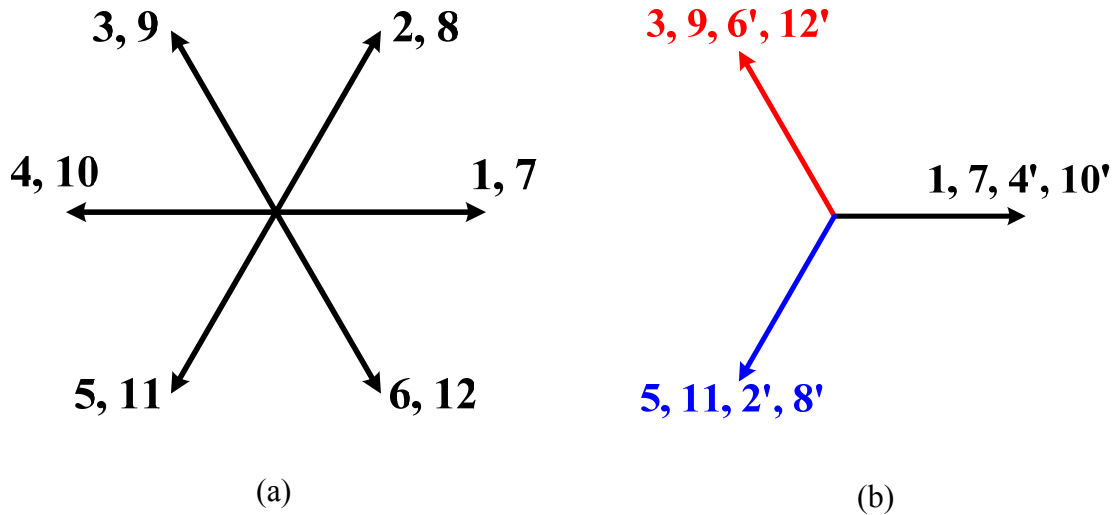


Fig. 2.20 Back-EMF phasors of 12/14 NS-NS. (a) Star of slots. (b) Coil-EMF phasors.

Therefore, the distribution factor  $k_d$  of NS-SN and NS-NS are the same, which is

$$k_d = \frac{\sin(Qv\alpha / 2)}{Q \sin(v\alpha / 2)} \quad (2.4)$$

where  $Q$  is the number of coil-EMF phasors per phase,  $\alpha$  is the angle between two adjacent coil-EMF phasors, and  $v$  is the harmonic order. For 12/14 FRPM machines with double-layer windings,  $Q=4$  and  $\alpha=0^\circ$ . Hence,  $k_d=1$  for the fundamental harmonic.

Considering the pitch factor of the concentrated winding, for NS-SN, the angular difference between two adjacent slot conductors for the  $v$ th back-EMF harmonic is

$$\theta_c = v2\pi N_r / N_s \quad (2.5)$$

and for NS-NS, it is

$$\theta_c = v(2\pi N_r / N_s - \pi) \quad (2.6)$$

Hence, the pitch factor can be obtained as

$$k_g = |\cos(\theta_c / 2)| \quad (2.7)$$

Based on (2.4)-(2.7), the fundamental winding factors of NS-SN and NS-NS are shown in Fig. 2.21. Comparing Fig. 2.21 with Fig. 2.18, it is found that the different torque variation trends of NS-SN and NS-NS are largely related to the winding factors. When  $15 < N_r < 20$ , NS-NS has larger winding factor, resulting in higher torque; when  $9 < N_r < 13$ , NS-SN has larger winding factor and higher torque. When  $N_r = 13$  and  $14$ , although the NS-SN has larger winding factor, its output torque is smaller than the NS-NS, which can be explained by the different working harmonics of two arrangements.

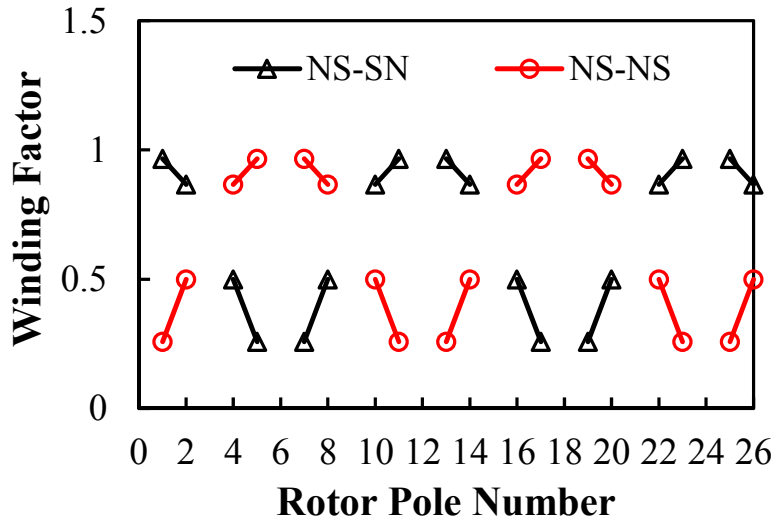


Fig. 2.21 Winding factors of 12-stator-slot NS-SN and NS-NS with different  $N_r$ .

### 2.3.2 Four Magnet Pieces on Each Stator Tooth

Considering NSNS-SNSN and NSNS-NSNS, the torque variations against  $N_r$  are shown in Fig. 2.22. Both PM arrangements have relatively high torque when  $N_r$  ranges from 10 to 20, and the 13-pole-rotor is preferred for NSNS-SNSN while the 14-pole-rotor is the best for NSNS-NSNS in terms of torque. Again, this phenomenon can be explained by the winding factors. For the

two machines, the coil-EMF phasors of the double-layer concentrated-winding are shown in Fig. 2.23. Based on (2.4)-(2.7), the winding factors of the machines are shown in Fig. 2.24. For NSNS-SNSN, the winding factor is higher when  $N_r=13$ ; for NSNS-NSNS, the winding factor is higher when  $N_r=14$ , both of which are consistent with the optimal  $N_r$  shown in Fig. 2.22.

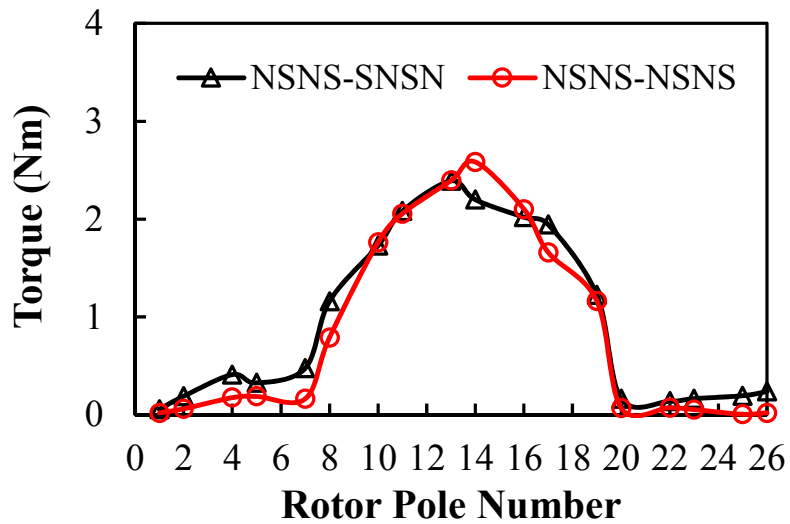


Fig. 2.22 Torque variation against  $N_r$  in NSNS-SNSN and NSNS-NSNS. ( $N_s=6$ )

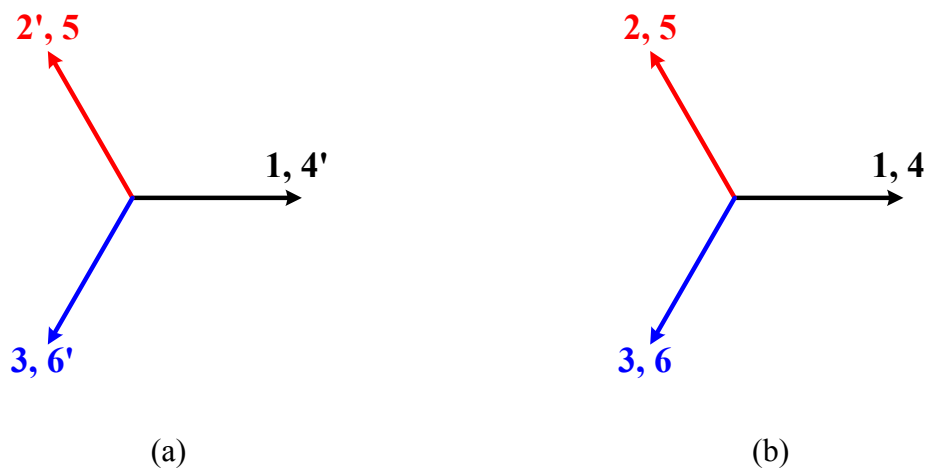


Fig. 2.23 Back-EMF phasors. (a) 6/14 NSNS-SNSN. (b) 6/14 NSNS-NSNS.



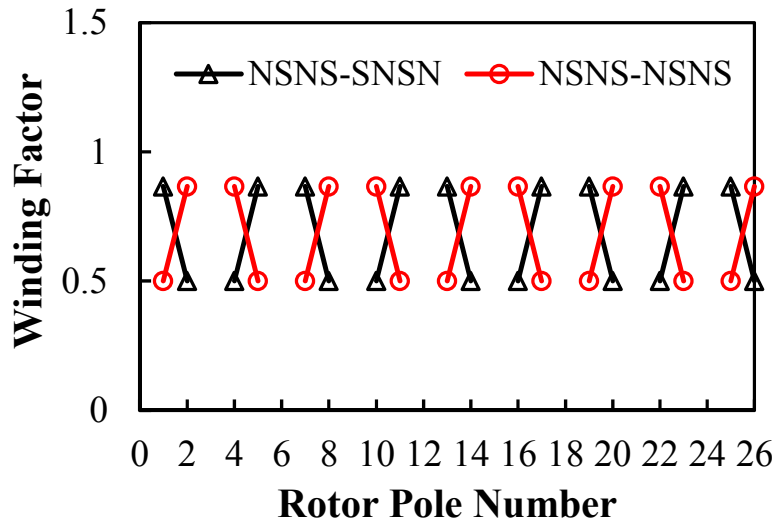


Fig. 2.24 Winding factors of 6-stator-slot NSNS-SNSN and NSNS-NSNS with different  $N_r$ .

## 2.4 Performance Comparison of Four 14-Rotor-Pole FRPM Machines with Different PM Arrangements

In the previous analysis, the optimal rotor pole number  $N_r$  of each PM arrangement has been identified, which is 13 for the 6-stator-slot NSNS-SNSN, and 14 for the 12-stator-slot NS-SN, 12-stator-slot NS-NS and 6-stator-slot NSNS-NSNS. It should be noted that the above conclusions are valid only when the concentrated-windings (CWs) are used. For some machines, the winding factor and average torque may be further improved when integer-slot distributed-windings (DWs) are used [MOR10a] [GAO17a]. For instance, as shown in Fig. 2.21, the winding factor of the 12/14 NS-NS is 0.5, and it can be improved to 1 when the short-pitch CWs are replaced with full-pitch DWs. However, because the machines with CWs always have higher slot filling factor and are easier to manufacture, and the aim of this chapter is to reveal the influence of PM arrangement on working harmonics and performance of the FRPM machine, only CWs are focused in this chapter. The performance difference among four arrangements with associated optimal  $N_r$  will be compared in the following. From Fig. 2.22, the torque of the 6-slot NSNS-SNSN with  $N_r=14$  is close to the highest value when  $N_r=13$ ,  $N_r$  is chosen as 14 for all the machines for simplicity.

The optimal parameters of the four machines are shown in Table 2.1, and their cross-sections are shown in Fig. 2.25. As can be seen, the stator teeth of the NSNS-SNSN and NSNS-NSNS are wider than those of the NS-SN and NS-NS since the flux through one stator tooth is much more due to the increased number of PM pieces mounted on single stator tooth. In addition,

there has a big difference of the ratio between the stator yoke thickness and the stator tooth width. For the NS-SN, the ratio is around 0.5 while that is larger than 1 for the NS-NS. This can be explained by  $p_{eq}$ , since for 12/14 NS-NS,  $p_{eq}=2$  and for 12/14 NS-SN,  $p_{eq}=4$ . The smaller the  $p_{eq}$ , the longer the magnetic path, and the thicker the stator yoke. Similarly, the stator yoke of the NSNS-NSNS is thinner than the NSNS-SNSN, thanks to the larger  $p_{eq}$ .

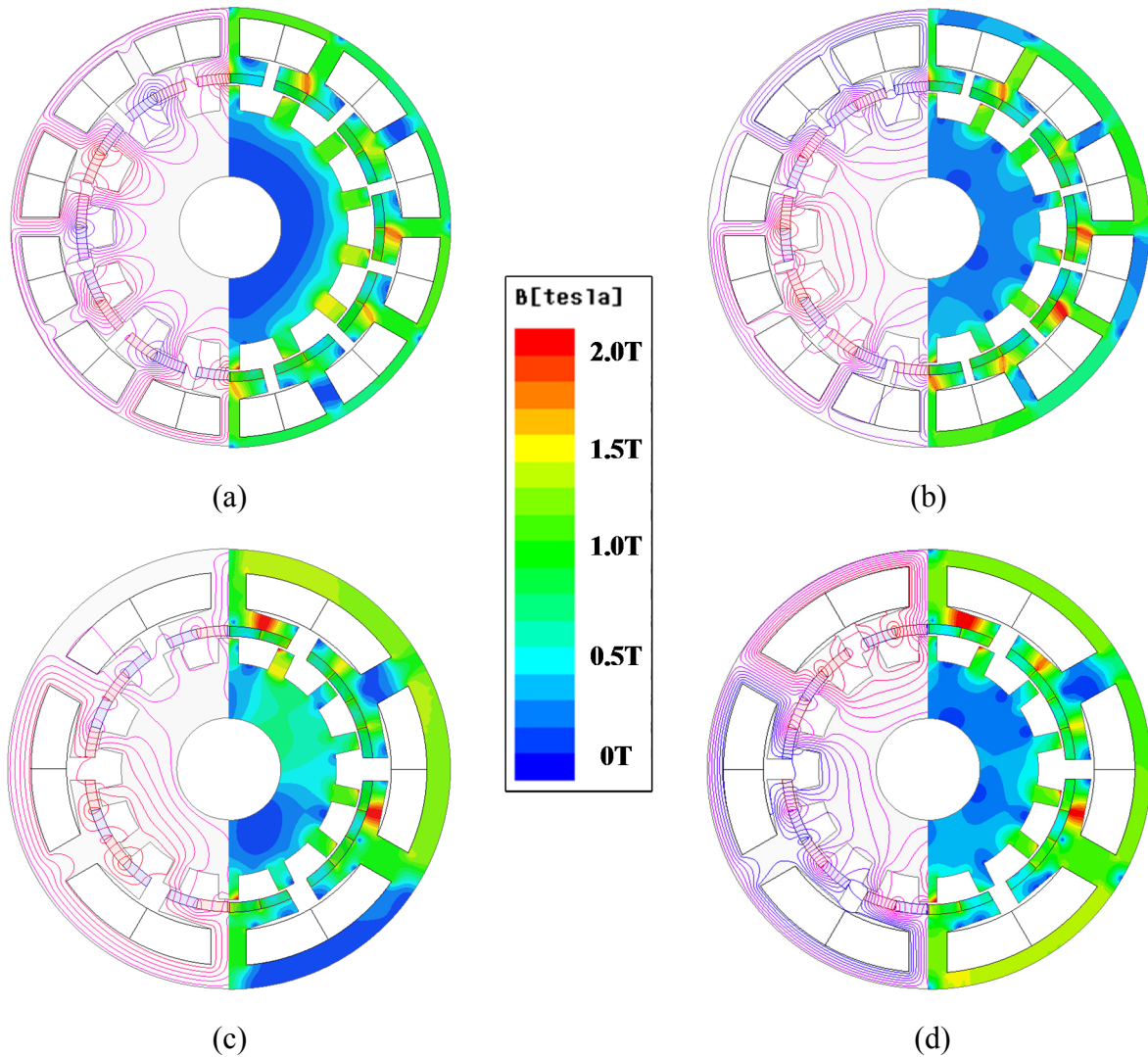
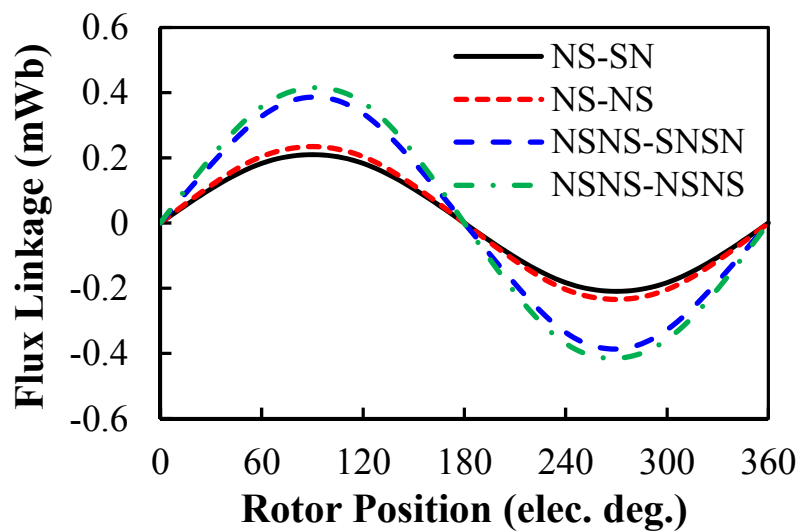


Fig. 2.25 Cross sections and full-load field distributions. (a) NS-SN. (b) NS-NS. (c) NSNS-SNSN. (d) NSNS-NSNS.

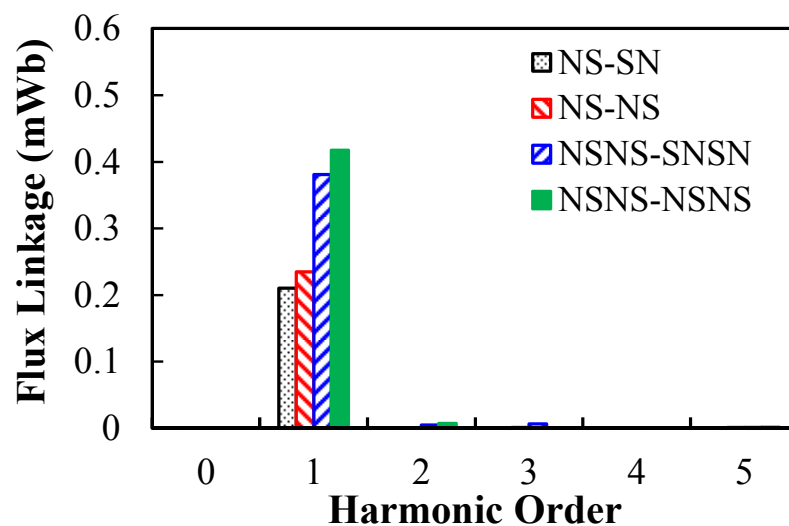
## 2.4.1 No-Load Performance

### 2.4.1.1 Flux Linkage

When the winding turns per phase  $N_{ph}$  are 4, the no-load phase flux linkages of different machines are shown in Fig. 2.26. As can be seen, the flux linkages of all the machines are bipolar, which are consistent with the previous analysis. All the machines have a near-sinusoidal waveform, especially for the NS-SN and the NS-NS. The 2nd harmonic exists in the NSNS-SNSN and NSNS-NSNS, while there is also a 3rd harmonic in the NSNS-SNSN.



(a)



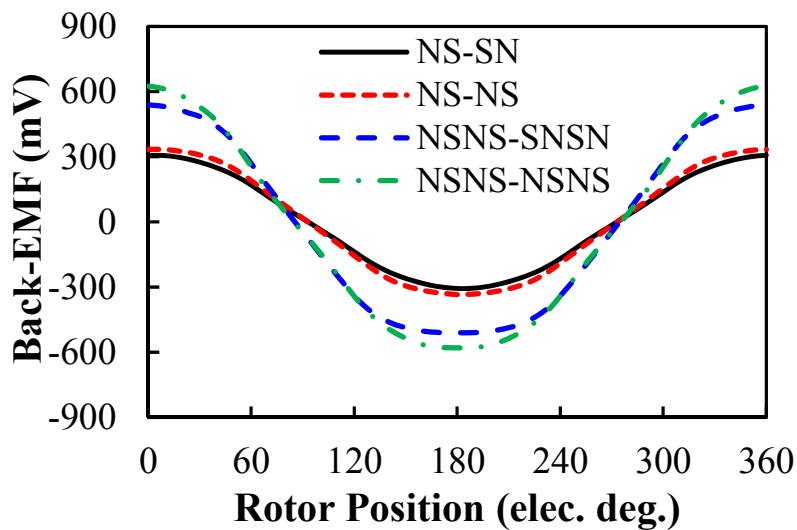
(b)

Fig. 2.26 Phase flux linkages of the four FRPM machines ( $N_{ph}=4$ ). (a) Waveforms. (b) Harmonic spectra.

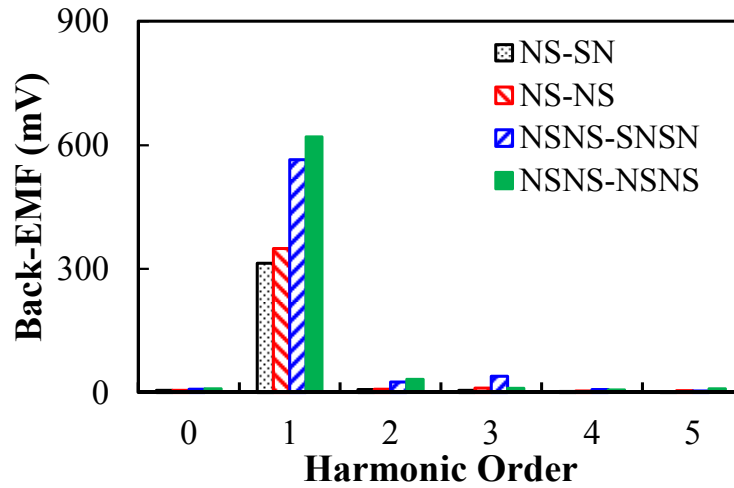
In terms of the fundamental flux linkage, the FRPM machines having opposite PM polarities of adjacent teeth always have larger magnitude of fundamental flux linkage than the FRPM machines having identical PM polarities of adjacent teeth. For instance, the NS-NS has 12% larger fundamental linkage than the NS-SN, and the NSNS-NSNS has 10% larger fundamental linkage than the NSNS-SNSN. Besides, the FRPM machines with four magnet pieces on each stator tooth have much larger fundamental flux linkage than the other two machines with two magnet pieces on each stator tooth. For instance, the NSNS-NSNS has the largest fundamental flux linkage, which is 98% larger than that of the most conventional NS-SN.

#### 2.4.1.2 Back-EMF

When the rotor speed  $n$  is 1000rpm and the winding turns per phase  $N_{ph}$  are 4, the no-load back-EMFs are shown in Fig. 2.27. Similar as flux linkage, the back-EMFs of machines with four magnet pieces on each stator tooth are much larger than the other two machines with two magnet pieces on each stator tooth. For instance, the proposed NSNS-NSNS has the highest back-EMF, which is 98% higher than the conventional NS-SN. In addition, the 2nd and 3rd harmonics exist in the NSNS-SNSN and NSNS-NSNS due to the harmonics of the flux linkage, which may cause larger torque pulsation.



(a)

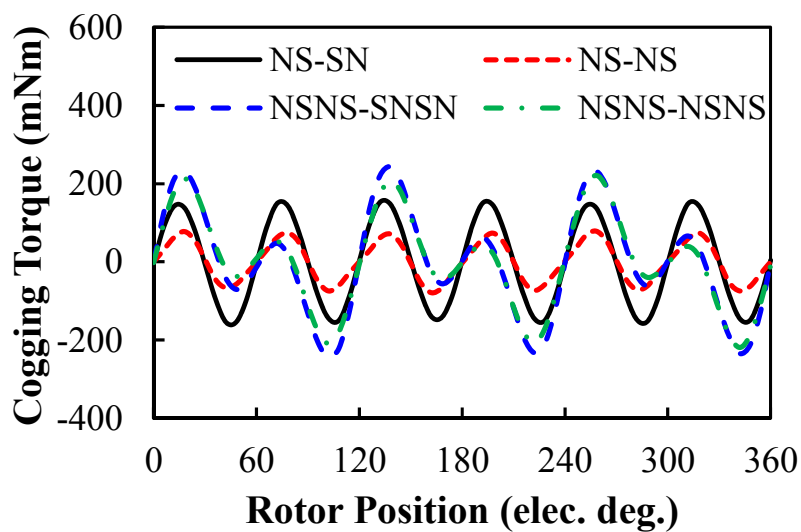


(b)

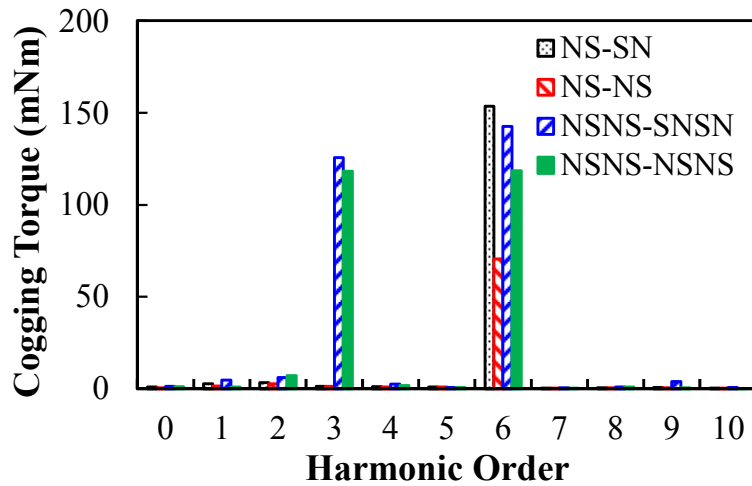
Fig. 2.27 Phase back-EMF of the four FRPM machines ( $n=1000\text{rpm}$ ,  $N_{ph}=4$ ). (a) Waveforms. (b) Harmonic spectra.

### 2.4.1.3 Cogging Torque

Fig. 2.28 shows the cogging torque of the four machines. Clearly, the PM arrangement has a big influence on the cogging torque. As can be seen, the fundamental orders of the cogging torque of the NS-SN and NS-NS are 6 while those of the NSNS-SNSN and NSNS-NSNS are 3. In addition, the NS-NS has the lowest cogging torque while the NSNS-SNSN and NSNS-NSNS have the largest. Therefore, for the applications where low torque ripple is required, the cogging torque reduction techniques should be utilized especially for the NSNS-SNSN and NSNS-NSNS [KIM05b].



(a)



(b)

Fig. 2.28 Cogging torque of the four FRPM machines. (a) Waveforms. (b) Harmonic Spectra.

#### 2.4.2 On-Load Torque Performance

When active copper loss  $p_{cu}=20W$ , the torque variations of the FRPM machines against current angle are firstly shown in Fig. 2.29. It should be noted that the current angle indicates the relative angle between the current phasor and the  $d$ -axis. When it is 90 elec. deg.,  $q$ -axis current ( $I_q$ ) is injected only, i.e.  $I_d=0$ . As can be seen, all the machines achieve the maximum torque when the current angle is approximately 90 elec. deg., indicating negligible reluctance torque. Such findings of NS-SN have been reported in [CHE11a]. Therefore, in this chapter,  $I_d=0$  control is adopted in all the optimisations and analyses.

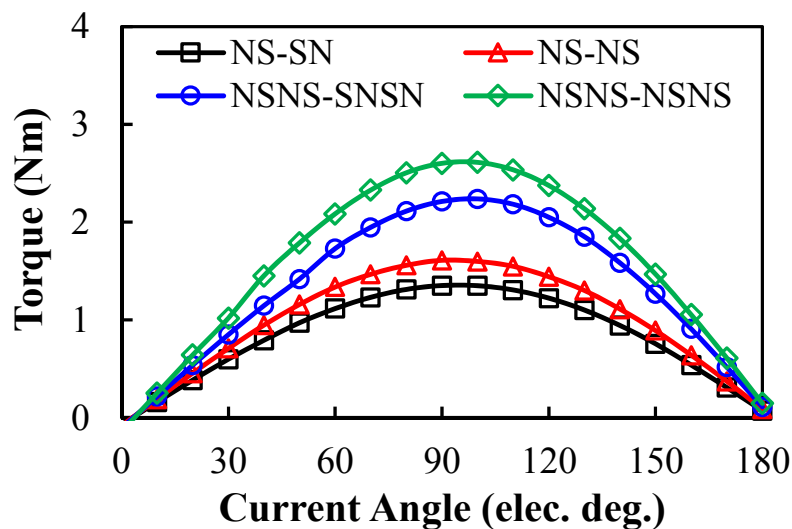
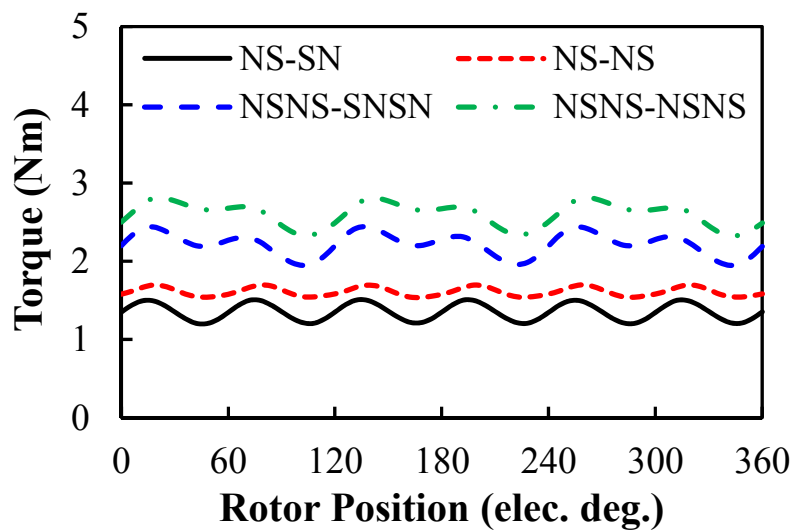
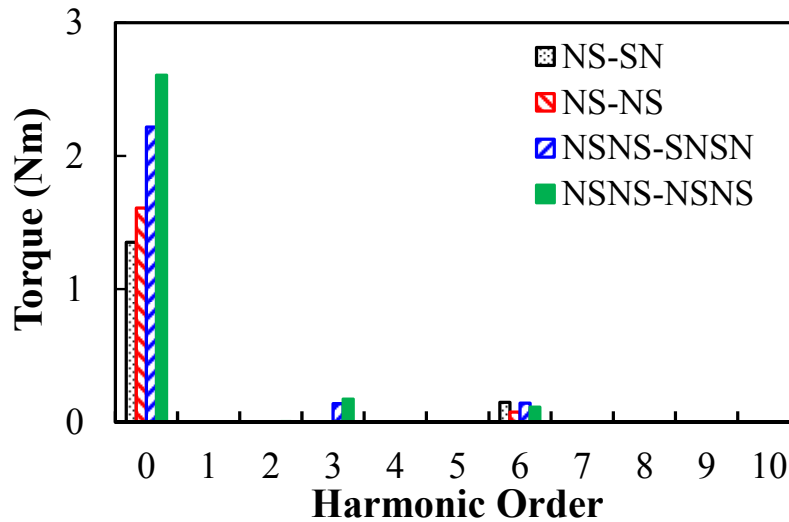


Fig. 2.29 Torque variations against current angle.

Fig. 2.30 shows the waveforms and harmonic spectra of the rated torque of the machines. The average torque of the proposed NSNS-NSNS is 2.6Nm, which is the highest and 93% higher than the lowest one of NS-SN arrangement. In addition, it should be noted that the torque ripples of the NSNS-SNSN and NSNS-NSNS are relatively larger especially compared to the NS-NS, which is resulted from the larger cogging torque and additional 2nd harmonic of the back-EMF. However, this problem can be effectively eliminated by various methods aiming at torque ripple minimization [KIM05b] [ZHU17b]. The full-load field distributions and flux densities of four machines are also shown in Fig. 2.25. It shows that the flux paths in the stator and rotor significantly vary with PM arrangement, which can be characterized by  $p_{eq}$ . In addition, for all the machines, the flux density in rotor teeth and stator tooth tips is higher than other regions.



(a)

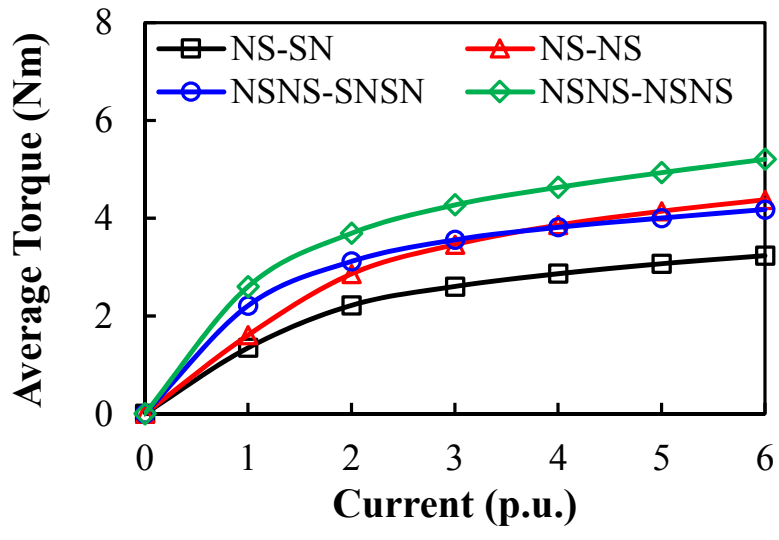


(b)

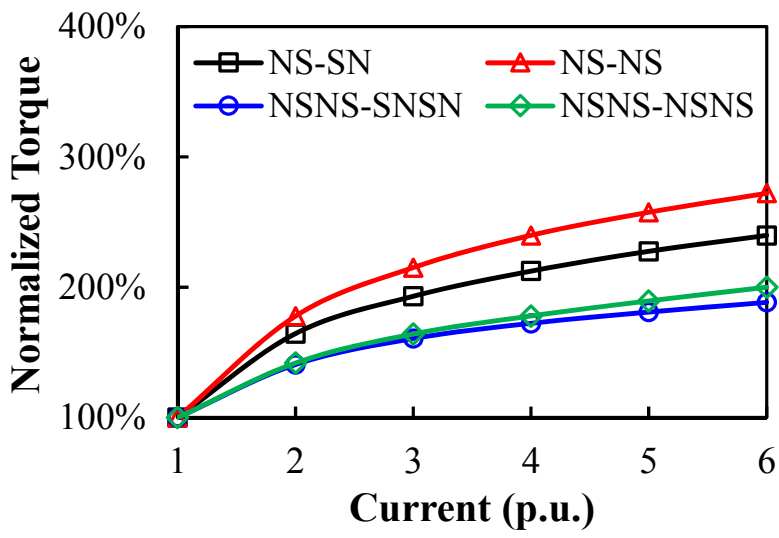
Fig. 2.30 Rated torque of the four FRPM machines ( $p_{cu}=20W$ ). (a) Waveforms. (b) Harmonic spectra.

To assess the over-load capability of the machines, the average torque variations against current are firstly shown in Fig. 2.31 (a). As can be seen, within the whole current range, the NSNS-NSNS always has the highest average torque while the NS-SN has the lowest. In addition, when the current  $I < 4$  p. u., the NSNS-SNSN has higher torque than the NS-NS, but the superiority becomes to be minor as the current increases. When  $I \geq 4$  p. u., the NS-NS turns to have higher torque. By setting the rated torque ( $p_{cu}=20W$ ) of each machine as benchmark, the normalised torque of the machines is shown in Fig. 2.31 (b). As can be seen, the over-load capability of the NSNS-NSNS and NSNS-SNSN is inferior to the NS-SN and NS-NS while that of the NS-NS is the best. This can be explained by the different self-inductances of the machines (see Fig. 2.32). It should be noted that the winding turns per phase  $N_{ph}$  are same for all the machines, which are 4. As can be seen, the self-inductances of all the machines decrease with current due to the saturation, and the self-inductances of the NSNS-SNSN and the NSNS-NSNS are similar, which are much higher than those of the NS-SN and the NS-NS. In addition, the NS-NS has the smallest self-inductance. The larger the self-inductance, the higher the armature field, the severer the saturation, and the worse the over-load capability.





(a)



(b)

Fig. 2.31 Torque variations against current. (a) Average torque. (b) Normalized average torque.

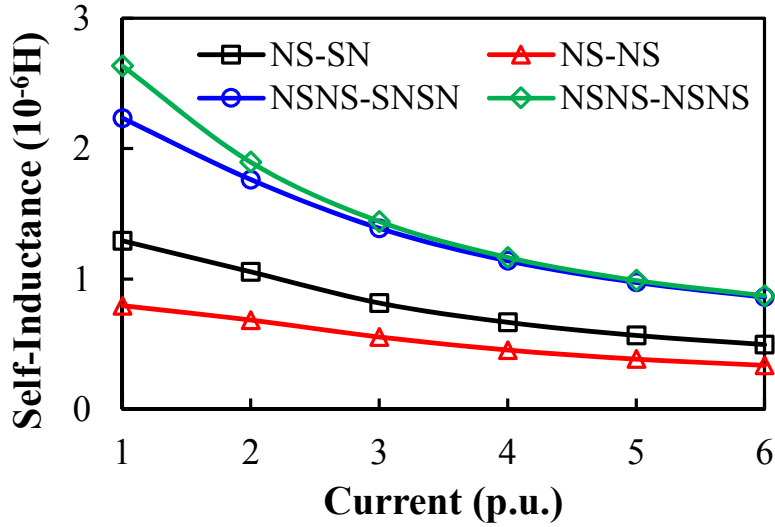


Fig. 2.32 Inductance variation against current. ( $N_{ph}=4$ )

### 2.4.3 Losses and Efficiency

Fig. 2.33 shows the full-load (i.e. copper loss equals 20W) iron loss variation against speed. As can be seen, the loss rapidly increases with speed, and it is higher in the NSNS-SNSN and NSNS-NSNS due to the higher average flux density in the stator (see Fig. 2.25) when compared to the NS-SN and NS-NS. At  $n=3000$ rpm, detailed iron loss distributions are shown in Fig. 2.34. It shows that the stator yoke together with the stator teeth account for the most proportion of the iron loss regardless of the PM arrangement and load condition. In terms of the losses of different PM arrangements, they are largely related to  $p_{eq}$ . Under no-load condition, the flux density in the stator and iron loss are determined by the PM field only. For the NS-NS,  $p_{eq}=2$  and it is smaller than that of the NS-SN which is 4. Therefore, the iron loss of the NS-NS is larger due to the longer magnetic path and corresponding higher average flux density in the stator yoke. When the machine operates under full-load condition, the flux density in the stator and iron loss are largely influenced by the armature field. For the NS-NS, the winding connection is equivalent to a conventional 12/4 rotor-PM machine while it is equivalent to a 12/8 PM machine for the NS-SN. It is well known that the harmonics of the armature field of a 12/4 integer-slot PM machine are smaller than a 12/8 fractional-slot PM machine [REF10]. Therefore, the iron loss produced by the armature field is smaller in the NS-NS. Similarly, the winding connection of the NSNS-SNSN is equivalent to a 6/2 integer-slot PM machine while it is equivalent to a 6/4 fractional-slot PM machine for the NSNS-NSNS. Therefore, the iron loss produced by the armature field of the NSNS-NSNS is larger than that of the NSNS-SNSN due to the increased field harmonics.

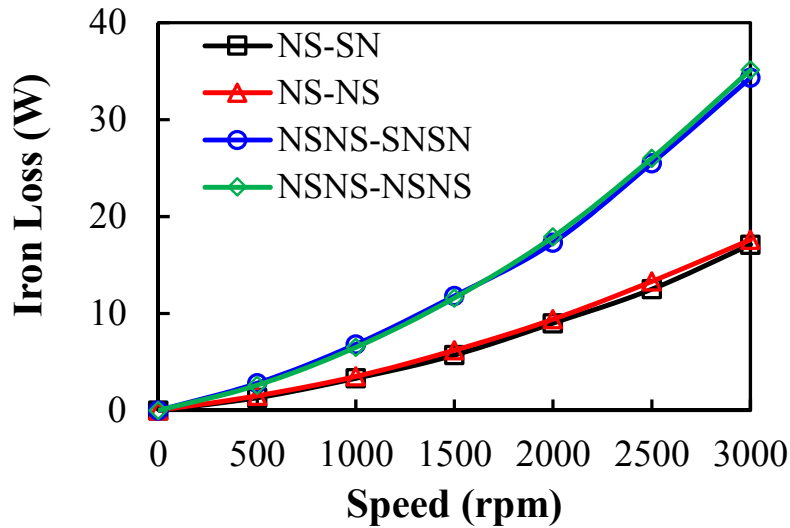


Fig. 2.33 Full-load iron loss variation against speed ( $p_{cu}=20W$ ).

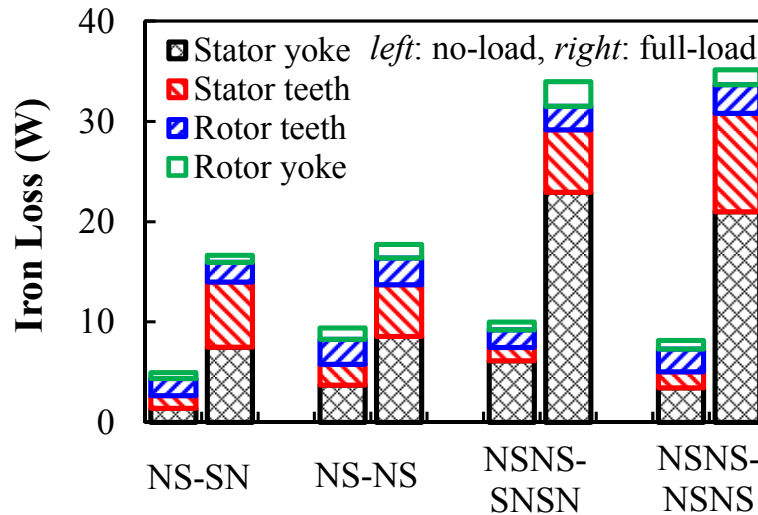


Fig. 2.34 Iron loss distributions ( $n=3000rpm$ ,  $p_{cu}=20W$ ).

Fig. 2.35 shows the full-load PM loss variation against speed. As can be seen, the NSNS-NSNS has the largest PM loss while the NS-NS has the lowest one. Considering the fact that all rotating harmonics in air-gap produce eddy current loss since the magnets are static, the major air-gap field harmonics (with magnitude exceeding 0.1T) of the NS-SN and NS-NS are listed in Table 2.4, and the rotational speed and corresponding frequency of each harmonic are calculated based on (2.1) and (2.2). As can be seen, for the NS-SN, there exist three rotating harmonics with different rotational speeds but the same frequency. In contrast, only two rotating harmonics exist in the NS-NS, making the PM loss smaller than the NS-SN. Similarly, Table 2.5 lists the major full-load field harmonics (with magnitude exceeding 0.1T) of the NSNS-SNSN and NSNS-NSNS. It can be found that the rotating harmonics in the NSNS-

NSNS are more abundant than those in the NSNS-SNSN. Therefore, the PM loss of the NSNS-SNSN is smaller than that of NSNS-NSNS.

Fig. 2.36 shows the variation of rated efficiency against speed. It should be noted that only copper loss, iron loss and PM loss are considered. As can be seen, all the machines exhibit the highest efficiency around 2500rpm. With rotor speed increasing from 2500rpm, the efficiencies gradually reduce. Within the speed range of 0-3000rpm, the NSNS-NSNS arrangement has the highest efficiency thanks to the improved torque density, while the NS-SN machine has the lowest efficiency.

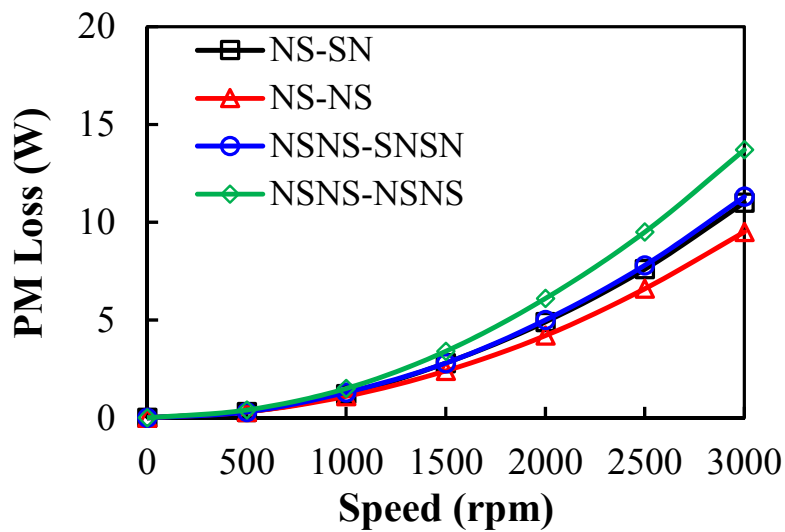


Fig. 2.35 PM loss variation against speed ( $p_{cu}=20W$ ).

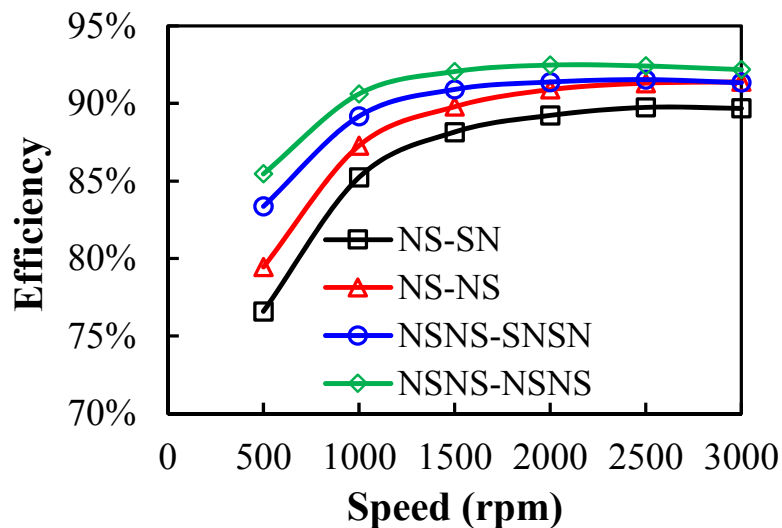


Fig. 2.36 Efficiency variation against speed.

Table 2.4 Full-load field harmonics of the NS-SN and NS-NS ( $p_{cu}=20W$ )

		<i>Static Harmonics</i>			<i>Rotating Harmonics</i>		
NS-SN	Order	6 <sup>th</sup>	18 <sup>th</sup>	42 <sup>nd</sup>	4 <sup>th</sup>	8 <sup>th</sup>	20 <sup>th</sup>
	Magnitude	0.66T	0.44T	0.17T	0.13T	0.18T	0.17T
	Speed	0	0	0	$-14/4\Omega_r$	$14/8 \Omega_r$	$14/20 \Omega_r$
	Frequency	0	0	0	$f$	$f$	$f$
NS-NS	Order	12 <sup>th</sup>	36 <sup>th</sup>		2 <sup>nd</sup>	26 <sup>th</sup>	
	Magnitude	0.77T	0.15T		0.21T	0.17T	
	Speed	0	0		$14/2\Omega_r$	$14/26 \Omega_r$	
	Frequency	0	0		$f$	$f$	

Table 2.5 Full-load field harmonics of the NSNS-SNSN and NSNS-NSNS ( $p_{cu}=20W$ )

		<i>Static Harmonics</i>				<i>Rotating Harmonics</i>		
NSNS-SNSN	Order	3 <sup>rd</sup>	9 <sup>th</sup>	15 <sup>th</sup>	45 <sup>th</sup>	1 <sup>st</sup>	29 <sup>th</sup>	
	Magnitude	0.28T	0.33T	0.63T	0.14T	0.23T	0.13T	
	Speed	0	0	0	0	$-14/1\Omega_r$	$14/29 \Omega_r$	
	Frequency	0	0	0	0	$f$	$f$	
NSNS-NSNS	Order	6 <sup>th</sup>	12 <sup>th</sup>	18 <sup>th</sup>	42 <sup>nd</sup>	2 <sup>nd</sup>	4 <sup>th</sup>	26 <sup>th</sup>
	Magnitude	0.13T	0.7T	0.25T	0.17T	0.23T	0.11T	0.16T
	Speed	0	0	0	0	$14/2\Omega_r$	$-14/4 \Omega_r$	$14/26 \Omega_r$
	Frequency	0	0	0	0	$f$	$f$	$f$

#### 2.4.4 Power Factor

Since the PM arrangement influences the average torque and inductance of the FRPM machine, the power factor of four PM arrangements are compared in the flowing. For the PM machine with negligible reluctance torque, the typical phasor diagram is shown in Fig. 2.37 ( $I_d=0$ ). To estimate the power factor of the machine, the  $d$ -axis voltage  $U_d$  and  $q$ -axis voltage  $U_q$  of the

machine are firstly expressed as (2.8) and (2.9). For simplicity, the voltage drop on the resistance is neglected. As can be seen,  $U_d$  is proportional to the angular frequency ( $\omega$ ),  $q$ -axis inductance ( $L_q$ ) and  $q$ -axis current ( $I_q$ );  $U_q$  is proportional to the angular frequency ( $\omega$ ) and PM flux linkage per pole ( $\psi_m$ ). The power factor ( $pf$ ) of the machine can then be obtained, as (2.10). By calculating  $L_q$ ,  $I_q$ , and  $\psi_m$ , the variations of power factor against torque of four arrangements are compared in Fig. 2.38. It shows that the NS-SN always has the lowest power factor because of the needed high armature field [GAO16a]. Although the NS-NS also needs higher armature field, particularly compared with the NSNS-NSNS, its power factor is the highest, thanks to the smaller inductance (see Fig. 2.32). It should be noted that for the high-torque region, the power factor of FRPM machines is relatively low due to the small  $\psi_m$  (resulted from high rotor pole number). The power factor improvement is a key challenge for FRPM machines since a low power factor will result in a high capacity of the inverter, which increases the cost of the whole system.

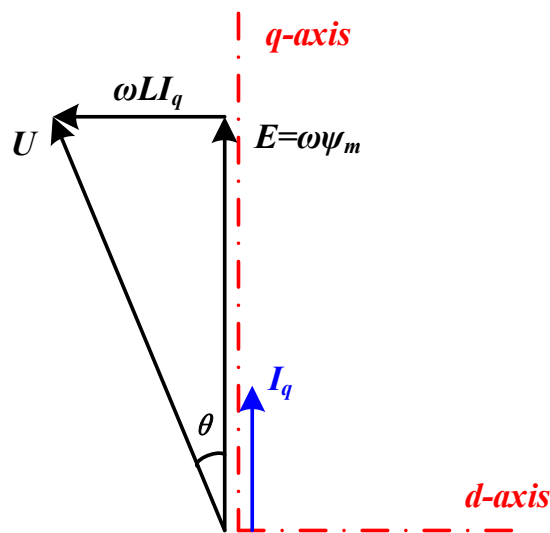


Fig. 2.37 Phasor diagram of FRPM machines.

$$U_d = -\omega L_q I_q + R I_d \approx -\omega L_q I_q \quad (2.8)$$

$$U_q = \omega(\psi_m + L_d I_d) + R I_q \approx \omega(\psi_m + L_d I_d) = \omega \psi_m \quad (2.9)$$

$$pf = \cos \theta = \frac{U_q}{\sqrt{U_d^2 + U_q^2}} = \frac{1}{\sqrt{1 + \left(\frac{L_q I_q}{\psi_m}\right)^2}} \quad (2.10)$$

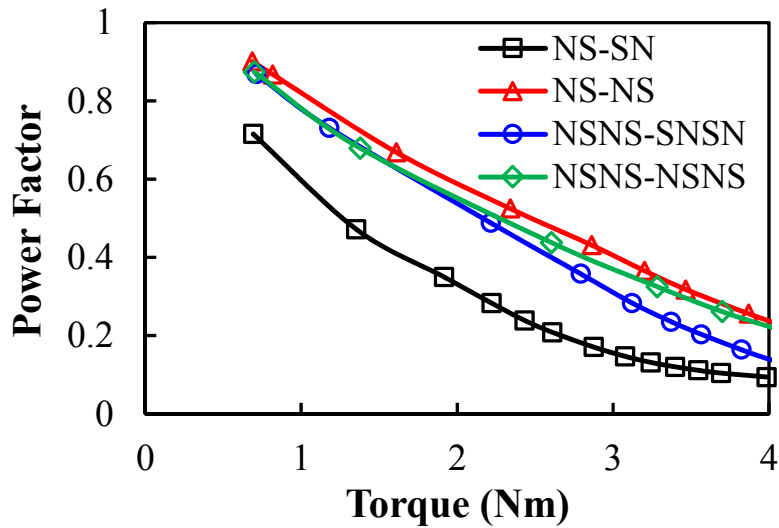


Fig. 2.38 Power factor variation against torque.

#### 2.4.5 Demagnetisation Withstand Capability

For PM machines working based on air-gap modulation, the PM thickness is a critical design parameter since it influences the equivalent air-gap length and the corresponding modulation effect. It has been proven that there is an optimal PM thickness  $h_m$  for FRPM machines with NS-SN arrangement [GAO16a]. Based on the machine parameters listed in Table 2.1, the influence of  $h_m$  on FRPM machines with different PM arrangement is shown in Fig. 2.39. For each PM arrangement, there always exists an optimal  $h_m$ . For the NS-SN and the NS-NS, it is 1.2mm, while it is 1.6mm for the NSNS-SNSN and the NSNS-NSNS.

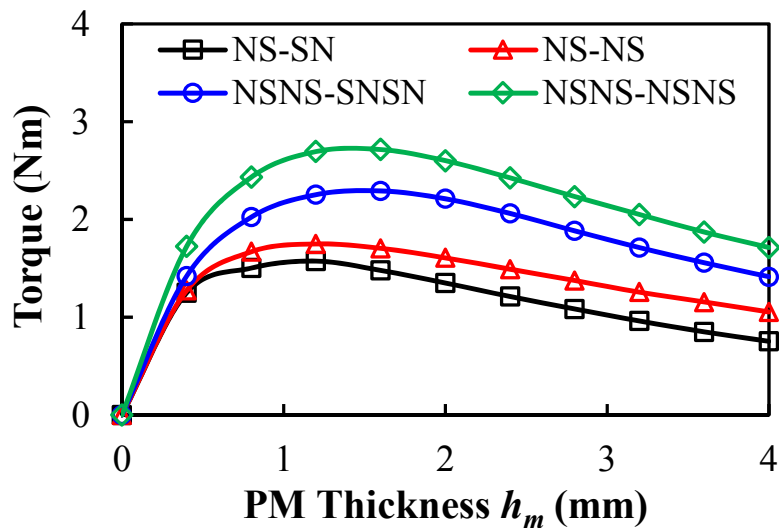


Fig. 2.39 Influence of PM thickness on torque of the FRPM machines.

Considering the manufacturability of the PM pieces,  $h_m$  is adjusted to 2mm for all the machines. By slightly increasing  $h_m$ , the demagnetization withstand capability of the machines can be also improved. Taking the 6/14 NSNS-NSNS as an example, the flux density in the magnetization direction of a single PM piece is shown in Fig. 2.40, when the machine operation temperature  $T$  is set as 100°C and a large minus  $d$ -axis current is injected ( $I_d = -5I_{rated}$ ). It can be found that when  $h_m = 1.6\text{mm}$ , a large area of the PM suffers high risk of demagnetization with flux density below 0T. In contrast, the demagnetization withstand capability of the machine is largely improved when  $h_m = 2\text{mm}$ .

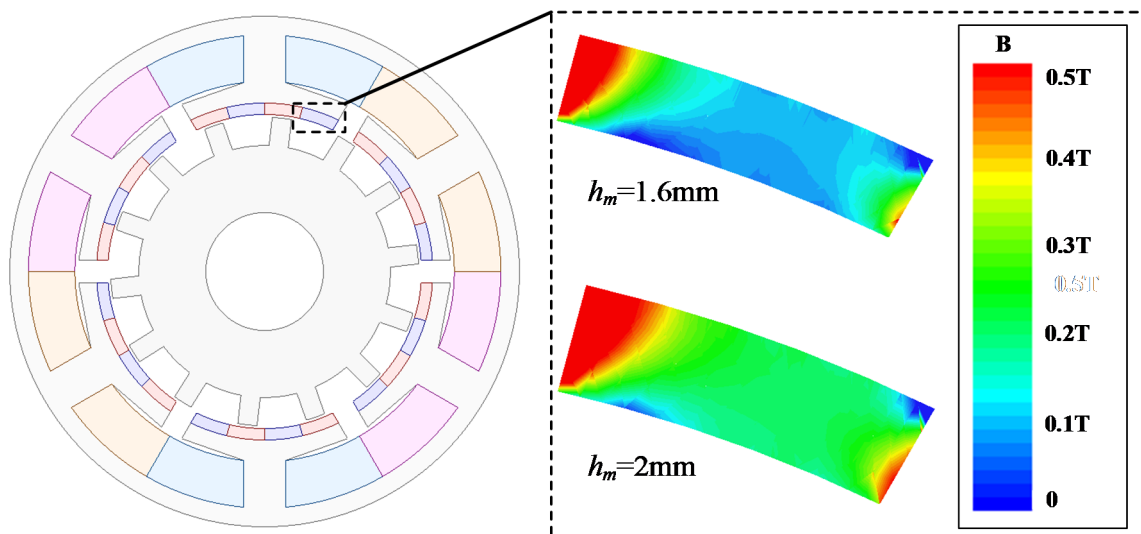


Fig. 2.40 Flux density in the magnetisation direction of the PM piece. ( $T = 100^\circ\text{C}$ ,  $I_d = -5I_{rated}$ ).

The demagnetisation withstand capability of the FRPM machines with different PM arrangements ( $h_m = 2\text{mm}$ ) are then compared in Fig. 2.41, when the machine operation temperature  $T$  is set as 100°C and a large minus  $d$ -axis current is injected ( $I_d = -5I_{rated}$ ). As can be seen, the NS-SN, NSNS-SNSN, and NSNS-NSNS have high risk of demagnetisation at the corner of the PM piece, and the latter two also have a demagnetisation area on the inner surface of the PM piece. In contrast, the NS-NS exhibits the best demagnetisation withstand capability since the whole PM piece has flux density over 0T. Such phenomenon can be explained by the inductances of the machines (see Fig. 2.32). The larger the inductance, the larger the armature field, the weaker the demagnetisation withstand capability.



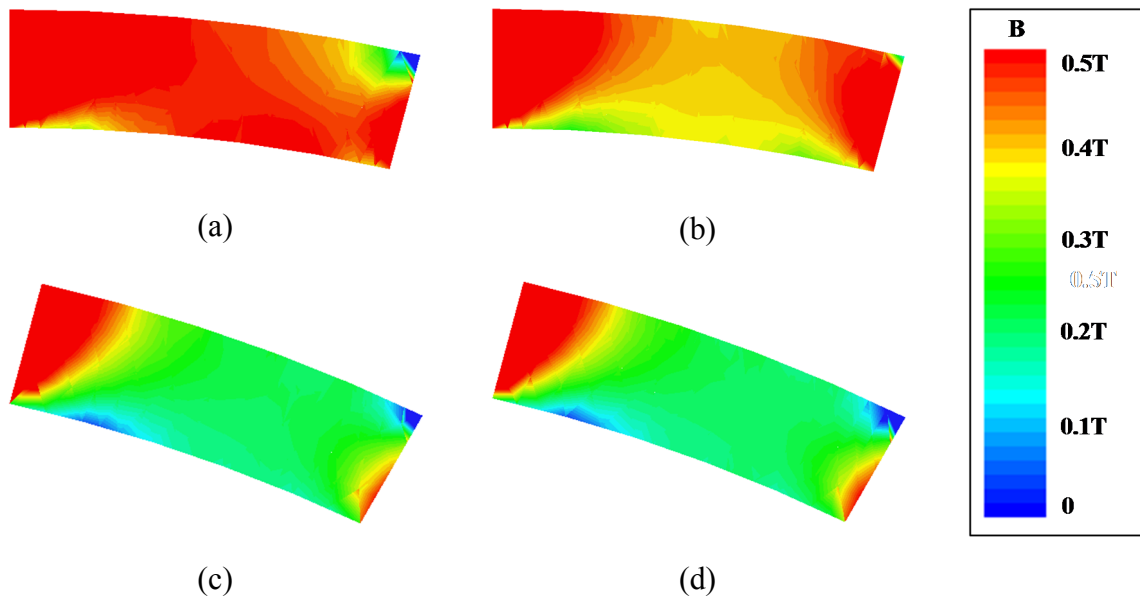
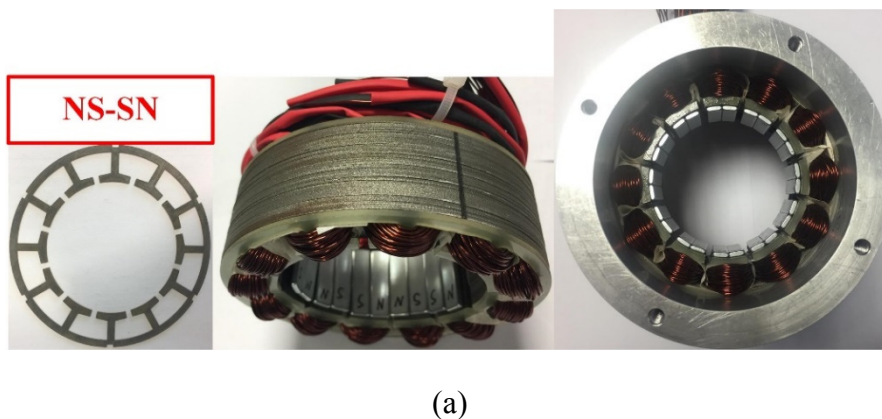


Fig. 2.41 Comparison of flux density in the magnetisation direction of a single PM piece ( $T=100^{\circ}\text{C}$ ,  $I_d=-5I_{rated}$ ). (a) NS-SN. (b) NS-NS. (c) NSNS-SNSN. (d) NSNS-NSNS.

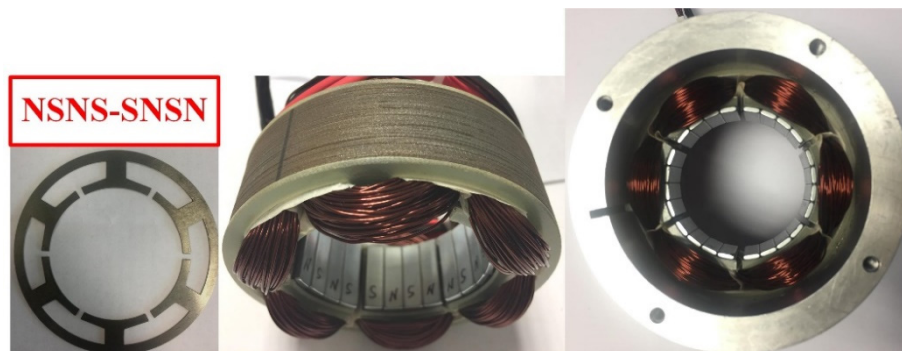
## 2.5 Experimental Validation

To verify the previous analyses, four 14-pole-rotor FRPM machines having different PM arrangements are manufactured, as shown in Fig. 2.42, together with their parameters listed in Table 2.6. It should be noted that all the prototypes have the same stator inner diameter and share the same rotor for simplicity. In addition, the NS-SN and NS-NS share the same stator lamination; the NSNS-SNSN and NSNS-NSNS share the same stator lamination. The PM thickness is 2mm. The drawings of the prototypes are shown in Appendix A.





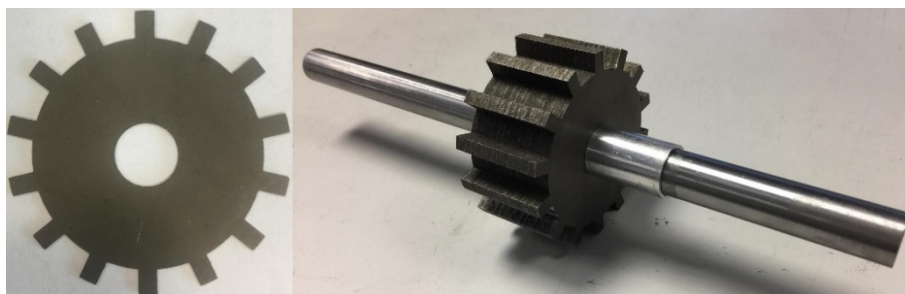
(b)



(c)



(d)



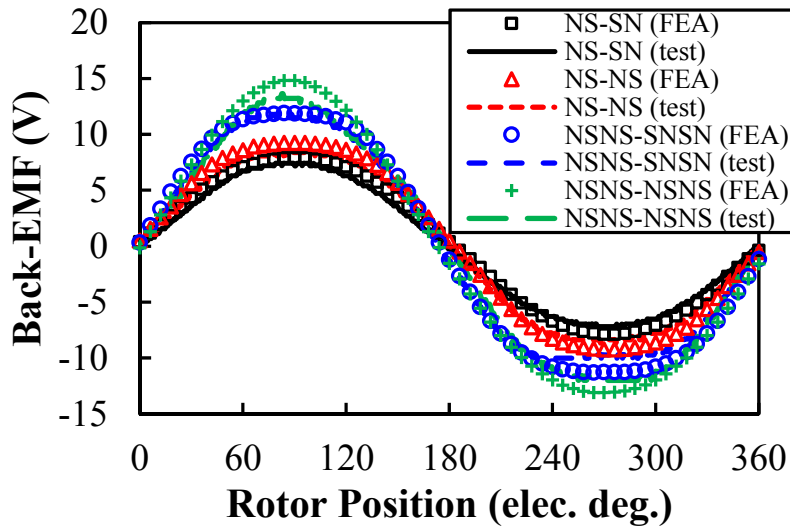
(e)

Fig. 2.42 Prototype machines. (a) 12-slot NS-SN stator. (b) 12-slot NS-NS stator. (c) 6-slot NSNS-SNSN stator. (d) 6-slot NSNS-NSNS stator. (e) Shared 14-pole rotor.

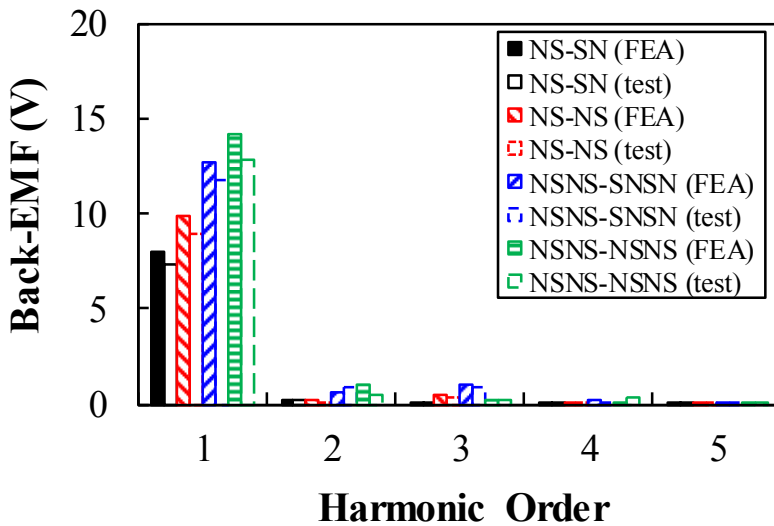
Table 2.6 Parameters of the FRPM prototypes with different PM arrangements

	NS-SN	NS-NS	NSNS-SNSN	NSNS-NSNS
Stator outer diameter $D$ (mm)			90	
Axial length $l$ (mm)			25	
Air-gap length $g$ (mm)			0.5	
Remanence of PM $B_r$ (T)			1.2	
Relative permeability of PM $\mu_r$			1.05	
Thickness of stator yoke $t_{sy}$ (mm)	3.2			4.2
Width of stator tooth $w_{st}$ (mm)	3.2			8.4
Width of stator slot opening $w_{so}$ (mm)	2.5			2.5
Split ratio $k_{sr}$			0.65	
PM thickness $h_m$ (mm)			2	
Width of rotor tooth $w_{rt}$ (mm)			3.6	

Fig. 2.43 (a) shows the measured and FE-predicted back-EMF waveforms of the four machines at  $n=400\text{rpm}$ , while their harmonic spectra are shown in Fig. 2.43 (b). It should be noted that to guarantee the same slot filling factor, the number of turns per coil  $n_c$  is 74 for the NS-SN and NS-NS, and it is 115 for the NSNS-SNSN and NSNS-NSNS. As can be seen, the measured back-EMF waveforms match well with the FEA results regardless of PM arrangement. For each PM arrangement, there is a 7%-9% decrease of the measured fundamental back-EMF magnitude over the FE-predicted value, and the errors can be attributed to the end-effect and manufacturing tolerance. Test results show that the NSNS-NSNS machine has the highest fundamental back-EMF, which is 72% higher than that of the NS-SN, 41% higher than that of the NS-NS, and 10% higher than that of the NSNS-SNSN.



(a)



(b)

Fig. 2.43 Measured and FE-predicted back-EMFs. ( $n=400\text{rpm}$ )

Based on the simple cogging torque and static torque measurement method introduced in Appendix B, the cogging torque and static torque of each machine are measured and compared with those obtained in FEA. Due to the high rotor pole number and corresponding limited torque measurement point, only torque waveforms without harmonic spectra are given. Fig. 2.44 shows the measured and FE-predicted cogging torque waveforms of the four machines. As can be seen, good agreement is achieved between the results. In addition, both the measured and FE-predicted cogging torques of the NSNS-SNSN and NSNS-NSNS are larger than those of the NS-NS and NS-SN.

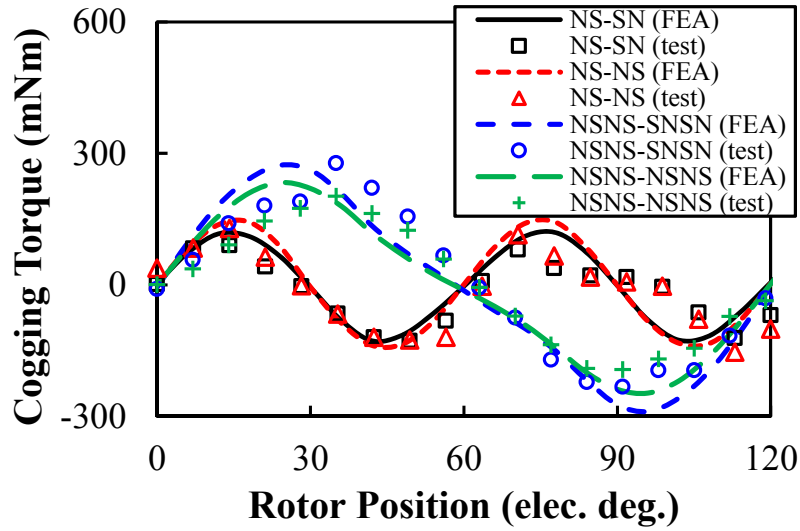


Fig. 2.44 Measured and FE-predicted cogging torques.

The variation of static torque against rotor position is measured by supplying three-phase windings with fixed DC current ( $I_a = -2I_b = -2I_c = I_{dc} = I_{rated}$ , and the rated current  $I_{rated}$  is corresponded to  $p_{cu} = 20W$ ). Fig. 2.45 shows the measured and FE-predicted static torques against rotor position of the four machines. Again, good agreement between the results can be observed. The maximum measured torque of the NSNS-NSNS is 2.3Nm, which is 96% higher than the NS-SN, 64% higher than the NS-NS, and 13% higher than the NSNS-SNSN.

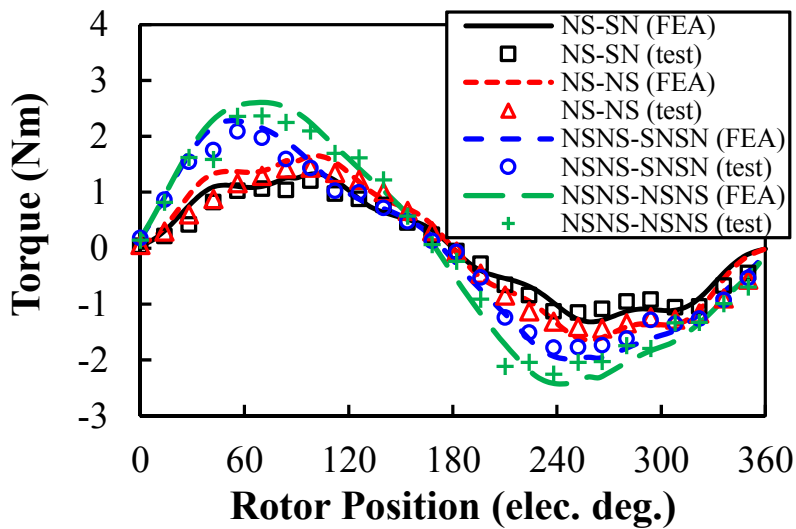


Fig. 2.45 Measured and FE-predicted static torques. ( $I_a = -2I_b = -2I_c = I_{rated}$ )

The torque variations of the four machines against current are compared in Fig. 2.46. As can be seen, the measured torque results match well with the FE-predicted values. Therefore, the highest torque density of the NSNS-NSNS FRPM machine is verified.

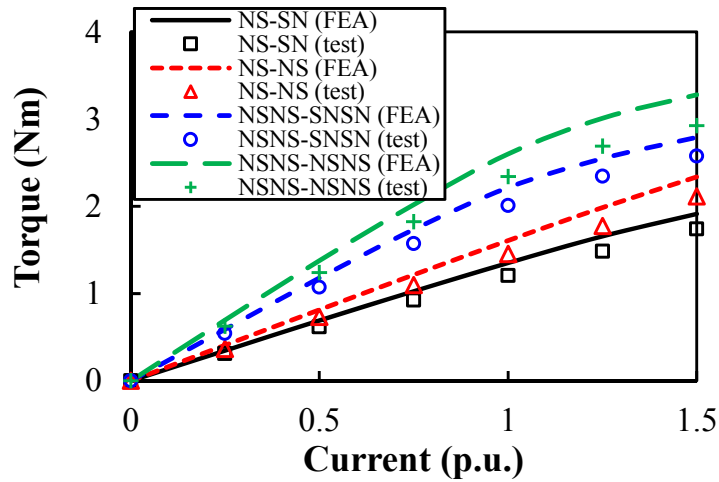


Fig. 2.46 Torque variations against current.

## 2.6 Conclusion

In this chapter, different PM arrangements of FRPM machines are analysed and compared. Based on the analysed machines, some findings can be summarised as follows:

1. The torque of a FRPM machine is produced by several dominant air-gap field harmonics. The working harmonics and resulted machine performance are greatly influenced by PM arrangement.
2. Each PM arrangement is preferable in a specific range of rotor pole number  $N_r$  to achieve high torque density, the optimal  $N_r$  is around 14 for the FRPM machines with 12 pairs of PMs.
3. Under the frequently used rotor pole number (e.g.  $N_r=14$ ), the FRPM machines with four PM pieces on each stator tooth have higher torque than those of the machines with two PM pieces, thanks to the enhanced armature field. The NSNS-NSNS arrangement offers the highest torque density and the highest efficiency.
4. In terms of the average torque of the FRPM machine, the opposite PM polarities of adjacent teeth rather than the identical one is preferred, since the concentrated PM field harmonic contents are more likely to be fully interacted with the armature field.
5. The power factor improvement is a key challenge for FRPM machines since the FRPM machines always have a low power factor due to the small flux linkage per pole (see Fig. 2.37). The low power factor will result in requirement of high capacity of the inverter, which increases the cost of the whole system and restricts the application of FRPM machines.



# **CHAPTER 3**

## **OPTIMAL NUMBER OF PM PIECES ON SINGLE STATOR TOOTH OF FLUX REVERSAL PERMANENT MAGNET MACHINE**

In this chapter, a unified analytical model of FRPM machines having different numbers of PM pieces on single stator tooth will be established, from which the optimal number of PM pieces on single stator tooth and the corresponding rotor pole number can be identified. Results show that by employing the optimal number of PM pieces instead of the conventional two on each stator tooth of the FRPM machine, additional back-EMF component can be generated which is beneficial to improve the torque. By using the developed analytical model, the influence of critical design parameters, including stator slot opening ratio, split ratio, PM thickness, and rotor slot ratio etc. will be investigated. Both FEA and experimental tests will be presented to validate the analytical analyses.

This chapter is published in *IEEE Trans. Energy Convers.*, 2018, doi: 10.1109/TEC.2018.2866765.

### **3.1 Introduction**

Among four kinds of stator-PM machines, the FRPM machine has less complex stator structure and simple SPM arrangement. However, due to large equivalent air-gap length for rotor-tooth modulation, the torque density of the FRPM machine is more likely to be smaller than the SFPM machine [CHE11a]. Therefore, the torque improvement of the FRPM machine is of great significance to boost its competitiveness against other machines and broaden its application prospect.

In chapter 2, the influence of PM polarities of adjacent teeth of FRPM machine has been investigated. With the aid of FEA, for the 14-rotor-pole FRPM machine, the electromagnetic performance of the four most commonly used PM arrangements have been compared. It reveals that the opposite PM polarities of adjacent teeth is preferred to maximise the torque. In addition, it has also been found that among the four PM arrangements, the two with four PM pieces on each stator tooth have higher torque than the others with two PM pieces on each stator tooth.



Therefore, an interesting question arises: what is the optimal number of PM pieces on single stator tooth of the FRPM machine?

To address this question, a unified analytical model of FRPM machines having different numbers of PM pieces on each stator tooth is established in this chapter, from which the machine back-EMF can be analytically derived and the optimal number of PM pieces on single stator tooth can be identified. To obtain a generalized conclusion, the determination of the associated rotor pole number, and the influence of design parameters including stator slot opening ratio, split ratio, PM thickness, rotor slot ratio, and stator slot number will also be investigated.

## **3.2 Working Principle of FRPM Machines with Different Number of PM Pieces on Single Stator Tooth**

### **3.2.1 Machine Configuration**

The most typical configuration of a three-phase FRPM machine is shown in Fig. 3.1 (a) (taking the 6-slot-stator FRPM machine for instance). As can be seen, the rotor of the FRPM machine is of pure reluctance structure, which has improved mechanical strength and is easy for manufacturing even if with high pole number. The non-overlapping concentrated armature windings are always wound around the stator teeth, resulting in short end-winding. Also, a pair of PMs is mounted on the inner surface of each stator tooth. As explained in chapter 2, with rotor rotating, the flux through the armature winding varies and the PM induced back-EMF interacts with the injected armature current to produce torque. The polarities of two adjacent PM pieces belonging to two stator teeth can be either identical or opposite (opposite in Fig. 3.1). In the case of identical polarities, the number of stator slot can be only even while that can be either even or odd in the case of opposite polarities.

In addition to the most typical configuration, the FRPM machines with increased number of PM pieces on single stator tooth have also been proposed and analysed. In [BOL02], the FRPM machine with increased PM pieces on each stator tooth is firstly proposed, i.e. four PM pieces instead of two, are mounted on each stator tooth, as shown in Fig. 3.1 (b). Ideally,  $2n_{pp}$  PM pieces can be mounted on each stator tooth, where  $n_{pp}$  is the number of PM pairs with minimum value being 1. Aiming at low-speed servo applications, a 12/28 FRPM machine with  $n_{pp}=2$  is optimised and analysed in [BOL02]. Although the working principle and winding

configuration of this kind of FRPM machine are then investigated in some other papers [MOR10a] [MOR10b], its performance difference against the conventional FRPM machine with  $n_{pp}=1$  has never been addressed. In addition, the analysis of the FRPM machine with  $n_{pp}>2$  has not been found in existing papers either. For instance, Fig. 3.1 (c) shows the FRPM machines with six PM pieces on each stator tooth ( $n_{pp}=3$ ). It should be noted that the associated rotor pole number varies with  $n_{pp}$ , which will be explained later.

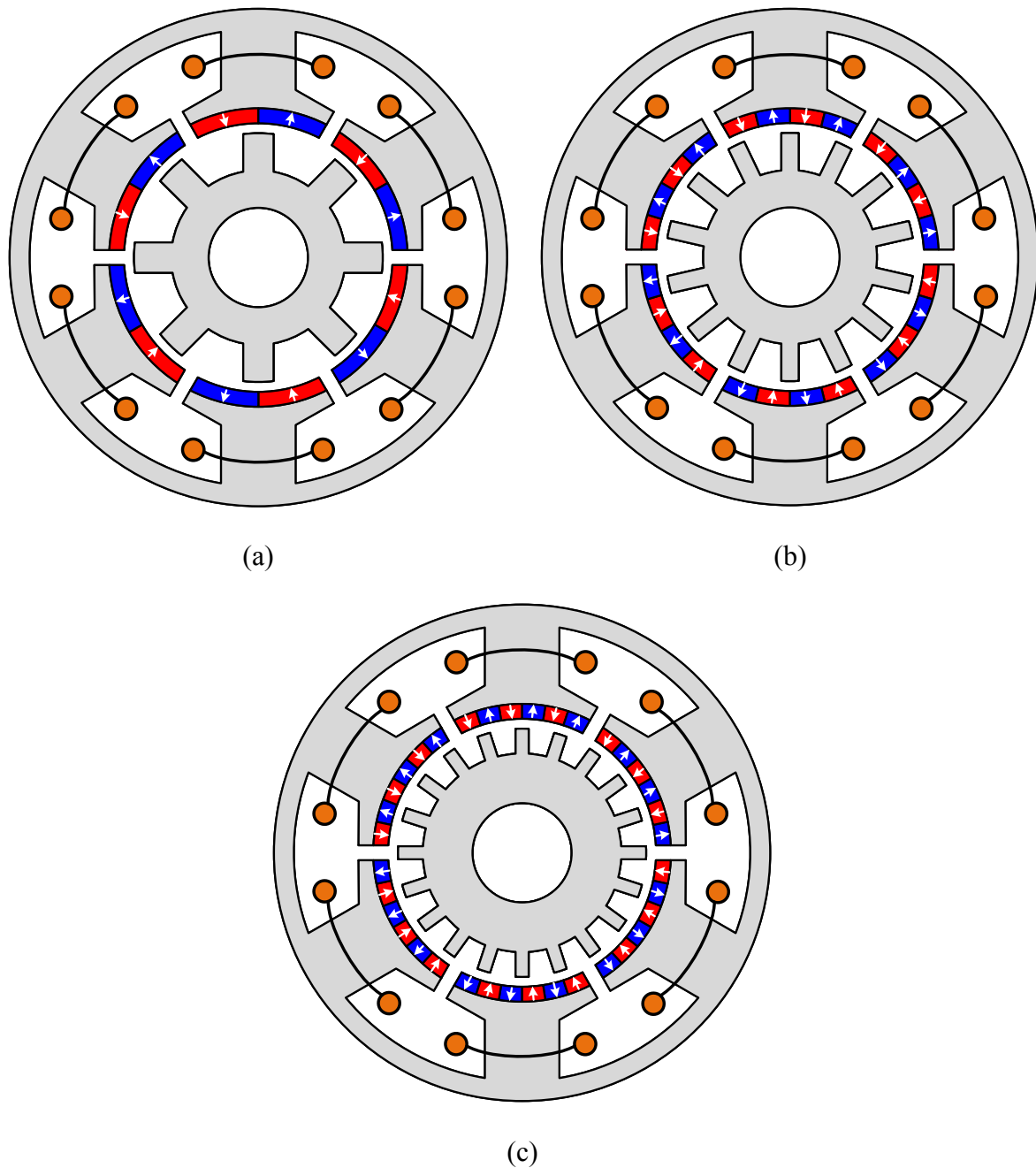


Fig. 3.1 FRPM machines with different numbers of magnet pieces on each stator tooth. (a) Conventional FRPM machine with  $n_{pp}=1$ . (b)  $n_{pp}=2$ . (c)  $n_{pp}=3$ .

### 3.2.2 Analytical Derivation of Machine Performance with Opposite PM Polarities of Adjacent Teeth

To investigate the operation principle of a FRPM machine and the influence of different numbers of PM pieces on single stator tooth, the analytical derivation of machine performance is conducted. To simplify the analysis, some assumptions are made as: 1) the saturation of the stator and rotor core is neglected; 2) the end-effect and fringing effect of the machine are neglected; 3) the magnets are radially-magnetized; 4) the dimensions of all PM pieces are the same.

In this chapter, the analytical expressions are deduced based on the FRPM machine with opposite PM polarities of adjacent teeth since its torque performance is proven to be better than its counterpart machine with identical PM polarities of adjacent teeth. Analytical derivation of the machine performance with identical PM polarities of adjacent teeth will be given in Appendix C.

The schematic of the FRPM machine considering  $npp$  is shown in Fig. 3.2. Some critical dimensional parameters including overall diameter ( $D$ ), inner radius of stator ( $R_{si}$ ), stator slot pitch ( $\tau_s$ ), width of stator slot opening ( $w_{so}$ ), PM height ( $h_m$ ), air-gap length ( $g$ ), rotor pole pitch ( $\tau_r$ ), and width of rotor slot opening ( $w_{ro}$ ) are also labelled.

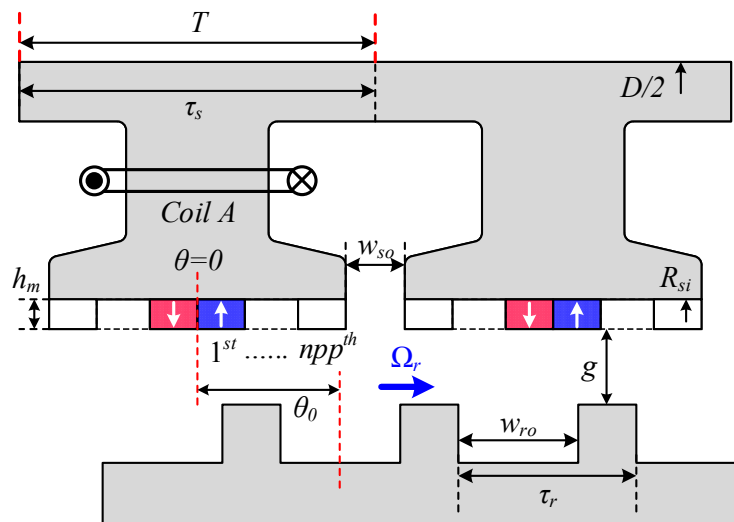


Fig. 3.2 Schematic of the FRPM machine with  $2npp$  PM pieces on single stator tooth.

On the basis of Ampere's circuital law, the magnetomotive force (MMF)-permeance model can be used to deduce the machine performance. Such a MMF-permeance model has been successfully implemented for the analysis of various machine topologies, such as SFPM

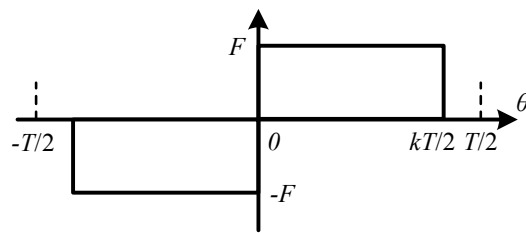
machine [GAU12], Vernier machine [LI16], and variable flux reluctance machine [HUA17b] etc. In [GAO17b], the MMF-permeance model has also been used to analyse the torque performance of the FRPM machine. However, the model is only focused on NS-SN (i.e.  $n_{pp}=1$ ). In this chapter, a unified MMF-permeance model will be established, in which  $n_{pp}$  can be considered and the contribution of working harmonics of PM MMF to back-EMF can be quantified.

Firstly, the no-load air-gap flux density of the FRPM machine can be given as

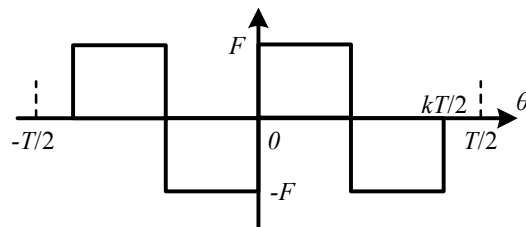
$$B(\theta, t) = F_{PM}(\theta) \Lambda_r(\theta, t) \quad (3.1)$$

where  $F_{PM}(\theta)$  is the PM MMF which is static under the stator reference frame, and  $\Lambda_r(\theta, t)$  is the specific relative air-gap permeance produced by the salient rotor which is dynamic due to the rotor rotation.

Considering the PM MMF of the machine, it is directly determined by the number of PM pairs on each stator tooth and the corresponding magnetisation directions. As shown in Fig. 3.2, since the PM arrangements of any two stator teeth are exactly the same, the PM MMFs are periodically distributed in the air-gap with a period  $T$  of  $\tau_s$ . By assuming the magnetisation direction of the 1st magnet piece outward, the PM MMF waveforms of different  $n_{pp}$  (1 to 3) are shown in Fig. 3.3.



(a)



(b)

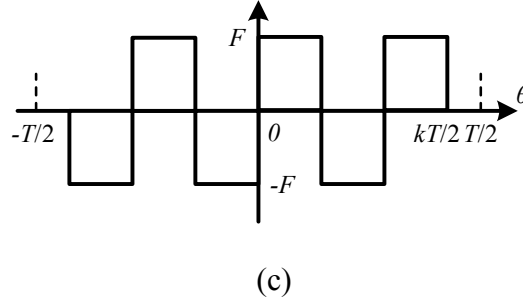


Fig. 3.3 PM MMF of FRPM machines. (a)  $npp=1$ . (b)  $npp=2$ . (c)  $npp=3$ .

The PM MMF can then be expressed in Fourier series, as

$$F_{PM}(\theta) = \sum_{i=1,2,3,\dots}^{\infty} F_i \sin(iN_s \theta) \quad (3.2)$$

where  $N_s$  is the number of stator slots,  $i$  is the order of Fourier series,  $F_i$  is the corresponding Fourier coefficient and is

$$F_i = \frac{4F}{TiN_s} \left[ -1 - (-1)^{npp} \cos(iN_s k \frac{T}{2}) + \sum_{j=1,2,3,\dots}^{npp+1} 2(-1)^{j-1} \cos(iN_s \frac{j-1}{npp} k \frac{T}{2}) \right] \quad (3.3)$$

where  $T=\tau_s=2\pi/N_s$ ,  $k=(1-w_{so}/\tau_s)$ ,  $F$  is related to the remanence ( $B_r$ ), height ( $h_m$ ), and relative permeability ( $\mu_r$ ) of the PM material, and  $F=B_r h_m / \mu_r \mu_0$ .

In terms of the relative air-gap permeance  $\Lambda_r(\theta, t)$ , it is essentially reflecting the slotting effect of the machine [WU12]. Based on the flux calculated for a slot-less machine, the conformal transformation can be used to evaluate  $\Lambda_r(\theta, t)$ , and there are many papers dealing with the mathematic expression of  $\Lambda_r(\theta, t)$ . In [ZHU93], a simple expression of  $\Lambda_r(\theta, t)$  is firstly presented by assuming the infinite slot depth and parallel slot in the machine, which can be used to calculate the radial flux component. Then, a complex form of  $\Lambda_r(\theta, t)$  is proposed in [ZAR06], from which both radial and tangential components of air-gap flux density can be obtained. Moreover, the expression of  $\Lambda_r(\theta, t)$  considering the doubly slotting effect of both stator and rotor slots is presented in [GAU12] [GAO17b]. Such expression has been proven to exhibit good accuracy for the machines with a reluctance rotor, albeit with a relative complex formula. Since the aim of the analytical model in this chapter is to investigate the influence of  $npp$  on machine performance rather than to improve the accuracy compared with FEA, the simple expression of  $\Lambda_r(\theta, t)$  in [ZHU93] is adopted, as

$$\Lambda_r(\theta, t) = \sum_{q=0,1,2,\dots}^{\infty} \Lambda_q \cos[qN_r(\theta - \theta_0 - \Omega_r t)] \quad (3.4)$$

and the Fourier coefficients can be obtained as

$$\Lambda_0 = \frac{\mu_0}{g'} (1 - 1.6\beta \frac{w_{ro}}{\tau_r}) \quad (3.5)$$

$$g' = g + \frac{h_m}{\mu_r} \quad (3.6)$$

$$\Lambda_q = -\beta \frac{4}{\pi q} \frac{\mu_0}{g'} \left[ \frac{1}{2} + \frac{(qw_{ro}/\tau_r)^2}{0.78125 - 2(qw_{ro}/\tau_r)^2} \right] \sin(1.6\pi q \frac{w_{ro}}{\tau_r}) \quad (3.7)$$

$$\beta = \frac{1}{2} \left[ 1 - \frac{1}{\sqrt{1 + (w_{ro}/2g')^2}} \right] \quad (3.8)$$

where  $\Omega_r$  is the angular speed of the rotor,  $N_r$  is the rotor pole number,  $q$  is the order of Fourier series, and  $\Lambda_q$  is the corresponding Fourier coefficient.

Substituting (3.2) and (3.4) into (3.1), the no-load air-gap flux density can then be expressed as

$$B(\theta, t) = \Lambda_0 \sum_{i=1,2,3,\dots}^{\infty} F_i \sin(iN_s \theta) + \sum_{i=1,2,3,\dots}^{\infty} \sum_{q=1,2,3,\dots}^{\infty} \frac{1}{2} F_i \Lambda_q \sin[(iN_s \pm qN_r)\theta \mp qN_r(\theta_0 + \Omega_r t)] \quad (3.9)$$

From (3.1)-(3.9), it can be observed that abundant air-gap flux density harmonics exist due to the rotor tooth modulation and the magnitudes of these harmonics highly depend on  $npp$ .

Considering the cogging torque of the machine, by using the virtual work method, it can be given as

$$T_c = -\frac{\partial W_c}{\partial \alpha} = -\frac{\partial W_c}{\partial (\Omega_r t)} \quad (3.10)$$

where  $\alpha$  is the rotor rotational angle, and  $W_c$  is the magnetic field energy which is equal to the co-energy stored in the air-gap and PMs of the machine under the assumption of infinite permeability of stator and rotor core, as

$$\begin{aligned}
W_c(t) &= \int \frac{1}{2\mu_0} B(\theta, t)^2 dV = \int \frac{1}{2\mu_0} F_{PM}(\theta)^2 \Lambda_r(\theta, t)^2 dV \\
&= \frac{l(R_{si}^2 - R_{ro}^2)}{2\mu_0} \int_0^{2\pi} F_{PM}(\theta)^2 \Lambda_r(\theta, t)^2 d\theta \\
&= \frac{\pi l(R_{si}^2 - R_{ro}^2)}{4\mu_0} \sum_{\frac{nN_r}{N_s}} F'_{\frac{nN_r}{N_s}} \Lambda'_n \cos[nN_r(\theta_0 + \Omega_r t)]
\end{aligned} \tag{3.11}$$

where  $l$  is axial length of the machine,  $R_{ro}$  is the outer radius of rotor,  $F'$  is the Fourier coefficient of  $F_{PM}(\theta)^2$ ,  $\Lambda'$  is the Fourier coefficient of  $\Lambda_r(\theta, t)^2$ , and  $n$  is the integer which makes  $(nN_r/N_s)$  an integer as well.

Then the cogging torque can be deduced as

$$T_c(t) = \frac{nN_r \pi l (R_{si}^2 - R_{ro}^2)}{4\mu_0} \sum_{\frac{nN_r}{N_s}} F'_{\frac{nN_r}{N_s}} \Lambda'_n \sin[nN_r(\theta_0 + \Omega_r t)] \tag{3.12}$$

The fundamental period of the cogging torque,  $N_c$ , is equal to the minimum  $n$ , and can be expressed as

$$N_c = n_{\min} = \frac{N_s}{\text{GCD}(N_r, N_s)} \tag{3.13}$$

From (3.13), it can be found that  $N_c$  is only related to  $N_s$  and the greatest common divisor (GCD) between  $N_r$  and  $N_s$  and is irrelevant to  $npp$ . This is because that the waveforms of  $F_{PM}(\theta)^2$  are exactly the same regardless of  $npp$ , as can be imagined from the waveform of  $F_{PM}(\theta)$  shown in Fig. 3.3.

As shown in Fig. 3.2, by integrating the air-gap flux density under the stator tooth, the flux through Coil A can be written as

$$\begin{aligned}
\lambda_A(t) &= n_c \int B(\theta, t) ds = n_c l R_{si} \int_{-k\pi/N_s}^{k\pi/N_s} B(\theta, t) d\theta \\
&= \sum_{i=1,2,3\dots}^{\infty} \sum_{q=1,2,3\dots}^{\infty} \frac{n_c l R_{si} F_i \Lambda_q}{(iN_s \pm qN_r)} \sin \left[ \left( \frac{iN_s \pm qN_r}{N_s} \right) k\pi \right] \sin [\mp qN_r(\theta_0 + \Omega_r t)]
\end{aligned} \tag{3.14}$$

where  $n_c$  is the number of series-connected turns of Coil A.

Correspondingly, the back-EMF of Coil A can be obtained as

$$e_A(t) = -\frac{d\lambda_A(t)}{dt} = \sum_{i=1,2,3\dots}^{\infty} \sum_{q=1,2,3\dots}^{\infty} \frac{\pm n_c l R_{si} F_i \Lambda_i q N_r \Omega_r}{(iN_s \pm qN_r)} \sin \left[ \left( \frac{iN_s \pm qN_r}{N_s} \right) k\pi \right] \cos [qN_r (\theta_0 + \Omega_r t)] \quad (3.15)$$

From (3.15), it can be seen that the air-gap flux density harmonics with the same  $q$  contribute to the back-EMF of the same frequency. Since  $\Lambda_1$  is much larger than the magnitudes of other permeance harmonics, the flux density harmonics with order being  $(iN_s \pm N_r)$  are all possible to produce the fundamental back-EMF, of which the magnitude can be expressed as

$$E_A = \sum_{i=1,2,3\dots}^{\infty} \frac{\pm n_c l R_{si} F_i \Lambda_1 N_r \Omega_r}{(iN_s \pm N_r)} \sin \left[ \left( \frac{iN_s \pm N_r}{N_s} \right) k\pi \right] \quad (3.16)$$

Obviously, the back-EMF is greatly influenced by  $npp$  because the magnitudes of the air-gap flux density harmonics are related to  $npp$ , as can be seen from (3.3) and (3.9).

By injecting sinusoidal phase current ( $I_d=0$ ), the average torque of the machine can be derived as

$$T = \frac{3}{2} n_{coil} k_d I_A E_A = \frac{3}{2} n_{ph} k_d I_A \sum_{i=1,2,3\dots}^{\infty} \frac{\pm l R_{si} F_i \Lambda_1 N_r \Omega_r}{(iN_s \pm N_r)} \sin \left[ \left( \frac{iN_s \pm N_r}{N_s} \right) k\pi \right] \quad (3.17)$$

where  $n_{coil}$  is the number of series-connected coils per phase,  $n_{ph}$  is the number of series-connected turns per phase,  $k_d$  is the distribution factor of the armature winding, and  $I_A$  is the peak value of the phase current.

### 3.3 Analysis of FRPM Machines with Different Numbers of PM Pieces

#### 3.3.1 Optimal Rotor Pole Number

It is clear that the rotor pole number  $N_r$  has a big influence on performance of the FRPM machine. In chapter 2, it has been proven that the 14-pole-rotor is suitable for the 12-slot-stator FRPM machine ( $npp=1$ ) in terms of the average torque. However, for different  $npp$ , the most suitable rotor pole number varies, which will be illustrated in the following.

Based on the analytical expressions and the fixed parameters listed in Table 3.1, the magnitude of the fundamental back-EMF is used to evaluate the performance of the FRPM machines with different stator slot/rotor pole combinations.



Table 3.1 Parameters of the FRPM machine in analytical model

Parameters	Value	Parameters	Value
Overall diameter ( $D$ )	90mm	Axial length ( $l$ )	25mm
Inner radius of stator ( $R_{si}$ )	31.5mm	Width of stator slot opening ( $w_{so}$ )	2.5mm
PM height ( $h_m$ )	2mm	Air-gap length ( $g$ )	0.5mm
Width ratio of rotor slot ( $w_{ro}/\tau_r$ )	0.7	Number of turns per coil ( $n_c$ )	1
Remanence of PM ( $B_r$ )	1.2T	Relative permeability of PM ( $\mu_r$ )	1.05

Taking  $N_s=6$  as an example, when the number of turns per coil  $n_c=1$  and the rotor speed  $n=4000\text{rpm}$ , the variation of the magnitude of fundamental back-EMF in a single coil against  $N_r$  is shown in Fig. 3.4. As can be seen, when  $npp$  ranges from 1 to 5, the optimal  $N_r$  are 6, 13, 19, 26, and 32, respectively. This can be explained by that the variation of flux is caused by the relative movement between rotor poles and PM pieces, a similar number of rotor pole and fundamental pole-pair of PM MMF is beneficial to fully utilize the PM field.

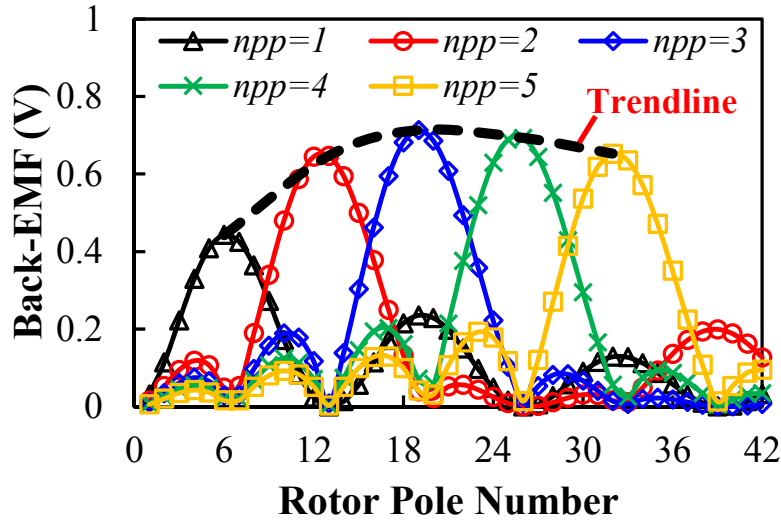


Fig. 3.4 Variations of the fundamental back-EMF magnitude of FRPM machines against rotor pole number. ( $N_s=6$ ,  $n_c=1$  and  $\Omega_r=2\pi\cdot4000/60$  rad/s)

Fig. 3.5 shows the harmonic spectra of the PM MMF. As can be seen, the harmonic order of the largest magnitude (i.e. the fundamental pole-pair of PM MMF) is related to  $npp$ , which is  $nppN_s$ . In addition, from (3.16), the back-EMF of the machine with a large  $N_r$  tends to be high when the rotor speed is fixed. Therefore, the optimal rotor pole number  $N_r$  should be  $(nppN_s+m)$ ,

where  $m=0, 1$  or  $2$ . Considering the fact that the unbalanced magnetic force may exist if  $N_r$  is odd, the suggested rotor pole number for a three-phase FRPM machine can be given as

$$N_r = nppN_s + 2 \quad (3.18)$$

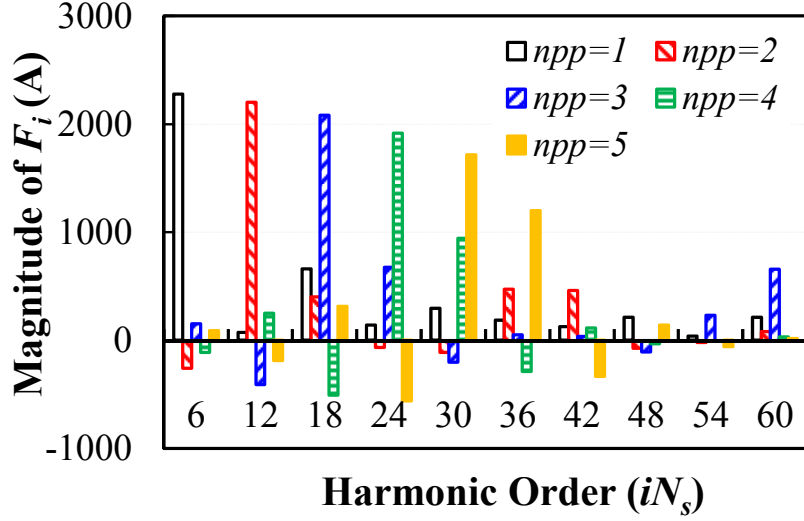


Fig. 3.5 Harmonic spectra of the PM MMFs ( $N_s=6$ ).

### 3.3.2 Identification of Working Harmonics of PM MMF

Considering the maximum back-EMF value of the FRPM machines with different  $npp$  (see the trend line in Fig. 3.4), when  $npp$  increases from 1, the back-EMF firstly increases and then reaches a maximum with  $npp=3$ , and it starts to decrease by further increasing  $npp$ . In comparison with the conventional FRPM machine with  $npp=1$ , the back-EMF of the FRPM machine with  $npp=3$  is improved by 61%.

To identify the best  $npp$  for the FRPM machine, and also explain the trend line of the performance variation against  $npp$ , it is necessary to quantify the contribution of each harmonic of the PM MMF. From (3.16), it is shown that the fundamental back-EMF is contributed by several PM MMF harmonics but with different weight factors, as

$$E_A \propto \sum_{i=1,2,3,\dots}^{\infty} \frac{\pm N_r \Lambda_1}{(iN_s \pm N_r)} \sin \left[ \left( \frac{iN_s \pm N_r}{N_s} \right) k\pi \right] F_i \propto \sum_{i=1,2,3,\dots}^{\infty} f_w^i F_i \quad (3.19)$$

The weight factor  $f_w^i$  of the  $iN_s$ th MMF harmonic can be defined as

$$f_w^i = \frac{N_r \Lambda_1}{(iN_s + N_r)} \sin \left[ \left( \frac{iN_s + N_r}{N_s} \right) k\pi \right] - \frac{N_r \Lambda_1}{(iN_s - N_r)} \sin \left[ \left( \frac{iN_s - N_r}{N_s} \right) k\pi \right] \quad (3.20)$$

Under the fixed parameters listed in Table 3.1 and the suggested rotor pole number in (3.18), the weight factor  $f_w^i$  of the 6-slot-stator FRPM machines with different  $npp$  can be calculated, as shown in Fig. 3.6. Not surprisingly, for each  $npp$ , the weight factor of the  $nppN_s$ th harmonic is the highest. Therefore, the fundamental back-EMF of the machine is largely resulted from the  $nppN_s$ th PM MMF since its magnitude is also the highest, as shown in Fig. 3.5. The  $nppN_s$ th PM MMF is then defined as *Principal* MMF in this chapter. In addition to *Principal* MMF, it is found that both weight factor and magnitude of the  $(npp+1)N_s$ th PM MMF are considerable especially when  $npp$  is large. The  $(npp+1)N_s$ th PM MMF is then defined as *Auxiliary* MMF. Table 3.2 shows the back-EMF contribution from both *Principal* and *Auxiliary* MMFs. For each  $npp$ , by setting the back-EMF produced by *Principal* MMF as benchmark, the normalized back-EMF produced by *Auxiliary* MMF is listed as well. It shows that the back-EMF contribution of *Auxiliary* MMF increases with  $npp$ , e.g. when  $npp=1$ , it is only 2% of the back-EMF produced by *Principal* MMF while it grows to 36% for  $npp=5$ . More importantly, the back-EMF resulted from these two MMF components accounts for more than 90% of the overall back-EMF. Therefore, it can be regarded that the back-EMF as well as the torque of the studied FRPM machines are mainly contributed by two working harmonics of the PM MMF, i.e. the  $nppN_s$ th and the  $(npp+1)N_s$ th.

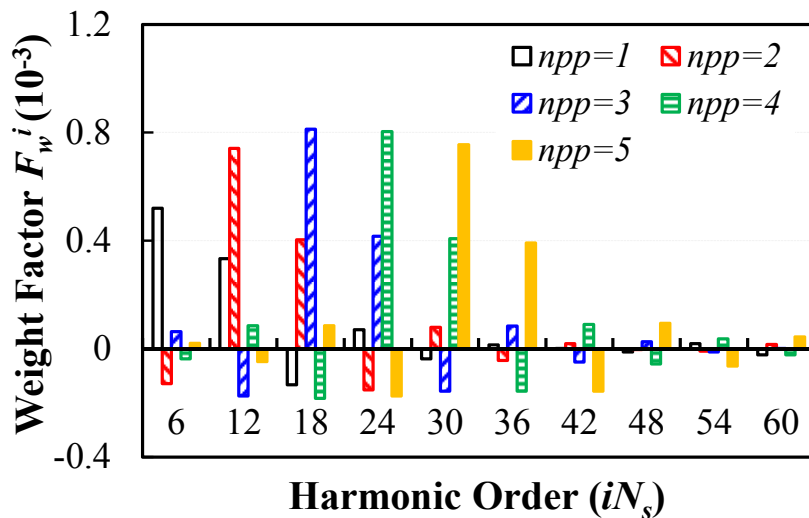


Fig. 3.6 Weight factors of the PM MMF harmonics ( $N_s=6$ ).

Table 3.2 Back-EMF contribution by *Principal* and *Auxiliary* MMF harmonics

$npp$	Overall Back-EMF	Produced by <i>Principal</i> MMF	Produced by <i>Auxiliary</i> MMF	Produced by other MMF harmonics
1	0.36V	0.38V (100%)	0.01V (2%)	-0.03V
2	0.59V	0.54V (100%)	0.05V (10%)	0
3	0.69V	0.56V (100%)	0.09V (17%)	0.04V
4	0.69V	0.51V (100%)	0.13V (25%)	0.05V
5	0.65V	0.43V (100%)	0.16V (36%)	0.06V

The back-EMFs produced by these two working harmonics are shown in Fig. 3.7, and can be used to explain the trend of the performance variation against  $npp$  shown in Fig. 3.4. It can be seen that the back-EMF produced by *Principal* MMF firstly increases with  $npp$  thanks to the increased weight factor shown in Fig. 3.6, and then it decreases due to the decreased magnitude as shown in Fig. 3.5. It achieves the maximum value when  $npp=3$ . In terms of the back-EMF produced by *Auxiliary* MMF, it always increases with  $npp$  since the magnitude of *Auxiliary* MMF largely increases with  $npp$ , as shown in Fig. 3.5. On the whole, when  $npp$  increases from 1, the performance of the FRPM machine is firstly improved due to the additional contribution of *Auxiliary* MMF. With the further increase of  $npp$ , the machine performance deteriorates due to the magnitude reduction of *Principal* MMF. Therefore, there exists an optimal  $npp$  for FRPM machine, and it is 3 when  $N_s=6$ .

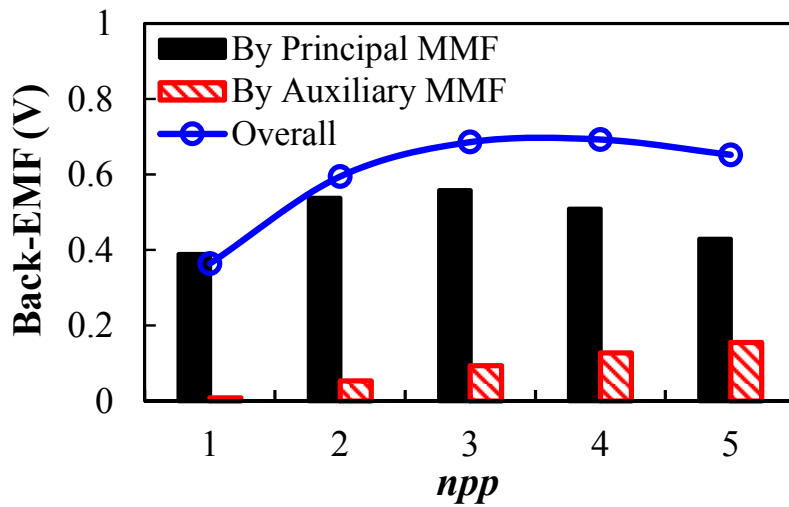


Fig. 3.7 Back-EMF produced by *Principal* MMF and *Auxiliary* MMF.

### 3.3.3 Influence of Number of PM Pieces on Cogging Torque

From (3.13), it is found that the fundamental period of cogging torque is determined by  $N_s$  and  $N_r$ . Although the optimal  $N_r$  varies with  $npp$  based on (3.18), the GCD ( $N_s$ ,  $N_r$ ) remains unchanged when  $N_s=6$ . Therefore,  $npp$  only affects the peak to peak value of the cogging torque, as shown in Fig. 3.8. The cogging torque decreases when  $npp$  increases from 1 to 4. In comparison with  $npp=4$ , the cogging torque with  $npp=5$  is larger. As shown in Fig. 3.3, the waveforms of  $F_{PM}(\theta)^2$  are exactly the same for different  $npp$ . However, for different  $npp$ , the cogging torque is related to different harmonics of  $F_{PM}(\theta)^2$ , of which the order can be obtained from (3.12) and is  $(3npp+1)$  when  $N_s=6$ . Fig. 3.9 shows the absolute value of harmonic magnitude of  $F_{PM}(\theta)^2$ , and the harmonics contributing to the fundamental cogging torques of different  $npp$  are also labelled. As can be seen, the magnitude variation of these harmonics matches well with the cogging torque variation in Fig. 3.8.

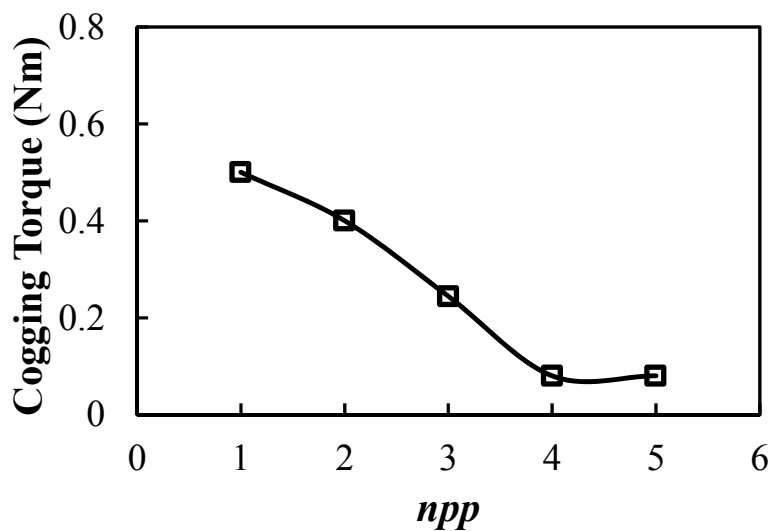


Fig. 3.8 Peak to peak values of the cogging torques with different  $npp$ .

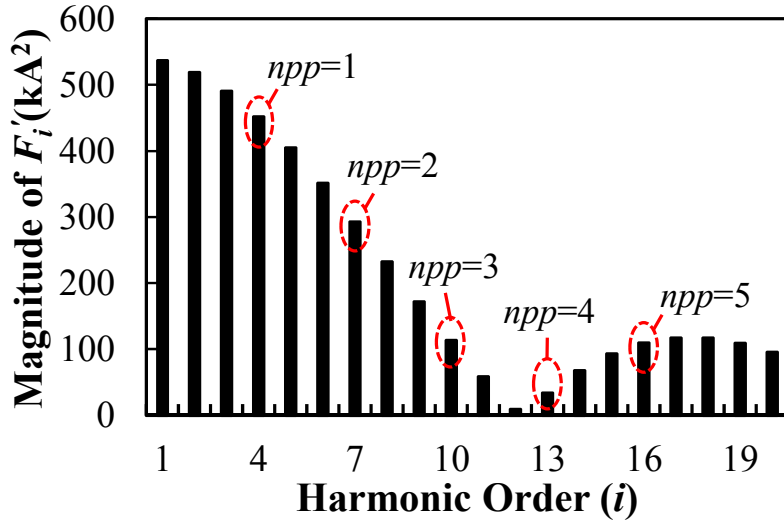


Fig. 3.9 Magnitudes of harmonics of  $F_{PM}(\theta)^2$ .

### 3.4 Influence of Design Parameters

To provide a simple design guidance of the FRPM machines analysed above, the influence of some key design parameters including stator slot opening ratio, split ratio, PM thickness, and rotor slot ratio, on the machine performance is investigated. Besides, the optimal  $npp$  for FRPM machines with different stator slot numbers is also investigated.

#### 3.4.1 Stator Slot Opening Ratio

Since the ratio of stator slot opening to stator slot pitch ( $w_{so}/\tau_s$ ) (designated as stator slot opening ratio) has a big influence on the distribution of the PM MMF, its influence on the machine performance is firstly investigated while other parameters are kept the same as Table 3.1. Fig. 3.10 shows the variation of the magnitude of the fundamental back-EMF against  $w_{so}/\tau_s$ . As can be seen, for each  $npp$ , there exists an optimal stator slot opening ratio. The larger the  $npp$ , the smaller the optimal  $w_{so}/\tau_s$ . For instance, the optimal stator slot opening ratio is 0.25 when  $npp=1$  while that is 0.1 when  $npp=3$ .

Considering the fact that the relative permeance is irrelevant to  $w_{so}/\tau_s$ , the magnitude variations of both *Principal* MMF and *Auxiliary* MMF are calculated to further explain the phenomenon, as shown in Fig. 3.11. As can be seen, when the ratio ( $w_{so}/\tau_s$ ) increases from 0 to 0.3, the magnitude of *Principal* MMF decreases regardless of  $npp$ . It means that the back-EMF produced by *Principal* MMF decreases with the ratio. In contrast, the magnitude of *Auxiliary* MMF as well as the corresponding back-EMF component tend to increase with the ratio, but

there exists an optimal value for  $npp > 2$ . Considering different  $npp$ , the sensitivity of the PM MMF to the ratio is the lowest for  $npp = 1$  and it increases with  $npp$ . Therefore, the optimal stator slot opening ratio is relatively large for  $npp = 1$  since it tends to utilize more *Auxiliary* MMF due to the high weight factor shown in Fig. 3.6. When  $npp$  increases, the optimal ratio becomes smaller since the *Principal* MMF rapidly decreases with the ratio and the optimal ratio for *Auxiliary* MMF also decreases.

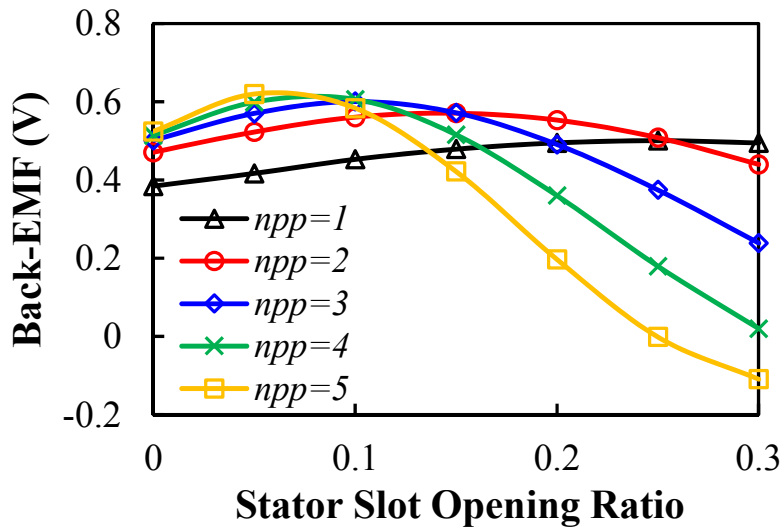
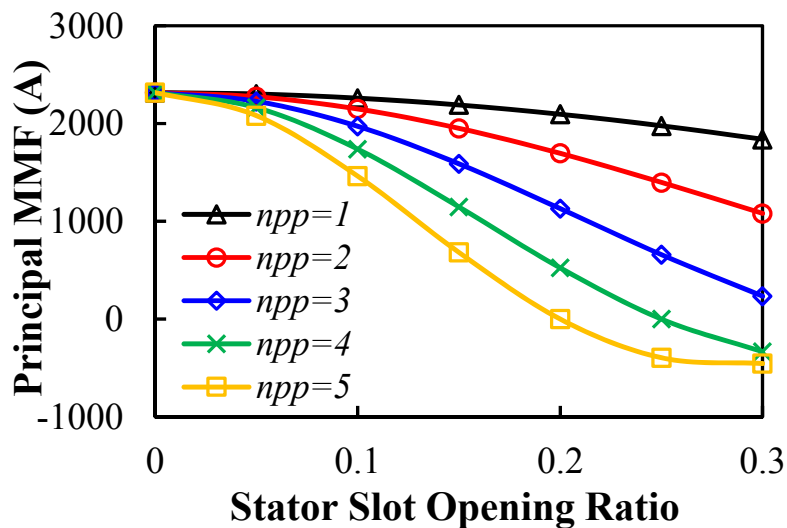
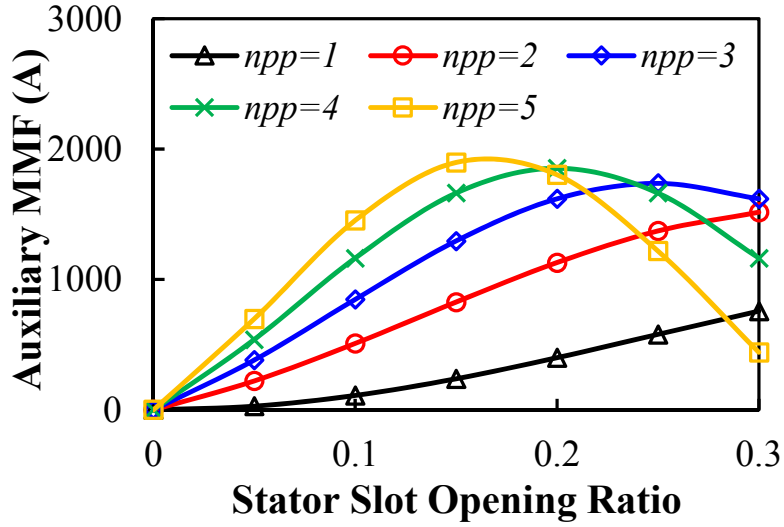


Fig. 3.10 Magnitudes of the fundamental back-EMFs with different  $w_{so}/\tau_s$ .



(a)



(b)

Fig. 3.11 Magnitude variation of PM MMF against stator slot opening ratio. (a) *Principal* MMF. (b) *Auxiliary* MMF.

### 3.4.2 Split Ratio

It is well-known that there should be an optimal split ratio ( $2R_{sl}/D$ ) for PM machines due to the trade-off between the magnetic loading and electric loading. To simplify the analysis of the influence of  $npp$  on the optimal value of split ratio, only the variation of back-EMF, i.e. the equivalent electric loading against split ratio is calculated by assuming the number of turns per coil  $n_c$  and other parameters unchanged as Table 3.1. As shown in Fig. 3.12, for all  $npp$ , the fundamental back-EMFs increase against split ratio but with different rates of increase, and the rate of increase is larger for a larger  $npp$ . Therefore, in comparison with the small  $npp$ , the optimal split ratio should be larger for the large  $npp$ . This can be further explained by the variation of the fundamental permeance  $\Lambda_1$  from (3.20), since the back-EMF is proportional to  $\Lambda_1$  which is related to  $N_r$ . For each  $npp$ , taking  $\Lambda_1$  with split ratio being 0.5 as benchmark, the variation of the normalised  $\Lambda_1$  against split ratio is shown in Fig. 3.13. As can be seen, the increase rate of the normalised  $\Lambda_1$  is larger for a larger  $npp$ , which is consistent with the variation of fundamental back-EMF shown in Fig. 3.12.



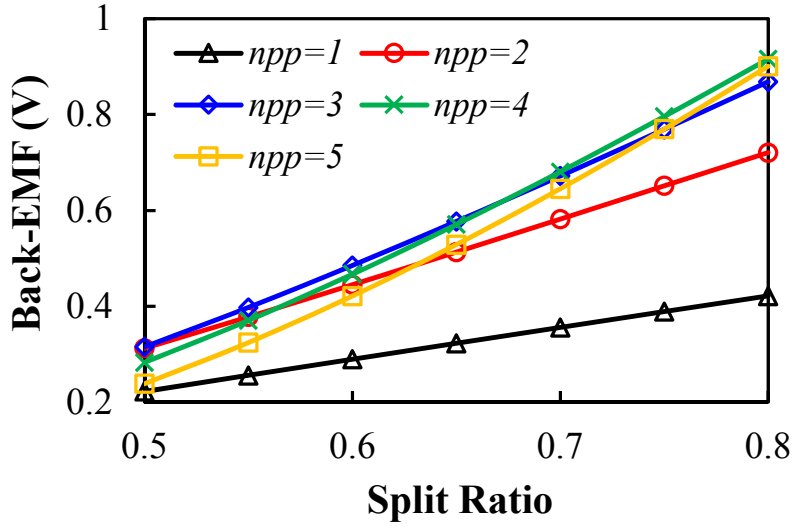


Fig. 3.12 Magnitude variation of fundamental back-EMF against split ratio.

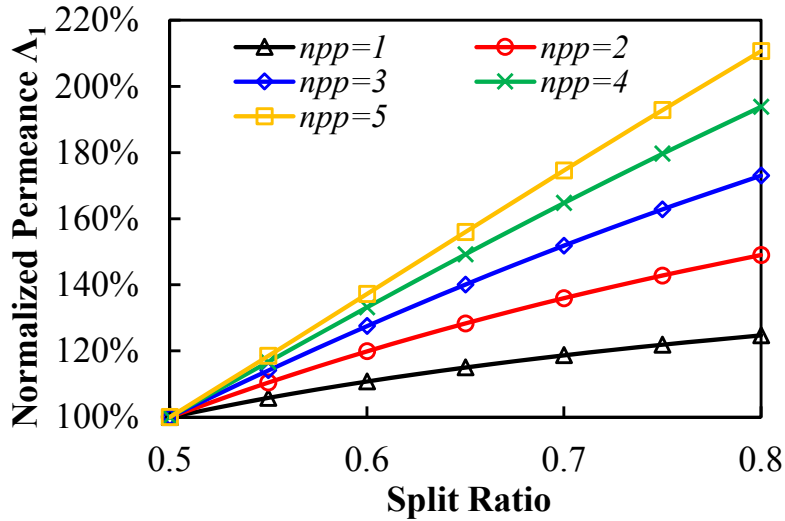


Fig. 3.13 Variation of normalised permeance  $\Lambda_1$  against split ratio.

### 3.4.3 PM Thickness

For the conventional PM machine, the back-EMF always increases as PM thickness  $h_m$  increases, although the machine may be saturated when the PMs are too thick. In contrast, it has been revealed that for the machine working based on air-gap field modulation, there always exists an optimal PM thickness  $h_m$  due to the rotor-tooth modulation effect [CHE11a]. Based on the analytical model in this chapter, it is clear that although  $h_m$  has almost no influence on the waveform (i.e. harmonic contents) of the PM MMF distribution, it largely affects the magnitudes of the PM MMF harmonics and the fundamental permeance  $\Lambda_1$ , as shown in (3.3)-(3.8). The influence of  $h_m$  on rotor-tooth modulation effect (i.e.  $\Lambda_1$ ) can then be quantified as follows.

Fig. 3.14 shows the magnitude variation of fundamental back-EMF of the FRPM machines against PM thickness  $h_m$ . As can be seen, for each  $npp$ , an optimal  $h_m$  exists. Such phenomenon can be further explained by the variation of normalised magnitudes of PM MMF harmonics and permeance  $\Lambda_1$  against PM thickness, as shown in Fig. 3.15. It should be noted that the magnitudes of PM MMF harmonics and the permeance  $\Lambda_1$  of  $h_m=0.4\text{mm}$  are set as the benchmark. As  $h_m$  increases, the magnitudes of PM MMF harmonics increase in a linear relationship while the magnitude of permeance  $\Lambda_1$  decreases in approximate parabolic type. Therefore, there would be a trade-off to maximise the back-EMF.

In terms of the different  $npp$ , it is found that the larger the  $npp$ , the smaller the optimal  $h_m$ . For example, for  $npp=1$ , the optimal  $h_m$  is 2mm while it is only 0.8mm for  $npp=5$ . Again, the variation of normalised permeance  $\Lambda_1$  can be used to explain this phenomenon. In comparison with a smaller  $npp$ , the normalised permeance  $\Lambda_1$  drops more rapidly against  $h_m$  for a larger  $npp$ . Therefore, the optimal  $h_m$  for a larger  $npp$  is relatively smaller which is beneficial to reduce the PM volume. However, for practical applications, the PM thickness cannot be selected too small due to the consideration of manufacturability and demagnetisation withstand capability. In chapter 2, the influence of  $h_m$  on demagnetisation withstand capability of the FRPM machine has been investigated. For the FRPM machines analysed in this chapter, the PM thickness of all  $npp$  is fixed to 2mm. Correspondingly, the optimal  $npp$  is 3, as shown in Fig. 3.14.

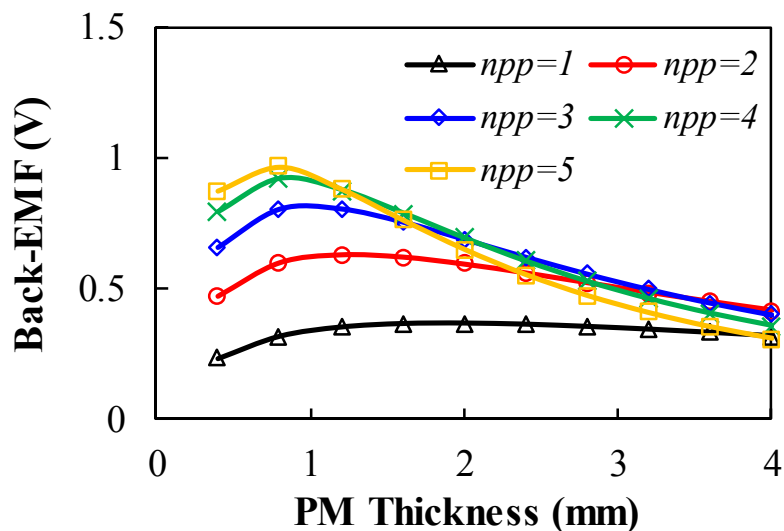


Fig. 3.14 Magnitude variation of fundamental back-EMF against PM thickness.

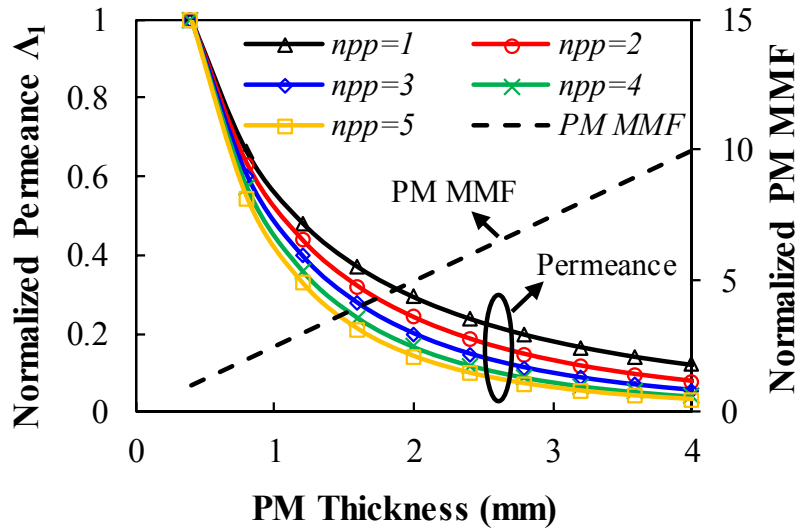


Fig. 3.15 Variation of normalised magnitudes of PM MMF harmonics and permeance  $\Delta_1$  against PM thickness.

### 3.4.4 Rotor Slot Ratio

The ratio of rotor slot width to rotor slot pitch ( $w_{ro}/\tau_r$ ) (designated as rotor slot ratio) directly determines the permeance distribution, thus having a significant influence on the performance of FRPM machines, as shown in Fig. 3.16. As can be seen, for each  $npp$ , there exists an optimal rotor slot ratio and the larger the  $npp$ , the larger the optimal rotor slot ratio. Besides, the back-EMF is more sensitive to rotor slot ratio when  $npp$  is large.

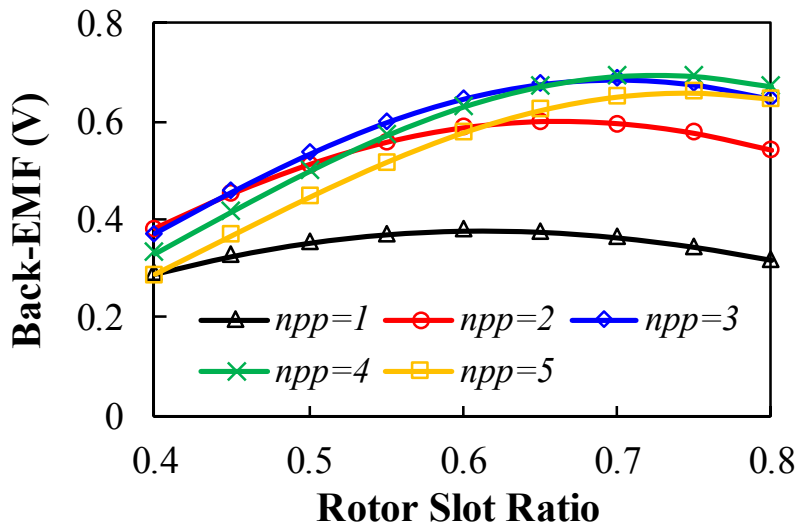


Fig. 3.16 Magnitude variation of fundamental back-EMF against rotor slot ratio.

By setting the magnitudes of permeance  $\Delta_1$  when rotor slot ratio is 0.4 as benchmark, the variation of normalised magnitudes of permeance  $\Delta_1$  is shown in Fig. 3.17. It is clear that the

larger the  $npp$ , the larger the optimal rotor slot ratio to maximise  $\Lambda_1$  and the more the sensitive of  $\Lambda_1$  to rotor slot ratio, which are all consistent with Fig. 3.16.

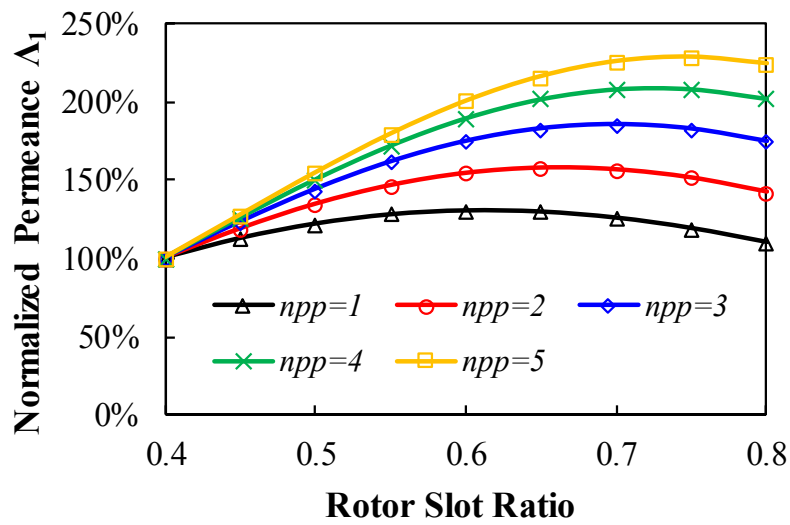


Fig. 3.17 Variation of normalised magnitudes of permeance  $\Lambda_1$  against rotor slot ratio.

### 3.4.5 Stator Slot Number

For FRPM machines with different numbers of stator slot  $N_s$ , the influence of  $npp$  is also investigated. Based on the parameters listed in Table 3.1, Fig. 3.18 shows the variation of the magnitude of the fundamental back-EMF against rotor pole number when  $N_s=12$ . Similar to Fig. 3.4, there is an optimal rotor pole number for each  $npp$ , and it is basically consistent with (3.18).

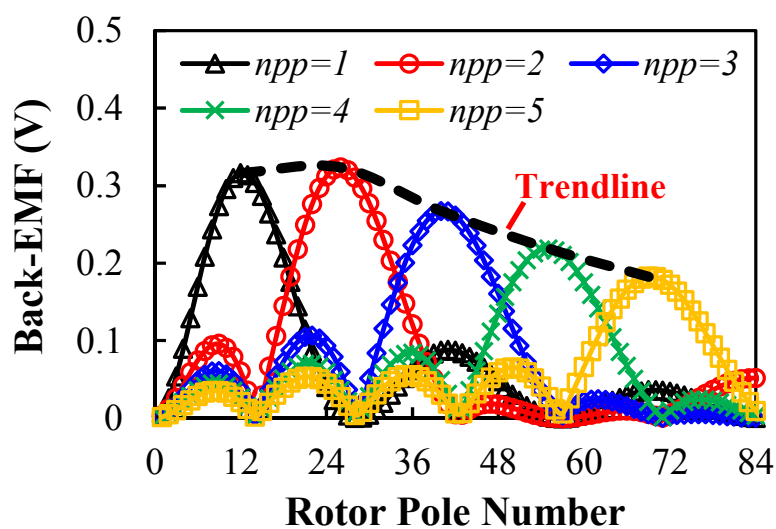


Fig. 3.18 Fundamental back-EMF variation against rotor pole number ( $N_s=12$ ).

For  $N_s=6$ , it has been proven that by increasing  $npp$  from 1 to the optimal value of 3, the back-EMF can be effectively improved mainly due to the increased weight factor of *Principal* MMF shown in Fig. 3.6, and increased magnitude of *Auxiliary* MMF shown in Fig. 3.5. However, for  $N_s=12$ , the optimal  $npp$  is 2 instead of 3, which can be observed from Fig. 3.18. This can be explained by the weight factor shown in Fig. 3.19. Compared with that shown in Fig. 3.6,  $npp=2$  has the highest weight factor of *Principal* MMF, and it drops rapidly with  $npp$ .

Similarly, the optimal  $npp$  for other  $N_s$  is identified and listed in Table 3.3. As can be seen, the optimal  $npp$  becomes 1 when  $N_s>12$ , i.e. the torque density of the machines cannot be improved by increasing the number of PM pieces on each stator tooth. This can be explained by the limited stator slot pitch under the fixed stator outer diameter  $D$  (90mm in this study). It should be noted that the optimal  $npp$  may vary with  $D$ . However, for different  $D$ , the optimal  $npp$  can still be determined and analysed by using the analytical model in this paper.

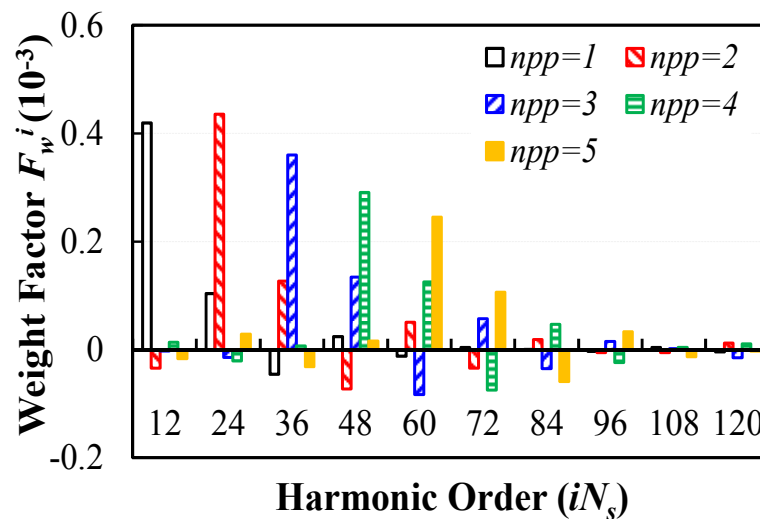


Fig. 3.19 Weight factors of PM MMF for  $N_s=12$ .

Table 3.3 Optimal  $npp$  for different numbers of stator slot

$N_s$	6	12	18	24
Optimal $npp$	3	2	1	1

### 3.5 Performance Validation by Finite Element Analysis

#### 3.5.1 Optimal Number of PM Pieces

To verify the findings obtained by the analytical model, the genetic-algorithm-based global optimisation by FEA is implemented for FRPM machines with different  $N_s$  and  $npp$ . To achieve a fair comparison, all the machines are optimised under the same effective space envelop ( $D=90\text{mm}$  and  $l=25\text{mm}$ ) and active copper loss ( $p_{cu}=20\text{W}$ ). The detailed parameters of the optimum FEA models are shown in Table 3.4 and Table 3.5. It should be noted that the PM thickness of all the machines is selected as 2mm to guarantee the mechanical strength and demagnetisation withstand capability.

Table 3.4 Parameters of optimum FEA models and prototypes of FRPM machines ( $N_s=6$ )

Parameters	FEA models					Prototypes		
	1	2	3	4	5	1	2	3
$npp$	1	2	3	4	5	1	2	3
Rotor pole number $N_r$	8	14	20	26	32	8	14	20
Overall diameter ( $D$ , mm)	90							
Axial length ( $l$ , mm)	25							
PM height ( $h_m$ , mm)	2mm							
PM property ( $B_r/u_r$ )	1.2T/1.05							
Split ratio ( $2R_{si}/D$ )	0.63	0.66	0.7	0.71	0.74	0.65		
Width ratio of stator slot opening ( $w_{sol}/\tau_s$ )	0.23	0.13	0.1	0.07	0.05	0.08		
Stator yoke thickness ( $t_{sy}$ , mm)	3.1	3.3	3.3	3.4	3.2	4.2		
Width of stator tooth ( $w_{st}$ , mm)	12.3	7.4	7.5	8.9	8.5	8.4		
Width ratio of rotor slot ( $w_{ro}/\tau_r$ )	0.67	0.72	0.76	0.75	0.75	0.75	0.7	0.7

Table 3.5 Parameters of optimum FEA models of FRPM machines ( $N_s=12, 18, \text{ and } 24$ )

Stator slot number ( $N_s$ )	12			18			24		
$npp$	1	2	3	1	2	3	1	2	3
Rotor pole number	14	26	38	20	38	56	26	50	74
Overall diameter ( $D$ , mm)	90								
Axial length ( $l$ , mm)	25								
PM height ( $h_m$ , mm)	2								
PM property ( $B_r/u_r$ )	1.2T/1.05								
Split ratio ( $2R_{sl}/D$ )	0.67	0.72	0.76	0.68	0.73	0.74	0.7	0.72	0.73
Width ratio of stator slot opening ( $w_{sol}/\tau_s$ )	0.13	0.09	0.07	0.13	0.11	0.1	0.16	0.14	0.14
Stator yoke thickness ( $t_{sy}$ , mm)	3.2	2.3	2.1	2.4	2.4	2.7	2.3	2.6	3.3
Width of stator tooth ( $w_{st}$ , mm)	3	3	2.5	2.7	2.5	3.2	2.2	2.6	3.1
Width ratio of rotor slot ( $w_{ro}/\tau_r$ )	0.73	0.73	0.73	0.73	0.77	0.77	0.68	0.69	0.73

Fig. 3.20 shows the average torque variation against  $npp$ . Apart from the results obtained by FEA, the analytically predicted torque values are also calculated based on the parameters of the optimum FEA models. As can be seen, for  $N_s=6$ , the FEA and analytical results match well with each other while for other  $N_s$ , the analytical value is slightly smaller than the FEA value, which is mainly attributed to the assumptions made in the analytical model. More importantly, for both FEA and analytical results, the optimal  $npp$  is 3 for  $N_s=6$ , while it is 2 for  $N_s=12$ , and 1 for  $N_s=18$  and 24. Therefore, the previous analysis of the optimal  $npp$  is verified by FEA.

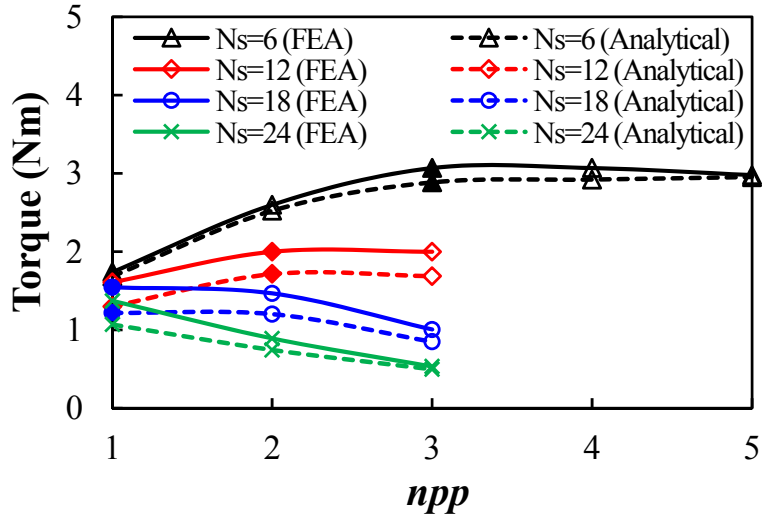


Fig. 3.20 Variation of torque of the FRPM machines against  $npp$ .

Taking  $N_s=6$  as an example, the performance of the FRPM machines with different  $npp$  (from 1 to 5) is compared in the following. As shown in Table 3.4, when  $npp$  increases from 1, both the split ratio and the rotor slot ratio increase, while the stator slot opening ratio decreases. Such phenomena are consistent with the previous analysis.

### 3.5.2 No-Load Performance

#### 3.5.2.1 Flux Distribution

The no-load air-gap flux densities of the machines with  $npp$  ranging from 1 to 5 are shown in Fig. 3.21-Fig. 3.25. As can be seen, the main harmonics of the air-gap flux density are largely influenced by  $npp$ . For each  $npp$ , the  $nppN_s$ th is the dominant harmonic while the  $(npp+1)N_s$ th harmonic is also of considerable magnitude. Due to the rotor-tooth modulation, additional harmonics are produced, particularly the  $(nppN_s+N_r)$ th and the  $(nppN_s-N_r)$ th.

Fig. 3.26 shows the no-load flux distribution of the machines when the flux linkage of phase A is maximum. As can be seen, the flux distributions are similar for the FRPM machines especially in stator and rotor yoke, despite of different  $npp$ . Such phenomenon can be explained by the equivalent pole-pair number  $p_{eq}$  introduced in chapter 2, as

$$p_{eq} = nppN_s - N_r \quad (3.21)$$

According to the preferred  $N_r$  shown in (3.18),  $p_{eq}$  can then be calculated, which is 2 for all  $npp$ . Therefore, the flux distributions in stator and rotor yoke of the FRPM machines are equivalent to those of a conventional 6-stator-slot/2-rotor-pole-pair rotor-PM machine.



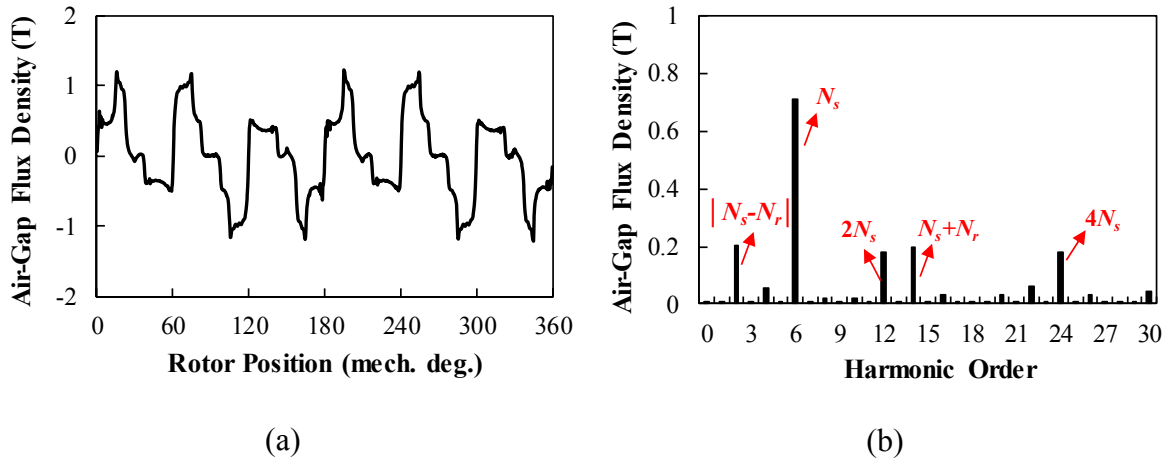


Fig. 3.21 No-load air-gap flux density for  $npp=1$  ( $N_s=6$ ). (a) Waveform. (b) Harmonic spectrum.

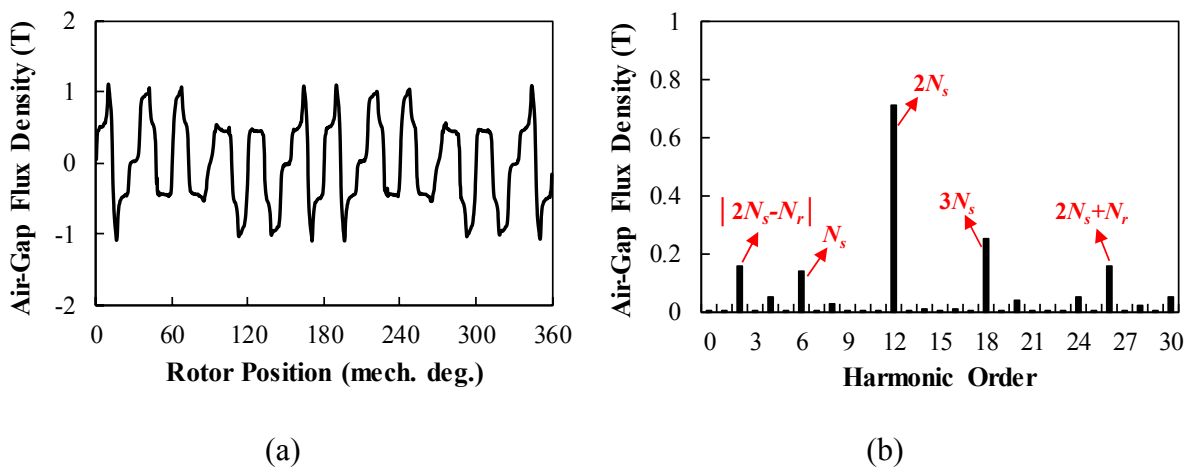


Fig. 3.22 No-load air-gap flux density for  $npp=2$  ( $N_s=6$ ). (a) Waveform. (b) Harmonic spectrum.

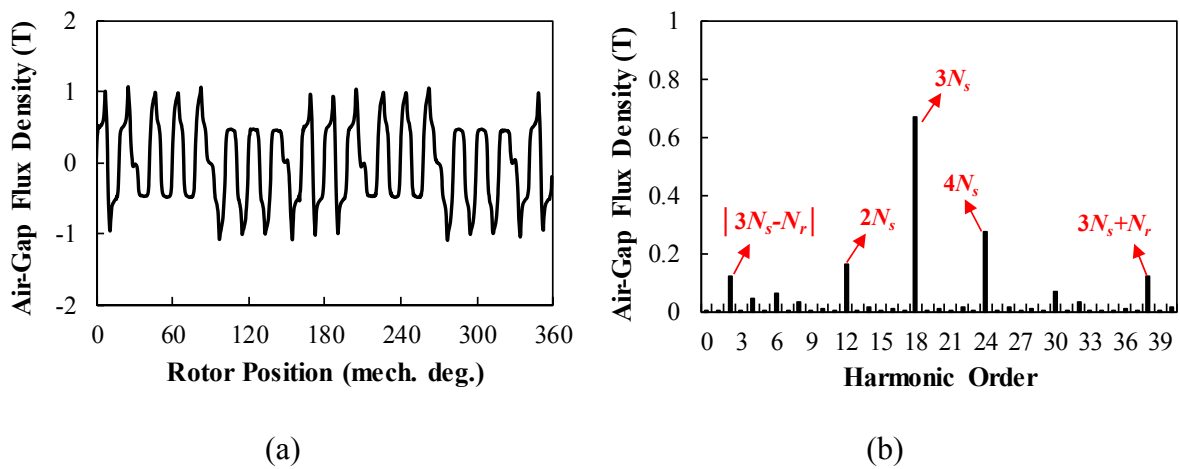


Fig. 3.23 No-load air-gap flux density for  $npp=3$  ( $N_s=6$ ). (a) Waveform. (b) Harmonic spectrum.

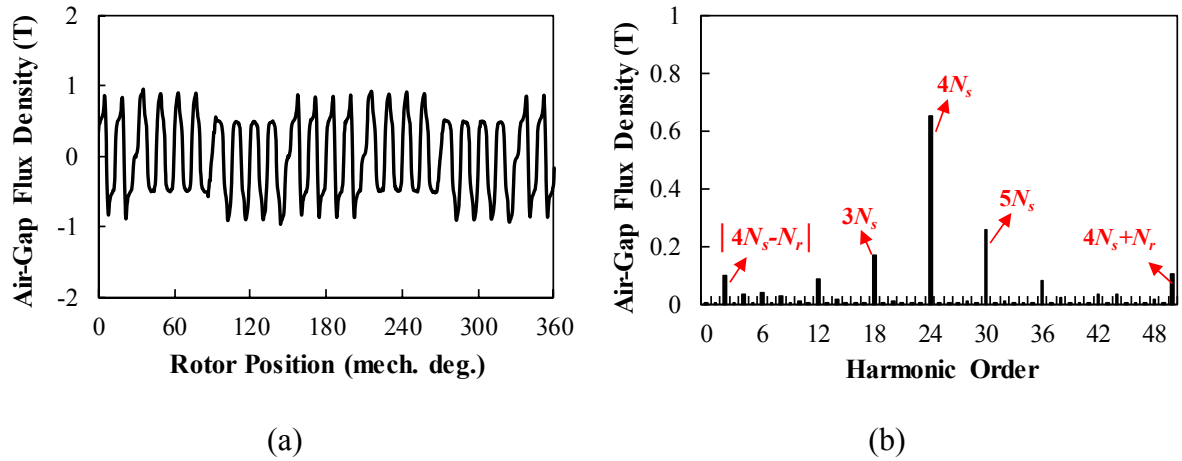


Fig. 3.24 No-load air-gap flux density for  $npp=4$  ( $N_s=6$ ). (a) Waveform. (b) Harmonic spectrum.

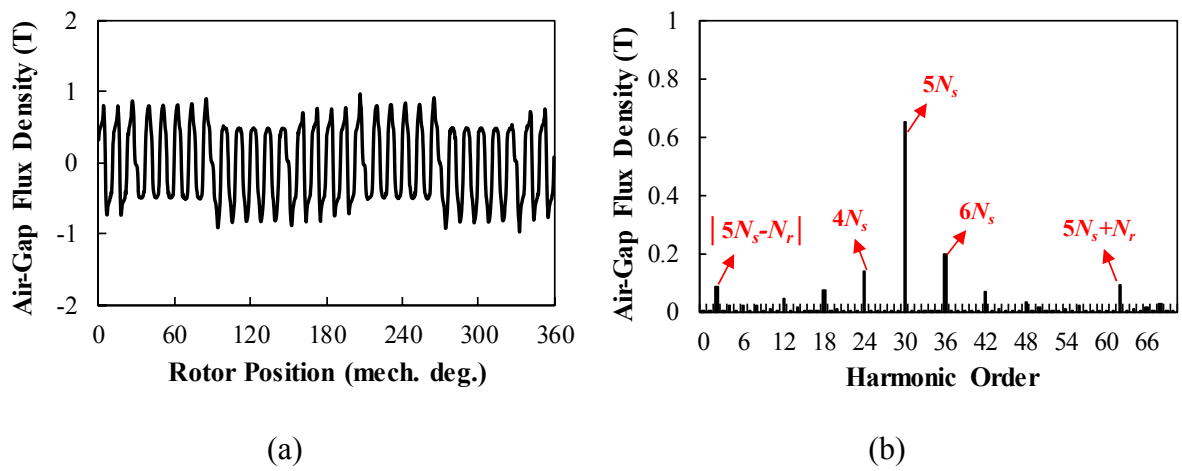
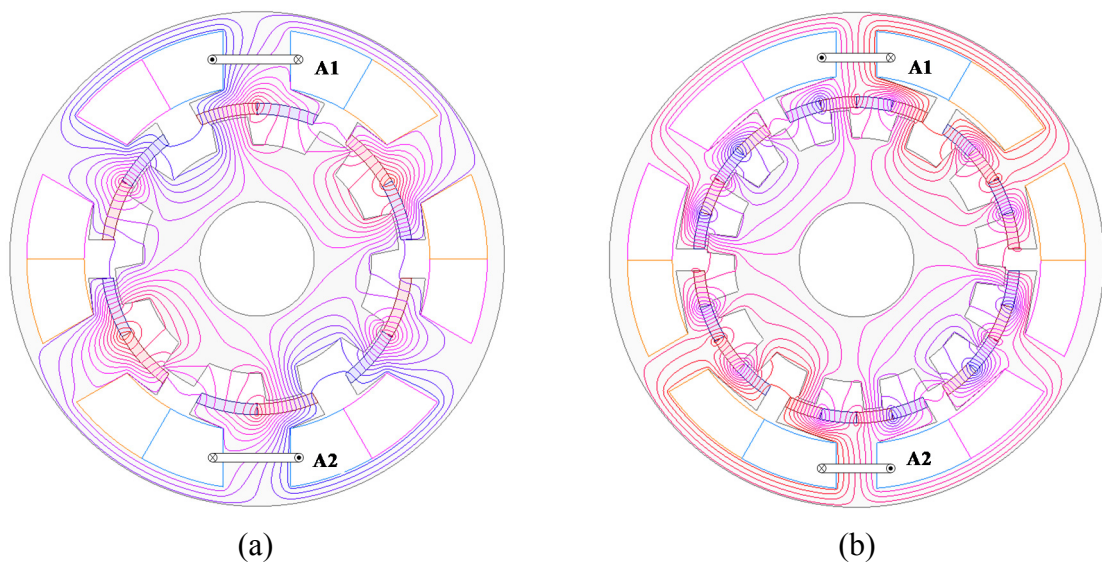


Fig. 3.25 No-load air-gap flux density for  $npp=5$  ( $N_s=6$ ). (a) Waveform. (b) Harmonic spectrum.



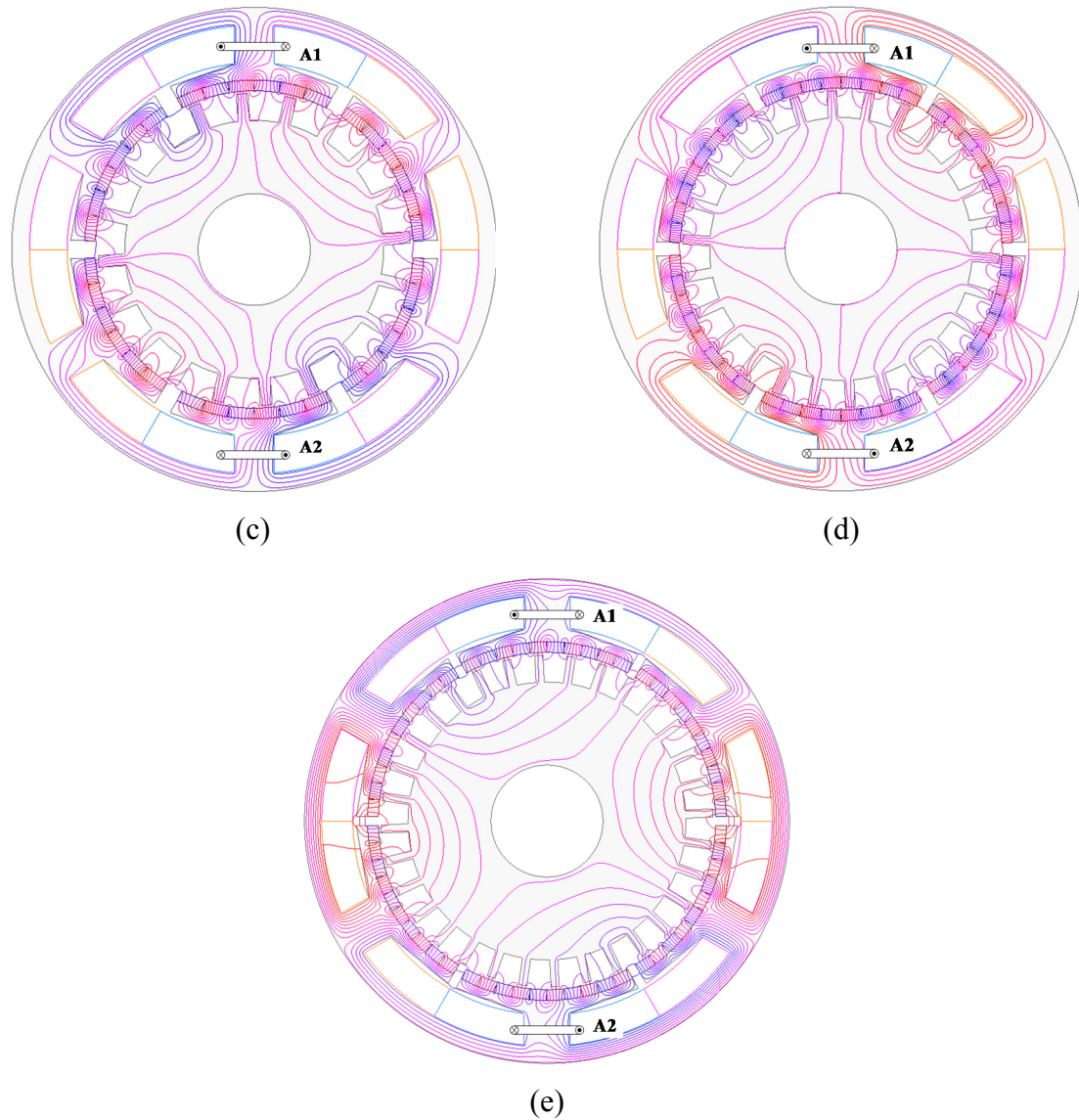
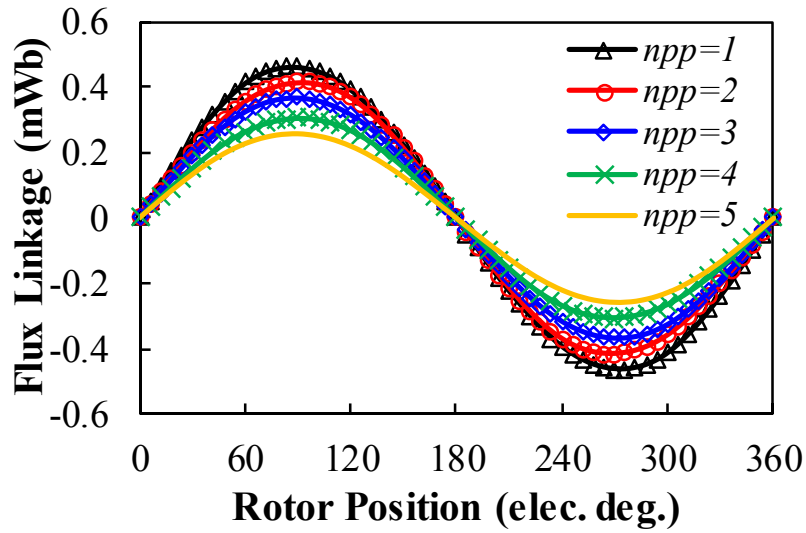


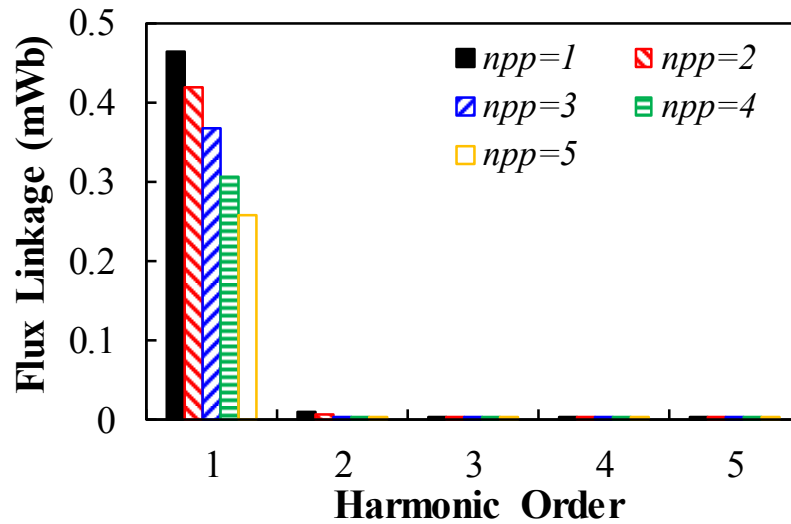
Fig. 3.26 No-load flux distributions when the flux linkage of phase A is maximum. (a)  $n_{pp}=1$ . (b)  $n_{pp}=2$ . (c)  $n_{pp}=3$ . (d)  $n_{pp}=4$ . (e)  $n_{pp}=5$ .

### 3.5.2.2 Flux Linkage

When the number of winding turns per phase  $N_{ph}$  is 4, the phase flux linkages of the machines are shown in Fig. 3.27. As can be seen, the flux linkages of all the machines are bipolar and have very few harmonics. In addition, the magnitude of the fundamental flux linkage decreases as  $n_{pp}$  increases due to the severer flux leakage. As shown in Fig. 3.26, when the flux linkage of phase A (i.e. coil A1 and coil A2) reaches its maximum value, although for each  $n_{pp}$ , the N-pole PM pieces under the coil are all aligned with rotor teeth, the flux leakage between the N-pole and S-pole PM pieces is severer for a larger  $n_{pp}$  since the width of a single PM piece is smaller.



(a)

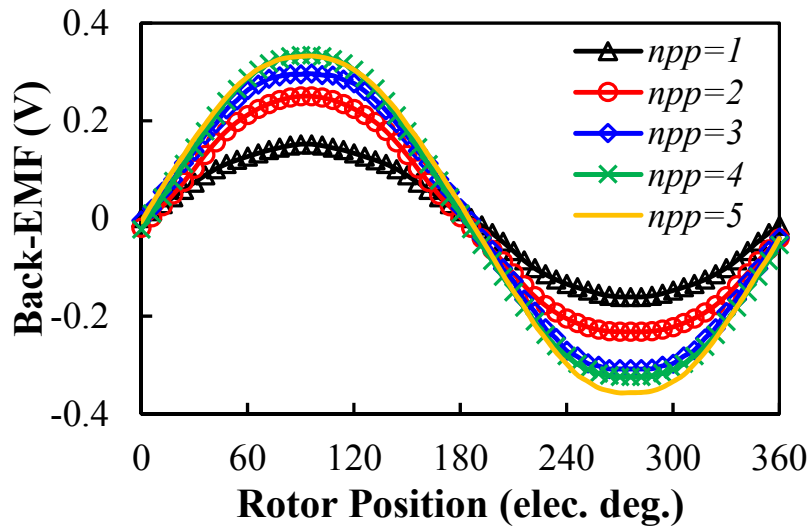


(b)

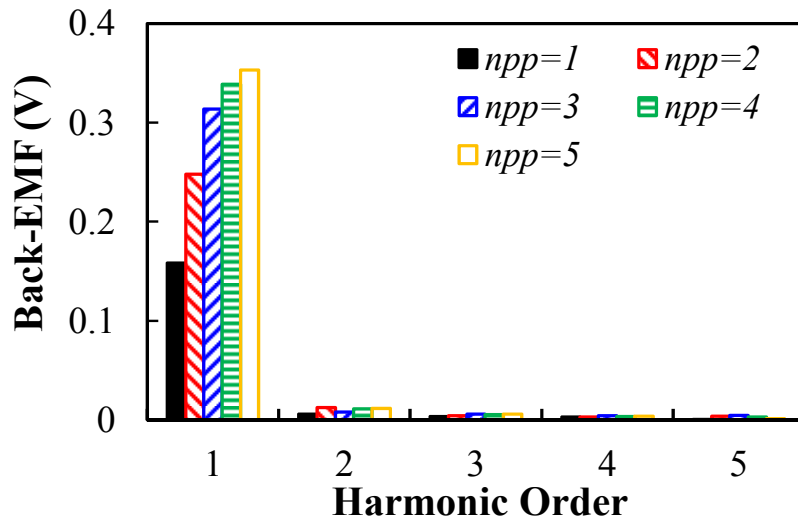
Fig. 3.27 Phase flux Linkage of the machines with different  $npp$ . (a) Waveforms. (b) Harmonic spectra.

### 3.5.2.3 Back-EMF

Fig. 3.28 shows the phase back-EMF of the machines at  $n=400$ rpm (the winding turns per phase  $N_{ph}$  are 4). As can be seen, all the back-EMF waveforms are sinusoidal, thanks to the less harmonics of the flux linkage. Although the flux linkage decreases as  $npp$  increases, the back-EMF of the machines increases against  $npp$ , thanks to the increased rotor pole number and frequency. As shown in Fig. 3.28, when  $npp$  increases from 1 to 3, the fundamental back-EMF is largely improved by 98%. By further increasing  $npp$ , the fundamental back-EMF still slightly increases because of the increased split ratio (see Table 3.4).



(a)

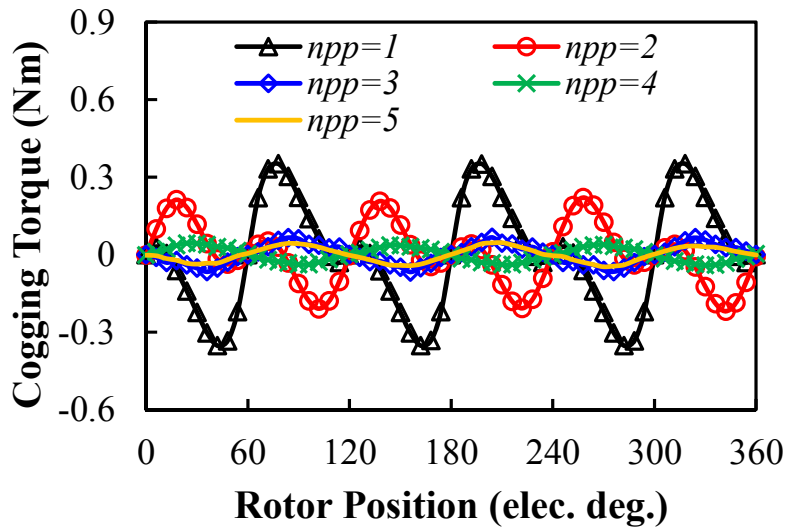


(b)

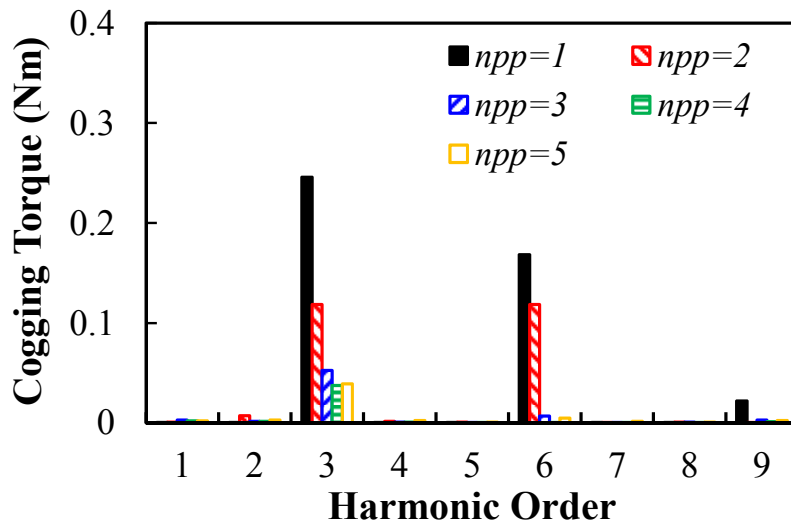
Fig. 3.28 Phase back-EMF of the machines with different  $npp$ . (a) Waveforms. (b) Harmonic spectra.

### 3.5.2.4 Cogging Torque

Fig. 3.29 shows the cogging torques of the five machines. As can be seen, the fundamental periods of cogging torque are all 3, but the magnitude firstly decreases with  $npp$  and achieves the minimum value when  $npp=4$ , which is consistent with Fig. 3.8.



(a)



(b)

Fig. 3.29 Cogging torque of the machines with different  $npp$ . (a) Waveforms. (b) Harmonic spectra.

### 3.5.3 On-Load Performance

When the effective copper loss  $p_{cu}=20W$ , the flux density distributions of the machines are shown in Fig. 3.30. Similar to the flux distributions shown in Fig. 3.26, the machines having different  $npp$  have a similar flux density distribution in stator yoke and stator teeth, of which the maximum flux density is around 1.5T. In addition, there are several local saturation regions in stator tooth tips of the machines with maximum flux density exceeding 2T.

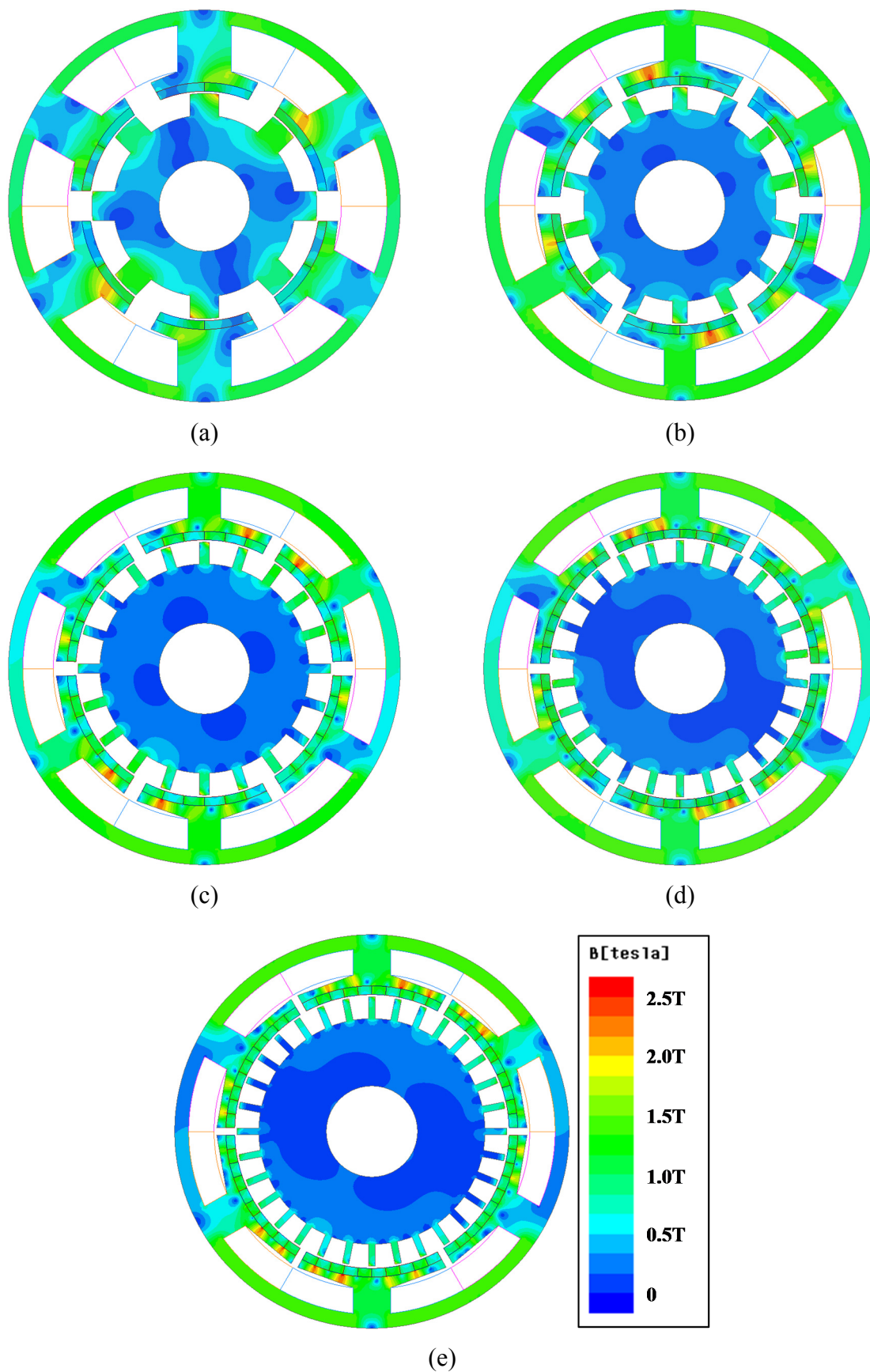
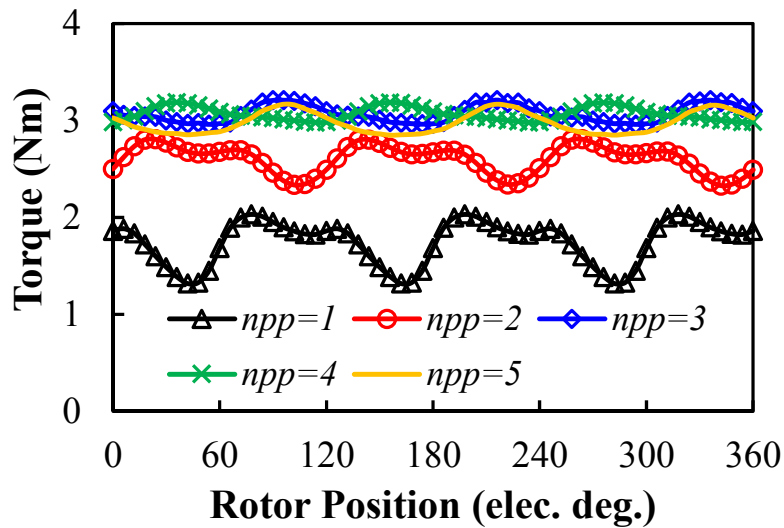
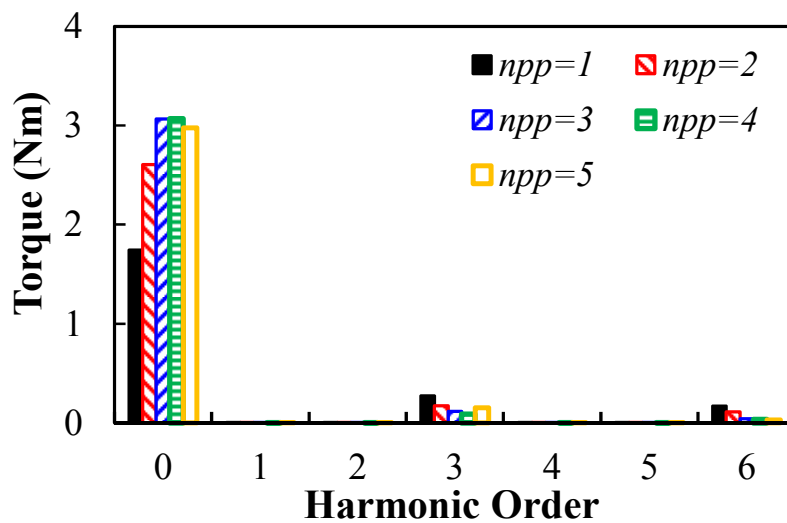


Fig. 3.30 Full-load flux density distributions. (a)  $npp=1$ . (b)  $npp=2$ . (c)  $npp=3$ . (d)  $npp=4$ . (e)  $npp=5$ .

Fig. 3.31 shows the rated torque of the machines when the effective copper loss  $p_{cu}=20\text{W}$ . As can be seen, the average torque  $T_{avg}$  firstly increases with  $npp$ . When  $npp=1$ ,  $T_{avg}=1.7\text{Nm}$  and it can be improved by 76% when  $npp$  increases to 3 ( $T_{avg}=3.1\text{Nm}$ ). Meanwhile, the torque ripple reduces from 41% to 8%, thanks to the reduced cogging torque shown in Fig. 3.29. When  $npp$  is further increased from 3, the average torque starts to decrease. Therefore, the optimal  $npp$  of 3 for  $N_s=6$  is verified.



(a)



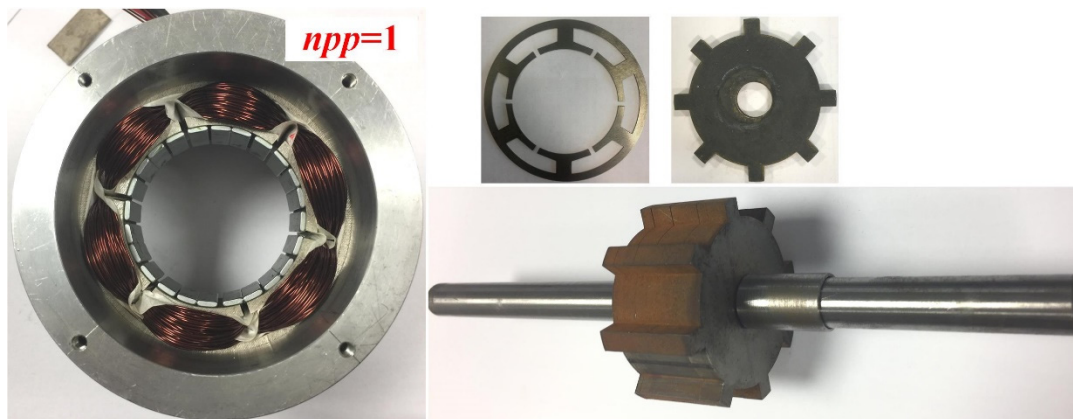
(b)

Fig. 3.31 Rated torque of the machines with different  $npp$ . (a) Waveforms. (b) Harmonic spectra.

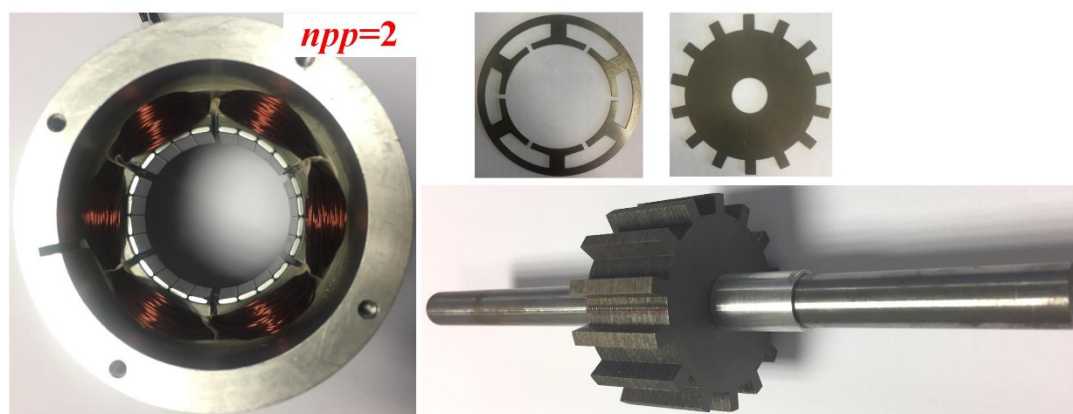


### 3.6 Experimental Validation

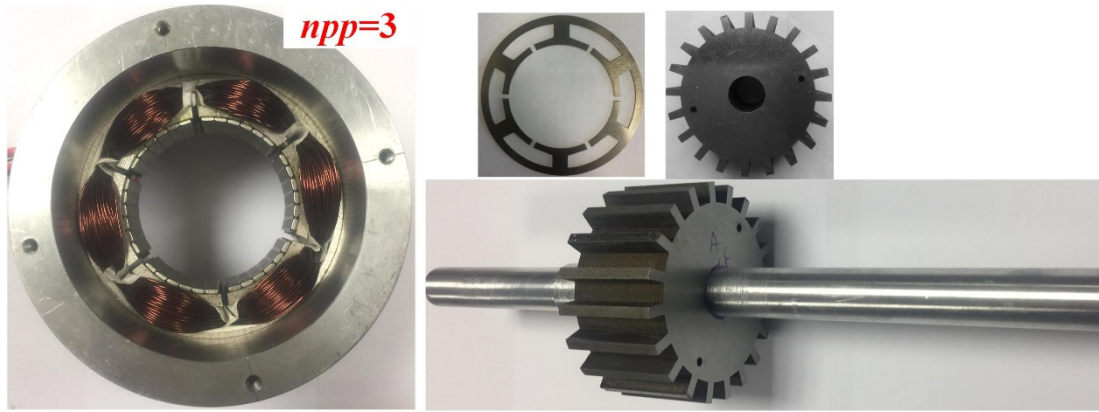
To further verify the conclusions aforementioned, 6-slot-stator prototype machines with different  $npp$  are manufactured, and their parameters are listed in Table 3.4. Since the machine overall diameter is relatively small ( $D=90\text{mm}$ ), only three prototypes ( $npp=1, 2$  and  $3$ ) are made to ease manufacturing and assembling of PMs and salient rotor. For simplicity, three machines share the same stator lamination, and for  $npp=1, 2$ , four PM pieces are mounted on each stator tooth. However, for  $npp=1$ , the polarities of four PM pieces are arranged as N-N-S-S, while that are arranged as N-S-N-S for  $npp=2$ , as shown in Fig. 3.32 (a), (b). The number of turns per coil is 115 for all the machines. In addition, for  $npp=1$ , the rotor pole number  $N_r$  is 8, as shown in Fig. 3.32 (a); for  $npp=2$ ,  $N_r=14$ , as shown in Fig. 3.32 (b); for  $npp=3$ ,  $N_r=20$ , as shown in Fig. 3.32 (c). The drawings of the prototypes are shown in Appendix A.



(a)



(b)



(c)

Fig. 3.32 Prototype machines ( $N_s=6$ ). (a)  $npp=1$ . (b)  $npp=2$ . (c)  $npp=3$ .

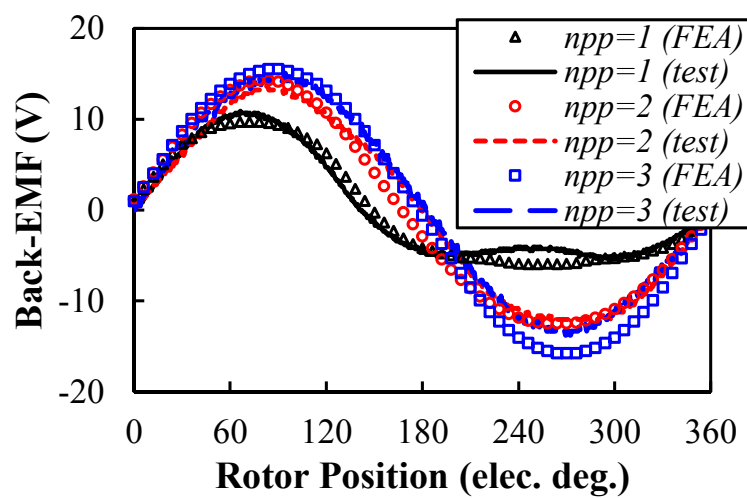
Fig. 3.33 (a) shows the measured and FE-predicted back-EMF waveforms of the machines when  $n=400$ rpm, while their harmonic spectra are shown in Fig. 3.33 (b). As can be seen, good agreement is achieved between the results especially for small  $npp$  (with magnitude difference of fundamental back-EMFs being 6%-8%), and the relatively large difference between measured and FE-predicted results for  $npp=3$  (with magnitude difference of fundamental back-EMFs being 14%) is attributed to the end-effect and larger manufacturing tolerance since the numbers of PM pieces and rotor pole are high. In addition, for  $npp=1$ , the back-EMF waveforms are asymmetric due to the large even harmonics, and  $npp=3$  has the maximum measured fundamental back-EMF, which is 13.9V and is improved by 82% when compared to that of  $npp=1$ .

By using the cogging torque measurement method introduced in Appendix B, Fig. 3.34 shows the measured and FE-predicted cogging torques of the machines. Due to the high rotor pole number and corresponding limited torque measurement point, only cogging torque waveforms are given. However, it can be clearly seen that the fundamental periods of the cogging torque of the machines are same but the peak to peak value decreases with  $npp$ . When  $npp=3$ , the peak to peak value of the measured cogging torque is 0.21Nm, which is much lower than that of  $npp=1$  (0.83Nm). Such phenomenon is consistent with the previous conclusions.

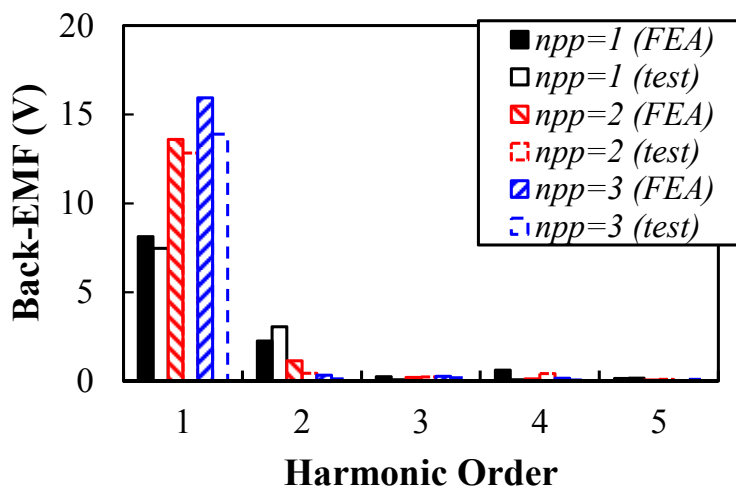
The variation of static torque with rotor position is measured by supplying three-phase windings with fixed dc current ( $I_a=-2I_b=-2I_c=I_{dc}=I_{rated}$ , and the rated current  $I_{rated}$  is corresponded to  $p_{cu}=20$ W). Fig. 3.35 shows the measured and FE-predicted static torques of the machines. As can be seen, the measured static torque waveforms match well with the FE-

predicted waveforms. With rated current injected, the maximum measured torque of  $npp=3$  is the largest, which is 2.6Nm and is 40% larger than that of  $npp=1$ .

The average torque variations of the four machines against current are compared in Fig. 3.36. As can be seen, the measured torque results match well with the FE-predicted values especially for  $npp=1$  and  $npp=2$ . Although the FE-predicted torque of  $npp=3$  is slightly higher than that of  $npp=2$ , the measured torques between  $npp=3$  and  $npp=2$  are quite similar, which is attributed to the relatively large manufacturing error of  $npp=3$ . Besides, it should be noted that the parameters of the prototypes are not exactly the same as the optimum models, as shown in Table 3.4. Nevertheless, the superior torque of  $npp=3$  over  $npp=1$  can be clearly observed.



(a)



(b)

Fig. 3.33 Measured and FE-predicted back-EMFs ( $n=400\text{rpm}$ ). (a) Waveforms. (b) Harmonic spectra.

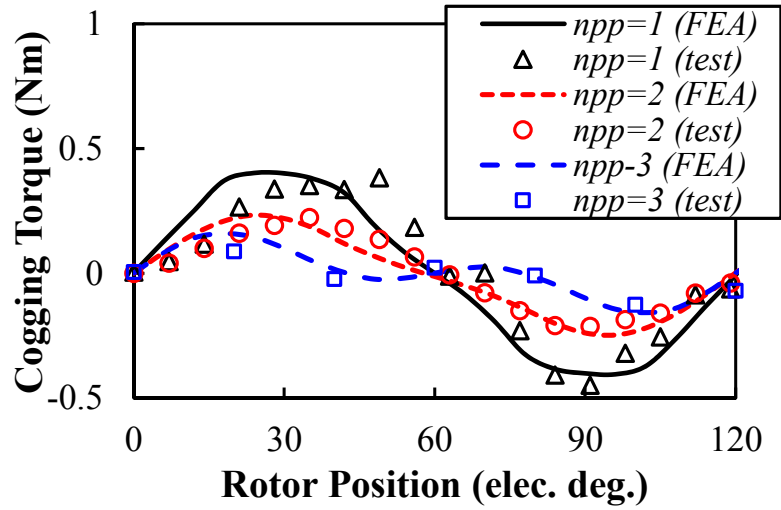


Fig. 3.34 Measured and FE-predicted cogging torques.

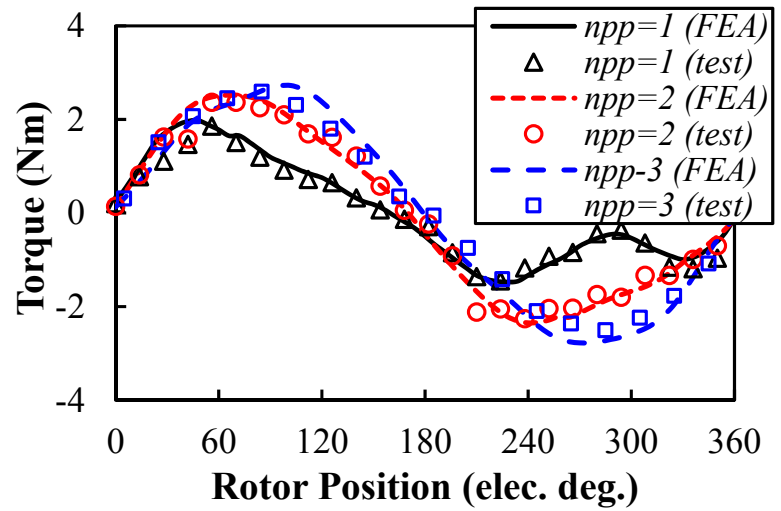


Fig. 3.35 Measured and FE-predicted static torques ( $I_a = -2I_b = -2I_c$ ).

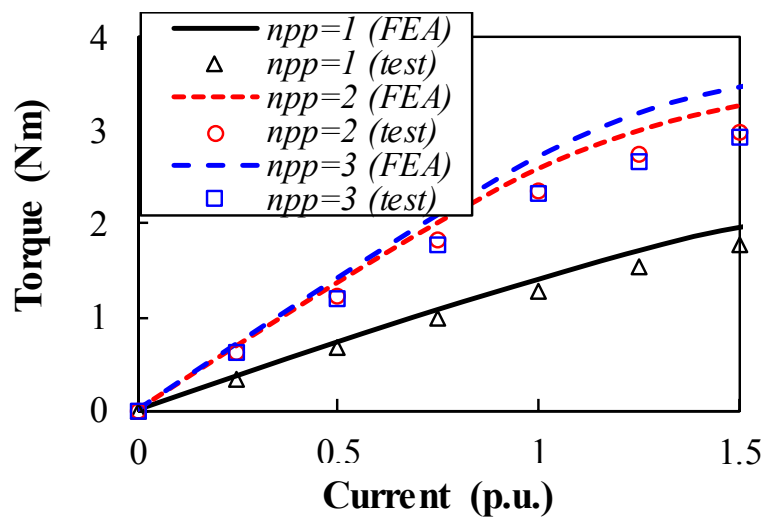


Fig. 3.36 Measured and FE-predicted average torque variations against current.

### 3.7 Conclusion

In this chapter, the influence of number of PM pieces on single stator tooth ( $n_{pp}$ ) on performance of FRPM machines is investigated. Based on the analysed machine dimensions, some findings can be summarised as follows:

1. For FRPM machines, there always exists an optimal number of PM pieces on single stator tooth to maximise the electromagnetic torque.
2. When  $N_s=6$  and  $D=90\text{mm}$ , compared with the conventional FRPM machine with  $n_{pp}$  being 1, the machine with the optimal  $n_{pp}$  of 3 has a much higher average torque (76% in this case). The improved performance is mainly because of the additional contribution by *Auxiliary* PM MMF.
3. Based on the unified analytical model of machines having different  $n_{pp}$ , the influence and design guidance of key design parameters including stator slot opening ratio, split ratio, PM thickness, rotor slot ratio and stator slot number can be clearly demonstrated from the perspective of PM MMF and permeance distribution.

## CHAPTER 4

# ANALYSIS OF FLUX REVERSAL PERMANENT MAGNET MACHINES WITH CONSEQUENT-POLE PM TOPOLOGIES

In this chapter, the FRPM machines with various consequent-pole PM (CPM) topologies will be comprehensively investigated. The torque improvement mechanism of CPM-FRPM machines over a SPM-FRPM machine and the influence of stator slot/rotor pole combinations of CPM-FRPM machines will firstly be analysed. Then four CPM topologies will be introduced and compared, from which the CPM topology with the highest torque density can be identified. The influence of critical design parameters especially the PM dimensions on the machine performance will also be parametrically investigated. By comparing the electromagnetic performance of CPM topologies with their SPM counterparts, the advantages and disadvantages of CPM topologies in FRPM machines, will be clearly revealed. Four FRPM prototypes will be manufactured and tested to verify the analyses.

This chapter is published in *IEEE Trans. Magn.* vol. 54, no. 11, 2018, doi: 10.1109/TMAG.2018.2839708.

### 4.1 Introduction

For most applications where a high torque density is preferred, the PM machines adopting high-energy rare-earth PM material are always adopted. However, the high PM consumption has become a great concern since such high-energy PMs suffer from fluctuant supply and high price. To overcome these demerits, both industry and academia have made great efforts to develop the techniques regarding PM reduction [BOL14] [RAM15] [JAH17]. Among various techniques, adopting consequent-pole PM (CPM) machine topology has proven to be an effective approach to reduce the PM volume and maintain the torque density. Such a technique has been well investigated for various machine topologies, such as fractional-slot PM machine [CHU15], magnetic gear [PEN14] [SHE17a], and Vernier machine [CHU11] etc.

As shown in Fig. 4.1, for conventional FRPM machines with PMs mounted on the inner surface of stator teeth, the large equivalent air-gap length resulted from SPM topology limits the field modulation effect of rotor teeth, thus impairing the torque performance. This characteristic has

been well explained in Chapter 3 since the PM thickness directly affects the magnitude of permeance harmonics. Therefore, alternate PM topologies instead of the conventional SPM topology deserve further investigation since they may offer some advantages in reducing the equivalent air-gap length. In [BOL02] and [KIM09], the inset-PM topology has been proposed and an improved machine performance is declared. However, the inset-PM topology may bring some difficulties in PM assembling due to the space limitation of stator teeth of the FRPM machine.

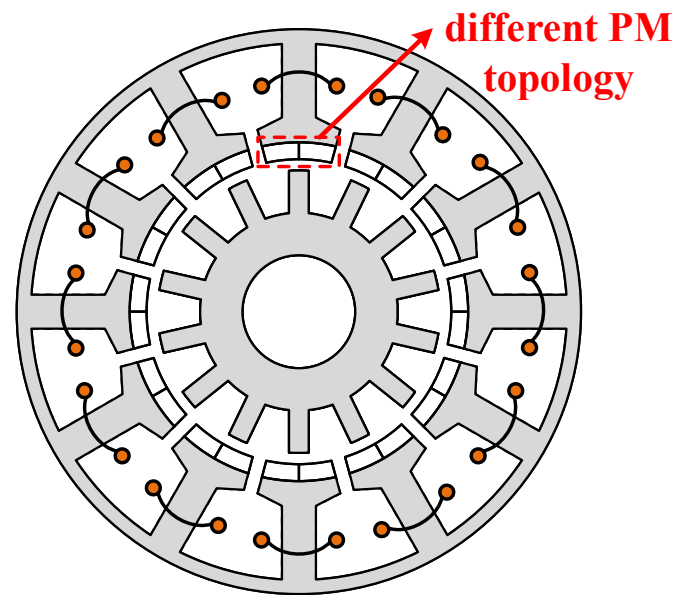


Fig. 4.1 Basic schematic of a FRPM machine.

With reference to the CPM topology in conventional rotor-PM machines and magnetic gears, the FRPM machine with CPM topology (denoted as CPM-FRPM) can be easily realised by replacing all the S-pole magnets with iron [GAO16b], as shown in Fig. 4.2. In [GAO16b], based on the conventional NS-SN SPM topology (see Fig. 4.2 (a)), a 12/16 stator slot/rotor pole CPM-FRPM is proposed and compared with its conventional counterpart of SPM structure (denoted as SPM-FRPM). Results show that the CPM-FRPM machine can provide higher torque with halved PM volume, which is attributed to the reduced flux leakage. However, the influence of stator slot and rotor pole combination on the performance of the CPM-FRPM machine has not been addressed up to date, which is actually an important issue and largely determines the effectiveness of torque improvement of CPM-FRPM machine. Moreover, based on the various SPM topologies investigated in Chapter 2, other CPM topologies can be proposed. Since different CPM topologies directly influence the PM fields in air-gap and

associated winding connections, their working harmonics and torque performance are quite different.

Therefore, the torque improvement mechanism of CPM-FRPM machine over SPM-FRPM machine and the influence of stator slot/rotor pole combination of CPM-FRPM machine will be the main topic of this chapter. In addition, four CPM-FRPM machines with different CPM topologies will be compared, from which the most promising CPM topology can be identified.

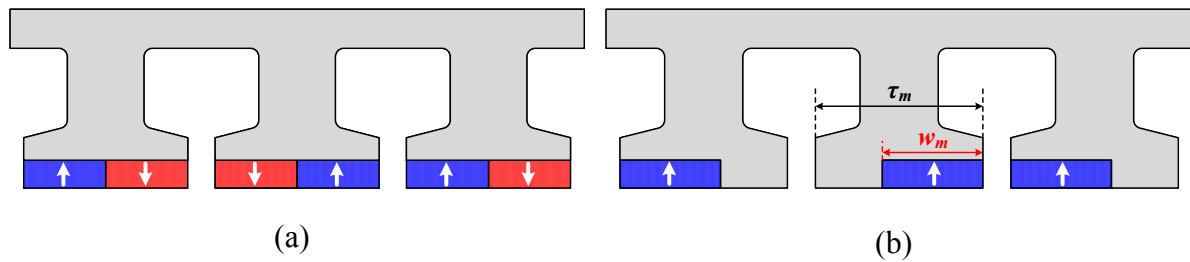


Fig. 4.2 Different PM topologies of FRPM machine. (a) SPM Topology. (b) CPM Topology.

## 4.2 Torque Improvement Mechanism of CPM-FRPM Machines

As shown in Fig. 4.2, the CPM-FRPM machine can be modified from the conventional SPM-FRPM machine by replacing all the S-pole magnets with iron. As a result, the iron poles together with the N-pole magnets will provide PM field the flux paths, making the working principle of flux modulation in the conventional SPM-FRPM machine still feasible in the CPM-FRPM machine. It should be noted that the PM usage of the CPM-FRPM machine is effectively reduced compared to the SPM-FRPM machine, and the PM width ratio ( $\alpha_m = w_m / \tau_m$  shown in Fig. 4.2 (b)) can be adjusted from 0 to 1 and affects both machine performance and PM usage.

In [GAO16b], the torque improvement of the CPM-FRPM machine is explained by the better utilization of PMs resulted from the reduced flux leakage. However, it should be noted that the working point of the PMs and the corresponding main flux decrease as well, making the explanation insufficient. Therefore, in this chapter, the torque improvement of the CPM-FRPM machine will be analysed from the perspective of the interaction between the PM field and the armature field.

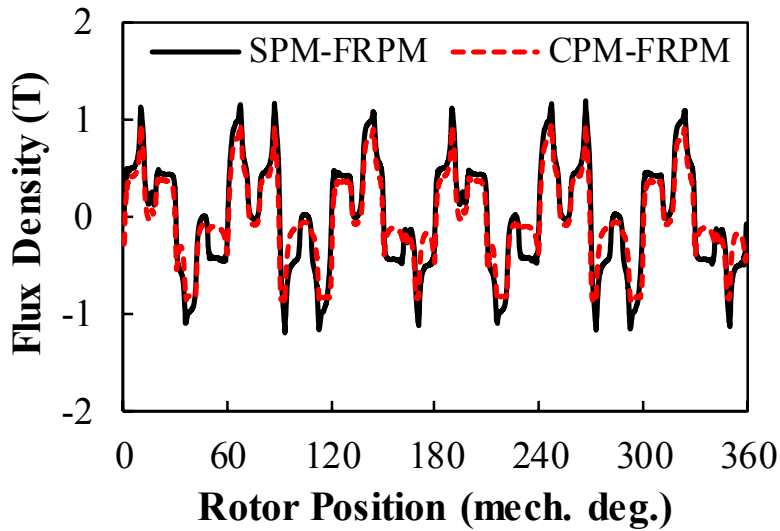
Taking 12/14 stator slot/rotor pole SPM-FRPM machine with NS-SN PM arrangement as an example for analysis, it is globally optimised, and its parameters are listed in Table 4.1. For simplicity, the analysed CPM-FRPM machine is initially obtained by simply replacing all the S-pole PMs of the studied SPM-FRPM machine with iron, i.e.  $\alpha_m = 0.5$ .



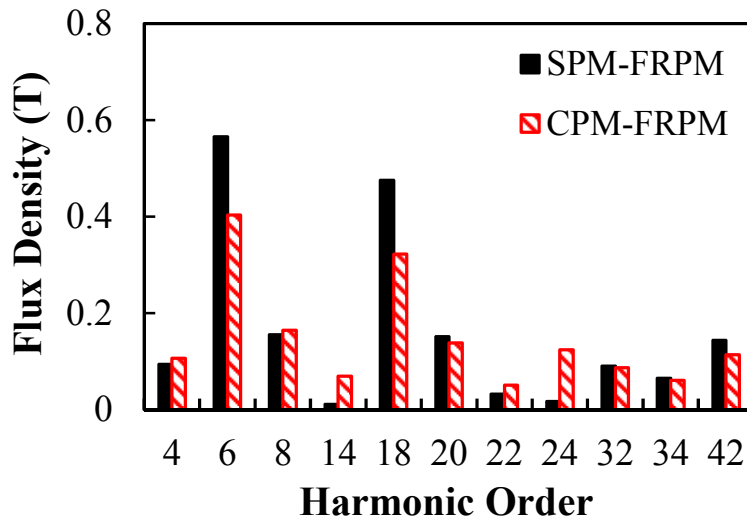
Table 4.1 Optimum parameters of SPM-FRPM Machines ( $N_s=12$ )

Parameters	Value							
Rotor pole number $N_r$	7	8	10	11	13	14	16	17
Stator outer diameter $D$ (mm)	90							
Axial length $l$ (mm)	25							
PM thickness $h_m$ (mm)	2							
Air-gap length $g$ (mm)	0.5							
Remanence of PM $B_r$ (T)	1.2							
Relative permeability of PM $\mu_r$	1.05							
Thickness of stator tooth $t_{sy}$ (mm)	4.6	2.9	2.2	2.2	2.1	2.1	2.2	2.4
Width of stator tooth $w_{st}$ (mm)	3.3	4.0	4.8	5.3	4.0	3.3	2.5	2.8
Inner radius of stator $R_{si}$ (mm)	28.8	30.6	30.6	31.1	31.1	31.1	31.1	32.0
Width of stator slot opening $w_{so}$ (mm)	1.2	1.3	1.5	1.8	2.8	3.5	4.4	4.6
Width of rotor tooth $w_{rt}$ (mm)	8	7.3	4.8	5.0	4.1	3.5	3.5	3.3

The air-gap field distribution of the two machines produced by the PM magnetomotive force (MMF) is firstly shown in Fig. 4.3 (a). As can be seen, besides the fundamental harmonic with order of  $N_s/2$  ( $N_s$  is the stator slot number), the PM fields of two machines are rich of harmonics, which can be clearly seen via the harmonic spectra, see Fig. 4.3 (b). It should be noted that only dominating harmonics are shown (with magnitude larger than 0.05T). For the SPM-FRPM machine, the harmonics of the PM MMF ( $nN_s/2$ ,  $n=1, 3, 5, \dots$ ) are of relatively large magnitudes (e.g. the 6th, the 18th, and the 42nd). In addition, due to the rotor-tooth modulation, other harmonics emerge with considerable magnitudes (e.g. the 4th, the 8th, the 20th etc.). Similar analyses for the SPM-FRPM machine have been presented in Chapter 2. In comparison with the SPM-FRPM machine, the field harmonic components of the CPM-FRPM machine are similar. However, the magnitudes of the major harmonics decrease due to the reduced PM usage. For instance, the magnitude of the 6th harmonic decreases from 0.57T to 0.40T (by 29%).



(a)

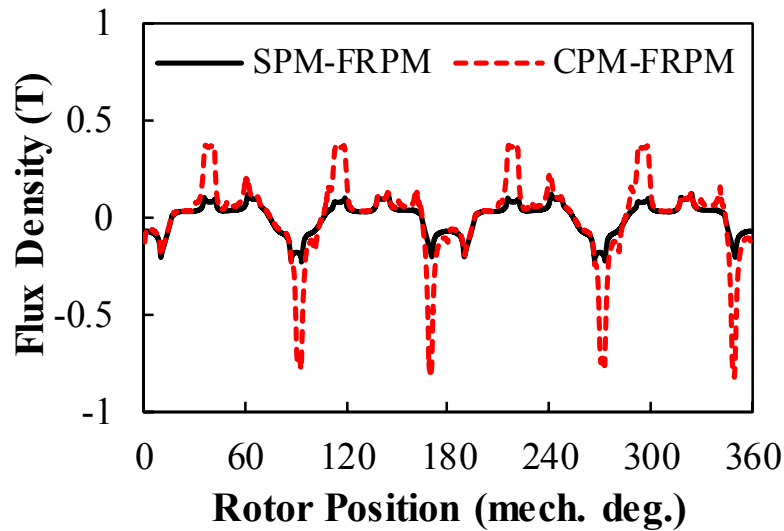


(b)

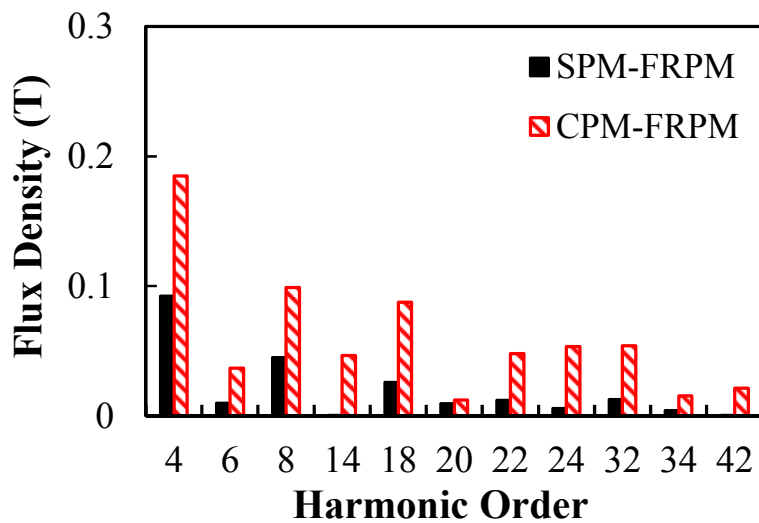
Fig. 4.3 Air-gap flux density produced by the PM MMF of two 12/14 FRPM machines ( $t=0$ ).  
 (a) Waveforms. (b) Harmonic spectra.

Similarly, the air-gap field distribution of the two machines produced by the armature MMF is calculated and shown in Fig. 4.4. For the SPM-FRPM machine, there are several dominant harmonics (e.g. the 4th, the 8th, and the 18th). It is well known that the harmonics of the armature field with the same order and rotational speed as those of the PM field can contribute to the torque production. Therefore, the average torque of the FRPM machine is contributed by several dominant harmonics rather than single working harmonic in the conventional rotor-PM machine. The detailed analyses of dominant working harmonics in SPM-FRPM machines have been presented in Chapter 2. As shown in Fig. 4.4 (b), considering the influence of CPM

topology on the armature field, the magnitudes of all harmonic components are largely improved, thanks to the reduced equivalent air-gap length. For instance, for the 4th harmonic, its magnitude is improved from 0.09T to 0.18T (by 100%); for the 8th harmonic, it is improved from 0.04T to 0.1T (by 121%). Therefore, in comparison with the conventional SPM-FRPM machine, the torque of the CPM-FRPM machine can be possibly improved thanks to the largely enhanced armature field although the PM field may decrease with a relatively small ratio.



(a)



(b)

Fig. 4.4 Air-gap flux density produced by the armature MMF of two 12/14 FRPM machines ( $t=0$ ). (a) Waveforms. (b) Harmonic spectra.

### 4.3 Average Torque Comparison of SPM- and CPM-FRPM Machines Having Different Stator Slot/Rotor Pole Combinations

Although the CPM-FRPM machine has potential to produce higher torque than its SPM counterpart, its effectiveness is largely influenced by the stator slot and rotor pole combination and will be analysed in the following.

#### 4.3.1 Influence of Rotor Pole Number

The torque performance of conventional 12-stator-slot SPM-FRPM machines with different rotor pole numbers ( $N_r$ ) is shown in Fig. 4.5. For each machine, finite element analysis (FEA)-based global optimisation is conducted aiming at the maximum output torque and the optimum parameters are given in Table 4.1. It should be noted that all the machines have the same stator outer diameter (90mm), stack length (25mm) and effective copper loss (20W). For each machine, concentrated-windings are adopted, resulting in short end-windings. The winding connections for each phase can be determined by using the approach introduced in Chapter 2. In addition, although the optimum PM thickness  $h_m$  of all the machines are smaller than 2mm,  $h_m$  is chosen as 2mm due to the consideration of manufacturability and demagnetisation withstand capability.

As can be seen from Fig. 4.5, when  $N_r=10, 11, 13, 14$  or  $16$ , the machine has high output torque and relatively low torque ripple. For these stator slot and rotor pole combinations, the torques of the corresponding CPM-FRPM machines are shown in Fig. 4.6 by simply replacing all the S-pole PMs of the SPM-FRPM machines with iron ( $\alpha_m = 0.5$ , and its influence will be investigated later). It shows that the torques of the CPM-FRPM machines are largely affected by  $N_r$  while the torques of the SPM-FRPM machines are similar. Taking the torque of each SPM-FRPM machine as benchmark, the normalised torque of each CPM-FRPM machine (defined as the torque ratio of CPM to SPM machine) with different rotor pole numbers is highlighted. As can be seen, when  $N_r=11, 13$ , and  $14$ , the torques of the CPM-FRPM machines are significantly improved when compared with their SPM-FRPM counterparts. On the contrary, the torque of the 16-pole CPM-FRPM machine has lower torque density than the SPM-FRPM machine. It should be noted that although the CPM-FRPM machines are not globally optimised, the influence of rotor pole number is clearly revealed by the performance difference of the CPM-FRPM machines having different  $N_r$ .

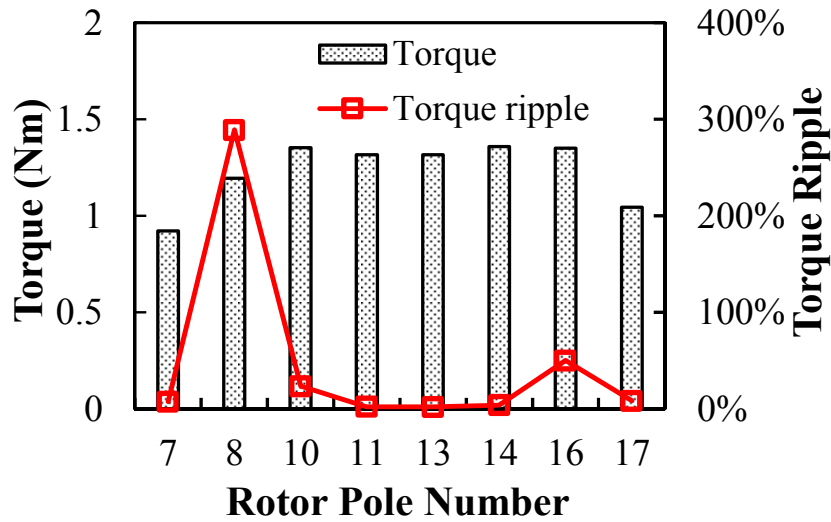


Fig. 4.5 Torque performance of SPM-FRPM machines with different  $N_r$  ( $N_s=12$ ).

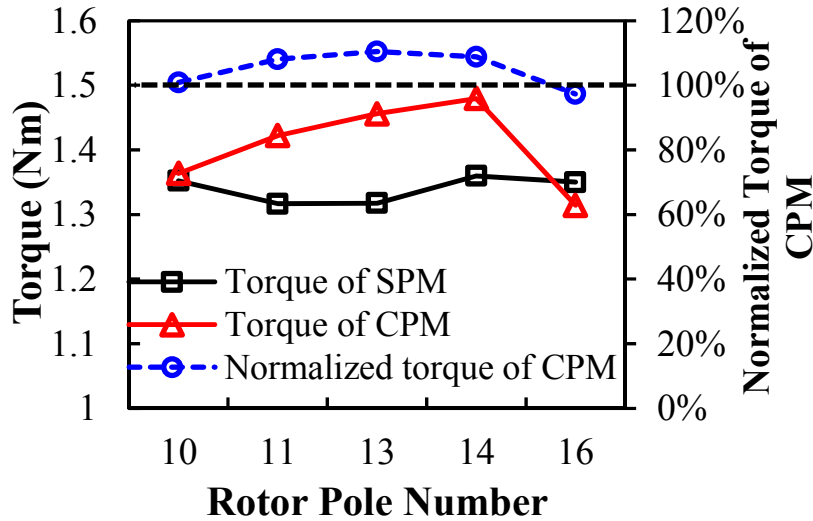


Fig. 4.6 Torque comparison of 12-stator-slot FRPM machines with SPM and CPM topologies.

### 4.3.2 Comparison of 12/14 and 12/16 FRPM Machines

To find out the reason why the rotor pole number affects the torque improvement of the 12-stator-slot CPM-FRPM machine, the 14-pole and 16-pole machines are chosen for detailed analysis. As can be seen from Fig. 4.6, the average torques of the two SPM-FRPM machines are similar. However, the torque of the 14-pole CPM-FRPM machine can be improved by 9% while that of the 16-pole CPM-FRPM machine decreases by 3%. This phenomenon can be explained by the different saturation conditions of the two machines. Both linear and non-linear ferromagnetic materials are set as the iron core material to reveal the influence of saturation. Taking the torque of each SPM-FRPM machine as benchmark, the normalised torque of the

corresponding CPM-FRPM machine is shown in Fig. 4.7. As can be seen, when ideal linear material is adopted, i.e. the saturation is neglected, the torque of the CPM-FRPM machines can be improved by around 20% regardless of  $N_r$ . In contrast, when the practical non-linear material is adopted, the benefits of the CPM-FRPM machines decrease apparently. It shows that the torque improvement of the 14-pole CPM-FRPM machine decreases to around 10% while the torque of the 16-pole CPM-FRPM machine is even smaller than its SPM-FRPM counterpart, indicating bigger influence of the non-linear core material on the performance of the 12/16 CPM-FRPM machine. In other words, the saturation of the 12/16 CPM-FRPM machine is much severer than the 12/14 CPM-FRPM machine, which can be verified by the full-load (corresponding to the effective copper loss  $p_{cu}=20W$ ) flux density distribution shown in Fig. 4.8. As can be seen, for the 12/14 CPM-FRPM machine, the maximum flux density of the stator yoke is only 1.4T. In contrast, for the 12/16 CPM-FRPM machine, most regions of the stator yoke suffer high flux density of 1.7T, which impairs the average torque.

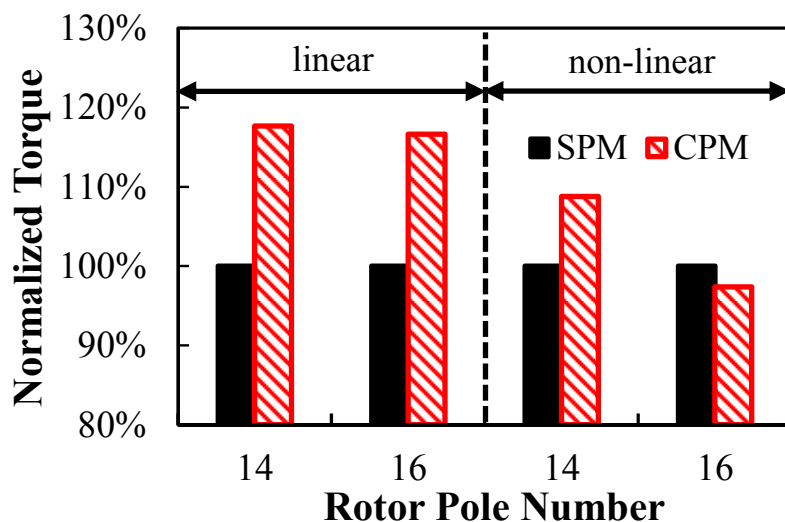


Fig. 4.7 Normalised torque of the 12/14 and 12/16 FRPM machines.

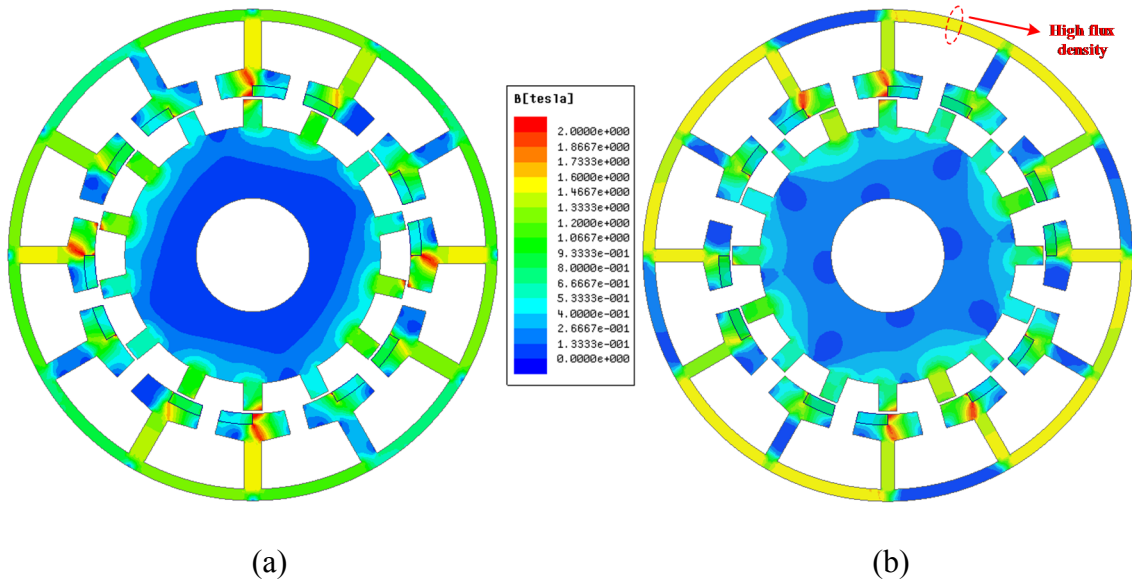


Fig. 4.8 Full-load flux density distributions of two 12-stator-slot CPM-FRPM machines. (a)  $N_r=14$ . (b)  $N_r=16$ .

The different saturation conditions of CPM-FRPM machines can be further explained by the equivalent pole-pair number  $p_{eq}$  of the machine. As introduced in Chapter 2, considering the field modulation mechanism in FRPM machines, although the  $N_s/2$ th and the  $3N_s/2$ th harmonics are the major components of the air-gap flux density (see Fig. 4.3), the rotor-tooth modulation has to be considered in terms of the flux distribution inside the stator and rotor core. Therefore, the equivalent pole-pair number  $p_{eq}$  can be defined as  $p_{eq}=\min ( | N_s/2-N_r | , | 3N_s/2-N_r | )$ , as shown in Table 2.2. When  $N_s=12$ , for the 14-pole machine,  $p_{eq}=4$ ; for the 16-pole machine,  $p_{eq}=2$ . The different  $p_{eq}$  can be verified by the flux distribution of two machines shown in Fig. 4.9. As can be seen, the flux distribution inside the stator and rotor cores of the 12/14 machine is similar as a conventional rotor-PM machine with pole-pair number  $p=4$ . Similarly, for the 12/16 FRPM machine, the flux distribution is equivalent to a conventional rotor-PM machine with  $p=2$ . Therefore, the stator yoke of the 12/16 CPM-FRPM machine is more likely to suffer high saturation due to the larger flux per pole caused by the smaller  $p_{eq}$ , which is consistent with Fig. 4.8.

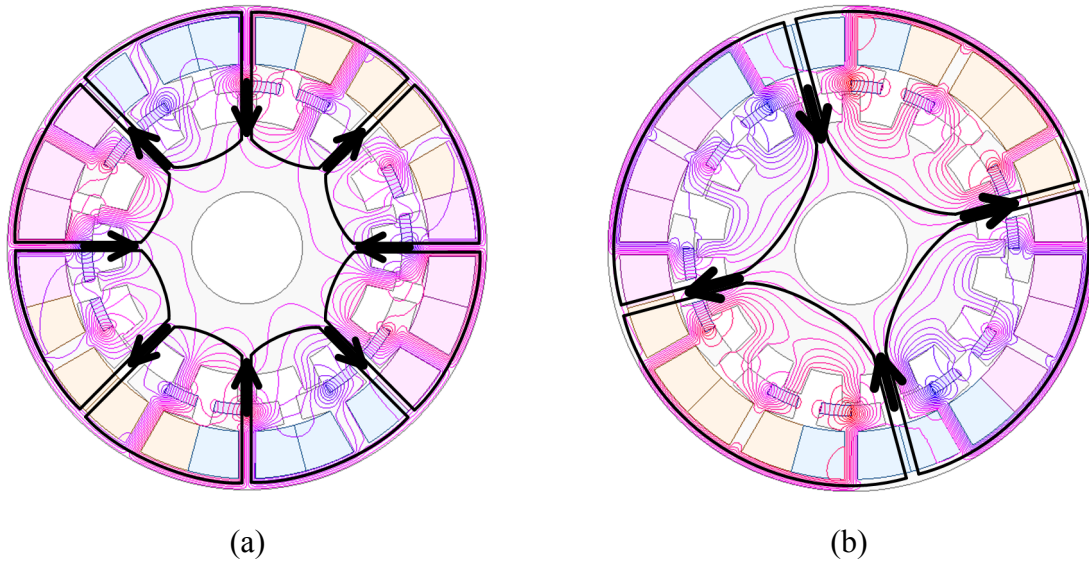


Fig. 4.9 Flux distributions and equivalent flux paths of two 12-stator-slot CPM-FRPM machines. (a)  $N_r=14$ . (b)  $N_r=16$ .

### 4.3.3 Influence of Stator Slot Number

In addition to the influence of rotor pole number  $N_r$ , the equivalent pole-pair number  $p_{eq}$  can be also used to analyse the influence of the stator slot number  $N_s$  on the torque improvement of the CPM-FRPM machine since it directly determines the flux distribution in the stator core as well as the saturation condition. Based on Table 2.2, for CPM-FRPM machines having different  $N_s$ , the variation of  $p_{eq}$  against  $N_r$  (ranging from  $N_s/2$  to  $3N_s/2$ ) is shown in Fig. 4.10. As can be seen, for each  $N_s$ ,  $p_{eq}$  achieves relatively high value when  $N_r$  is close to  $N_s$ . In addition, the larger the  $N_s$ , the higher the maximum  $p_{eq}$ .

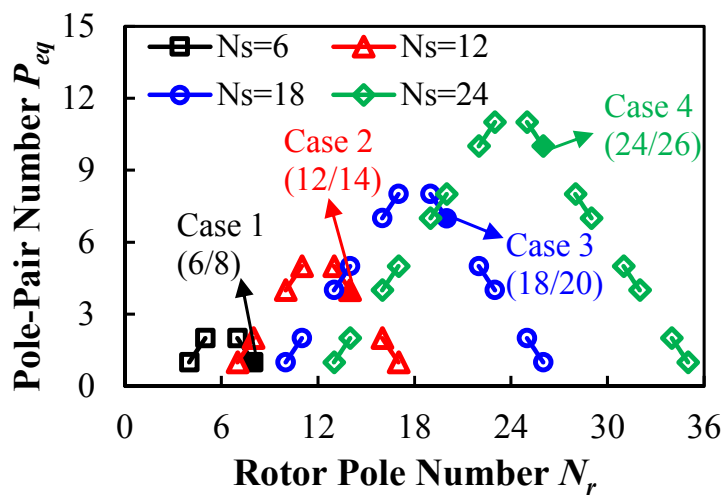


Fig. 4.10 Equivalent pole-pair number  $p_{eq}$  of CPM-FRPM machines having different stator slot/rotor pole combinations.



To investigate the influence of  $N_s$  and corresponding  $p_{eq}$ , for each  $N_s$ , one design case is selected when  $p_{eq}$  achieves the maximum value, as labelled in Fig. 4.10. For Case 1 (6/8),  $p_{eq}=1$ ; for Case 2 (12/14),  $p_{eq}=4$ ; for Case 3 (18/20),  $p_{eq}=7$ ; for Case 4 (24/26),  $p_{eq}=10$ . It should be noted that only even number of  $N_r$  is chosen due to the consideration of unbalanced magnetic force. For each study case, the corresponding SPM-FRPM and CPM-FRPM machines are globally optimised under the same overall size and copper loss for maximum torque. Table 4.2 lists the parameters of the optimum models. As can be seen, one more design parameter, i.e. PM width ratio ( $\alpha_m=w_m/\tau_m$ ), is considered for the CPM-FRPM machines, and for all the design cases, the optimum  $\alpha_m$  is within 0.55-0.6. In other words, the optimum PM width is larger than the adjacent iron pole, as shown in Fig. 4.2 (b).

Table 4.2 Optimum parameters of FRPM machines with different stator slot/rotor pole combinations

Parameter	SPM-FRPM				CPM-FRPM			
Stator slot number $N_s$	6	12	18	24	6	12	18	24
Rotor pole number $N_r$	8	14	20	26	8	14	20	26
Stator outer diameter $D$ (mm)	90							
Axial length $l$ (mm)	25							
PM thickness $h_m$ (mm)	2							
Air-gap length $g$ (mm)	0.5							
Remanence of PM $B_r$ (T)	1.2							
Relative permeability of PM $\mu_r$	1.05							
Thickness of stator tooth $t_{sy}$ (mm)	4.6	2.1	1.3	1.3	5.7	2.2	1.7	1.5
Width of stator tooth $w_{st}$ (mm)	10.2	3.3	2.8	2.5	10.2	4.6	3	2.6
Inner radius of stator $R_{si}$ (mm)	27.5	31.1	31.5	32.9	25.9	28.6	30.4	30.9
Width of stator slot opening $w_{so}$ (mm)	8.3	3.5	1.9	1.2	8.8	3.6	2.1	1.2
Width of rotor tooth $w_{rt}$ (mm)	6.1	3.5	2.6	1.9	6.4	3.8	3.1	2.3
PM width ratio $\alpha_m$	/				0.57	0.56	0.59	0.56

Fig. 4.11 shows the average torque of each machine, and by taking the torque of the SPM-FRPM machine as benchmark, the normalised torque of the CPM-FRPM machine of each design case is shown as well. As can be seen, for the SPM-FRPM machine, the torque decreases with  $N_s$ , i.e. Case 1 (6/8) has the highest torque. However, the torque improvement of the CPM-FRPM machine increases with  $N_s$ . For Case 1 (6/8), the torque of the CPM-FRPM machine is only 95% of the SPM-FRPM counterpart while the torque of the CPM-FRPM machine can be improved by 55% for Case 4 (24/26). Therefore, under the studied overall diameter (90mm), the torque of the CPM-FRPM machine in Case 2 (12/14) turns to be the maximum. In conclusion, the larger the  $N_s$ , the possible the higher  $p_{eq}$ , and the larger the torque improvement of the CPM-FRPM machine over its SPM-FRPM counterpart.

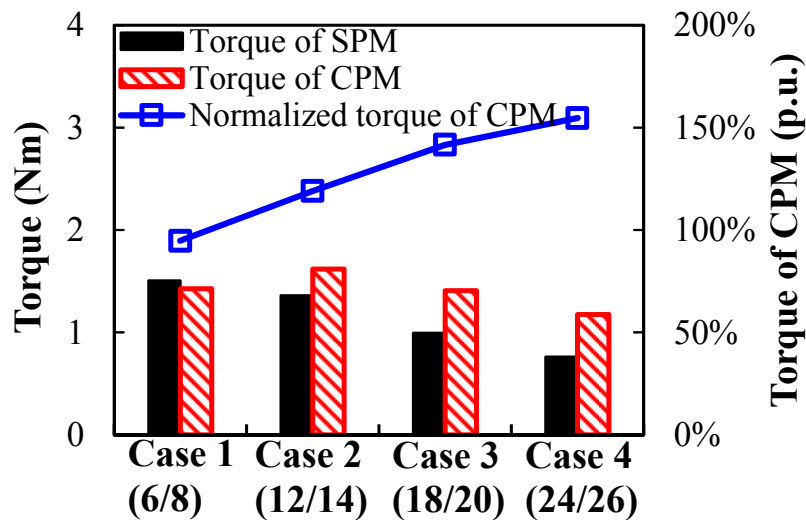


Fig. 4.11 Average torque comparison of machines for different cases

#### 4.4 Analysis of FRPM Machines with Different CPM Topologies

The above analyses are all based on the specific CPM topology shown in Fig. 4.12 (a), which can be derived from the NS-SN SPM topology presented in Chapter 2. By replacing the S-pole PM with ferromagnetic iron pole on each stator tooth, one PM piece together with the adjacent ferromagnetic iron pole make the magnitude and direction of flux through the coil vary with the relative rotor position. Moreover, the magnetisation directions of PMs are identical for all the stator teeth, but the PM locations are different for two adjacent stator teeth. Therefore, the CPM topology can be designated as N/Fe-Fe/N.

With reference to the other three SPM topologies investigated in Chapter 2, i.e. NS-NS, NSNS-SNSN, and NSNS-NSNS, three new types of CPM topologies are proposed in this chapter, as shown in Fig. 4.12 (b)-(d), which are designated as N/Fe-N/Fe, N/Fe/N/Fe-Fe/N/Fe/N, and N/Fe/N/Fe-N/Fe/N/Fe, respectively. Similar as N/Fe-Fe/N (Type1), each stator tooth of N/Fe-N/Fe (Type2) has one PM piece and one ferromagnetic iron pole. However, the PM locations of all the stator teeth are identical. Both N/Fe/N/Fe-Fe/N/Fe/N (Type3) and N/Fe/N/Fe-N/Fe/N/Fe (Type4) have two PM pieces and two ferromagnetic iron poles on each stator tooth, and the PM locations of two adjacent stator teeth are different for the former, while they are the same for the latter. In Chapter 2, it has been proven that the torque of a conventional FRPM machine with SPM topology is contributed by the interaction of several harmonic pairs. Considering that PM MMF distribution is changed, and additional modulation is introduced due to the CPM topology, the distribution and working harmonics of air-gap flux density of FRPM machines with CPM topologies become more complex and deserve further investigation. Moreover, it is obvious that different CPM topologies directly influence the PM fields in air-gap and associated winding connections, their working harmonics and torque performance are quite different, which will be illustrated in the following.

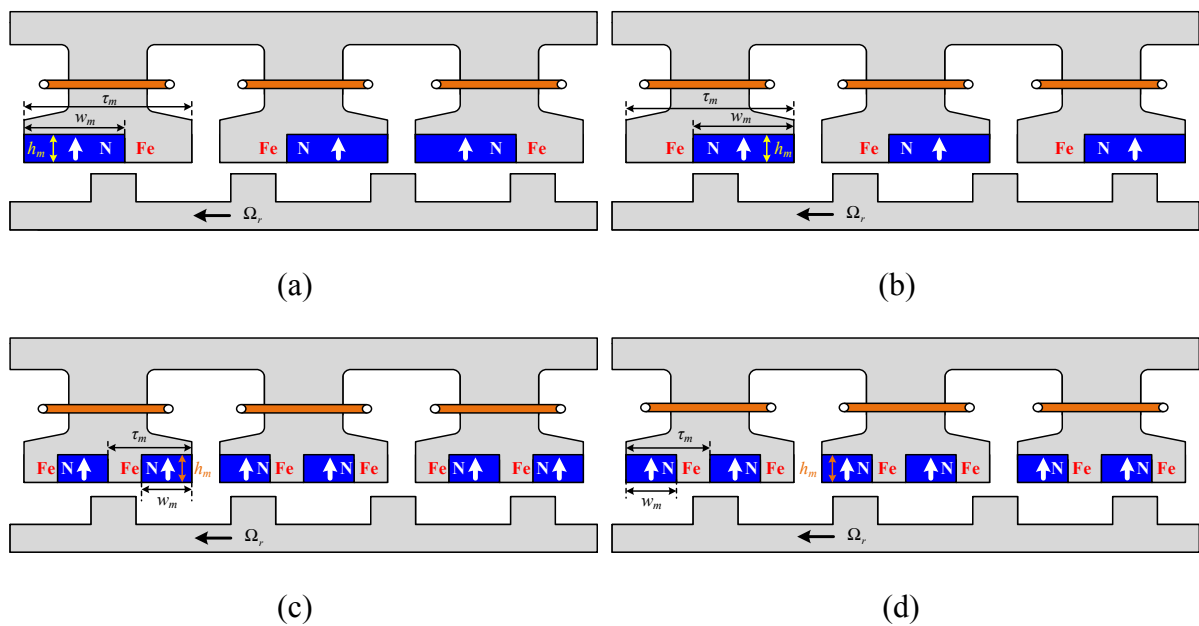


Fig. 4.12 FRPM machines with different CPM topologies. (a) Type1: N/Fe-Fe/N. (b) Type2: N/Fe-N/Fe. (c) Type3: N/Fe/N/Fe-Fe/N/Fe/N. (d) Type4: N/Fe/N/Fe-N/Fe/N/Fe.

#### 4.4.1 Air-Gap Flux Density

Aiming at maximum torque density, four 14-pole-rotor FRPM machines with different CPM topologies are globally optimised under the same machine size and effective copper loss (20W). Meanwhile, for each CPM topology, its SPM counterpart is also optimised. Their parameters are listed in Table 4.3. It should be noted that for Type1 and Type2, the stator slot number  $N_s=12$  while it is 6 for Type3 and Type4. The air-gap flux density resulted from both PM MMF and armature MMF of different CPM topologies are shown in Fig. 2.11, Fig. 4.14, Fig. 4.15, and Fig. 4.16, respectively. As can be seen, both PM field and armature field of the four CPM topologies are totally different.

Similar as SPM-FRPM machine, the harmonic pole-pair number of PM field of CPM-FRPM machine can still be expressed as

$$p_{m,k} = |mp + kN_r| \quad (4.1)$$

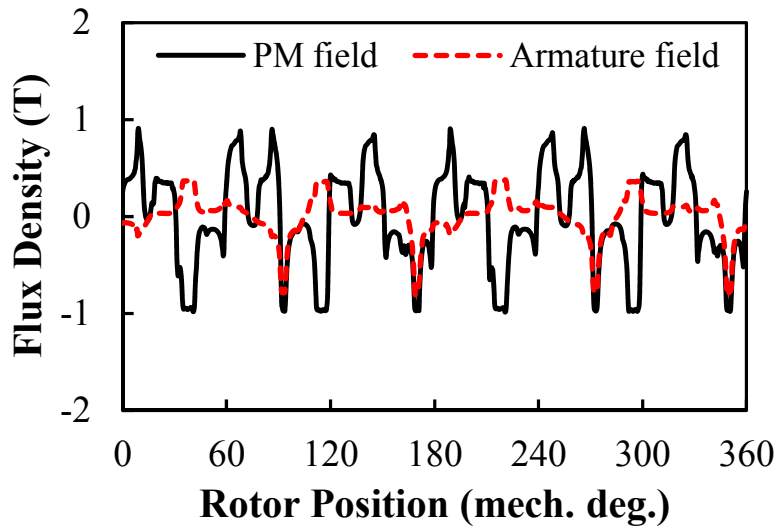
where  $p$  is the fundamental pole-pair number of PM MMF,  $N_r$  is the rotor pole number,  $m$  and  $k$  are the orders of Fourier series of PM MMF and permeance harmonics.

Obviously, PM field is largely related to CPM topology since it directly influences  $p$  and the order and magnitude of  $p_{m,k}$ . As listed in Table 4.4, for Type1 and Type3,  $p=N_s/2$  due to the different PM locations of the adjacent stator teeth; for Type3 and Type4,  $p=N_s$  since the PM locations of all the stator teeth are identical. Correspondingly, the orders and magnitudes of major harmonics (with magnitude larger than 0.2T) of the topologies are all different.

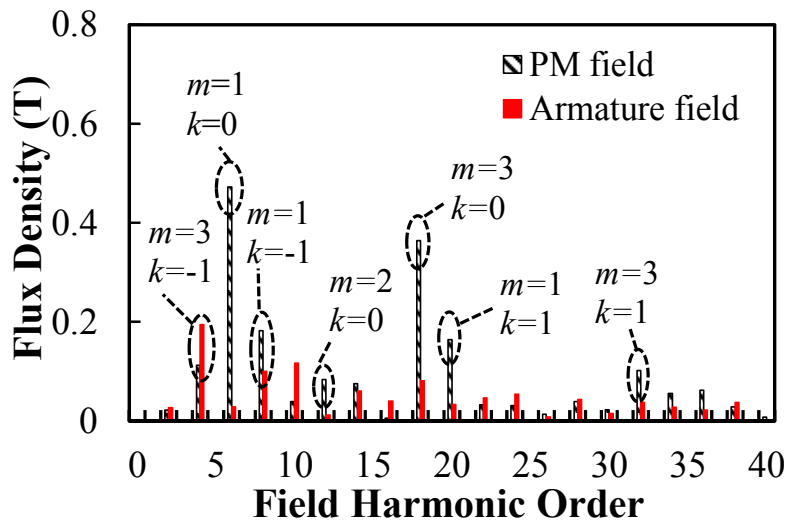
Considering the winding configurations of different CPM topologies, the equivalent pole-pair number  $p_{eq}$  is utilized, thus the windings can be arranged based on the conventional theory of star of slots. Based on Table 4.4,  $p_{eq}=4$  for Type1;  $p_{eq}=2$  for Type2;  $p_{eq}=1$  for Type3 and  $p_{eq}=2$  for Type4, which are the same as SPM-FRPM machines shown in Table 2.2. When the concentrated windings (CWs) are adopted, the armature fields of four topologies are also compared in Fig. 2.11-Fig. 4.16. As can be seen, abundant harmonics exist due to the utilisation of CWs, rotor-tooth modulation and stator iron-poles modulation. Again, the orders and magnitudes of major harmonics are all different and Type3 and Type4 have higher magnitudes than the other two types, which may produce higher torque.

Table 4.3 Optimum parameters of FRPM machines with different SPM and CPM topologies

	FEA models								Prototypes			
	Type1		Type2		Type3		Type4		Type2		Type4	
	CPM	SPM	CPM	SPM	CPM	SPM	CPM	SPM	CPM	SPM	CPM	SPM
$N_s$		12				6			12		6	
$D$						90						
$l$						25						
$g$						0.5						
$h_m$						2						
$B_r/u_r$						1.2T/1.05						
$t_{sy}$	2.2	2.1	3.1	3.2	5.8	4.8	4.0	3.3	3.2		4.2	
$w_{st}$	4.6	4.0	3.5	3.0	7.6	6.8	8.4	7.4	3.2		8.4	
$R_{si}$	30.6	31.1	29.7	30.2	30.6	29.1	29.7	29.7			29.3	
$w_{so}$	3.2	2.5	2.3	1.9	4.7	4.6	5.0	4.1			2.5	
$w_{rt}$	3.6	3.5	3.4	3.2	3.4	3.6	3.8	3.4			3.6	
$r_m$	0.56	/	0.64	/	0.60	/	0.66	/	0.60	/	0.60	/
$a_r$	0.32	0.27	0.28	0.26	0.27	0.3	0.31	0.28			0.30	

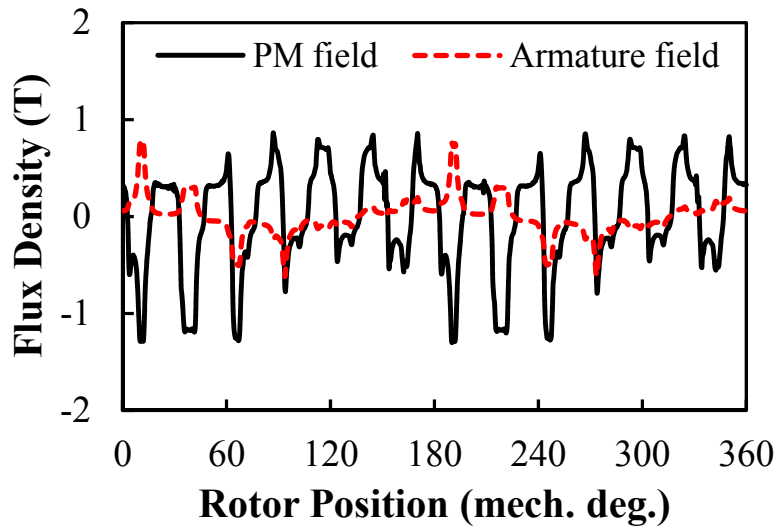


(a)

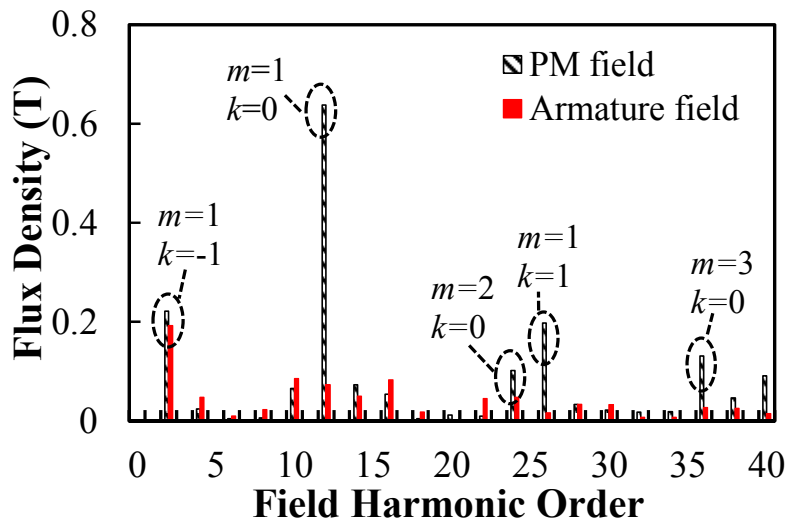


(b)

Fig. 4.13 Air-gap flux density produced by PM MMF and armature MMF in the 12/14 N/Fe-Fe/N CPM-FRPM (Type 1) machine ( $t=0$ ). (a) Waveforms. (b) Harmonic spectra.

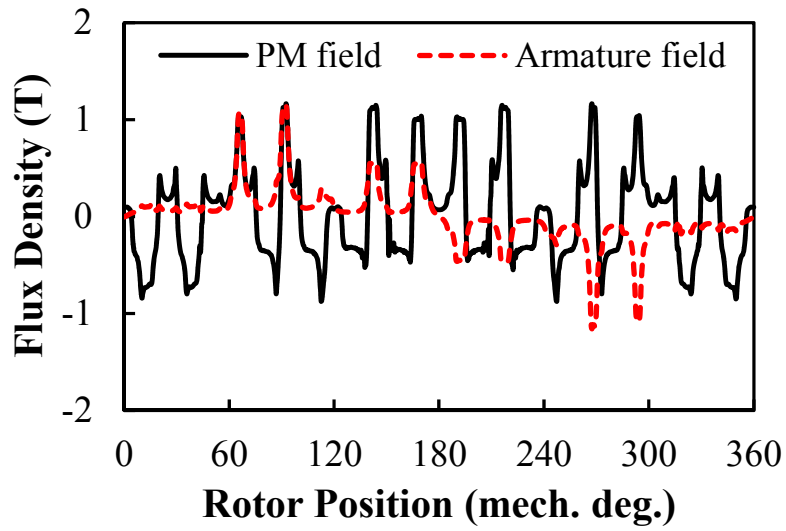


(a)

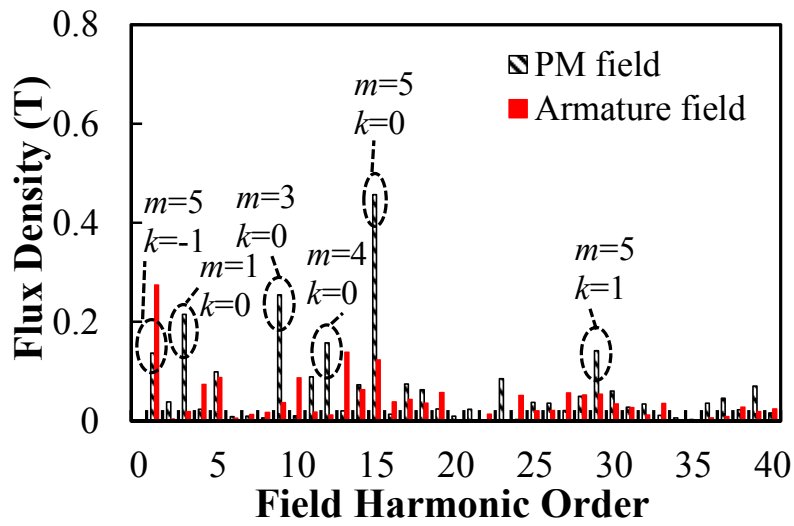


(b)

Fig. 4.14 Air-gap flux density produced by PM MMF and armature MMF in the 12/14 N/Fe-N/Fe CPM-FRPM (Type 2) machine ( $t=0$ ). (a) Waveforms. (b) Harmonic spectra.



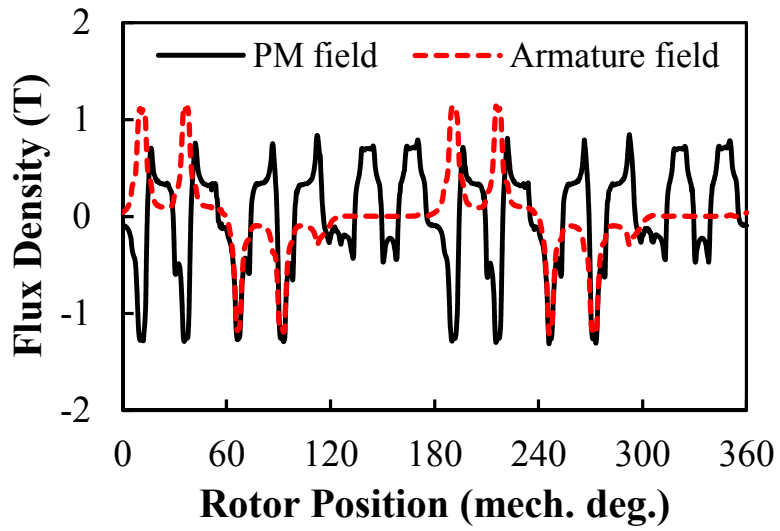
(a)



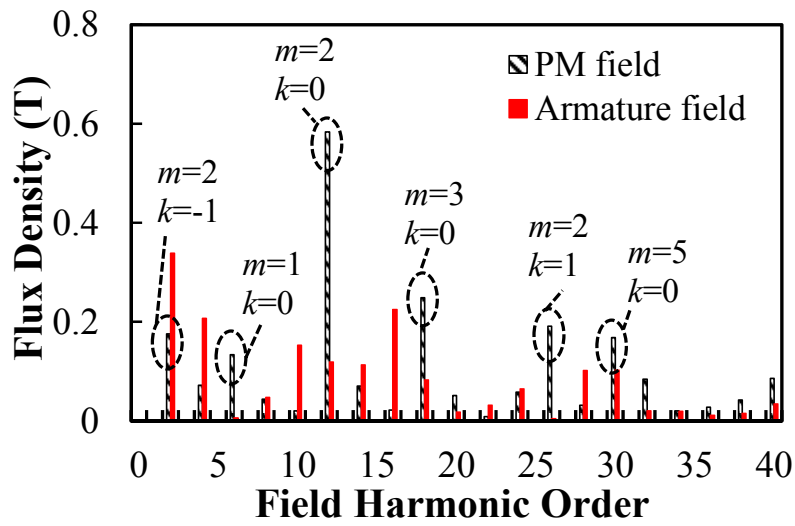
(b)

Fig. 4.15 Air-gap flux density produced by PM MMF and armature MMF in the 6/14 N/Fe/N/Fe-Fe/N/Fe/N CPM-FRPM (Type 3) machine ( $t=0$ ). (a) Waveforms. (b) Harmonic spectra.





(a)



(b)

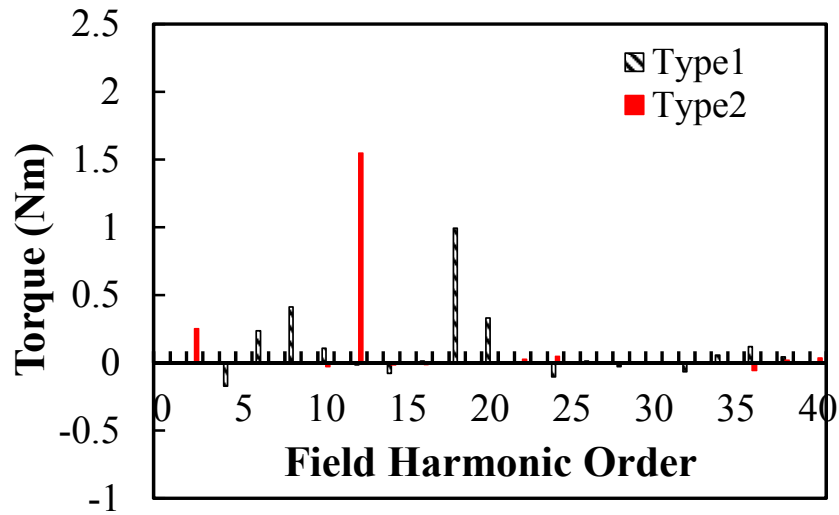
Fig. 4.16 Air-gap flux density produced by PM MMF and armature MMF in the 6/14 N/Fe/N/Fe-N/Fe/N/Fe CPM-FRPM (Type 4) machine ( $t=0$ ). (a) Waveforms. (b) Harmonic spectra.

Table 4.4 Pole-pair numbers of FRPM machines with different CPM topologies

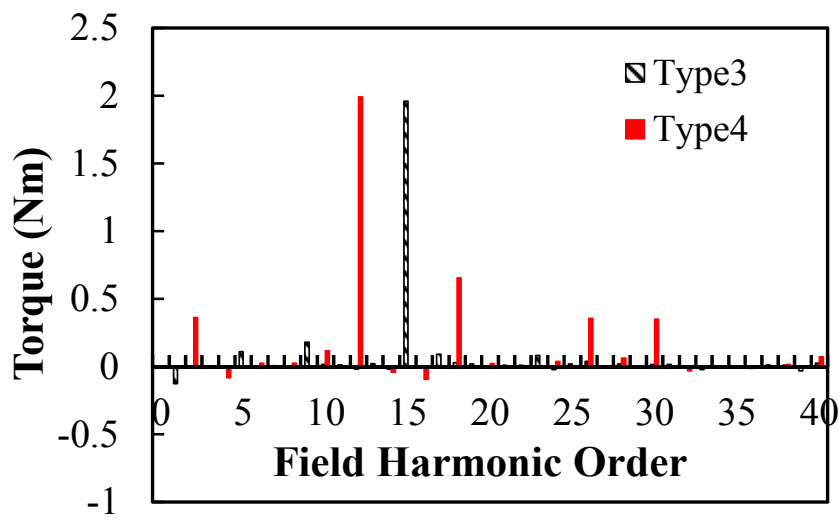
CPM type	Type1	Type2	Type3	Type4
$p$	$N_s/2$	$N_s$	$N_s/2$	$N_s$
Major field harmonics	$N_s/2, 3N_s/2$	$N_s$	$3N_s/2, 5N_s/2$	$2N_s, 3N_s$
$p_{eq}$	$\min( N_s/2 - N_r ,  3N_s/2 - N_r )$	$ N_s - N_r $	$\min( 3N_s/2 - N_r ,  5N_s/2 - N_r )$	$\min( 2N_s - N_r ,  3N_s - N_r )$

#### 4.4.2 Torque Contribution of Working Harmonics

From the above analysis, it is clear that different CPM topologies have different harmonic pairs of PM field and armature field. To further identify and compare the working harmonic pairs, the torque contribution of each field harmonic is obtained by using Maxwell tensor, as shown in Fig. 4.17. Similar as SPM-FRPM machines, the torques of different CPM-FRPM machines are all contributed by several field harmonics. However, the orders and their contributions are totally different. For Type1 and Type4, the torque contributions are scattered while those are relatively concentrated for Type2 and Type 3, as highlighted in Table 4.5 and Table 4.6. In addition, Type3 and Type4 are more likely to have higher torque than Type1 and Type2, thanks to the improved armature field. Compared with Type3, the torque of Type4 is higher since more harmonic pairs with considerable magnitudes (e.g. the 2nd, 18th, 26th etc.) are utilised. Such results are similar to the performance comparison results of different SPM-FRPM machines introduced in Chapter 2.



(a)



(b)

Fig. 4.17 Torque contribution of field harmonics of different CPM-FRPM machines. (a) Type1, 2. (b)Type3, 4.

Table 4.5 Torque proportion of field harmonics in Type1 and Type2 CPM-FRPM machines

	$p$	$p-N_r$	$p+N_r$	$2p$	$2p-N_r$	$2p+N_r$	$3p$	$3p-N_r$	$3p+N_r$
Type1	6 <sup>th</sup> (12%)	8 <sup>th</sup> (22%)	20 <sup>th</sup> (18%)	12 <sup>th</sup> (-1%)	2 <sup>nd</sup> (0%)	26 <sup>th</sup> (1%)-	18 <sup>th</sup> (53%)	4 <sup>th</sup> (-9%)	32 <sup>nd</sup> (-4%)
Type2	12 <sup>th</sup> (82%)	2 <sup>nd</sup> (13%)	26 <sup>th</sup> (0%)	24 <sup>th</sup> (3%)	10 <sup>th</sup> (-2%)	38 <sup>th</sup> (1%)	36 <sup>th</sup> (-3%)	22 <sup>nd</sup> (0%)	50 <sup>th</sup> (1%)

Table 4.6 Torque proportion of field harmonics in Type3 and Type4 CPM-FRPM machines

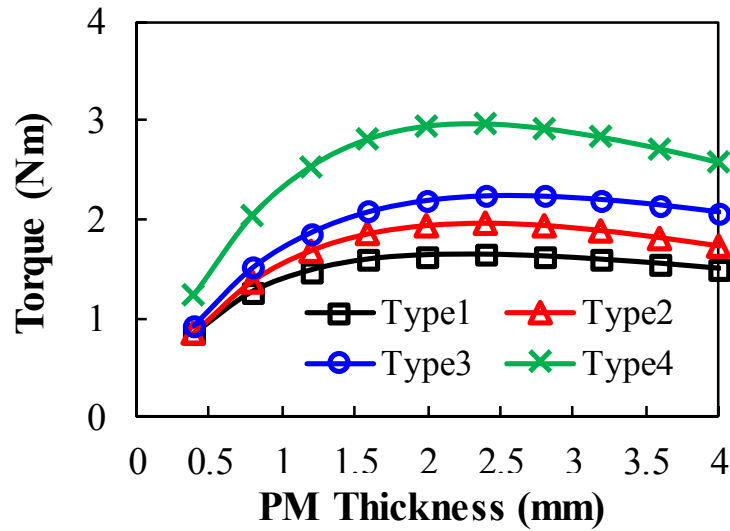
	$p$	$p-N_r$	$p+N_r$	$2p$	$2p-N_r$	$2p+N_r$	$3p$
Type3	3 <sup>rd</sup> (0%)	11 <sup>th</sup> (1%)	17 <sup>th</sup> (4%)	6 <sup>th</sup> (0%)	8 <sup>th</sup> (0%)-	22 <sup>nd</sup> (0%)	9 <sup>th</sup> (8%)
Type4	6 <sup>th</sup> (1%)	8 <sup>th</sup> (1%)	20 <sup>th</sup> (1%)	12 <sup>th</sup> (58%)	2 <sup>nd</sup> (11%)	26 <sup>th</sup> (10%)	18 <sup>th</sup> (19%)
	$3p-N_r$	$3p+N_r$	$4p-N_r$	$5p$	$5p-N_r$	$5p+N_r$	$6p$
Type3	5 <sup>th</sup> (5%)	23 <sup>rd</sup> (4%)	2 <sup>nd</sup> (0%)	15 <sup>th</sup> (89%)	1 <sup>st</sup> (-6%)	29 <sup>th</sup> (0%)	18 <sup>th</sup> (1%)
Type4	4 <sup>th</sup> (-2%)	32 <sup>nd</sup> (-1%)	10 <sup>th</sup> (3%)	30 <sup>th</sup> (10%)	16 <sup>th</sup> (-3%)	44 <sup>th</sup> (-3%)	36 <sup>th</sup> (0%)

#### 4.4.3 Influence of PM Dimensions

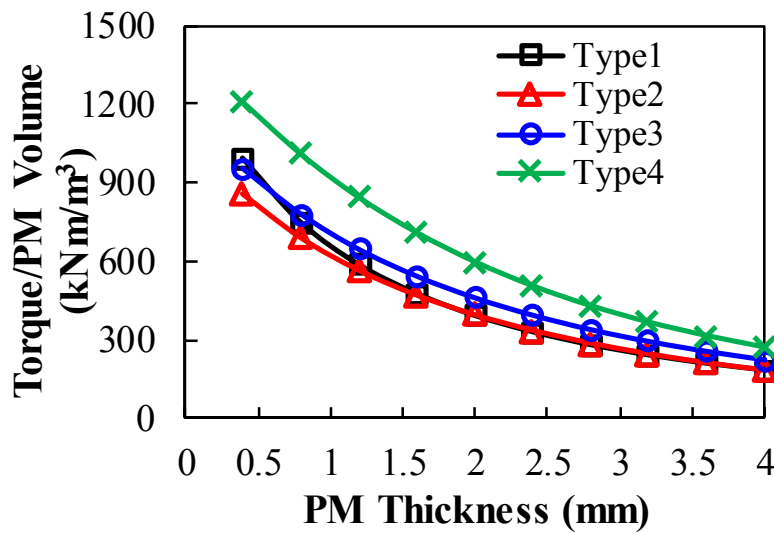
As labelled in Fig. 4.12, both PM width ratio ( $a_m=w_m/\tau_m$ ) and thickness ( $h_m$ ) are critical parameters for CPM-FRPM machines since they directly affect the magnitudes of PM MMF and equivalent air-gap length [CHU11] [CHU12] [DOR10]. Therefore, the influence of  $h_m$  and  $a_m$  on the performance of CPM-FRPM machines will be parametrically analysed.

##### 4.4.3.1 PM Thickness

Based on the machine parameters listed in Table 4.3, the influence of  $h_m$  on machine performance is shown in Fig. 4.18. As can be seen, for each CPM topology, there exists an optimal  $h_m$  (around 2-2.4mm), which is similar as the conventional SPM topology since the rotor-tooth modulation effect may deteriorate with  $h_m$ . Type4 and Type3 CPM topologies have higher average torque than Type1 and Type2, and Type4 CPM machine has the maximum average torque. In addition, as can be seen from Fig. 4.18(b), for all the CPM topologies, the torque per PM volume always decreases with  $h_m$ . Again, Type4 has the maximum torque and torque per PM volume thanks to the large average torque.



(a)



(b)

Fig. 4.18 Influence of PM thickness  $h_m$  on machine performance. (a) Average torque. (b) Torque per PM volume.

#### 4.4.3.2 PM Width Ratio

The influence of PM width ratio  $a_m$  on average torque of the machines is shown in Fig. 4.19 (a). As can be seen, for each machine, its average torque can be improved by properly increasing  $a_m$  from 0.5, but there exists an optimal  $a_m$  (normally around 0.6-0.65) due to the saturation of the stator iron poles. In addition, Type4 always has the highest torque while Type1 has the lowest. Fig. 4.19 (b) shows the variation of torque per PM volume against  $a_m$ . As can be seen, Type2 machine achieve the maximum PM utilisation ratio when  $a_m$  is around 0.6 while the other three machines have the maximum PM utilisation ratio when  $a_m$  is around 0.5. In

addition, within the whole range of  $a_m$ , Type4 has the highest torque per PM volume thanks to the high average torque.

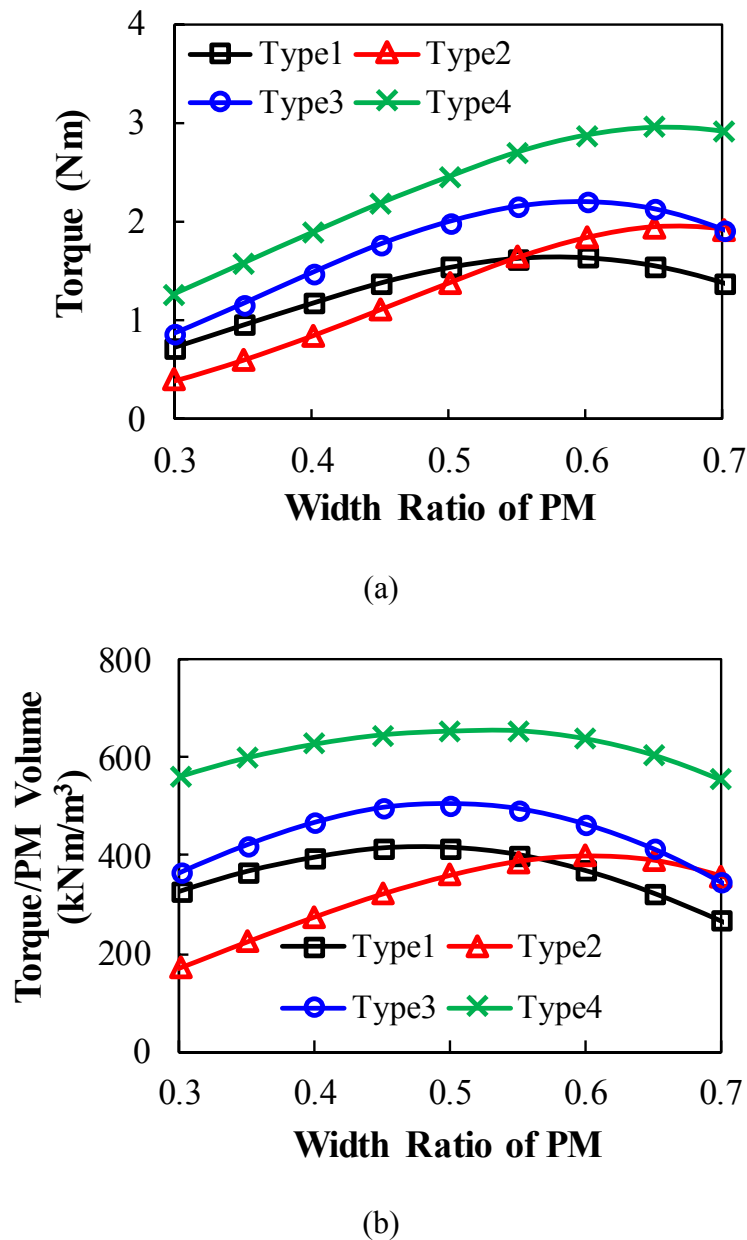


Fig. 4.19 Influence of PM width ratio  $a_m$  on machine performance. (a) Average torque. (b) Torque per PM volume.

In addition to the average torque,  $a_m$  significantly influences the cogging torque, back-EMF waveform and corresponding torque ripple of the CPM-FRPM machines. Fig. 4.20 shows the variation of the peak to peak value of the cogging torque against  $a_m$ . It shows that the cogging torque is largely related to the CPM topology and Type2 has the lowest cogging torque. In addition, the cogging torque is sensitive to  $a_m$  since the harmonics of the no-load air-gap flux density are directly determined by  $a_m$ . When  $a_m$  is much higher or lower than 0.5, considerable

even-order harmonics of the PM MMF emerge, which is more likely to cause large cogging torque.

Fig. 4.21 shows the variation of the line back-EMF total harmonic distortion (THD) against  $\alpha_m$ . Similarly, CPM topology largely affects the back-EMF THD, and the THD is relatively low for Type2. Besides, the back-EMF THD is more likely to achieve a small value when  $\alpha_m$  is near 0.5, which can still be explained by the even-order harmonics of the PM MMF.

Fig. 4.22 shows the rated torque ripple of the CPM-FRPM machines with different  $\alpha_m$ . In addition to the cogging torque and back-EMF distortion,  $\alpha_m$  also affects the saturation of the iron poles with current injection, resulting in extra torque ripple. Therefore,  $\alpha_m$  cannot be very large since the larger the  $\alpha_m$ , the severer the saturation of the iron poles. From Fig. 4.22, the optimum  $\alpha_m$  should be selected around 0.45-0.55 if a small torque ripple is desired.

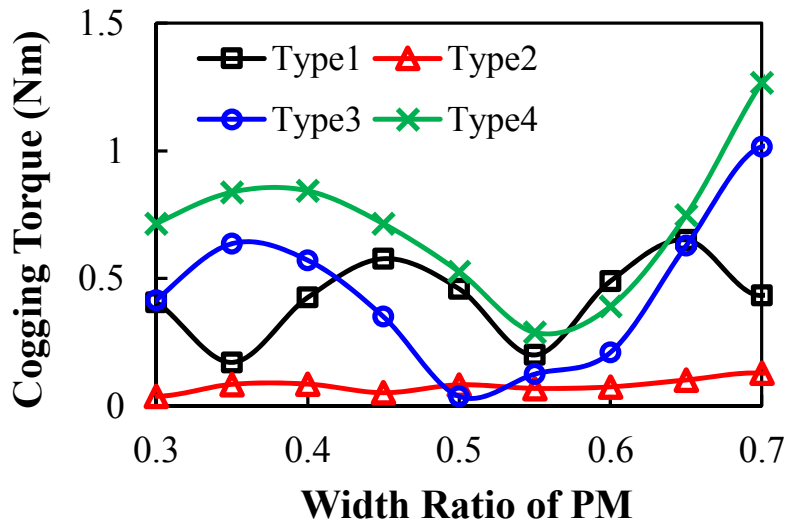


Fig. 4.20 Cogging torque variation of CPM-FRPM machines against  $\alpha_m$ .

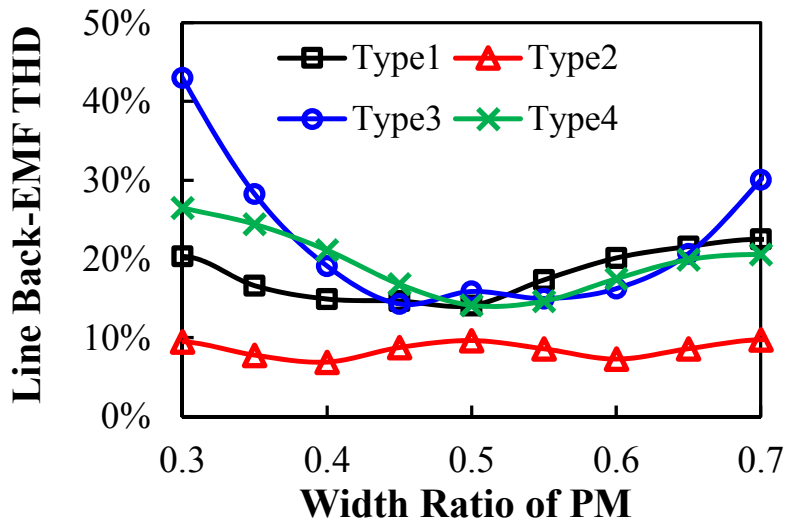


Fig. 4.21 Back-EMF THD variation of CPM-FRPM machines against  $a_m$ .

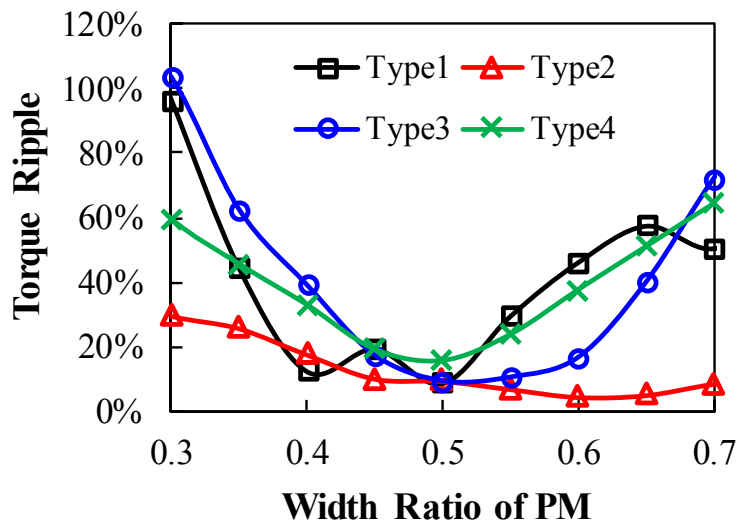


Fig. 4.22 Torque ripple variation of CPM-FRPM machines against  $a_m$ .

#### 4.4.4 Torque Improvement over SPM Topologies

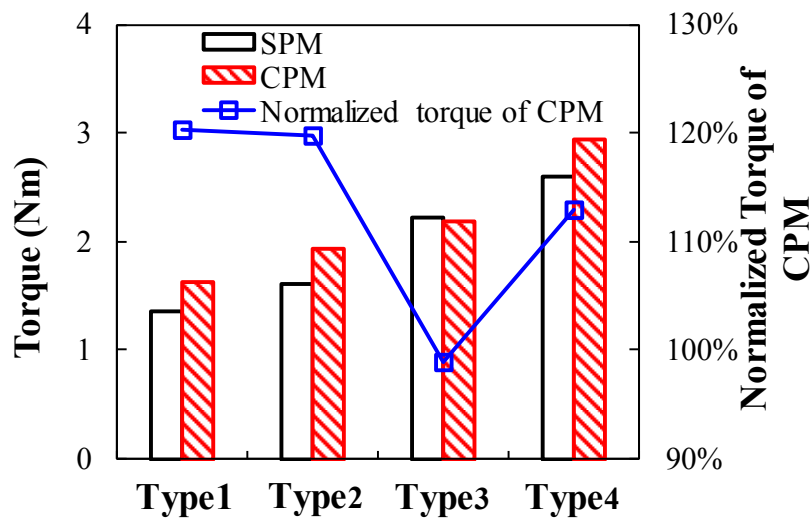
Considering the torque improvement of each CPM topology over its SPM counterpart, the torque performance of FRPM machines with different CPM and SPM topologies is calculated based on the machine parameters shown in Table 4.3, as shown in Fig. 4.23.

As can be seen from Fig. 4.23 (a), for either SPM or CPM, 1) the machines with identical PM locations on two adjacent stator teeth are more likely to produce higher torque than those with different PM locations, e.g. for CPM topology, Type2 (N/Fe-N/Fe) has 18% higher torque than Type1 (N/Fe-Fe/N), Type4 (N/Fe/N/Fe-N/Fe/N/Fe) has 34% higher torque than Type3 (N/Fe/N/Fe-Fe/N/Fe/N); 2) the machines with two PM pairs on each stator tooth produce

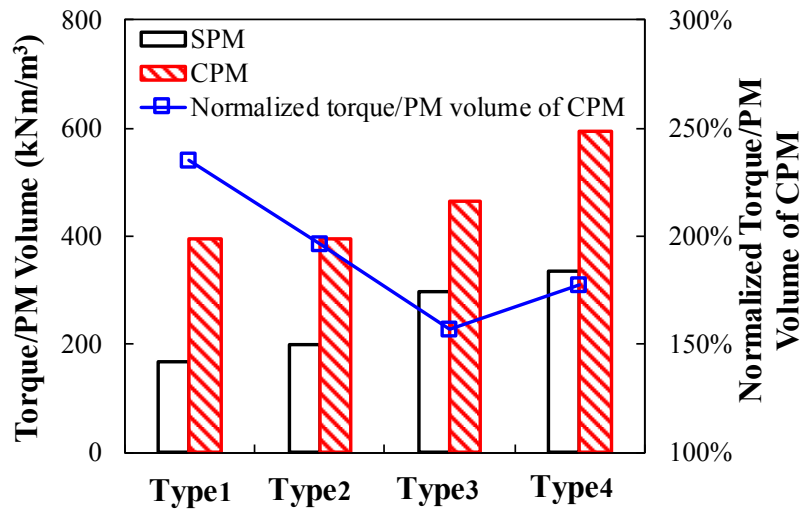


higher torque than those with one PM pair, e.g. for CPM topology, Type3 has 34% higher torque than Type1, Type4 has 52% higher torque than Type2. The conclusions are also applied to the torque per PM volume of the machines, as shown in Fig. 4.23 (b).

For each machine type, by setting the performance of SPM topology as benchmark, the normalised performance of the CPM topology is also shown in Fig. 4.23. As can be seen, the torque improvement of CPM over SPM is largely related to machine type. In addition to Type3, the torque of all other CPM types can be improved, and Type1 has the largest improvement (by 20%). This phenomenon can be explained by different equivalent pole-pair numbers  $p_{eq}$  of the machines, as shown in Fig. 4.24. For example,  $p_{eq}=1$  for Type3 while it is 2 for Type4. Therefore, the stator yoke of Type3 is more likely to suffer high saturation due to the larger flux per pole caused by the smaller  $p_{eq}$ . The improvement of armature field and torque of the CPM topology over SPM topology is then restricted. Thanks to the reduced PM volume as well as improved or similar average torque, the torque per PM volume of all CPM topologies can be largely improved (over 150%), making them suitable for low-cost applications, see Fig. 4.23 (b).

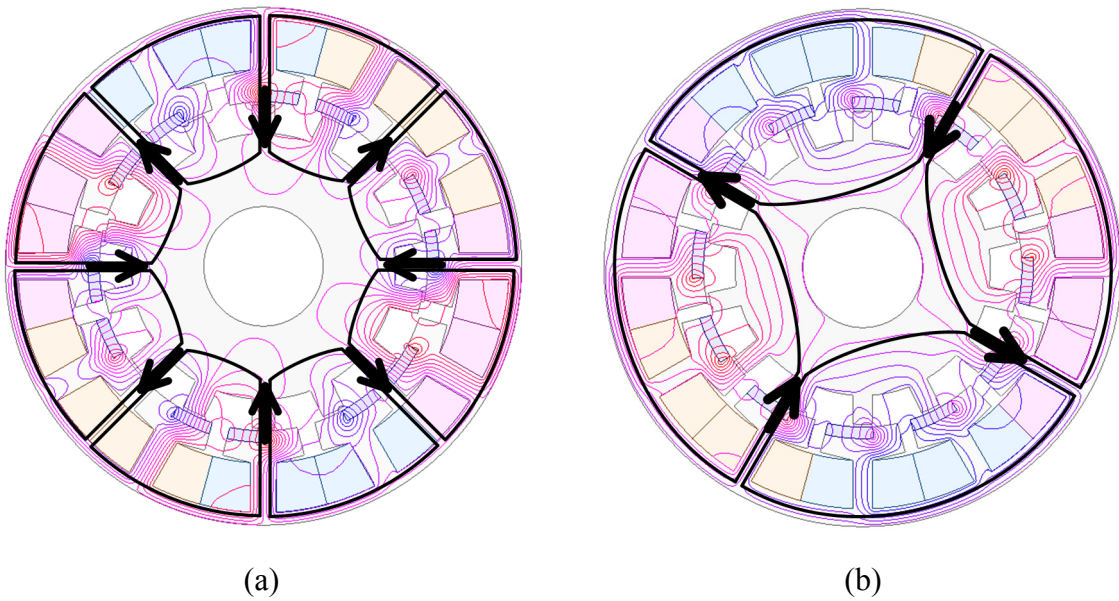


(a)



(b)

Fig. 4.23 Performance comparison of FRPM machines with different SPM and CPM topologies. (a) Torque. (b) Torque per PM volume.



(a)

(b)

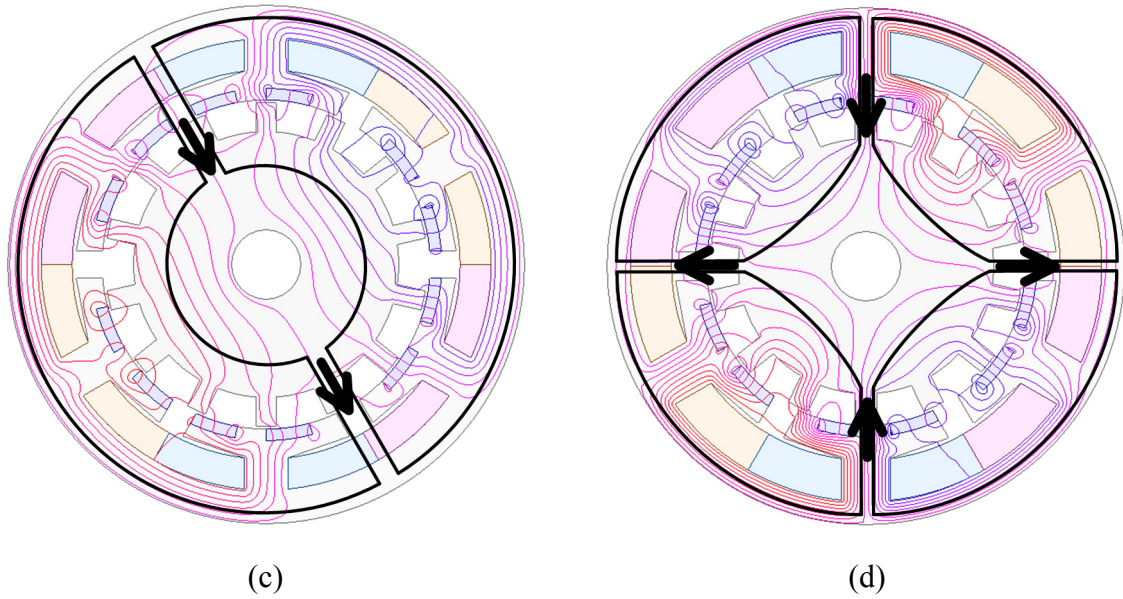


Fig. 4.24 No-load flux distribution and  $p_{eq}$  of FRPM machines with different CPM topologies. (a) Type1. (b) Type2. (c) Type3. (d) Type4.

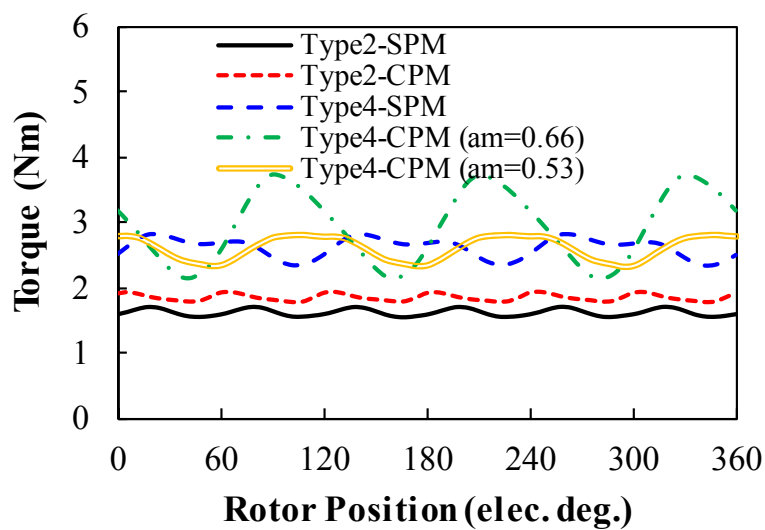
#### 4.5 Performance Comparison of 14-Rotor-Pole SPM and CPM-FRPM Machines

In the previous analyses, it has been proven that in addition to Type3, the CPM-FRPM machine always has higher average torque than its counterpart SPM-FRPM machine, and its PM usage can be largely reduced. In addition to the average torque, the detailed performance comparison of CPM-FRPM machines with SPM-FRPM machines will be presented to give a more comprehensive understanding of both advantages and disadvantages of CPM topology. It should be noted that only Type2 and Type4 are chosen for analysing since for both CPM- and SPM-FRPM machines, Type2 has higher torque than Type1 and Type4 has higher torque than Type3. Therefore, the two 12/14 FRPM machines (i.e. Type2) and two 6/14 FRPM machines (i.e. Type4) will be compared in the following.

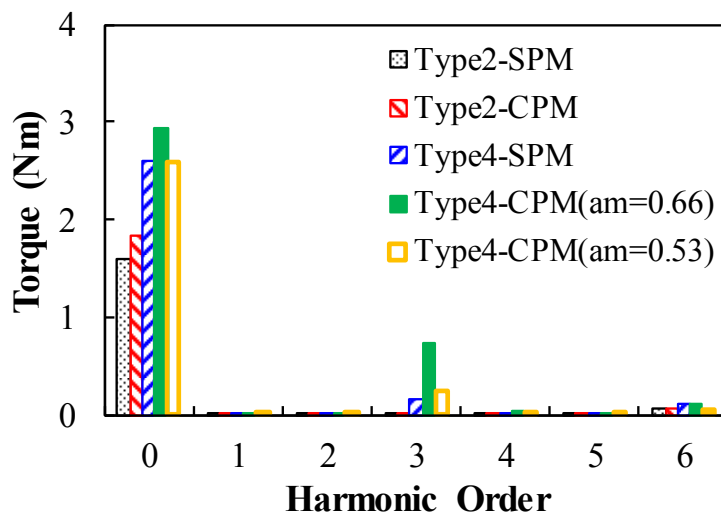
##### 4.5.1 On-Load Torque and Flux Density Distribution

Based on the optimum parameters shown in Table 4.3, the rated torque (corresponding to  $p_{cu}=20W$ ) of the machines are shown in Fig. 4.25 and Table 4.7. It should be noted that all the machines are optimised for maximum torque only. As can be seen, for Type2, the average torque  $T_{avg}$  of the CPM-FRPM machine is 20% higher than the SPM-FRPM machine while its torque ripple is also 46% lower. For Type4, the average torque of the CPM-FRPM machine is 13% higher than the SPM-FRPM machine. However, the torque ripple of the Type4 CPM-

FRPM machine is 54%, which is much higher when compared to the SPM-FRPM machine and is unacceptable for most applications. Since the PM width ratio  $\alpha_m$  has a big influence on the torque ripple (see Fig. 4.22 ), it is manually adjusted from its original optimum value of 0.66 to a modified value of 0.53 to mitigate the torque ripple, as verified in Fig. 4.25. The torque ripple of the modified CPM-FRPM machine is reduced to 18.6% which is similar to that of the SPM-FRPM machine. Although the average torque  $T_{avg}$  of the modified CPM-FRPM decreases, it is still competitive with that of the SPM-FRPM machine. Therefore, for Type4, the subsequent performance comparison will focus on the SPM-FRPM machine and the modified CPM-FRPM machine.



(a)



(b)

Fig. 4.25 Rated torque of the machines. (a) Waveforms. (b) Harmonic spectra.

Table 4.7 Average torque and torque ripple of the machines

	Type2-SPM	Type2-CPM	Type4-SPM	Type4-CPM ( $a_m=0.66$ )	Type4-CPM ( $a_m=0.53$ )
$T_{avg}$	1.61	1.93	2.60	2.94	2.60
Torque ripple	10.0%	5.4%	18.4%	54.3%	18.6%

When active copper loss  $p_{cu}=20W$ , the torque variations of the FRPM machines against current angle are firstly shown in Fig. 4.26. It should be noted that the current angle indicates the relative angle between the current phasor and the  $d$ -axis. When it is 90 elec. deg.,  $q$ -axis current ( $I_q$ ) is injected only, i.e.  $I_d=0$ . As can be seen, for both SPM and CPM topologies, the machine achieves the maximum torque when the current angle is approximately 90 elec. deg., indicating negligible reluctance torque. Therefore, in this chapter,  $I_d=0$  control is adopted in all the optimisations and analyses.

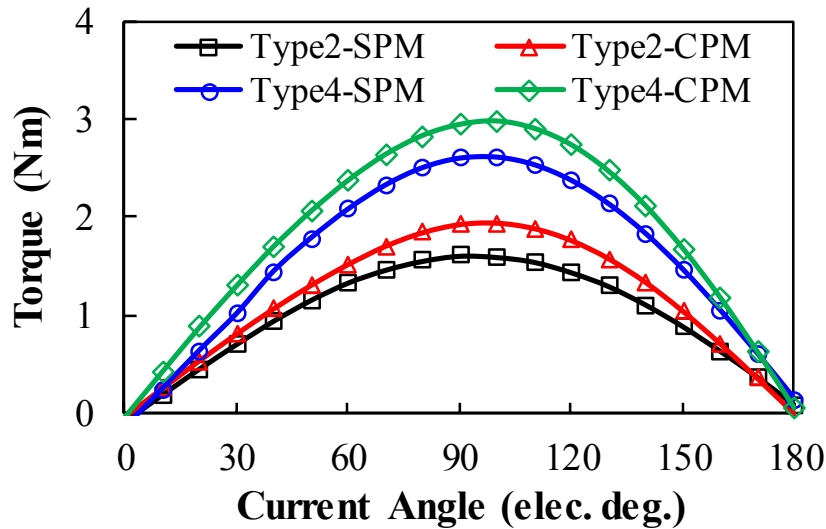


Fig. 4.26 Torque variations against current angle.

Fig. 4.27 shows the cross sections and full-load flux distributions of the four machines. As can be seen, for each machine type, the width of stator tooth and stator yoke thickness of the CPM-FRPM machine are larger than those of the SPM-FRPM machines, due to the increased armature field, which has been analysed before. In addition, for each machine, the maximum flux density in stator yoke is around 1.6-1.8T while the stator tooth tips may suffer saturation with maximum flux density exceeding 2T.

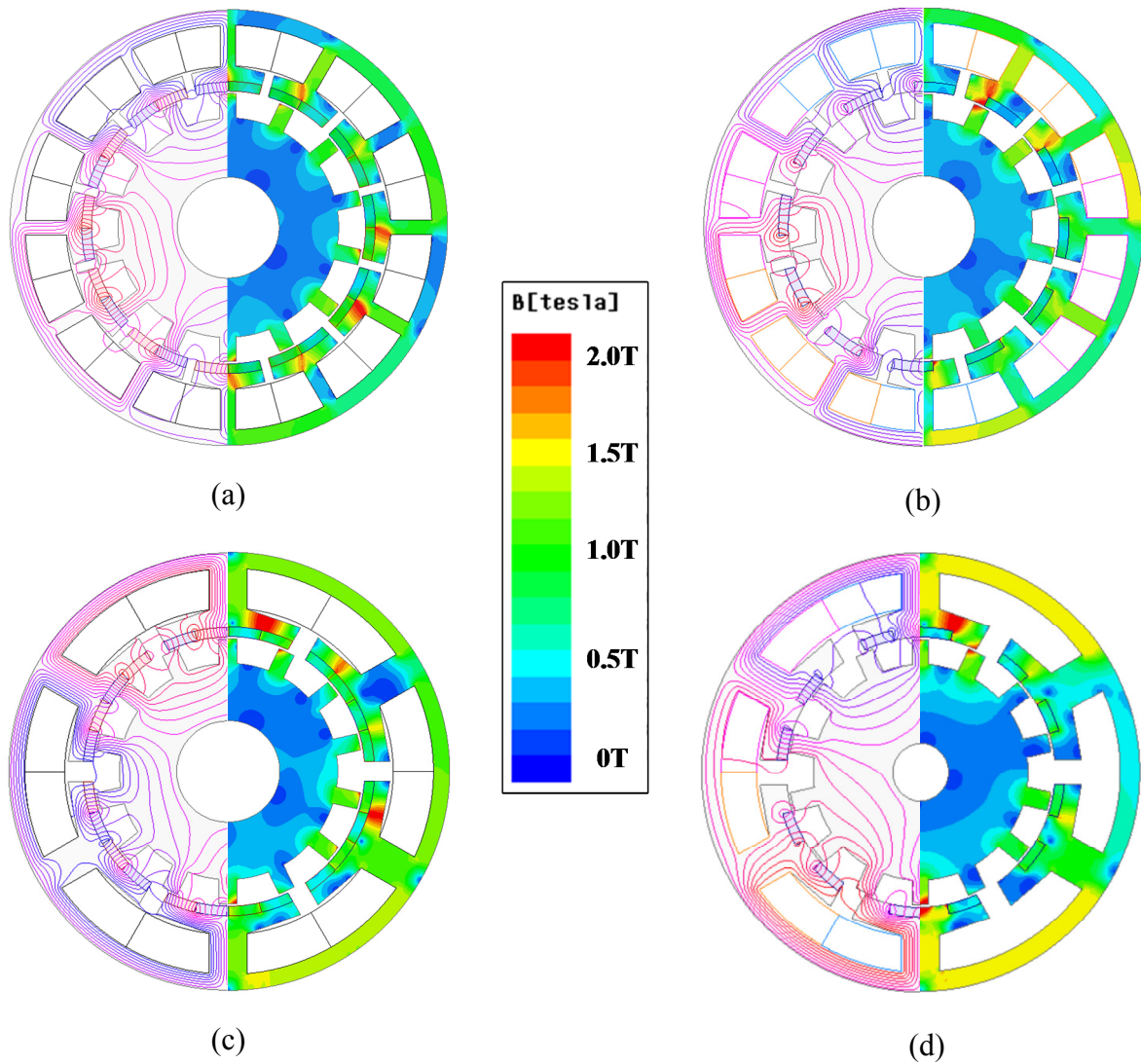


Fig. 4.27 Cross sections and full-load field distributions of machines. (a) Type2 SPM-FRPM. (b) Type2 CPM-FRPM. (c) Type4 SPM-FRPM. (d) Type4 CPM-FRPM.

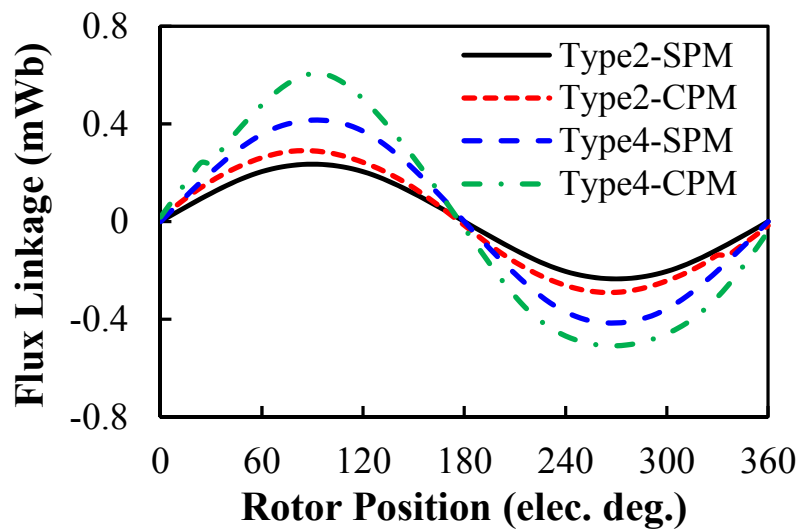
## 4.5.2 No-Load Performance

### 4.5.2.1 Flux Linkage

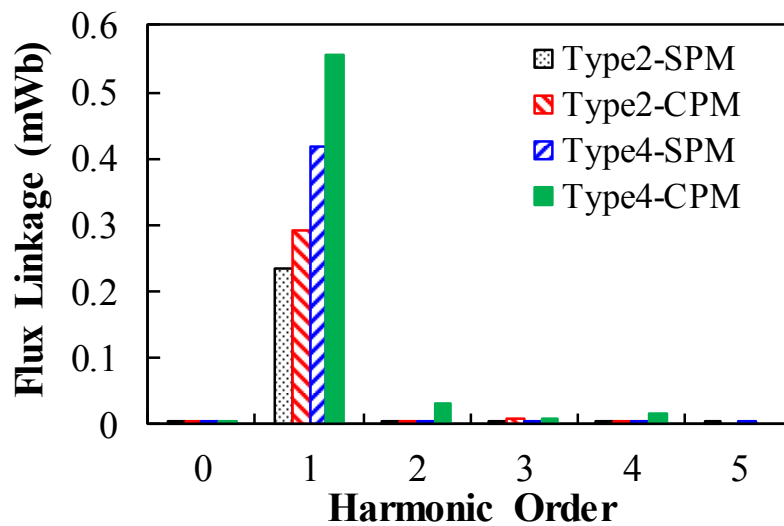
When the winding turns per phase  $N_{ph}$  are 4, the no-load phase flux linkages of different machines are shown in Fig. 4.28. As can be seen, the flux linkages of all the machines are bipolar. In addition to the Type4 CPM machine, the other three machines have a near-sinusoidal waveform. A relatively large 2nd and 4th harmonics exist in the Type4 CPM machine, while will result in back-EMF harmonics.

In terms of the fundamental flux linkage, the CPM-FRPM machines always have larger magnitude than the SPM-FRPM machines. For instance, the Type2 CPM-FRPM machine has

25% larger fundamental linkage than the Type2 SPM-FRPM machine, and the Type4 CPM-FRPM machine has 20% larger fundamental linkage than the Type4 SPM-FRPM machine.



(a)



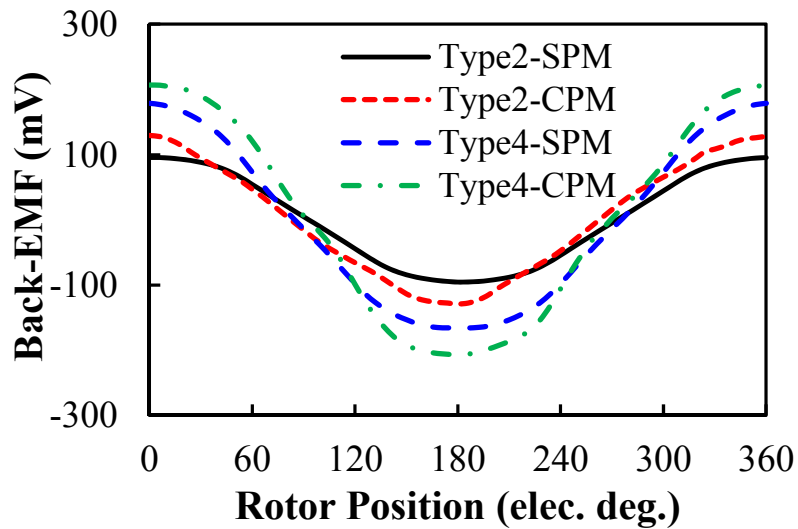
(b)

Fig. 4.28 Phase flux linkages of the four FRPM machines ( $N_{ph}=4$ ). (a) Waveforms. (b) Harmonic spectra.

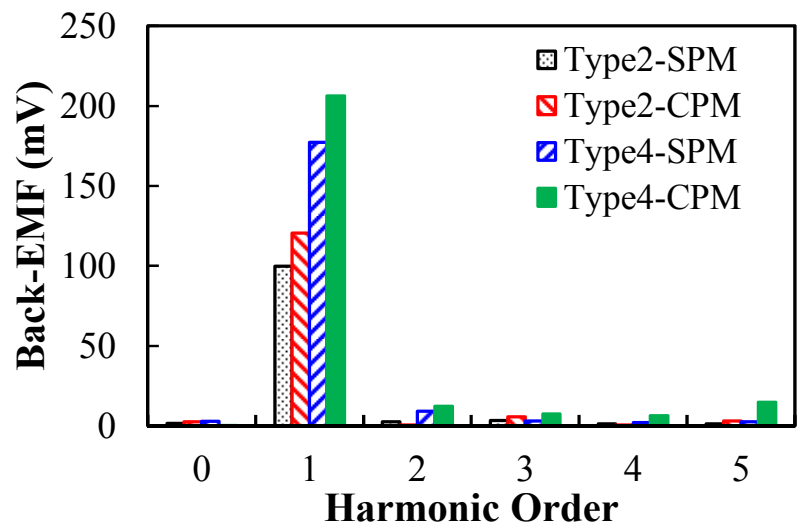
#### 4.5.2.2 Back-EMF

When the rotor speed  $n$  is 1000rpm and the winding turns per phase  $N_{ph}$  are 4, the no-load phase back-EMFs are shown in Fig. 4.29. Similar to the flux linkage, the back-EMFs of CPM-FRPM machines have larger fundamental magnitude than their counterpart SPM-FRPM machines. For instance, the Type2 CPM-FRPM machine has 25% larger fundamental back-EMF than the Type2 SPM-FRPM machine, and the Type4 CPM-FRPM machine has 20% larger fundamental

back-EMF than the Type4 SPM-FRPM machine. In addition, the high-order back-EMF harmonics exist in the Type4 CPM-FRPM machine due to the harmonics of the flux linkage, which contribute to a large torque pulsation component.



(a)



(b)

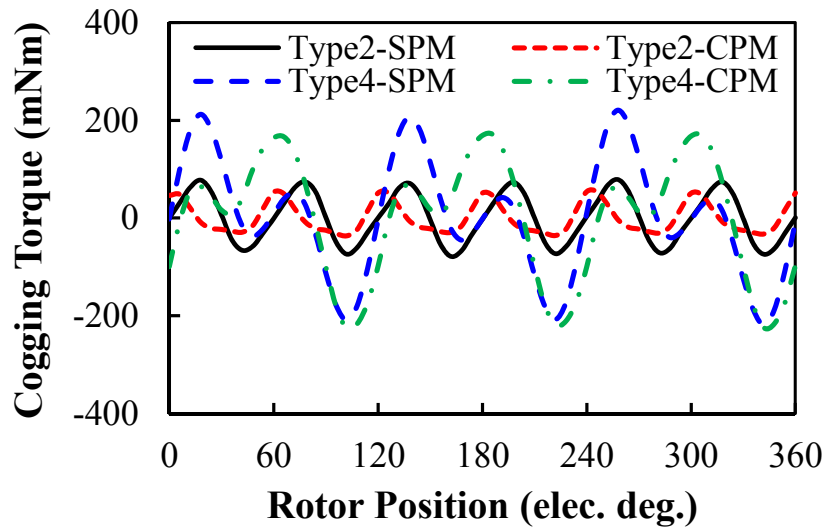
Fig. 4.29 Phase back-EMF of the four FRPM machines ( $n=1000\text{rpm}$ ,  $N_{ph}=4$ ). (a) Waveforms. (b) Harmonic spectra.

#### 4.5.2.3 Cogging Torque

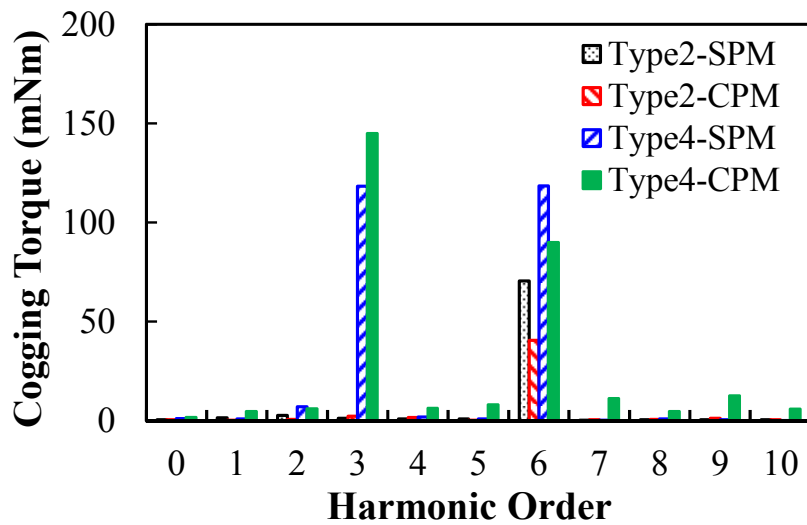
Fig. 4.30 shows the cogging torque of the four machines. As can be seen, the fundamental orders of the cogging torque of the Type2 machines are 6 while those of the Type4 machines are 3, which are consistent with the main torque ripple harmonics shown in Fig. 4.25. In addition, the Type2 machines have lower cogging torque than the Type4 machines, and for



each machine type, the CPM- and SPM-FRPM machines have similar peak to peak value of the cogging torque. Therefore, for the applications where low cogging torque is required, the cogging torque reduction techniques should be utilised especially for the Type4 machines [KIM05b].



(a)



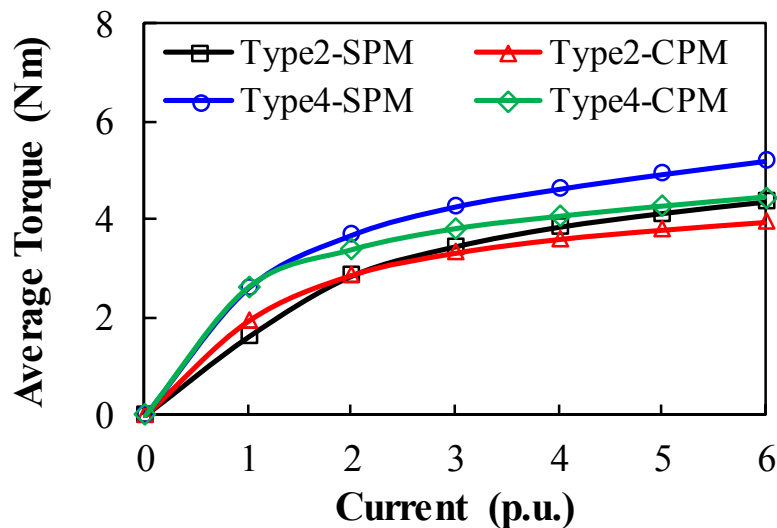
(b)

Fig. 4.30 Cogging torque of the four FRPM machines. (a) Waveforms. (b) Harmonic Spectra.

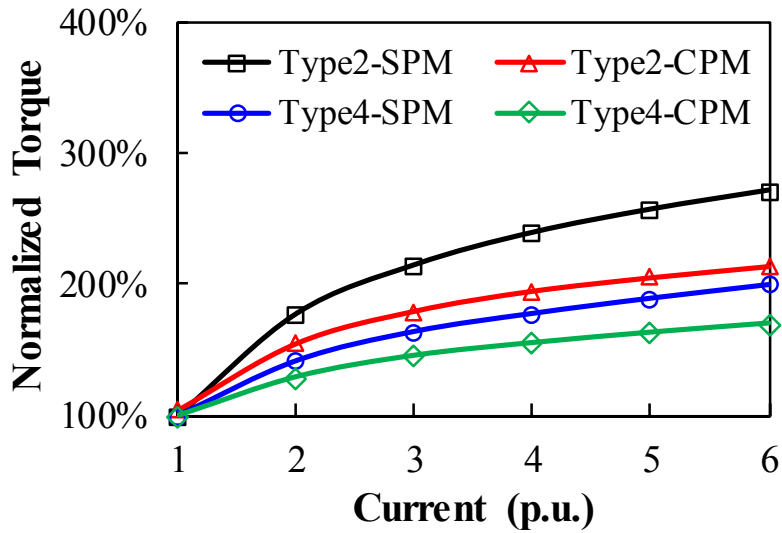
### 4.5.3 Over-Load Torque Capability and Inductance

To assess the over-load capability of the machines, the average torque variations against current are firstly shown in Fig. 4.31 (a). As can be seen, when the current is low, the CPM-FRPM

machines have similar or higher average torque than the corresponding SPM-FRPM machines. However, the average torque of SPM-FRPM machines is improved more significantly as current increases. For instance, when current is 1 p.u., the average torque of the Type2 CPM-FRPM machine is 20% higher than that of the Type2 SPM-FRPM machine while it is 4% lower when current is 3 p.u. Therefore, the inferior over-load capability of the CPM-FRPM machine is revealed. More clearly, by setting the rated torque (i.e.  $p_{cu}=20W$ ) of each machine as benchmark, the normalised torque of the machines under different load conditions is shown in Fig. 4.31 (b). As can be seen, within the whole current region, the over-load capability of the Type2 machines is better than that of the Type4 machines, and Type2 SPM-FRPM machine has the best over-load capability. This can be further explained by the different self-inductances of the machines (see Fig. 4.32). It should be noted that the winding turns per phase  $N_{ph}$  are same for all the machines, which are 4. As can be seen, the self-inductances of all the machines decrease with current due to the saturation and the self-inductances of the Type4 machines are larger than those of the Type2 machines due to the reduced stator slot number. In terms of the comparison of SPM and CPM machines, it is found that the CPM machines always have larger inductance than the SPM machines due to the reduced equivalent air-gap length. It can be concluded that the larger the self-inductance, the higher the armature field, the severer the saturation, and the worse the over-load capability.



(a)



(b)

Fig. 4.31 Torque variations against current. (a) Average torque. (b) Normalised average torque.

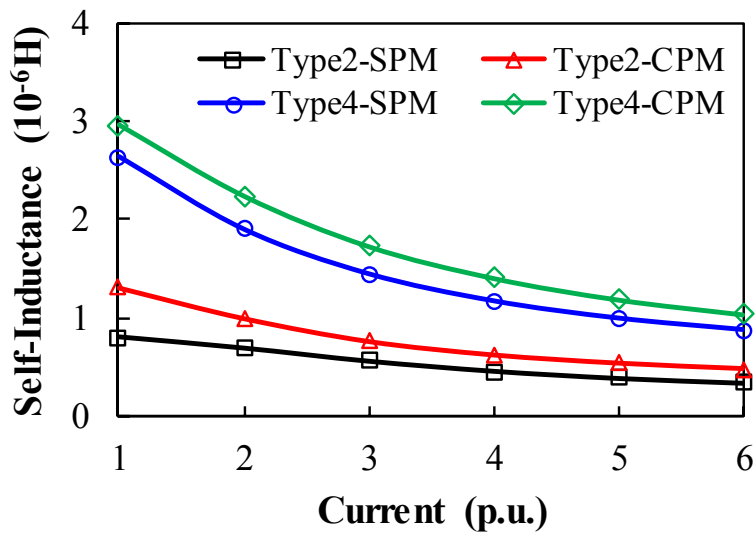


Fig. 4.32 Inductance variation against current. ( $N_{ph}=4$ )

#### 4.5.4 Losses and Efficiency

Fig. 4.33 shows the full-load iron loss variation against speed. As can be seen, the loss rapidly increases with speed, and it is higher in the Type4 machines due to the higher average flux density in the stator (see Fig. 4.27) when compared to the Type2 machines. In addition, it is found that the CPM machines always have higher core loss than the SPM machines due to the larger armature field and resulted high flux density especially in stator core.

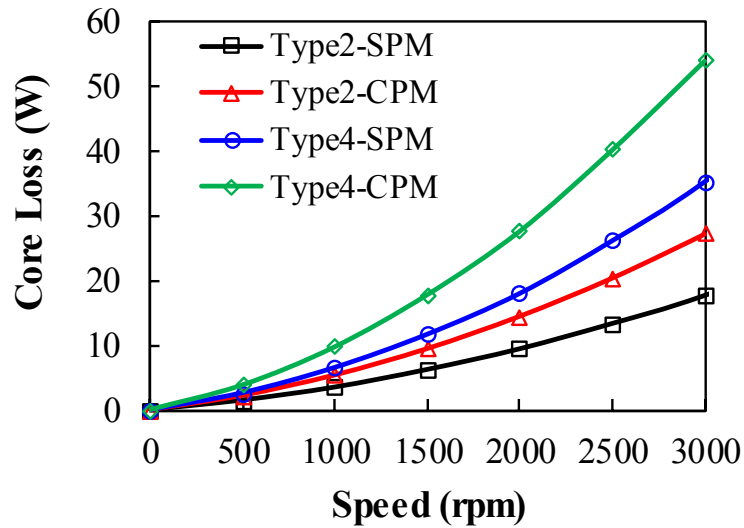


Fig. 4.33 Full-load iron loss variation against speed ( $p_{cu}=20W$ ).

Fig. 4.34 shows the full-load PM loss variation against speed. As can be seen, unlike core loss shown in Fig. 4.33, the PM loss of CPM machines is always lower than that of SPM machines, which is mainly resulted from the reduced PM volume. Fig. 4.35 shows the variation of rated efficiency against speed. As can be seen, all the machines exhibit the highest efficiency around 2000-2500rpm. With rotor speed increasing from 2500rpm, the efficiencies gradually reduce. When the speed is relatively low, the CPM machines have much higher efficiency than the SPM machines due to the improved average torque. As speed increases, the advantage of CPM machines over SPM machines tends to be minor because of the rapidly increased core loss in CPM machines (see Fig. 4.33).

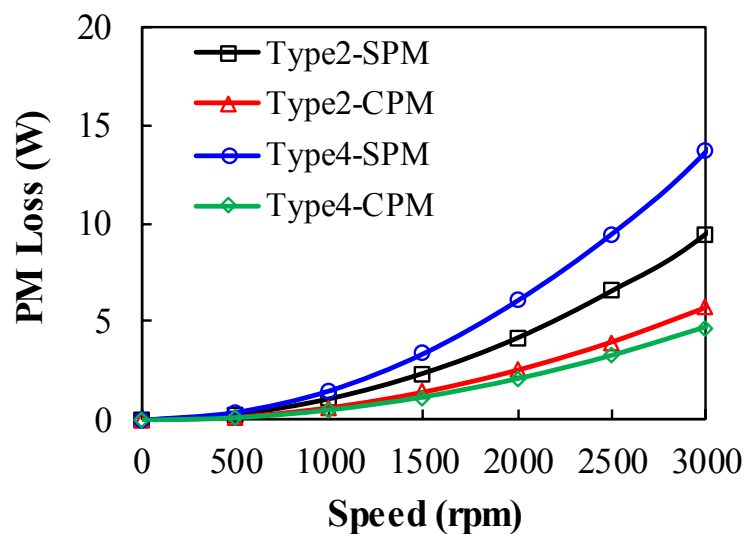


Fig. 4.34 PM loss variation against speed ( $p_{cu}=20W$ ).

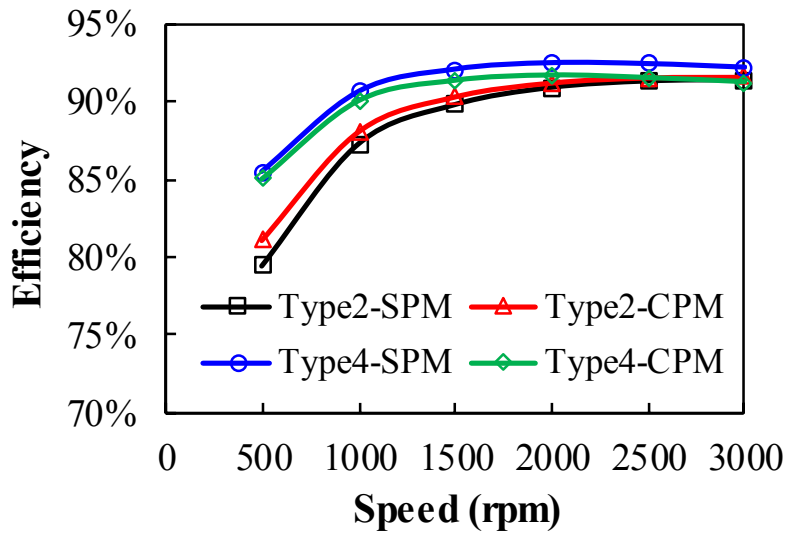


Fig. 4.35 Efficiency variation against speed.

#### 4.5.5 Power Factor

Considering that the PM topology influences the average torque and inductance of the FRPM machine, the power factor of different FRPM machines are compared in Fig. 4.36. Since both CPM and SPM machines have negligible reluctance torque (see Fig. 4.26), the power factor ( $pf$ ) of the machines can still be expressed as (2.10). As can be seen, when torque is relatively low, the CPM machines have slightly higher power factor than the SPM machines thanks to the lower armature field (i.e. lower current level) required for the torque production. As torque increases, the SPM machines tend to have higher power factor than the CPM machines since the CPM machines have higher inductance (see Fig. 4.36).

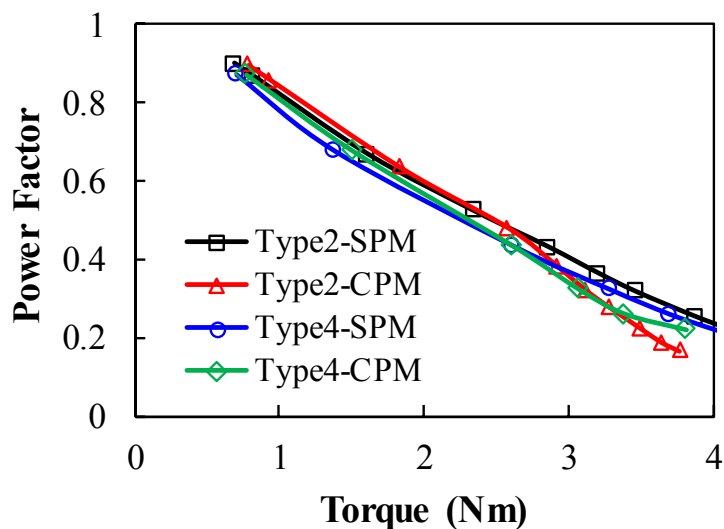


Fig. 4.36 Power factor variation against torque.

#### 4.5.6 Demagnetisation Withstand Capability

The demagnetisation withstand capability of the FRPM machines with different PM topologies are compared in Fig. 4.37, when the machine operation temperature  $T$  is set as  $100^{\circ}\text{C}$  and a large minus  $d$ -axis current is injected ( $I_d = -5I_{rated}$ ). As can be seen, the Type4 machines suffer high risk of demagnetisation and the Type4 CPM topology exhibits the worst demagnetisation withstand capability. Such phenomenon can be explained by the inductance of the machines (see Fig. 4.32). The larger the inductance, the larger the armature field, the weaker the demagnetisation withstand capability.

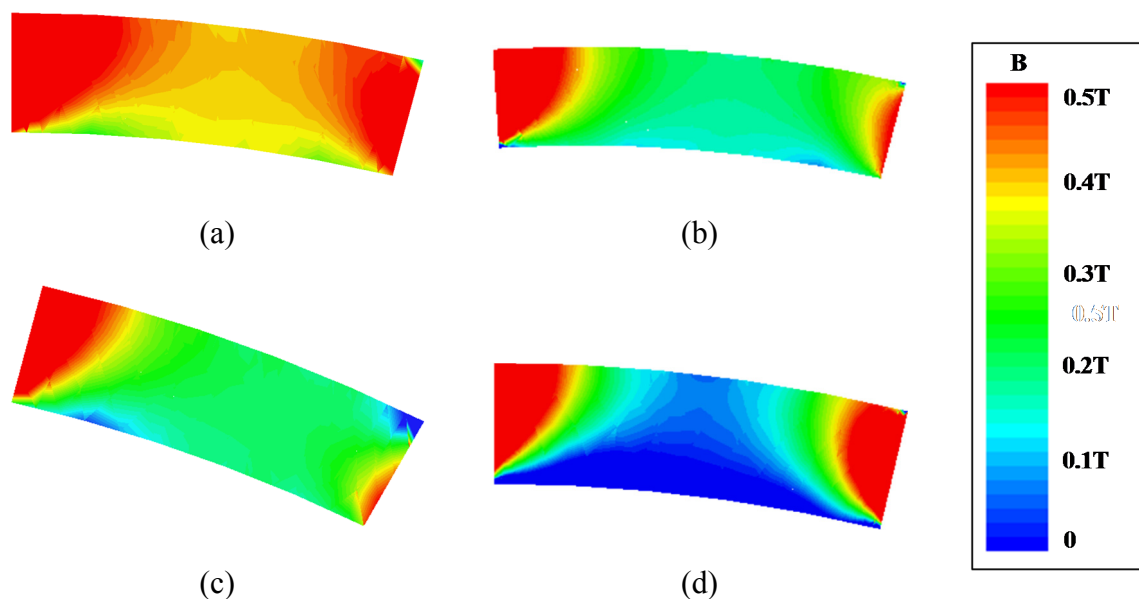


Fig. 4.37 Comparison of flux density in the magnetisation direction of a single PM piece ( $T=100^{\circ}\text{C}$ ,  $I_d=-5I_{rated}$ ). (a) Type2-SPM. (b) Type2-CPM. (c) Type4-SPM. (d) Type4-CPM.

#### 4.5.7 3-D End-Effect Analysis

Although the machine with CPM topology may have advantages of reduced PM volume and maintained or even improved average torque, its end-effect should be carefully assessed [WU16b] [SHE17a] [GE16]. By adopting 3D FEA in JMAG, the end-effects of FRPM machines with CPM and SPM topologies are investigated and compared.

The no-load 3D flux vector plot of the Type2 SPM-FRPM machine is shown in Fig. 4.38 while that of the Type2 CPM-FRPM machine is shown in Fig. 4.39. As can be seen, the flux density of the CPM-FRPM machine is higher than that of the SPM-FRPM machine, especially in stator yoke, which is consistent with the previous analysis. Considering the end region flux leakage vectors of the two machines shown in Fig. 4.40, the axial flux leakage is severer in the CPM

topology and this is mainly attributed to the high saturation in iron poles of stator teeth [WU16b]. Besides, the no-load 3D flux vector plots of Type4 SPM-FRPM machine is shown in Fig. 4.41 while that of Type4 CPM-FRPM machine is shown in Fig. 4.42. Similar to the Type2 machine, the Type4 CPM-FRPM machine has higher flux density in stator yoke and severer axial flux leakage in the end region, as shown in Fig. 4.43.

In general, for FRPM machines with CPM topologies, the torque benefit will be partially counteracted by the large end-effect. Moreover, for practical machine systems, the large end flux leakage may magnetise the mechanical components of the machines, such as the shaft, bearing, and screws, which will impair reliability and life span of the machine [LI19]. Therefore, for the design of CPM-FRPM machines, it is necessary to conduct 3D FEA to verify the machine performance and for applications where end flux leakage mitigation is required, additional techniques should be further investigated, such as adopting more complicated CPM topologies or flux barriers [LI19]. The influence of end-effect on back-EMF, cogging torque, static torque, and torque-current characteristics of CPM machines will be reported in the next section.

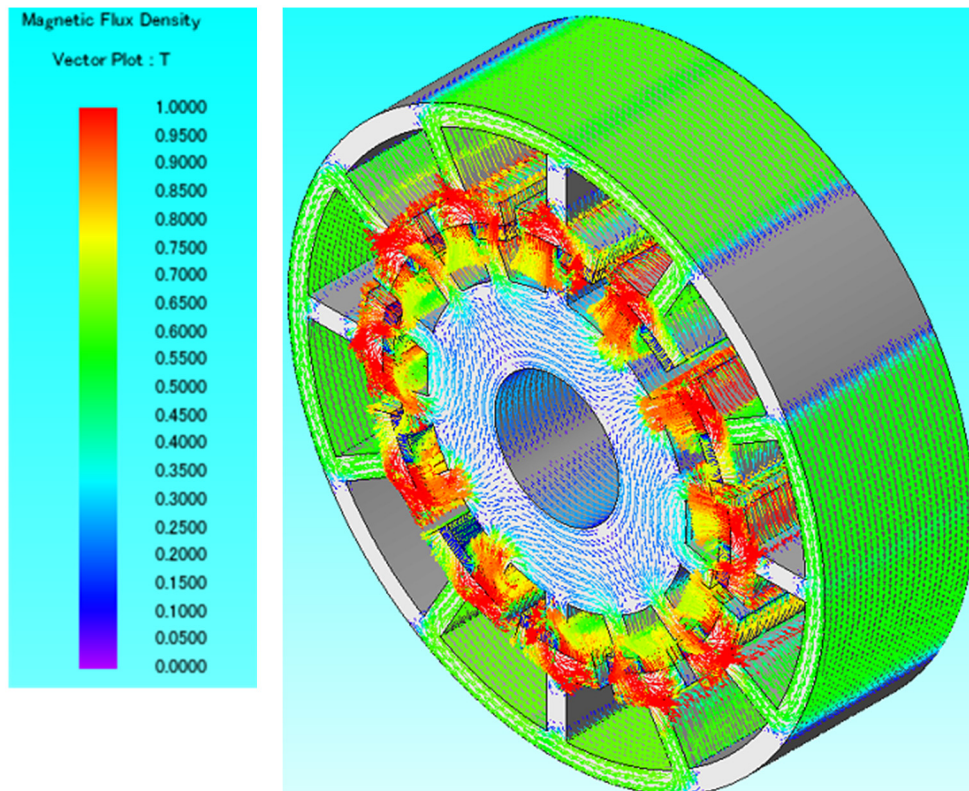


Fig. 4.38 No-load 3D flux vector plot of Type2 SPM-FRPM machine.

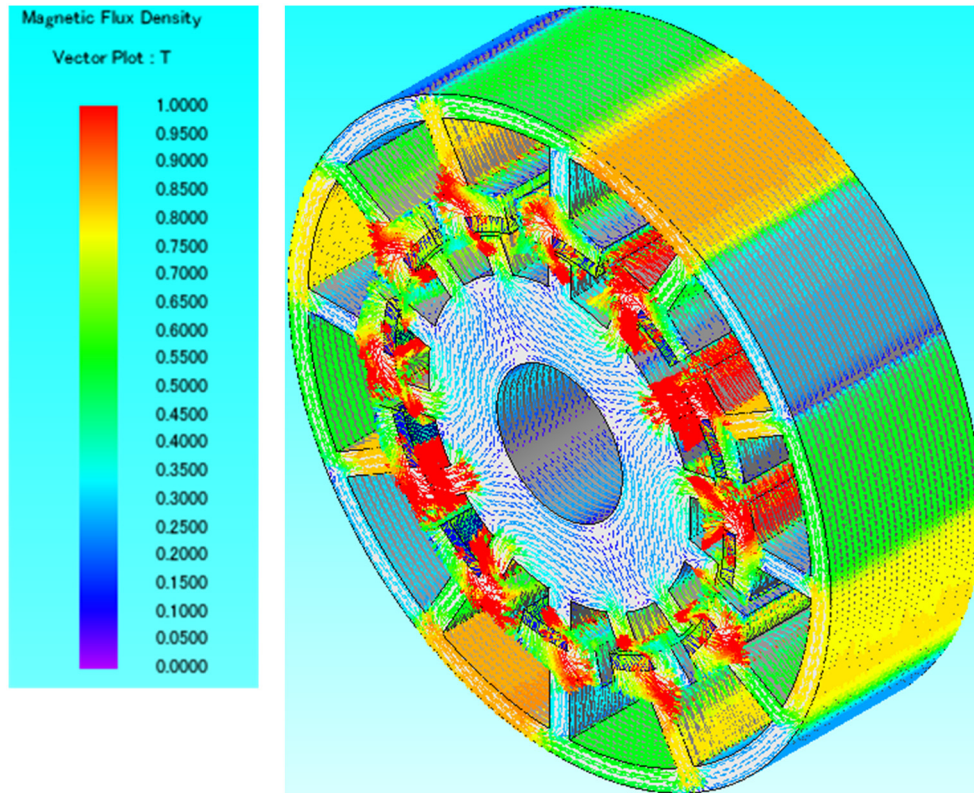


Fig. 4.39 No-load 3D flux vector plot of Type2 CPM-FRPM machine.

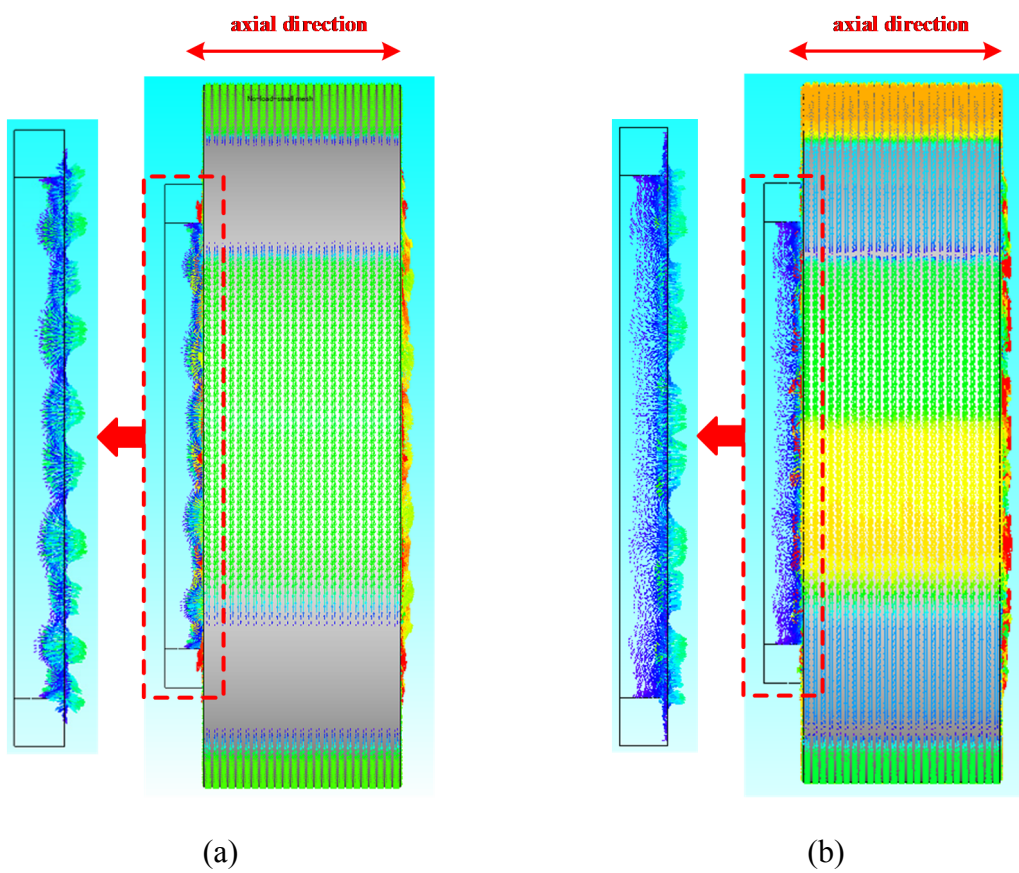


Fig. 4.40 End magnetic flux leakage of Type2 machines. (a) SPM-FRPM. (b) CPM-FRPM.



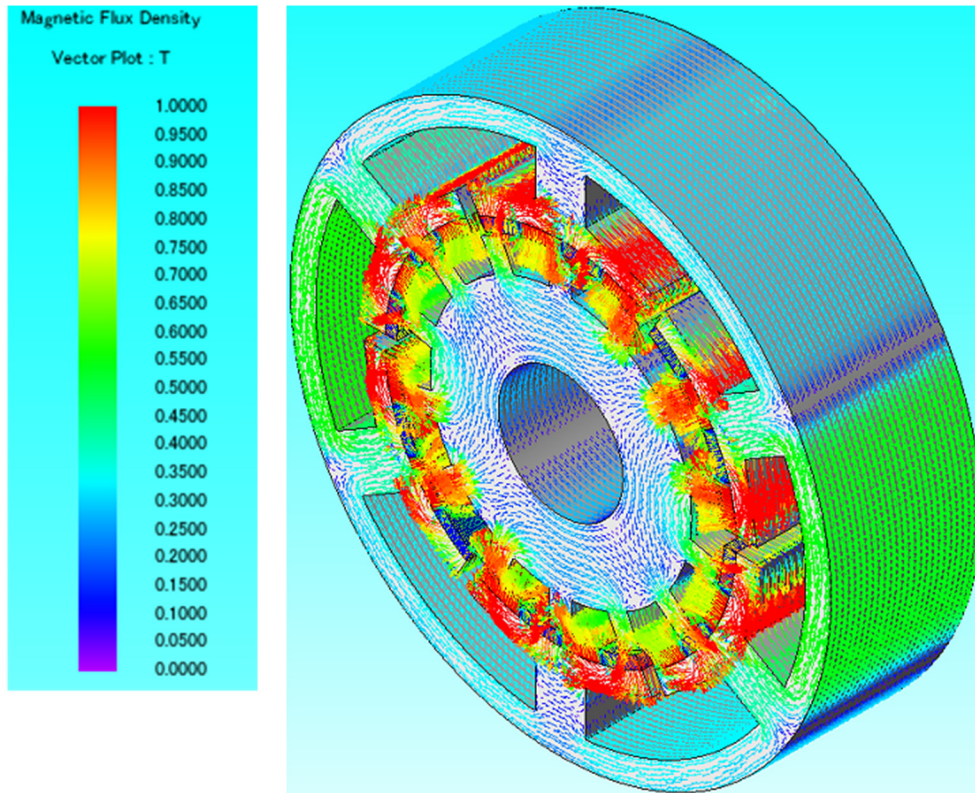


Fig. 4.41 No-load 3D flux vector plot of Type4 SPM-FRPM machine.

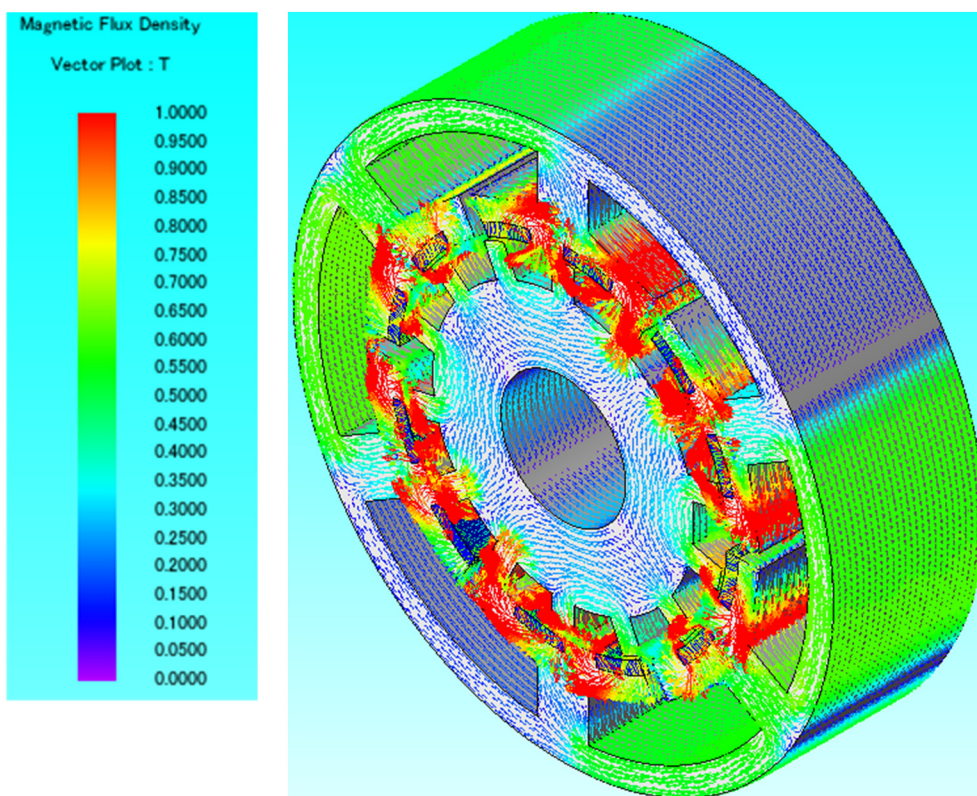


Fig. 4.42 No-load 3D flux vector plot of Type4 CPM-FRPM machine.

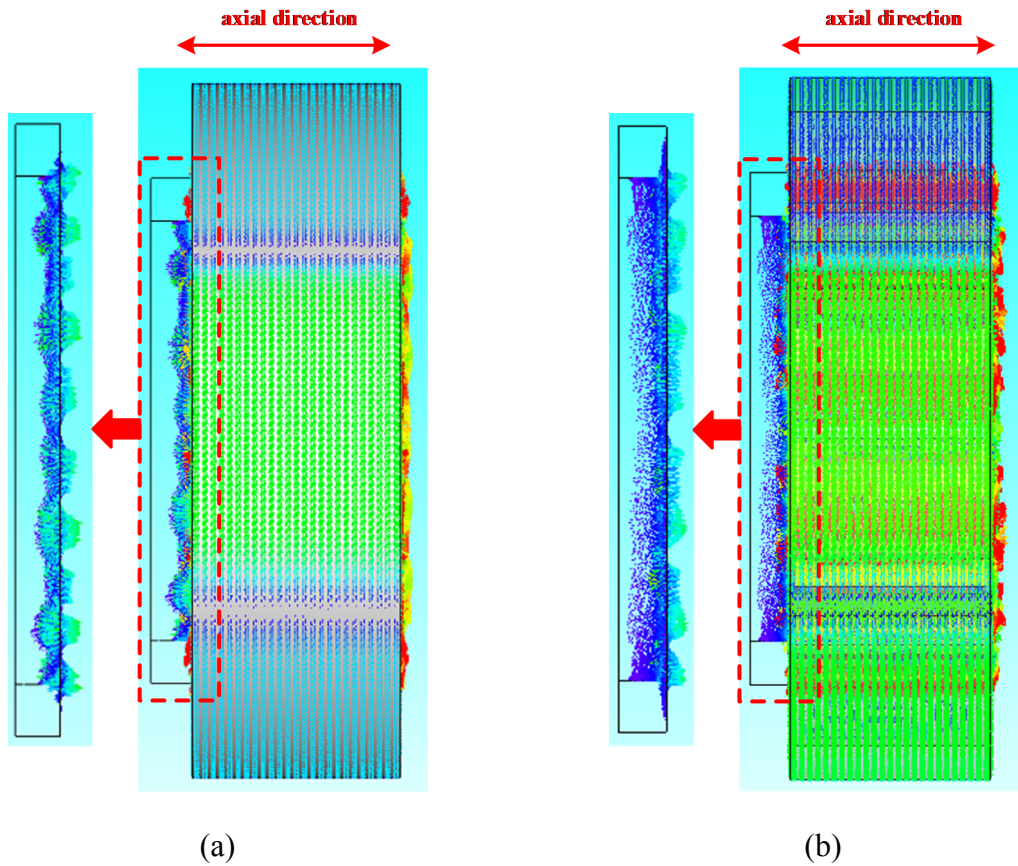


Fig. 4.43 End magnetic flux leakage of Type4 machines. (a) SPM-FRPM. (b) CPM-FRPM.

#### 4.6 Experimental Validation

To validate the previous analyses of FRPM machines with different PM topologies, two SPM and two CPM prototypes of Type2 and Type4 are manufactured and tested. Fig. 4.44 shows the machine prototypes, and their parameters are listed in Table 4.3. For simplicity, the four machines share the same 14-pole rotor, and the parameters of the prototypes are not exactly the same as the optimum FEA models. Besides, the machine end-caps and housings are all made of aluminium to avoid the influence of axial flux leakage to these mechanical components. Under the same slot filling factor, the number of series turns per coil  $n_c$  is 74 for the Type2-SPM and CPM machines, and it is 115 for the Type4-SPM and CPM machines.

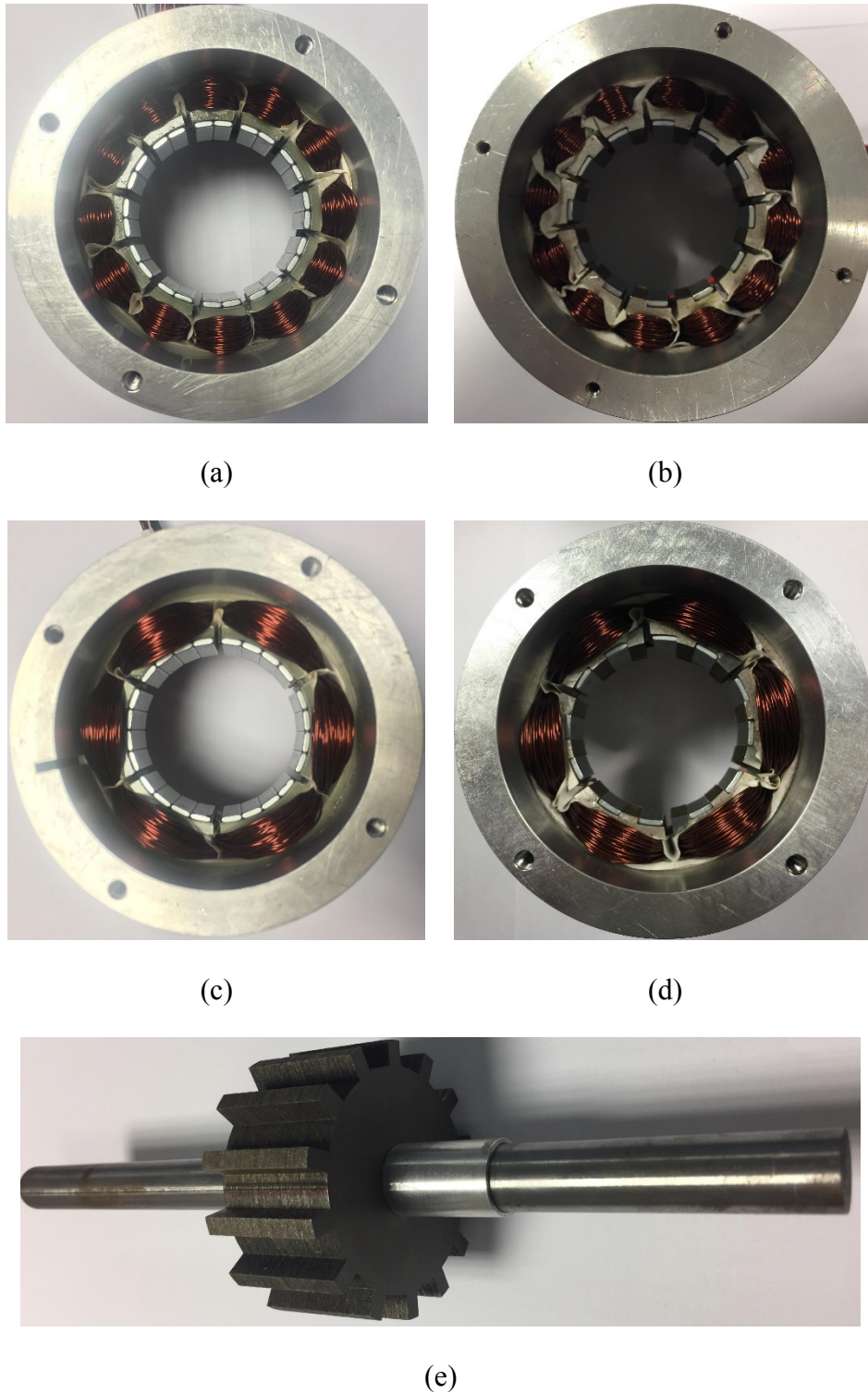


Fig. 4.44 Prototypes. (a) Type2-SPM stator. (b) Type2-CPM stator. (c) Type4-SPM stator. (d) Type4-CPM stator. (e) Shared 14-pole-rotor.

The measured and FE-predicted back-EMFs of the four machines ( $n=400\text{rpm}$ ) are shown in Fig. 4.45, Fig. 4.46, Fig. 4.47, and Fig. 4.48, respectively. Both 2D FE and 3D FE predicted back-EMFs are given, and the magnitudes of fundamental back-EMFs are summarised in Table

4.8. As can be seen, for the two SPM machines, a good agreement between the back-EMF waveforms can be observed while the measured back-EMF waveforms of the CPM machines have some deviations against the FE-predicted waveforms. In terms of the fundamental back-EMF shown in Table 4.8, the 3D FE-predicted back-EMFs are always smaller than the 2D FE results due to the end-effect. For the SPM machines, the 3D FE-predicted fundamental back-EMFs are around 97% of the 2D FE-predicted results. In contrast, the 3D FE-predicted fundamental back-EMFs of the CPM machines are around 94% of the 2D FE-predicted results, indicating larger end-effect in CPM machines (as shown in Fig. 4.40 and Fig. 4.43). As for the measured results, there are approximately a 10% reduction against 2D results for the SPM machines while for the CPM machines, the measured back-EMFs are even smaller. For instance, the measured back-EMF of the Type4-CPM machine is only 80% of the 2D-predicted value. Such errors can be attributed to the manufacture imperfection especially for the CPM topologies. For instance, there may exist additional gaps between the PM pieces and adjacent iron poles, which will result in a large equivalent air-gap length and deteriorate the back-EMF. Despite of the large end-effect and manufacturing imperfections in CPM topologies, the improved back-EMFs of CPM topologies can still be verified since both CPM machines have higher measured back-EMFs than their SPM counterparts.

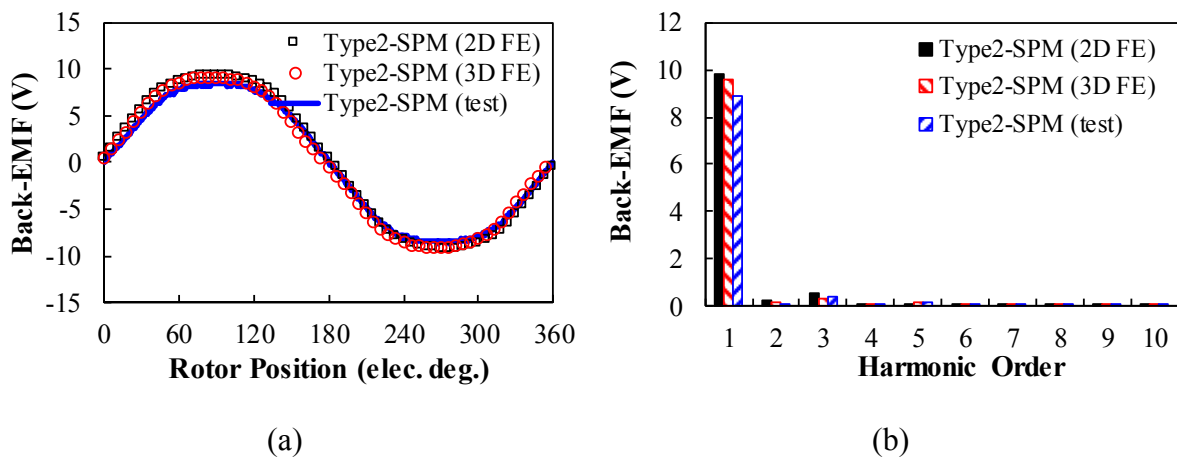


Fig. 4.45 Measured and FE-predicted back-EMFs of Type2-SPM machine. ( $n=400\text{rpm}$ ) (a) Waveforms. (b) Harmonic spectra.

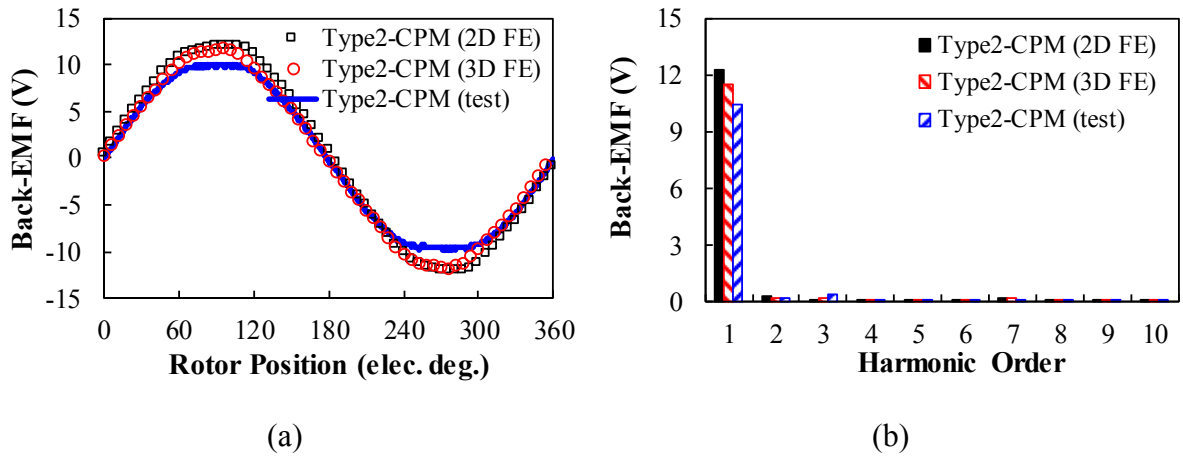


Fig. 4.46 Measured and FE-predicted back-EMFs of Type2-CPM machine. ( $n=400\text{rpm}$ ) (a) Waveforms. (b) Harmonic spectra.

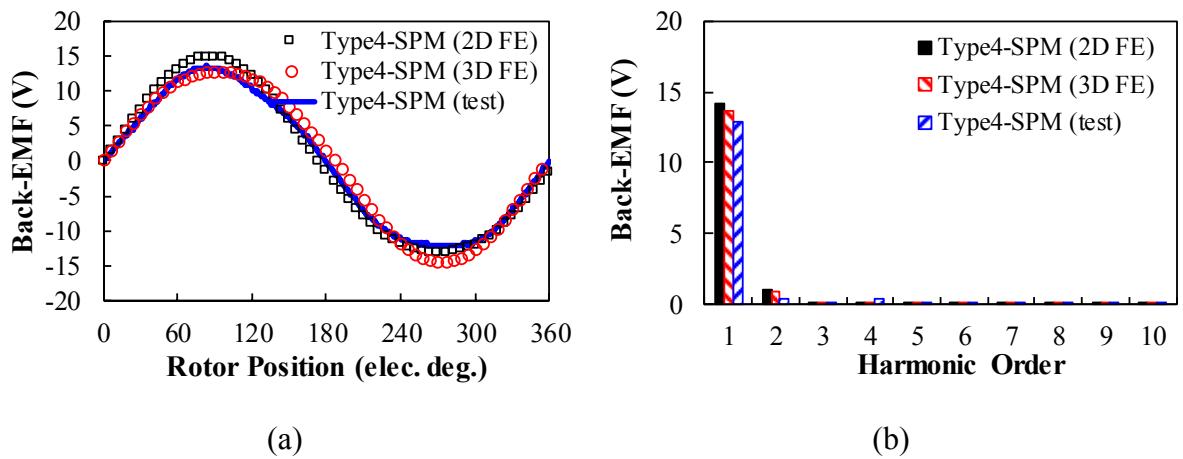


Fig. 4.47 Measured and FE-predicted back-EMFs of Type4-SPM machine. ( $n=400\text{rpm}$ ) (a) Waveforms. (b) Harmonic spectra.

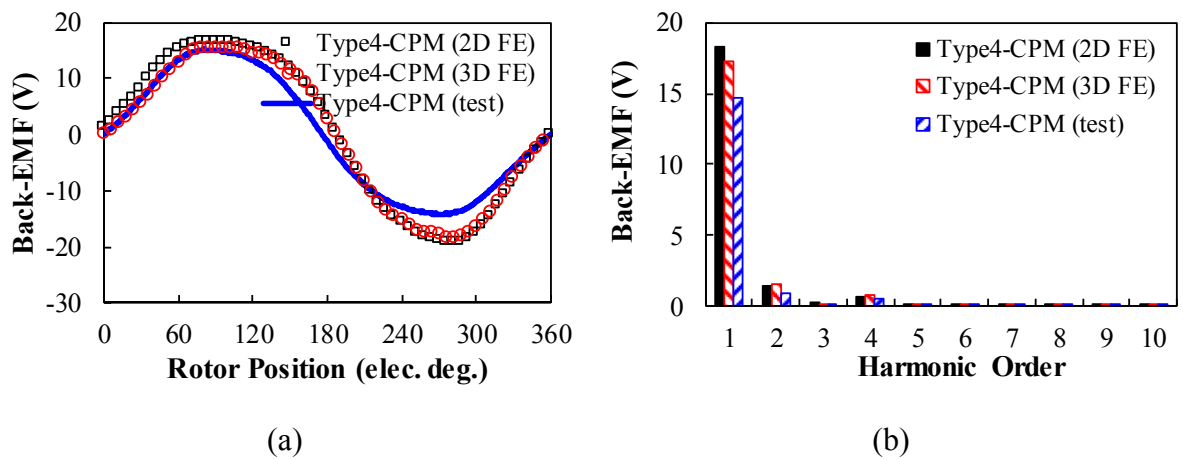


Fig. 4.48 Measured and FE-predicted back-EMFs of Type4-CPM machine. ( $n=400\text{rpm}$ ) (a) Waveforms. (b) Harmonic spectra.

Table 4.8 FE-predicted and measured fundamental back-EMFs

PM topology	Type2		Type4	
	SPM	CPM	SPM	CPM
2D-FE	9.8 V (100%)	12.3 V (100%)	14.2 V (100%)	18.3 V (100%)
3D-FE	9.6V (97.4%)	11.5V (94.0%)	13.7V (96.7%)	17.3V (94.2%)
test	8.9V (90.5%)	10.4V (84.8%)	12.8V (90.5%)	14.7V (80.4%)

Based on the simple cogging torque measurement method introduced in Appendix B, the cogging torque of each machine is measured and compared with those obtained by 2D and 3D FE, as shown in Fig. 4.49 and Fig. 4.50. Due to the high rotor pole number and corresponding limited torque measurement point, only torque waveforms without harmonic spectra are given. As can be seen, for each machine, a good agreement between the results is achieved and the minor difference can be attributed to the measurement error and manufacturing tolerance. In addition, the measured and FE-predicted cogging torques of the Type4 machines are larger than those of the Type2 machines, and the Type2 CPM-FRPM machine has the lowest cogging torque.

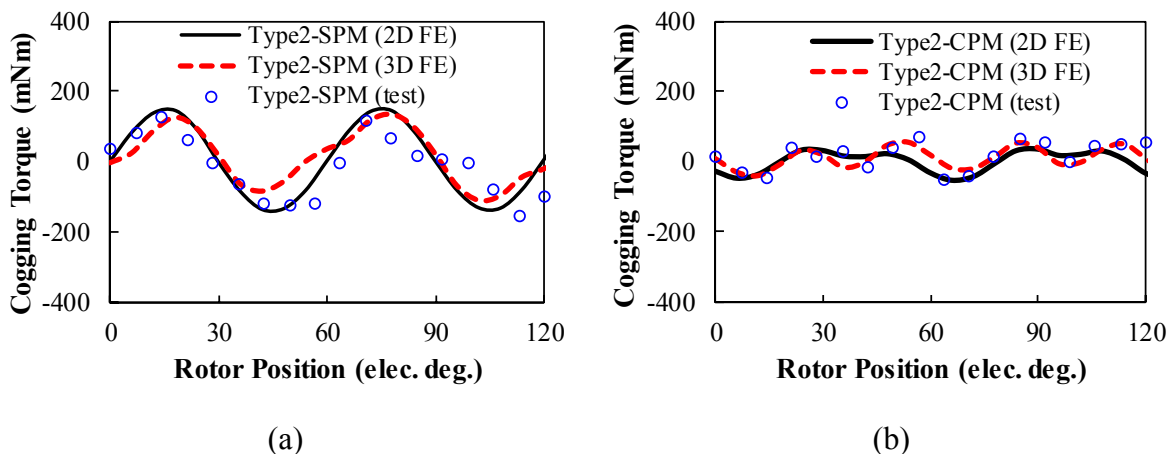


Fig. 4.49 Measured and FE-predicted cogging torques of Type2 machines. (a) SPM-FRPM machine. (b) CPM-FRPM machine.

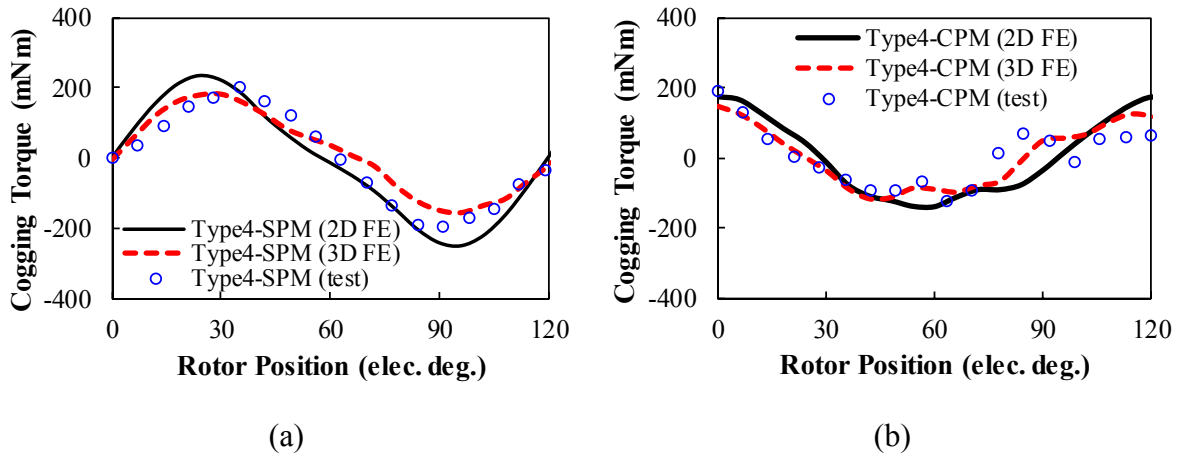


Fig. 4.50 Measured and FE-predicted cogging torques of Type4 machines. (a) SPM-FRPM machine. (b) CPM-FRPM machine.

The variations of static torque of the machines are measured by supplying three-phase windings with fixed DC current ( $I_a = -2I_b = -2I_c = I_{dc} = I_{rated}$ , and the rated current  $I_{rated}$  is corresponded to  $p_{cu} = 20W$ ), as shown in Fig. 4.51 and Fig. 4.52. Similar as back-EMF results, for SPM machines, the measured static torques match well with the FEA results while they are obviously lower for CPM machines especially for the Type4 CPM machine. However, the measured maximum static torques of the CPM machines are still larger than those of the SPM machines, albeit with almost halved PM volume, from which the previous analyses can be verified.

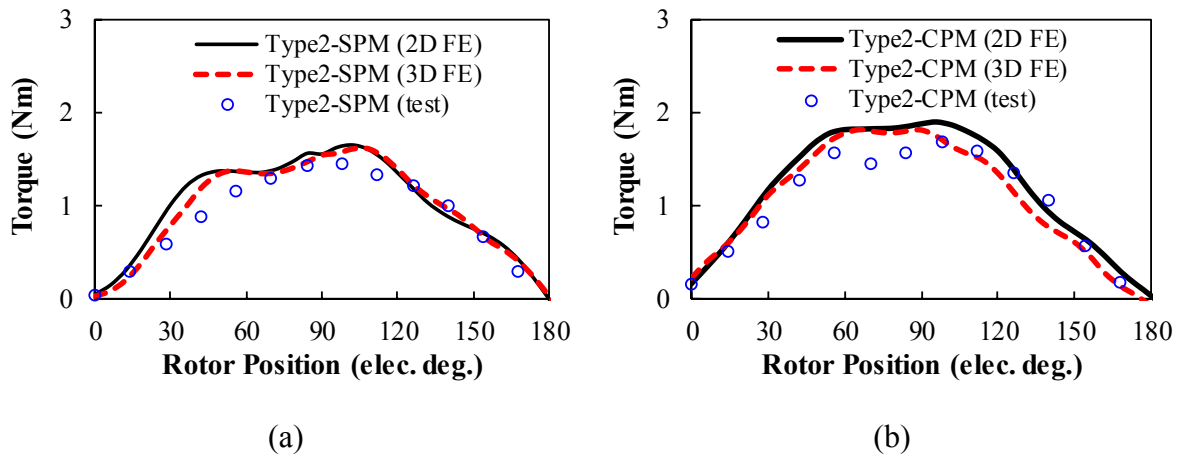


Fig. 4.51 Measured and FE-predicted static torques of Type2 machines. (a) SPM-FRPM machine. (b) CPM-FRPM machine.

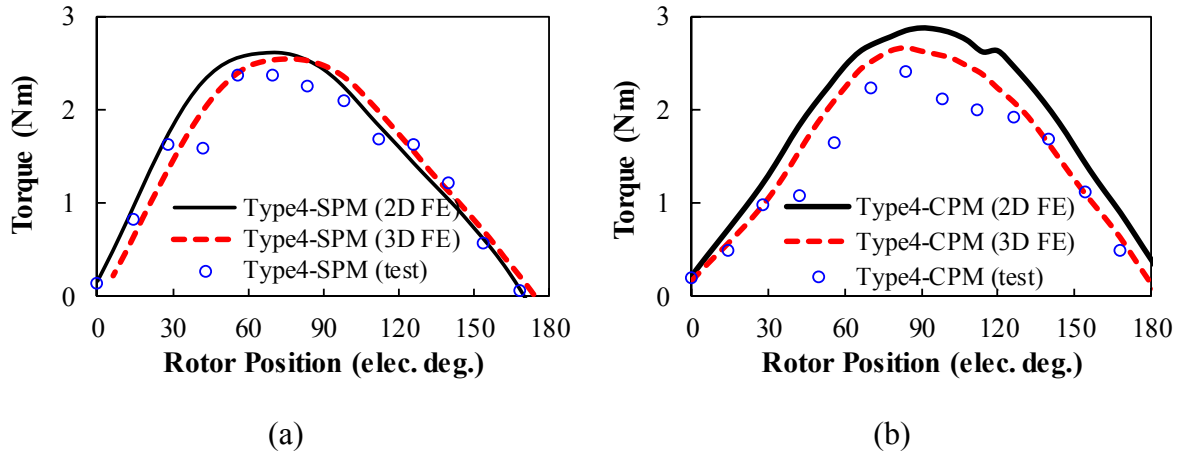


Fig. 4.52 Measured and FE-predicted static torques of Type4 machines. (a) SPM-FRPM machine. (b) CPM-FRPM machine.

The variations of average torque of the four machines against current are also compared in Fig. 2.46. As can be seen, the measured torque variation results match well with the FE-predicted torque variation trends. When the current is relatively low, the measured torques of the CPM machines are higher compared with the SPM machines. As current increases, the average torques of the SPM machines tend to be higher, thanks to the less saturation and smaller inductance, which have been analysed.

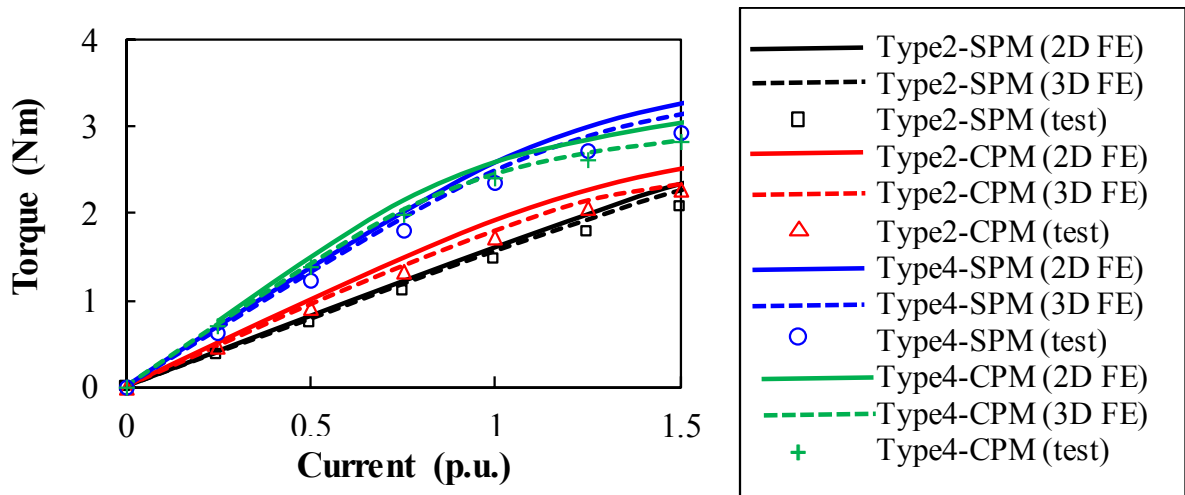


Fig. 4.53 Measured and FE-predicted torque variations against current.

## 4.7 Conclusion

In this chapter, different PM topologies of FRPM machines are analysed and compared. Based on the analysed machines, some findings can be summarised as follows:



1. The torque improvement of the CPM machine over SPM machine is largely influenced by the stator slot/rotor pole combination due to different equivalent pole-pair numbers and saturation conditions.
2. The torque of the CPM-FRPM machine can be improved by properly increasing the PM width ratio while the torque ripple is sensitive to the PM width ratio.
3. The CPM machines with identical PM locations on two adjacent stator teeth are more likely to produce higher torque than those with different PM locations (i.e. Type2 has 18% higher torque than Type1, and Type4 has 34% higher torque than Type3).
4. In comparison with the SPM-FRPM machine, the CPM-FRPM machine offers advantages of high average torque and less PM volume. However, the over-load capability and demagnetisation withstand capability of the CPM-FRPM machine tend to be worse due to the increased inductance.
5. The CPM-FRPM machine has large end-effects, which should be well considered and analysed for practical applications.

# **CHAPTER 5**

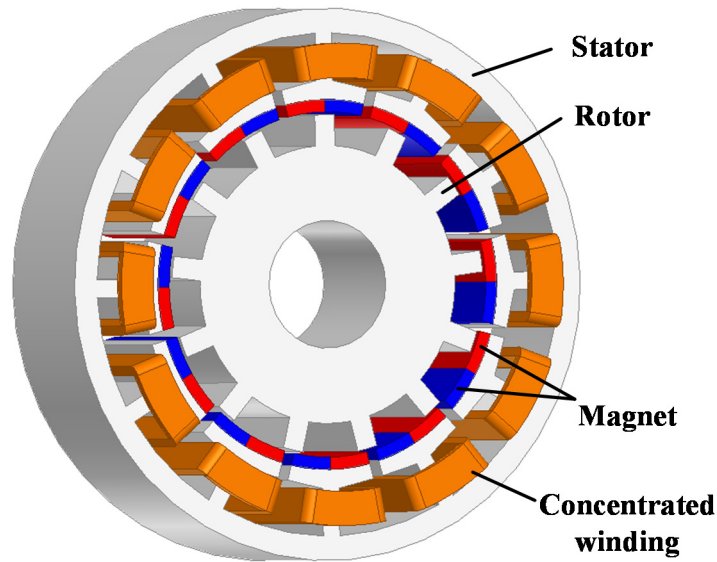
## **COMPARATIVE ANALYSIS OF FLUX REVERSAL PERMANENT MAGNET MACHINES WITH TOROIDAL AND CONCENTRATED WINDINGS**

In this chapter, the FRPM machine with toroidal windings will be presented and analysed with reference to conventional concentrated windings. Firstly, the influence of rotor pole numbers on performance of the FRPM machine with conventional concentrated windings will be investigated. It is found that although the 12/13 stator slot/rotor pole FRPM machine has a high back-EMF, the pitch factor and magnet flux utilization ratio of concentrated windings are very low. By adopting toroidal windings instead of concentrated windings in the 12/13 FRPM machine, the pitch factor and resulted torque performance can be effectively improved. Finite element analysis shows that the 12/13 FRPM machine with toroidal windings can produce 79% higher torque density than its counterpart with concentrated windings. Then, the critical design parameters and electromagnetic performance of FRPM machines with both winding types will be analysed and compared. It is shown that the machine with toroidal windings has higher torque, efficiency, power factor and lower torque ripple, making it particularly suitable for low-speed, high-torque, and axial length limited applications. In addition, other feasible stator slot/rotor pole combinations to use toroidal winding will be identified, with the aid of equivalent pole-pair number in the FRPM machine. Finally, two 12/13 FRPM prototypes with toroidal windings and concentrated windings will be tested to validate the analyses.

### **5.1 Introduction**

Thanks to the development of high-energy-product permanent magnet (PM) material, PM machines have now been widely utilised in various applications [LEV08] [REF10] [EMA08]. For applications where low-speed and high-torque are required, such as marine propulsion, wind power generation, servo drives, etc., direct-drive PM machine systems have been a hot research topic since mechanical transmission devices can be simplified or even eliminated. With both PMs and windings equipped in stator, stator-PM machines are regarded as one of promising direct-drive PM machine concepts due to the improved rotor robustness and heat management capability [CHE11a].

As one category of stator-PM machines, the FRPM machine was firstly proposed in [DEO97] and then have been extensively investigated in last decades. Fig. 5.1 (a) shows a conventional three-phase FRPM machine. As can be seen, a pair of PMs with alternate polarities is mounted on the inner surface of each stator tooth and the rotor is of simple salient-pole structure. Besides, the tooth-coils are wound around stator teeth, resulting in short end-windings. Clearly, when the rotor rotates, for each stator tooth, the areas of the two PM pieces directly facing the rotor teeth vary against the rotor position, resulting in bipolar flux and back-EMF waveforms in the tooth-coil. Detailed flux variations against rotor position of the FRPM machine have been analysed in Chapter 2. Moreover, based on the recently developed air-gap field modulation/magnetic gearing effect theory [CHE17] [MOR10b] [GAO17b] [ZHU19], the working principle of FRPM machines can now be further recognized, which has been presented in Chapter 3. That is, although the fundamental pole-pair numbers of PM MMF/field and armature MMF/field are different, additional PM field and armature field pairs with the same pole-pair number and rotational speed can be produced after the rotor-tooth modulation, thus contributing to the torque production.



(a)

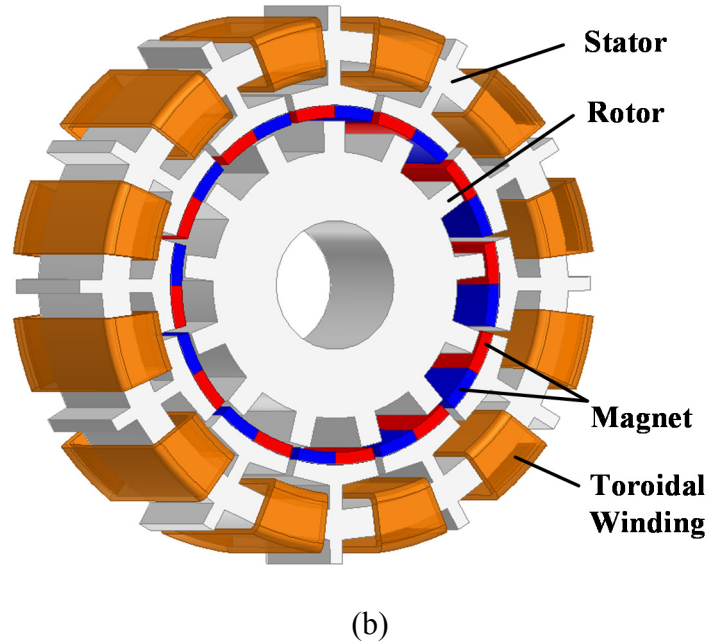


Fig. 5.1 Configuration of FRPM machines. (a) Conventional CW-FRPM machine. (b) Proposed TW-FRPM machine.

Although a FRPM machine inherently shares the similarities of working principle with a SFPM machine [WU15c], a Vernier machine [QU11] and other flux-modulated/ magnetically geared machines [LI15a] [FU16], its torque density is relatively low. For example, in [CHE11a], three kinds of stator-PM machines are qualitatively compared. It was stated that the FRPM machine is more likely to have inferior torque density compared to the SFPM machine, which is attributed to the larger equivalent air-gap length in FRPM machine.

It should be noted that to avoid the bulky system, a high torque density is always the most critical requirement for a direct-drive PM machine to be used in low-speed and high-torque applications. Therefore, the torque density improvement of FRPM machine is of great significance to promote its application prospect. Some useful torque improvement techniques can be summarised as follows:

- Stator slot ( $N_s$ ) /rotor pole ( $N_r$ ) combinations: the suitable  $N_s/N_r$  combinations to maximise the machine torque have been revealed from both analytical analysis and FEA. For example, in [GAO16a], it shows that when  $N_s=12$ , the preferred region of  $N_r$  is from 10 to 17, while the 12/14 combination tends to have the maximum torque density. The similar findings have also been reported in Chapter 2.
- PM arrangements: various aspects including the relative PM polarities of adjacent stator

teeth (see Chapter 2), the optimal number of PM pieces on single stator tooth (see Chapter 3), the alternate PM structures, such as consequent-pole PM (see Chapter 4), inset-PM [BOL02] [KIM09], and the unequal PM pieces [GAO18a] have been investigated.

- Topology variation: a novel dual-stator FRPM machine is proposed in [ZHU15] and a novel FRPM machine with a whole PM ring attached in the stator bore is analysed in [LI18]. Both topologies can enhance the torque density in certain circumstances.
- Winding configurations: in addition to the tooth-coil shown in Fig. 5.1 (a), i.e. concentrated winding (CW), the distributed winding (DW) can be also adopted for specific  $N_s/N_r$  combinations [ZHU19] [MOR10a] [GAO17a]. For example, in [GAO17a], a 12/17 FRPM machine with DW is shown to exhibit higher torque than a 12/14 FRPM machine with CW when the end-winding length is neglected.

As a continuation and further study of various winding configurations, this chapter deals with the feasibility of using toroidal winding (TW) in a FRPM machine, which has not been reported in any literature although TW has been widely used in other types of electrical machines [LI15b] [JEN12] [VIR13] [LEE06] [BOR14] [MUL99]. Fig. 5.1 (b) shows the FRPM machine equipped with TW (denoted as TW-FRPM machine). As can be seen, the coils are wound around the stator yoke instead of the stator tooth, which differs with the FRPM machine with CW shown in Fig. 5.1 (a) (denoted as CW-FRPM machine).

In general, the purpose of using TW (or called drum winding) in a machine can be illustrated from the following two perspectives:

- TW is particularly suitable for machines where the axial length is limited, the winding pole-pair number  $p_a$  is low, and the stator slot number  $N_s$  is relatively large. In such cases, CW results in a very low winding factor while DW has an excessive long end-winding, both of which are undesirable. For example, TW intrinsically suits the open-slot type Vernier machine [LI15b], since  $p_a$  of a Vernier machine is always low, and  $N_s$  is always large to achieve a high gear ratio. Another good example is that a 4-pole folded-strip toroidally wound induction machine is comprehensively analysed in [JEN12] regarding its performance and manufacture, aiming at a specific rim-driven application where the axial-length is strictly limited.
- TW provides high flexibility in changing coil connections for specific applications. For example, in [VIR13], TW is utilized to change  $p_a$  for a multi-speed induction machine and in

[LEE06], TW is adopted in a switched reluctance machine to use commercialized 6-switch converter.

In this chapter, the rationality and significance of TW-FRPM machine will be explained from the first perspective. The major findings/contributions of this chapter are: (1) revealing that the CW-FRPM machines with preferred  $N_s/N_r$  combinations are equivalent to conventional PM machines with a low winding pole-pair number, and thus TW can be a very effective approach to improve the machine torque; (2) presenting a comprehensive comparative analysis between the TW-FRPM machine and the conventional CW-FRPM machine, including electromagnetic performance and key design parameters; (3) a TW-FRPM prototype is manufactured and tested for the first time.

## 5.2 Working Principle and Pitch Factor Improvement of FRPM Machine

### 5.2.1 Working Principle and Influence of Rotor Pole Number of CW-FRPM Machine

In Chapter 3, it has been proven that the fundamental no-load back-EMF of a CW-FRPM machine is contributed by the fundamental air-gap permeance harmonic  $\Lambda_1$  (resulted from the reluctance rotor) and all PM MMF harmonics  $F_i$  ( $i$  is the harmonic order). For different  $F_i$ , their contributions to the back-EMF are different, which can be characterised by the weight factor  $w_i^f$ , as

$$E_{A1-CW} = \sum_{i=1,2,3\dots}^{\infty} E_i = n_c l R_{si} \Omega_r \Lambda_1 \sum_{i=1,2,3\dots}^{\infty} w_i^f F_i \quad (5.1)$$

$$w_i^f = \frac{N_r}{(iN_s + N_r)} \sin \left[ \left( \frac{iN_s + N_r}{N_s} \right) k\pi \right] - \frac{N_r}{(iN_s - N_r)} \sin \left[ \left( \frac{iN_s - N_r}{N_s} \right) k\pi \right] \quad (5.2)$$

where  $E_{A1-CW}$  is the fundamental back-EMF in a single coil A1 of CW-FRPM machine,  $n_c$  is the number of turns per coil,  $l$  is the stack length,  $R_{si}$  is the stator inner radius,  $\Omega_r$  is the angular speed of rotor,  $N_s$  is the stator slot number, and  $N_r$  is the rotor pole number.

Clearly, the stator slot and rotor pole combinations have a significant influence on the machine back-EMF, since  $N_s$  and  $N_r$  directly determine the weight factor  $w_i^f$ . Based on the machine parameters listed in Table 5.1, when  $N_s=12$ , the influence of  $N_r$  on back-EMF of the three-phase CW-FRPM machine is shown in Fig. 5.2. As can be seen, when  $N_r$  ranges from 10 to 14 (labelled as Region A), the CW-FRPM machine has much higher back-EMF than the other  $N_r$ .

Such conclusions are consistent with the existing literatures [GAO17b], i.e. the 12/10, 12/11, 12/13, and 12/14 are typically preferred  $N_s/N_r$  combinations (aiming at  $N_s=12$ ). This can be explained by the fact that similar numbers of  $N_s$  and  $N_r$  are helpful to utilize the flux of all the PM pieces simultaneously.

Table 5.1 Parameters of the 12/13 FRPM machines

Parameters	Analytical and FE models			Prototypes	
	CW-FRPM	TW-FRPM	DW-FRPM	CW-FRPM	TW-FRPM
Overall diameter $D$			90		
Active stack length $l$			25		
Air-gap length $g$			0.5		
Property of PM material $B_r/\mu_r$			1.2T/1.02		
Slot filling factor $f_s$			0.4		
Rated speed $n$ (rpm)			400		
Thickness of stator yoke $t_{sy}$	4	4.9	6	3.2	4.9
Width of stator tooth $w_{st}$	2.9	2.2	4.5	3.2	2.2
Inner radius of stator $R_{si}$	30.2	29	29.2	29.3	
Height of stator tooth tip $h_{so}$	2.5	2.7	1.7	3	2.7
Width of stator slot opening $w_{so}$	1.7	1.5	1.5	2.5	1.2
PM height $h_m$	1.6	1.6	2	2	
Width ratio of rotor slot $w_{ro}/\tau_r$	0.74	0.71	0.74	0.7	0.7
Height of protruded stator tooth $h_{sp}$	--	3.9	--	--	3.6
Slot area for a coil side $S$ (mm <sup>2</sup> )	64.1	61.4	52.0	73.1	61.4
End-winding length $l_{end}$	17.5	14.8	14.5	17.9	13.8
Number of turns per coil $n_c$	65	62	53	74	62
Rated current $I_r$ (A)	3.4	3.5	4.2	3.2	3.5
Average torque $T_{avg}$ (Nm)	1.45	2.60	4.11	1.28	2.47
Torque density $T_{avg}/V_{eff}$ (kNm/m <sup>3</sup> )	9.1	16.3	25.8	8.0	15.5

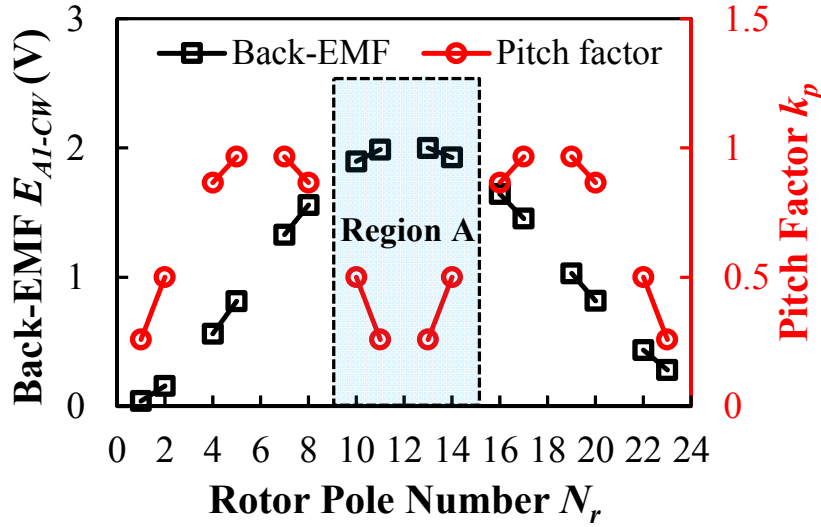


Fig. 5.2 Influence of  $N_r$  on back-EMF and pitch factor of the three-phase CW-FRPM machine.

Considering the pitch factor ( $k_p$ ) of the CW-FRPM machine, the star of slots of the conventional PM machine can be used since the PM arrangement of all the stator teeth are same (see Fig. 5.1 (a)). Thus,  $k_p$  can be obtained as

$$k_p = \left| \cos\left(\frac{\pi N_r}{N_s} - \frac{\pi}{2}\right) \right| \quad (5.3)$$

As shown in Fig. 5.2, for Region A with high  $E_{AI-CW}$ ,  $k_p$  is quite low. For example, when  $N_r=13$ ,  $k_p$  is only 0.26 and  $k_p=0.5$  when  $N_r=14$ , which can be clearly understood through the star of slots shown in Fig. 5.3. When CW is adopted, the electric angle between the two sides of a coil (e.g. phasor 1 and phasor 2) is lower than 90 deg., indicating insufficient utilization of the PM flux per pole.

To sum up, although the back-EMF of CW-FRPM machine can be maximized by properly selecting  $N_s/N_r$  combination, its flux per pole cannot be fully utilized. Thus, TW-FRPM machine can effectively improve the flux utilization ratio and the corresponding machine performance.



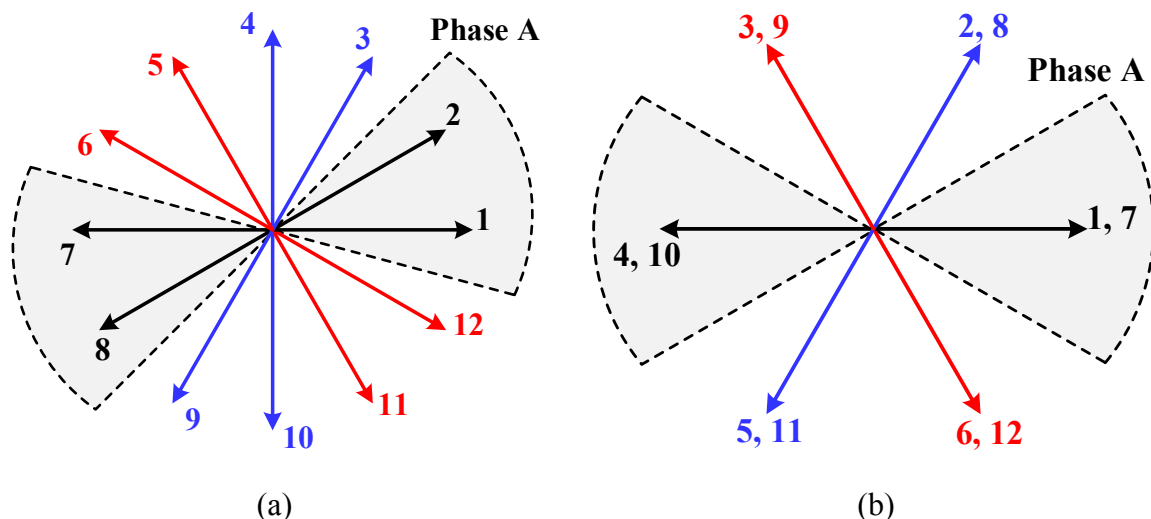


Fig. 5.3 Star of slots of CW-FRPM machines. (a) 12/13. (b) 12/14.

### 5.2.2 Pitch Factor Improvement by Using Toroidal Winding

For the CW-FRPM machine, although the fundamental back-EMF achieves a relatively high level in the preferred  $N_s/N_r$  Region A, the machine potential is not fully developed (especially for 12/11 and 12/13). In other words, the machine performance may be largely improved if the flux utilization ratio is improved. For this reason, replacing CW with TW turns to be an effective technique to boost the machine performance.

Taking 12/13 FRPM machine as an example, the different flux linkages between CW and TW can be clearly observed in Fig. 5.4. At this specific rotor position where both CW and TW link the flux to the largest extent, the PM pieces contributing to the flux (i.e. those directly facing the rotor teeth) are highlighted. As can be seen, although  $N_r=13$ , the flux path pattern in stator and rotor cores is equivalent to a conventional PM machine with a fundamental pole-pair number  $p_a$  being 1. Therefore, for CW, it only links a small portion of the flux per pole while for TW, it can link most of the flux, resulting in a much higher pitch factor.

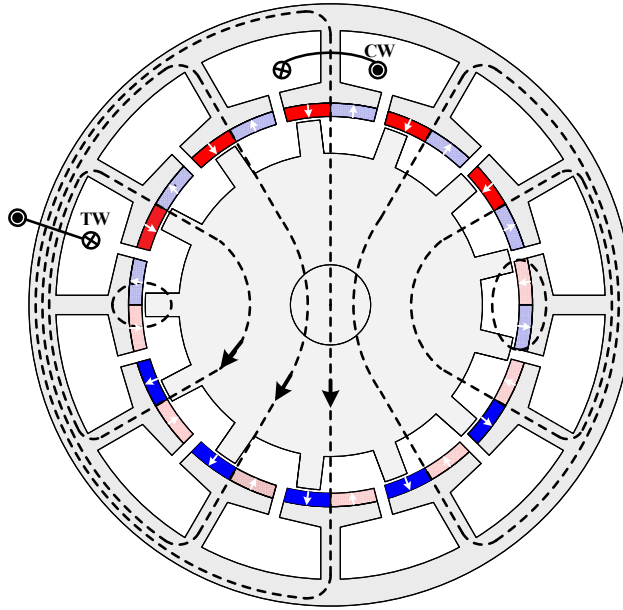


Fig. 5.4 Flux path through CW and TW in a 12/13 FRPM machine.

### 5.3 Optimisation and Critical Design Parameters

Based on the above analyses, although the TW-FRPM machine may have better performance than the CW-FRPM machine, the optimization of both machines should be carefully considered to make a fair evaluation. For example, the space occupied by the external coil side of TW must be considered (see Fig. 5.4).

#### 5.3.1 Optimisation of FRPM Machines

For low-speed and high-torque applications, the copper loss is always the dominant component of the total losses [LI15b]. Hence, in this paper, the effective copper loss of the machine is kept constant while other dimensional parameters are optimized. The design parameters of CW-FRPM and TW-FRPM machines are shown in Fig. 5.5 and Fig. 5.6, respectively. The genetic-algorithm-based global optimization in ANSYS commercial finite-element (FE) software is adopted, which enables the simultaneous optimization of multi-parameters [ZHU11b]. The fixed and optimized parameters in the optimization process are shown in Table 5.2. Some instructions are as follows:

- The only optimization goal is to achieve the maximum output torque under fixed overall diameter  $D$  (90mm), active stack length  $l$  (25mm) and air-gap length  $g$  (0.5mm);
- The optimization is conducted under the fixed effective copper loss (on side-a and side-c

shown in Fig. 5.5 and Fig. 5.6)  $p_{cu\_eff}=20W$ . Based on the obtained optimal motor dimensions, the length and copper loss of the end-winding (side-b and side-d) will then be calculated for the ease of investigating the influence of stack length on machine performance;

- For TW-FRPM machine, the space occupied by the outer coil side (side-c) is considered via the height of protruded stator tooth  $h_{sp}$ . Besides, to make the slot areas ( $S$ ) for two coil sides (i.e. side-a and side-c) identical,  $h_{sp}$  and the height of stator tooth ( $h_{st}$ ) satisfy  $\pi(D^2/4-R_{so}^2)-N_s w_{st} h_{sp} = \pi(R_{co}^2-R_{ci}^2)-N_s w_{st} h_{st}$ ;

- The number of turns per coil  $n_c$  and rated current  $I_r$  are determined by assuming a fixed slot filling factor  $f_s$  (set as 0.4) and copper wire diameter  $d$  (0.71mm in this case), as

$$n_c = \frac{4Sf_s}{\pi d^2} \quad (5.4)$$

$$I_r = \sqrt{\frac{p_{cu\_eff} \pi d^2}{N_s n_c \rho 8l}} \quad (5.5)$$

where  $\rho$  is the resistivity of the copper wire.

After the global optimization, the parameters of the optimum CW-FRPM and TW-FRPM FE models are listed in Table 5.1. Then, the end-winding length ( $l_{end}$ ) of both machines are calculated to obtain the additional copper loss, as

$$l_{end} = \pi \tau_c \quad (5.6)$$

where  $\tau_c$  is the average coil pitch of the machine, for the TW-FRPM machine,  $\tau_c=(t_{sy}+h_{sp}+t_{sy}+h_{st})/2$ , and for the CW-FRPM machine,  $\tau_c=[\pi(R_{co}+R_{ci})/N_s+w_{st}]/2$ , see Fig. 5.5 and Fig. 5.6.  $l_{end}$  of the machines are also listed in Table 5.1.

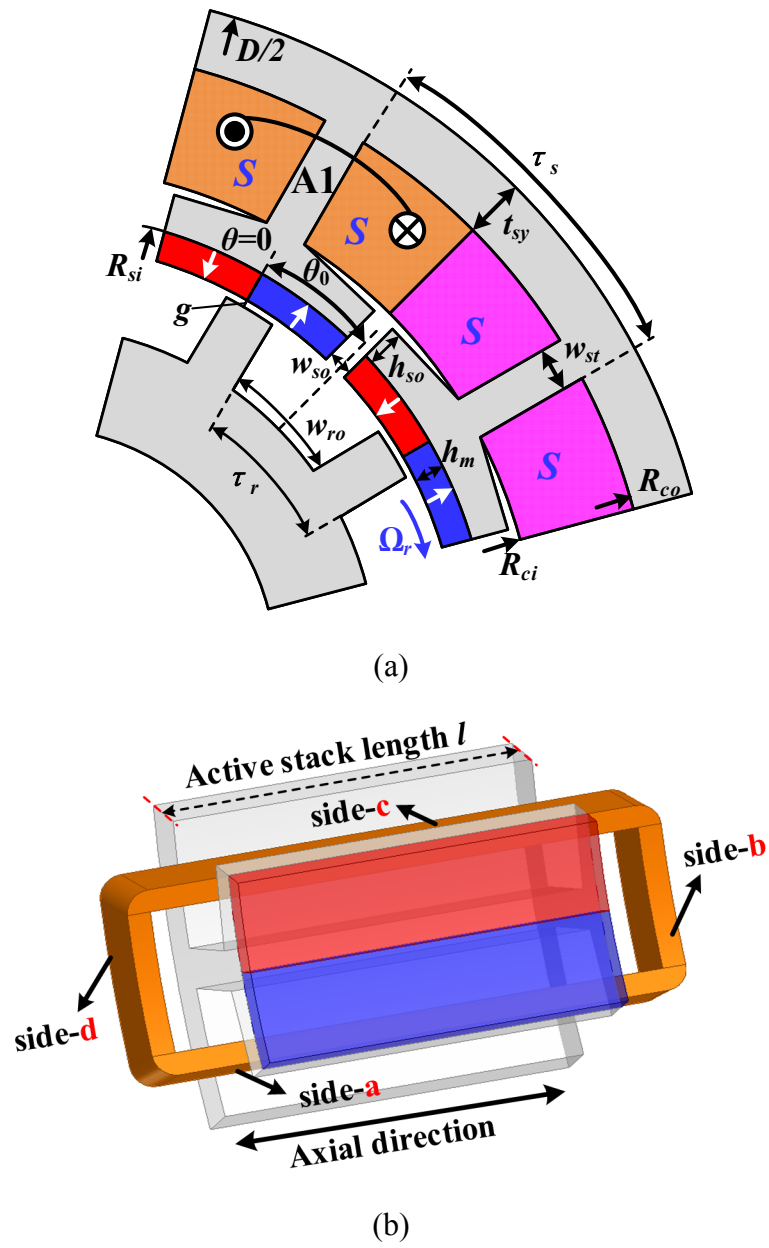


Fig. 5.5 Major design parameters and coil schematic of CW-FRPM machines. (a) Parameters. (b) Coil sides.

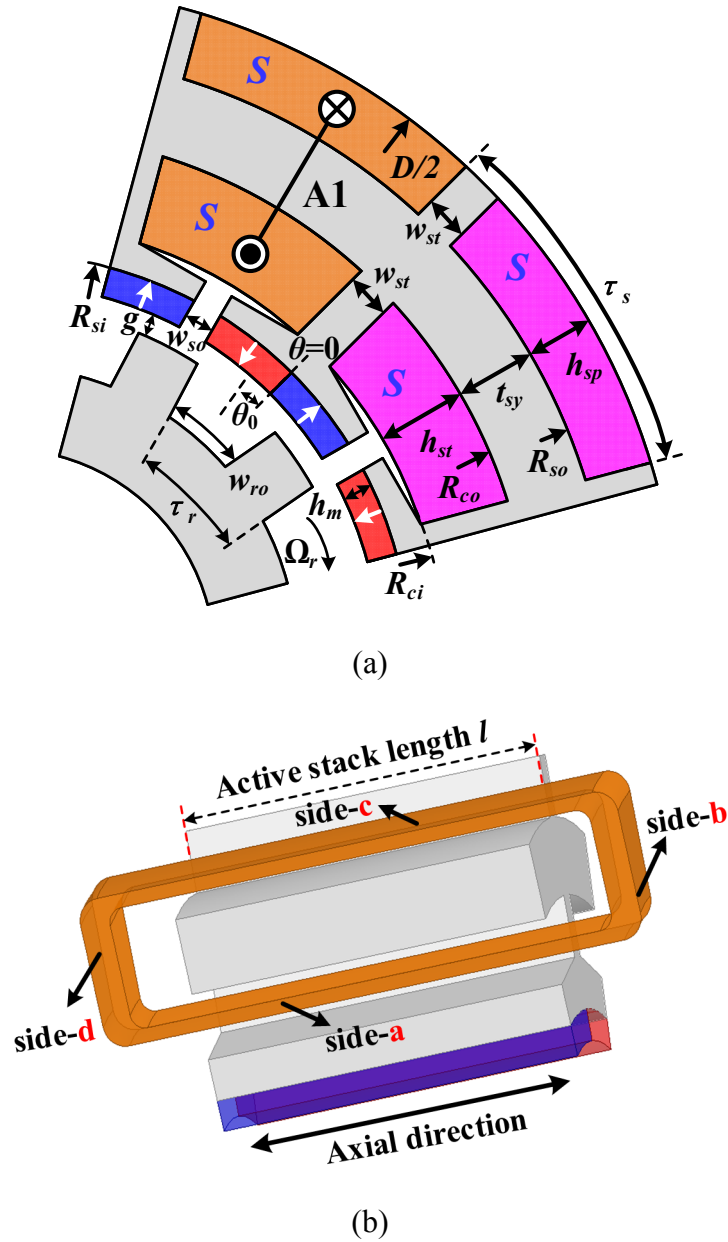


Fig. 5.6 Major design parameters and coil schematic of TW-FRPM machines. (a) Parameters. (b) Coil sides.

Table 5.2 Fixed and Optimized Dimensional Parameters

	Fixed parameters	Optimized parameters
CW-FRPM	$D, l, g$	$t_{sy}, w_{st}, R_{si}, h_{so}, w_{so}, h_m, w_{ro}/\tau_r$
TW-FRPM		$h_{sp}, w_{st}, t_{sy}, R_{si}, h_{so}, w_{so}, h_m, w_{ro}/\tau_r$

### 5.3.2 Influence of Critical Design Parameters

For FRPM machines, several critical parameters, such as PM thickness ( $h_m$ ), width of stator slot opening ( $w_{so}$ ), thickness of stator yoke ( $t_{sy}$ ), and width of stator tooth ( $w_{st}$ ) etc., have significant influence on rotor-tooth modulation and resulted machine performance [GAO16a]. Thus, these parameters will be parametrically investigated based on the optimum machine designs in Table 5.1.

Since  $h_m$  and  $w_{so}$  directly determine the PM dimensions, their influence on the machine average torque  $T_{avg}$  is firstly shown in Fig. 5.7. As can be seen, for each FRPM machine, there exists an optimal  $h_m$ , and it is only 1.6mm for the studied machines. This can be explained by that  $h_m$  influences the equivalent air-gap length and the corresponding the modulation effect of the reluctance rotor. When the PMs are too thick, the magnitude of the fundamental permeance decreases although that of the PM MMF increases. In contrast, the influence of  $w_{so}$  on  $T_{avg}$  of the machines is relatively less significant. Moreover, with the optimal  $h_m$  and  $w_{so}$ , the average torque of the TW-FRPM machine is 2.60Nm, which is 79% higher than that of the CW-FRPM machine (1.45Nm).

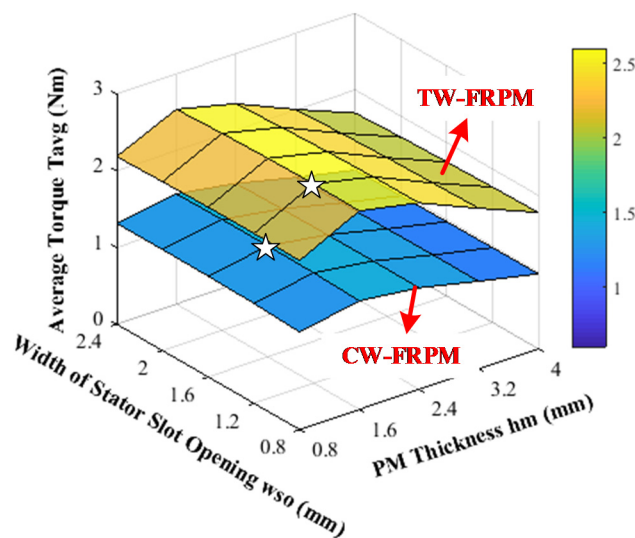


Fig. 5.7 Torque variation against  $h_m$  and  $w_{so}$ .

Fig. 5.8 shows the torque variation against the thickness of stator yoke ( $t_{sy}$ ) and the width of stator tooth ( $w_{st}$ ). As can be seen, the optimal  $t_{sy}$  is around 5mm for both machines while the optimal  $w_{st}$  is smaller (2.2mm for the CW-FRPM machine and 2.9mm for the TW-FRPM machine). This phenomenon can be explained by the machine flux distribution (see Fig. 5.4). The flux through the stator yoke is higher than that through the stator tooth, thus resulting in a thick stator yoke.

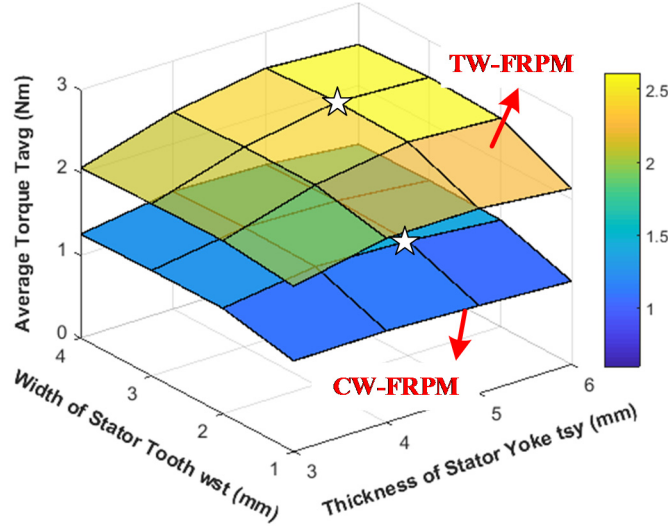


Fig. 5.8 Torque variation against  $t_{sy}$  and  $w_{st}$ .

#### 5.4 Performance Comparison of FRPM Machines

In the previous analysis, it is revealed that the torque of a 12/13 FRPM machine can be largely improved by replacing CW with TW, thanks to the improved pitch factor. Therefore, it is expected that a higher machine torque can be also achieved by using distributed-winding (DW) in the machine (denoted as DW-FRPM machine) since DW always has a high pitch factor [MOR10a]. However, it should be noted that the long end-winding will compromise the torque benefit of the DW-FRPM machine, which should be carefully evaluated.

Following the machine optimization process introduced before, a 12/13 DW-FRPM machine is optimized under the same  $D$ ,  $l$ ,  $g$ , and effective copper loss  $p_{cu\_eff}$  as the TW- and CW-FRPM machines. The optimum parameters are listed in Table 5.1, and the end-winding length  $l_{end}$  is also calculated based on (5.6). From Table 5.1, it shows that the DW-FRPM machine has the maximum average torque  $T_{avg}$  while its end-winding is excessively long since its coil pitch is 6 (see Fig. 5.3 (a)). By keeping the rated current  $I_r$  of the machines as constant and accounting for the additional copper loss of end-winding, the influence of active stack length  $l$  on machine performance is depicted in Fig. 5.9. The torque per total copper loss ( $T_{avg}/p_{cu\_total}$ ) is set as an indicator to evaluate the machines. As can be seen, within the whole range of  $l$ , the TW-FRPM machine always has the highest  $T_{avg}/p_{cu\_total}$  because of the largely improved torque and the shortest end-winding. In terms of the DW-FRPM machine, its  $T_{avg}/p_{cu\_total}$  is even lower than that of the CW-FRPM machine when  $l$  is small, due to the longest end-winding. For the studied FRPM machines of  $D=90\text{mm}$  and  $l=25\text{mm}$ , the torque per copper loss of the proposed TW-FRPM machine is  $0.082\text{Nm/W}$ , which is 91% higher than that of the CW-FRPM machine

(0.043Nm/W), and 173% higher than that of the DW-FRPM machine (0.030Nm/W).

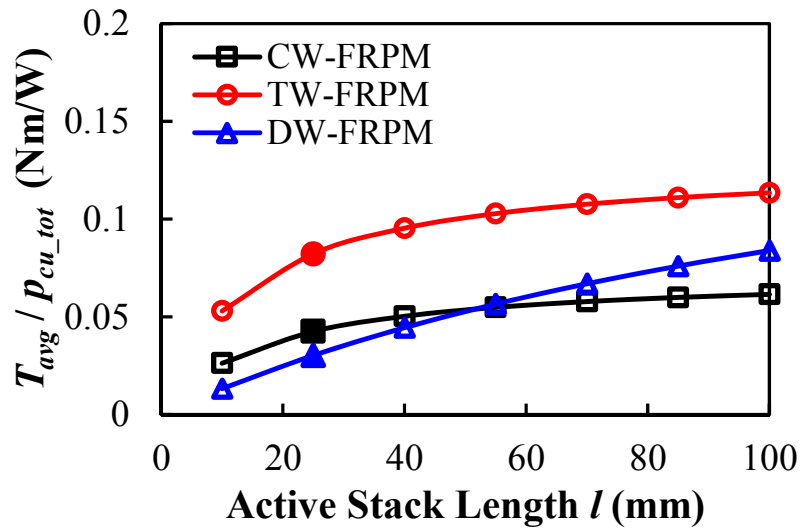


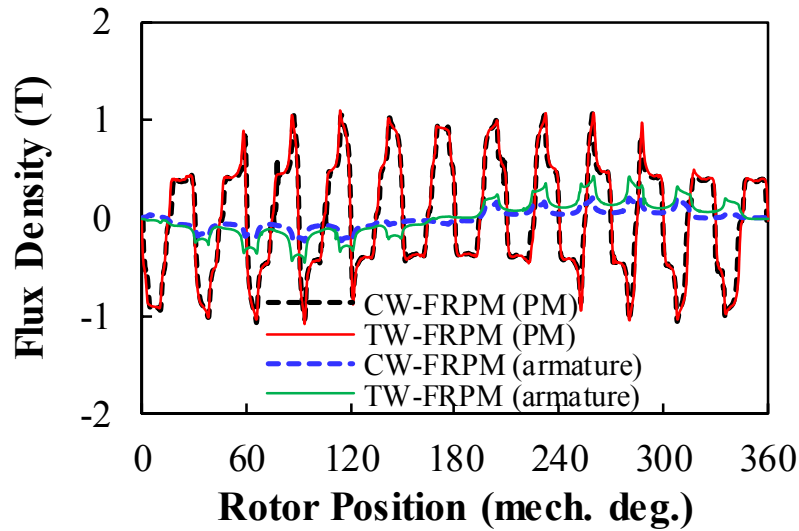
Fig. 5.9 Influence of active stack length on average torque per total copper loss of the three machines.

Therefore, the focus of this chapter is still on the performance comparison between the TW-FRPM and CW-FRPM machines since both machines have a short end-winding and relatively better torque performance for applications where  $l$  is limited. Based on Table 5.1, in addition to the average torque, detailed performance of the 12/13 TW-FRPM machine will be analysed and compared with the 12/13 CW-FRPM machine, aiming to provide a comprehensive evaluation of the machines.

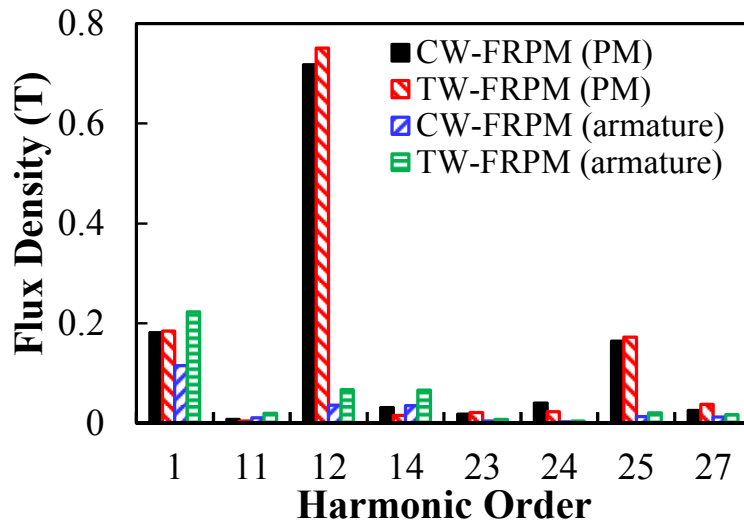
#### 5.4.1 Air-Gap Field and Winding Pole-Pair Number

The no-load PM fields of the two machines are shown in Fig. 5.10. As can be seen, for each machine, the major PM field harmonic is the 12<sup>th</sup>, which equals  $N_s$  and additional harmonics emerge (e.g. the 1<sup>st</sup> and the 25<sup>th</sup>) due to the rotor-tooth modulation. Besides, the PM fields of the two machines are similar, for both waveform and harmonic spectrum.





(a)



(b)

Fig. 5.10 Air-gap fields produced by both PM MMF and armature MMF. (a) Waveforms. (b) Harmonic spectra (with magnitude > 0.02 T).

Fig. 5.11 shows the no-load flux distributions of the two machines when the flux linkage of the coil A1 is maximum. As can be seen, the flux distribution patterns inside the stator and rotor cores of the two machines are very similar, which can be characterized by the equivalent pole-pair number ( $p_{eq}$ ). More specifically, although the flux density distribution in the air-gap is mainly determined by the waveform of the PM MMF with fundamental order being  $N_s$ , the flux distributions inside the stator and rotor are determined by the flux after rotor-teeth modulation. As introduced in Chapter 2, based on the “magnetic gearing effect” introduced in [MOR10b],

and considering that the  $N_s^{\text{th}}$  PM MMF and the  $N_r^{\text{th}}$  permeance have the highest magnitude, the equivalent pole-pair number  $p_{eq}$  is defined as

$$p_{eq} = |N_s - N_r| \quad (5.7)$$

For the 12/13 FRPM machines,  $p_{eq}=1$  and the equivalent flux patterns are also shown in Fig. 5.11. Therefore, the flux and resulted back-EMF of the coil A1 of the TW-FRPM machine are much larger than those of the CW-FRPM machine due to the different coil locations of the two machines.

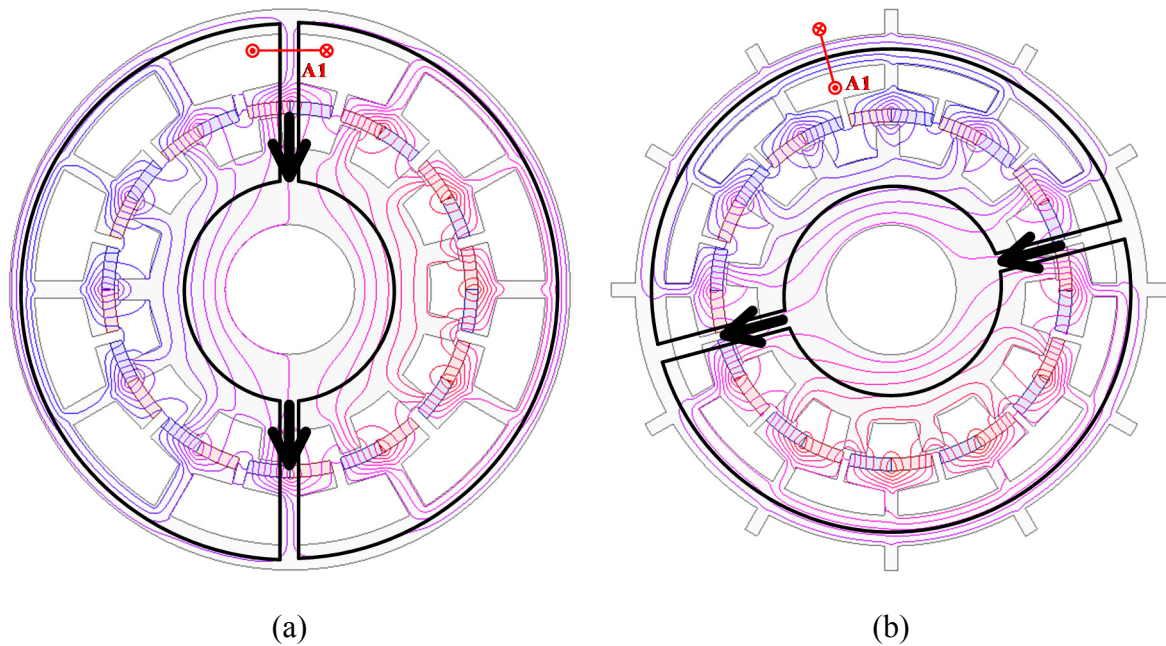


Fig. 5.11 No-load flux distribution and equivalent flux pattern. (a) 12/13 CW-FRPM machine. (b) 12/13 TW-FRPM machine

Considering the field produced by the armature winding, it is also shown in Fig. 5.10. As can be seen, the fundamental winding pole-pair number  $p_a$  is equal to  $p_{eq}$ , and additional field harmonics are produced due to the rotor-tooth modulation. Therefore, there are several harmonic pairs of the armature field and the PM field with considerable magnitude ( $>0.02\text{T}$ ), which are all contributing to the torque production. Such a feature of multi-working harmonics of a FRPM machine has been revealed in Chapter 2. More importantly, it can be observed that the TW-FRPM machine has a higher magnitude of armature field than the CW-FRPM machine, which will result in a higher average torque.

### 5.4.2 No-Load Performance

Fig. 5.12 compares the phase back-EMFs of the two machines ( $n=400\text{rpm}$ ). As can be seen, the magnitude of the fundamental back-EMF of the TW-FRPM machine is 16.0V, which is 81% higher than that of the CW-FRPM machine (8.8V). Besides, both machines have a low harmonic distortion (THD) in back-EMF.

As revealed in Chapter 3, the cogging torque of a FRPM machine is largely related to  $N_s/N_r$  combination, for machines with a large lowest common multiple (LCM), its cogging torque is always small, which is beneficial to achieve a smooth output torque. Fig. 5.13 shows the cogging torque of the two machines. As can be seen, the cogging torques of the machines are small especially for the 12/13 TW-FRPM machine.

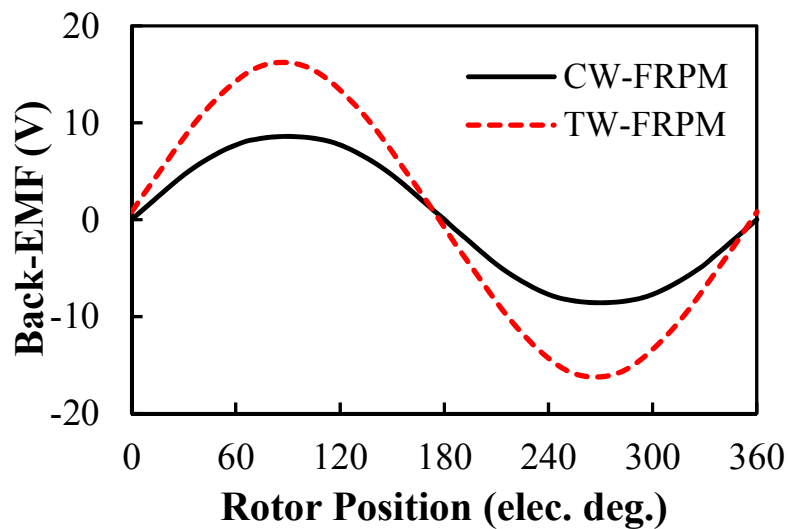


Fig. 5.12 No-load back-EMF of CW- and TW-FRPM machines.

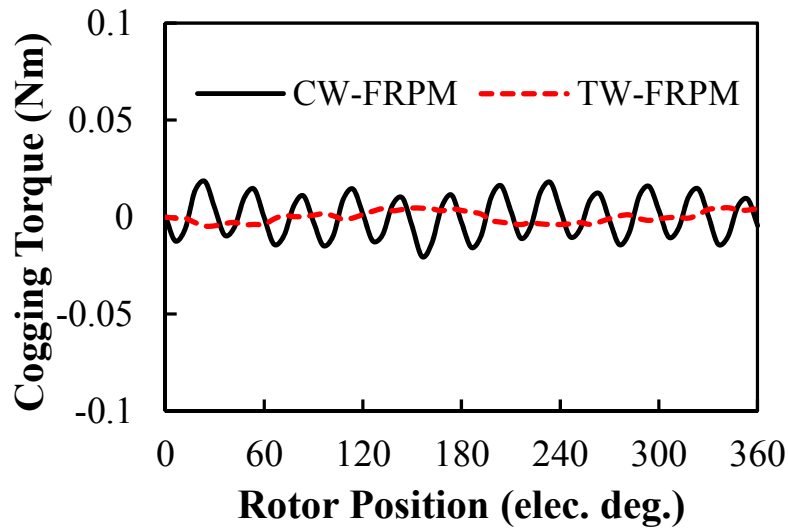


Fig. 5.13 Cogging torque of CW- and TW-FRPM machines.

### 5.4.3 On-Load Torque Performance

Fig. 5.14 shows the torque-current angle characteristic of the FRPM machines. It should be noted that the current angle indicates the relative angle between the current phasor and the  $d$ -axis. When it is 90 elec. deg.,  $q$ -axis current ( $I_q$ ) is injected only, i.e.  $I_d=0$ . As can be seen, all the machines achieve maximum torque when the current angle is approximately 100 elec. deg., indicating small reluctance torque. Therefore, for simplicity,  $I_d=0$  is adopted in all the optimizations and analyses in this paper.

Fig. 5.15 shows the rated torque waveforms of the machines. As can be seen, the average torque  $T_{avg}$  of the proposed TW-FRPM machine is 2.60Nm, which is 79% higher than that of the CW-FRPM machine. Besides, both the machines have a low torque ripple, especially for the TW-FRPM machine (only 1.9%), thanks to the small THD of the back-EMF and low cogging torque.

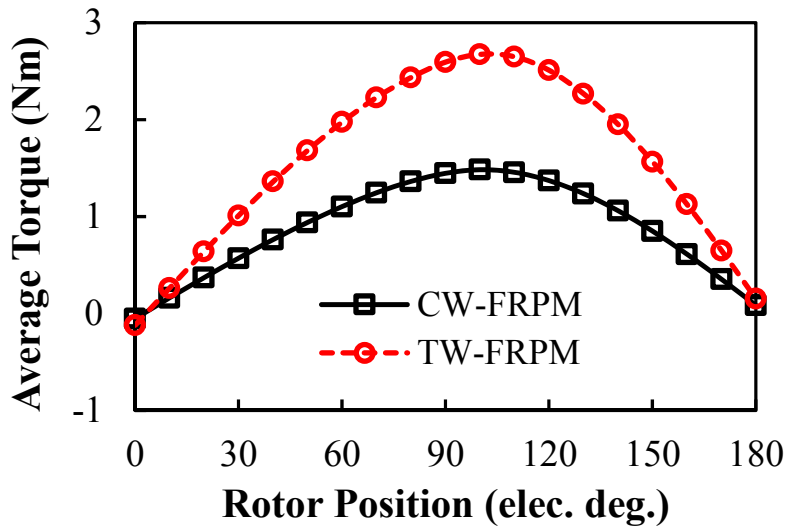


Fig. 5.14 Torque-current angle characteristic of CW- and TW-FRPM machines.

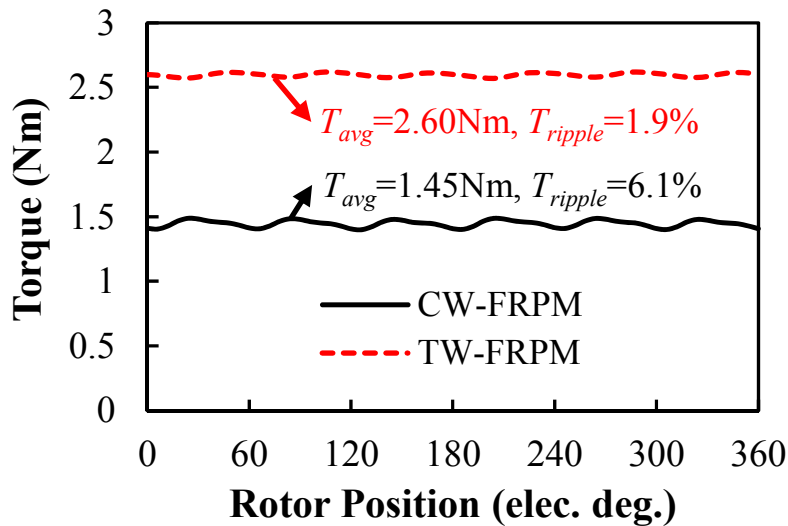


Fig. 5.15 Rated torque waveforms of CW- and TW-FRPM machines.

The flux density distributions of the machines under rated condition (i.e.  $I=1$ p.u.) are shown in Fig. 5.16. As can be seen, for the CW-FRPM machine, the maximum flux density in stator yoke is around 1.5T and a small area of stator tooth tip suffers magnetic saturation with maximum flux density over 2T. For the TW-FRPM machine, the high flux density region is more evenly distributed in stator yoke with flux density around 1.4T. Similarly, a small area of stator tooth tip suffers magnetic saturation. Overall, the correctness of the optimization of the machines can be verified.

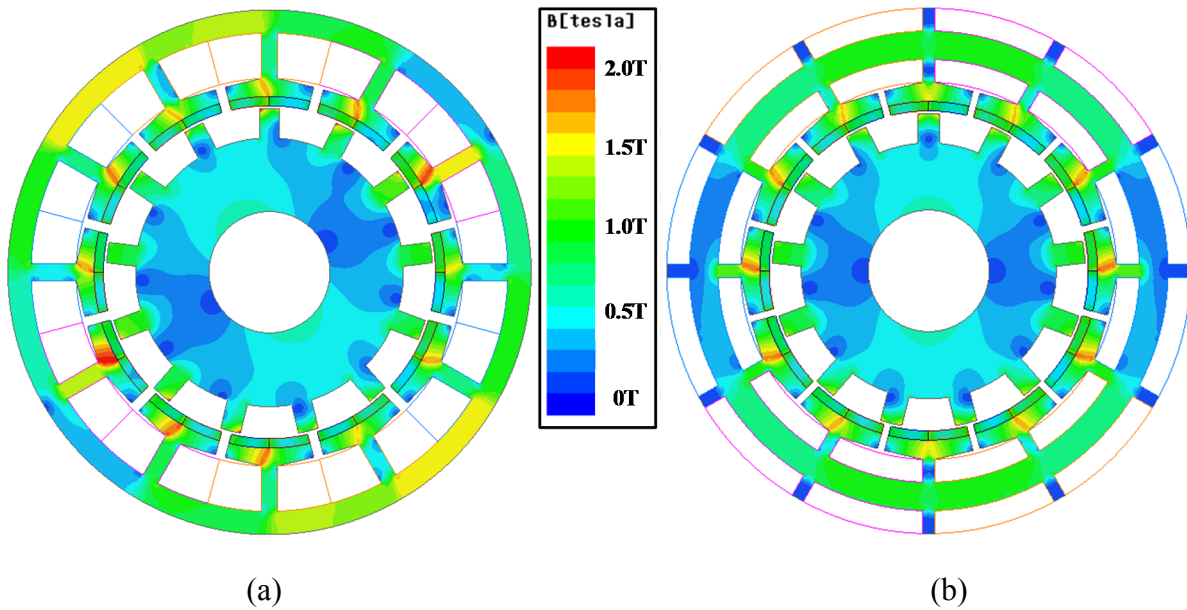


Fig. 5.16 Full-load flux density distribution ( $I=1\text{p.u.}$ ). (a) CW-FRPM machine. (b) TW-FRPM machine.

#### 5.4.4 Inductance

Besides the torque performance, the winding configuration directly determines the machine inductance, which will affect the corresponding performance, such as torque-current characteristic, losses, and power factor etc. Fig. 5.17 compares the phase inductance of the two FRPM machines. As can be seen, all the inductances decrease with current due to the saturation. The self-inductance of the TW-FRPM machine is about 1.7 times of the CW-FRPM machine because of the smaller magnetic reluctance of the flux path for the armature field. In addition, for the CW-FRPM machine, the mutual inductance between two phases is negligible, which is common for a short-pitch CW machine [REF06]. For the TW-FRPM machine, the mutual inductance is negative and around 1/3 of its self-inductance, which is similar to an integer-slot DW machine [REF06].

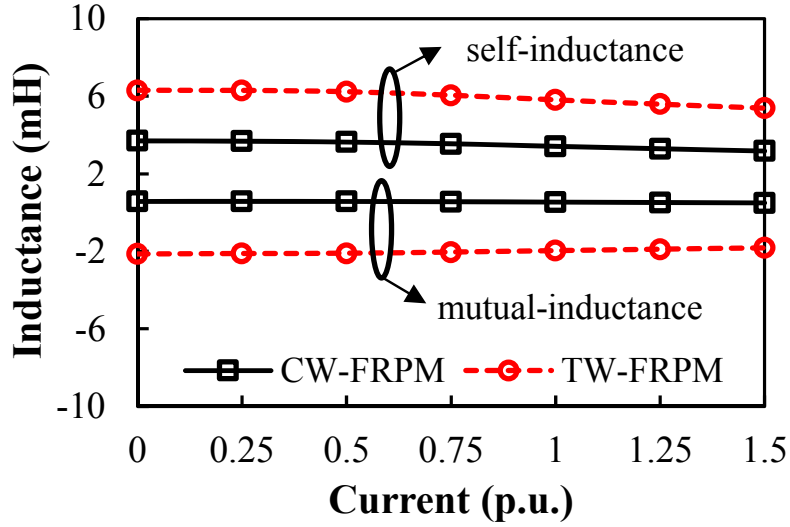


Fig. 5.17 Phase inductances of CW- and TW-FRPM machines.

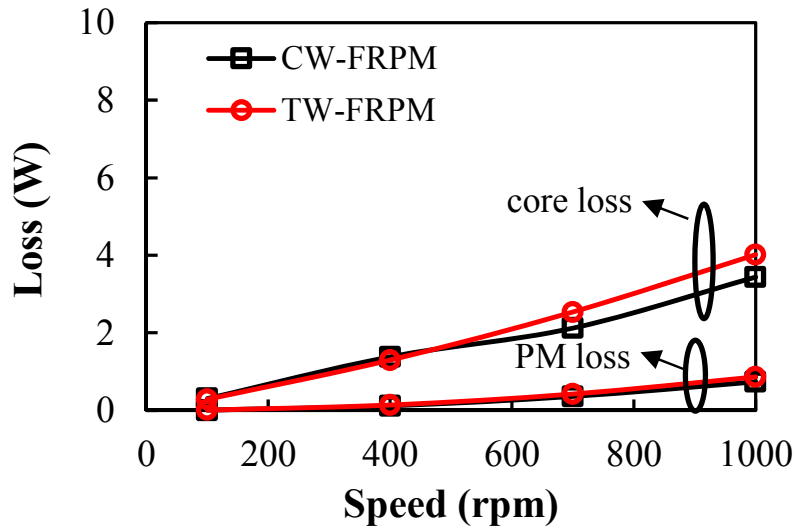
#### 5.4.5 Losses and Efficiency

Fig. 5.18 predicts the variation of core loss and PM loss against rotor speed, together with the influence of load condition (i.e. current  $I$ ). The PM loss is predicted based on the material property of N35SH (the conductivity is 625000S/m), and the core loss is calculated based on

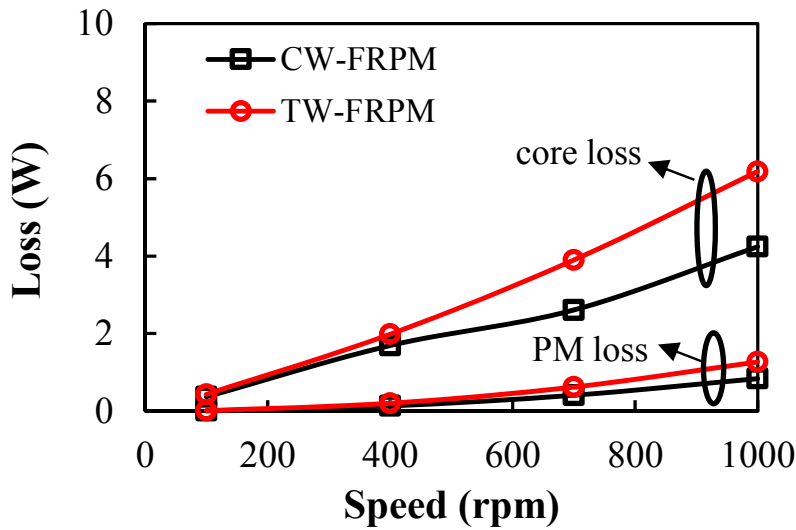
$$p_{core} = p_h + p_c + p_e = k_h f (B_m)^2 + k_c (f B_m)^2 + k_e (f B_m)^{1.5} \quad (5.8)$$

where  $f$  is the frequency,  $B_m$  is the amplitude of the flux,  $k_h$ ,  $k_c$ , and  $k_e$  are the hysteresis, eddy-current, and excess core loss coefficient, respectively.  $k_h$ ,  $k_c$ , and  $k_e$  are related to the adopted core lamination (B35A300 in this study).

As can be seen from Fig. 5.18, within the whole speed region, the core loss is larger than the PM loss and the TW-FRPM machine has larger core loss compared with the CW-FRPM machine, especially for a large current (see Fig. 5.18(b)). This can be explained by the large inductance in TW-FRPM machine, since the armature field is proportional to the inductance and current.



(a)



(b)

Fig. 5.18 Loss variation against speed of CW- and TW-FRPM machines. (a) Half load ( $I=0.5p.u.$ ). (b) Full load ( $I=1p.u.$ ).

The efficiency variation against speed is also predicted in Fig. 5.19. It should be noted that only core loss, PM loss and copper loss are considered in the calculation of efficiency, as

$$\eta = \frac{P_{em}}{P_{em} + p_{core} + p_{PM} + p_{cu\_total}} \quad (5.9)$$

As can be seen from Fig. 5.19, when  $n < 1000rpm$ , the machine efficiency increases against  $n$  since the output power  $P_{em}$  increases with  $n$ . In addition, the machine efficiency is largely influenced by the load condition since the copper loss is the dominant loss component. The



larger the current, the larger the copper loss and the lower the efficiency. More importantly, despite of the higher core losses (see Fig. 5.18), the proposed TW-FRPM machine has much higher efficiency than the CW-FRPM machine, thanks to the improved output power/torque. For example, when  $n=400\text{rpm}$ , for the TW-FRPM machine, the rated efficiency is 76.2% while it is only 62.8% for the CW-FRPM machine.

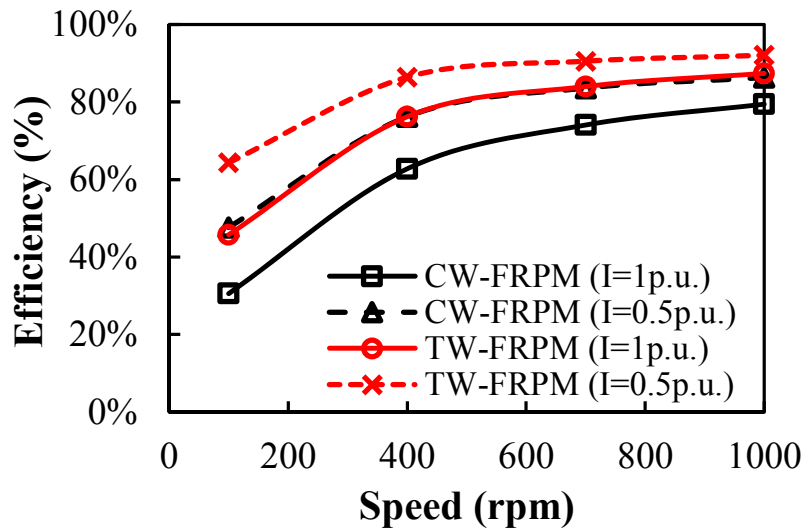


Fig. 5.19 Efficiency of CW- and TW-FRPM machines.

#### 5.4.6 Torque-Current Characteristic

Fig. 5.20 shows the torque-current characteristic of the two machines. As can be seen, within the whole current range ( $I \leq 1.5\text{p.u.}$ ), the TW-FRPM machine always has much higher torque than the CW-FRPM machine although its torque increase ratio against  $I$  is relatively lower. Again, this can be explained by the machine inductance. For the TW-FRPM machine, due to the larger inductance, its magnetic saturation is severer especially for high current.

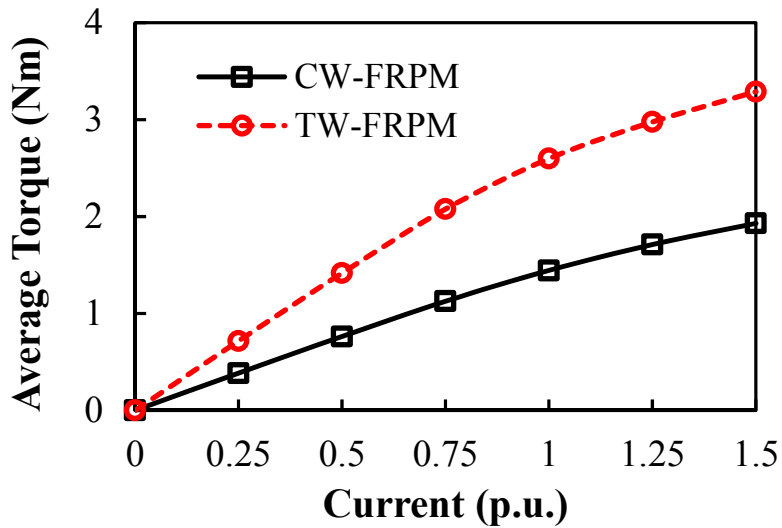


Fig. 5.20 Torque-current characteristics of CW- and TW-FRPM machines.

#### 5.4.7 Power Factor

Fig. 5.21 compares the power factors of the two machines within the whole effective copper loss range ( $\leq 45\text{W}$ ). As can be seen, when  $p_{cu\_eff}=45\text{W}$ , the torque of the TW-FRPM machine is 70% higher than that of the CW-FRPM machine. Besides, under the fixed torque, the power factor of the TW-FRPM machine is always larger than that of the CW-FRPM machine since the demanded armature field (current) is reduced [GAO16b]. For example, when the machine output torque is 2Nm, the power factor of the TW-FRPM machine is 0.7 while it is only 0.58 for the CW-FRPM machine.

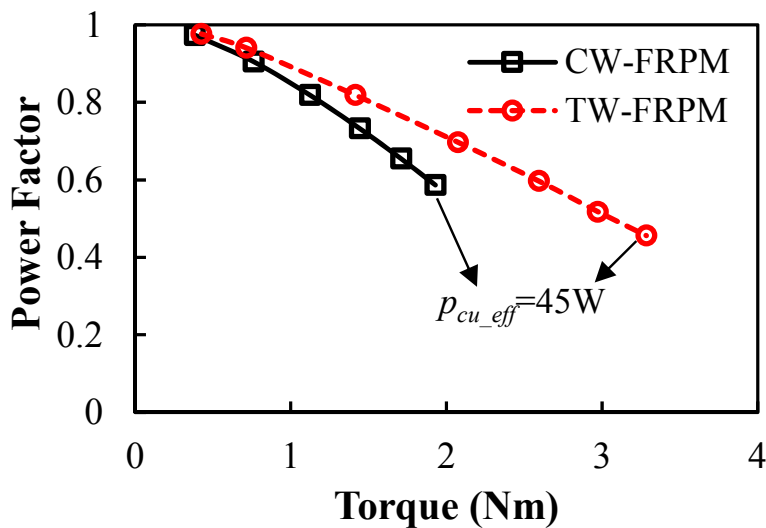


Fig. 5.21 Power factor of CW- and TW-FRPM machines.

## 5.5 Preferred Slot/Pole combinations for TW-FRPM Machine

Although the 12/13 TW-FRPM machine is proven to exhibit better performance than the CW-FRPM machine, the other feasible stator slot/rotor pole ( $N_s/N_r$ ) combinations should be identified to provide a general design guidance for TW-FRPM machine. Based on  $p_{eq}$  in (5.7), the slot per pole per phase ( $spp$ ) of a FRPM machine is

$$spp = N_s / 2mp_{eq} \quad (5.10)$$

where  $m$  is the phase number of the machine.

For CW-FRPM machines, the pitch factor can be obtained as

$$k_{p-cw} = \cos[\pi(1 - 1/mspp) / 2] \quad (5.11)$$

Based on the pitch factor improvement mechanism of TW-FRPM machine, the torque of the TW-FRPM machine can be improved when  $k_{p-cw} < 1/2$ , thus,  $spp$  should be

$$spp > (3/m) \quad (5.12)$$

Therefore, based on (5.7) (5.10) and (5.12), the fitness of using TW in FRPM machines with different  $N_s/N_r$  combinations can be determined. Taking three phase ( $m=3$ ) and  $N_s=12$  as an example, when  $N_r$  ranges from 10 to 14, the torque variations of both CW-FRPM and TW-FRPM machine are shown in Fig. 5.22. It should be noted that all the machines are globally optimized for maximum torque.

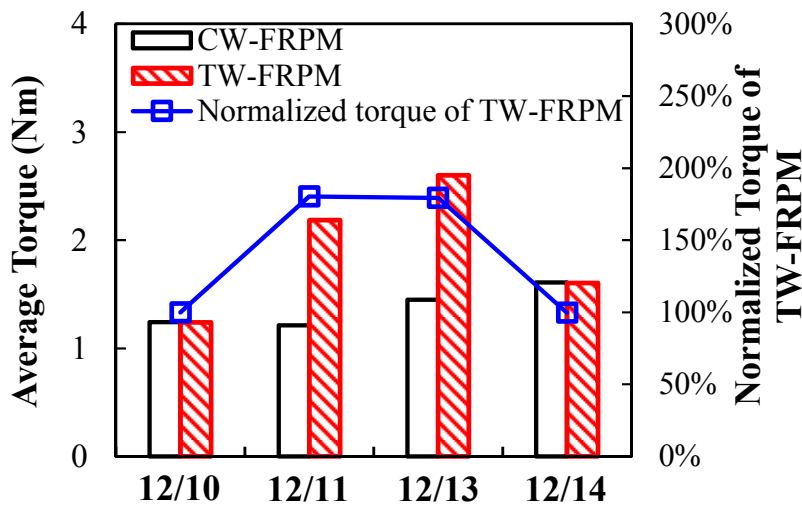
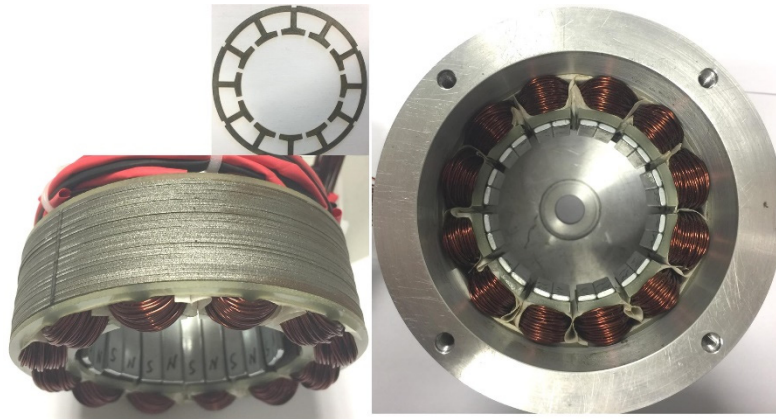


Fig. 5.22 Influence of  $N_s/N_r$  combination on machine torque.

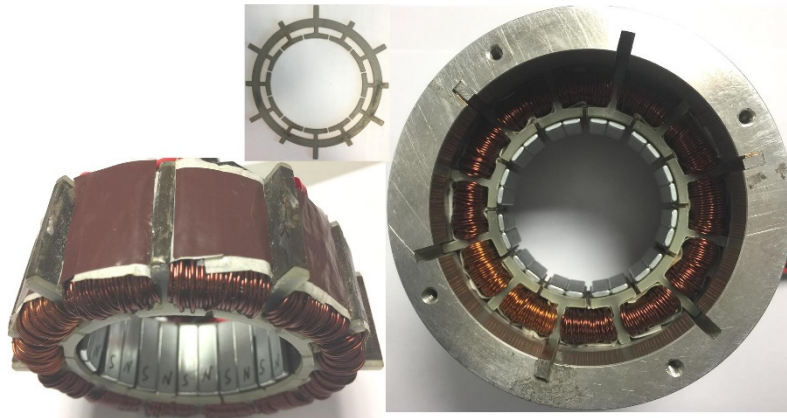
As can be seen, for CW-FRPM machine, the average torque of 12/14 is slightly higher than that of the other  $N_s/N_r$ ; for TW-FRPM machine, the 12/13 and 12/11 have significantly higher torque than the 12/10 and 12/14. For each  $N_s/N_r$ , by setting the torque of CW-FRPM machine as a benchmark, the normalized torque of TW-FRPM machine is also depicted. As can be observed, for the 12/11 and 12/13, TW-FRPM machine has much higher torque while the torque cannot be improved for the 12/10 and 12/14. Such phenomenon is consistent with (5.12) since for 12/11 and 12/13,  $spp=2$  while  $spp=1$  for 12/10 and 12/14.

## 5.6 Experimental Validation

To verify the analyses aforementioned, a 12/13 TW-FRPM machine and a 12/13 CW-FRPM machine are manufactured and tested, as shown in Fig. 5.23. Their parameters are listed in Table 5.1. It should be noted that there are some small differences between the parameters of the prototypes and the optimum FE models. For example, the inner radius of stator  $R_{si}$  of the two prototypes are slightly adjusted from its optimal value in order to share the same rotor; the PM thickness  $h_m$  of the prototypes are adjusted to 2mm due to the consideration of mechanical strength. The CAD drawings of the prototypes will be given in Appendix A.



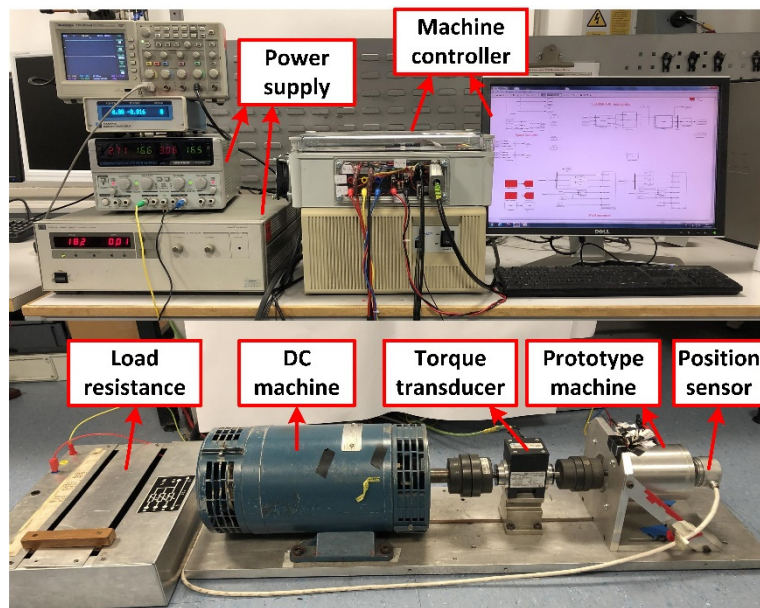
(a)



(b)



(c)



(d)

Fig. 5.23 Prototype machines. (a) CW-FRPM stator. (b) TW-FRPM stator. (c) Shared 13-pole rotor. (d) Test rig.

Fig. 5.24 shows the measured and FE-predicted back-EMFs of the two machines at  $n=400\text{rpm}$ . As can be seen, the measured back-EMF matches well with the FEA result. Test results show

that the TW-FRPM machine has 80% higher fundamental back-EMF than the CW-FRPM machine.

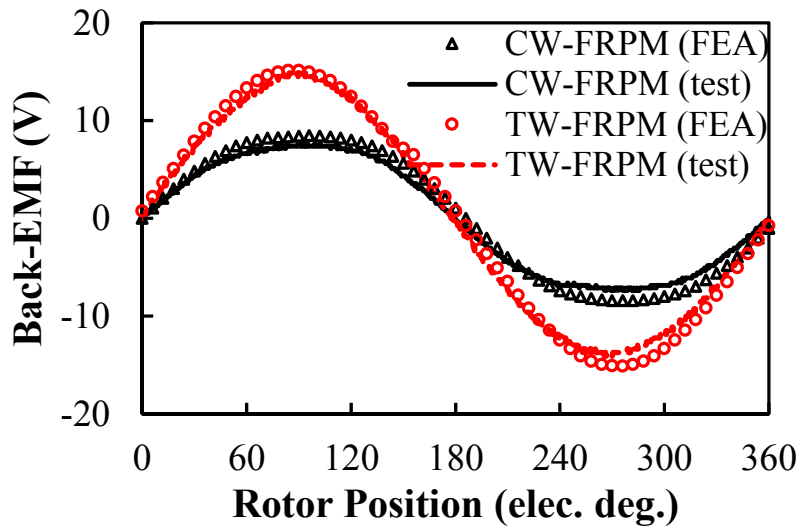


Fig. 5.24 Measured and FE-predicted rated back-EMF waveforms.

By using the static cogging torque measurement method introduced in [ZHU09b], the cogging torques of the two machines are compared in Fig. 5.25. As can be seen, for each machine, the FE-predicted cogging torque is very small, due to the  $N_s/N_r$  combination. In terms of the measured cogging torque, it is relatively larger, which can be attributed to the manufacture imperfection, such as slight rotor eccentricity. However, the measured cogging torque is still of a low peak to peak value when compared with the machine average torque.

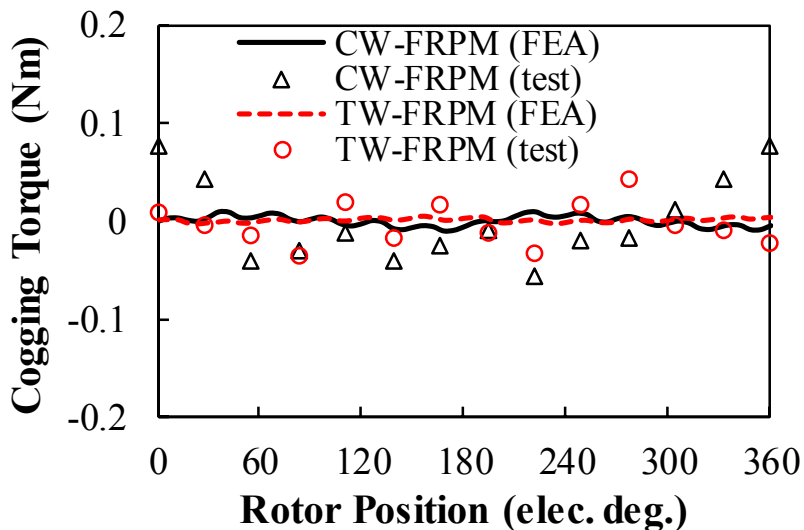


Fig. 5.25 Measured and FE-predicted cogging torques.

When  $I_d=0$  is applied, the torque-current characteristics of the two machines are measured, as

shown in Fig. 5.26. As can be seen, the measured torque-current variations match well with the FE-predicted curves albeit with relatively lower torque value. This can be explained by the end-effect and manufacture imperfection. More importantly, within the whole current range, the measured torque of the TW-FRPM machine is much higher than that of the CW-FRPM machine. Thus, the improved torque density of the TW-FRPM machine can be verified. For example, when  $I=0.5$  p.u., for the TW-FRPM machine, the measured average torque is 1.17 Nm and is 92% larger than that of the CW-FRPM machine (0.61Nm). The measured torque waveforms are also shown in Fig. 5.27. As can be seen, the measured torque ripple of the 12/13 FRPM machines is low regardless of the winding configuration, which is consistent with FEA.

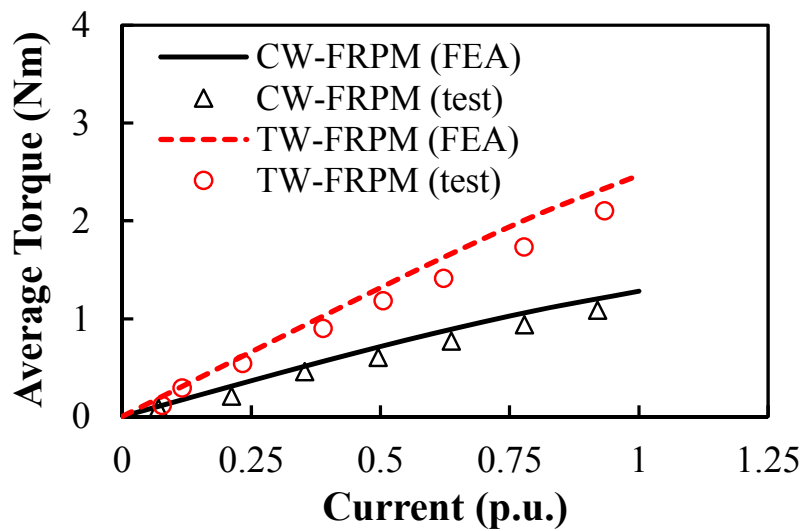


Fig. 5.26 Measured and FE-predicted torque-current characteristics.

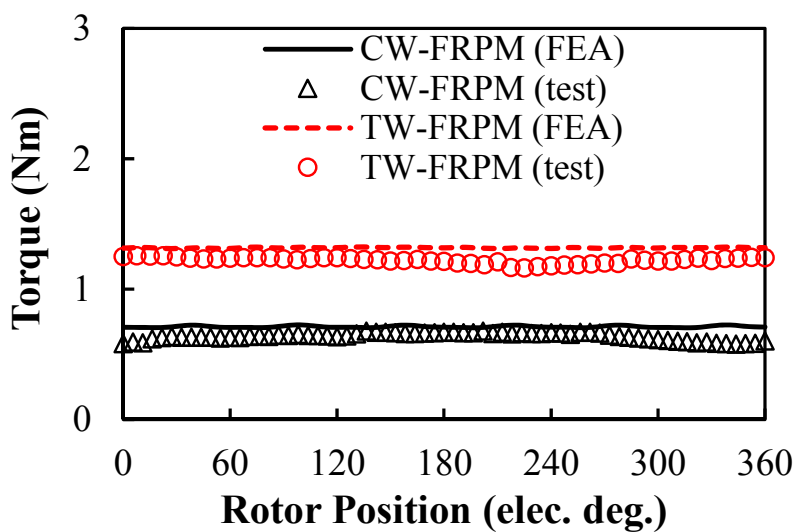


Fig. 5.27 Measured and FE-predicted torque waveforms ( $I=0.5$ p.u.)

By measuring the phase voltage, phase current, rotor speed and torque, both the efficiency and power factor of the machines can be obtained. Fig. 5.28 shows the efficiency variation of the machines against speed ( $I=0.5$  p.u.). As can be seen, for each machine, the measured efficiency increases as the speed increases, due to the improved output power. Since the mechanical losses of the test rig is difficult to be considered in FEA, the measured efficiency is lower. In addition, the efficiency of the TW-FRPM machine is always higher than that of the CW-FRPM machine, thanks to the improved torque and corresponding higher output power. Fig. 5.29 shows the power factor of the machines. Again, the measured power factor matches well with the FEA and under a fixed output torque, the TW-FRPM machine has a higher power factor since the required armature current is lower.

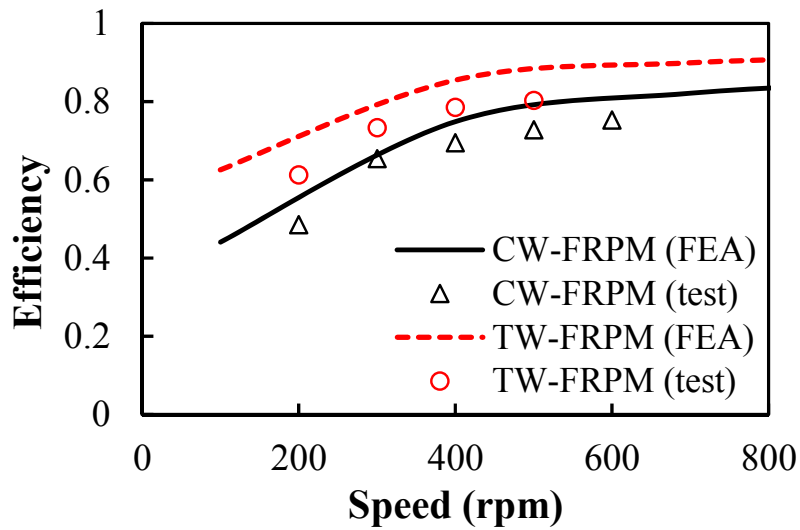


Fig. 5.28 Measured and FE-predicted efficiency. ( $I=0.5$ p.u.)

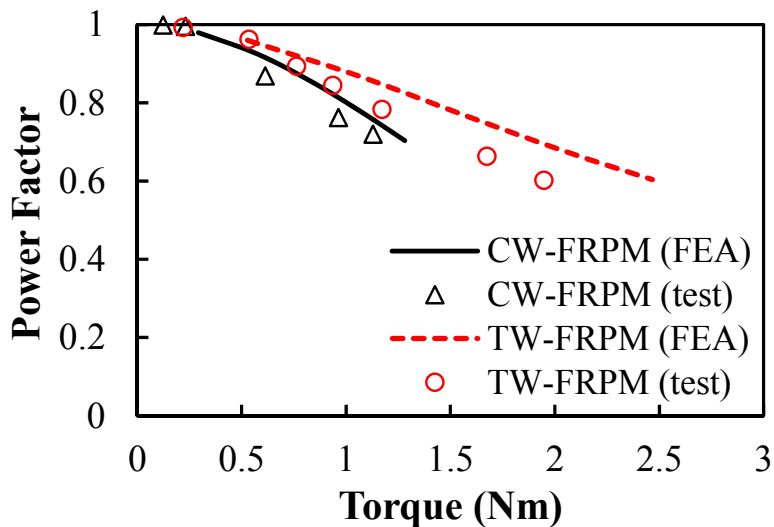


Fig. 5.29 Measured and FE-predicted power factor.



## 5.7 Conclusion

In this chapter, the FRPM machine equipped with toroidal windings is proposed and analysed, with a purpose of enhancing the machine torque performance. With both FEA and experiment results, the detailed performance comparison between the proposed TW-FRPM machine and the conventional CW-FRPM machine is presented. Some findings are summarised as follows:

1. The stator slot/rotor pole ( $N_s/N_r$ ) combination greatly influences the average torque of the CW-FRPM machine, and the preferred  $N_s/N_r$  combination can be identified via both FE and analytical methods. However, the CW-FRPM machine with a preferred  $N_s/N_r$  combination is inherently accompanied by a low pitch factor.
2. Thanks to the improved pitch factor and short end-winding, adopting TW instead of CW in a FRPM machine with specific  $N_s/N_r$  combination can be an effective approach to boost the machine torque and relevant performance. Such TW-FRPM machines are ideally suitable for applications where the axial-length is limited.

# CHAPTER 6

## COMPARATIVE STUDY OF AIR-GAP FIELD MODULATION IN FLUX REVERSAL AND VERNIER PERMANENT MAGNET MACHINES

In this chapter, the torque production mechanisms of FRPM machines and Vernier PM machines will be compared based on the unified airgap field modulation theory. Working harmonics of PM MMF and airgap permeance in two conventional 6-stator-slot/10-rotor-pole-pair machines will be analytically identified and compared. It is revealed that the fundamental PM MMF together with all permeance harmonics contribute to the torque production of a Vernier machine whereas all PM MMF harmonics but only the fundamental permeance in a FRPM machine produces the torque. Thanks to the utilised large DC component of the airgap permeance, the torque density of a Vernier machine is more likely to be higher than that of a conventional FRPM machine. Influence of critical dimensional parameters on the machine performance, such as PM thickness and slot width ratio of the flux modulation pole, will also be investigated. Both FEA and experimental validation will be conducted to verify the conclusions. In addition to the conventional FRPM machine, the performance of various FRPM machines proposed and analysed in the previous chapters will also be summarised and compared with that of the Vernier machine. Results show that some FRPM machines can have similar or even higher torque density than the Vernier machine while their PM volume can be largely reduced.

This chapter is published in *IEEE Trans. Magn.* vol. 54, no. 11, 2018, doi: 10.1109/TMAG.2018.2837898.

### 6.1 Introduction

With the recently developed theories of magnetic gearing effect/airgap field modulation [ATA01] [CHE17], the working principles of many machine topologies, such as magnetically geared machine [CHA07c] [ATA08] [WAN09], stator-PM machine [WU15c] [MOR10b], Vernier machine [QU11], variable flux reluctance machine [HUA17b] etc., have been analysed and/or re-recognized now.

Among various airgap field modulation-based machines, FRPM and Vernier machines are two typical topologies offering advantage of simple mechanical structure, such as single airgap, SPM structure, and integrated flux modulation poles (FMPs), as shown in Fig. 6.1. For both machines, the PM MMF harmonics (resulted from SPM) interact with the permeance harmonics produced by FMPs, thus producing abundant field harmonics in the airgap. The pole pair number of the main harmonic of the PM field is no longer required to be equal to that of the armature field [MOR10b] [TOB00], which differs from the conventional PM machine.

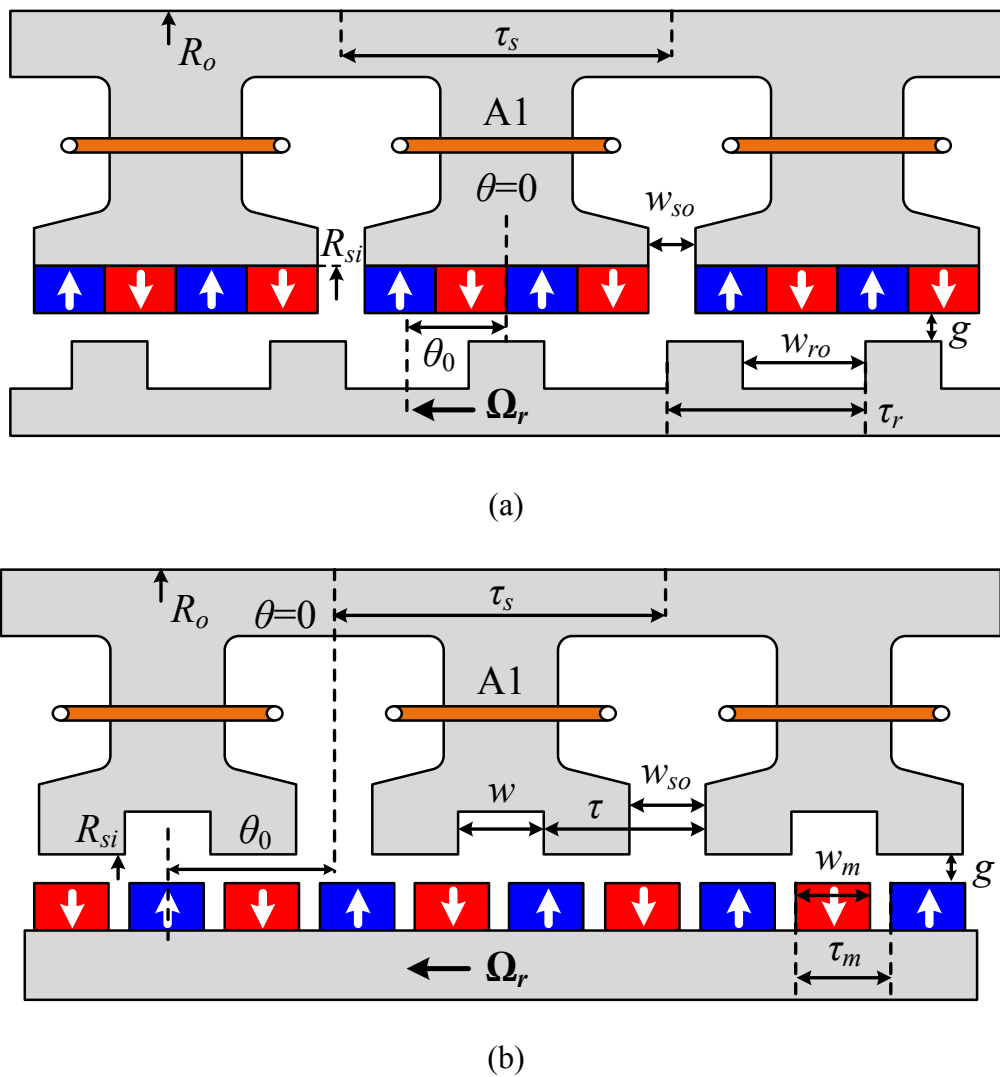


Fig. 6.1 Schematics of machines with single airgap, SPM structure and integrated flux modulation poles. (a) FRPM machine. (b) Vernier machine.

For a FRPM machine shown in Fig. 6.1 (a), its developments in recent decades have been summarised in Chapter 1, and some new perspectives of analysing and improving the

performance of a FFPM machine have also been presented in the previous chapters of this thesis.

As for the Vernier machine, according to different stator and winding configurations [TOB99], there are mainly two categories, which are open-slot, distributed-winding Vernier machine and split-pole, concentrated-winding Vernier machine. In general, the latter machine has advantages of short end-winding, compact machine size and good fault tolerance capability [LI10] [HO11] [XU15], making it particularly suitable for direct-drive applications with limited axial length. Fig. 6.1 (b) shows a conventional Vernier machine with split-pole and concentrated-windings [OKA13]. As can be seen, a concentrated tooth-coil is wound around each stator tooth with two FMPs attached to the inner surface, resulting in short end-winding and compact stator design. The existing research on Vernier machines with concentrated tooth-coil windings is mainly on working principle and topology variation. The air-gap flux modulation and/or magnetic gearing effect of Vernier machines have been investigated in [QU11] [LIU17] and some analytical methods to deduce the machine performance have been reported in [JIA11] [KIM14] [ONE16]. In addition, various aspects of structure optimisation and topology variation of Vernier machines, such as the optimal number FMPs, uneven distribution of FMPs [ZOU17], multi-phase [LIU12] and CPM rotor [CHU13], have also been investigated.

Although the FRPM and Vernier machines share the similarities in working principle, there is no systematic analysis and comparison between them which can be found in existing literatures. Therefore, in this chapter, the torque production mechanisms and electromagnetic performance of conventional FRPM machines and Vernier PM machines will be compared based on the unified airgap field modulation theory, and some promising FRPM machines analysed in the previous chapters will also be summarised.

## **6.2 Machine Configuration and Working Principle**

As introduced in Chapter 3, the PM MMF-permeance model has proven to be an effective analytical approach to deduce the performance of machines working based on air-gap field modulation. Therefore, based on this well-developed PM MMF-permeance model, the operation principles of FRPM and Vernier machines will be deduced, and the no-load back-EMF is used to assess and compare their performance. For simplicity, some assumptions are

made as: 1) the saturation of the stator and rotor core is neglected; 2) the end-effect and fringing effect of the machine are neglected; 3) the PMs are radially-magnetized.

The no-load airgap flux density of the machines is given as

$$B(\theta, t) = F_{PM}(\theta, t)\Lambda(\theta, t) \quad (6.1)$$

where  $F_{PM}(\theta, t)$  is the PM MMF produced by the SPM structure, and  $\Lambda(\theta, t)$  is the specific air-gap permeance function produced by the salient FMPs.

### 6.2.1 FRPM Machine

In Chapter 2, it has been revealed that the NSNS-NSNS FRPM machine has relatively higher average torque among various PM arrangements. Therefore, in this chapter, the NSNS-NSNS is chosen as the representative FRPM machine to compare with the Vernier machine. As shown in Fig. 6.1 (a), for a conventional NSNS-NSNS FRPM machine, two pairs of PMs are mounted on the inner surface of each stator tooth with adjacent PMs belonging to different stator teeth having opposite polarities, and the rotor consists of several FMPs, producing static PM MMF and rotating permeance harmonics. Since the unified PM MMF-analytical model of FRPM machines with different number of PM pieces ( $2npp$ ) has been established in Chapter 3, the performance of NSNS-NSNS (i.e.  $npp=2$ ) can be easily deduced as follows.

The static PM MMF can be expressed in Fourier series, as

$$F_{PM}(\theta) = \sum_{i=1,2,3,\dots}^{\infty} F_i \sin(iN_s \theta) \quad (6.2)$$

where  $N_s$  is the number of stator slot,  $i$  is the order of Fourier series,  $F_i$  is the corresponding Fourier coefficient and can be obtained according to the PM MMF waveform, as

$$F_i = \frac{2F}{i\pi} \left[ 1 + \cos(ik\pi) - 2 \cos\left(i \frac{\pi}{2} k\right) \right] \quad (6.3)$$

where  $k=(1-w_{so}/\tau_s)$ ,  $\tau_s=2\pi/N_s$ ,  $F$  is related to the remanence ( $B_r$ ), height ( $h_m$ ), and relative permeability ( $\mu_r$ ) of the PM material, and  $F=B_r h_m / \mu_r \mu_0$ .

Regarding the permeance distribution, it can be written as

$$\Lambda(\theta, t) = \sum_{q=0,1,2,\dots}^{\infty} \Lambda_q \cos[qN_r(\theta - \theta_0 - \Omega_r t)] \quad (6.4)$$

where  $\Omega_r$  is the angular speed of the rotor,  $N_r$  is the rotor pole number,  $q$  is the order of Fourier series, and  $\Lambda_q$  is the corresponding Fourier coefficient, which can be obtained by using the conformal transformation [ZHU93], and has already been given in Chapter 3, see (3.5)-(3.8).

Therefore, the no-load air-gap flux density can be rewritten as

$$B(\theta, t) = \Lambda_0 \sum_{i=1,2,3,\dots}^{\infty} F_i \sin(iN_s \theta) + \sum_{i=1,2,3,\dots}^{\infty} \sum_{q=1,2,3,\dots}^{\infty} \frac{1}{2} F_i \Lambda_q \sin[(iN_s \pm qN_r)\theta \mp qN_r(\theta_0 + \Omega_r t)] \quad (6.5)$$

Considering the flux through the single coil A1, it is

$$\begin{aligned} \lambda_A(t) &= n_c \int B(\theta, t) ds = n_c l R_{si} \int_{-k\pi/N_s}^{k\pi/N_s} B(\theta, t) d\theta \\ &= \sum_{i=1,2,3,\dots}^{\infty} \sum_{q=1,2,3,\dots}^{\infty} \frac{n_c l R_{si} F_i \Lambda_q}{(iN_s \pm qN_r)} \sin\left[\left(\frac{iN_s \pm qN_r}{N_s}\right) k\pi\right] \sin[\mp qN_r(\theta_0 + \Omega_r t)] \end{aligned} \quad (6.6)$$

where  $n_c$  is the number of turns per coil,  $l$  is the machine stack length,  $R_{si}$  is the stator inner radius.

Correspondingly, its back-EMF can be obtained as

$$\begin{aligned} e_A(t) &= -\frac{d\lambda_A(t)}{dt} = \sum_{i=1,2,3,\dots}^{\infty} \sum_{q=1,2,3,\dots}^{\infty} \frac{\pm n_c l R_{si} F_i \Lambda_q q N_r \Omega_r}{(iN_s \pm qN_r)} \sin\left[\left(\frac{iN_s \pm qN_r}{N_s}\right) k\pi\right] \\ &\quad \square \cos[qN_r(\theta_0 + \Omega_r t)] \end{aligned} \quad (6.7)$$

From (6.5)-(6.7), it is clear that abundant harmonics exist in the no-load airgap flux density, however, only those with same  $q$  can contribute to the back-EMF with same frequency.

## 6.2.2 Vernier Machine

As shown in Fig. 6.1 (b), the rotor of Vernier machine is of SPM structure and the flux modulation iron poles are located on the stator, resulting in static permeance and rotating PM MMF harmonics. Theoretically, the number, width and depth of the auxiliary slots on stator teeth are changeable, making the permeance distribution more complex. In this study, each tooth has one auxiliary slot and its width is set as equal to the stator slot opening ( $w=w_{so}$ ) while its depth is regarded as infinite for simplicity. Thus, the number of FMPs is  $2N_s$ , and the

permeance expressions of (3.5)-(3.8) are still feasible. The static permeance distribution is then expressed as

$$\Lambda(\theta) = \sum_{q=0,1,2,\dots}^{\infty} \Lambda_q \cos(2qN_s\theta) \quad (6.8)$$

The rotating PM MMF of Vernier machine can be written as

$$F_{PM}(\theta, t) = \sum_{i=1,2,3,\dots}^{\infty} F_i \sin[ip_m(\theta - \theta_0 - \Omega_r t)] \quad (6.9)$$

$$F_i = \frac{4F}{i\pi} [\sin(i\pi/2)\sin(i\pi\alpha/2)] \quad (6.10)$$

where  $p_m$  is the pole-pair number of rotor PM, and  $\alpha = w_m/\tau_m$ , see Fig. 6.1 (b).

Substituting (6.1) with (6.8) and (6.9), the flux density is

$$B(\theta, t) = \frac{1}{2} \sum_{i=1,2,3,\dots}^{\infty} \sum_{q=0,1,2,\dots}^{\infty} F_i \Lambda_q \sin[(ip_m \pm 2qN_s)\theta - ip_m(\theta_0 + \Omega_r t)] \quad (6.11)$$

Similarly, the flux and back-EMF of coil A1 can be deduced as

$$\begin{aligned} \lambda_A(t) &= n_c \int B(\theta, t) ds = n_c l R_{si} \int_{\pi w/2N_s\tau}^{2\pi/N_s - \pi w/2N_s\tau} B(\theta, t) d\theta \\ &= \sum_{i=1,3,5,\dots}^{\infty} \sum_{q=0,1,2,\dots}^{\infty} \frac{n_c l R_{si} F_i \Lambda_q}{ip_m \pm 2qN_s} \sin \left[ (ip_m \pm 2qN_s) \left( \frac{\pi w}{2N_s\tau} - \frac{\pi}{N_s} \right) \right] \sin \left[ ip_m \left( \theta_0 + \frac{\pi}{N_s} + \Omega_r t \right) \right] \end{aligned} \quad (6.12)$$

$$\begin{aligned} e_A(t) &= -d\lambda_A(t)/dt = \sum_{i=1,3,5,\dots}^{\infty} \sum_{q=0,1,2,\dots}^{\infty} \frac{-ip_m \Omega_r n_c l R_{si} F_i \Lambda_q}{ip_m \pm 2qN_s} \sin \left[ (ip_m \pm 2qN_s) \left( \frac{\pi w}{2N_s\tau} - \frac{\pi}{N_s} \right) \right] \\ &\quad \square \cos \left[ ip_m \left( \theta_0 + \frac{\pi}{N_s} + \Omega_r t \right) \right] \end{aligned} \quad (6.13)$$

Again, abundant no-load flux density harmonics exist in Vernier machines. However, only those with same  $i$  contribute to the back-EMF with same frequency, see (6.13).

### 6.2.3 Different Working Harmonics of Two Kinds of Machines

Comparing (6.7) with (6.13), it is found that the working harmonics of PM MMF and permeance distribution are totally different between two kinds of machines.

For the FRPM machine, all PM MMF harmonics ( $F_i$ ) but only fundamental permeance ( $\Lambda_1$ ) contributes to the production of fundamental back-EMF, and there is a unique weight factor ( $w^f_i$ ) for each harmonic of PM MMF. The fundamental back-EMF ( $E_A$ ) of coil A can be given as

$$\begin{aligned} E_A &= \sum_{i=1,2,3\dots}^{\infty} E_i = n_c l R_{si} \Omega_r \Lambda_1 \sum_{i=1,2,3\dots}^{\infty} w^f_i F_i \\ &= \sum_{i=1,2,3\dots}^{\infty} \frac{\pm n_c l R_{si} F_i \Lambda_1 N_r \Omega_r}{(iN_s \pm N_r)} \sin \left[ \left( \frac{iN_s \pm N_r}{N_s} \right) k\pi \right] \end{aligned} \quad (6.14)$$

The weight factor ( $w^f_i$ ) for each PM MMF harmonic can be expressed as

$$w^f_i = \frac{N_r}{(iN_s + N_r)} \sin \left[ \left( \frac{iN_s + N_r}{N_s} \right) k\pi \right] + \frac{-N_r}{(iN_s - N_r)} \sin \left[ \left( \frac{iN_s - N_r}{N_s} \right) k\pi \right] \quad (6.15)$$

For the Vernier machine, only fundamental PM MMF ( $F_1$ ) but all permeance harmonics ( $\Lambda_q$ ) are effective. Similarly, there is a weight factor ( $w^v_q$ ) for each permeance harmonic. The weight factor and fundamental back-EMF ( $E_A$ ) of coil A can be given as

$$\begin{aligned} E_A &= \sum_{q=0,1,2\dots}^{\infty} E_q = n_c l R_{si} \Omega_r F_1 \sum_{q=0,1,2\dots}^{\infty} w^v_q \Lambda_q \\ &= \sum_{q=0,1,2\dots}^{\infty} \frac{-p_m \Omega_r n_c l R_{si} F_1 \Lambda_q}{p_m \pm 2qN_s} \sin \left[ (p_m \pm 2qN_s) \left( \frac{\pi w}{2N_s \tau} - \frac{\pi}{N_s} \right) \right] \end{aligned} \quad (6.16)$$

$$\begin{aligned} w^v_q &= \frac{-p_m}{p_m + 2qN_s} \sin \left[ (p_m + 2qN_s) \left( \frac{\pi w}{2N_s \tau} - \frac{\pi}{N_s} \right) \right] \\ &+ \frac{-p_m}{p_m - 2qN_s} \sin \left[ (p_m - 2qN_s) \left( \frac{\pi w}{2N_s \tau} - \frac{\pi}{N_s} \right) \right] \end{aligned} \quad (6.17)$$

For clarity, the working harmonics of PM MMF and permeance distribution of FRPM and Vernier machines are summarised in Table 6.1.

To make a fair comparison between FRPM and Vernier machines and quantify the contribution of each harmonic, the back-EMFs of two machines with same stator slot number ( $N_s=6$ ) and rotor pole-pair number ( $N_r=p_m=10$ ) are analytically calculated. Their basic parameters are listed in Table 6.2.



Table 6.1 Working harmonics of PM MMF and Permeance Distribution

	FRPM	Vernier
PM MMF ( $F_i$ )	$F_i (i=1, 2, 3\dots)$	$F_1$
Permeance ( $\Lambda_q$ )	$\Lambda_1$	$\Lambda_q (q=0, 1, 2\dots)$
Back-EMF ( $E_a$ )	$n_c l R_{si} \Omega_r \cdot \Lambda_1 \sum_{i=1,2,3\dots}^{\infty} w_i^f F_i$	$n_c l R_{si} \Omega_r \cdot F_1 \sum_{q=0,1,2\dots}^{\infty} w_q^v \Lambda_q$
Weight factor ( $w$ )	$w_i^f = \frac{\pm N_r}{i N_s \pm N_r} \cdot \sin \left[ (i N_s \pm N_r) k \pi / N_s \right]$	$w_q^v = \frac{-p_m}{p_m \pm q 2 N_s} \cdot \sin \left[ (p_m \pm 2 q N_s) \left( \frac{\pi w}{2 N_s \tau} - \frac{\pi}{N_s} \right) \right]$

Table 6.2 Parameters of FRPM and Vernier machines (units: mm)

Parameters	Analytical		FEA		Prototype	
	FRPM	Vernier	FRPM	Vernier	FRPM	Vernier
Stator slot number $N_s$			6			
Rotor pole number $N_r/p_m$			10			
Overall stator diameter $D$			90			
Effective axial length $l$			25			
Airgap length $g$			0.5			
PM property $B_r, \mu_r$			1.2T, 1.05			
Stator inner radius $R_{si}$	30		31.1	28.4	29.3	21
PM thickness $h_m$	2		1.6	2.4	2	2.5
Slot width ratio of FMP	0.5		0.67	0.5	0.7	0.5
Stator slot opening $w_{so}$	2		1.3	7.4	2.5	5.6

For the FRPM machine, Fig. 6.2 shows the magnitude ( $F_i$ ), weight factor ( $w_i^f$ ) and back-EMF contribution of each PM MMF harmonic. As can be seen, the 2<sup>nd</sup> harmonic ( $F_2$ ) is the dominant

component of the PM MMF and the 3<sup>rd</sup> PM MMF harmonic is also of considerable magnitude. In terms of  $w_i^f$ , both  $i=1$  and  $i=2$  have a relatively large magnitude and it is the largest for  $i=2$ . When  $i>2$ ,  $w_i^f$  decreases rapidly. Based on (6.14), the back-EMF contribution of each PM MMF harmonic is calculated. As can be seen, the fundamental back-EMF is mainly produced by  $F_2$ , thanks to its high magnitude and weight factor. In addition,  $F_1$  accounts for the second largest proportion of the fundamental back-EMF. However, its produced fundamental back-EMF is of opposite phase of that produced by  $F_2$ , thus reducing the overall fundamental back-EMF. The two main components of the fundamental back-EMF are summarised in Table 6.3. Basically, it can be regarded that the overall fundamental back-EMF is produced by  $F_1$  and  $F_2$  only.

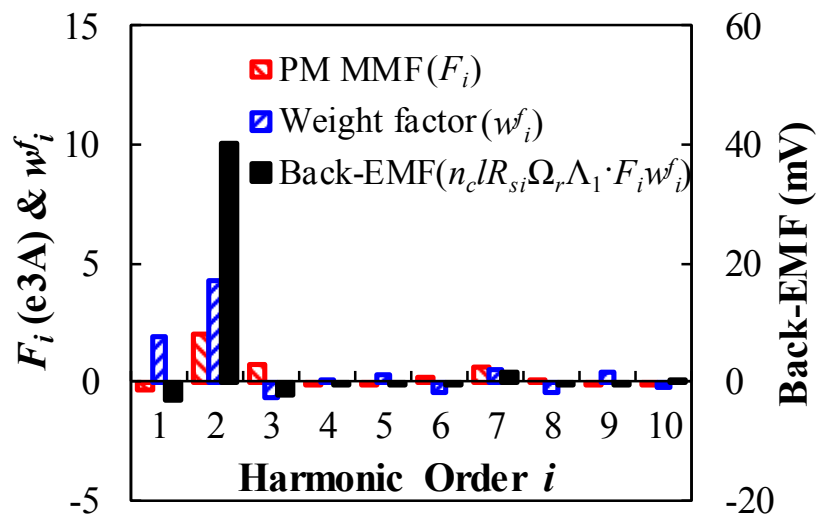


Fig. 6.2 Harmonics of PM MMF of the 6/10 FRPM machine and their weight factors and contributions to back-EMF ( $n_c=1$ ,  $n=400$ r/min).

For the Vernier machine, Fig. 6.3 shows the magnitude ( $\Lambda_q$ ), weight factor ( $w^v_q$ ) and back-EMF contribution of each permeance harmonic. As can be seen, when  $q>1$ , the magnitudes of  $\Lambda_q$  and  $w^v_q$  are all negligible. Although the weight factor  $w^v_1 > w^v_0$ , the magnitude of DC permeance ( $\Lambda_0$ ) is much larger than that of the fundamental permeance component ( $\Lambda_1$ ). Therefore, in addition to  $\Lambda_1$ , the large  $\Lambda_0$  is utilised to interact with  $F_1$ , producing additional back-EMF component with considerable proportion (54.7% in this case), see Table 6.3.

Although  $\Lambda_1$  and the main PM MMF harmonic ( $F_2$  for the NSNS-NSNS FRPM machine,  $F_1$  for the Vernier machine) interact with each other to produce the fundamental back-EMF component for the two machines, it is clear that the Vernier machine is more likely to have better performance than the FRPM machine. This can be explained by the fact that for the FRPM machine, additional fundamental back-EMF component resulted from  $F_1$  is negligible,

due to the low magnitude of  $F_1$ ; for the Vernier machine, additional fundamental back-EMF component resulted from  $\Lambda_0$  is considerable, thanks to its large magnitude.

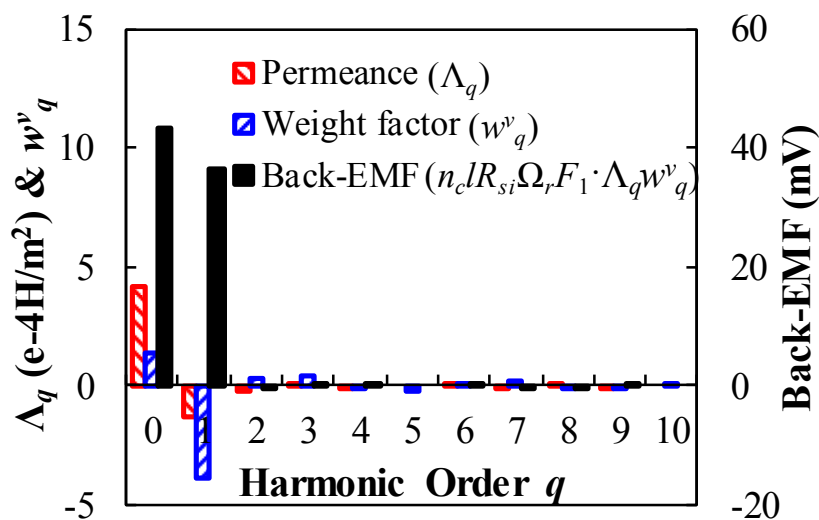


Fig. 6.3 Harmonics of permeance distribution of the 6/10 Vernier machine and their weight factors and contributions to back-EMF ( $n_c=1$ ,  $n=400$ r/min).

Table 6.3 Main components contributing to the fundamental back-EMF

	Back-EMF	Principal component	Secondary component
FRPM	35.8mV	$\Lambda_1$ with $w_2^v F_2$ (112.5%)	$\Lambda_1$ with $w_1^v F_1$ (-9.0%)
Vernier	79.5mV	$F_1$ with $w_0^v \Lambda_0$ (54.7%)	$F_1$ with $w_1^v \Lambda_1$ (45.8%)

### 6.3 Influence of Critical Design Parameters

Based on the parameters in Table 6.2, the better performance of Vernier machine has been revealed (see Table 6.3). Further, it is essential to analyse and compare the influence of critical design parameters on performance of the two machines.

#### 6.3.1 PM Thickness

Since PM thickness  $h_m$  directly affects the magnitude of PM MMF and equivalent airgap length, its influence on machine performance is obvious. Based on Table 6.2, by changing  $h_m$  and keeping all other parameters constant, the influence of PM thickness on machine fundamental back-EMF is shown in Fig. 6.4. The performance of original  $h_m=2$ mm is set as benchmark, so as to provide a clear illustration. As can be seen, there is an optimal  $h_m$  for both machines. For

the FRPM machine, the optimal  $h_m$  is smaller (1.2mm) and the back-EMF rapidly decreases with  $h_m$ . In contrast, for the Vernier machine, the back-EMF only slightly decreases when  $h_m$  is too large. Based on Table 6.2 and Table 6.3, the influence of  $h_m$  on either permeance-related (for FRPM machine, it is  $\Lambda_1$ ; for Vernier machine, it is  $w^y_0\Lambda_0+w^y_1\Lambda_1$ ) or PM MMF-related (for FRPM machine, it is  $w^f_1F_1+w^f_2F_2$ ; for Vernier machine, it is  $F_1$ ) component of the back-EMF is separated and shown in Fig. 6.5 (a). It shows that the influence of  $h_m$  on permeance-related component of two machines is quite different, due to the different variation trends of  $\Lambda_0$  and  $\Lambda_1$  against  $h_m$ , see Fig. 6.5 (b). Since the fundamental back-EMF of FRPM machine only depends on  $\Lambda_1$  which is more sensitive to  $h_m$ ,  $h_m$  cannot be selected too large, resulting in small PM MMF and inferior performance.

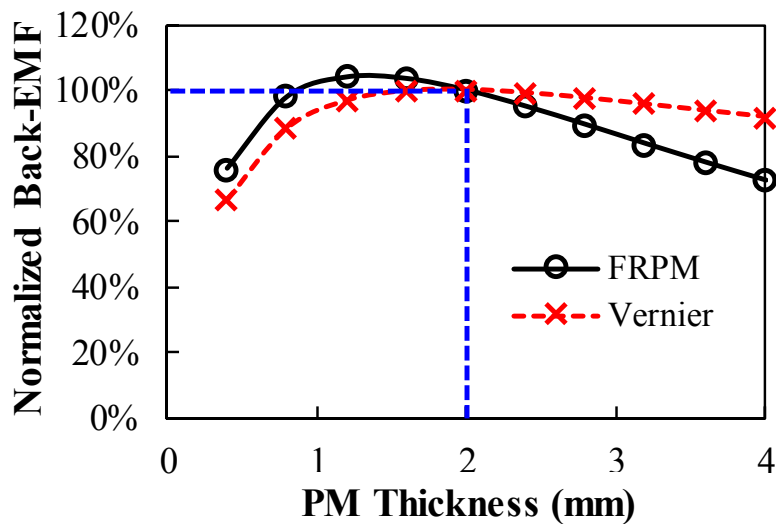
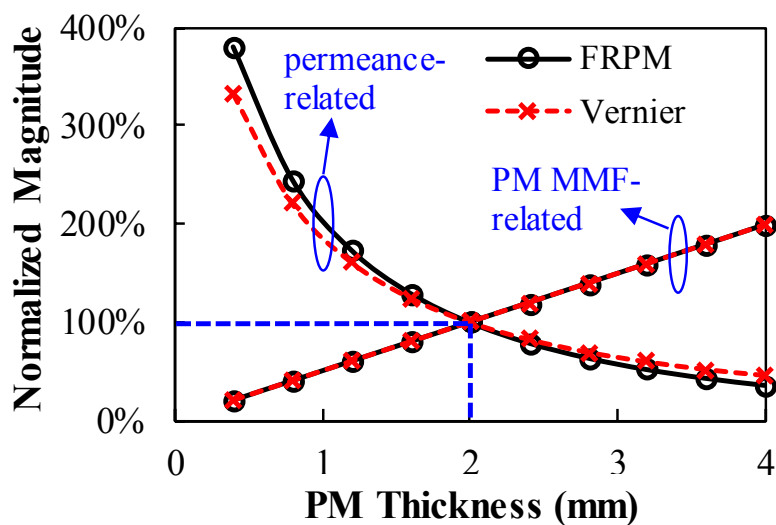
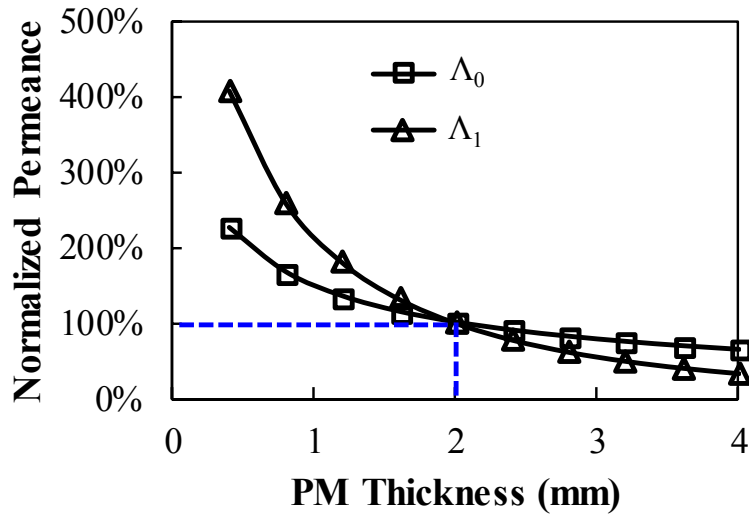


Fig. 6.4 Influence of PM thickness  $h_m$  on back-EMF.



(a)



(b)

Fig. 6.5 Influence of  $h_m$ . (a) On permeance and PM-MMF. (b) On  $\Lambda_0$  and  $\Lambda_1$ .

### 6.3.2 Slot Width Ratio

Fig. 6.6 shows the influence of slot width ratio of FMP ( $w_{ro}/\tau_r$  in FRPM machine and  $w/\tau$  in Vernier machine) on machine fundamental back-EMF, and the slot width ratio of 0.5 is set as benchmark to normalise the influence. As can be seen, there is an optimal slot width ratio to maximise the machine performance. It is smaller than 0.5 for the Vernier machine, while it is larger than 0.5 for the FRPM machine. Moreover, the performance of FRPM machine is more sensitive to the slot width ratio. Again, this can be further explained by the influence of slot width ratio on permeance-related and PM MMF-related component of the back-EMF since  $\Lambda_1$  is more sensitive to the slot width ratio, as shown in Fig. 6.7.

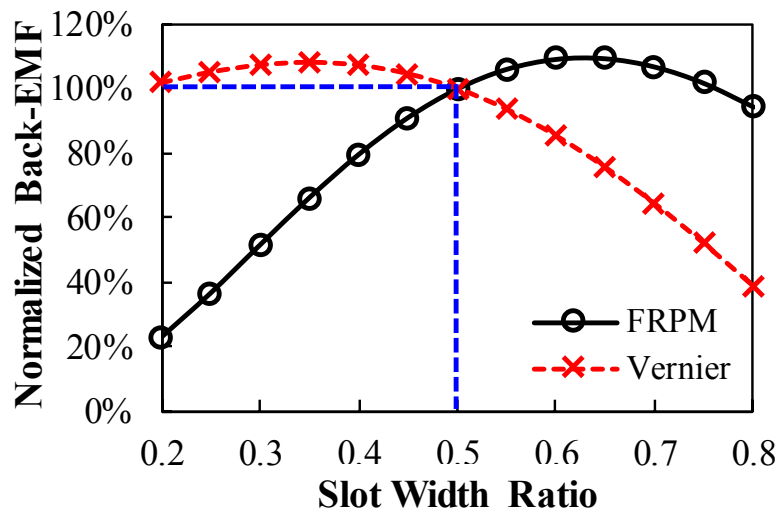
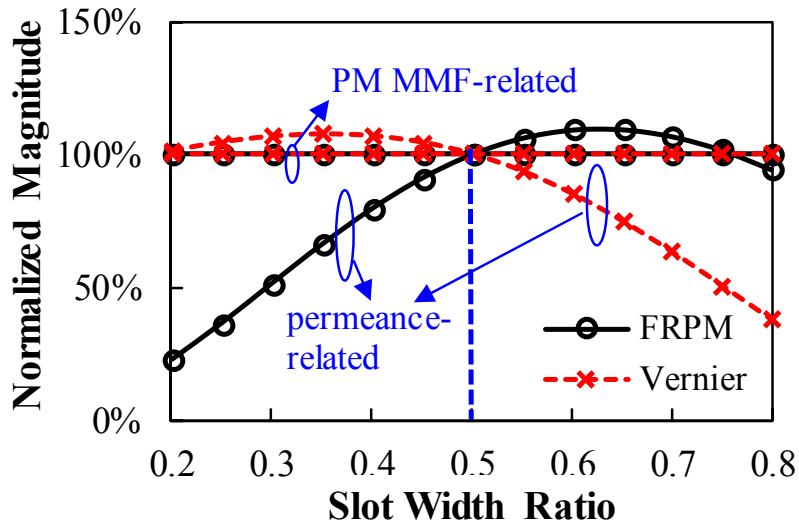
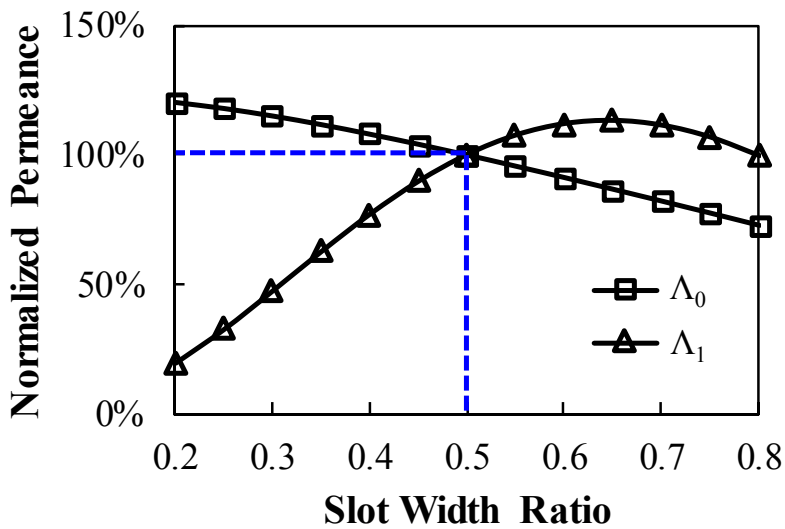


Fig. 6.6 Influence of slot width ratio of FMP on fundamental back-EMF.



(a)



(b)

Fig. 6.7 Influence of slot width ratio of FMP. (a) On permeance and PM-MMF. (b) On  $\Lambda_0$  and  $\Lambda_1$ .

## 6.4 Finite Element and Experimental Validation

### 6.4.1 Finite Element Validation

To validate the previous analytical analyses, both the 6/10 NSNS-NSNS FRPM and Vernier machines are globally optimised by FEA, aiming at the maximum torque under the same stator outer diameter (90mm), axial length (25mm), and copper loss (20W). Their parameters are listed in Table 6.2.

### 6.4.1.1 No-Load Performance

Fig. 6.8 shows the cross-section and no-load flux distribution of the two machines. As can be seen, the optimal PM thickness of the 6/10 FRPM machine is thinner while its slot width ratio of FMPs is larger, which are all consistent with the previous analyses.

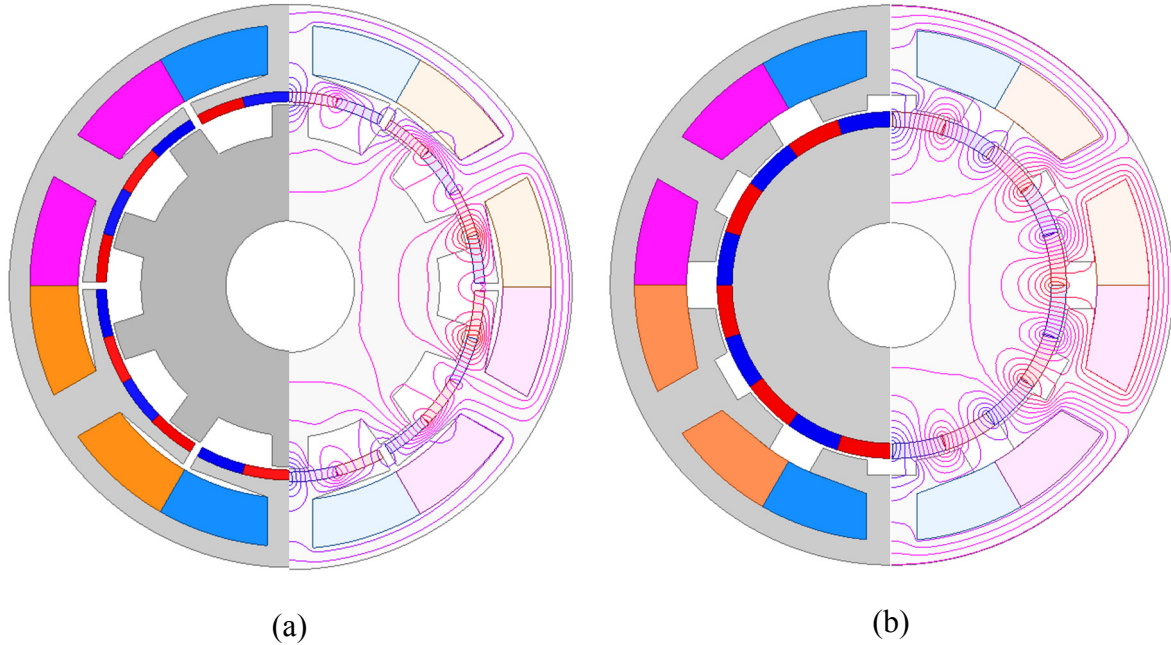


Fig. 6.8 Cross-section and no-load flux distribution of the two machines. (a) 6/10 FRPM machine. (b) 6/10 Vernier machine.

The cogging torques of the two machines are compared in Fig. 6.9. From Chapter 3, the fundamental period of cogging torque of a FRPM machine is

$$N_c = \frac{N_s}{\text{GCD}(N_r, N_s)} \quad (6.18)$$

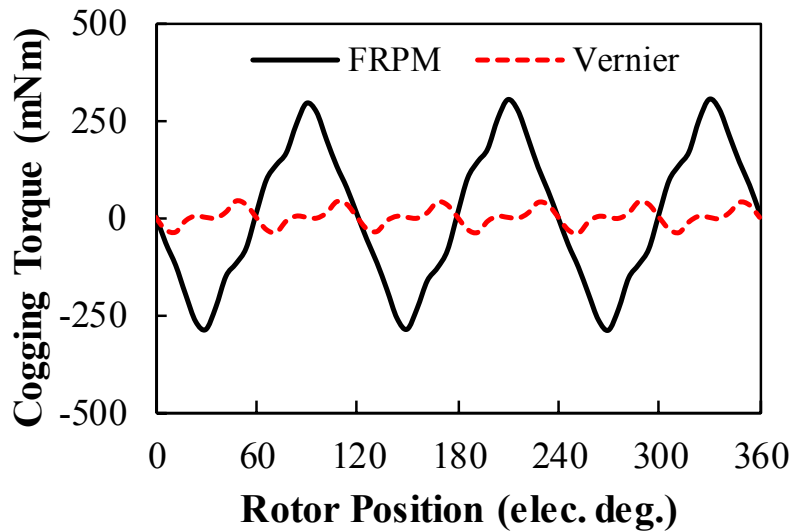
where GCD is the greatest common divisor.

For a Vernier machine, its fundamental period of cogging torque is the same as a conventional rotor-PM machine with stator slot number of  $2N_s$  and rotor pole-pair number of  $p_m$ . Therefore, its fundamental period of cogging torque can be expressed as [ZHU00]

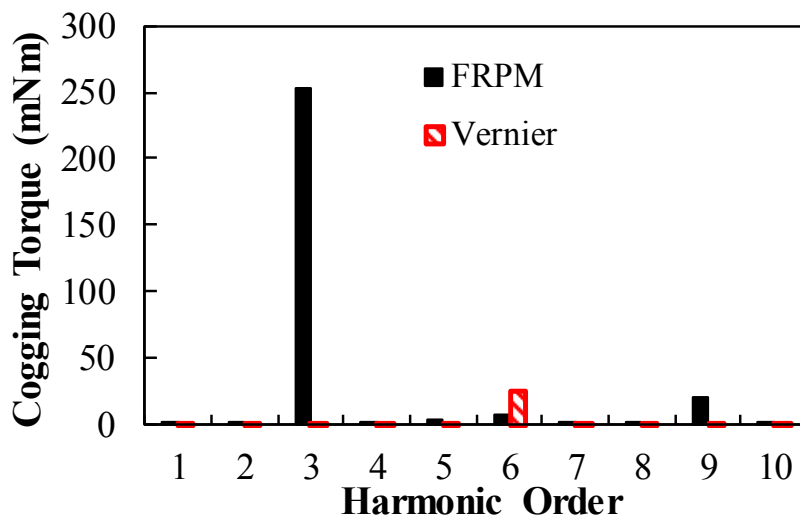
$$N_c = \frac{\text{LCM}(2p_m, 2N_s)}{P_m} \quad (6.19)$$

where LCM is the lowest common multiple.

As can be seen from Fig. 6.9, for the 6/10 FRPM machine,  $N_c=3$  and for the 6/10 Vernier machine,  $N_c=6$ , which are consistent with (3.13) and (6.19). In addition, the peak to peak value of cogging torque of the FRPM machine is quite large, which will cause a large 3<sup>rd</sup> harmonic torque ripple. In contrast, the cogging torque of the Vernier machine is small, which is beneficial to low torque ripple.



(a)



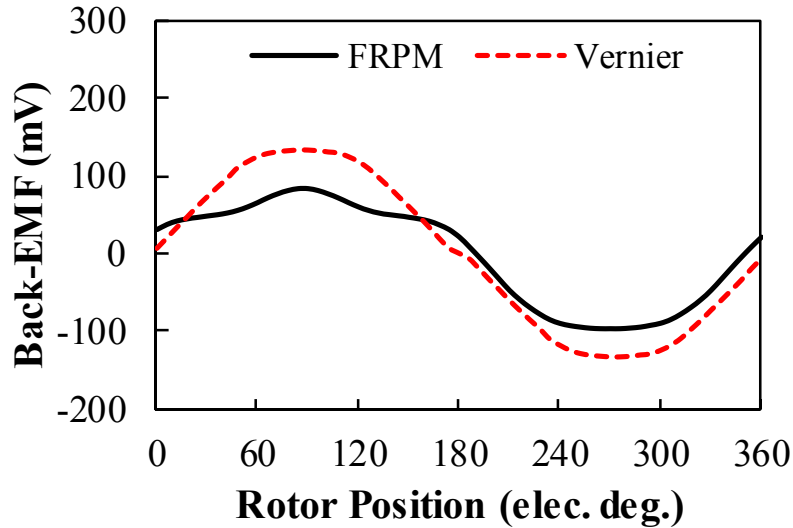
(b)

Fig. 6.9 Cogging torque of two machines. (a) Waveforms. (b) Harmonic spectra.

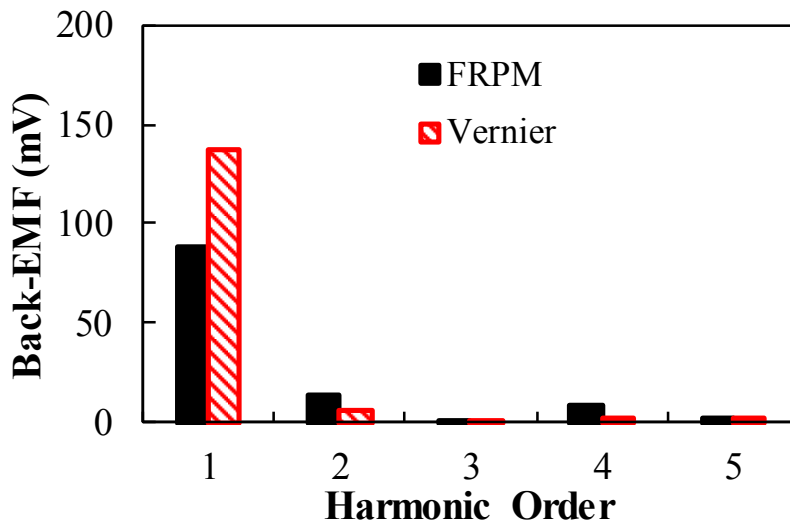
When the number of turns per coil  $n_c$  is 1, the phase back-EMFs at  $n=400$ rpm of the two machines are shown in Fig. 6.10. As can be seen, the magnitude of the fundamental back-EMF of the Vernier machine is 136.9mV, which is 54.8% higher than that of the FRPM machine (88.4mV). In addition, the 2<sup>nd</sup> and the 4<sup>th</sup> back-EMF harmonic components of the FRPM



machine are quite large, which will cause additional 3<sup>rd</sup> harmonic torque ripple. In contrast, the phase back-EMF THD of the Vernier machine is 5.6%, which is much lower than that of the FRPM machine (19.4%).



(a)



(b)

Fig. 6.10 Back-EMF of two machines ( $n_c=1$ ,  $n=400$ rpm). (a) Waveforms. (b) Harmonic spectra.

#### 6.4.1.2 On-Load Performance

With the rated current injected, the full-load flux density distributions of the two machines are shown in Fig. 6.11. As can be seen, both machines have an average flux density around 1.5T in stator yoke and stator teeth. In addition, the tooth-tips of the two machines are more vulnerable to magnetic saturation.

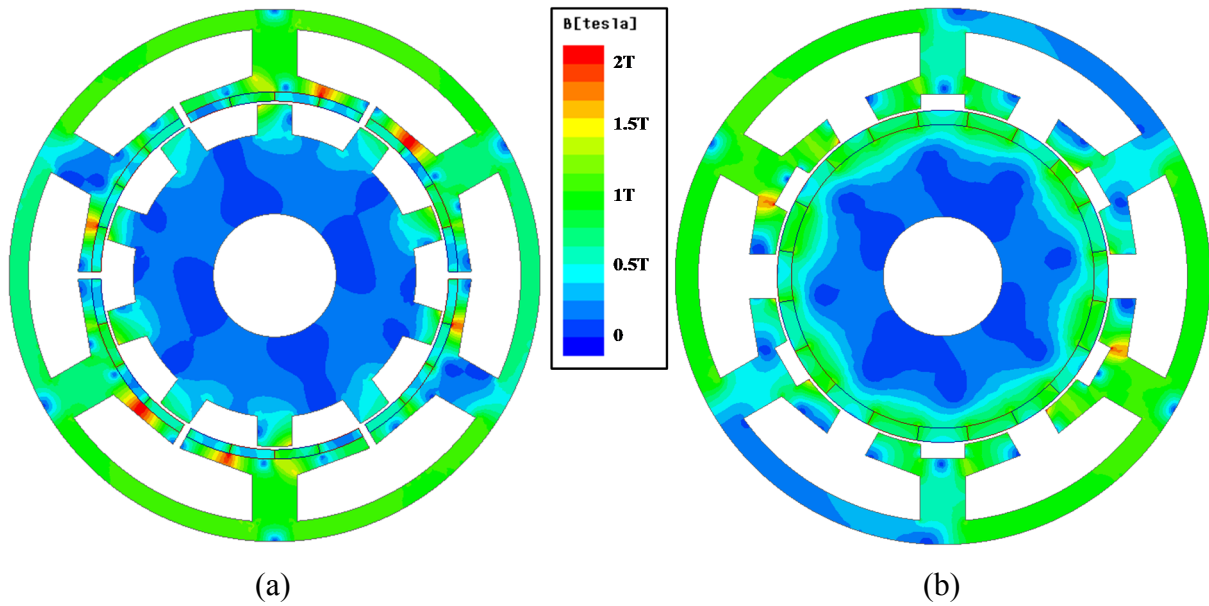
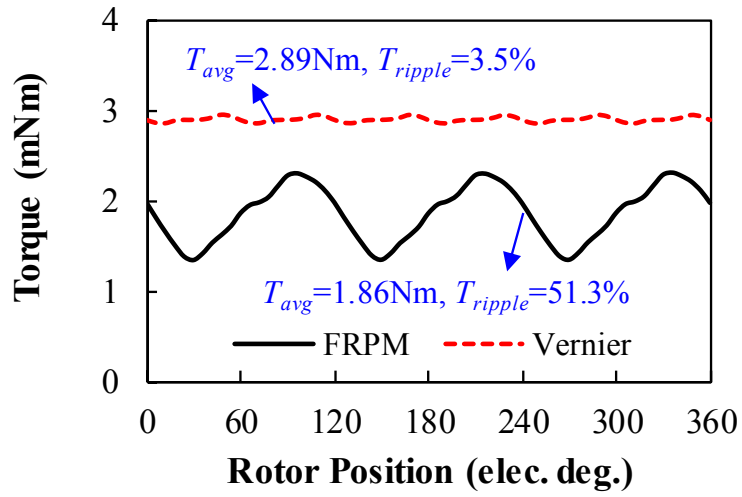


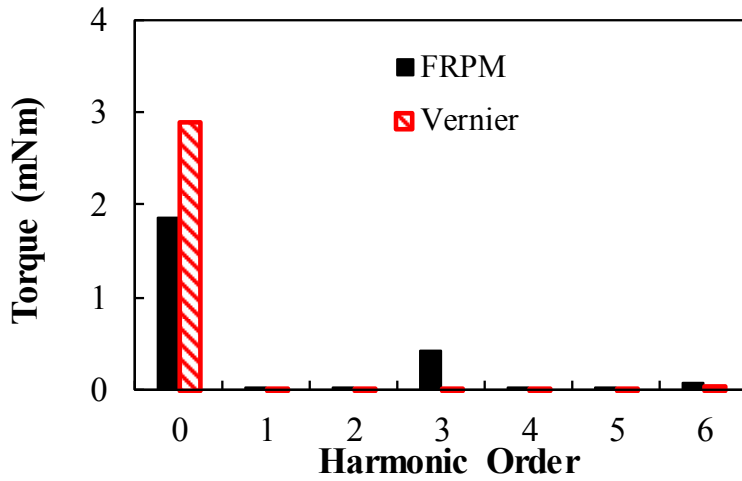
Fig. 6.11 Full-load flux density distribution. (a) 6/10 FRPM machine. (b) 6/10 Vernier machine.

The rated torques of the two machines are shown in Fig. 6.12. As can be seen, the average torque of the Vernier machine is 2.89Nm, which is 55.4% higher than that of the FRPM machine (1.86Nm). This can be explained by the larger fundamental back-EMF of the Vernier machine. Besides, the torque ripple of the Vernier machine is only 3.5% while that of the FRPM machine is 51.3% due to the large cogging torque and abundant back-EMF harmonics. Therefore, the superior torque performance of the 6/10 Vernier machine over the 6/10 FRPM machine is verified.

The different average torque of the FRPM and Vernier machine can be further explained by the air-gap flux density, as shown in Fig. 6.13 and Fig. 6.14, respectively. As can be seen, the PM field of the FRPM machine is weaker than that of the Vernier machine due to the thinner PM thickness. In terms of the armature field, although the fundamental pole-pair numbers  $p_a$  of the two machines are the same ( $p_a=2$ ), the magnitude of the FRPM machine is relatively lower. This can be explained by the lower DC permeance in the FRPM machine since its slot width ratio of FMPs is larger (see Table 6.2).

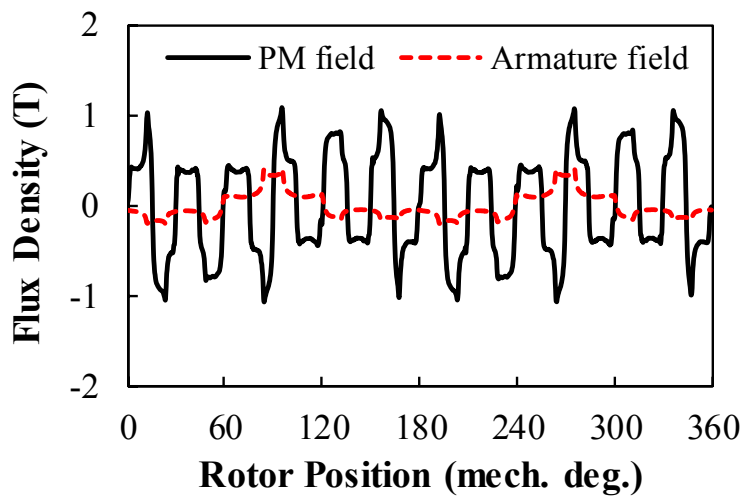


(a)

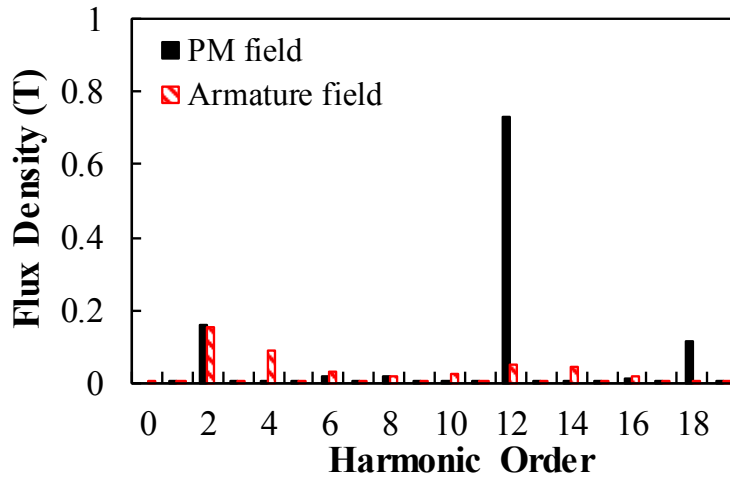


(b)

Fig. 6.12 Rated torque of two machines. (a) Waveforms. (b) Harmonic spectra.

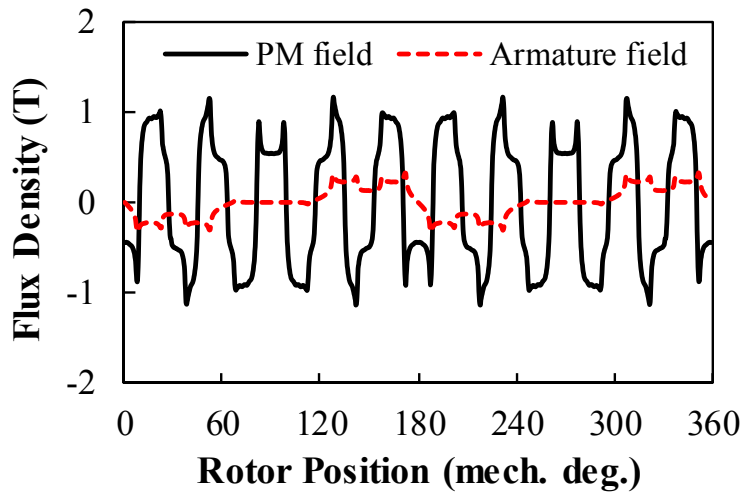


(a)

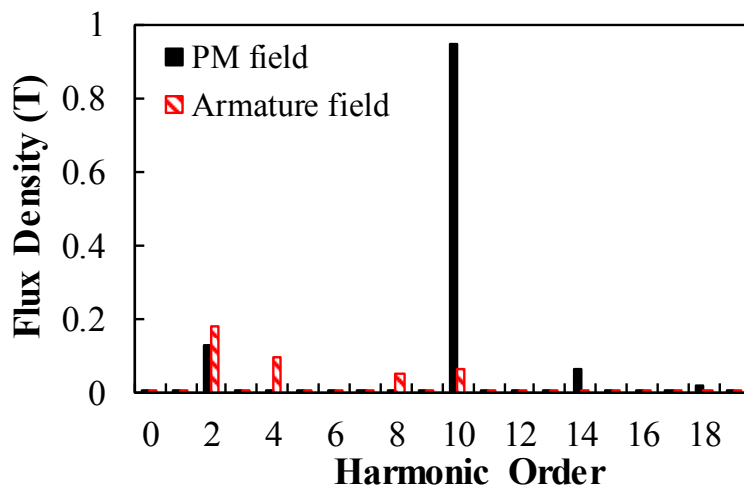


(b)

Fig. 6.13 Air-gap flux density of 6/10 FRPM machine.



(a)



(b)

Fig. 6.14 Air-gap flux density of 6/10 Vernier machine.

The torque-current characteristics of the two machines are shown in Fig. 6.15. As can be seen, within the whole current range, the Vernier machine always has higher torque density. Fig. 6.16 compares the power factor of the two machines. As can be seen, the power factors decrease with the load condition (i.e. current) and the Vernier machine has higher power factor, thanks to the higher PM flux linkage. For example, when the output torque is 1.5Nm, the power factor of the Vernier machine is 0.86 while it is only 0.55 for the FRPM machine.

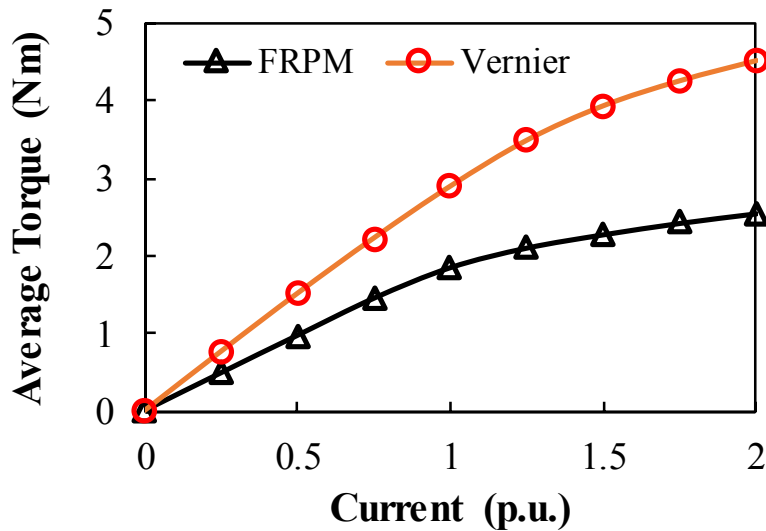


Fig. 6.15 Torque-current characteristic of the two machines.

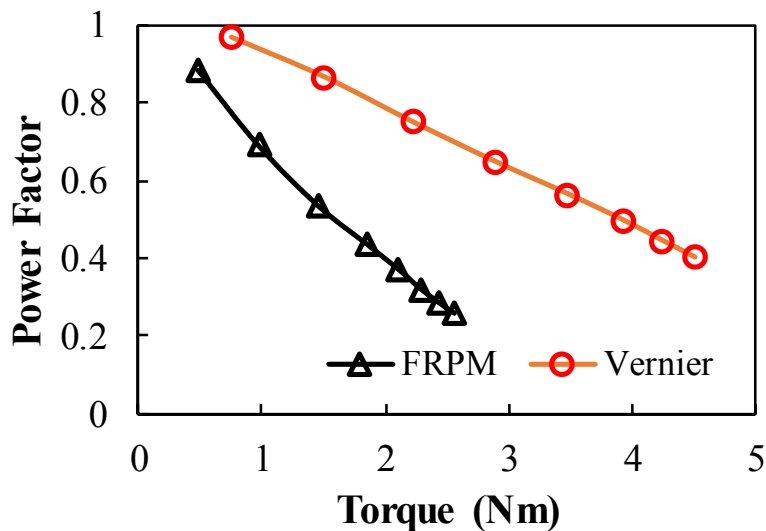


Fig. 6.16 Power factor variation against output torque.

Under the same effective copper loss of 20W, Fig. 6.17 compares the efficiency of the two machines. It should be noted that only core loss, PM loss and DC copper loss are considered in the calculation of efficiency. Again, it shows that the Vernier machine has higher efficiency

due to the improved torque. For example, when  $n=400\text{rpm}$ , the efficiency of the Vernier machine is 84.7% while it is only 77.9% for the FRPM machine.

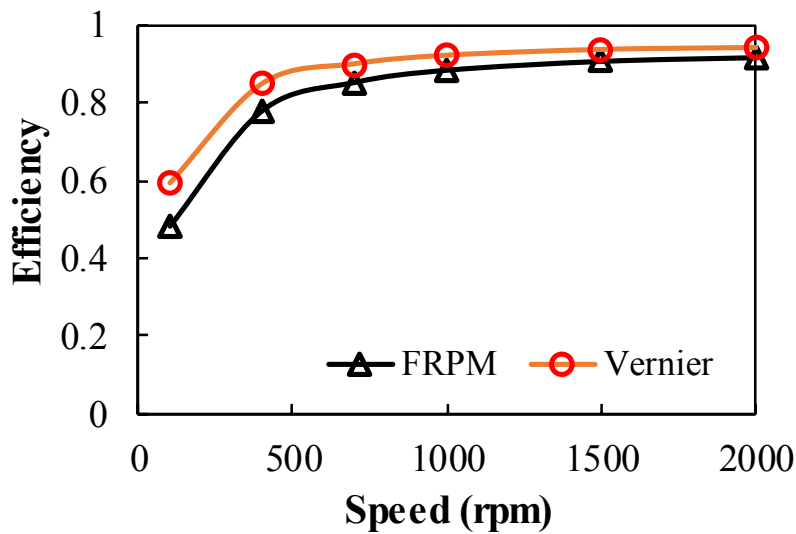


Fig. 6.17 Efficiency variation against speed.

#### 6.4.1.3 Influence of Design Parameters

The influence of PM thickness and slot width ratio of FMP on average torque is shown and compared in Fig. 6.18 and Fig. 6.19, respectively. As can be seen, the optimal  $h_m$  of the FRPM machine is 1.6mm, while that of the Vernier machine is 2.4mm; the optimal slot width ratio of FMP is 0.65 for the FRPM machine, while it is 0.5 for the Vernier machine. In addition, the average torque of the FRPM machine is more sensitive to both PM thickness and slot width ratio of FMP, which is consistent with Fig. 6.4 and Fig. 6.6.

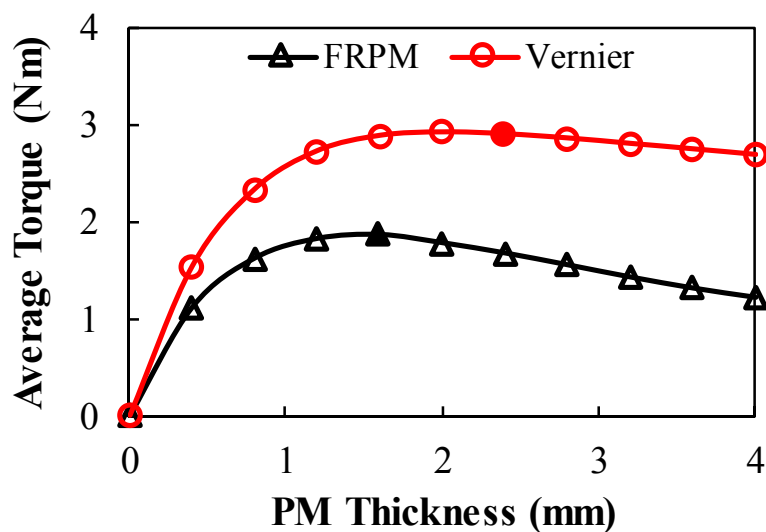


Fig. 6.18 Influence of PM thickness on average torque.

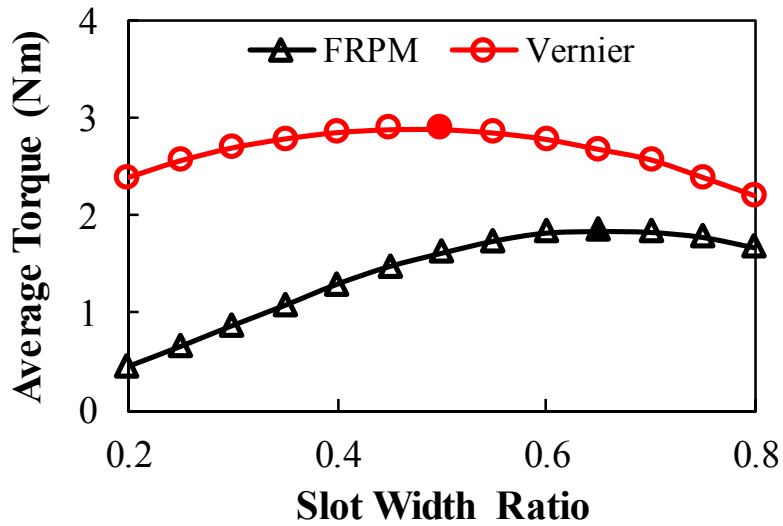
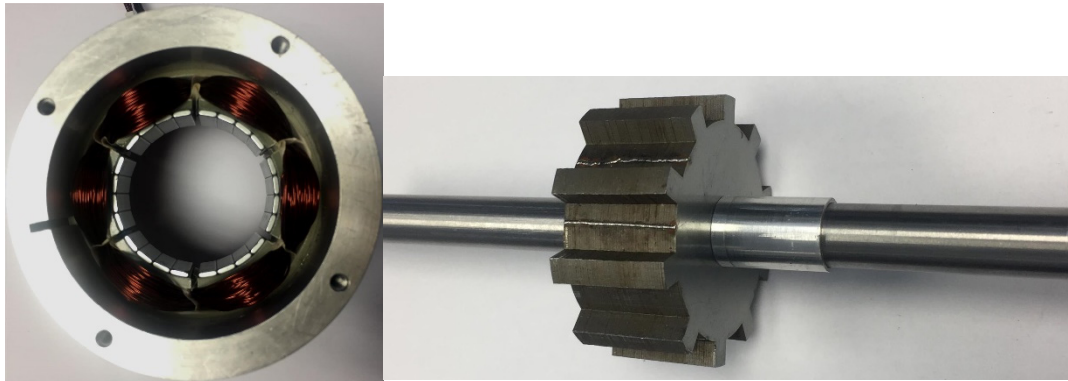


Fig. 6.19 Influence of slot with ratio of FMPs on average torque.

### 6.4.2 Experimental Validation

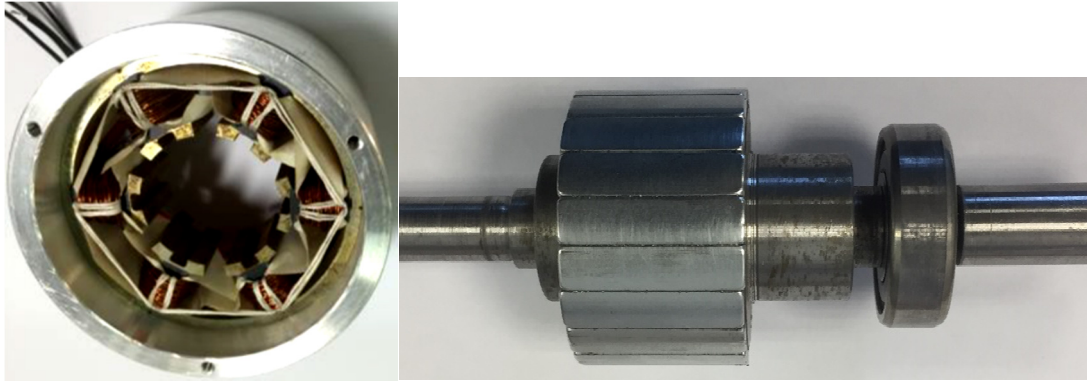
To further validate the analytical and FE analyses, a 6/10 FRPM prototype and a 6/10 Vernier prototype are manufactured and tested. Fig. 6.20 shows the machine prototypes, and Table 6.2 lists their parameters. It should be noted that the parameters of the prototypes are not strictly identical to the optimal FEA models when considering some practical manufacturing issues. The CAD drawings of the prototypes are given in Appendix A.



(a)

Fig. 6.20 Prototypes. (a) FRPM machine ( $N_s=6, N_r=10$ ). (b) Vernier machine ( $N_s=6, p_m=10$ ).

Fig. 6.21 (a) shows the measured and FE-predicted back-EMF waveforms of the two machines at  $n=400$ rpm. Besides, based on the back-EMF derivations shown in (6.14) and (6.16), the analytical-predicted back-EMF waveforms are also presented. Under the same slot filling factor, the number of series turns per phase is 64 for the FRPM machine, and it is 100 for the

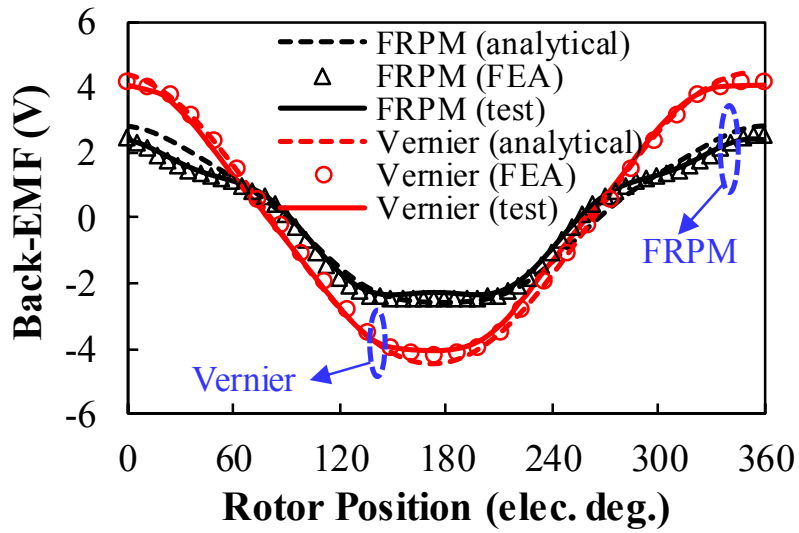


(b)

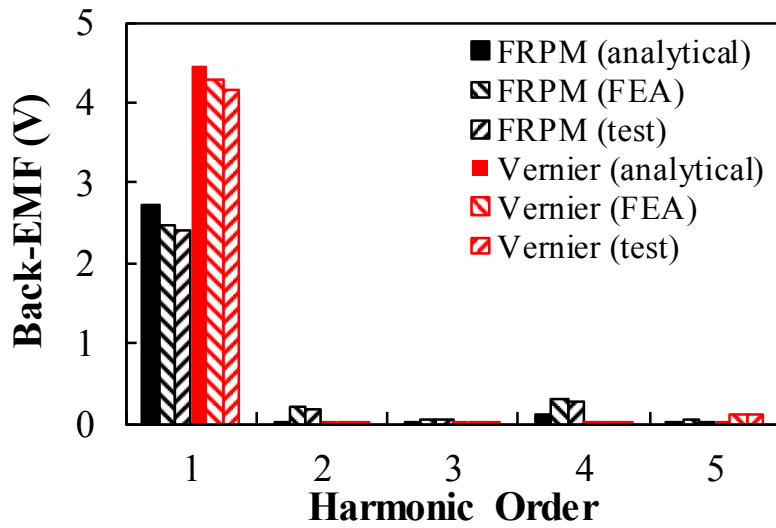
Vernier machine. As can be seen, for the 6/10 Vernier machine, the back-EMF waveforms match well with each other; for the 6/10 FRPM machine, the measured back-EMF waveform matches well with the FEA result while there are some deviations for the analytical result. The harmonic spectra of the back-EMFs are then shown in Fig. 6.21 (b). As can be seen, for the Vernier machine, its measured fundamental back-EMF is 4.17V, which is slightly lower than the FEA result (4.27V) and the analytical result (4.45V) due to the end-effect and manufacture imperfection. Besides the fundamental back-EMF component, the other harmonics are all negligible. For the FRPM machine, the measured fundamental back-EMF is 2.40V, which is slightly lower than the FEA result (2.48V) and the analytical result (2.73V). There are considerable 2<sup>nd</sup> and 4<sup>th</sup> harmonics in FE-predicted and tested back-EMFs, making the waveforms not sinusoidal. The lower magnitudes of the 2<sup>nd</sup> and 4<sup>th</sup> harmonics of the analytically predicted back-EMF are mainly because of the relatively imprecise expressions of the high-order permeance harmonics in the analytical derivations [GAO17a]. Despite of this, it is clear that the 6/10 Vernier machine has much higher fundamental back-EMF than the 6/10 FRPM machine.

Based on the cogging torque measurement method introduced in Appendix B, the cogging torque of each machine are measured and compared with those obtained in FEA. Due to the high rotor pole number and corresponding limited torque measurement point, only cogging torque waveforms without harmonic spectra are given. Fig. 6.22 shows the measured and FE-predicted cogging torque waveforms of the two machines. As can be seen, for both measured and FE-predicted cogging torques, the 6/10 FRPM machine has much larger peak to peak value than the 6/10 Vernier machine. In addition, the fundamental period of 3 of the 6/10 FRPM machine is verified.





(a)



(b)

Fig. 6.21 Measured and FE-predicted back-EMFs. ( $n=400\text{rpm}$ ) (a) Waveforms. (b) Harmonic spectra.

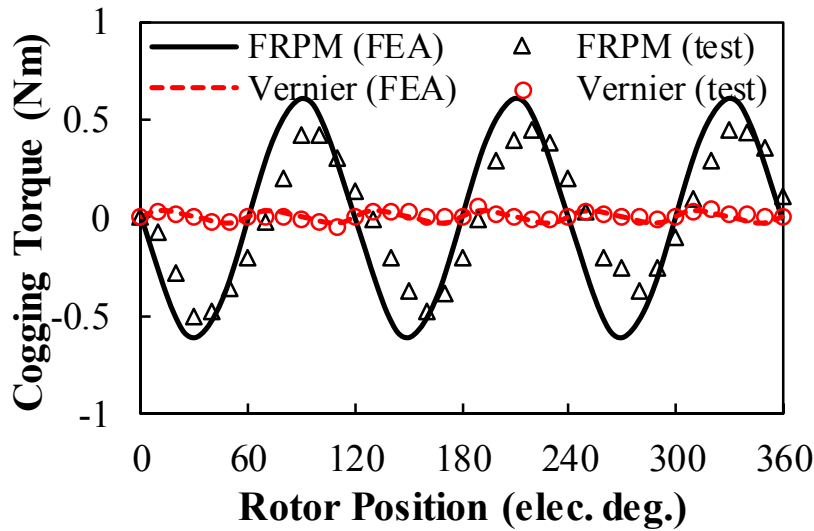


Fig. 6.22 Measured and FE-predicted cogging torques.

By supplying three-phase windings with fixed DC current ( $I_a=-2I_b=-2I_c=I_{dc}=0.6I_{rated}$ , and the rated current  $I_{rate}$  is corresponded to  $p_{cu}=20W$ ), the variations of static torque are measured and shown in Fig. 6.23. As can be seen, good agreements between the FEA results and test results can be observed. More importantly, the maximum measured torque of the Vernier machine is larger than that of the FRPM machine. The torque-current characteristics of the two machines are then measured, as shown in Fig. 6.24. Again, the measured torques match well with the FE-predicted torques, and within the whole current range, the Vernier machine has much higher torque than the FRPM machine. For example, when  $I=1$  p.u., the measured torque of the Vernier machine is 2.18Nm, which is 41% higher than that of the FRPM machine. Therefore, the higher torque density of the 6/10 Vernier machine over the 6/10 FRPM machine is verified.

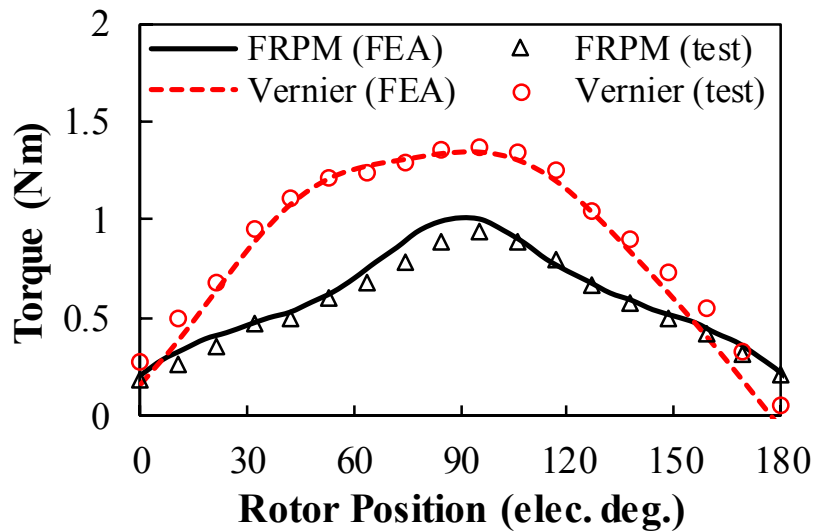


Fig. 6.23 Measured and FE-predicted static torques. ( $I_a=-2I_b=-2I_c=0.6I_{rated}$ )

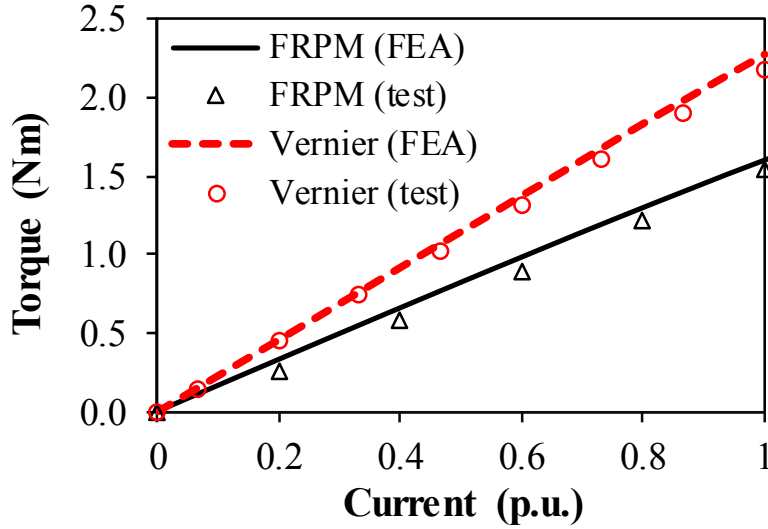


Fig. 6.24 Measured and FE-predicted torque-current characteristics.

## 6.5 Performance Summary of Various FRPM Machines and Vernier Machine

Although the 6/10 Vernier machine is proven to have better performance than the 6/10 FRPM machine, it should be noted that there are more feasible stator slot ( $N_s$ )/rotor pole ( $N_r$ ) combinations for FRPM machines while the stator slot ( $N_s$ )/rotor pole ( $p_m$ ) combinations for Vernier machine is relatively limited.

To maximise the torque of a Vernier machine with concentrated-windings,  $N_s$ ,  $p_m$ , the number of FMP of each stator tooth  $N_p$ , and the winding pole-pair number  $p_a$  should satisfy [TOB00]

$$N_p N_s - p_a = p_m \quad (6.20)$$

For example, when  $N_s=6$  and concentrated-windings are employed,  $p_a$  is normally selected as 2 to achieve a high armature field. Even if we consider a wide  $p_m$  range (e.g. from 5 to 15),  $p_m$  can only be 10 with  $N_p=2$ . In other words, 6/10 is the only feasible  $N_s/p_m$  combination for a 6-stator-slot Vernier machine when  $p_m$  is from 5 to 15. This can be verified since 6/10 is a very commonly used  $N_s/p_m$  combination in existing literatures of Vernier machine with concentrated windings [OKA13] [ONE16].

In contrast, for a FRPM machine, if the same  $p_m$  range of 5 to 15 is considered, there are many other feasible  $N_s/N_r$  combinations in addition to 6/10. For example, as analysed in Chapter 2, 6/10, 6/11, 6/13 and 6/14 are all preferred  $N_s/N_r$  combinations for a FRPM machine (with either NSNS-NSNS or NSNS-SNSN PM arrangement) to achieve a good performance.

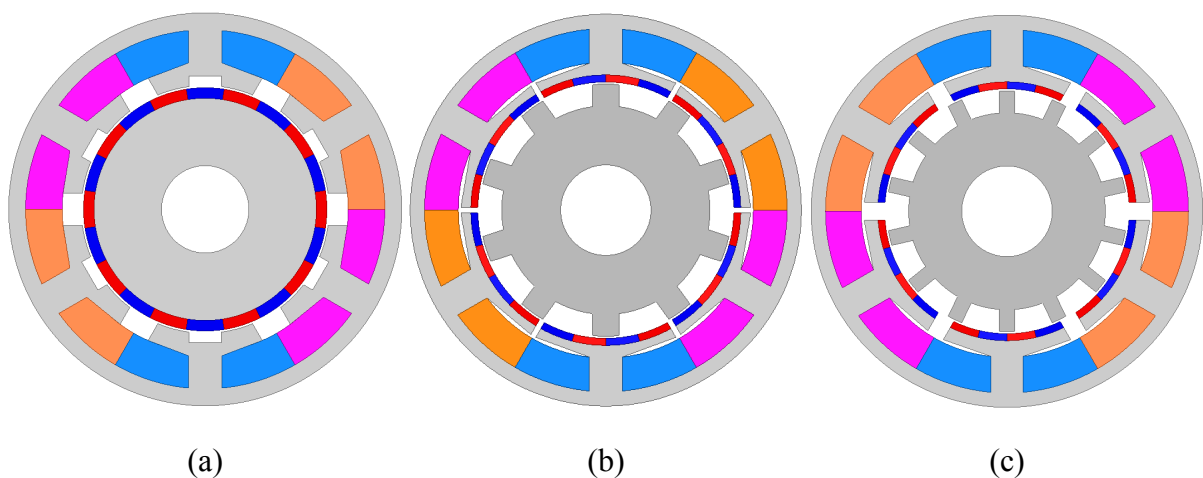
In addition, in the previous chapters of this thesis, some techniques and several novel machine topologies have been proposed to improve the performance of FRPM machine. Therefore, it would be interesting to know how these FRPM machines perform against the Vernier machine. Thus, based on the analyses in the previous chapters, some promising FRPM machines will be identified, and their performance will be summarised and compared with the 6/10 Vernier machine.

In Chapter 2, it has been proven that the 6/14 FRPM machine with NSNS-NSNS arrangement (designated as 6/14 FRPM machine) has the maximum torque density among various PM arrangements and  $N_s/N_r$  combinations.

In Chapter 4, it has been proven that for FRPM machines with consequent-pole PM structures, the 6/14 FRPM machine with N/Fe/N/Fe-N/Fe/N/Fe CPM structure (denoted as 6/14 CPM-FRPM machine) has the maximum torque density.

In Chapter 5, it has been proven that the 12/13 FRPM machine equipped with toroidal winding (denoted as 12/13 TW-FRPM machine) can improve the torque density significantly.

Therefore, these three promising FRPM machines are selected and compared with the original 6/10 Vernier machine and 6/10 FRPM machine. In addition, a conventional 12/8 SPM machine is also introduced as a reference to compare with other machines. As shown in Fig. 6.25, the six machines are all globally optimised using genetic algorithm for maximum torque under fixed effective copper loss of 20W. The machine parameters are listed in Table 6.4. As can be observed from Fig. 6.25, all the machines have a simple mechanical structure such as single air-gap, rigid stator, simple PM structure etc.



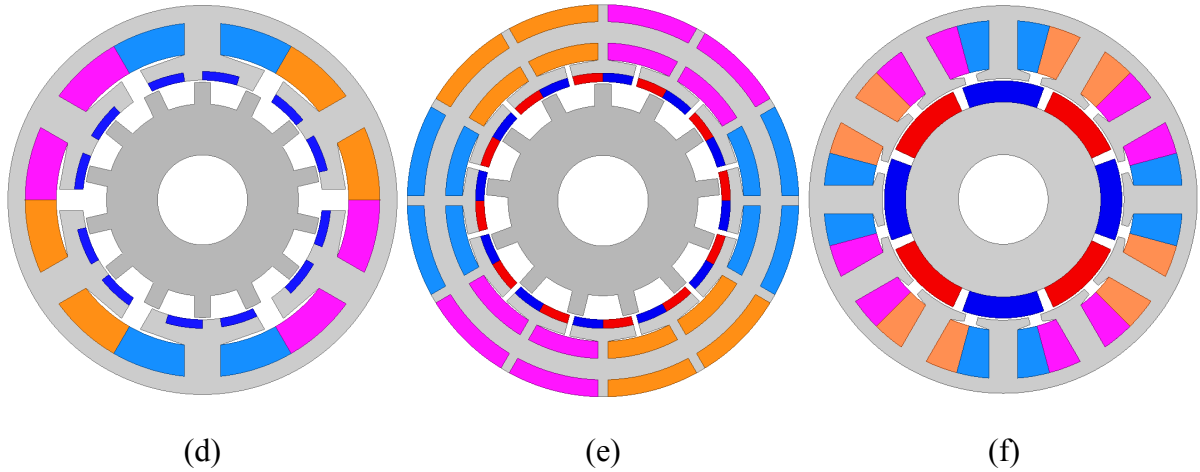


Fig. 6.25 Cross-sections of the machines. (a) 6/10 Vernier machine. (b) 6/10 FRPM machine. (c) 6/14 FRPM machine. (d) 6/14 CPM-FRPM machine. (e) 12/13 TW-FRPM machine. (f) 12/8 SPM machine.

The electromagnetic performance of the machines is summarised in Table 6.5. It should be noted that all the machines have the same stator outer diameter (90mm) and active axial length (25mm). Hence, the active volume  $V_{ac}$  is the same for all the machines, and the torque comparison results are equivalent to the torque density (i.e. torque per machine active volume) comparison results. As can be observed from Table 6.5, in comparison with the original 6/10 FRPM machine, the torque density of other three FRPM machines can be largely improved, making it competitive or even higher against that of the 6/10 Vernier machine and the 12/8 SPM machine. For example, the 6/14 FRPM machine has a torque density ( $T_{avg}/V_{ac}$ ) of  $17.0\text{kNm/m}^3$  and  $T_{avg}/V_{ac}$  of the 12/13 TW-FRPM machine is  $16.3\text{kNm/m}^3$ . Both are larger than that of the 12/8 SPM machine and exceed 90% of  $T_{avg}/V_{ac}$  of the 6/10 Vernier machine. Moreover, the 6/14 CPM-FRPM machine has the highest  $T_{avg}/V_{ac}$  among all the machines, thanks to the reduced reluctance for the armature field. In terms of the PM volume  $V_{PM}$ , it can be found that all the FRPM machines have smaller  $V_{PM}$  than the Vernier machine and the SPM machine due to the smaller PM thickness. Correspondingly, the torque per PM volume  $T_{avg}/V_{PM}$  of the machines are also calculated. As can be seen, in addition to the 6/10 FRPM machine, all other three FRPM machines have more than 20% higher  $T_{avg}/V_{PM}$  than the Vernier machine. The 6/14 CPM-FRPM machine has the highest  $T_{avg}/V_{PM}$  since its average torque is the highest and PM volume is the lowest. The 12/8 SPM machine has the lowest  $T_{avg}/V_{PM}$  since its PM volume is the highest, as shown in Table 6.5.

It should be noted that the comparison results in Table 6.5 are predicted based on the optimum machine models designed for the maximum torque density under the fixed copper loss.

However, as revealed in Fig. 6.4, the torque improvement against the PM thickness  $h_m$  is very limited when  $h_m$  is of a relatively large value. For example, for the 6/10 Vernier machine, the torque improvement is less than 5% when  $h_m$  increases from 1.2mm to 2mm. To demonstrate and compare the PM utilisation ratio (i.e.  $T_{avg}/V_{PM}$ ) of different machines more clearly, Table 6.6 compares the PM volume and PM utilisation ratio of the machines when the machines give the same output torque (1.86Nm). The PM thickness of each machine is adjusted from its optimum value to output the same torque. As can be seen, the 6/14 FRPM, the 6/14 CPM-FRPM, and the 12/13 TW-FRPM machines can still have a higher  $T_{avg}/V_{PM}$  than the 6/10 Vernier machine and the 12/8 SPM machine.

Table 6.4 Parameters of the Vernier, SPM, and FRPM machines (length units: mm)

	6/10 Vernier	6/10 FRPM	6/14 FRPM	6/14 CPM- FRPM	12/13 TW- FRPM	12/8 SPM
Stator outer diameter $D$				90		
Axial length $l$				25		
Air-gap length $g$				0.5		
Remanence of PM $B_r$				1.2T		
Relative permeability of PM $\mu_r$				1.05		
Thickness of stator yoke $t_{sy}$	3.9	3.3	3.3	4	4.9	3.4
Width of stator tooth $w_{st}$	7.8	7.6	7.4	8.4	2.2	6.7
Width of stator slot opening $w_{so}$	7.4	1.3	4.1	5	1.2	2.9
Stator inner radius $R_{si}$	28.4	31.1	29.7	29.7	29.0	28.0
PM thickness $h_m$	2.4	1.6	1.6	2	1.6	4.9
PM width ratio	--	--	--	0.66	--	--
Width of rotor tooth $w_{rt}$	--	6.0	3.5	3.8	3.8	--
Height of protruded stator tooth $h_{sp}$	--	--	--	--	3.9	--

Table 6.5 Performance comparison of Vernier, SPM, and FRPM machines

	6/10 Vernier	6/10 FRPM	6/14 FRPM	6/14 CPM- FRPM	12/13 TW- FRPM	12/8 SPM
Machine active volume $V_{ac}$ (mm <sup>3</sup> )	159043	159043	159043	159043	159043	159043
PM volume $V_{PM}$ (mm <sup>3</sup> )	10047	7291	7785	4968	6504	17183
Average Torque $T_{avg}$ (Nm)	2.89	1.86	2.71	2.94	2.60	2.42
Rated speed $n$ (r/min)	400	400	400	400	400	400
Power $P_{em}$ (W)	121.1	77.9	113.5	123.2	108.9	101.4
Torque per machine volume $T_{avg}/V_{ac}$ (kNm/m <sup>3</sup> )	18.2	11.7	17.0	18.5	16.3	15.2
Power per machine volume $P_{em}/V_{ac}$ (kW/m <sup>3</sup> )	761.2	489.9	713.7	774.3	684.8	637.4
Torque per PM volume $T_{avg}/V_{PM}$ (kNm/m <sup>3</sup> )	287.6	255.1	348.1	591.8	399.8	140.8
Power per PM volume $P_{em}/V_{PM}$ (kW/m <sup>3</sup> )	12049	10686	13990	24789	16745	5899

Table 6.6 Torque density of Vernier, SPM, and FRPM machines ( $T_{avg}=1.86\text{Nm}$ )

	6/10 Vernier	6/10 FRPM	6/14 FRPM	6/14 CPM- FRPM	12/13 TW- FRPM	12/8 SPM
PM thickness $h_m$ (mm)	0.54	1.6	0.46	0.7	0.55	0.8
PM volume $V_{PM}$ ( $\text{mm}^3$ )	2318	7291	1826	1781	2281	3035
Torque per PM volume $T_{avg}/V_{PM}$ ( $\text{kNm}/\text{m}^3$ )	801.8	255.1	1020.5	1047.2	814.9	612.2
Power per PM volume $P_{em}/V_{PM}$ ( $\text{kW}/\text{m}^3$ )	33587	10654	42746	43866	34135	25644

## 6.6 Conclusion

In this chapter, a conventional 6/10 FRPM machine and a conventional 6/10 Vernier machine are analysed and compared in detail based on the unified theory of airgap field modulation. In addition, based on the investigations in the previous chapters, several promising FRPM machines are also identified and compared with the Vernier machine. Some findings can be summarised as follows:

1. The fundamental PM MMF together with all permeance harmonics contribute to the torque production of Vernier machine whereas all PM MMF harmonics but only the fundamental permeance in FRPM machine produces the torque.
2. For Vernier and FRPM machines having the same stator slot/rotor pole combination (6/10 in this study), the Vernier machine tends to have higher torque density than the FRPM machine, thanks to the utilised large DC component of airgap permeance.
3. The performance of FRPM machine is more sensitive to the design parameters, e.g. the PM thickness and the slot width ratio of FMPs, since the fundamental component of airgap permeance is more sensitive to these parameters in comparison with the DC component.
4. The FRPM machine has more feasible  $N_s/N_r$  combinations while the  $N_s/p_m$  combinations of the Vernier machine are relatively limited. By using the identified optimal  $N_s/N_r$  combination (i.e. 6/14) or other effective torque improvement techniques (including



consequent-pole PM structure and toroidal winding), the FRPM machine can have competitive or even higher torque density than the Vernier machine. Meanwhile, its PM volume can be largely reduced when compared with the Vernier machine.

# CHAPTER 7

## GENERAL CONCLUSIONS AND FUTURE WORK

### 7.1 General Conclusions

This thesis presents a comprehensive investigation into a promising machine category, i.e. the flux reversal permanent magnet machines, for low-speed and high-torque direct drive applications. The advantages of the FRPM machines are summarised as follows:

- With high-energy-product PMs adopted, the FRPM machines can exhibit higher torque density and efficiency than those machines without PMs, such as the switched reluctance machines, the induction machines, and the wound-field machines etc.;
- As a member of the stator-PM machines, the rotor of the FRPM machines is of a simple salient pole structure and both the armature windings and PMs are accommodated on stator-side, which enable a more robust rotor and a more effective heat management when compared to the rotor-PM machines;
- Since the PMs are mounted on the inner surface of the stator, the mechanical structure of the stator is simpler and more rigid when compared to the other stator-PM machines in which a modular stator structure is required, or PMs are placed on stator slot-openings.

The working mechanism of FRPM machines is thoroughly analysed in this thesis, and various aspects of improving the torque performance of FRPM machines are investigated. Several novel FRPM machine topologies are proposed for the first time. Some findings and conclusions are detailed below.

#### 7.1.1 Working Mechanism and analysis methods of FRPM machines

The salient pole rotor structure of the FRPM machines produces a certain permeance distribution in the air-gap, thus modulating the PM MMF and armature MMF. Correspondingly, both the air-gap PM field and armature field are rich of harmonics, Fig. 2.9.

There are mainly two perspectives to analyse the working mechanism of the FRPM machines, i.e. from the interaction between the PM field and the armature field and from the interaction between the back EMF and the current, respectively.

From the perspective of interaction between the PM field and the armature field, the harmonic

pairs of the air-gap PM field and armature field having the same pole-pair number and rotational speed can produce a steady torque component. With the obtained radial and tangential components of the air-gap fields in FEA, the Maxwell stress tensor (see (2.3)) can be used to identify the working field harmonics and quantify their contributions to the torque production. It is found that the torque of the FRPM machines is contributed by several working field harmonics, rather than one working field harmonic as in the conventional PMSMs, Fig. 2.17.

From the perspective of interaction between the back EMF and the current, the no-load air-gap PM field can be derived based on the PM MMF-permeance analytical model (see (3.1)). Then, by directly integrating the PM field under the corresponding stator teeth, the flux linkage and back-EMF of the stator coils can be obtained. As detailed in Chapter 3 and Chapter 6, the fundamental back-EMF  $E_A$  of a coil can be expressed as

$$E_A = \sum_{i=1,2,3\dots}^{\infty} E_i = n_c l R_{st} \Omega_r \Lambda_1 \sum_{i=1,2,3\dots}^{\infty} w_i^f F_i \quad (7.1)$$

It is found that

- All PM MMF harmonics  $F_i$  but only the fundamental permeance  $\Lambda_1$  produces the fundamental back-EMF;
- Different PM MMF harmonics have different contributions to the fundamental back-EMF, which can be characterised by the unique weight factor  $w_i^f$  of each PM MMF harmonic;
- The fundament back-EMF of a FRPM machine is largely related to the  $N_s/N_r$  combination and PM arrangement method, since  $\Lambda_1$  is influenced by  $N_r$  (see (3.7)),  $w_i^f$  is influenced by both  $N_s$  and  $N_r$  (see (6.15)), and  $F_i$  is influenced by PM arrangement, such as the number of PM pieces on each stator tooth (see (3.3));

Therefore, for a given FRPM machine, its back-EMF contribution of each PM MMF harmonic can be quantified, e.g. the magnitude, weight factor, and resulted back-EMF contribution of each  $F_i$  of a conventional 6/10 FRPM machine are shown in Fig. 6.2.

Despite the advantages aforementioned, the topology evolution and torque improvement are of great significance in further boosting the competitiveness of the FRPM machines, due to the relatively lower torque density compared to some popular PM machine topologies. For example, as pointed out in [CHE11a], the conventional FRPM machines are more likely to

have lower torque density than the switched flux PM machines since the larger equivalent air-gap length (resulted from the SPM structure) may deteriorate the rotor-tooth modulation effect. In this thesis, based on the unified air-gap field modulation theory, the conventional FRPM machines are compared with another popular machine topology, i.e. the Vernier PM machines. As presented in Chapter 6, it is revealed that unlike the FRPM machines, the large DC permeance component  $\Lambda_0$  contributes to the back-EMF production in a Vernier machine, making the torque density of a conventional FRPM machine always inferior to the Vernier machine (see Fig. 6.2 and Fig. 6.3). Under the same machine dimensions ( $D=90\text{mm}$ ,  $l=25\text{mm}$ ) and copper loss ( $p_{cu}=20\text{W}$ ), a conventional FRPM machine and a Vernier machine with the same  $N_s/N_r$  combination (i.e. 6/10) are optimised for maximum torque, and their torque performance is summarised in Table 7.1. It shows that the torque density (per active volume) of the 6/10 FRPM machine is 36% lower than that of the 6/10 Vernier machine. Again, this highlights the significance of torque improvement of the FRPM machines.

### 7.1.2 Developed FRPM Machine Topologies

In this thesis, several novel FRPM machine topologies are proposed and analysed for the first time, including the machines with various CPM topologies and the machines with TWs. The FRPM machines with different CPM topologies are proposed and compared in Chapter 4. It is found that the CPM-FRPM machines may have higher torque density over the SPM machines, thanks to the improved armature field and enhanced air-gap field modulation effect (see Fig. 4.4). However, the torque improvement of the CPM-FRPM machines is largely influenced by  $N_s/N_r$  combination due to the different equivalent pole-pair numbers and saturation conditions (see Fig. 4.6). Among various CPM topologies, the 6/14 N/Fe/N/Fe-N/Fe/N/Fe CPM-FRPM machine is proven to have the highest torque density (see Fig. 4.23). In order to achieve the high pitch factor and short end-windings simultaneously, the FRPM machine equipped with toroidal windings is also proposed and analysed (see Chapter 5). Based on the established PM MMF-permeance model for the conventional FRPM machines with concentrated windings, it is found the preferred  $N_s/N_r$  combinations are inherently accompanied by a very low pitch factor (see Fig. 5.2). By using toroidal windings in these  $N_s/N_r$  combinations, the pitch factor can be largely improved while the end-windings are even shorter. For example, the 12/13 TW-FRPM machine is proven to have 79% higher torque density than the 12/13 CW-FRPM machine while its efficiency and power factor are also higher (see Fig. 5.15, Fig. 5.19, and Fig. 5.21).

The developed topologies in this thesis enrich the diversity of FRPM machines, and some topologies are proven to exhibit better performance than the conventional FRPM machines.

### 7.1.3 Performance Improvement and Comparison

In addition to the newly developed FRPM machine topologies, various aspects of improving the torque density of the conventional FRPM machines are investigated, from which some effective approaches are identified.

Four conventional PM arrangements of the FRPM machines are analysed and compared in Chapter 2. It is found that the  $N_s/N_r$  combination greatly affects the torque density of a FRPM machine, regardless of PM arrangements (see Fig. 2.18 and Fig. 2.22). In terms of the PM polarities of adjacent teeth, it is revealed that the opposite PM polarities of adjacent teeth rather than the identical one is preferred, since the concentrated PM field harmonic contents are more likely to be fully interacted with the armature field. For example, the NSNS-NSNS PM arrangement has 17% higher torque density than the NSNS-SNSN PM arrangement (see Fig. 2.17 and Table 2.3). Besides, the 6/14 NSNS-NSNS FRPM machine is proven to exhibit the highest torque density among the FRPM machines with four PM arrangements and various  $N_s/N_r$  combinations (see Fig. 2.30). The optimal number of PM pieces on single stator tooth ( $n_{pp}$ ) of a FRPM machine is also identified. Based on the unified PM MMF-permeance analytical model, it is found that there always exists an optimal  $n_{pp}$  to maximise the electromagnetic torque (see Fig. 3.4). Correspondingly, the rotor pole number also varies against  $n_{pp}$  (see (3.18)). For example, for the FRPM machines with  $N_s=6$ , the optimal  $n_{pp}$  is proven to be 3 and the optimal 6/20 FRPM machine (i.e.  $n_{pp}=3$ ) can have 76% higher average torque over the conventional 6/8 FRPM machine (i.e.  $n_{pp}=1$ ), thanks to the additional contribution by *Auxiliary* PM MMF (see Fig. 3.31 and Table 3.2).

Moreover, the performance of various FRPM machines are summarised and compared with the popular 6/10 Vernier and 12/8 SPM machines in Table 7.1. As can be seen, the 6/14 NSNS-NSNS FRPM machine can improve the torque density over the original 6/10 NSNS-NSNS FRPM machine by 45%. Although its torque density is still 6% lower than that of the 6/10 Vernier machine, its torque per PM volume is much higher (27.3% higher) due to the reduced PM volume. In addition, the 6/14 NSNS-NSNS FRPM machine has a better performance over the 12/8 SPM machine in terms of both torque density and PM utilisation ratio. In comparison with the 6/14 SPM-FRPM machine, the CPM-FRPM machine offers advantages of high average torque and less PM volume. It is found that the torque density of the 6/14 CPM-FRPM

machine is even higher than the 6/10 Vernier machine while its PM volume is largely reduced, resulting in a 30.6% higher torque per PM volume. Besides, the torque density of the 12/13 TW-FRPM machine reaches over 90% of that of the 6/10 Vernier machine while its torque per PM volume is slightly higher.

Therefore, it can be concluded that the investigation conducted in this thesis is a useful guidance in analysing and designing high-performance FRPM machines. With the deep understanding and investigation of the working mechanism and various torque improvement approaches, several promising FRPM machine topologies have been identified, which can have competitive or even higher torque density against other popular machine topologies, e.g. the Vernier machine and the SPM machine. Meanwhile, the PM volume of the FRPM machines are much lower. It should be noted that the investigations and conclusions in this thesis are based on specified machine dimensions (i.e. active stator diameter  $D=90\text{mm}$  and active length  $l=25\text{mm}$ ). It would be expected that the influence of machine size and working condition on machine performance may vary for different machines. For example, when the machine size is larger, the electric loading of the machine is also higher (a fixed current density is assumed) [KIR15], thus causing a severer saturation and restricting the torque density of those machines with a relatively larger inductance, such as CW-FRPM machines (see Fig. 4.32) and TW-FRPM machines (see Fig. 5.17). However, the working mechanisms and various torque improvement concepts of FRPM machines presented in this thesis are still applicable for different machine dimensions. For a different machine size or working condition, the different machine topologies can still be assessed and compared according to the analysis approaches introduced in this thesis.

It is believed that with the ever-increasing torque performance and other inherent advantages, the FRPM machines would be a very promising machine candidate for assorted low-speed, high-torque direct-drive applications.

Table 7.1 Performance comparison of Vernier, SPM, and FRPM machines

	6/10 Vernier	6/10 FRPM	6/14 FRPM	6/14 CPM- FRPM	12/13 TW- FRPM	12/8 SPM
Machine active volume $V_{ac}$ (mm <sup>3</sup> )	159043	159043	159043	159043	159043	159043
Average torque $T_{avg}$ (Nm)	2.89	1.86	2.71	2.94	2.60	2.42
Torque per machine volume $T_{avg}/V_{ac}$ (kNm/m <sup>3</sup> )	18.2	11.7	17.0	18.5	16.3	15.2
PM volume $V_{PM}$ when output torque is 1.86Nm (mm <sup>3</sup> )	2318	7291	1826	1781	2281	3035
Torque per PM volume $T_{avg}/V_{PM}$ when output torque is 1.86Nm (kNm/m <sup>3</sup> )	801.8	255.1	1020.5	1047.2	814.9	612.2

## 7.2 Future Works

Based on the investigation in this thesis, some future works could be proposed as follows:

- Combining different torque improvement methods to further increase the torque density of the FRPM machines, e.g. using toroidal windings in CPM-FRPM machines;
- Investigating the influence of various rotor pole shaping methods on average torque and torque ripple;
- Investigation of parasitic effect in FRPM machines, such as PM eddy current loss, magnetic force on PMs, noise and vibration etc;
- Improvement of power factor of FRPM machines, such as dual-rotor topology;
- Extending various radial-field single air-gap FRPM machine topologies to other machine types, e.g. using toroidal windings in axial-field FRPM machines where dual air-gaps are always adopted.

## REFERENCES

- [ATA01] K. Atallah, and D. Howe, "A novel high-performance magnetic gear," *IEEE Trans. Magn.*, vol. 37, no. 41, pp. 2844–2846, Jul. 2001.
- [ATA08] K. Atallah, J. Rens, S. Mezani, and D. Howe, "A novel 'pseudo' direct-drive brushless permanent magnet machine," *IEEE Trans. Magn.*, vol. 44, no. 12, pp. 4605–4617, Nov. 2008.
- [ATA12] K. Atallah, J. Wang, S. D. Calverley, and S. Duggan, "Design and operation of a magnetic continuously variable transmission," *IEEE Trans. Ind. Appl.*, vol. 48, no. 4, pp. 1288–1295, May 2012.
- [BIA06] N. Bianchi, S. Bolognani, M. D. Pr e, and G. Grezzani, "Design considerations for fractional-slot winding configurations of synchronous machines," *IEEE Trans. Ind. Appl.*, vol. 42, no. 4, pp. 997–1006, Aug. 2006.
- [BOL02] I. Boldea, J. Zhang, and S. A. Nasar, "Theoretical characterization of flux reversal machine in low speed servo drives-the pole-PM configuration," *IEEE Trans. Ind. Appl.*, vol. 38, no. 6, pp. 1549–1557, Dec. 2002.
- [BOL14] I. Boldea, L. N. Tutelea, L. Parsa, and D. Dorrell, "Automotive electric propulsion systems with reduced or no permanent magnets: An overview," *IEEE Trans. Ind. Electron.*, vol. 61, no. 10, pp. 5696–5711, Oct. 2014.
- [BOL96] I. Boldea, E. Serban, and R. Babau, "Flux-reversal stator-PM single phase generator with controlled DC output," in *Proc. OPTIM'96*, vol. 4, Brasov, Romania, 1996, pp. 1124–1134.
- [BOR14] A. Borisavljevic, S. Jumayev, and E. Lomonova, "Toroidally-wound permanent magnet machines in high-speed applications," in *Int. Conf. Elect. Mach. (ICEM 2014)*, Berlin, Germany, 2014, pp. 2588–2593.
- [CHA07a] K.T. Chau and C.C. Chan, "Emerging energy-efficient technologies for hybrid electric vehicles," *Proc. IEEE*, Vol. 95, No. 4, pp. 821–835, Apr. 2007.
- [CHA07b] C.C. Chan, "The state of the art of electric, hybrid, and fuel cell vehicles," *Proc. IEEE*, Vol. 95, No. 4, pp. 704–718, Apr. 2007.
- [CHA07c] K. T. Chau, Z. Dong, J. Z. Jiang, C. H. Liu, and Y. J. Zhang, "Design of a magnetic-gearred outer-rotor permanent-magnet brushless motor for electric vehicles," *IEEE Trans. Magn.*, vol. 43, no. 6, pp. 2504–2506, Jun. 2007.
- [CHE00a] J. Y. Chen, C. V. Nayar, and L. Y. Xu, "Design and finite-element analysis of an outer-rotor permanent-magnet generator for directly coupled wind turbines," *IEEE Trans. Magn.*, vol. 36, no. 5, pp. 3802–3809, Sep. 2000.
- [CHE00b] M. Cheng, K. T. Chau, C. C. Chan, E. Zhou, and X. Huang, "Nonlinear varying-network magnetic circuit analysis for doubly salient permanent magnet motors," *IEEE Trans. Magn.*, vol. 36, pp. 339–348, Jan. 2000.
- [CHE10a] J. T. Chen and Z. Q. Zhu, "Winding configurations and optimal stator and rotor pole combination of flux-switching PM brushless AC machines," *IEEE Trans. Energy Convers.*, vol. 25, no. 2, pp. 293–302, Jun. 2010.



- [CHE10b] J. T. Chen and Z. Q. Zhu, "Comparison of all- and alternate-poles-wound flux-switching pm machines having different stator and rotor pole numbers," *IEEE Trans. Ind. Appl.*, vol. 46, no. 4, pp. 1406–1415, Jul./Aug. 2010.
- [CHE11a] M. Cheng, W. Hua, J. Zhang, and W. Zhao, "Overview of stator-permanent magnet brushless machines," *IEEE Trans. Ind. Electron.*, vol. 58, no. 11, pp. 5087–5101, Nov. 2011.
- [CHE11b] J. T. Chen, Z. Q. Zhu, S. Iwasaki, and R. P. Deodhar, "Influence of slot opening on optimal stator and rotor pole combination and electromagnetic performance of switched-flux PM brushless AC machines," *IEEE Trans. Ind. Appl.*, vol. 47, no. 4, pp. 1681–1691, Jul./Aug. 2011.
- [CHE11c] J. T. Chen, Z. Q. Zhu, S. Iwasaki, and R. P. Deodhar, "A novel E-core switched-flux PM brushless AC machine," *IEEE Trans. Ind. Appl.*, vol. 47, no. 3, pp. 1273–1282, May/Jun. 2011.
- [CHE11d] J. T. Chen, Z. Q. Zhu, S. Iwasaki, and R. P. Deodhar, "A novel hybrid-excited switched-flux brushless AC machine for EV/HEV applications," *IEEE Trans. Veh. Technol.*, vol. 60, no. 4, pp. 1365–1373, May 2011.
- [CHE14] Y. Chen, W. N. Fu, S. L. Ho, and H. Liu, "A quantitative comparison analysis of radial-flux, transverse-flux, and axial-flux magnetic gears," *IEEE Trans. Magn.*, vol. 50, no.11, Nov. 2014, Art. ID 8104604.
- [CHE17] M. Cheng, P. Han, and W. Hua, "General airgap field modulation theory for electrical machines," *IEEE Trans. Ind. Electron.*, vol. 64, no.8, pp. 6063-6074, Aug. 2017.
- [CHU07] S. U. Chung, D. H. Kang, J. H. Chang, J. W. Kim, and J. Y. Lee, "New configuration of flux reversal linear synchronous motor," in *Int. Conf. Elect. Mach. Syst. (ICEMS 2007)*, Seoul, South Korea, 2007, pp. 864–867.
- [CHU08] S. Chung, H. Lee, and S. Hwang, "A novel design of linear synchronous motor using FRM topology," *IEEE Trans. Magn.*, vol. 44, no. 6, pp. 1514–1517, Jun. 2008.
- [CHU11] S. Chung, J. Kim, B. Woo, D. Hong, J. Lee, and D. Koo, "A novel design of modular three - phase permanent magnet Vernier machine with consequent pole rotor," *IEEE Trans. Magn.*, vol. 47, no. 10, pp. 4215 - 4218, Oct. 2011
- [CHU12] S. Chung, J. Kim, D. Koo, B. Woo, D. Hong, and J. Lee, "Fractional slot concentrated winding permanent magnet synchronous machine with consequent pole rotor for low speed direct drive," *IEEE Trans. Magn.*, vol. 48, no. 11, pp. 2965–2968, Nov. 2012
- [CHU13] S. U. Chung, Y. Do Chun, B. C. Woo, D. K. Hong, and J. Y. Lee, "Design considerations and validation of permanent magnet Vernier machine with consequent pole rotor for low speed servo applications," *J. Elect. Eng. Technology*, vol. 8, no. 5, pp. 1146–1151, Sep. 2013.
- [CHU15] S. U. Chung, J. W. Kim, Y. D. Chun, B. C. Woo, and D. K. Hong, "Fractional slot concentrated winding PMSM with consequent pole rotor for a low-speed direct drive: reduction of rare earth permanent magnet," *IEEE Trans. Energy Convers.*, vol. 30, no.1, pp. 103-109, Mar. 2015.

- [CRI15] J. M. Crider and S. D. Sudhoff, "An inner rotor flux-modulated permanent magnet synchronous machine for low-speed high-torque applications," *IEEE Trans. Energy Convers.*, vol. 30, no. 3, pp. 1247–1254, Sep. 2015.
- [DEO97] R. Deodhar, S. Andersson, I. Boldea, and T. J. E. Miller, "The flux reversal machine: A new brushless doubly-salient permanent magnet machine," *IEEE Trans. Ind. Appl.*, vol. 33, no. 4, pp. 925–934, Jul. 1997.
- [DOR10] D. G. Dorrell, M. Popescu, and D. M. Ionel, "Unbalanced magnetic pull due to asymmetry and low-level static rotor eccentricity in fractional-slot brushless permanent-magnet motors with surface-magnet and consequent-pole rotors," *IEEE Trans. Magn.*, vol. 46, no. 7, pp. 2675–2685, Jul. 2010.
- [EMA08] A. Emadi, Y. J. Lee, and K. Rajashekar, "Power electronics and motor drives in electric, hybrid electric, and plug-in hybrid electric vehicles," *IEEE Trans. Ind. Electron.*, vol. 55, no. 6, pp. 2237–2245, Jun. 2008.
- [FRA15] T. V. Frandsen, L. Mathe, N. I. Berg, R. K. Holm, T. N. Matzen, P. O. Rasmussen, and K. K. Jensen, "Motor integrated permanent magnet gear in a battery electrical vehicle," *IEEE Trans. Ind. Appl.*, vol. 51, no. 2, pp. 1516–1525, Mar. 2015.
- [FU16] W. N. Fu and Y. Liu, "A unified theory of flux-modulated electric machines," in *Int. Symp. Elect. Eng. (ISEE 2016)*, Hong Kong, China, 2016.
- [GAO16a] Y. Gao, R. Qu, D. Li, J. Li, and L. Wu, "Design of three-phase flux-reversal machines with fractional-slot windings," *IEEE Trans. Ind. Appl.*, vol. 52, no. 4, pp. 2856–2864, Jul. 2016.
- [GAO16b] Y. Gao, R. Qu, D. Li, J. Li, and G. Zhou, "Consequent-pole flux-reversal permanent-magnet machine for electric vehicle propulsion," *IEEE Trans. Appl. Supercond.*, vol. 26, no. 4, Jun. 2016.
- [GAO17a] Y. Gao, R. Qu, D. Li, and J. Li, "Design procedure of flux reversal permanent magnet machines," *IEEE Trans. Ind. Appl.*, vol. 53, no. 5, pp. 4232–4241, Apr. 2017.
- [GAO17b] Y. Gao, R. Qu, D. Li, and J. Li, "Torque performance analysis of three-phase flux reversal machines," *IEEE Trans. Ind. Appl.*, vol. 53, no. 3, pp. 2110–2119, Mar. 2017.
- [GAO18a] Y. Gao, D. Li, R. Qu, and Z. Liang, "Analysis of novel flux reversal permanent-magnet machine with multi MMF working harmonics," in *IEEE Energy Conv. Congress Expo. (ECCE 2018)*, Portland, OR, 2018, pp. 6484–6491.
- [GAO18b] Y. Gao, D. Li, R. Qu, X. Fan, J. Li, and H. Ding, "A novel hybrid excitation flux reversal machine for electric vehicle propulsion," *IEEE Trans. Veh. Technol.*, vol. 67, no. 1, pp. 171–182, Jan. 2018.
- [GAU12] B. Gaussens, E. Hoang, O. De La Barrière, J. Saint-Michel, M. Lecrivain, and M. Gabsi, "Analytical approach for air-gap modeling of field-excited flux-switching machine: No-load operation," *IEEE Trans. Magn.*, vol. 48, no. 9, pp. 2505–2517, 2012.
- [GE16] X. Ge, Z. Q. Zhu, J. Li, and J. T. Chen, "A spoke-type IPM machine with novel alternate airspace barriers and reduction of unipolar leakage flux by step-

- staggered rotor,” *IEEE Trans. Ind. Appl.*, vol. 52, no. 6, pp. 4789–4797, Nov. 2016.
- [GER10] J. F. Gieras, *Permanent magnet motor technology*, 3<sup>rd</sup> ed. Boca Raton, FL: CRC Press, 2010.
- [GHA17] M. Ghasemian, F. Tahami, and G. Reza zadeh, “A comparative analysis of permanent magnet flux reversal generators with distributed and concentrated winding,” in *Annu. Conf. IEEE Ind. Electron. Soc. (IECON 2017)*, Beijing, China, 2017, pp. 1657–1661.
- [HAN03] D. Hanselman, *Brushless permanent magnet motor design*, 2<sup>nd</sup> ed. Lebanon, OH: Magna Physis, 2003.
- [HEL09] R. Hellinger and P. Mnich, “Linear motor-powered transportation: History, present status, and future outlook,” *Proc. IEEE*, vol. 97, no. 11, pp. 1892–1900, Nov. 2009.
- [HEN10] J. R. Hendershot and T. J. E. Miller, *Design of brushless permanent-magnet machines*, 3<sup>rd</sup> ed. Venice, FL: Motor Design Books LLC, 2010.
- [HO11] S. L. Ho, S. Niu, and W. N. Fu, “Design and comparison of Vernier permanent magnet machines,” *IEEE Trans. Magn.*, vol. 47, no. 10, pp. 3280–3283, Oct. 2011.
- [HOA97] E. Hoang, H. B. Ahmed, and J. Lucidarme, “Switching flux permanent magnet polyphased synchronous machines,” in *Eur. Conf. power Electron. Appl. (EPE 97)*, Trondheim, Norway, 1997.
- [HUA05] W. Hua, Z. Q. Zhu, M. Cheng, Y. Pang, and D. Howe, “Comparison of flux-switching and doubly-salient permanent magnet brushless machines,” in *Int. Conf. Elect. Mach. Syst. (ICEMS 2005)*, Nanjing, China, 2005.
- [HUA10] W. Hua, Z. Z. Wu, and M. Cheng, “A novel three-phase flux-reversal permanent magnet machine with compensatory windings,” in *Int. Conf. Elect. Mach. Syst. (ICEMS 2010)*, Incheon, South Korea, 2010, pp. 1117–1121.
- [HUA15] W. Hua, P. Su, M. Shi, G. Zhao, and M. Cheng, “The influence of magnetizations on bipolar stator surface-mounted permanent magnet machines,” *IEEE Trans. Magn.*, vol. 51, no. 3, Mar. 2015.
- [HUA17a] W. Hua, W. Huang, and F. Yu, “Improved model-predictive-flux-control strategy for three-phase four-switch inverter-fed flux-reversal permanent magnet machine drives,” *IET Electr. Power Appl.*, vol. 11, no. 5, pp. 717–728, May 2017.
- [HUA17b] L. R. Huang, J. H. Feng, S. Y. Guo, J. X. Shi, W. Q. Chu, and Z. Q. Zhu, “Analysis of torque production in variable flux reluctance machine,” *IEEE Trans. Energy Convers.*, vol. 32, no. 4, pp. 1297–1308, Dec. 2017.
- [HUA18] W. Hua, X. Zhu, and Z. Wu, “Influence of coil pitch and stator-slot/rotor-pole combination on back-EMF harmonics in flux-reversal permanent magnet machines,” *IEEE Trans. Energy Convers.*, vol. 33, no. 3, pp. 1330–1341, Sept. 2018.
- [HUS16] E. K. Hussain, K. Atallah, M. O. R. S. Dragan, R. E. Clark, and M. S. Sheffield, “Pseudo direct drive electrical machines for flight control surface actuation,”

in *IET Int. Conf. Power Electron. Mach. Drives (PEMD 2016)*, Glasgow, UK, 2016.

- [HUS17] T. Husain, I. Hasan, Y. Sozer, I. Husain, and E. Muljadi, “A comprehensive review of permanent magnet transverse flux machines for direct drive applications,” in *IEEE Energy Conv. Congress Expo. (ECCE 2017)*, Cincinnati, OH, 2017, pp. 1255-1262.
- [IFE12] C. J. Ifedi and B. C. Mecrow and J. D. Widmer and G. J. Atkinson and S. T. M. Brockway and D. Kostic-Perovic, “A high torque density, direct drive in-wheel motor for electric vehicles”, in *IET Int. Conf. Power Electron. Mach. Drives (PEMD 2012)*, Bristol, UK, 2012.
- [ISH06] D. Ishak, Z. Q. Zhu, and D. Howe, “Comparison of PM brushless motors, having either all teeth or alternate teeth wound,” *IEEE Trans. Energy Convers.*, vol. 21, no. 1, pp. 95–103, Mar. 2006.
- [IWA94] N. Iwabuchi, A. Kawahara, and T. Kume, “A novel high-torque reluctance motor with rare-earth magnet,” *IEEE Trans. Ind. Appl.*, vol. 30, no. 3, May 1994.
- [JAH17] T. Jahns, “Getting rare-earth magnets out of EV traction machines: A review of the many approaches being pursued to minimize or eliminate rare-earth magnets from future EV drivetrains,” *IEEE Electrific. Mag.*, vol. 5, no. 1, pp. 6-18, Mar. 2017
- [JEN12] B. B. Jensen, A. G. Jack, G. J. Atkinson, and B. C. Mecrow, “Performance of a folded-strip toroidally wound induction machine,” *IEEE Trans. Ind. Electron.*, vol. 59, no. 5, pp. 2217–2226, May 2012.
- [JIA09a] L. N. Jian, K. T. Chau, Y. Gong, J. Z. Jiang, C. Yu, and W. L. Li, “Comparison of coaxial magnetic gears with different topologies,” *IEEE Trans. Magn.*, vol. 45, no.10, pp. 4526-4529, Oct. 2009.
- [JIA09b] L. Jian and K. T. Chau, “A novel electronic-continuously variable transmission propulsion system using coaxial magnetic gearing for hybrid electric vehicles,” *J. Asian Electr. Veh.*, vol. 7, no. 2, pp. 1291–1296, Dec. 2009.
- [JIA09c] L. Jian, K. T. Chau, and J. Z. Jiang, “A magnetic-gear outer-rotor permanent-magnet brushless machine for wind power generation,” *IEEE Trans. Ind. Appl.*, vol. 45, no. 3, pp. 954–962, May 2009.
- [JIA11] L. Jian, K. T. Chau, and C. C. Chan, “Analytical method for magnetic field calculation in a low-speed permanent-magnet harmonic machine,” *IEEE Trans. Energy Convers.*, vol. 26, no. 3, pp. 862–870, Sept. 2011.
- [JIA12] L. Jian, W. Gong, G. Xu, J. Liang, and W. Zhao, “Integrated magnetic-gear machine with sandwiched armature stator for low-speed large-torque applications,” *IEEE Trans. Magn.*, vol. 48, no. 11, pp. 4184–4187, Nov. 2012.
- [KAH14] S. Kahourzade, A. Mahmoudi, H. W. Ping, and M. N. Uddin, “A comprehensive review of axial-flux permanent-magnet machines,” *Can. J. Electr. Comput. Eng.*, vol. 37, pp. 19–33, 2014.
- [KIM04] T. H. Kim and J. Lee, “A study of the design for the flux reversal machine,” *IEEE Trans. Magn.*, vol. 40, no. 4, pp. 2053–2055, Jul. 2004.

- [KIM05a] T. H. Kim, S. H. Won, K. Bong, and J. Lee, "Reduction of cogging torque in flux-reversal machine by rotor teeth pairing," *IEEE Trans. Magn.*, vol. 41, no. 10, pp. 3964–3966, Oct. 2005.
- [KIM05b] Y.-S. Kim, T. H. Kim, Y. T. Kim, W. S. Oh, and J. Lee, "Various design techniques to reduce cogging torque in flux-reversal machines," in *Int. Conf. Elect. Mach. Syst. (ICEMS 2005)*, Nanjing, China, 2005, pp. 261–263.
- [KIM05c] T. H. Kim, K. B. Jang, Y. Do Chun, and J. Lee, "Comparison of the characteristics of a flux reversal machine under the different driving methods," *IEEE Trans. Magn.*, vol. 41, no. 5, pp. 1916–1919, May 2005.
- [KIM05d] T. H. Kim and J. Lee, "Influences of PWM mode on the performance of flux reversal machine," *IEEE Trans. Magn.*, vol. 41, no. 5, pp. 1956–1959, May 2005.
- [KIM07] T. H. Kim and J. Lee, "Comparison of the iron loss of a flux-reversal machine under four different PWM modes," *IEEE Trans. Magn.*, vol. 43, no. 4, pp. 1725–1728, Apr. 2007.
- [KIM09] T. H. Kim, "A study on the design of an inset-permanent-magnet-type flux-reversal machine," *IEEE Trans. Magn.*, vol. 45, no. 6, pp. 2859–2862, May 2009.
- [KIM14] B. Kim and T. A. Lipo, "Operation and design principles of a PM Vernier motor," *IEEE Trans. Ind. Appl.*, vol. 50, no. 6, pp. 3656–3663, Nov./Dec. 2014.
- [KIR15] J. L. Kirtley, A. Banerjee, and S. Englebretson, "Motors for ship propulsion," *Proc. IEEE*, vol. 103, no. 12, pp. 2320–2332, Dec. 2015.
- [LEE06] J. Y. Lee, B. K. Lee, and W. T. Lee, "Dynamic analysis of toroidal winding switched reluctance motor driven by 6-switch converter," *IEEE Trans. Magn.*, vol. 42, no. 4, pp. 1275–1278, Apr. 2006.
- [LEV08] E. Levi, "Multiphase electric machines for variable-speed applications," *IEEE Trans. Ind. Electron.*, vol. 55, no. 5, pp. 1893–1909, May 2008.
- [LI10] J. Li, K. T. Chau, J. Z. Jiang, C. Liu, and W. Li, "A new efficient permanent-magnet vernier machine for wind power generation," *IEEE Trans. Magn.*, vol. 46, no. 6, pp. 1475–1478, Jun. 2010.
- [LI12] J. Li and K. T. Chau, "Performance and cost comparison of permanent-magnet vernier machines," *IEEE Trans. Appl. Supercond.*, vol. 22, no. 3, Jun. 2012.
- [LI15a] D. Li, R. Qu, and J. Li, "Topologies and analysis of flux-modulation machines," in *IEEE Energy Conv. Congress Expo. (ECCE 2015)*, Montreal, QC, 2015, pp. 2153–2160.
- [LI15b] D. Li, R. Qu, J. Li, and W. Xu, "Consequent-pole toroidal-winding outer-rotor Vernier permanent-magnet machines," *IEEE Trans. Ind. Appl.*, vol. 51, no. 6, pp. 4470–4481, Nov./Dec. 2015.
- [LI16] D. Li, R. Qu, and J. Li, "Analysis of Torque Capability and Quality in Vernier Permanent-Magnet Machines," *IEEE Trans. Ind. Appl.*, vol. 52, no. 1, pp. 125–135, Jan./Feb. 2016.
- [LI18] D. Li, Y. Gao, R. Qu, J. Li, Y. Huo, and H. Ding, "Design and analysis of a flux reversal machine with evenly distributed permanent magnets," *IEEE Trans. Ind. Appl.*, vol. 54, no. 1, pp. 172–183, Jan. 2018.

- [LI19] J. Li, K. Wang, F. Li, S. S. Zhu, and C. Liu, "Elimination of even-order harmonics and unipolar leakage flux in consequent-pole PM machines by employing N-S-iron-S-N-iron Rotor," *IEEE Trans. Ind. Electron.*, vol. 66, no. 3, pp. 1736–1747, Mar. 2019.
- [LIA95] Y. Liao, F. Liang, and T. A. Lipo, "A novel permanent magnet motor with doubly salient structure," *IEEE Trans. Ind. Appl.*, vol. 31, no. 5, pp. 1069–1078, Nov. 1995.
- [LIU12] G. Liu, J. Yang, W. Zhao, J. Ji, and Q. Chen, "Design and analysis of a new fault-tolerant permanent-magnet Vernier machine for electric vehicles," *IEEE Trans. Magn.*, vol. 48, no. 11, pp. 4176–4179, Nov. 2012.
- [LIU17] Y. Liu and Z. Q. Zhu, "Magnetic gearing effect in Vernier permanent magnet synchronous machines," in *IEEE Energy Conv. Congress Expo. (ECCE 2017)*, Cincinnati, OH, 2017, pp. 5025-5032
- [LU18] Q. Lu and W. Mei, "Recent development of linear machine topologies and applications," *CES Trans. Elec Machines and Systems*, vol. 2, no. 1, pp. 65-72, Mar. 2018.
- [MOR08a] D. S. More and B. G. Fernandes, "Novel three phase flux reversal machine with full pitch winding," in *Int. Conf. Power Electron.*, Daegu, South Korea, 2008, pp. 1007-1012.
- [MOR08b] D. S. More, H. Kalluru, and B. G. Fernandes, "Comparative analysis of flux reversal machine and fractional slot concentrated winding PMSM," in *Annu. Conf. IEEE Ind. Electron.*, Orlando, FL, 2017, pp. 1131–1136.
- [MOR10a] D. S. More and B. G. Fernandes, "Power density improvement of three phase flux reversal machine with distributed winding," *IET, Electr. Power Appl.*, vol. 4, no. 2, pp. 109–120, Feb. 2010.
- [MOR10b] D. S. More and B. G. Fernandes, "Analysis of flux-reversal machine based on fictitious electrical gear," *IEEE Trans. Energy Convers.*, vol. 25, no. 4, pp. 940–947, Dec. 2010.
- [MOR13] D. S. More and B. G. Fernandes, "Modelling and performance of three-phase 6/14 pole flux reversal machine," *IET Electr. Power Appl.*, vol. 7, no. 2, pp. 131–139, Feb. 2013.
- [MUL99] E. Muljadi, C. P. Butterfield, and Y. H. Wan, "Axial-flux modular permanent-magnet generator with a toroidal winding for wind-turbine applications," *IEEE Trans. Ind. Appl.*, vol. 35, no. 4, pp. 831–836, Jul./Aug. 1999.
- [OKA13] K. Okada, N. Niguchi, and K. Hirata, "Analysis of a Vernier motor with concentrated windings," *IEEE Trans. Magn.*, vol. 49, no. 5, pp. 2241–2244, May 2013.
- [ONE16] Y. Oner, Z. Q. Zhu, L. Wu, X. Ge, H. Zhan, and J. Chen, "Analytical on-load subdomain field model of permanent magnet Vernier machines," *IEEE Trans. Ind. Electron.*, vol. 63, no. 7, pp. 4105–4117, Jul. 2016.
- [PEL11] G. Pellegrino and C. Gerada, "Modeling of flux reversal machines for direct drive applications," in *Proc. Euro. Conf. Power Electron. Appl.*, Birmingham, UK, 2011.

- [PEN14] S. Peng, W. N. Fu, and S. L. Ho, "A novel high torque-density triple-permanent-magnet-excited magnetic gear," *IEEE Trans. Magn.*, vol. 50, no.11, Nov. 2014, Art. ID 8001704.
- [POL05] H. Polinder, B.C. Mecrow, A.G. Jack, P. G. Dickinson, and M. A. Mueller, "Conventional and TFPM linear generators for direct-drive wave energy conversion," *IEEE Trans. Energy Convers.*, vol. 20, no. 2, pp. 260–267, Jun. 2005.
- [POL06] H. Polinder, F. F. A. van der Pijl, G. J. de Vilder, and P. J. Tavner, "Comparison of direct-drive and geared generator concepts for wind turbines," *IEEE Trans. Energy Convers.*, vol. 21, no.3, pp. 725-733, Sep. 2006.
- [PRA17] V. Prakht, V. Dmitrievskii, V. Kazakbaev, and S. Sarapulov, "Steady-state model of a single-phase flux reversal motor," in *Int. Conf. Power Elect. Engin.*, Riga, Latvia, 2017.
- [QU11] R. Qu, D. Li, and J. Wang, "Relationship between magnetic gears and Vernier machines," in *Int. Conf. Elect. Mach. Syst. (ICEMS 2011)*, Beijing, China, 2011.
- [RAM15] T. Raminosa, A. El-Refaie, D. Pan, K.-K. Huh, J. Alexander, K. Grace, S. Grubic, S. Galimoto, P. Reddy, and X. Shen, "Reduced rare-earth flux-switching machines for traction applications," *IEEE Trans. Ind. Appl.*, vol. 51, no. 4, pp. 2959-2971, Jul./Aug. 2015.
- [RAS05] P. O. Rasmussen, T. O. Andersen, F. T. Joergensen, and O. Nielsen, "Development of a high-performance magnetic gear," *IEEE Trans. Ind. Appl.*, vol. 41, no.3, pp. 764 - 770, May/June. 2005.
- [RAU55] S. E. Rauch and L. J. Johnson, "Design principle of the flux switch alternator," *Trans. Inst. Elect. Eng.*, vol. 74, no. 3, pp. 1261–1268, Jan. 1955.
- [REF06] A. M. El-Refaie and T. M. Johns, "Experimental verification of optimal flux weakening in surface PM machines using concentrated windings," *IEEE Trans. Ind. Appl.*, vol. 42, no. 2, pp. 443–453, Mar./Apr. 2006.
- [REF10] A. M. El-Refaie, "Fractional-slot concentrated-windings synchronous permanent magnet machines: Opportunities and challenges," *IEEE Trans. Ind. Electron.*, vol. 57, no. 1, pp. 107–121, Jan. 2010.
- [REF13] A. M. El-Refaie, "Motors/generators for traction/propulsion applications: A review," *IEEE Veh. Technol. Mag.*, vol. 8, no. 1, pp. 90–99, Mar. 2013.
- [SHE17a] J. X. Shen, H. Y. Li, H. Hao and M. J. Jin, "A coaxial magnetic gear with consequent-pole rotors," *IEEE Trans. Energy Convers.*, vol. 32, no. 1, pp. 267-275, Mar. 2017.
- [SHE17b] J. X. Shen, H. Y. Li, H. Hao, M. J. Jin, and Y. C. Wang, "Topologies and performance study of a variety of coaxial magnetic gears," *IET Electr. Power Appl.*, vol. 11, no.7, pp. 1160-1168, Aug. 2017.
- [SPO03] E. Spooner and L. Haydock, "Vernier hybrid machines," *IEE Proceedings-Electric Power Appl.*, vol. 150, no. 6, pp. 655–662, Nov. 2003.
- [TAN10] Y. Q. Tang and Y. P. Liang, *Analysis and Calculation of Electromagnetic Field in Electrical Machines*. Beijing, China: CMP, 2010.

- [TLA16] P. M. Tlali, S. Gerber, and R. J. Wang, "Optimal design of an outer-stator magnetically geared permanent magnet machine," *IEEE Trans. Magn.*, vol. 52, no. 2, Feb. 2016, Art. ID 8100610.
- [TOB00] A. Toba, T. A. Lipo, "Generic torque-maximizing design methodology of surface permanent-magnet Vernier machine," *IEEE Trans. Ind. Appl.*, vol. 36, no. 6, pp. 1539–1545, Nov./Dec. 2000.
- [TOB99] A. Toba and T. A. Lipo, "Novel dual-excitation permanent magnet Vernier machine," *IEEE Ind. Appl. Conf.*, Phoenix, AZ, 1999, pp. 2539–2544.
- [VAK08] G. Vakil, P. Upadhyay, N. Sheth, a. Patel, a. Tiwari, and D. Miller, "Torque ripple reduction in the flux reversal motor by rotor pole shaping and stator excitation," in *Int. Conf. Elect. Mach. Syst. (ICEMS 2008)*, Wuhan, China, 2008, pp. 2980–2985.
- [VIR13] B. Virlan, S. Benelghali, A. Simion, L. Livadaru, R. Outbib, and A. Munteanu, "Induction motor with outer rotor and ring stator winding for multispeed applications," *IEEE Trans. Energy Convers.*, vol. 28, no. 4, pp. 999–1007, Dec. 2013.
- [WAN01] C. X. Wang, I. Boldea, and S. A. Nasar, "Characterization of three phase flux reversal machine as an automotive generator," *IEEE Trans. Energy Convers.*, vol. 16, no. 1, pp. 74–80, Mar. 2001.
- [WAN08a] J. Wang, K. Atallah, Z.Q. Zhu, and D. Howe, "Modular three-phase permanent-magnet brushless machines for in-wheel applications" *IEEE Trans. on Vehicle Tech.*, Vol. 57, No. 5, pp. 2714- 2720, Sep. 2008.
- [WAN08b] L. L. Wang, J. X. Shen, Y. Wang, and K. Wang, "A novel magnetic-geared outer-rotor permanent-magnet brushless motor," in *IET Int. Conf. Power Electron. Mach. Drives (PEMD 2008)*, York, UK, 2008, pp. 33-36.
- [WAN09] L. L. Wang, J. X. Shen, P. C. K. Luk, W. Z. Fei, C. F. Wang, and H. Hao, "Development of a magnetic-geared permanent-magnet brushless motor," *IEEE Trans. Magn.*, vol. 45, no. 10, pp. 4578–4581, Sep. 2009.
- [WAN11] J. B. Wang, K. Atallah, and S. D. Carvley, "A magnetic continuously variable transmission device," *IEEE Trans. Magn.*, vol. 47, no. 10, pp. 2815–2818, Oct. 2011.
- [WAN99] C. Wang, S. A. Nasar, and I. Boldea, "Three-phase flux reversal machine (FRM)," *Proc. IEE. Elec. Power Appl.*, vol. 146, no. 2, pp. 139–146, Mar. 1999.
- [WEH88] H. Weh, H. Hoffman, and J. Landrath, "New permanent magnet excited synchronous machine with high efficiency at low speeds," in *Proc. Int. Conf. Electrical Machines*, Pisa, Italy, 1988, pp. 35–40.
- [WU12] L. J. Wu, Z. Q. Zhu, D. A. Staton, M. Popescu, and D. Hawkins, "Comparison of analytical models of cogging torque in surface-mounted PM machines," *IEEE Trans. Ind. Electron.*, vol. 59, no. 6, pp. 2414–2425, Jun. 2012.
- [WU14] D. Wu, J. T. Shi, Z. Q. Zhu, and X. Liu, "Electromagnetic performance of novel synchronous machines with permanent magnets in stator yoke," *IEEE Trans. Magn.*, vol. 50, no. 9, Sep. 2014.



- [WU15a] Z. Z. Wu, Z. Q. Zhu, and J. T. Shi, "Novel doubly salient permanent magnet machines with partitioned stator and iron pieces rotor," *IEEE Trans. Magn.*, vol. 51, no. 5, May 2015.
- [WU15b] Z. Z. Wu and Z. Q. Zhu, "Partitioned stator flux reversal machine with consequent-pole PM stator," *IEEE Trans. Energy Convers.*, vol. 30, no. 4, pp. 1472–1482, Dec. 2015.
- [WU15c] Z. Z. Wu and Z. Q. Zhu, "Analysis of air-gap field modulation and magnetic gearing effects in switched flux permanent magnet machines," *IEEE Trans. Magn.*, vol. 51, no. 5, May 2015, Art. ID 8105012.
- [WU16a] Z.Z. Wu and Z.Q. Zhu, "Analysis of magnetic gearing effect in partitioned stator switched flux PM machines," *IEEE Trans. Energy Convers.*, vol.31, no.4, pp.1239-1249, Dec. 2016.
- [WU16b] Z. Z. Wu and Z. Q. Zhu, "Comparative analysis of end effect in partitioned stator flux reversal machines having surface-mounted and consequent pole permanent magnets," *IEEE Trans. Magn.*, vol. 52, no. 7, pp. 18–21, Jul. 2016.
- [XU14] L. Xu, W. Zhao, J. Ji, G. Liu, Y. Du, Z. Fang, and L. Mo, "Design and analysis of a new linear hybrid excited flux reversal motor with inset permanent magnets," *IEEE Trans. Magn.*, vol. 50, no. 11, Nov. 2014.
- [XU15] L. Xu, G. Liu, W. Zhao, J. Ji, H. Zhou, W. Zhao, and T. Jiang, "Quantitative comparison of integral and fractional slot permanent magnet Vernier motors," *IEEE Trans. Energy Convers.*, vol. 30, no. 4, pp. 1483–1495, Dec. 2015.
- [YAN14a] Y. Yang, J. Zhang, L. Ma, X. Wang, and N. Wang, "The electromagnetic performance calculation and comparison of flux reversal machine with different winding topologies," in *Int. Conf. Elect. Mach. Syst. (ICEMS 2014)*, Hangzhou, China, 2014, pp. 605-609.
- [YAN14b] Y. Yang, X. Wang, and Z. Zhang, "Analytical calculation of magnetic field and electromagnetic performance of flux reversal machines," *IET Electr. Power Appl.*, vol. 8, no. 5, pp. 178–188, May 2014.
- [YAN19a] H. Yang, Z. Q. Zhu, H. Lin, H. Li, and S. Lyu, "Analysis of consequent-pole flux reversal permanent magnet machine with biased flux modulation theory," *IEEE Trans. Ind. Electron.*, early access, 2019.
- [YAN19b] H. Yang, S. Lyu, Z. Q. Zhu, Y. Liu, and H. Lin, "Design and analysis of novel asymmetric-stator-pole flux reversal PM machine," *IEEE Trans. Ind. Electron.*, early access, 2019.
- [YAS16] P400 Series: Compact axial flux motors and generators, Abingdon: YASA Motors Ltd., 2016. [Online]. Available: [http://www.yasamotors.com/wp-content/uploads/2015/09/YASA\\_P400\\_Product\\_Sheet.pdf](http://www.yasamotors.com/wp-content/uploads/2015/09/YASA_P400_Product_Sheet.pdf).
- [YIN15] X. Yin, P. Pfister and Y. Fang, "A novel magnetic gear: toward a higher torque density," *IEEE Trans. Magn.*, vol. 51, no.11, Nov. 2015, Art. ID 8002804.
- [ZAR06] D. Zarko, D. Ban, and T. A. Lipo, "Analytical calculation of magnetic field distribution in the slotted air gap of a surface permanent-magnet motor using complex relative air-gap permeance," *IEEE Trans. Magn.*, vol. 42, no. 7, pp. 1828–1837, Jul. 2006.

- [ZHA09] J. Z. Zhang, M. Cheng, Z. Chen, and W. Hua, "Comparison of stator-mounted permanent-magnet machines based on a general power equation," *IEEE Trans. Energy Convers.*, vol. 24, no. 4, pp. 826–834, Dec. 2009.
- [ZHA14] W. Zhao, J. Ji, G. Liu, Y. Du, and M. Cheng, "Design and analysis of a new modular linear flux-reversal permanent-magnet motor," *IEEE Trans. Appl. Supercond.*, vol. 24, no. 3, pp. 3–7, Jun. 2014.
- [ZHA17] G. Zhao, W. Hua, G. Zhang, and X. Zhu, "The influence of dummy slots on stator surface-mounted permanent magnet machines," *IEEE Trans. Magn.*, vol. 53, no. 6, Jun. 2017.
- [ZHE13] P. Zheng, J. Bai, C. Tong, Y. Sui, Z. Song, and Q. Zhao, "Investigation of a novel radial magnetic-field-modulated brushless double-rotor machine used for HEVs," *IEEE Trans. Magn.*, vol. 49, no. 3, pp. 1231–1241, Mar. 2013.
- [ZHU00] Z. Q. Zhu and D. Howe, "Influence of design parameters on cogging torque in permanent magnet machines," *IEEE Trans. Energy Convers.*, vol. 15, no. 4, pp. 407–412, Dec. 2000.
- [ZHU07] Z. Q. Zhu and D. Howe, "Electrical machines and drives for electric, hybrid, and fuel cell vehicles," *Proc. IEEE*, Vol. 95, No. 4, pp. 746–765, Apr. 2007.
- [ZHU08] Z. Q. Zhu, J. T. Chen, Y. Pang, D. Howe, S. Iwasaki, and R. Deodhar, "Analysis of a novel multi-tooth flux-switching PM brushless AC machine for high torque direct-drive applications," *IEEE Trans. Magn.*, vol. 44, no. 11, pp. 4313–4316, Nov. 2008.
- [ZHU09a] Z. Q. Zhu, A. S. Thomas, J. T. Chen, and G. W. Jewell, "Cogging torque in flux-switching permanent magnet machines," *IEEE Trans. Magn.*, vol. 45, no. 10, pp. 4708–4711, Oct. 2009.
- [ZHU09b] Z. Q. Zhu, "A simple method for measuring cogging torque in permanent magnet machines," in *Proc. IEEE Power Energy Soc. Gen. Meet.*, Calgary, AB, 2009.
- [ZHU10] Z. Q. Zhu and J. T. Chen, "Advanced flux-switching permanent magnet brushless machines," *IEEE Trans. Magn.*, vol. 46, no. 6, pp. 1447–1453, Jun. 2010.
- [ZHU11a] Z. Q. Zhu, "Switched flux permanent magnet machines-Innovation continues," in *Int. Conf. Elect. Mach. Syst. (ICEMS 2011)*, Beijing, China, 2011.
- [ZHU11b] Z. Q. Zhu and X. Liu, "Individual and global optimization of switched flux permanent magnet motors," in *Int. Conf. Elect. Mach. Syst. (ICEMS 2011)*, Beijing, China, 2011.
- [ZHU12] Z. Q. Zhu, "Recent advances on permanent magnet machines," *Trans. China Electrotechnical Society*, vol. 27, no.3, pp. 1-11, Mar. 2012.
- [ZHU14] Z. Q. Zhu and D. Evans, "Overview of recent advances in innovative electrical machines-with particular reference to magnetically geared switched flux machines," in *Int. Conf. Elect. Mach. Syst. (ICEMS 2014)*, Hangzhou, China, 2014.
- [ZHU15] Z. Q. Zhu, Z. Z. Wu, D. Evans, and W. Q. Chu, "Novel electrical machines having separate PM excitation stator," *IEEE Trans. Magn.*, vol. 51, no. 4, Apr. 2015, Art. No. 8104109.

- [ZHU16] Z. Q. Zhu, H. Hua, D. Wu, J. T. Shi, and Z. Z. Wu, "Comparative study of partitioned stator machines with different PM excitation," *IEEE Trans. Ind. Appl.*, vol. 52, no. 1, pp. 199–208, Jan./Feb. 2016.
- [ZHU17a] X. Zhu and W. Hua, "An improved configuration for cogging torque reduction in flux-reversal permanent magnet machines," *IEEE Trans. Magn.*, vol. 53, no. 6, pp. 6–9, Jun. 2017.
- [ZHU17b] X. Zhu, W. Hua, and Z. Wu, "Cogging torque suppression in flux-reversal permanent magnet machines," *IET Elect. Power Appl.*, vol. 12, no. 1, pp. 135–143, Dec. 2017.
- [ZHU17c] S. Zhu, T. Cox, and C. Gerada, "Comparative study of novel tubular flux-Reversal transverse flux permanent magnet linear machine," in *IEEE Energy Conv. Congress Expo. (ECCE 2017)*, Cincinnati, OH, 2018, pp. 4282-4287.
- [ZHU18a] Z. Q. Zhu, M. F. H. Khatab, H. Y. Li and Y. Liu, "A novel axial flux magnetically geared machine for power split application," *IEEE Trans. Ind. Appl.*, vol. 54, no. 6, pp. 5954–5966, Nov. 2018.
- [ZHU18b] Z. Q. Zhu, "Overview of novel magnetically geared machines with partitioned stators," *IET Electr. Power Appl.*, vol. 12, no. 5, pp. 595–604, Apr. 2018.
- [ZHU19] X. Zhu, W. Hua, W. Wang, and W. Huang, "Analysis of back-EMF in flux-reversal permanent magnet machines by air-gap field modulation theory," *IEEE Trans. Ind. Electron.*, vol. 66, no. 5, pp. 3344–3355, May 2019.
- [ZHU93] Z. Q. Zhu and D. Howe, "Instantaneous magnetic field distribution in brushless permanent magnet DC motors. III: Effect of stator slotting," *IEEE Trans. Magn.*, vol. 29, no. 1, pp. 143–151, Jan. 1993.
- [ZOU17] T. Zou, D. Li, R. Qu, D. Jiang, and J. Li, "Advanced high torque density PM Vernier machine with multiple working harmonics," *IEEE Trans. Ind. Appl.*, vol. 53, no. 6, pp. 5295–5304, Nov./Dec. 2017.

# APPENDIX A

## CAD DRAWINGS OF PROTOTYPES

Stator laminations:

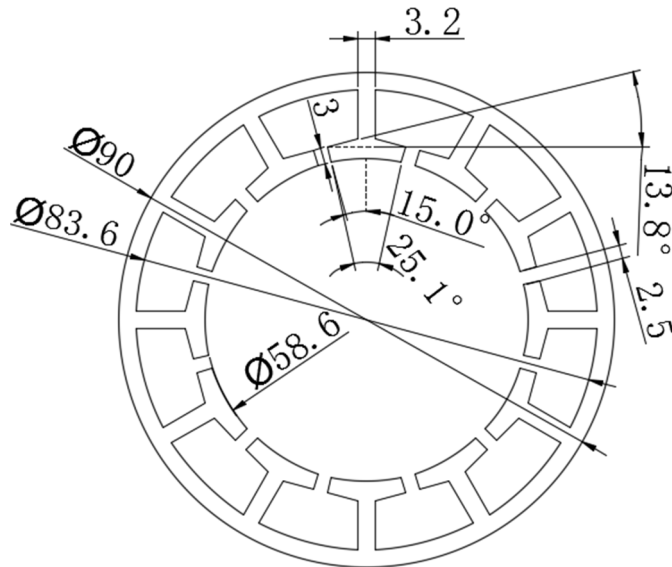


Fig. A.1 12-slot stator dimensions for SPM-FRPM machines.

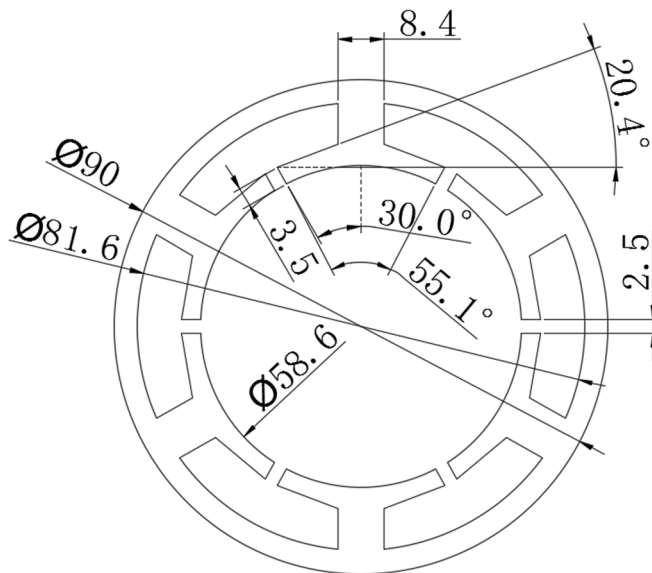


Fig. A.2 6-slot stator dimensions for SPM-FRPM machines.

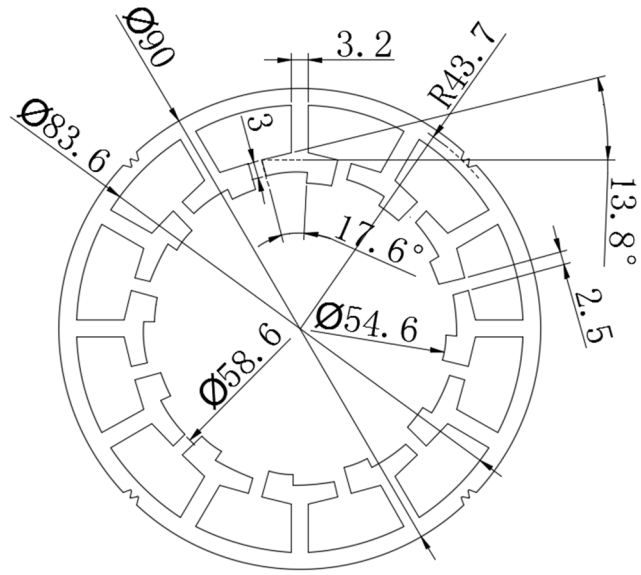


Fig. A.3 12-slot stator dimensions for 12/14 CPM-FRPM machine.

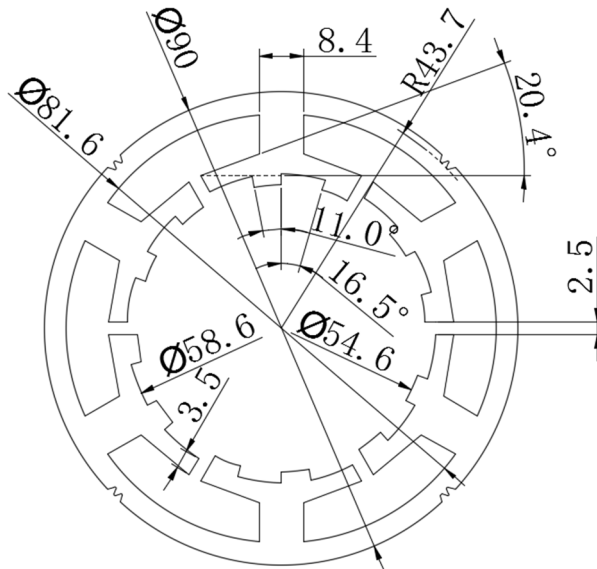


Fig. A.4 6-slot stator dimensions for 6/14 CPM-FRPM machine.

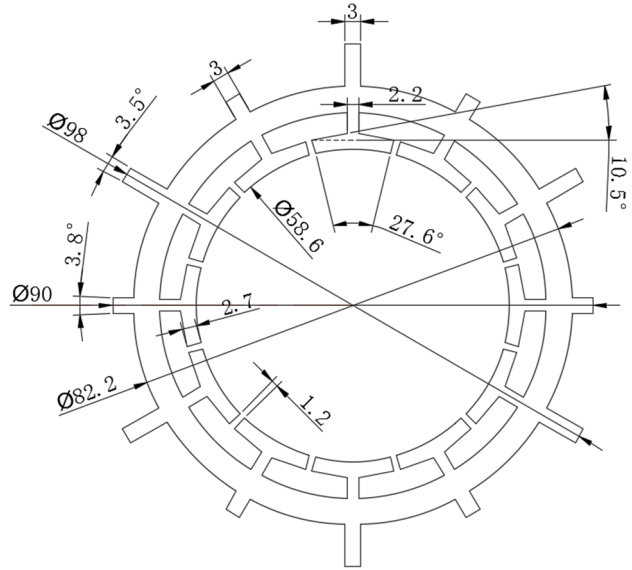


Fig. A.5 12-slot stator dimensions for 12/13 TW-FRPM machine.

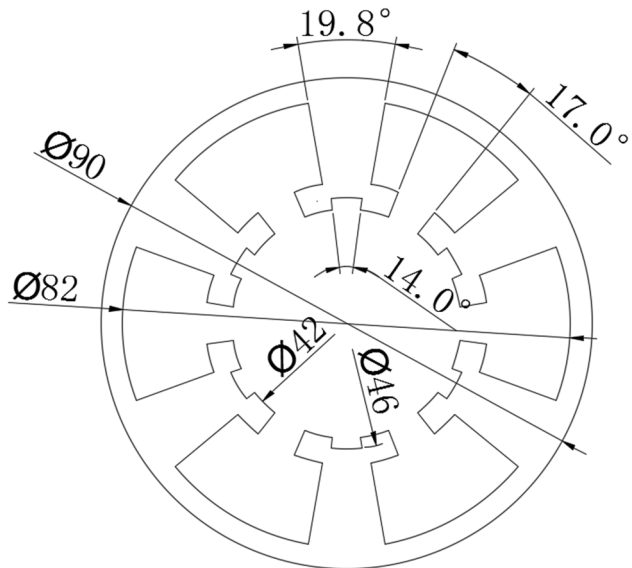


Fig. A.6 6-slot stator dimensions for 6/10 Vernier machine.

**Rotor laminations:**

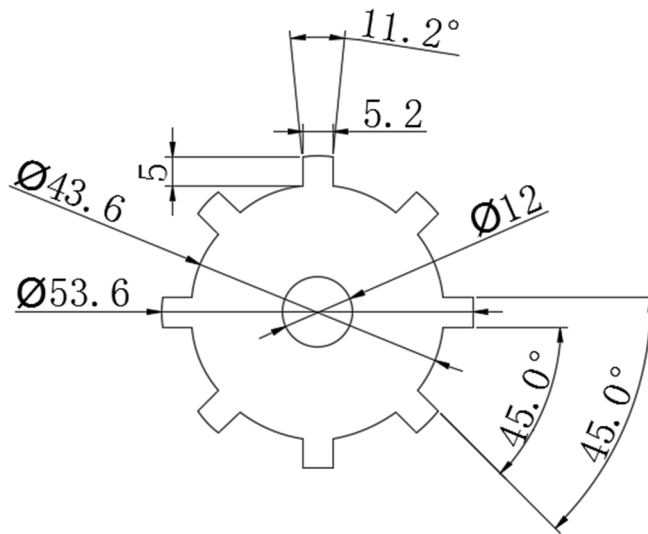


Fig. A.7 8-pole rotor dimensions for 6/8 FRPM machine.

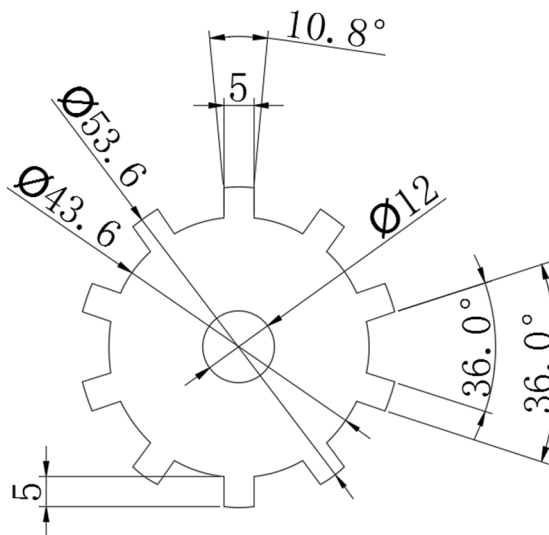


Fig. A.8 10-pole rotor dimensions for 6/10 FRPM machine.

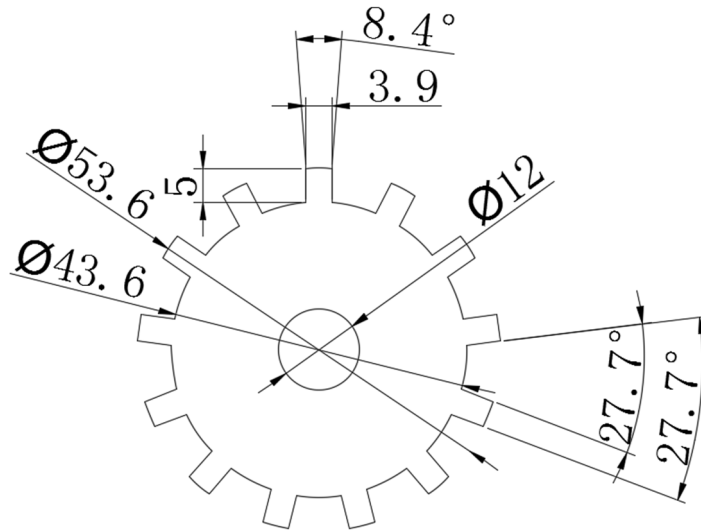


Fig. A.9 13-pole rotor dimensions for 12/13 FRPM machines.

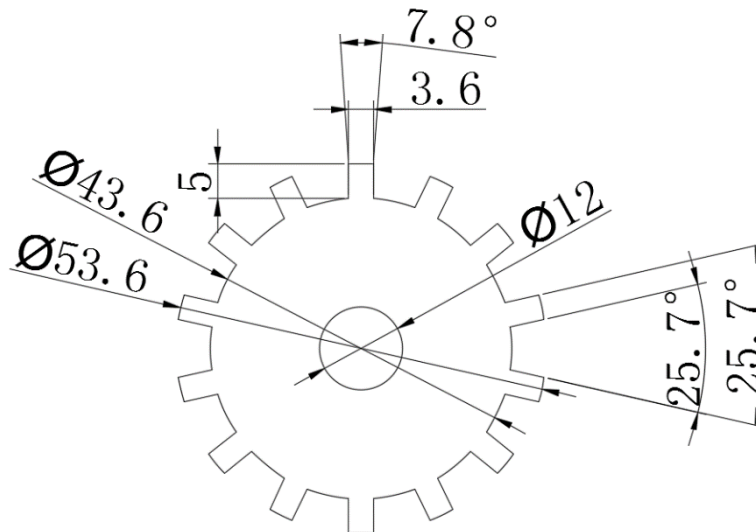


Fig. A.10 14-pole rotor dimensions for both SPM- and CPM-FRPM machines.



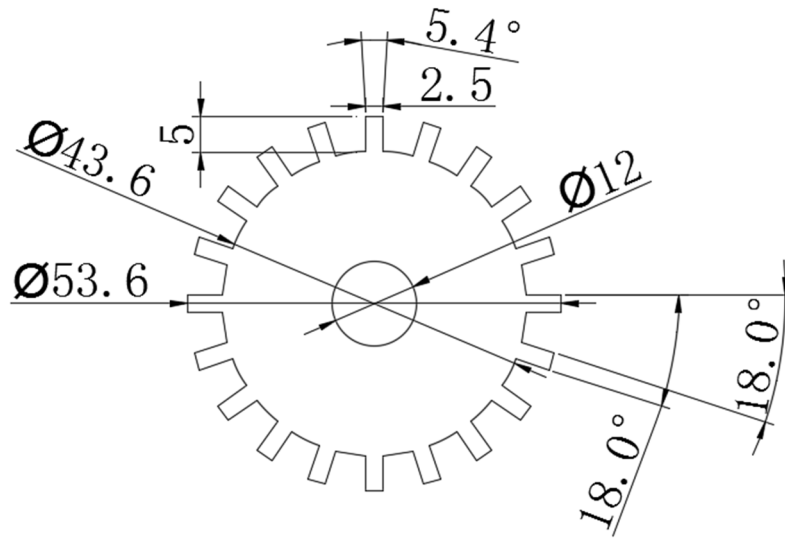


Fig. A.11 20-pole rotor dimensions for 6/20 FRPM machine.

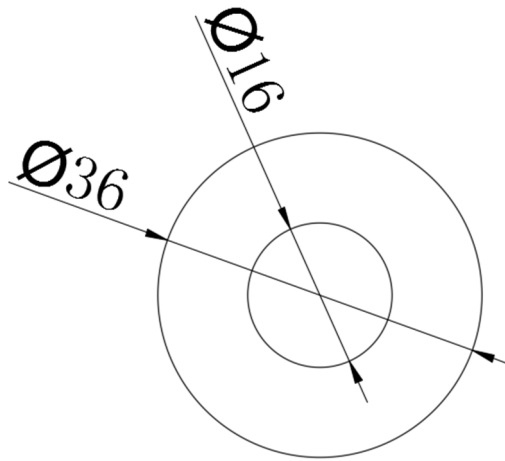


Fig. A.12 Rotor dimensions for 6/10 Vernier machine.

**PM dimensions:**

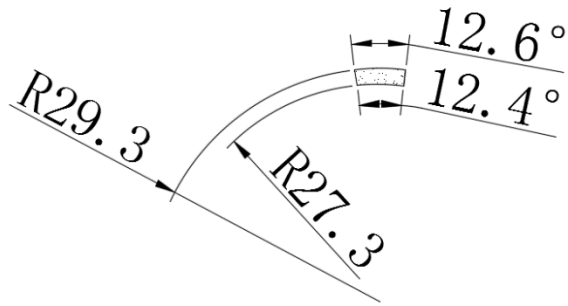


Fig. A.13 PM dimensions for 12-stator-slot SPM-FRPM machines.

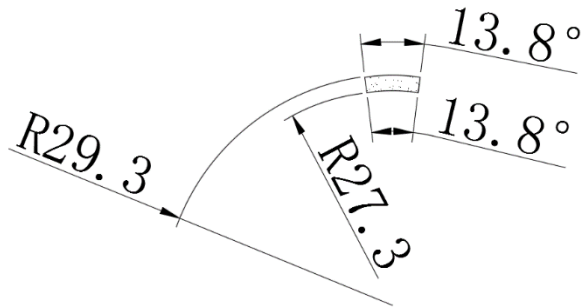


Fig. A.14 PM dimensions for 6-stator-slot SPM-FRPM machines.

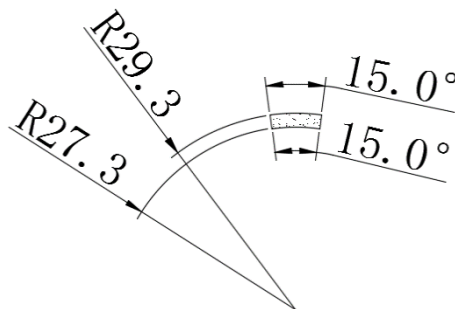


Fig. A.15 PM dimensions for 12/14 CPM-FRPM machines.

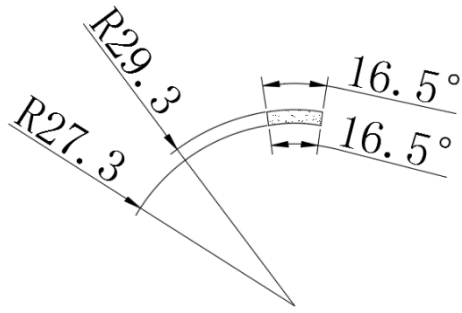


Fig. A.16 PM dimensions for 6/14 CPM-FRPM machines.

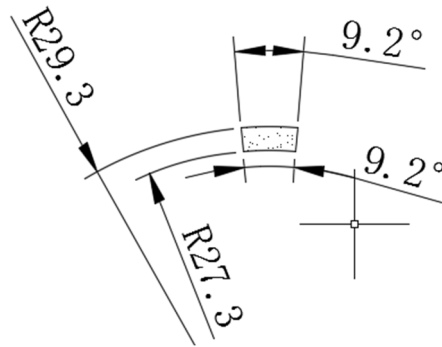


Fig. A.17 PM dimensions for 6/20 FRPM machine

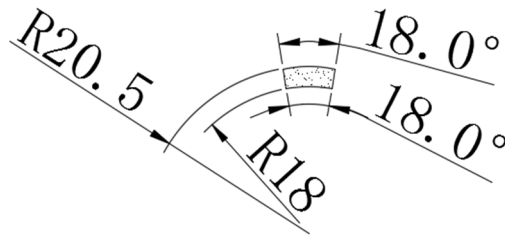


Fig. A.18 PM dimensions for 6/10 Vernier machine.

**BH and Loss Curves of Core Laminations:**

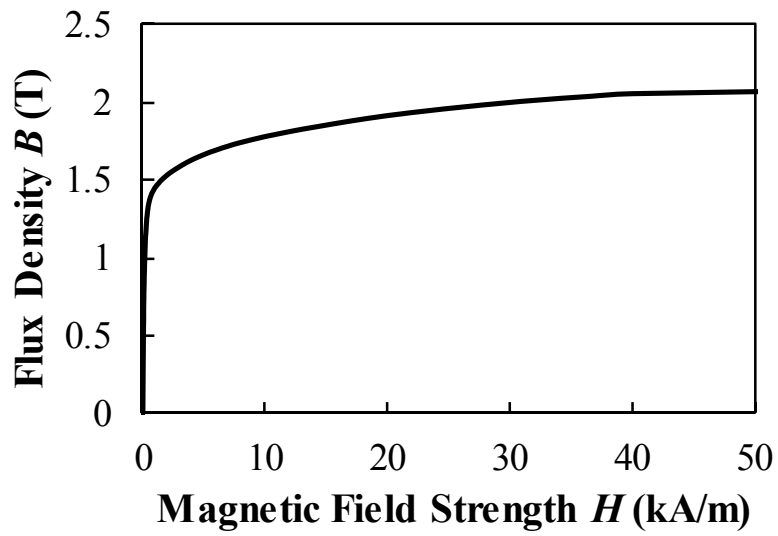


Fig. A.19 BH curve of core laminations.

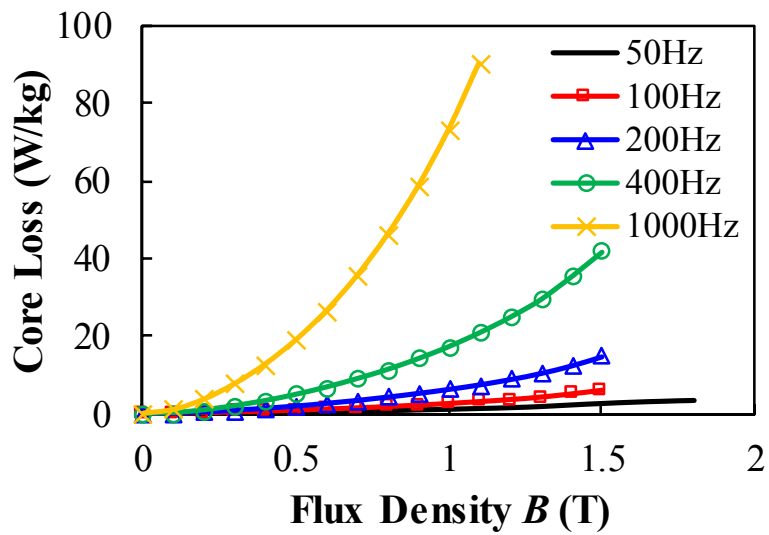
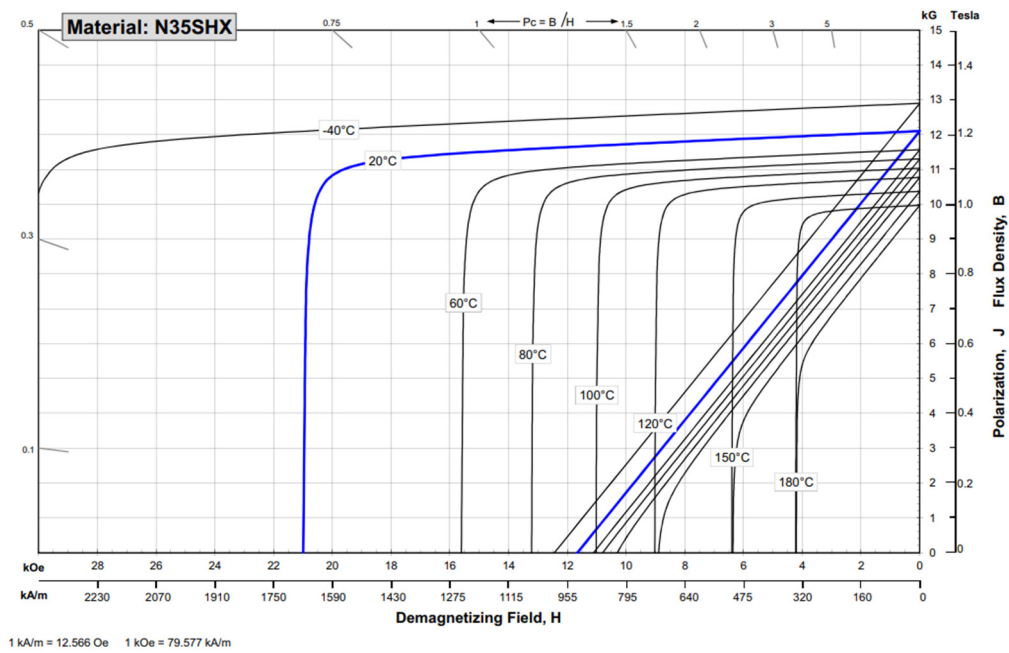


Fig. A.20 Loss curves of core laminations.

## PM Properties:



Magnetic Properties	Characteristic	Units	min.	nominal	max.
	<b>B<sub>r</sub></b> , Residual Induction		Gauss	11,700	12,100
		mT	1170	1210	1250
<b>H<sub>cB</sub></b> , Coercivity		Oersteds	11,000	11,500	12,000
		kA/m	876	915	955
<b>H<sub>cJ</sub></b> , Intrinsic Coercivity		Oersteds	20,000		
		kA/m	1,592		
<b>BH<sub>max</sub></b> , Maximum Energy Product		MGOe	33	36	38
		kJ/m <sup>3</sup>	263	283	302

Fig. A.21 Magnetic properties of N35SH magnet (provided by Arnold Magnetic Technologies).

## APPENDIX B

### COGGING TORQUE AND STATIC TORQUE MEASURING METHOD

The simple test method for measuring the cogging torque waveform is firstly proposed in [ZHU09b], and the test rig is shown in Fig. B.1. The stator of the prototype machine is clamped on a lathe, while the rotor shaft is connected with a balanced beam. The bar at one end of the beam is supported by the digital scale with a pre-weight exerted on. There is an angular degree indication on the lathe, which enables a precise indication of the relative rotor position to the stator when the stator is turned.

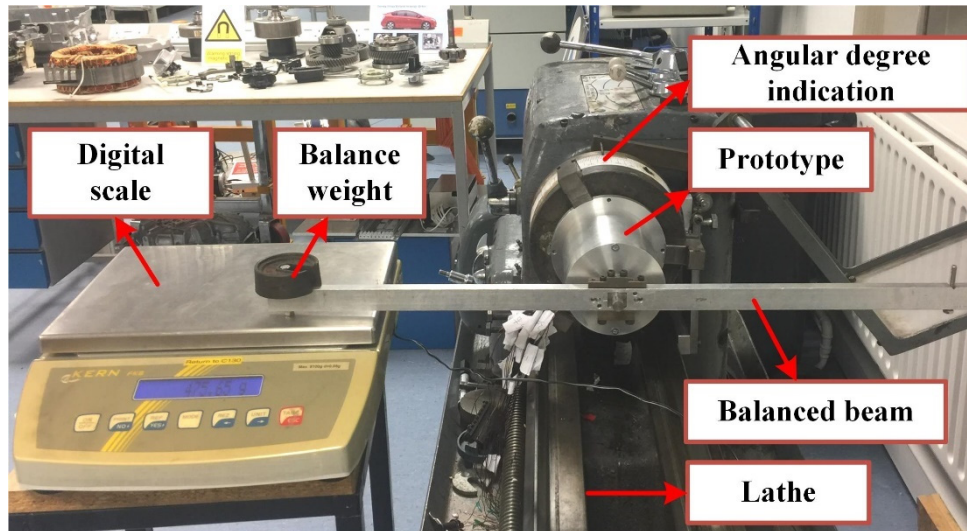


Fig. B.1 Test rig for measuring cogging torque and static torque waveforms.

When the beam is adjusted to the level position, the cogging torque value  $T_c$  under one certain rotor position can be given as

$$T_c = 9.8(m_{sca} - m_{pre})L_b \quad (\text{B.1})$$

where  $m_{sca}$  is the weight display of the digital scale,  $m_{pre}$  is the pre-weight of the balance weight,  $L_b$  is the arm length of the bar at the end of the beam, and 9.8 is the value of gravitational acceleration (meters per second squared).

By manually rotating the lathe to different rotor positions, the cogging torque waveform can be obtained. The test rig can be also used to measure the static torque waveforms, and the

corresponding winding connections are shown in Fig. B.2. With a fixed DC current injected (i.e.  $I_a = -2I_b = -2I_c = I_{dc}$ ), the value of the static torque can be also obtained based on (B.1).

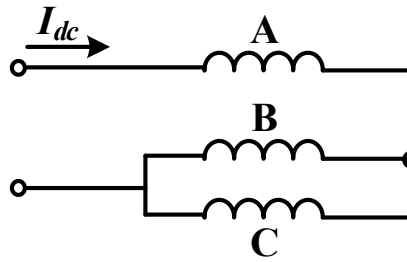


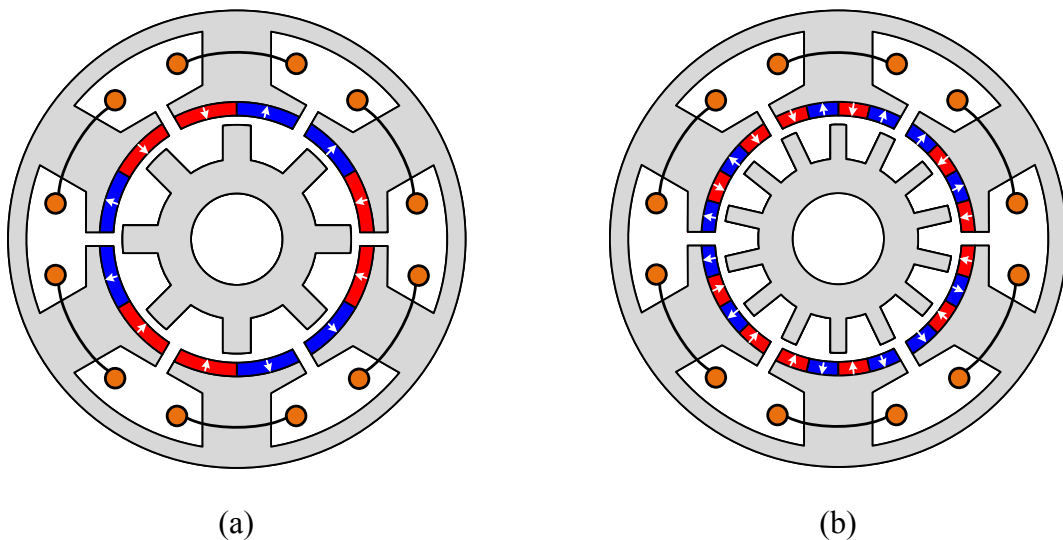
Fig. B.2 Winding connections for measuring static torque waveform.

## APPENDIX C

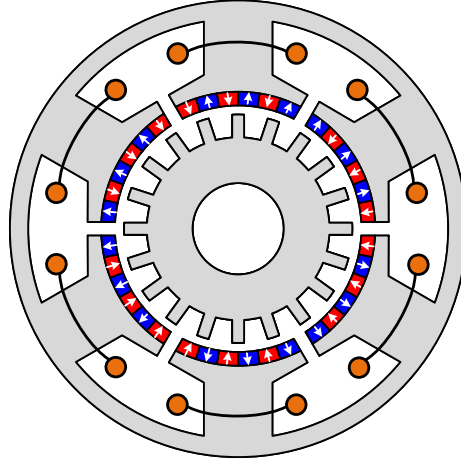
### ANALYTICAL PERFORMANCE DERIVATION OF FLUX REVERSAL PERMANENT MAGNET MACHINES WITH IDENTICAL PM POLARITIES OF ADJACENT TEETH

In chapter 3, the unified analytical model of FRPM machines with opposite PM polarities of adjacent teeth is established, from which the performance of machines having different number of PM pieces on single stator tooth can be derived. Similarly, the performance of FRPM machines with identical PM polarities of adjacent teeth will be analytically deduced in the following.

For FRPM machines with identical PM polarities of adjacent teeth, the most typical configuration of a three-phase machine is shown in Fig. 3.1 (a) (taking the 6-slot-stator FRPM machine for instance). The non-overlapping concentrated armature windings are always wound around the stator teeth, resulting in short end-winding. Also, a pair of PMs is mounted on the inner surface of each stator tooth. In FRPM machines with opposite PM polarities of adjacent teeth, the number of stator slot can be either even or odd. In contrast, the number of stator slot of FRPM machines with identical PM polarities of adjacent teeth can be only even. Besides, by increasing the number of PM pairs  $n_{pp}$  on single stator tooth, other FRPM machines can be proposed, as shown in Fig. 3.1 (a), and (b). Ideally,  $2n_{pp}$  PM pieces can be mounted on each stator tooth with minimum  $n_{pp}$  being 1.







(c)

Fig. C.1 FRPM machines with identical PM polarities of adjacent teeth and different  $n_{pp}$ . (a)  $n_{pp}=1$ . (b)  $n_{pp}=2$ . (c)  $n_{pp}=3$ .

The unified analytical model of FRPM machines with identical PM polarities of adjacent teeth will be given in the following. To simplify the analysis, some assumptions are made as: 1) the saturation of the stator and rotor cores is neglected; 2) the end-effect and fringing effect of the machine are neglected; 3) the magnets are radially-magnetized; 4) the dimensions of all PM pieces are the same.

The schematic of the FRPM machine considering  $n_{pp}$  is shown in Fig. 3.2. Some critical dimensional parameters including overall diameter ( $D$ ), inner radius of stator ( $R_{si}$ ), stator slot pitch ( $\tau_s$ ), width of stator slot opening ( $w_{so}$ ), PM height ( $h_m$ ), air-gap length ( $g$ ), rotor pole pitch ( $\tau_r$ ), and width of rotor slot opening ( $w_{ro}$ ) are also labelled.

Based on the magnetomotive force (MMF)-permeance model, the no-load air-gap flux density of the FRPM machine can be given as

$$B(\theta, t) = F_{PM}(\theta) \Lambda_r(\theta, t) \quad (C.1)$$

where  $F_{PM}(\theta)$  is the PM MMF which is static under the stator reference frame, and  $\Lambda_r(\theta, t)$  is the specific relative air-gap permeance produced by the salient rotor which is dynamic due to the rotor rotation.

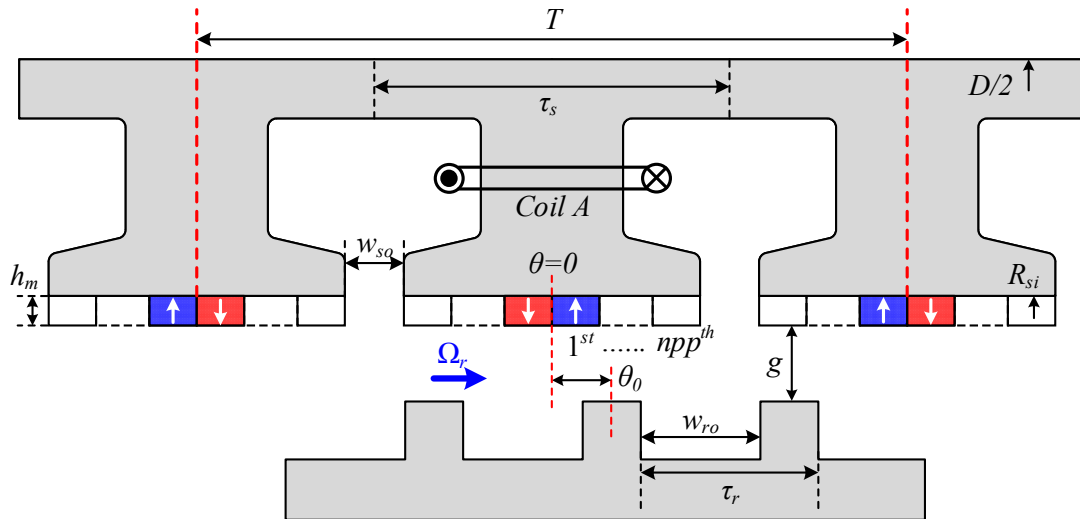
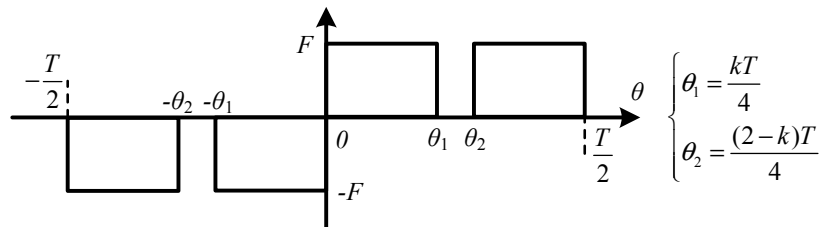
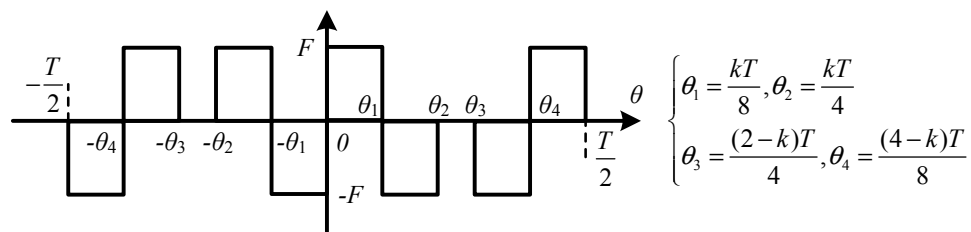


Fig. C.2 Schematic of the FRPM machine with  $2npp$  PM pieces on single stator tooth and identical PM polarities of adjacent teeth.

Considering the PM MMF of the machine, it is directly determined by the number of PM pairs on each stator tooth and the corresponding magnetisation directions. As shown in Fig. 3.2, since the PM arrangements of the adjacent two stator teeth are not the same, the PM MMF periodically distributes in the air-gap with period ( $T$ ) being  $2\tau_s$ . By assuming the magnetisation direction of the 1st magnet piece outward, the PM MMF waveforms of different  $npp$  (1 to 3) are shown in Fig. 3.3.



(a)



(b)

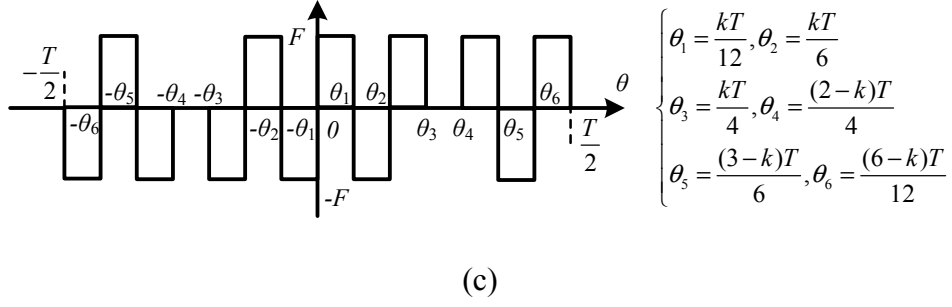


Fig. C.3 PM MMF waveform of FRPM machines. (a)  $npp=1$ . (b)  $npp=2$ . (c)  $npp=3$ .

The PM MMF can then be expressed in Fourier series, as

$$F_{PM}(\theta) = \sum_{i=1,2,3,\dots}^{\infty} F_i \sin(i \frac{N_s}{2} \theta) \quad (C.2)$$

where  $N_s$  is the number of stator slots,  $i$  is the order of Fourier series,  $F_i$  is the corresponding Fourier coefficient and is

$$F_i = \frac{8F}{TiN_s} \left\{ \begin{aligned} & -1 - (-1)^{npp} \cos\left(\frac{iN_s}{2} k \frac{T}{4}\right) + \cos\left(\frac{iN_s}{2} \frac{T}{2}\right) - (-1)^{npp+1} \cos\left[\frac{iN_s}{2} \left(\frac{T}{2} - k \frac{T}{4}\right)\right] + \\ & \sum_{j=1,2,\dots}^{npp+1} 2(-1)^{j-1} \cos\left[\frac{iN_s}{2} \frac{j-1}{npp} k \frac{T}{4}\right] + \sum_{j=1,2,\dots}^{npp+1} 2(-1)^j \cos\left[\frac{iN_s}{2} \left(\frac{T}{2} - \frac{j-1}{npp} k \frac{T}{4}\right)\right] \end{aligned} \right\} \quad (C.3)$$

where  $T=2\tau_s=4\pi/N_s$ ,  $k=(1-w_{so}/\tau_s)$ ,  $F$  is related to the remanence ( $B_r$ ), height ( $h_m$ ), and relative permeability ( $\mu_r$ ) of the PM material, and  $F=B_r h_m / \mu_r \mu_0$ .

Comparing  $F_i$  between (3.3) and (3.3), it can be seen that the PM polarities of adjacent teeth significantly affects the PM MMF distribution.

In terms of the relative air-gap permeance  $\Lambda_r(\theta, t)$ , it is

$$\Lambda_r(\theta, t) = \sum_{q=0,1,2,\dots}^{\infty} \Lambda_q \cos[qN_r(\theta - \theta_0 - \Omega_r t)] \quad (C.4)$$

and the Fourier coefficients are totally the same as FRPM machines with opposite PM polarities of adjacent teeth, which can be found in (3.4)-(3.8).

Therefore, the no-load air-gap flux density can be expressed as

$$B(\theta, t) = \Lambda_0 \sum_{i=1,2,3,\dots}^{\infty} F_i \sin(i \frac{N_s}{2} \theta) + \sum_{i=1,2,3,\dots}^{\infty} \sum_{q=1,2,3,\dots}^{\infty} \frac{1}{2} F_i \Lambda_q \sin[(i \frac{N_s}{2} \pm q N_r) \theta \mp q N_r (\theta_0 + \Omega_r t)] \quad (C.5)$$

From (C.1)-(3.9), it can be observed that abundant air-gap flux density harmonics exist due to the rotor tooth modulation and the magnitudes of these harmonics highly depend on  $npp$ .

The magnetic field energy as well as the co-energy can be expressed as

$$\begin{aligned} W_c(t) &= \int \frac{1}{2\mu_0} B(\theta, t)^2 dV = \int \frac{1}{2\mu_0} F_{PM}(\theta)^2 \Lambda_r(\theta, t)^2 dV \\ &= \frac{l(R_{si}^2 - R_{ro}^2)}{2\mu_0} \int_0^{2\pi} F_{PM}(\theta)^2 \Lambda_r(\theta, t)^2 d\theta \\ &= \frac{\pi l(R_{si}^2 - R_{ro}^2)}{4\mu_0} \sum_{\frac{nN_r}{N_s}} F_{\frac{nN_r}{N_s}}' \Lambda_n' \cos[nN_r(\theta_0 + \Omega_r t)] \end{aligned} \quad (C.6)$$

where  $l$  is axial length of the machine,  $R_{ro}$  is the outer radius of rotor,  $F'$  is the Fourier coefficient of  $F_{PM}(\theta)^2$ ,  $\Lambda'$  is the Fourier coefficient of  $\Lambda_r(\theta, t)^2$ , and  $n$  is the integer which makes  $(nN_r/N_s)$  an integer as well.

Then the cogging torque can be deduced as

$$T_c(t) = -\frac{\partial W_c}{\partial \alpha} = -\frac{\partial W_c}{\partial(\Omega_r t)} \frac{nN_r \pi l (R_{si}^2 - R_{ro}^2)}{4\mu_0} \sum_{\frac{nN_r}{N_s}} F_{\frac{nN_r}{N_s}}' \Lambda_n' \sin[nN_r(\theta_0 + \Omega_r t)] \quad (C.7)$$

The fundamental period of the cogging torque,  $N_c$ , is equal to the minimum  $n$ , and can be expressed as

$$N_c = n_{\min} = \frac{N_s}{\text{GCD}(N_r, N_s)} \quad (C.8)$$

From (3.13), it can be found that  $N_c$  is only related to  $N_s$  and the greatest common divisor (GCD) between  $N_r$  and  $N_s$  and is irrelevant to  $npp$ . This is because that the waveforms of  $F_{PM}(\theta)^2$  are exactly the same regardless of  $npp$ , as can be imagined from the waveform of  $F_{PM}(\theta)$  shown in Fig. 3.3. In comparison with the FRPM machines with opposite PM polarities of adjacent teeth, the cogging torque of the FRPM machines with identical PM polarities of adjacent teeth is exactly the same since the waveform of  $F_{PM}(\theta)^2$  are all the same.

As shown in Fig. 3.2, by integrating the air-gap flux density under the stator tooth, the flux through Coil A can be written as

$$\begin{aligned}\lambda_A(t) &= n_c \int B(\theta, t) ds = n_c l R_{si} \int_{-k\pi/N_s}^{k\pi/N_s} B(\theta, t) d\theta \\ &= \sum_{i=1,2,3,\dots}^{\infty} \sum_{q=1,2,3,\dots}^{\infty} \frac{2n_c l R_{si} F_i \Lambda_q}{(iN_s \pm 2qN_r)} \sin \left[ \left( \frac{iN_s \pm 2qN_r}{2N_s} \right) k\pi \right] \sin [\mp qN_r(\theta_0 + \Omega_r t)]\end{aligned}\quad (C.9)$$

where  $n_c$  is the number of series-connected turns of Coil A.

Correspondingly, the back-EMF of Coil A can be obtained as

$$\begin{aligned}e_A(t) &= -\frac{d\lambda_A(t)}{dt} = \sum_{i=1,2,3,\dots}^{\infty} \sum_{q=1,2,3,\dots}^{\infty} \frac{\pm 2n_c l R_{si} F_i \Lambda_q q N_r \Omega_r}{(iN_s \pm 2qN_r)} \\ &\quad \sin \left[ \left( \frac{iN_s \pm 2qN_r}{2N_s} \right) k\pi \right] \cos [qN_r(\theta_0 + \Omega_r t)]\end{aligned}\quad (C.10)$$

From (3.15), it can be seen that the air-gap flux density harmonics with the same  $q$  contribute to the back-EMF of the same frequency. Since  $\Lambda_1$  is much larger than the magnitudes of other permeance harmonics, the flux density harmonics with order being  $(iN_s/2 \pm N_r)$  are all possible to produce the fundamental back-EMF, of which the magnitude can be expressed as

$$E_A = \sum_{i=1,2,3,\dots}^{\infty} \frac{\pm 2n_c l R_{si} F_i \Lambda_1 N_r \Omega_r}{(iN_s \pm 2N_r)} \sin \left[ \left( \frac{iN_s \pm 2N_r}{2N_s} \right) k\pi \right] \quad (C.11)$$

Obviously, the back-EMF is greatly influenced by  $n_{pp}$  because the magnitudes of the air-gap flux density harmonics are related to  $n_{pp}$ , as can be seen from (3.3) and (3.9).

By injecting sinusoidal phase current ( $I_d=0$ ), the average torque of the machine can be derived as

$$T = \frac{3}{2} n_{coil} I_A E_A = \frac{3}{2} n_{ph} k_d I_A \sum_{i=1,2,3,\dots}^{\infty} \frac{\pm 2l R_{si} F_i \Lambda_1 N_r \Omega_r}{(iN_s \pm 2N_r)} \sin \left[ \left( \frac{iN_s \pm 2N_r}{2N_s} \right) k\pi \right] \quad (C.12)$$

where  $n_{coil}$  is the number of series-connected coils per phase,  $n_{ph}$  is the number of series-connected turns per phase,  $k_d$  is the distribution factor of the armature winding, and  $I_A$  is the peak value of the phase current.



# APPENDIX D

## PUBLICATIONS

### Journal Papers:

- [1] Z. Q. Zhu, **H. Y. Li**, R. Deodhar, A. Pride, and T. Sasaki, “Recent developments and comparative study of magnetically geared machines,” *CES Trans. Elect. Mach. Syst.*, vol. 2, no.1, pp. 13-22, Mar. 2018. (**Chapter 1**)
- [2] **H. Y. Li** and Z. Q. Zhu, “Influence of adjacent teeth magnet polarities on performance of flux reversal permanent magnet machine,” *IEEE Trans. Ind. Appl.*, vol. 55, no. 1, pp. 354–365, Jan./Feb. 2019. (**Chapter 2**)
- [3] **H. Y. Li** and Z. Q. Zhu, “Optimal number of magnet pieces of flux reversal permanent magnet machines,” *IEEE Trans. Energy Convers.*, early access, doi: 10.1109/TEC.2018.2866765. (**Chapter 3**)
- [4] **H. Y. Li** and Z. Q. Zhu, “Analysis of flux reversal permanent magnet machines with different consequent-pole PM topologies,” *IEEE Trans. Magn.*, vol. 54, no.11, Nov. 2018, Art. ID 8105305. (**Chapter 4**)
- [5] **H. Y. Li** and Z. Q. Zhu, “Investigation of stator slot and rotor pole combination of flux reversal permanent magnet machine with consequent-pole PM structure,” *IET J. Eng.*, in press. (**Chapter 4**)
- [6] **H. Y. Li**, Z. Q. Zhu, and H. Hua, “Comparative analysis of flux reversal permanent magnet machines with toroidal and concentrated windings,” *IEEE Trans. Ind. Electron.*, under review. (**Chapter 5**)
- [7] **H. Y. Li**, Y. Liu, and Z. Q. Zhu, “Comparative study of airgap field modulation in flux reversal and Vernier permanent magnet machines,” *IEEE Trans. Magn.*, vol. 54, no.11, Nov. 2018, Art. ID 8105206. (**Chapter 6**)
- [8] Y. Liu, **H. Y. Li**, and Z. Q. Zhu, “A high power factor Vernier machine with coil-pitch of two slot pitches,” *IEEE Trans. Magn.*, 2018, vol. 54, no.11, Nov. 2018, Art. ID 8105405.
- [9] Z. Q. Zhu, M. F. H. Khatab, **H. Y. Li**, and Y. Liu, “A novel axial flux magnetically geared machine for power split application,” *IEEE Trans. Ind. Appl.*, vol. 54, no. 6, pp. 5954–5966, Nov. 2018.
- [10] H. Yang, Z. Q. Zhu, H. Lin, **H. Y. Li**, and S. Lyu, “Analysis of consequent-pole flux reversal permanent magnet machine with biased flux modulation theory,” *IEEE Trans. Ind. Electron.*, early access, doi: 10.1109/TIE.2019.2902816.
- [11] M. Zheng, Z. Q. Zhu, S. Cai, **H. Y. Li**, and Y. Liu, “Influence of magnetic saturation and rotor eccentricity on back-EMF of novel hybrid-excited stator slot opening permanent magnet machine,” *IEEE Trans. Magn.*, vol. 54, no.11, Nov. 2018, Art. ID 8105905.

- [12]M. Zheng, Z. Q. Zhu, S. Cai, **H. Y. Li**, and Y. Liu, “Influence of stator and rotor pole number combinations on the electromagnetic performance of stator slot-opening PM hybrid-excited machine,” *IEEE Trans. Magn.*, early access, doi: 10.1109/TMAG.2019.2903769.
- [13]M. F. H. Khatab, Z. Q. Zhu, **H. Y. Li**, and Y. Liu, “Comparative study of axial flux magnetically geared machine with conventional axial flux YASA machine,” *CES Trans. Elect. Mach. Syst.*, vol. 2, no. 4, pp. 392–398, Dec. 2018.
- [14]M. F. H. Khatab, Z. Q. Zhu, **H. Y. Li**, and Y. Liu, “Influence of static and dynamic rotor/stator misalignments in axial flux magnetically geared machine,” *IET J. Eng.*, in press.

#### Conference Papers:

- [15]**H. Y. Li** and Z. Q. Zhu, “Optimal flux modulation pole number in Vernier permanent magnet synchronous machines,” in *IEEE Energy Conv. Congress Expo. (ECCE 2018)*, Portland, OR, 2018, pp. 2343-2350.
- [16]**H. Y. Li** and Z. Q. Zhu, “Comparative study of airgap field modulation in flux reversal and Vernier permanent magnet machines,” in *IEEE Int. Magnetics. Conf. (INTERMAG 2018)*, Singapore, 2018.
- [17]**H. Y. Li** and Z. Q. Zhu, “Investigation of stator slot and rotor pole combination of flux reversal permanent magnet machine with consequent-pole PM structure,” in *IET Int. Conf. Power Electron. Mach. Drives (PEMD 2018)*, Liverpool, UK, 2018.
- [18]**H. Y. Li** and Z. Q. Zhu, “Analysis of flux reversal permanent magnet machines with different consequent-pole PM topologies,” in *IEEE Int. Magnetics. Conf. (INTERMAG 2018)*, Singapore, 2018.
- [19]**H. Y. Li** and Z. Q. Zhu, “Influence of magnet arrangement on performance of flux reversal permanent magnet machine,” in *IEEE Int. Elect. Mach. Drives. Conf. (IEMDC 2017)*, Miami, FL, 2017.
- [20]M. F. H. Khatab, Z. Q. Zhu, **H. Y. Li**, and Y. Liu, “Optimal design of a novel axial flux magnetically geared PM machine,” *Int. Conf. Ecological Veh. Renewable Energies (EVER 2017)*, Monte Carlo, Monaco, 2017.
- [21]Z. Q. Zhu, H. Yang, S. Cai, **H. Y. Li**, Y. Liu, J. Mipo, and S. Personnaz, “Hybrid excited stator slot PM machines with overlapping windings,” *Int. Conf. Elect. Mach. (ICEM 2018)*, Alexandroupoli, Greece, 2018, pp. 2185-2191.
- [22]H. Yang, Z. Q. Zhu, S. Cai, **H. Y. Li**, Y. Liu, J. Mipo, and S. Personnaz, “Performance comparison of stator slot PM machines with non-overlapping and overlapping windings,” *Int. Conf. Elect. Mach. (ICEM 2018)*, Alexandroupoli, Greece, 2018, pp. 2283-2289.
- [23]H. Yang, Z. Q. Zhu, Y. Liu, **H. Y. Li**, and J. Mipo, “Comparative study of doubly salient machines with/without stator slot permanent magnets,” in *IEEE Int. Elect. Mach. Drives. Conf. (IEMDC 2017)*, Miami, FL, 2017.